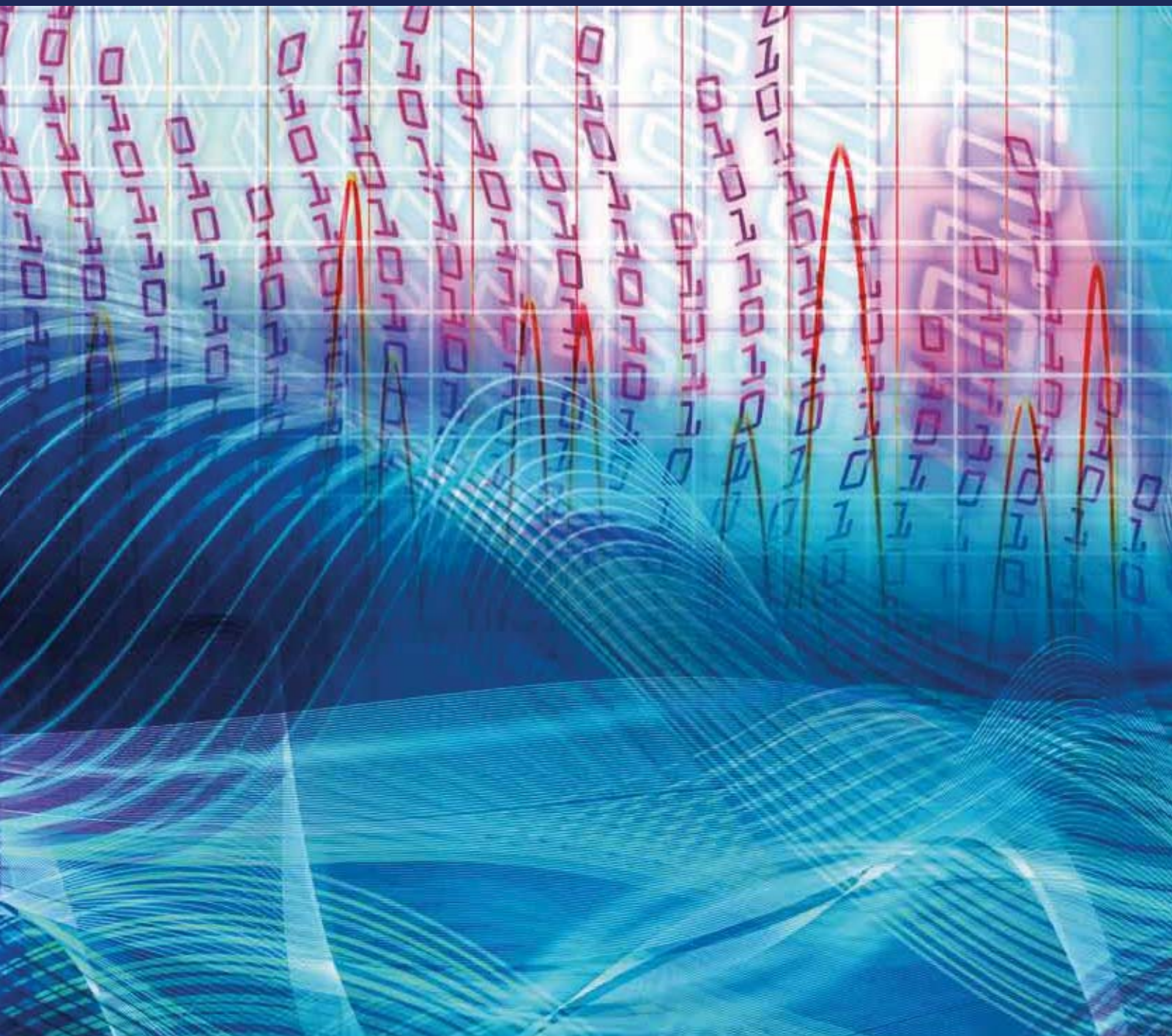


# Image Processing and Analysis in Biomechanics

Guest Editors: João Manuel R. S. Tavares and R. M. Natal Jorge





---

# **Image Processing and Analysis in Biomechanics**

## **Image Processing and Analysis in Biomechanics**

Guest Editors: João Manuel R. S. Tavares and  
R. M. Natal Jorge



---

Copyright © 2010 Hindawi Publishing Corporation. All rights reserved.

This is a special issue published in volume 2010 of "EURASIP Journal on Advances in Signal Processing." All articles are open access articles distributed under the Creative Commons Attribution License, which permits unrestricted use, distribution, and reproduction in any medium, provided the original work is properly cited.

## **Editor-in-Chief**

Phillip Regalia, Institut National des Télécommunications, France

## **Associate Editors**

Adel M. Alimi, Tunisia  
Kenneth Barner, USA  
Yasar Becerikli, Turkey  
Kostas Berberidis, Greece  
Jose Carlos Bermudez, Brazil  
Enrico Capobianco, Italy  
A. Enis Cetin, Turkey  
Jonathon Chambers, UK  
Mei-Juan Chen, Taiwan  
Liang-Gee Chen, Taiwan  
Huaiyu Dai, USA  
Satya Dharamipragada, USA  
Kutluayil Dogancay, Australia  
Florent Dupont, France  
Frank Ehlers, Italy  
Sharon Gannot, Israel  
M. Greco, Italy  
Irene Y. H. Gu, Sweden  
Fredrik Gustafsson, Sweden  
Ulrich Heute, Germany  
Sangjin Hong, USA  
Jiri Jan, Czech Republic  
Magnus Jansson, Sweden  
Sudharman K. Jayaweera, USA

Soren Holdt Jensen, Denmark  
Mark Kahrs, USA  
Moon Gi Kang, South Korea  
Walter Kellermann, Germany  
Lisimachos P. Kondi, Greece  
Alex Chichung Kot, Singapore  
C.-C. Jay Kuo, USA  
Ercan E. Kuruoglu, Italy  
Tan Lee, China  
Geert Leus, The Netherlands  
T.-H. Li, USA  
Husheng Li, USA  
Mark Liao, Taiwan  
Y.-P. Lin, Taiwan  
Shoji Makino, Japan  
Stephen Marshall, UK  
C. Mecklenbräuker, Austria  
Gloria Menegaz, Italy  
Ricardo Merched, Brazil  
Marc Moonen, Belgium  
Vitor Heloiz Nascimento, Brazil  
Christophoros Nikou, Greece  
Sven Nordholm, Australia  
Patrick Oonincx, The Netherlands

Douglas O'Shaughnessy, Canada  
Björn Ottersten, Sweden  
Jacques Palicot, France  
Ana Perez-Neira, Spain  
Wilfried R. Philips, Belgium  
Aggelos Pikrakis, Greece  
Ioannis Psaromiligkos, Canada  
Athanasios Rontogiannis, Greece  
Gregor Rozinaj, Slovakia  
Markus Rupp, Austria  
William Allan Sandham, UK  
Bulent Sankur, Turkey  
Ling Shao, UK  
Dirk Slock, France  
Y.-P. Tan, Singapore  
João Manuel R. S. Tavares, Portugal  
George S. Tombras, Greece  
Dimitrios Tzovaras, Greece  
Bernhard Wess, Austria  
Jar-Ferr Yang, Taiwan  
Azzedine Zerguine, Saudi Arabia  
Abdelhak M. Zoubir, Germany

## Contents

**Image Processing and Analysis in Biomechanics**, João Manuel R. S. Tavares and R. M. Natal Jorge  
Volume 2010, Article ID 287929, 1 page

**Colour Image Segmentation Using Homogeneity Method and Data Fusion Techniques**,  
Salim Ben Chaabane, Mounir Sayadi, Farhat Fnaiech, and Eric Brassart  
Volume 2010, Article ID 367297, 11 pages

**2D-3D Registration of CT Vertebra Volume to Fluoroscopy Projection: A Calibration Model Assessment**,  
P. Bifulco, M. Cesarelli, R. Allen, M. Romano, A. Fratini, and G. Pasquariello  
Volume 2010, Article ID 806094, 8 pages

**Three-Dimensional Morphometry of Single Endothelial Cells with Substrate Stretching and Image-Based Finite Element Modeling**, Hiroshi Yamada, Norihide Mouri, and Shinji Nobuhara  
Volume 2010, Article ID 616091, 10 pages

**Computer Aided Modeling of Human Mastoid Cavity Biomechanics Using Finite Element Analysis**,  
Chia-Fone Lee, Peir-Rong Chen, Wen-Jeng Lee, Yuan-Fang Chou, Jyh-Horng Chen, and Tien-Chen Liu  
Volume 2010, Article ID 203037, 9 pages

**Recovery of Myocardial Kinematic Function without the Time History of External Loads**, Heye Zhang,  
Bo Li, Alistair A. Young, and Peter J. Hunter  
Volume 2010, Article ID 310473, 9 pages

**In Vivo Measurement of Glenohumeral Joint Contact Patterns**, Michael J. Bey, Stephanie K. Kline,  
Roger Zuel, Patricia A. Kolowich, and Terrence R. Lock  
Volume 2010, Article ID 162136, 6 pages

**Adding Image Constraints to Inverse Kinematics for Human Motion Capture**, Antoni Jaume-i-Capó,  
Javier Varona, Manuel González-Hidalgo, and Francisco J. Perales  
Volume 2010, Article ID 142354, 13 pages

**Segmentation, Reconstruction, and Analysis of Blood Thrombus Formation in 3D 2-Photon Microscopy Images**, Jian Mu, Xiaomin Liu, Małgorzata M. Kamocka, Zhiliang Xu, Mark S. Alber, Elliot D. Rosen,  
and Danny Z. Chen  
Volume 2010, Article ID 147216, 8 pages

**Evaluation of a Validation Method for MR Imaging-Based Motion Tracking Using Image Simulation**,  
Kevin M. Moerman, Christian M. Kerskens, Caitríona Lally, Vittoria Flamini, and Ciaran K. Simms  
Volume 2010, Article ID 942131, 11 pages

**Optical Flow Active Contours with Primitive Shape Priors for Echocardiography**, Ali K. Hamou and  
Mahmoud R. El-Sakka  
Volume 2010, Article ID 836753, 10 pages

**A New Method to Calibrate Attachment Angles of Data Loggers in Swimming Sharks**, Shizuka Kawatsu,  
Katsufumi Sato, Yuuki Watanabe, Susumu Hyodo, Jason P. Breves, Bradley K. Fox, E. Gordon Grau,  
and Nobuyuki Miyazaki  
Volume 2010, Article ID 732586, 6 pages

**Analysis and Modelling of Muscles Motion during Whole Body Vibration**, M. Cesarelli, A. Fratini, P. Bifulco, A. La Gatta, M. Romano, and G. Pasquariello  
Volume 2010, Article ID 972353, 9 pages

**Nonlinear Synchronization for Automatic Learning of 3D Pose Variability in Human Motion Sequences**, M. Mozerov, I. Rius, X. Roca, and J. González  
Volume 2010, Article ID 507247, 10 pages

**Determination of Three-Dimensional Left Ventricle Motion to Analyze Ventricular Dyssynchrony in SPECT Images**, Marina de Sá Rebelo, Ann Kirstine Hummelgaard Aarre, Karen-Louise Clemmesen, Simone Cristina Soares Brandão, Maria Clementina Giorgi, José Cláudio Meneghetti, and Marco Antonio Gutierrez  
Volume 2010, Article ID 290695, 9 pages

**3D Elbow Kinematics with Monoplanar Fluoroscopy: *In Silico* Evaluation**, L. Tersi, S. Fantozzi, and R. Stagni  
Volume 2010, Article ID 142989, 10 pages

**Efficient and Low-Cost 3D Structured Light System Based on a Modified Number-Theoretic Approach**, Tomislav Pribanić, Hrvoje Džapo, and Joaquim Salvi  
Volume 2010, Article ID 474389, 11 pages

**Toward the Development of Virtual Surgical Tools to Aid Orthopaedic FE Analyses**, Srinivas C. Tadepalli, Kiran H. Shivanna, Vincent A. Magnotta, Nicole A. Kallemeyn, and Nicole M. Grosland  
Volume 2010, Article ID 190293, 7 pages

**Soft Tissue Structure Modelling for Use in Orthopaedic Applications and Musculoskeletal Biomechanics**, E. A. Audenaert, P. Mahieu, T. van Hoof, and C. Pattyn  
Volume 2010, Article ID 389356, 9 pages

**Imaging Arterial Fibres Using Diffusion Tensor Imaging—Feasibility Study and Preliminary Results**, Vittoria Flamini, Christian Kerskens, Kevin M. Moerman, Ciaran K. Simms, and Caitríona Lally  
Volume 2010, Article ID 904091, 13 pages

## *Editorial*

# **Image Processing and Analysis in Biomechanics**

**João Manuel R. S. Tavares and R. M. Natal Jorge**

*Faculty of Engineering, University of Porto, Rua Dr. Roberto Frias, s/n 4200-465 Porto, Portugal*

Correspondence should be addressed to João Manuel R. S. Tavares, tavares@fe.up.pt

Received 16 December 2009; Accepted 16 December 2009

Copyright © 2010 J. M. R. S. Tavares and R. M. Natal Jorge. This is an open access article distributed under the Creative Commons Attribution License, which permits unrestricted use, distribution, and reproduction in any medium, provided the original work is properly cited.

Computational methodologies of signal processing and analysis based on 1D-4D data are commonly used in different applications. In particular, image processing and analysis methodologies have enjoyed increasing deployment in automated recognition, human-machine interfaces, computer-aided diagnostics, robotic surgery, and many other areas; however, in the last years their application in Biomechanics has gained special attention.

This issue of the EURASIP Journal on Advances in Signal Processing constitutes the special issue related with Image Processing and Analysis applied to biomechanical systems, including data compression, data fusion, image segmentation, image registration, objects recognition, objects modeling, tracking and motion analysis, shape reconstruction, 3D vision, and virtual reality. One important feature to retainment of this special issue is the interdisciplinary of works resulting from the collaboration between mechanical engineers, electrical engineers, biomedical engineers, medical doctors, computational engineers, biologists, physicians, mathematicians, among others.

The success of this special issue is directed and associated with the high significance on analysis and simulation of biomechanical structures from images and their challenging problems, regarding geometric modeling, numerical modeling, material models and experimental methodologies, as well as their real application and validation. This great interest has been revealed by users, students, researchers, and all who are interested on areas related with signal processing, image processing and analysis, medical imaging, computational and experimental biomechanics, enhanced computation, and software applications.

For this special issue, 31 works were submitted from 18 countries: Belgium, Brazil, Canada, China, Croatia, Czech Republic, France, India, Iran, Ireland, Italy, Japan, Morocco,

New Zealand, Spain, Taiwan, Tunisia, and USA. After the review done by 55 international experts, 19 works were accepted for publication.

The guest editors would like to express their deep gratitude to the Editor-in-Chief and Associate Editors of EURASIP Journal on Advances in Signal Processing for this opportunity, to all authors that shared their excellent works with us and to all members of the Scientific Committee of this special issue that help us in the review process.

*João Manuel R. S. Tavares  
R. M. Natal Jorge*

## Research Article

# Colour Image Segmentation Using Homogeneity Method and Data Fusion Techniques

Salim Ben Chaabane,<sup>1</sup> Mounir Sayadi,<sup>1,2</sup> Farhat Fnaiech,<sup>1,2</sup> and Eric Brassart<sup>2</sup>

<sup>1</sup>SICISI Unit, High school of sciences and techniques of Tunis (ESSTT), 5 Av. Taha Hussein, 1008 Tunis, Tunisia

<sup>2</sup>Laboratory for Innovation Technologies (LTI-UPRES EA3899), Electrical Power Engineering Group (EESA), University of Picardie Jules Verne, 7, rue du Moulin Neuf, 80000 Amiens, France

Correspondence should be addressed to Salim Ben Chaabane, ben\_chaabane\_salim@yahoo.fr

Received 17 December 2008; Revised 25 March 2009; Accepted 11 May 2009

Recommended by João Manuel R. S. Tavares

A novel method of colour image segmentation based on fuzzy homogeneity and data fusion techniques is presented. The general idea of mass function estimation in the Dempster-Shafer evidence theory of the histogram is extended to the homogeneity domain. The fuzzy homogeneity vector is used to determine the fuzzy region in each primitive colour, whereas, the evidence theory is employed to merge different data sources in order to increase the quality of the information and to obtain an optimal segmented image. Segmentation results from the proposed method are validated and the classification accuracy for the test data available is evaluated, and then a comparative study versus existing techniques is presented. The experimental results demonstrate the superiority of introducing the fuzzy homogeneity method in evidence theory for image segmentation.

Copyright © 2010 Salim Ben Chaabane et al. This is an open access article distributed under the Creative Commons Attribution License, which permits unrestricted use, distribution, and reproduction in any medium, provided the original work is properly cited.

## 1. Introduction

Image segmentation is considered as an important basic operation for meaningful analysis and interpretation of acquired images [1, 2]. In this framework, colour image segmentation has wide applications in many areas [3, 4], and many different techniques have been developed.

Most published results of colour image segmentation are based on gray level image segmentation methods with different colour representations. Most gray level image segmentation techniques such as histogram thresholding, clustering, region growing, edge detection, fuzzy methods, and neural networks can be extended to colour images. Gray level segmentation methods can be applied directly to each component of a colour space, and then the results can be combined in some way to obtain a final segmentation result.

In the Red, Green, Blue (RGB) representation, the colour of each pixel is usually represented on the basis of the three primary colours (red, green, and blue), but it can be coded in other representation systems which are grouped together according to their different properties. RGB is suitable for colour display, but inappropriate for colour scene

segmentation and analysis because of the high correlation among the R, G, and B components [5]. In this context, image segmentation using data fusion techniques appears to be an interesting method.

Data fusion is a technique which simultaneously takes into account heterogeneous data coming from different sources, in order to obtain an optimal set of objects for investigation. Of the existing data fusion methods such as probability theory [6], fuzzy logic [7–9], possibility theory [10], evidence theory [11, 12], the Dempster-Shafer (DS) evidence theory [13], is a powerful and flexible mathematical tool for handling uncertain, imprecise, and incomplete information. In the case of evidence theory, the determination of mass function is a crucial step of fusion process.

In the past, many authors have addressed this problem using different methods [14–17], and several researchers have, in particular, investigated the relationship between fuzzy sets and Dempster-Shafer evidence theory. Most of the literature using fuzzy sets has been focused on automatically determining the mass function in the DS evidence theory [17, 18]. Recently, most analytic fuzzy methods have been

derived from Bezdek's Fuzzy C-Means (FCM) [19, 20]. However, this algorithm has a considerable drawback in noisy environments, and the degrees of membership resulting from FCM do not correspond to the intuitive concept of belonging or compatibility. Also, the Hard C-Means (HCM) [21] is one of the oldest clustering methods in which HCM memberships are hard (i.e., 1 or 0). This method is used to learn the prototypes of clusters or classes, and the cluster centers are used as prototypes.

In this context, Gautier et al. [22] aim at providing a help to the doctor for the follow-up of the diseases of the spinal column. The objective is to rebuild each vertebral lumbar rachis starting from a series of cross-sections. From an initial segmentation obtained by using the Snakes, active contour models, one seeks a segmentation which represents as well as possible the anatomical contour of the vertebra, in order to give the doctors a schema of the points really forming part of the vertebra. The methodology is based on the application of the belief theory to fusion information. However, the active contour models do not require image preprocessing and provide a closed contour of the object, however typical problems remain difficult to solve including the initialization of the model.

With the same objective, Zimmermann and Zysno [14], have shown through empirical studies that the good Model for Membership Functions is based on the Distance of a point from a prototypical member (MMFD). However, one of the major factors that influences the determination of appropriate groups of points is the "distance measure" chosen for the problem at hand. Also, Zhu et al. [17], and Ben Chaabane et al. [23] have proposed a method of automatically determining the mass function for image segmentation problems. The idea is to assign, at each image pixel level, a mass function that corresponds to a membership function in fuzzy logic. The degrees of membership of each pixel are determined by applying fuzzy c-means (FCM) clustering to the gray levels of the image.

In another study, Vannoorenberghe et al. [16] and Ben Chaabane et al. [24] have proposed an information model obtained from training sets extracted from the pixel intensity of the image. In their papers, the authors described the estimation of the Model Mass Function method based on the Assumption of Gaussian Distribution (MMFAGD) and histogram thresholding and applied on synthetic and biomedical images that contain only two classes. However, the differences between the various works cited above occur in the method of mass functions estimation, and in the application.

In this paper an investigation of how the user can choose the best a priori knowledge for determining the mass function in Dempster-Shafer evidence theory is described. We shall assume a Gaussian distribution for estimating the mass function. So, this work may be seen to be straightforwardly complementary to that in the paper proposed by Vannoorenberghe et al. [16] and Ben Chaabane et al. [24]. In their paper, the authors suggested that the user has to search for a suitable method for determining the a priori knowledge. Hence, this paper is devoted to this task, applied

to colour image segmentation that contains more than two classes. The idea is based on the histogram thresholding of the homogeneity and data fusion techniques. The concept of the histogram of the homogeneity was discussed in [25], which is used to express the local and global information among pixels in an image. Histogram analysis is applied to find all major homogeneous regions in the three primitive colours. The assumption of a Gaussian distribution is used to calculate the mass function of each pixel. Once the mass functions are determined for each primitive colour to be fused, the DS combination rule and decision are applied to obtain the final segmentation.

Section 2 introduces the proposed method for colour image segmentation. The experimental results are discussed in Section 3, and the conclusion is given in Section 4.

## 2. Proposed Method

For colour images with RGB representation, the colour of a pixel is a mixture of the three primitive colours red, green, and blue. RGB is suitable for colour display, but not good for colour scene segmentation and analysis because of the high correlation among the R, G, and B components [5, 26]. By high correlation, we mean that if the intensity changes, all the three components will change accordingly. In this context, colour image segmentation using evidence theory appears to be an interesting method. However, to fuse different images using DS theory, the appropriate determination of mass function plays a crucial role, since assignation of a pixel to a cluster is given directly by the estimated mass functions. In the present study, the method of generating the mass functions is based on the assumption of a Gaussian distribution. To do this, histogram analysis is applied simultaneously to both the homogeneity and the colour feature domains. These are used to extract homogeneous regions in each primitive colour. Once the mass functions are estimated, the DS combination rule is applied to obtain the final segmentation results.

**2.1. Homogeneity Histogram Analysis.** Histogram thresholding is one of the widely used techniques for monochrome image segmentation, but it is based on only gray levels and does not take into account the spatial information of pixels with respect to each other. A comprehensive survey of image thresholding methods is provided in [27]. Cheng et al. [25, 28, 29], proposed a fuzzy homogeneity method to overcome this limitation. In this paper, we employ the concept of the homogeneity histogram to extract homogeneous regions in each primitive colour.

Assume  $g_{xy}$  is the intensity of a pixel  $p_{xy}$  at the location  $(x, y)$  in an  $(M \times N)$  image,  $w_{xy}^{(1)}$  is a size  $(d \times d)$  window centered at  $(x, y)$  for the computation of variation,  $w_{xy}^{(2)}$  is a size  $(t \times t)$  window centered at  $(x, y)$  for the computation of discontinuity. Let us choose a  $5 \times 5$  window for computing the standard deviation of a pixel  $p_{xy}$ , and a  $3 \times 3$  window for computing the edge. However,  $w_{xy}^{(1)}$  and  $w_{xy}^{(2)}$  are the

local regions where the homogeneity features for pixel are calculated. By assuming, that the signals are ergodic, the standard deviation describes the contrast within a local region [30], and is calculated for a pixel  $p_{xy}$  as follows:

$$\nu_{xy} = \sqrt{\frac{1}{d^2} \sum_{p=x-(d-1)/2}^{x+(d-1)/2} \sum_{q=y-(d-1)/2}^{y+(d-1)/2} (g_{pq} - \mu_{xy})^2}, \quad (1)$$

where  $x \geq 2$ ,  $p \leq M - 1$ ,  $y \geq 2$ , and  $q \leq N - 1$ .

$\mu_{xy}$  is the mean of the gray levels within window  $w_{xy}$  and is defined by:

$$\mu_{xy} = \frac{1}{d^2} \sum_{p=x-(d+1)/2}^{x+(d-1)/2} \sum_{q=y-(d+1)/2}^{y+(d-1)/2} g_{pq}. \quad (2)$$

The discontinuity is a measure of abrupt changes in gray levels of pixels  $p_{xy}$ , that is, the discontinuity is described by its edge value, and could be obtained by applying edge detectors to the corresponding region. There are many different edge operators: Sobel, Canny, Derish, Laplace, and so forth, but their functions and performances are not the same. In spite of all the efforts, none of the proposed operators are fully satisfactory in real world cases. Applying different operators to a noisy image shows that, the second derivative operators exhibit better performance than classical operators, but require more computations because the image is first smoothed with a Gaussian function and then the gradient is computed [31]. Liu and Haralick [32] have evaluated the performance of edge detection algorithms.

Since it is not necessary to find the accurate locations of the edges, and due to its simplicity, the Sobel operator for calculating the discontinuity and the magnitude of the gradient at location  $(x, y)$  are used for their measurement [30]:

$$c_{xy} = \sqrt{G_{x'}^2 + G_{y'}^2}, \quad (3)$$

where  $G_{x'}$  and  $G_{y'}$  are the components of the gradient in the  $x'$  and  $y'$  directions, respectively.

The homogeneity is represented by:

$$h(g_{xy}, w_{xy}^{(1)}, w_{xy}^{(2)}) = 1 - E(g_{xy}, w_{xy}^{(2)}) \times V(g_{xy}, w_{xy}^{(1)}), \quad (4)$$

where

$$V(g_{xy}, w_{xy}^{(1)}) = \frac{\nu_{xy}}{\max\{\nu_{xy}\}}, \quad (5)$$

$$E(g_{xy}, w_{xy}^{(2)}) = \frac{c_{xy}}{\max\{c_{xy}\}},$$

$c_{xy}$  and  $\nu_{xy}$  are, respectively, the discontinuity and the standard deviation of a pixel  $p_{xy}$  at the location  $(x, y)$ ,  $2 \leq x \leq M - 1$  and  $2 \leq y \leq N - 1$ .

However, the size of the windows has an influence on the calculation of the value of the homogeneity. The window should be big enough to allow enough local information about the pixel to be involved in the computation of the

homogeneity. Furthermore, using a larger window in the computation of the homogeneity increases the smoothing effect, and makes the derivative operations less sensitive to noise [13]. However, smoothing the local area might hide some abrupt changes of the local region. Also, a large window causes significant processing time. In our case, the sizes of the windows are selected experimentally over 120 images. Weighting the pros and cons, experimentally, a  $5 \times 5$  window for computing the standard deviation of the pixel, and a  $3 \times 3$  window for computing the edge are chosen.

Once the homogeneity histogram has been determined, a typical segmentation method based on histogram analysis is applied to each primitive colour. Sezgin and Sankur [27] have examined and evaluated the quantitative performance of several thresholding techniques. Finally, a peak finding algorithm whose general form is reviewed as follows [25].

Input an  $M \times N$  image with gray levels zero to 255.

Suppose a homogeneity histogram of an image represented by a function  $h(i)$ , where  $i$  is an integer,  $0 \leq i \leq 255$  and the value of the homogeneity at each location of an image has a range from  $[0, 1]$ .

*Step 1.* Find the set of points  $p_i$  corresponding to the local maximums of the histogram.

The result forms a set  $P_0$ :

$$P_0 = \{(i), h(i) \mid h(i) > h(i-1), h(i) > h(i+1), 1 \leq i \leq 254\}. \quad (6)$$

*Step 2.* Find significant peaks in set  $P_0$ .

The result forms a set  $P_1$ :

$$P_1 = \{(p_i), h(p_i) \mid h(p_i) > h(p_{i-1}), h(p_i) > h(p_{i+1}), p_i \in P_0\}. \quad (7)$$

*Step 3.* Thresholding: includes three substeps.

- (i) Remove small peaks: for any peak  $j$ , if  $(h(j)/h(i_{\max})) < 0.05$ , then the peak  $j$  is removed, where  $i_{\max}$  is the value of the highest peak.
- (ii) Choose one peak among two peaks ( $p_1$  and  $p_2$ ) if they are too close to each other. If  $(p_2 - p_1) \leq 12$  then  $h = \max(h(p_1), h(p_2))$ .
- (iii) Remove a peak if the valley between two peaks is not significant.

*Comments.* The first substep below Step 2.1 related to the thresholding is used for removing the small peaks compared with the biggest. For any peak  $j$ , if  $(h(j)/h(i_{\max})) < 0.05$ , then peak  $j$  is removed. The threshold 0.05 is based on the experiments over more than 120 images. Since the value of the homogeneity at each location of an image has a range from  $[0, 1]$ ,  $h(i_{\max})$  is equal to 1. Therefore, the points with  $h(i_{\max}) < 0.05$  will be removed.

The second substep below Step 2.1 is to select one peak from two peaks close to each other. For two peaks  $h(p_1)$  and  $h(p_2)$ ,  $p_2 > p_1$ , if  $(p_2 - p_1) \leq 12$ , then  $h = \max(h(p_1), h(p_2))$ . Thus, the peak with the biggest value is chosen.

Finally, the third substep of Step 2.1 is applied for removing a peak if the valley between two peaks is not significant. The valley is not deep enough to separate the two peaks, if  $h_{\text{aver}_1}/h_{\text{aver}_2} > 0.75$ , where  $h_{\text{aver}_1}$  is the average value among the points between peaks  $p_1$  and  $p_2$  indicated by

$$h_{\text{aver}_1} = \frac{\sum_{p_i=p_1}^{p_i=p_2} h(p_i)}{p_2 - p_1 + 1}, \quad (8)$$

and  $h_{\text{aver}_2}$  is the average value for the two peaks defined by

$$h_{\text{aver}_2} = \frac{h(p_1) + h(p_2)}{2}. \quad (9)$$

The distance 12 between two peaks is selected experimentally over 120 images. It is a minimum threshold used to choose one of these two peaks. Also, the threshold 0.75 is based on the experiments over than 120 images.

**2.2. Use of DS Evidence Theory for Image Segmentation.** The purpose of segmentation is to partition the image into homogeneous regions. The idea of using DS evidence theory for image segmentation is to fuse one by one the pixels coming from the three images. The homogeneity method is applied to the three primitive colours. Then, the segmented results are combined using the Dempster-Shafer evidence theory to obtain the final segmentation results.

Dempster-Shafer Theory (DS) is a mathematical theory of evidence [11, 12]. This theory can be interpreted as a generalization of probability theory where probabilities are assigned to sets as opposed to mutually exclusive singletons. In traditional probability theory, evidence is associated with only one possible event.

In DS theory, evidence can be associated with multiple possible events, for example, sets of events. One of the most important features of Dempster-Shafer theory is that the model is designed to cope with varying levels of precision regarding the information.

In the present study, the clusters ( $C_i$ ) are generated by the homogeneity method from the frame of discernment  $\Omega$  composed of  $n$  single mutually exclusive subsets  $H_n$ , which are symbolized by

$$\Omega = \{H_1, H_2, \dots, H_n\} = \{C_i\}, \quad 1 \leq i \leq n. \quad (10)$$

In order to express a degree of confidence for each proposition  $A$  of  $2^\Omega$ , it is possible to associate an elementary mass function  $m(A)$  which indicates the degree of confidence that one can give to this proposition. Formally, this description of  $m$  can be represented with the following three equations:

$$\begin{aligned} m : 2^\Omega &\longrightarrow [0, 1], \\ m(\emptyset) &= 0, \\ \sum_{A_n \subseteq \Omega} m(A) &= 1. \end{aligned} \quad (11)$$

The quantity  $m(A)$  is interpreted as the belief strictly placed on  $A$ . This quantity differs from a probability by the totality of the total belief which is distributed not only on the simple

classes but also on the composed classes. This modelling shows the impossibility of dissociating several hypotheses. Hence, it is the principal advantage of this theory, but on the other hand, it represents the main difficulty of this method.

In the following, we give some useful definitions. In fact if  $m(A) > 0$  then  $A$  is called a focal element.

The union of all the focal elements of a mass function is called the core  $N$  of the mass function given by the following equation:

$$N = \{A \in 2^\Omega / m(A) > 0\}. \quad (12)$$

Credibility  $\text{Cr}(\cdot)$  and plausibility  $\text{Pl}(\cdot)$  functions are derived from the mass function. However, the *credibility* for a set  $H_n$  is defined as the sum of all the basic probability assignments of the proper subsets ( $A$ ) of the set of interest ( $H_n$ ) ( $A \subseteq H_n$ ), see (13). The value  $\text{Cr}(H_n)$  denotes the minimal degree of belief in the hypothesis  $H_n$ :

$$\text{Cr}(H_n) = \sum_{A \subseteq H_n} m(A). \quad (13)$$

The *Plausibility* is the sum of all the basic probability assignments of the sets ( $A$ ) that intersect the set of interest ( $H_n$ ) ( $A \cap H_n = \emptyset$ ), see (14). The value  $\text{Pl}(H_n)$  gives the maximal degree of belief in the hypothesis  $H_n$ :

$$\text{Pl}(H_n) = \sum_{A \cap H_n \neq \emptyset} m(A). \quad (14)$$

The Dempster rule of combination is critical to the original concept of Dempster-Shafer theory. Dempster's rule combines multiple belief functions through their basic probability assignments ( $m$ ). These belief functions are defined on the same frame of discernment, but are based on independent arguments or bodies of evidence. The combination rule results in a belief function based on conjunctive-pooled evidence.

The combination is performed by the orthogonal sum of Dempster, and is expressed for  $n$  sources as

$$\begin{aligned} \bigoplus_{i=1}^n m_i(H_n) \\ = \frac{1}{1-k} \sum_{A_1 \cap A_2 \cap \dots \cap A_n = H_n} m_1(A_1)m_2(A_2) \dots m_n(A_n), \end{aligned} \quad (15)$$

where  $H_n, A_1, \dots, A_n$  are subsets of  $\Omega$ , and

$$k = \sum_{A_1 \cap A_2 \cap \dots \cap A_n = \emptyset} m_1(A_1)m_2(A_2) \dots m_n(A_n). \quad (16)$$

Specifically, the combination (called the joint  $m_{12}$ ) is calculated from the aggregation of two mass functions  $m_1$  and  $m_2$  and given as follows:

$$\forall H_i \subseteq \Omega, \quad m_{12}(H_i) = \frac{1}{1-K} \sum_{A_1 \cap A_2 = H_i} m_1(A_1)m_2(A_2), \quad (17)$$

where  $K$  is defined by [11]:

$$K = \sum_{A_1 \cap A_2 = \emptyset} m_1(A_1)m_2(A_2), \quad (18)$$

$K$  represents the basic probability mass associated with conflict. This is determined by summing the products of mass functions of all sets where the intersection is an empty set.

This rule is commutative and associative. The denominator in Dempster's rule,  $(1 - K)$ , is a normalization factor, which evaluates the conflict between the two sources  $A_1$  and  $A_2$ .

The DS theory of evidence is a rich model of uncertainty handling as it allows the expression of partial belief [9].

**2.2.1. Mass Function of Simple Hypotheses.** Masses of simple hypotheses  $C_i$  are obtained from the assumption of Gaussian Distributions of the grey level  $g_{xy}$  to cluster  $i$  as follows:

$$m_q^{xy}(C_i) = \frac{1}{\sigma_i \sqrt{2\pi}} \exp \frac{-(g_{xy}^q - \mu_i)^2}{2\sigma_i^2}, \quad (19)$$

where  $g_{xy}^q$  is the intensity of a pixel  $p_{xy}$  at the location  $(x, y)$  for one of the three information sources ( $q = 1, 2, 3$ ). The values  $\mu_i = E(g_{xy}^q)$  and  $\sigma_i^2 = E(g_{xy}^q - E(g_{xy}^q))^2$  are, respectively, the mean and the variance on the class  $C_i$  present in each primitive colour (R, G, and B). E denoted the mathematical expectation.

**2.2.2. Mass Function of Double Hypotheses.** The mass function assigned to double hypotheses depends on the mass functions of each hypothesis.

In fact, if there is a high ambiguity in assigning a grey level  $g_{xy}$  to cluster  $r$  or  $s$ , that is,  $|m_q^{xy}(C_r) - m_q^{xy}(C_s)| < \varepsilon$ , where  $\varepsilon$  is the thresholding value, then a double hypotheses is formed. In the present study,  $\varepsilon$  was fixed at 0.1.

Once the double hypotheses (composed of two simple hypotheses) are formed, their joint mass is calculated according to the following formula:

$$m_q^{xy}(C_r \cup C_s) = \frac{1}{\sigma_{rs} \sqrt{2\pi}} \exp \frac{-(g_{xy}^q - \mu_{rs})^2}{2\sigma_{rs}^2}, \quad (20)$$

with  $\mu_{rs} = (\mu_r + \mu_s)/2$  and  $\sigma_{rs} = \max(\sigma_r, \sigma_s)$ .

In the case where the double hypotheses  $C_j$  are composed of more than two simple hypotheses, their joint mass is determined as follows:

$$m_q^{xy}(C_1 \cup C_2 \cup \dots \cup C_M) = \frac{1}{\sigma_j \sqrt{2\pi}} \exp \frac{-(g_{xy}^q - \mu_j)^2}{2\sigma_j^2}, \quad (21)$$

where  $\mu_j = (1/M) \sum_{i=1}^M \mu_i$ ,  $\sigma_j = \max(\sigma_1, \sigma_2, \dots, \sigma_M)$  and  $2 < M \leq N$ .

Once the mass functions of the three images are estimated, their combination is performed using the orthogonal sum that can be represented as follows:

$$m(C_i) = m_1(C_i) \oplus m_2(C_i) \oplus m_3(C_i) \quad (22)$$

with  $\oplus$  is the sum of DS orthogonal rule.

After calculating the orthogonal sum of the mass functions for the three images, the decisional procedure for classification purpose consists in choosing one of the most likely hypotheses  $C_i$ . The proposed method can be described by a flowchart given in Figure 1.

### 3. Experimental Results

In this section, several results of the simulations on the segmentation of medical and synthetic colour images (Figure 5), which illustrate the ideas presented in the previous section, are given.

In order to evaluate the performance of the proposed algorithm on the segmentation of colour cell images (which is a challenging problem in this field), the segmentation results of the datasets are reported. Consequently, a synthetic image dataset is developed and used for numerical evaluation purpose.

First the segmentation results in RGB colour space by applying the proposed method to red, green, and blue colour features, respectively, are presented. In this case, we find that the regions are recognized for example in red and green components but are not identified by the blue component. This shows the lack of information when using only one information source and may be explained by the high degree of correlation among of the three components of the RGB colour space.

The experimentation is carried out on a medical image provided by a cancer hospital Figure 2(a) and used as an original image. The results are shown in Figures 2(b), 2(c), and 2(d).

The problem of the incorrectly segmentation is also illustrated in Figure 2(b), the resulting image has four cells, while in Figures 2(c) and 2(d) the resulting image by using homogeneity histogram thresholding has only three and two cells, respectively.

Comparing the results, we can find that the cells are much better segmented in (b) than in (c) and (d). Also, the first resulting image contains some missing features in one of the cells, which do not exist in the other resulting images. This demonstrates the necessity of using the fusion process

Also let us compare the performance of our proposed algorithm to those in other published reports that have recently been applied to colour images. These include Zimmermann and Zysno [14], Vannoorenberghe et al. [16], Ben Chaabane et al. [24], Zhu et al. [17], and Ben Chaabane et al. [23].

The segmentation results are shown in Figures 3, 4, 6, and 7.

Firstly let us present a colour image that contains two classes. To highlight its performance let us compare it with the MMFD [14] and MMFAGD [24] algorithms.

Secondly let us work on more realistic images containing multiple classes and compare the performance of our method with other methods that use FCM [23], and HCM [21] algorithms as tools for the estimation of mass functions in the Dempster-Shafer evidence theory. Figures 3, 4, 6, and 7 show the obtained results of the proposed method.

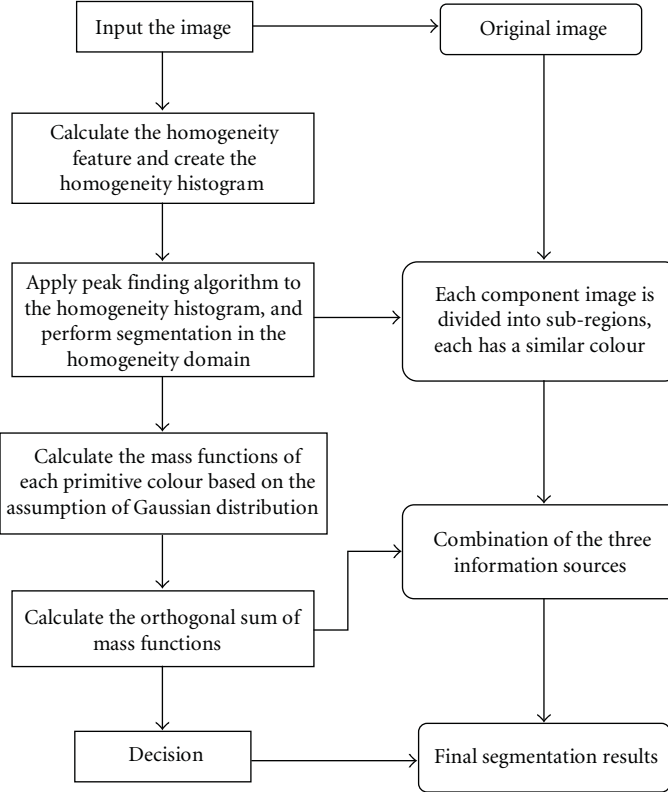


FIGURE 1: Flowchart of the proposed method.

The original images are artificial, that is, generated with a user defined classification, and are stored in RGB format. Each of the primitive colours (red, green, and blue) takes 8 bits and has an intensity range from 0 to 255.

Figure 3 shows a comparison of the results between the traditional methods MMFD [14], MMFADG [24], and the proposed method. However, the image shown in Figure 3(b) represents the original image  $I$  where a “Salt and pepper” noise of  $D$  density was added. This affects approximately  $(D \times (N \times M))$  pixels. The value of  $D$  is 0.02.

The final images using the MMFD and MMFAGD algorithms and the homogeneity for the determination of mass functions in DS theory are shown in Figures 3(c), 3(d), and 3(e), respectively.

Comparing Figures 3(c), 3(d), and 3(e), one can find that the cell is much better segmented in (e) than those in (c) and (d), also the first and the second images contain some holes in the cell and some pixels were incorrectly segmented. These do not exist in the correctly segmented image, but after the redefining process, only a few singularity points are left in the final image as shown in Figure 3(e).

Accordingly, the dark blue colour of the cell is identified by the proposed method (Figure 3(e)), but is not seen in other traditional methods (Figures 3(c) and 3(d)).

It can be seen from Table 1 that 31.77%, 20.44%, and 2.73% of pixels were incorrectly segmented in Figures 3(c), 3(d), and 3(e), respectively. However, the two regions are correctly segmented in Figure 3(e), using the complementary

information provided by the three primitive colours and consequently a good estimation of mass function by homogeneity, even in the presence of a noise (without the filtering step) is recorded.

In fact, the experimental results indicate that the proposed method, which uses both local and global information for mass function calculation in DS evidence theory, is more accurate than the traditional methods in terms of segmentation quality as denoted by segmentation sensitivity, see Table 1.

In the method based on traditional histogram thresholding [16, 24] only global information is considered in the histogram analysis.

To provide insights into the proposed method, we have compared the performance of the proposed method with those of the corresponding Hard and Fuzzy C-Means algorithms. The method was also tested on synthetic images and compared with other existing methods, see Figure 4.

Figure 4 shows a synthetic input image that contains a multicomponent object with complicated boundaries and different component sizes. This figure consists of mainly six kinds of objects. After applying the HCM and FCM algorithms for the estimation of the mass function in DS evidence theory, followed by the data fusion techniques, the resulting image is divided into only four and five regions, respectively. But, using the proposed segmentation method, the resulting image is divided into six regions.

TABLE 1: Segmentation sensitivity from MMFD and DS, MMFAGD and DS and homogeneity method and DS for the data set shown in Figure 5.

	MMFD and DS	MMFAGD and DS	Homogeneity and DS (proposed method)
	Sensitivity segmentation (%)		
Image 1	66.84	72.94	94.23
Image 2	68.23	79.66	97.27
Image 3	72.56	83.19	90.84
Image 4	85.11	88.91	98.11
Image 5	75.42	76.86	96.85
Image 6	63.71	81.45	98.58
Image 7	83.54	93.88	98.36
Image 8	66.78	79.33	95.37
Image 9	75.84	77.85	99.85
Image 10	54.85	75.17	96.97
Image 11	62.74	74.43	81.13
Image 12	45.37	68.45	97.72

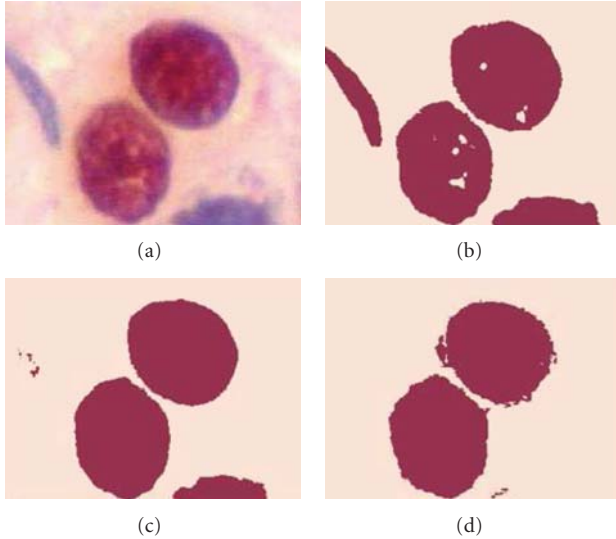


FIGURE 2: Segmentation results on a colour image. (a) Original image ( $256 \times 256 \times 3$ ) with gray level spread on the range  $[0, 255]$ . (b) Red resulting image by homogeneity histogram-based method. (c) Green resulting image by homogeneity histogram-based method. (d) Blue resulting image by homogeneity histogram-based method. The selected thresholds are 147, 110, and 194, respectively.

In brief, the experimental results conform to the visualized colour distribution in the objects. However, the new classes that appeared in Figure 6(d), tend to increase the size of some regions (yellow regions), and to shrink other regions (flowers), and some incorrectly segmented pixels are present in Figure 6(c), such as the extra blue contouring in the bottom centre flower.

The improved experimental results have been achieved by the proposed method based on the homogeneity histogram which can be used to generate a mass function that has a typical interpretation, that is, the resulting partition

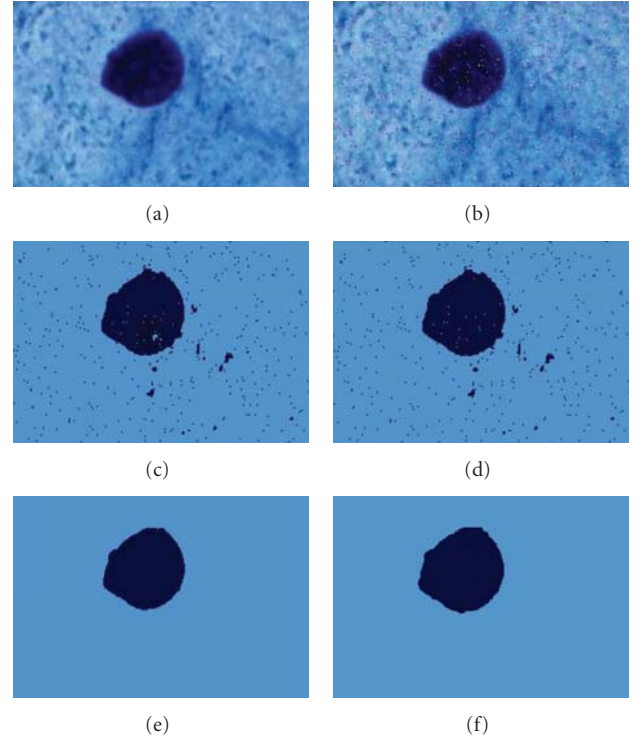


FIGURE 3: Comparison of the proposed segmentation method with other existing methods on a medical image (2 classes, 1 cell). (a) Original image with RGB representation ( $256 \times 256 \times 3$ ), (b) colour cell image disturbed with a “salt and pepper” noise, (c) segmentation based on MMFD and DS (d) segmentation based on MMFAGD and DS, (e) segmentation based on homogeneity and DS, and (f) reference segmented image.

of the data can be interpreted as the compatibilities of the points with the class prototypes, while the HCM and FCM methods use only the gray level to determine the degree of membership of each pixel.

TABLE 2: Segmentation sensitivity from HCM and DS, FCM and DS and homogeneity method and DS for the data set shown in Figure 5.

	HCM and DS	FCM and DS	Homogeneity and DS (proposed method)
	Sensitivity segmentation (%)		
Image 1	86.74	89.45	94.23
Image 2	61.82	88.92	97.27
Image 3	73.76	87.25	90.84
Image 4	89.21	96.68	98.11
Image 5	78.62	90.15	96.85
Image 6	72.33	87.78	98.58
Image 7	73.64	96.88	98.36
Image 8	61.48	88.79	95.37
Image 9	73.38	99.63	99.85
Image 10	64.42	79.58	96.97
Image 11	44.93	69.07	81.13
Image 12	56.87	67.31	97.72

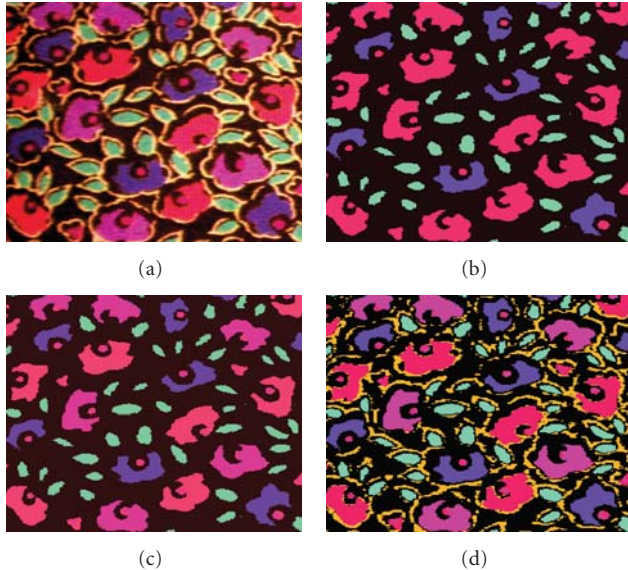


FIGURE 4: Comparison of the proposed segmentation method with other existing methods on a synthetic image (6 classes). (a) Original image ( $256 \times 256 \times 3$ ): colour synthetic image with RGB description, (b) segmentation based on HCM and DS, (c) segmentation based on FCM and DS, and (d) segmentation based on homogeneity and DS.

Comparing Figures 4(b), 4(c), and 4(d), one can see that the different objects of the image are much better segmented in (d) than those in (b) and (c).

Figures 6 and 7 show other comparison results on a complex medical image. The segmentation results are obtained using the HCM, the FCM and Homogeneity method.

They correspond, respectively, to Figures 6(b), 6(c), and 6(d) in Figure 6. The cells are exactly and homogeneously segmented in Figure 6(d), which is not the case of Figures 6(b) and 6(c).

To evaluate the performance of the proposed segmentation algorithm, its accuracy was recorded.

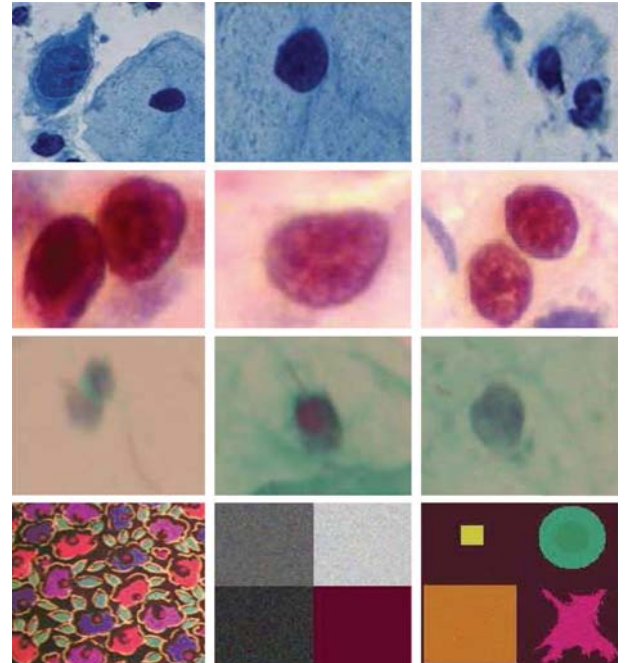


FIGURE 5: Data set used in the experiment. Twelve were selected for a comparison study. The patterns are numbered from 1 through 12, starting at the upper left-hand corner.

Regarding the accuracy, Tables 1 and 2 list the segmentation sensitivity of the different methods for the data set used in the experiment.

The segmentation sensitivity [33, 34] is determined as follows:

$$\text{Sens} = \frac{N_{\text{pcc}}}{N \times M} \times 100, \quad (23)$$

with Sens,  $N_{\text{pcc}}$ ,  $N \times M$  correspond, respectively, to the segmentation sensitivity (%), number of correctly classified pixels and dimension of the image. The acquisition of the correct classified pixels is not a manual process; hence

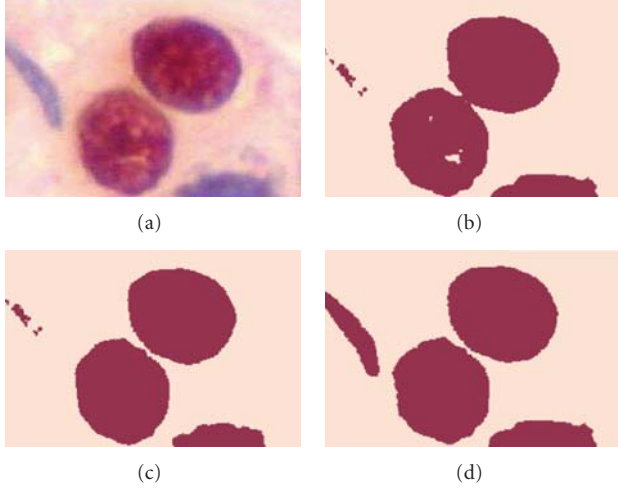


FIGURE 6: Comparison of the proposed segmentation method with other existing methods on a complex medical image (2 classes, various cells). (a) Original image ( $256 \times 256 \times 3$ ): colour medical image with RGB description, (b) segmentation based on HCM and DS, (c) segmentation based on FCM and DS, and (d) segmentation based on homogeneity and DS.

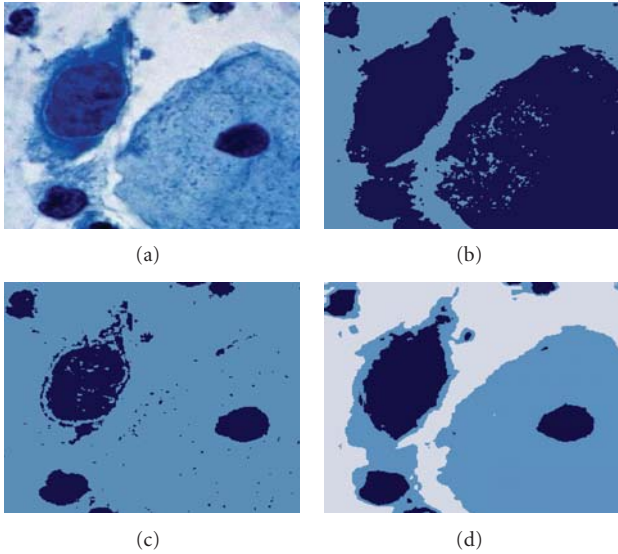


FIGURE 7: Comparison of the proposed segmentation method with other existing methods on a complex medical image (3 classes, various cells). (a) Original image ( $256 \times 256 \times 3$ ): colour cells image with RGB description, (b) segmentation based on HCM and DS, (c) segmentation based on FCM and DS, and (d) segmentation based on homogeneity and DS.

software based on a reference image is run. It consists of a small program which compares the labels of the obtained pixels and the reference pixels as shown in Figure 3(f). The correctly classified pixel denotes a pixel with a label equal to its corresponding pixel in the reference image. The labeling of the original image is generated by the user based on the image used for segmentation.

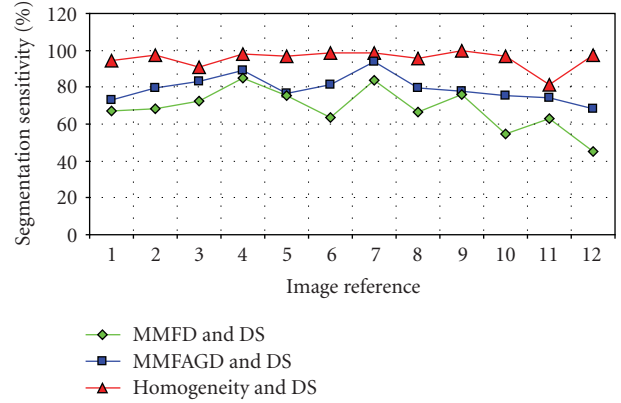


FIGURE 8: Segmentation sensitivity plots using MMFD and DS, MMFAGD and DS and homogeneity method and DS for the data set shown in Figure 5.

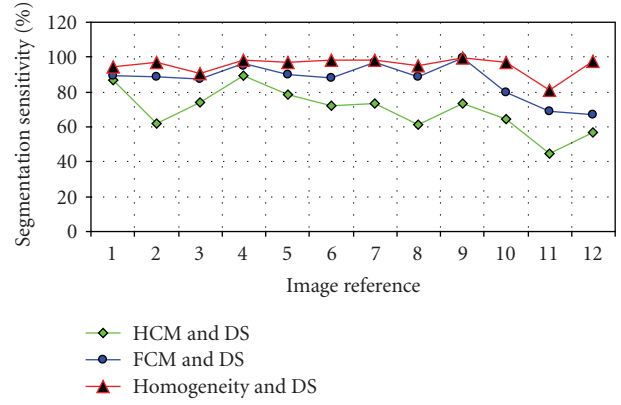


FIGURE 9: Segmentation sensitivity plots using HCM and DS, FCM and DS and homogeneity method and DS for the data set shown in Figure 5.

In fact, the experimental results presented in Figure 6(d) are quite consistent with the visualized colour distributions in the objects, which make it possible to do an accurate measurement of cell volumes.

Parts (b), (c), and (d) of Figure 7 show other segmentation results and were obtained using HCM, FCM algorithms, and the homogeneity method, as used for the DS mass determination.

In Figure 7(a), only three colours are needed to represent the colour image (dark blue, blue, and background). In Figures 7(b) and 7(c), the resulting image has only two colours. In Figure 7(d), the resulting image has three colours.

The partition resulting by the HCM is less accurate, and the partition resulting by FCM is not satisfactory either.

The performance of the homogeneity method is quite acceptable. In fact, one can observe in Figures 7(b) and 7(c) that 13.26% and 10.55% of pixels were incorrectly segmented for the HCM and FCM methods, respectively. However, this demonstrates that the mass functions resulting from the two algorithms, do not always correspond to the intuitive concept of degree of belonging or compatibility,

and the generated mass functions do not have a typical interpretation. Moreover, the HCM and FCM algorithms are unstable in noisy environments. However, errors were largely reduced when exploiting simultaneously the three images through the use of the DS fusion method including the homogeneity histogram.

Indeed, only 5.77% of pixels were incorrectly segmented in Figure 7(d). This good performance between these methods can also be easily assessed by visually comparing the segmentation results.

The segmentation sensitivity values reported in Tables 1 and 2 are plotted in Figures 8 and 9, respectively.

Figure 8 shows two segmentation sensitivity plots using traditional methods such as MMFD and MMFAGD compared with the proposed method plot.

Figure 9 shows two other segmentation sensitivity plots using automatic methods such as HCM and FCM compared with the proposed method plot.

As seen on both Figures 8 and 9, the proposed method plot is clearly located on the top of the other methods plots.

Referring to segmentation sensitivity plots given in Figure 9, one observes that 27.67%, 12.22%, and 1.42% of pixels were incorrectly segmented in Figures 6(b), 6(c), and 6(d), respectively. Comparing Figures 6(b) and 6(c) with Figure 6(d), the resulting image by the proposed method is much clearer than the one given by the HCM and FCM methods.

## 4. Conclusion

In this paper, we have proposed a new method for colour image segmentation based on homogeneity histogram thresholding and data fusion techniques. In the first phase, uniform regions are identified in each primitive colour via a thresholding operation on a newly defined homogeneity histogram. Then, the DS combination rule and decision are applied to fuse the three primitive colours.

The results obtained show the generic and robust character of the method in the sense that the local and global information were involved in the fusion process. On the other hand, in the estimation of mass function, we have used the local and global information. The results obtained demonstrated the significant improved performance in segmentation. The proposed method can be useful for colour image segmentation.

Nevertheless, there are some drawbacks to our proposed method. The used image models are mainly based on some a priori knowledge such as the mean and the standard deviation of each region of the image to be segmented. Also, in all our work, we have considered only one image for each application, whereas, many realizations of the same image fused together may be very helpful to the segmentation process. Furthermore, the research of other optimal models to estimate the mass functions in the Dempster-Shafer evidence theory and the fusion of imperfect information coming from different colour images are an important aspect of our present work. Also, the proposed method assumes that we have a reference image, which should be

labelled by the user for comparison purposes. In practice, this is not realisable; hence advanced intelligent software for classification based on the Kohonen Neural Network may be used in parallel with the proposed segmentation procedure to avoid the manually labelling of the image by the user.

## References

- [1] E. Navon, O. Miller, and A. Averbuch, "Color image segmentation based on adaptive local thresholds," *Image and Vision Computing*, vol. 23, no. 1, pp. 69–85, 2005.
- [2] S. Kasaei and M. Hasanzadeh, "Fuzzy image segmentation using membership connectedness," *EURASIP Journal on Advances in Signal Processing*, vol. 2008, Article ID 417293, 13 pages, 2008.
- [3] H. D. Cheng, X. H. Jiang, Y. Sun, and J. Wang, "Color image segmentation: advances and prospects," *Pattern Recognition*, vol. 34, no. 12, pp. 2259–2281, 2001.
- [4] R. Etienne-Cummings, P. Pouliquen, and M. A. Lewis, "A vision chip for color segmentation and pattern matching," *EURASIP Journal on Applied Signal Processing*, vol. 2003, no. 7, pp. 703–712, 2003.
- [5] X. Gao, K. Hong, P. Passmore, L. Podladchikova, and D. Shaposhnikov, "Colour vision model-based approach for segmentation of traffic signs," *EURASIP Journal on Image and Video Processing*, vol. 2008, Article ID 386705, 7 pages, 2008.
- [6] R. Bradley, "A unified Bayesian decision theory," *Theory and Decision*, vol. 63, no. 3, pp. 233–263, 2007.
- [7] I. Bloch and H. Maitre, "Fusion of image information under imprecision," in *Aggregation and Fusion of Imperfect Information*, B. Bouchon-Meunier, Ed., Series studies in fuzziness, Physical Verlag, pp. 189–213, Springer, 1997.
- [8] S.-L. Dong, J.-M. Wei, T. Xing, and H.-T. Liu, "Constraint-based fuzzy optimization data fusion for sensor network localization," in *Proceedings of the 2nd International Conference on Semantics Knowledge and Grid (SKG '06)*, p. 59, November 2006.
- [9] C. Lucas and B. N. Araabi, "Generalization of the Dempster-Shafer theory: a fuzzy-valued measure," *IEEE Transactions on Fuzzy Systems*, vol. 7, no. 3, pp. 255–270, 1999.
- [10] D. Dubois and H. Prade, "Possibility theory and its applications: a retrospective and prospective view," in *Proceedings of the IEEE International Conference on Fuzzy Systems*, vol. 1, pp. 5–11, May 2003.
- [11] A. P. Dempster, "Upper and lower probabilities induced by multivalued mapping," *Annals of Mathematical Statistics*, vol. 38, pp. 325–339, 1967.
- [12] G. Shafer, *A Mathematical Theory of Evidence*, Princeton University Press, 1976.
- [13] T. Denœux, "A k-nearest neighbor classification rule based on Dempster-Shafer theory," *IEEE Transactions on Systems, Man & Cybernetics*, vol. 25, no. 5, pp. 804–813, 1995.
- [14] H.-J. Zimmermann and P. Zysno, "Quantifying vagueness in decision models," *European Journal of Operational Research*, vol. 22, no. 2, pp. 148–158, 1985.
- [15] K. Raghu and J. M. Keller, "A possibilistic method to clustering," *IEEE Transactions on Fuzzy Systems*, vol. 1, no. 2, 1993.
- [16] P. Vannoorenberghe, O. Colot, and D. De Brucq, "Color image segmentation using Dempster-Shafer's theory," *IEEE International Conference on Image Processing (ICIP '99)*, vol. 4, pp. 300–304, October 1999.

- [17] Y. M. Zhu, L. Bentabet, O. Dupuis, V. Kaftandjian, D. Babot, and M. Rombaut, "Automatic determination of mass functions in Dempster-Shafer theory using fuzzy c-means and spatial neighborhood information for image segmentation," *Optical Engineering*, vol. 41, no. 4, pp. 760–770, 2002.
- [18] R. R. Yager, "Class of fuzzy measures generated from a Dempster-Shafer belief structure," *International Journal of Intelligent Systems*, vol. 14, no. 12, pp. 1239–1247, 1999.
- [19] J. C. Bezdek, *Pattern Recognition with Fuzzy Objective Function Algorithms*, Plenum Press, New York, NY, USA, 1981.
- [20] M. N. Ahmed, S. M. Yamany, N. Mohamed, A. A. Farag, and T. Moriarty, "A modified fuzzy C-means algorithm for bias field estimation and segmentation of MRI data," *IEEE Transactions on Medical Imaging*, vol. 21, no. 3, pp. 193–199, 2002.
- [21] R. Duda and P. Hart, *Pattern Classification and Scene Analysis*, John Wiley & Sons, New York, NY, USA, 1973.
- [22] L. Gautier, A. Taleb-Ahmed, M. Rombaut, J. G. Postaire, and H. Leclet, "Help to decision of segmentation of pictures by Dempster-Shafer theory: application to MRI sequence," *Editions Scientifiques et Médicales Elsevier SAS*, vol. 22, no. 6, pp. 378–392, 2001.
- [23] S. Ben Chaabane, M. Sayadi, F. Fnaiech, and E. Brassart, "Dempster-Shafer evidence theory for image segmentation: application in cells images," *International Journal of Signal Processing*, vol. 5, no. 1, 2009.
- [24] S. Ben Chaabane, M. Sayadi, F. Fnaiech, and E. Brassart, "Color image segmentation based on Dempster-Shafer evidence theory," in *Proceedings of the Mediterranean Electrotechnical Conference (MELECON '08)*, pp. 862–866, 2008.
- [25] H. D. Cheng, C. H. Chen, H. H. Chiu, and H. Xu, "Fuzzy homogeneity approach to multilevel thresholding," *IEEE Transactions on Image Processing*, vol. 7, no. 7, pp. 1084–1088, 1998.
- [26] E. Littmann and H. Ritter, "Adaptive color segmentation—a comparison of neural and statistical methods," *IEEE Transactions on Neural Networks*, vol. 8, no. 1, pp. 175–185, 1997.
- [27] M. Sezgin and B. Sankur, "Survey over image thresholding techniques and quantitative performance evaluation," *Journal of Electronic Imaging*, vol. 13, no. 1, pp. 146–168, 2004.
- [28] H.-D. Cheng and Y. Sun, "A hierarchical approach to color image segmentation using homogeneity," *IEEE Transactions on Image Processing*, vol. 9, no. 12, pp. 2071–2082, 2000.
- [29] H. D. Cheng, X. H. Jiang, and J. Wang, "Color image segmentation based on homogram thresholding and region merging," *Pattern Recognition*, vol. 35, no. 2, pp. 373–393, 2002.
- [30] R. C. Gonzalez and P. Wintz, *Digital Image Processing*, Addison-Wesley, Reading, Mass, USA, 1987.
- [31] M. Heath, S. Sarkar, T. Sanocki, and K. Bowyer, "Comparison of edge detectors: a methodology and initial study," in *Proceedings of the IEEE Computer Society Conference on Computer Vision and Pattern Recognition*, pp. 143–148, 1996.
- [32] G. Liu and R. M. Haralick, "Assignment problem in edge detection performance evaluation," in *Proceedings of the IEEE Computer Society Conference on Computer Vision and Pattern Recognition*, vol. 1, pp. 26–31, 2000.
- [33] V. Grau, A. U. J. Mewes, M. Alcañiz, R. Kikinis, and S. K. Warfield, "Improved watershed transform for medical image segmentation using prior information," *IEEE Transactions on Medical Imaging*, vol. 23, no. 4, pp. 447–458, 2004.
- [34] R. O. Duda, P. E. Hart, and D. G. Sorkin, *Pattern Classification*, Wiley-Interscience, New York, NY, USA, 2000.

## Research Article

# 2D-3D Registration of CT Vertebra Volume to Fluoroscopy Projection: A Calibration Model Assessment

P. Bifulco,<sup>1</sup> M. Cesarelli,<sup>1</sup> R. Allen,<sup>2</sup> M. Romano,<sup>1</sup> A. Fratini,<sup>1</sup> and G. Pasquariello<sup>1</sup>

<sup>1</sup>Department of Biomedical, Electronic and Telecommunication Engineering, University of Naples Federico II, 80125 Napoli, Italy

<sup>2</sup>Institute of Sound and Vibration Research, University of Southampton, Southampton SO17 1BJ, UK

Correspondence should be addressed to P. Bifulco, pabifulc@unina.it

Received 28 April 2009; Accepted 22 May 2009

Recommended by João Manuel R. S. Tavares

This study extends a previous research concerning intervertebral motion registration by means of 2D dynamic fluoroscopy to obtain a more comprehensive 3D description of vertebral kinematics. The problem of estimating the 3D rigid pose of a CT volume of a vertebra from its 2D X-ray fluoroscopy projection is addressed. 2D-3D registration is obtained maximising a measure of similarity between Digitally Reconstructed Radiographs (obtained from the CT volume) and real fluoroscopic projection. X-ray energy correction was performed. To assess the method a calibration model was realised a sheep dry vertebra was rigidly fixed to a frame of reference including metallic markers. Accurate measurement of 3D orientation was obtained via single-camera calibration of the markers and held as true 3D vertebra position; then, vertebra 3D pose was estimated and results compared. Error analysis revealed accuracy of the order of 0.1 degree for the rotation angles of about 1 mm for displacements parallel to the fluoroscopic plane, and of order of 10 mm for the orthogonal displacement.

Copyright © 2010 P. Bifulco et al. This is an open access article distributed under the Creative Commons Attribution License, which permits unrestricted use, distribution, and reproduction in any medium, provided the original work is properly cited.

## 1. Introduction

Intervertebral kinematics closely relates to the functionality of spinal segments and can provide useful diagnostic information. Direct measurement of the intervertebral kinematics *in vivo* is very problematic due to its intrinsic inaccessibility. The use of a fluoroscopic device can provide a continuous 2D screening of a specific spinal tract (e.g., cervical, lumbar) during spontaneous motion of the patient, with an acceptable, low X-ray dose. 2D kinematics can be extrapolated from fluoroscopic sequences. Most of the previous works [1–8] were confined to the estimation of planar motion (most on sagittal plane) and are based on the assumption of absence of out-of-plane coupled motion (e.g., axial rotation). Coupled motion can be neglected in sagittal (flexion-extension) motion (mainly due to anatomic symmetry), but in lateral bending, where a coupled axial rotation is certainly present [9], this approximation is no longer valid.

The knowledge of 3D positioning (pose) of vertebrae with time can lead to full 3D kinematics analysis, or at least to evaluate the presence of out-of-plane motion (rotation).

External skin markers do not provide accurate intervertebral motion description [10, 11], and invasive positioning of markers inserted in the vertebrae is not generally viable. In order to allow clinical application, 3D kinematics analysis should be performed by means of readily available, and minimally invasive, instrumentation, combined with an appropriate image processing technique.

In this study, a method for 3D pose estimation of vertebrae based on single plane-projection (e.g., Digital Video Fluoroscopy, DVF) combined with available CT-data [12–17] is proposed. By processing common CT slices it is possible to extract a 3D model of a vertebra, and by subsequent processing using ray-casting techniques it is possible to produce Digitally Reconstructed Radiographs (DRRs), simulating the 3D radiograph formation process. Comparing the DRRs with the real fluoroscopic image it is possible to estimate the real 3D orientation of the vertebra when screened by fluoroscopy (Figure 1).

To assess the accuracy and the repeatability of the method *invitro*, a calibration model consisting of a sheep dry vertebra rigidly fixed to an X-ray transparent frame of reference was designed in order to independently evaluate its 3D pose by

means of a single camera calibration procedure. The errors with respect to the estimate provided by the calibration procedure were evaluated.

It is anticipated that such a method will also be helpful in a number of other contexts such as Computer Assisted Surgery (CAS) [18–23], Radiotherapy Planning (RTP) and functional evaluation of implanted prosthesis [24–26].

## 2. Materials and Methods

**2.1. Summary of the Methodology.** In this study an in vitro assessment is performed of a method for 3D pose estimation of a vertebra with respect to a fluoroscopic imaging system, based upon the comparison between Digital Video Fluoroscopy (DVF) images and DRRs. The 3D pose estimation is a first step in a full 3D motion analysis [12, 13, 24–26].

Previous studies [4, 6, 14, 27] showed that fluoroscopy is well-suited to *in vivo* spine kinematics analysis because of the capability of screening patients during free motion with an acceptably low X-ray dosage and because of the wide availability of fluoroscopes in the clinical environment. However, this technique is limited to planar motion analysis and this assumption is valid only for pure flexion-extension movements. More information is needed in order to estimate 3D motion. Segmented CT volumes can provide an accurate model of a 3D vertebral shape and different X-ray attenuation of its features. Such a 3D vertebral model can be used to compute DRRs.

To estimate the 3D pose of a vertebra, the true DVF image is compared to an opportune set of differently oriented DRRs; the 3D parameters belonging to the DRR which maximise a predefined similarity index, are held as the vertebra 3D pose estimation. The similarity index employed in this study is the image zero-mean, cross-correlation coefficient. Zero-mean Normalized Cross-Correlation (ZNCC) is a widely used similarity function in template matching as well as in motion analysis. Let  $I$  be the image under examination, of size  $R$  by  $C$  pixels,  $T$  the template, of size  $M$  by  $N$  pixels, and  $Ic(x, y)$  be the subimage of  $I$  at position  $(x, y)$  having the same size as the template  $T$ , and let  $\langle Ic \rangle$  and  $\langle T \rangle$  be the computed mean of  $T$  and of  $Ic(x, y)$  respectively. The Normalized Zero-mean Normalized Cross-Correlation between the template  $T$  and the image  $I$  at position  $(x, y)$  is defined as

$$\text{ZNCC}(x, y) = \frac{\sum_{i=1}^M \sum_{j=1}^N [I(x+i, y+j) - \langle Ic \rangle] \cdot [T(i, j) - \langle T \rangle]}{\sqrt{\sum_{j=1}^N \sum_{i=1}^M [I(x+i, y+j) - \langle Ic \rangle]^2} \cdot \sqrt{\sum_{i=1}^M \sum_{j=1}^N [T(i, j) - \langle T \rangle]^2}}. \quad (1)$$

The DRR that best matches the real DVF image is searched by means of an iterative, gradient-driven procedure.

In this work the *in vivo* accuracy and repeatability of the method was assessed using a calibration object. The results of

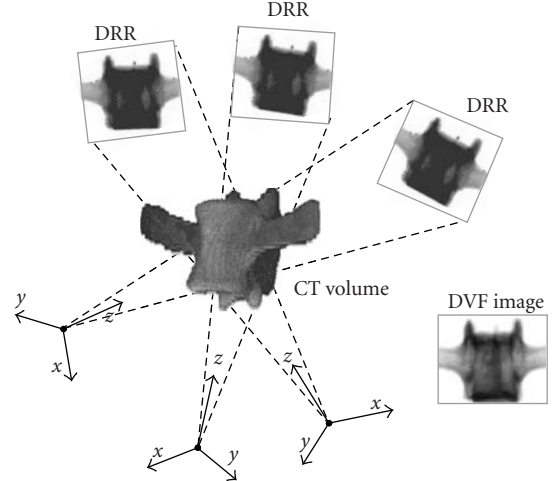


FIGURE 1: General sketch of the proposed method. A 3D CT vertebra model is available (the vertebra's 3D rendering is shown at centre). A DRR can be reconstructed from any orientation and distance. DRRs can be matched with a real DVF radiographic projection using a similarity index. The DRR that maximises the similarity with the real image is searched for. This procedure provides the vertebral 3D pose estimation.

the registrations between the DVF images and the CT volume were compared to an accurate 3D pose estimation obtained by means of fiducial markers embedded in the calibration object.

**2.2. Reconstruction of Digital Radiographs.** A number of techniques to compute DRRs have been proposed in the literature (see [28]). In this study, DRRs are computed from CT data using a ray-casting algorithm [29, 30]. This technique simulates the radiographic image formation process (see Figure 2).

A few simplifications are involved: X-ray is monochromatic radiation, traversing as straight lines throughout the matter (scattering effects are neglected); x-rays source (focus) is small (ideally a point) and is positioned at a finite distance from the radiographic plane; the attenuation through the body is described by the following equation for monochromatic radiation [31]:

$$I = I_0 \cdot e^{-\int \mu(x) \cdot dx}, \quad (2)$$

where  $I$  is the intensity of the X-ray radiation at the radiographic plane,  $I_0$  is the intensity of X-ray radiation at the source,  $\mu(x)$  is the linear attenuation coefficient of the voxel at  $x$  whose width is  $dx$  (notice that the effect of beam-hardening [32] is not considered). The relationship between CT-data (represented as Hounsfield Units, HU) and the corresponding attenuation coefficient  $\mu$  is represented by the equation [31]:

$$HU = 1000 \cdot \frac{\mu - \mu_{\text{water}}}{\mu_{\text{water}}}, \quad (3)$$

where  $\mu_{\text{water}}$  is approximately  $0.2 \text{ cm}^{-1}$  for an X-ray source at 120 kVp.

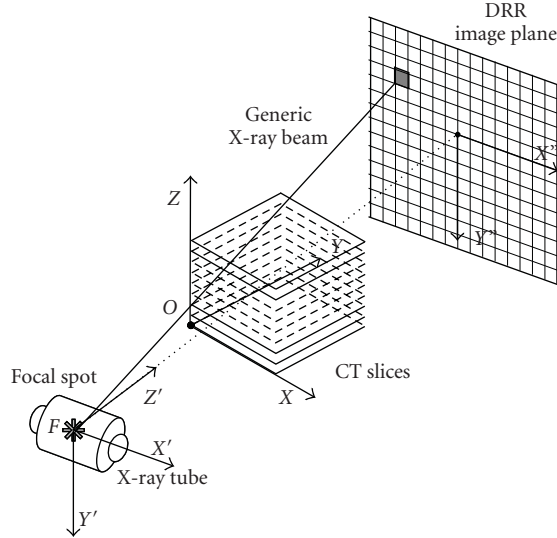


FIGURE 2: Algorithm for the simulation of the radiographic process. X-rays are modelled as straight lines (generic X-ray beam) through matter. The radiographic DRR image plane and X-rays are sampled. X-ray attenuation values of the CT 3D model are integrated together with a generic ray in order to obtain the grey-level of the corresponding pixel of the DRR.

To reconstruct a radiograph, the radiographic plane (DRR image plane in Figure 2) is subdivided into a number of pixels, each pixel is ideally connected by a straight line with the X-ray source, and absorption coefficients in the CT volume are summated along this line (generic X-ray beam in Figure 2). Therefore the summation provides the brightness value of the radiographic pixel under examination. Three-linear interpolation [33] of CT data was used to estimate X-ray absorption at a generic point within the CT volume.

**2.3. CT and DVF X-Rays Energy Equalisation.** Typical CT scanners operate at a peak voltage of about 120 kVp. In fluoroscopy, peak voltages of 40–80 kVp are used. The energy of the X-ray photons, and therefore the  $\mu$  values, are influenced by the peak voltage. The energy dependency of the attenuation coefficients is highly nonlinear [32]. The energy corresponding to the peak of the spectrum has the strongest effect on the attenuation coefficients: we use this energy to perform the correction. The wavelength at the peak ( $\lambda_{\text{peak}}$ ) is approximately given by [34]:  $\lambda_{\text{peak}} = 2/V_{\text{peak}}$ , where  $V_{\text{peak}}$  is the peak voltage expressed in kVp and  $\lambda_{\text{peak}}$  is expressed in nm. The corresponding energy can be calculated using the following formula [32]:  $E = 1.24/\lambda_{\text{peak}}$ , where  $E$  is expressed in keV. Before reconstruction of DRRs, CT data must be corrected by multiplication of a correction factor  $\gamma$ , computed using the following formula:

$$\mu_{\text{DVF}} = \mu_{\text{CT}} \cdot \left( \frac{\mu_{\text{DVF}}}{\rho} \right) \cdot \left( \frac{\rho}{\mu_{\text{CT}}} \right) = \mu_{\text{CT}} \cdot \gamma, \quad (4)$$

where  $\mu_{\text{DVF}}$  and  $\mu_{\text{CT}}$  indicate the  $\mu$  of the material at DVF and at CT energy respectively; the ratio between  $\mu$  and the  $\rho$  (density of the material) is called the mass attenuation

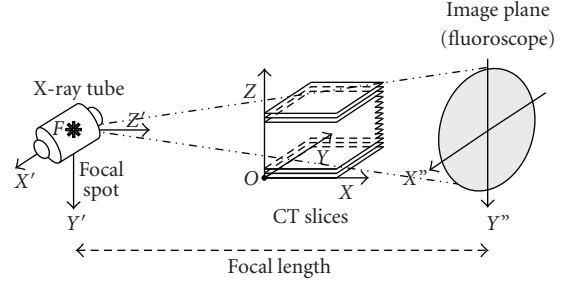


FIGURE 3: Different frame of references employed in the study of the 3D pose estimation of the vertebral model. The main frame of reference ( $OXYZ$ ) is related to CT slices and patient. The other frame of reference ( $FX'Y'Z'$ ) is fixed to the DVF device: where  $F$  is the X-ray focal spot,  $x$  and  $y$  axes describe the orientation of the image plane and the  $z$  axis represents the direction connecting  $F$  with the radiographic image centre (focal length). Orientation of the DVF frame of reference is described by a translation vector (e.g.,  $X, Y, Z$  in Table 1, which represent the X-ray focal spot coordinates with respect to the CT frame of reference) and the Euler angles ( $\phi, \theta, \varphi$  rotation angles about the axes  $x, y$  and  $z$ ).

coefficient. Notice that the lower the peak voltage, the larger the difference between the correction factors for bone and for the other tissues. So the peak voltage is a parameter that determines the contrast between the bone and the other tissues on DVF images. Tabled mass attenuation coefficients versus x-ray energy, for several materials, can be found in Johns and Cunningham [32]; mass attenuation coefficients corresponding to the voltages of the actual devices used in this work are not reported in the table, and were therefore obtained by linear interpolation. To perform energy correction, two thresholds are fixed, in order to separate high density (compact) bone and low density (cancellous) bone within the CT volume: for each voxel whose Hounsfield Unit lies in the predefined range the corresponding correction factor is computed.

**2.4. Estimation of the 3D Pose by Maximising the Cross-Correlation Index.** A rigid body in space has 6 degrees of freedom. The pose is determined by the 3D coordinates of the focus (X-ray source) and the Euler angles of the fluoroscopic image plane, which are both expressed in the frame of reference of the CT volume (see Figure 3).

In order to estimate the 3D pose of the vertebra, a set of DRRs using different positioning is generated. The actual radiograph is compared to a set of DRRs by means of a cross-correlation index. The DRR that maximises the cross-correlation is found using a procedure that adopts an iterative step-refinement approach. In the first steps of the iterative procedure the space of the focus coordinates and of the Euler angles is sampled at a low resolution (10 mm, 5 degrees resp.). The DRRs are reconstructed using an initial resolution of approximately 2 mm/pixel; the true DVF is resampled using the same resolution to allow calculation of the cross-correlation. The time required to compute a low-resolution DRR is short and it is possible to screen a wide region of the cross-correlation function to avoid

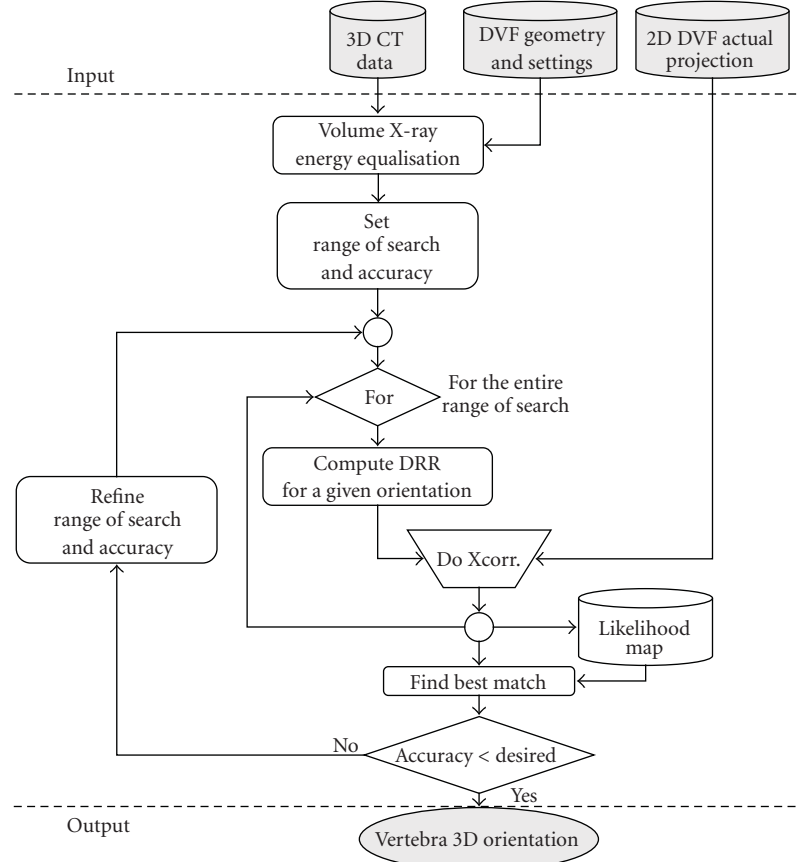


FIGURE 4: Flow-chart of the 2D-3D registration procedure.

being trapped in local maxima. In the subsequent steps of the iterative procedure the sampling resolution of the space and of the Euler angles is progressively increased (5 mm, 1 mm; 1 degree, 0.1 degrees). In principle, it is possible to increase the resolution further but at high resolutions the data (CT and DVF) sampling errors become predominant. The flow-chart (Figure 4) presents the main stages of the algorithm.

CT volume of the vertebra, actual 2D fluoroscopic projection and information about CT and DVF device (e.g., DVF focal distance, pixels and voxel dimensions, X-ray KVp, etc.) are the input data. A preliminary step to correct the CT Hounsfield numbers was performed (see the CT and DVF X-rays energy equalisation paragraph). To start the search for vertebra orientation parameters an initial range of search with a low accuracy for the 6 degrees of freedom parameters ( $x, y, z, \phi, \theta, \varphi$ ) was chosen. A set of differently oriented DRR are then computed (for the DRR procedure refer to the Reconstruction of digital radiographs paragraph). Each DRR is then cross-correlated with the actual DVF image and a likelihood map (function of the 6 parameters) is generated. The maximum of the likelihood map is searched and the corresponding 6 parameters are considered the current best estimate of vertebra pose and orientation. The process is iterated, by refining the range of search and by increasing the accuracy of the parameters, until a desired accuracy

is reached. Since the DRR algorithm is particularly time consuming, the multiscale approach (increasing accuracy) and the gradient-driven maximum search helps to reduce the total computation time.

**2.5. The Calibration Model.** In a previous study the feasibility of the method was evaluated by means of a computer simulation [35, 36]. In this work, in order to perform an *in vitro* assessment of the method, a calibration model was designed. It was realised with a dried sheep vertebra fixed to a radiographically transparent block (72 by 40 by 34 mm in Perspex) in which eight fiducial markers (3 mm diameter metallic spheres) were inserted (see Figure 5). Fiducial markers were used to perform an accurate 3D pose estimation of the calibration object, these results were held as reference. CT data and DVF images of the calibration model were acquired.

CT data were acquired by means of a spiral CT scanner (GE 16-slice) set to 120 kVp, 100 mAs with an image resolution 0.5 mm/pixel, 0.75 mm slice thickness. The DVF image was acquired by means of a 9 inch, digital video-fluoroscopy system(GE Advantx) set to 50 kVp, 1 mAs with an image resolution of 0.3 mm/pixel. An accurate estimate of the 3D pose of the calibration model with respect to the fluoroscopic system was obtained with a single camera

TABLE 1: An example of the 3D pose parameters of the calibration model, estimated via a single camera calibration by means of the metallic markers.

	Focus Co-ordinates (mm); Translation			Euler's angles (deg); Rotations		
	X	Y	Z	$\varphi$	$\theta$	$\psi$
Mean	-751.22	119.94	49.99	-1.53	89.98	-90.10
SD	5.78	0.12	0.12	0.55	0.11	0.11

TABLE 2: Means and standard deviations (SD) of the errors in computing the 6 parameters of the 3D vertebral pose with respect to the reference value obtained via metallic marker camera calibration. The letters refer to the type of correction performed (see text).

Mean	X (mm)	Y (mm)	Z (mm)	$\varphi$ (deg)	$\theta$ (deg)	$\psi$ (deg)
A	38.25	3.03	-2.88	-0.13	-0.16	0.52
B	37.61	2.04	-1.74	-0.13	-0.16	0.48
C	22.58	1.87	-1.52	-0.12	-0.16	0.37
D	12.17	1.64	-1.13	-0.10	-0.16	0.49
SD	X (mm)	Y (mm)	Z (mm)	$\varphi$ (deg)	$\theta$ (deg)	$\psi$ (deg)
A	10.97	7.19	9.94	0.61	0.71	0.67
B	8.56	7.89	9.89	0.62	0.73	0.60
C	10.02	7.54	9.12	0.61	0.72	0.72
D	4.99	7.68	9.19	0.61	0.70	0.43



FIGURE 5: Picture of the realised calibration model. The dried sheep vertebra (anterior view) fixed to a radiographically transparent Perspex block measuring 72 mm by 40 mm by 34 mm with eight 3 mm diameter metallic markers inserted.

calibration procedure, using the eight fiducial markers [37, 38].

An intensity-weighted method was used to find the coordinates of the centroid of the fiducial markers both in the CT scan and in the DVF image [39, 40]. The markers were previously segmented using a threshold-based algorithm. For each marker the 2D coordinates of the centroid of its projection on the DVF image were measured. The centroid was calculated as the intensity-weighted average of the coordinates of the pixels belonging to the marker. Measurement error was estimated by repeating measures using various thresholds. In the CT data each marker occupied three-to-four slices. The 3D coordinates of a marker centroid were measured as an intensity-weighted

average of the pixel coordinates on each slice in which the marker was visible. In order to evaluate the precision of the single camera calibration, a Monte Carlo simulation was performed adding random noise (standard deviation equal to estimated noise on measured markers of 2 mm) to measured marker coordinates and recalculating the 3D pose of the model.

### 3. Results

Table 1 presents an example of the 3D pose parameters of the calibration model, independently estimated by means of the single camera, Monte Carlo simulation, calibration procedure using the radiographically transparent frame. The mean values resemble the positioning of the DVF frame of reference with respect to the CT as shown in Figure 3. These results were used as a reference from which to compute the final errors in estimated pose parameters. As example, Figure 6 shows a real DVF of the calibration object beside its correspondent DRR obtained by the CT 3D vertebra model.

To evaluate the accuracy and the precision of the method for 3D pose estimation, presented in the previous section, a set of trials was carefully designed.

It is assumed that an accurate simulation of the radiographic process should produce the best results in 3D pose estimation. However, the more accurate the simulation process, the larger is the computing time required. With this in mind, 4 cases were considered in order to evaluate the influence of the simulation process on the accuracy and precision of 3D pose estimation.

Preprocessing of CT data (segmentation and X-ray energy correction) was performed in the Matlab environment. To speed up DRR computation, all the software required was developed in C++.

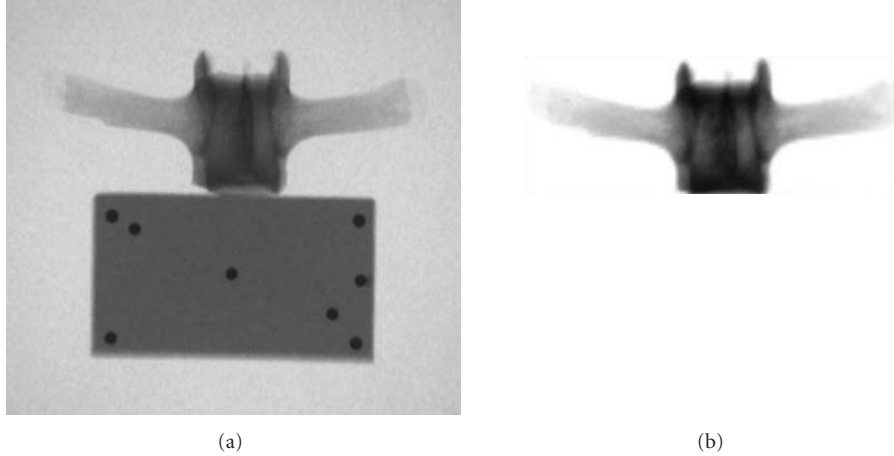


FIGURE 6: A real antero-posterior DVF of the calibration object (a): the radio-transparent frame attached below the vertebra and the inserted metallic markers are also visible; an equally oriented DRR (b) obtained by the CT 3D vertebra model is shown for comparison.

In order to evaluate the influence of these various factors, the 4 trials were performed:

- (a) using CT data with no corrections at all;
- (b) performing only exponential correction in (1) but not the  $\mu$  correction;
- (c) performing only attenuation coefficient  $\mu$  correction (energy) of CT data;
- (d) performing both corrections.

For each trial, 70 registrations were accomplished within a total of 280 registrations. Errors with respect to the “true pose” registration (obtained via the metallic marker camera calibration) were computed. The results of the 4 trials are presented in Table 2. For each trial the mean errors of the  $x, y, z$  coordinates (in mm) and in Euler angles (in degrees) are reported. The standard deviations (SD) of errors are also reported.

The results show that, for each trial, the mean error is of approximately 0.1 degree for Euler angles and about 2 mm for coordinates parallel to the radiographic plane. The coordinate perpendicular to the radiographic plane, instead, is subjected to a more significant error (about 15 mm). In general errors decrease by applying the described corrections.

#### 4. Discussion and Conclusions

This paper has described an automatic method for 3D pose estimation of a vertebra by means of CT and digital video-fluoroscopy and an *in vitro* assessment using a calibration object was performed.

The method is based upon a comparison (by means of cross-correlation) between DVF images and DRRs obtained using the CT 3D vertebral model. The DRR is obtained by simulating the radiographic process in an accurate manner, taking into account the effect of the difference of X-ray energy between CT and DVF imaging modalities. The

algorithm for the reconstruction of digital radiographs is based on a ray-casting approach.

The 3D parameters belonging to the DRR that maximises the cross-correlation were considered as the estimators of the 3D pose of the vertebra. An iterative (gradient driven), step-refinement, multiscale approach was used to reliably estimate the absolute maxima of the cross-correlation function described by variables representing the 6 degrees of freedom of a rigid body (vertebra).

To perform an assessment of the method, a calibration model, with embedded fiducial markers, was designed in order to allow an accurate estimate of the 3D pose as a baseline. An appropriate set of trials was designed to investigate the possibility of not simulating accurately the radiographic process.

From the results it can be inferred that accuracy and precision of the 3D pose estimation increases when the simulation becomes more accurate, in particular, taking into account the effect of X-ray energies and the exponential attenuation of X-ray through matter.

The method presents satisfactory results in the computation of Euler angles and of focus coordinates parallel to the radiographic plane. However, the coordinates orthogonal to the radiographic plane are subjected to more significant errors. Nevertheless, in practical cases, this information is known via positioning of the patient with respect to the DVF device.

To explain this fact it should be observed that a displacement in the direction perpendicular to the radiographic plane causes a “zoom effect”. This “zoom” is clearly visible only if the displacement is of the order of 10–15 mm. Therefore the cross-correlation index is not able to distinguish between 2 DVF images obtained with orthogonal coordinates differing less than 10–15 mm.

It is worth mentioning that by using the calibration model, the effect of soft tissue and adjacent vertebrae has been neglected. Therefore the presented results reasonably represent an upper limit for the accuracy and precision

achievable in real applications. However, recent further study involving the analysis of the cervical spine motion in human patients seems to confirm the applicability of such a methodology [41]. Current work aims to evaluate the use of first derivatives of DVF images to improve and speed up the template matching process [42].

## References

- [1] J. Dimnet, L. P. Fischer, G. Gonon, and J. P. Carret, "Radiographic studies of lateral flexion in the lumbar spine," *Journal of Biomechanics*, vol. 11, no. 3, pp. 143–150, 1978.
- [2] I. A. F. Stokes, D. G. Wilder, J. W. Frymoyer, and M. H. Pope, "Assessment of patients with low-back pain by biplanar radiographic measurement of intervertebral motion," *Spine*, vol. 6, no. 3, pp. 233–240, 1981.
- [3] A. C. Breen, R. Allen, and A. Morris, "Spine kinematics: a digital videofluoroscopic technique," *Journal of Biomedical Engineering*, vol. 11, no. 3, pp. 224–228, 1989.
- [4] H. van Mameren, J. Drukker, H. Sanches, and J. Beursgens, "Cervical spine motion in the sagittal plane (I) range of motion of actually performed movements, an X-ray cinematographic study," *European Journal of Morphology*, vol. 28, no. 1, pp. 47–68, 1990.
- [5] H. van Mameren, H. Sanches, J. Beursgens, and J. Drukker, "Cervical spine motion in the sagittal plane II: position of segmental averaged instantaneous centers of rotation—a cineradiographic study," *Spine*, vol. 17, no. 5, pp. 467–474, 1992.
- [6] J. M. Muggleton and R. Allen, "Automatic location of vertebrae in digitized videofluoroscopic images of the lumbar spine," *Medical Engineering and Physics*, vol. 19, no. 1, pp. 77–89, 1997.
- [7] P. Bifulco, M. Cesarelli, R. Allen, J. Muggleton, and M. Bracale, "Automatic vertebrae recognition throughout a videofluoroscopic sequence for intervertebral kinematics study," in *Time Varying Image Processing and Moving Object Recognition*, Cappellini, Ed., vol. 4, pp. 213–218, Elsevier, Amsterdam, The Netherlands, 1996.
- [8] B. McCane, T. I. King, and J. H. Abbott, "Calculating the 2D motion of lumbar vertebrae using splines," *Journal of Biomechanics*, vol. 39, no. 14, pp. 2703–2708, 2006.
- [9] A. A. White III and M. M. Panjabi, "The basic kinematics of the human spine: a review of past and current knowledge," *Spine*, vol. 3, no. 1, pp. 12–20, 1978.
- [10] X. Zhang and J. Xiong, "Model-guided derivation of lumbar vertebral kinematics in vivo reveals the difference between external marker-defined and internal segmental rotations," *Journal of Biomechanics*, vol. 36, no. 1, pp. 9–17, 2003.
- [11] P. Cerveri, A. Pedotti, and G. Ferrigno, "Kinematical models to reduce the effect of skin artifacts on marker-based human motion estimation," *Journal of Biomechanics*, vol. 38, no. 11, pp. 2228–2236, 2005.
- [12] P. Bifulco, M. Cesarelli, M. Roccasalva Firenze, E. Verso, M. Sansone, and M. Bracale, "Estimation of the 3D positioning of anatomic structures from radiographic projection and volume knowledge," in *Proceedings of the 8th Mediterranean Conference on Medical and Biological Engineering and Computing (MEDICON '98)*, 1998, CD-ROM: 2.5.
- [13] P. Bifulco, M. Cesarelli, E. Verso, M. Roccasalva Firenze, M. Sansone, and M. Bracale, "Simulation of the radiography formation process from CT patient volume," in *Proceedings of the 8th Mediterranean Conference on Medical and Biological Engineering and Computing (MEDICON '98)*, 1998, CD-ROM: 2.5.
- [14] P. Bifulco, M. Cesarelli, R. Allen, M. Sansone, and M. Bracale, "Automatic recognition of vertebral landmarks in fluoroscopic sequences for analysis of intervertebral kinematics," *Medical and Biological Engineering and Computing*, vol. 39, no. 1, pp. 65–75, 2001.
- [15] W. Birkfellner, J. Wirth, W. Burgstaller, et al., "A faster method for 3D/2D medical image registration—a simulation study," *Physics in Medicine and Biology*, vol. 48, no. 16, pp. 2665–2679, 2003.
- [16] T. Rohlfing, D. B. Russakoff, J. Denzler, K. Mori, and C. R. Maurer Jr., "Progressive attenuation fields: fast 2D-3D image registration without precomputation," *Medical Physics*, vol. 32, no. 9, pp. 2870–2880, 2005.
- [17] D. B. Russakoff, T. Rohlfing, J. R. Adler Jr., and C. R. Maurer Jr., "Intensity-based 2D-3D spine image registration incorporating a single fiducial marker," *Academic Radiology*, vol. 12, no. 1, pp. 37–50, 2005.
- [18] A. Hamadeh, S. Lavallee, and P. Cinquin, "Automated 3-dimensional computed tomographic and fluoroscopic image registration," *Computer Aided Surgery*, vol. 3, no. 1, pp. 11–19, 1998.
- [19] J.-M. Mac-Thiong, C. E. Aubin, J. Dansereau, J. A. de Guise, P. Brodeur, and H. Labelle, "Registration and geometric modelling of the spine during scoliosis surgery: a comparison study of different pre-operative reconstruction techniques and intra-operative tracking systems," *Medical and Biological Engineering and Computing*, vol. 37, no. 4, pp. 445–450, 1999.
- [20] J. Weese, R. Gocke, G. P. Penney, P. Desmedt, T. M. Buzug, and H. Schumann, "Fast voxel-based 2D/3D registration algorithm using a volume rendering method based on the shear-warp factorization," in *Medical Imaging 1999: Image Processing*, vol. 3661 of *Proceedings of SPIE*, pp. 802–810, 1999.
- [21] S. Lavallee and R. Szeliski, "Recovering the position and orientation of free-form objects from image contours using 3D distance maps," *IEEE Transactions on Pattern Analysis and Machine Intelligence*, vol. 17, no. 4, pp. 378–390, 1995.
- [22] S. Lavallee, R. Szeliski, and L. Bruniee, "Anatomy based registration of three-dimensional medical images, range images, X-ray projections, and three-dimensional models using octree-splines," in *Computer Integrated Surgery: Technology and Clinical Applications*, MIT Press, Cambridge, Mass, USA, 1995.
- [23] A. Hurvitz and L. Joskowicz, "Registration of a CT-like atlas to fluoroscopic X-ray images using intensity correspondences," *International Journal of Computer Assisted Radiology and Surgery*, vol. 3, no. 6, pp. 493–504, 2008.
- [24] S. A. Banks and W. A. Hodge, "Accurate measurement of three-dimensional knee replacement kinematics using single-plane fluoroscopy," *IEEE Transactions on Biomedical Engineering*, vol. 43, no. 6, pp. 638–649, 1996.
- [25] S. Zuffi, A. Leardini, F. Catani, S. Fantozzi, and A. Cappello, "A model-based method for the reconstruction of total knee replacement kinematics," *IEEE Transactions on Medical Imaging*, vol. 18, no. 10, pp. 981–991, 1999.
- [26] S. Hirokawa, M. Abrar Hossain, Y. Kihara, and S. Ariyoshi, "A 3D kinematic estimation of knee prosthesis using X-ray projection images: clinical assessment of the improved algorithm for fluoroscopy images," *Medical and Biological Engineering and Computing*, vol. 46, no. 12, pp. 1253–1262, 2008.
- [27] P. Bifulco, M. Cesarelli, M. Sansone, R. Allen, and M. Bracale, "Fluoroscopic analysis of inter-vertebral lumbar motion: a

- rigid model fitting technique,” in *Proceedings of the World Congress on Medical Physics and Biomedical Engineering*, p. 714, 1997.
- [28] J. Alakuijala, U.-M. Jaske, S. Sallinen, H. Helminen, and J. Laitinen, “Reconstruction of digital radiographs by texture mapping, ray casting and splatting,” in *Proceedings of the 18th Annual International Conference of the IEEE Engineering in Medicine and Biology*, vol. 2, pp. 643–645, 1996.
  - [29] L. M. Gottesfeld Brown and T. E. Boult, “Registration of planar film radiographs with computed tomography,” in *Proceedings of the Workshop on Mathematical Methods in Biomedical Image Analysis (MMBIA '96)*, pp. 42–51, 1996.
  - [30] J. Weese, G. P. Penney, P. Desmedt, T. M. Buzug, D. L. G. Hill, and D. J. Hawkes, “Voxel-based 2-d/3-d registration of fluoroscopy images and CT scans for image-guided surgery,” *IEEE Transactions on Information Technology in Biomedicine*, vol. 1, no. 4, pp. 284–293, 1997.
  - [31] Z. Cho, J. P. Jones, and M. Singh, *Foundations of Medical Imaging*, Wiley Interscience, New York, NY, USA, 1993.
  - [32] H. E. Johns and J. R. Cunningham, *The Physics of Radiology*, Charles C. Thomas, Springfield, Ill, USA, 1983.
  - [33] S. R. Marschner and R. J. Lobb, “An evaluation of reconstruction filters for volume rendering,” in *Proceedings of the IEEE Conference on Visualization (Visualization '94)*, pp. 100–107, Washington, DC, USA, 1994.
  - [34] G. J. van der Plaats and P. Vlijbrief, *Medische Rontgentechniek in de Diagnostiek*, Uitgeversmaatschappij de Tijdstroom, 1978.
  - [35] P. Bifulco, M. Sansone, M. Cesarelli, R. Allen, and M. Bracale, “Estimation of out-of-plane vertebra rotations on radiographic projections using CT data: a simulation study,” *Medical Engineering and Physics*, vol. 24, no. 4, pp. 295–300, 2002.
  - [36] P. Bifulco, M. Sansone, M. Cesarelli, and M. Bracale, “In-vivo evaluation of cervical spine intervertebral kinematics by means of digital fluoroscopy: experimental set-up,” in *Proceedings of the 2nd European Medical & Biological Engineering Conference (EMBEC '02)*, Vienna, Austria, December 2002.
  - [37] J. Dapena, E. A. Harman, and J. A. Miller, “Three-dimensional cinematography with control object of unknown shape,” *Journal of Biomechanics*, vol. 15, no. 1, pp. 11–19, 1982.
  - [38] H. Hatze, “High-precision three-dimensional photogrammetric calibration and object space reconstruction using a modified DLT-approach,” *Journal of Biomechanics*, vol. 21, no. 7, pp. 533–538, 1988.
  - [39] C. B. Bose and I. Amir, “Design of fiducials for accurate registration using machine vision,” *IEEE Transactions on Pattern Analysis and Machine Intelligence*, vol. 12, no. 12, pp. 1196–1200, 1990.
  - [40] G. Chiorboli and G. P. Vecchi, “Comments on “design of fiducials for accurate registration using machine vision”,” *IEEE Transactions on Pattern Analysis and Machine Intelligence*, vol. 15, no. 12, pp. 1330–1332, 1993.
  - [41] M. Sansone, P. Bifulco, M. Cesarelli, and M. Bracale, “Evaluation of spine kinematics after surgical intervention: a feasibility study,” in *Proceedings of the Medicon and Health Telematics*, Ischia, Italy, July-August 2004.
  - [42] P. Bifulco, M. Cesarelli, M. Romano, R. Allen, and T. Cerciello, “Vertebrae tracking through fluoroscopic sequence: a novel approach,” in *Proceedings of the World Congress on Medical Physics and Biomedical Engineering: The Triennial Scientific Meeting of the IUPESM*, Munich, Germany, September 2009.

## Research Article

# Three-Dimensional Morphometry of Single Endothelial Cells with Substrate Stretching and Image-Based Finite Element Modeling

Hiroshi Yamada, Norihide Mouri, and Shinji Nobuhara

Department of Biological Functions and Engineering, Graduate School of Life Science and Systems Engineering, Kyushu Institute of Technology, 2-4 Hibikino, Wakamatsu-Ku, Kitakyushu 808-0196, Japan

Correspondence should be addressed to Hiroshi Yamada, [yamada@life.kyutech.ac.jp](mailto:yamada@life.kyutech.ac.jp)

Received 6 April 2009; Accepted 8 June 2009

Recommended by João Manuel R. S. Tavares

Morphologically accurate reproduction of the behavior of endothelial cells is a key to understanding their mechanical behavior in cyclically inflated arteries and to quantitatively correlating this with cellular responses. We developed a novel technique to measure the three-dimensional geometry of cells on the substrate being stretched. We obtained sliced images of cells using confocal laser-scanning microscopy, and created image-based finite element models in the unloaded state assuming neo-Hookean material. Comparison of numerical predictions and experiments involving six cells when the substrate was stretched by 15% showed that the deformed geometry agreed with an average error of  $<0.55\text{ }\mu\text{m}$ , roughly one-hundredth the size of a cell, for the lower half of the range of cellular height. Numerical sensitivity analyses showed that the cellular deformation under substrate stretching, that is, displacement boundaries, is insensitive to the absolute value of the elastic modulus, but depends on the nuclear to cytoplasmic modulus ratio.

Copyright © 2010 Hiroshi Yamada et al. This is an open access article distributed under the Creative Commons Attribution License, which permits unrestricted use, distribution, and reproduction in any medium, provided the original work is properly cited.

## 1. Introduction

Arterial endothelial cells are exposed to periodic blood flow and undergo associated cyclic deformation. Their morphological changes and remodeling are mediated by these mechanical conditions. Therefore, it is important to determine the effects of the mechanical fields quantitatively by measuring the deformation of a cell, for example, with confocal laser-scanning microscopy (CLSM), and reproducing it accurately with a finite element model. Adequate modeling is a key to understand the mechanical behavior of a cell under substrate deformation and to correlate quantitatively the cellular and intracellular responses with mechanical factors.

The deformation of an adherent cell has been measured at the cellular or subcellular level after stretching the substrate or applying a force to the cell to identify the cell deformation behavior or force—displacement relationship [1]. The cellular and intracellular strains have been estimated in two dimensions on the horizontal plane perpendicular

to the light axis of a microscope. To do so, one uses the relative displacement of fluorescent markers on the plasma membrane surface [2] and fluorescent [3] or nonfluorescent [4] markers in the cytoplasm, the correlation of cellular images captured as the fluorescence intensity texture on undeformed or deformed substrates [5, 6], or a comparison of the central cross-section of a cell (a chondrocyte in a gel) in CLSM images between the uncompressed and compressed states [7].

A hybrid technique for characterizing adherent cells combines mechanical measurement and finite element analysis [1, 8–10] as described below. For the three-dimensional (3D) modeling and stress analysis of cells subject to fluid shear stress, Ohashi et al. [8] measured the cellular free surface of bovine aortic endothelial cells in culture using an atomic force microscope, and Ferko et al. [10] measured the cytoplasm and nucleus in the same type of cell using total internal reflection fluorescence microscopy. They characterized the cell as an isotropic linear elastic material.

Hyperelastic material models have also been applied to improve the analysis of a cell undergoing large deformation. Caille et al. [1] modeled neo-Hookean material for a cell with Young's moduli ( $E$ ) ranging from 100 to 2500 Pa and 500 to 25000 Pa for the cytoplasm and nucleus, respectively, compressed between parallel plates. Yamada et al. [11] and Yamada and Matsumura [12] modeled neo-Hookean material for a cell on a substrate being stretched with  $E = 775$  Pa, 5100 Pa, and 775 kPa for the cytoplasm, nucleus, and substrate, respectively. Jean et al. [13] modeled neo-Hookean material to reproduce cell rounding behavior with  $E = 5000$  Pa, 500–1500 Pa, 500 Pa, and 1000 Pa for the nucleus, cytoskeleton, cytosol, and cortical layer, respectively. Tracqui and Ohayon [14] used a second-order equation of the first invariant of the right Cauchy-Green deformation tensor for a cell body subjected to the rotation of embedded beads, and modeled neo-Hookean material with  $E = 900$  Pa and 5100 Pa for the basal cell cortex and nucleus, respectively. However, the 3D geometry of an entire cell body in a theoretical model has never been compared to experimental measurements made under deformation.

Therefore, we examined the 3D deformation characteristics of cultured aortic endothelial cells under substrate stretching. We used CLSM to obtain the 3D geometry of cells on unstretched and uniaxially stretched substrate as a set of horizontally sliced images. Next we made a 3D finite element model of unstretched cells assuming incompressible isotropic hyperelastic material. Then we compared the 3D geometry of each measured stretched cell with the theoretical prediction based on a finite element analysis. We also evaluated the effects of the elasticity of intracellular components to obtain an accurate finite element analysis reproduction of cellular deformation due to substrate stretching.

## 2. Materials and Methods

**2.1. Materials and Cell Culture.** Porcine thoracic aortas obtained from a slaughterhouse were excised to remove endothelial cells [15]. The cells were dispersed in 35 mm dishes coated with type I collagen (Iwaki, Chiba, Japan) with D-MEM (Gibco, Grand Island, NY, USA) containing 10% fetal bovine serum (Gibco) and a 1% mixture of penicillin, streptomycin, and neomycin (Gibco). The cells were cultured in an incubator kept at 37°C in a 100% humidified atmosphere with 5% carbon dioxide. When the cells were 70%–80% confluent, they were detached with 0.05% trypsin–EDTA (Gibco) and subcultured in 35 mm tissue culture dishes (Iwaki).

The 32 × 32 × 0.1 mm bottom membrane in a silicone chamber (10-cc; Strex, Osaka, Japan) was coated with 1 mL 50 µg/mL fibronectin from porcine plasma (Wako Pure Chemical Industries, Osaka, Japan). Young's modulus of the membrane was 1267 kPa at room temperature. Cells from the second to fourth passages were transferred to the silicon membrane with 2 mL solution at a concentration of 25,600 cells/mL for seeding the cells at 5000 cells/cm<sup>2</sup> to avoid cell-to-cell contact.

**2.2. Fluorescent Staining.** After incubation overnight (13–16 hours), the cells were stained by replacing the culture medium (D-MEM) with 10 µM calcein-AM (Dojindo, Kumamoto, Japan) and incubated for 30 minutes. Then the dish was rinsed once with D-PBS (Gibco) and filled with culture medium.

**2.3. Image Acquisition of Unstretched and Stretched Cells.** The chamber was mounted on the stretching apparatus of a microscopic stage (see Figure 1). The temperature of the bath was kept at 34–37°C by circulating hot water in the tube. An unstretched cell was scanned horizontally using CLSM (FV300-BX51WI; Olympus, Tokyo, Japan) with a 60 × water immersion objective after adjusting the voltage of the photomultiplier tube so as to obtain brightness intensities within 256 levels. Then the following steps were repeated to obtain the 3D geometry of each cell.

- (1) A cell in the unstretched state was scanned horizontally at 0.25-µm height intervals over a height range of 20 µm using CLSM to acquire a series of fluorescent images (800 × 600 pixels, 0.167 µm/pixel) within 3 minutes.
- (2) The silicone membrane was stretched for 30 seconds to a 15.1% strain at strain increments of 1.51% using a pair of pulse stages connected to a programmable controller (PS-30E-0 & CAT II; Chuo Precision Industrial, Tokyo, Japan). The focus of the cell was adjusted manually through a light microscope after each strain increment.
- (3) The cells were scanned between 1 and 4 minutes after reaching the applied strain. The scanning procedure was the same as that used for the unstretched state.

**2.4. Compensation for Fading Fluorescence Intensity and Determination of the Intensity Threshold.** We obtained equivalent thresholds of fluorescence intensity for the initial image scanned in the unstretched state and that scanned in the stretched state. As a pretest, cells were scanned in three dimensions using CLSM twice, 3 minutes apart. To determine the border of the cell body, excluding the very thin peripheral region, we chose a threshold,  $T_1$ , as the level from which the intensity increased abruptly. The brightest 20 × 20-pixel region in the image of the cell bottom was chosen in the first scan. Then the ratio of the mean intensity,  $r$ , was calculated by comparing the intensity in the second scan. The threshold in the second scan,  $T_2$ , was assumed to be proportional to the ratio  $T_2 = T_1 \times r$ .

We scanned four cells using CLSM to validate the chosen threshold. Each cell was scanned horizontally at 0.25-µm height intervals. Each cell was divided into bottom, middle, and top height regions. The bottom and middle regions were chosen at least 1 µm lower than the top of the cell. For example, if the height of the cell was 5.5 µm, the top and bottom images were obtained at heights of 5 µm and 0 µm, respectively, and the middle images were obtained at heights of 1–4 µm at 1-µm intervals.

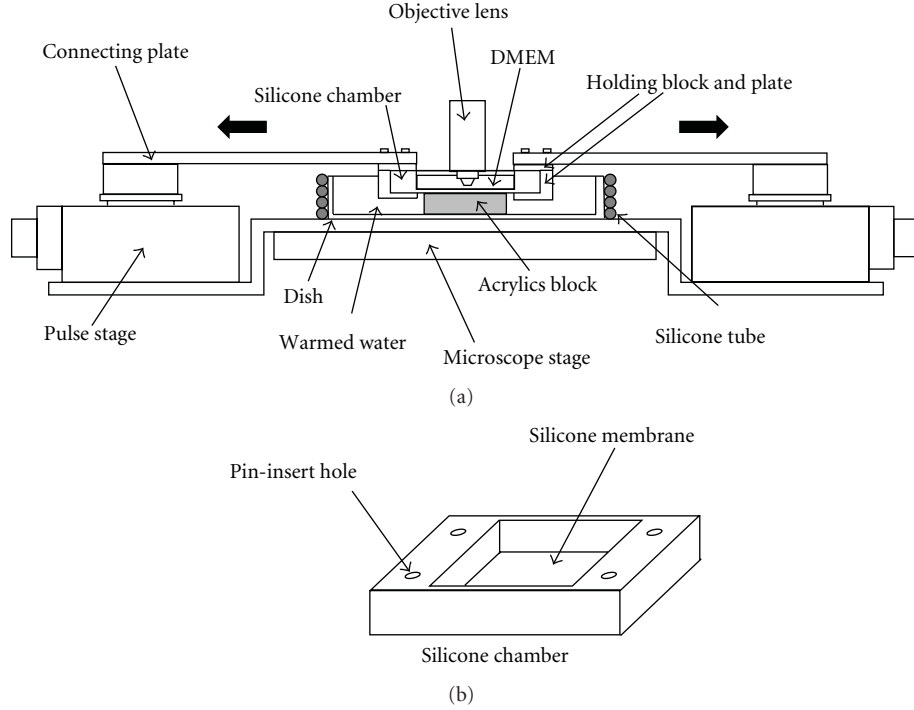


FIGURE 1: Experimental setup (a) with a silicone chamber (b). The right and left edges of the silicone chamber were grasped with a holding block and plate, and we inserted cylindrical pins into the four holes of the chamber to transmit a force from the connecting plates to the chamber. The chamber was stretched by moving the pair of pulse stages with a controller. The acrylic block kept the silicone membrane flat. A surfactant added to the water in the dish reduced the friction significantly between the acrylic block and the silicone membrane when stretching.

**2.5. Image Processing.** For unstretched cells, a candidate image of the cell bottom was chosen temporarily for each individual cell. Then a threshold value of the fluorescence intensity was obtained for a temporary cellular outline in which the intensity increased abruptly. A contour map was drawn for a series of sliced cell images using Igor Pro version 5 (WaveMetrics, Lake Oswego, OR, USA). The image that had the largest area surrounded by the outline was defined as the cell bottom because the substrate not stained with fluorescent markers was undetectable. Then the threshold of the cell was determined for that image.

Using the intensity threshold of the cell bottom, we redrew the contours for the other images at  $1\text{-}\mu\text{m}$  height intervals. From the average intensities of  $20 \times 20$ -pixel squares in a cell region, we sought a peak value in the unstretched state and then calculated the corresponding average value in the same square in the stretched state, ignoring the deformation of the square of interest. The threshold value in the stretched state was calculated by taking the product of the threshold in the unstretched state and the average intensity in the stretched state divided by the average intensity in the unstretched state. A contour map was drawn for the cell in the stretched state using this threshold.

**2.6. Geometric Modeling and Finite Element Analysis.** The coordinates of the points on the cellular outline were extracted manually to obtain a smooth outline for each image

extending from the bottom to the top of the cell until the outline was difficult to identify due to the lack of staining in the top region. The coordinates of the outlines of the cell of interest were imported into Rhinoceros version 3 (Robert McNeel and Associates, Seattle, WA, USA). Closed curves were drawn using the points of cell outlines on the planes with a height interval of  $1\text{ }\mu\text{m}$ . Using the loft command, a free surface of the cell was constructed from a set of closed curves of cell outlines and an additional very small circle that was  $0.5$  or  $1\text{ }\mu\text{m}$  above the top slice. Then, a solid 3D model of the cell was reconstructed using the cap command and was connected to a plate of the substrate ( $60 \times 60 \times 1.5\text{ }\mu\text{m}$ ) at the bottom of the cell. This solid model was imported into Abaqus/CAE (SIMULIA, Providence, RI, USA). The geometric model was partitioned into the two regions of cell and substrate, and the material properties in Table 1 were assigned to each of these. The model was meshed with 10-node tetrahedral hybrid elements (element type C3D10MH). The finite element analysis was carried out using Abaqus/Standard version 6.7 (SIMULIA).

We postulated that the strain energy function of the neo-Hookean material was given by

$$W = C(I_1 - 3), \quad (1)$$

where  $I_1$  is the first invariant of the right Cauchy-Green deformation tensor and  $C$  is the material constant, which is one-sixth of Young's modulus  $E$  for infinitesimal strains. The

TABLE 1: Material constant  $C$  (Pa) in (1) determined for various finite element models.

Model	Cytoplasm	Nucleus	Cortical layer	SF band	Substrate
$A_1, \dots, A_6$ (Figure 6)	129	129	N/A	N/A	211000
$B_1$	16.7	850	N/A	N/A	211000
$B_2$	417	850	N/A	N/A	211000
$B_3$	16.7	16.7	N/A	N/A	211000
$B_4$	16.7	167	N/A	N/A	211000
$B_5$	167	167	N/A	N/A	211000
$B_6$	167	1667	N/A	N/A	211000
$B_7$ (Figure 7(a))	129	850	N/A	N/A	211000
$B_8$ (Figure 7(b))	129	129	N/A	N/A	211000

Models  $B_i$  ( $i = 1, \dots, 8$ ) have the same profile as model  $A_1$  (see left in Figure 5(b)) and a region of the nucleus (see Figure 7).

material constant  $C$  was defined as 129 Pa for a cell [1] and 211 kPa for the substrate (model  $A_1$  in Table 1).

Displacements of  $\pm 4.53 \mu\text{m}$  (15.1% of the tensile strain) and  $\pm 0.90 \mu\text{m}$  (3.0% of the compressive strain) were applied to the sides of the substrate as boundary conditions. We obtained these strain values experimentally after all the image acquisitions were complete by averaging the relative displacements of four ink marks in a  $1 \times 1 \text{ mm}$  square while the silicone substrate was stretched. These marks were plotted at nine locations in a  $10 \times 10 \text{ mm}$  square at the center of the  $32 \times 32 \text{ mm}$  square membrane. The upper surface of the substrate (the cell bottom) was held at the same height to obtain the cellular deformation with respect to the substrate surface.

**2.7. Error Estimation for Cell Outlines at Various Heights.** The average error in the cellular outlines was estimated between the first and second pretest scans and between the experimental data and theoretical predictions. The error was calculated by adding all the areas surrounded by segments of the outline,  $S_1 + S_2 + \dots + S_n$  and dividing the sum by the perimeter of the shorter outline for the pretest scans or the perimeter of the theoretical model for the comparison between experimental and theoretical results (see Figure 2). Rigid body motion was removed by matching the cell bottom outline in an image of the stretched state to that obtained by applying the substrate deformation to the cell bottom outline for the unstretched state. For the finite element analysis results, the two-dimensional (2D) displacement was calculated for nodes at each height range in the unstretched state, that is,  $h = 0$  and  $n - 0.05 \mu\text{m} \leq h \leq n + 0.05 \mu\text{m}$ ,  $n = 1, 2, \dots$ , neglecting the component in the height direction.

**2.8. Sensitivity of the Cellular Deformation to the Elasticity of Intracellular Components: A Numerical Study.** We investigated the effects of the elasticity of the intracellular components numerically, focusing mainly on the cytoplasm and nucleus during the cell deformation. We prepared finite element models ( $B_1, \dots, B_8$ ) with the same geometry as model  $A_1$  and various material constant values corresponding to Young's moduli for the spread of endothelial cells reported by Caille et al. [1], to investigate the sensitivity of the cellular deformation to the elasticity of the cytoplasm

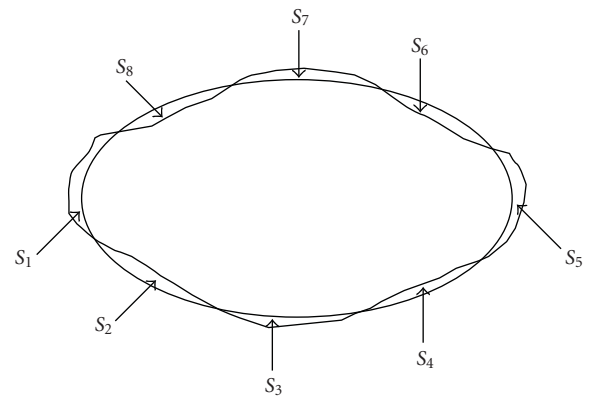


FIGURE 2: Estimate of the average distance between the two outlines of a cell at each height level:  $(S_1 + S_2 + \dots + S_n)/\text{perimeter}$ .

and nucleus (see Table 1). The cytoplasm and nucleus were completely connected at their boundaries. We compared the deformation of the cellular free surface obtained using the above analyses.

The sensitivity to the amount of substrate stretching was also investigated for model  $A_1$ . With  $x$  and  $y$  denoted as the axes of stretching and the transverse directions, respectively, the substrate strains were varied as  $(\varepsilon_x, \varepsilon_y) = (0.151, -0.031), (0.101, -0.031)$ , and  $(0.151, 0)$ .

### 3. Results

The ratio ( $r$ ) of the mean intensity in the central  $20 \times 20$ -pixel region in the second scan to that in the first scan was  $0.73 \pm 0.05$  (mean  $\pm$  SD) for the bottom images of four cells. Table 2 summarizes the error estimates for the cell outlines that were identified by the  $T_1$  and  $T_2$  threshold values. The  $r$ -value was used to compensate for fluorescence fading in the latter. In the bottom and middle regions, the average error was  $0.24$  to  $0.26 \mu\text{m}$ , or less than one-hundredth of the cell size. The top region had a large average error of  $0.44 \mu\text{m}$ , which was significantly different from the average values for the other regions ( $P < .05$  using a statistical  $t$ -test).

Figure 3 shows an example set of fluorescence intensity images of an endothelial cell stained with calcein-AM. The

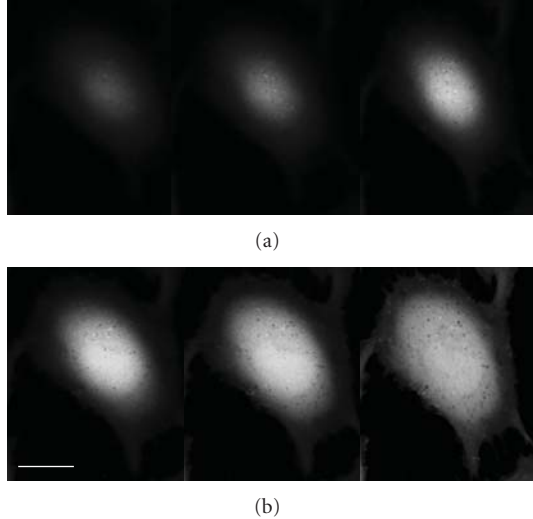


FIGURE 3: Fluorescence intensity images of an endothelial cell at heights of 5, 4, 3 (a, left to right), 2, 1, and 0  $\mu\text{m}$  (b, left to right), where 0  $\mu\text{m}$  is the cell bottom. The cell was stained with calcein-AM. Bar: 20  $\mu\text{m}$ .

TABLE 2: Distance error for the outlines of each cell between the first and second measurements using CLSM ( $n = 4$ ). The outline derived from the second measurement was compensated for fluorescent fading.

Region	Average ( $\mu\text{m}$ )	SD ( $\mu\text{m}$ )	Average $\pm$ 1.28 SD ( $\mu\text{m}$ )
Top	0.44	0.14	0.26/0.62
Middle	0.26	0.12	0.11/0.41
Bottom	0.24	0.09	0.13/0.35

The average  $\pm$  1.28 SD covers 90% of the error distribution.

images are located at heights of 5, 4, 3, 2, 1, and 0  $\mu\text{m}$ , where 0  $\mu\text{m}$  corresponds to the cell bottom. The intensity in the cell region tended to decrease at higher levels.

Figure 4(a) shows an example of the fluorescence intensity contours at the cell bottom (right image in Figure 3(b)), and Figure 4(b) shows a side view of a surface plot of the intensity. Based on the results in Figure 4(b), the intensity threshold for identifying the cell outline was determined to be 55.

Figure 5 shows the geometries of typical finite element models of measured single cells on the substrate before and after stretching. In the geometrical modeling, a small circle was added to the top of the cell at a height of 0.5 or 1.0  $\mu\text{m}$  above the highest outline. For the substrate, the edges to the right and left of the figure were stretched by 15.1%, whereas those on the other sides were compressed by 3.0%. The distribution of the maximum principal strain during stretching was plotted on the surfaces of the cell and substrate (right panels in Figure 5).

Table 3 shows the mean and SD of the nominal strain components in the stretching, transverse, and height directions at various height levels of the cell models in Figure 5. The strain components in the stretching and transverse

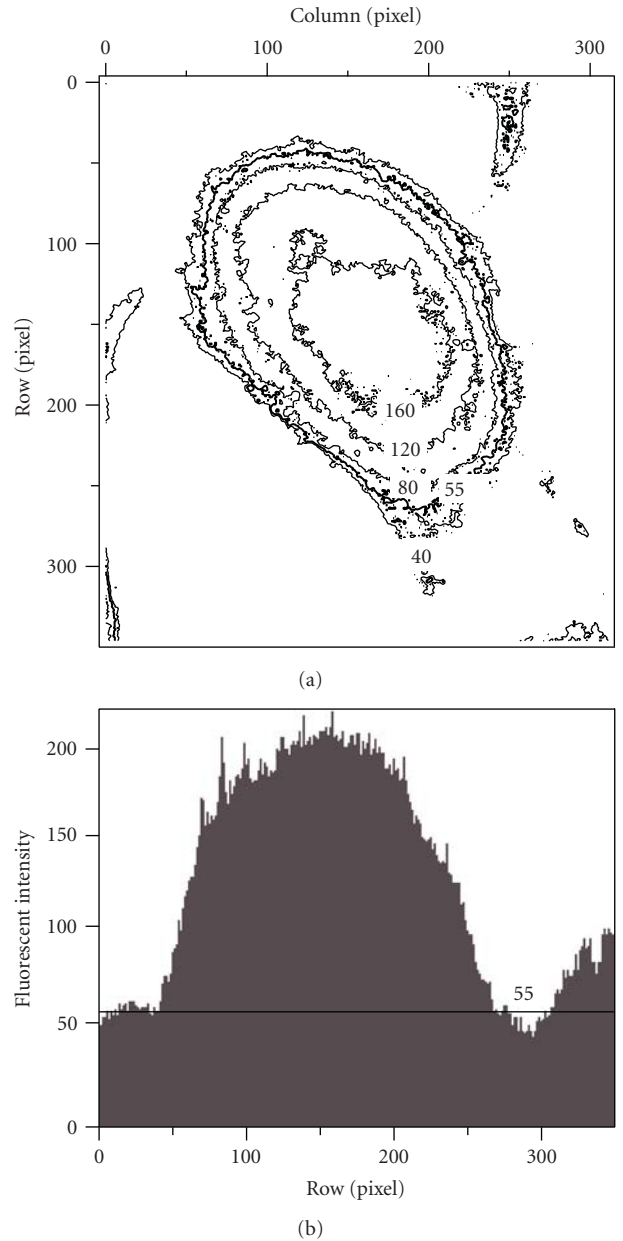


FIGURE 4: (a) Contours of the fluorescence intensity at the cell bottom (right image in Figure 3(b)). The thick contour corresponds to the threshold value 55. (b) A side view of the surface plot of the intensity was used to determine the threshold value of 55.

directions were almost equal to the strain of the substrate at the cell bottom; the former strain component decreased gradually, whereas the latter remained relatively constant with increasing height. The strain component in the height direction was 11% compressive in the bottom region and decreased toward zero with increasing height.

Figure 6 compares (a) the contours measured in the unstretched state (blue lines) to those smoothed to make the 3D geometric models (red lines) and (b) the contours measured in the stretched state (blue lines) to the ones predicted by the finite element analysis (red lines). In the

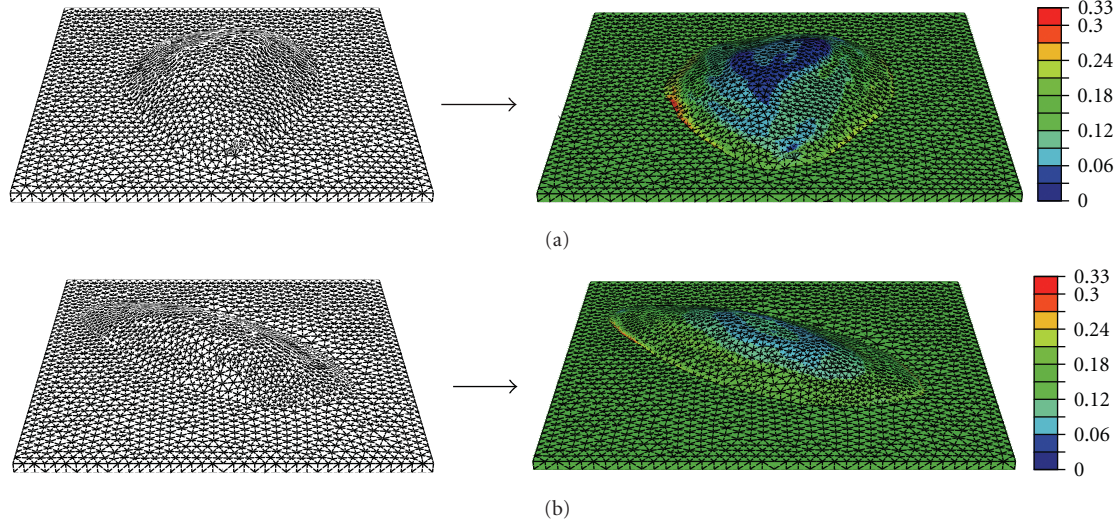


FIGURE 5: Geometry of typical finite element models of a cell on the substrate before and after stretching. In the left panels, the substrate is 60- $\mu\text{m}$ -square before stretching. In the right panels, the distribution of the maximum principal strain is also shown for cells when the substrate is stretched in the horizontal direction by 15.1%. The cell in the top line is model  $A_2$ , and its profile is made from the images in Figure 3. The cell in the bottom line is model  $A_1$ .

TABLE 3: Mean (SD) of nominal strain components in the stretching, transverse, and height directions at various height levels of cell models. The values in the upper and lower rows in the table were obtained from the upper cell model (height: 7  $\mu\text{m}$  in the unstretched state) and the lower cell model (height: 5.5  $\mu\text{m}$  in the unstretched state) in Figure 5, respectively. The substrate was deformed with strains of 15.1% in the stretching direction and -3% in the transverse direction. Extrapolated values for element nodes from integration-point values were averaged over each height range.

Height ranges ( $\mu\text{m}$ )	Stretching direction (%)	Transverse direction (%)	Height direction (%)
0	16.0 (1.0)	-3.0 (0.2)	-10.8 (0.4)
	15.8 (1.0)	-2.9 (0.3)	-10.7 (0.5)
0.95–1.05	13.4 (1.0)	-3.5 (0.6)	-8.3 (1.2)
	14.0 (1.0)	-3.9 (0.6)	-8.5 (1.0)
1.95–2.05	11.3 (1.6)	-3.5 (0.5)	-6.6 (1.5)
	13.5 (1.6)	-3.9 (0.8)	-8.2 (0.7)
2.95–3.05	10.3 (1.2)	-3.6 (0.4)	-5.9 (1.0)
	10.7 (0.6)	-3.9 (0.5)	-5.9 (1.0)
3.95–4.05	9.2 (1.0)	-3.6 (0.4)	-4.9 (0.9)
	9.3 (0.5)	-3.7 (0.3)	-4.8 (0.6)
4.95–5.05	7.4 (1.1)	-3.4 (0.4)	-3.6 (0.9)
	8.4 (0.8)	-3.7 (0.2)	-4.2 (0.6)
5.95–6.05	5.6 (1.4)	-3.0 (0.3)	-2.2 (1.1)
	N/A	N/A	N/A

figure, the horizontal direction is the stretching direction, and the height interval of each contour is 1  $\mu\text{m}$ . The cell was elongated in the substrate-stretching direction, with an associated slight compression in the transverse direction.

Table 4 summarizes the distance error between the outlines obtained from the measurements in the stretched state and those obtained from finite element analyses for six cells. In the third column, the relative error of the displacement is listed with respect to the mean 2D displacement of the cellular free surface at the same height level. For the lower

half of the cells, the average distance error was 0.41 to 0.55  $\mu\text{m}$ , or 24% to 48% of the mean displacement at the same height level, whereas these values were 0.86 to 1.28  $\mu\text{m}$  or 128% to 278% for the upper half of the cells. Such large relative errors resulted from dividing the distance error by a small mean displacement which decreased toward zero with increasing height.

Figures 7(a) and 7(b) compare the displacement in the height direction in the major and minor cross-sections between models  $B_7$  and  $B_8$  to illustrate the effect of nuclear

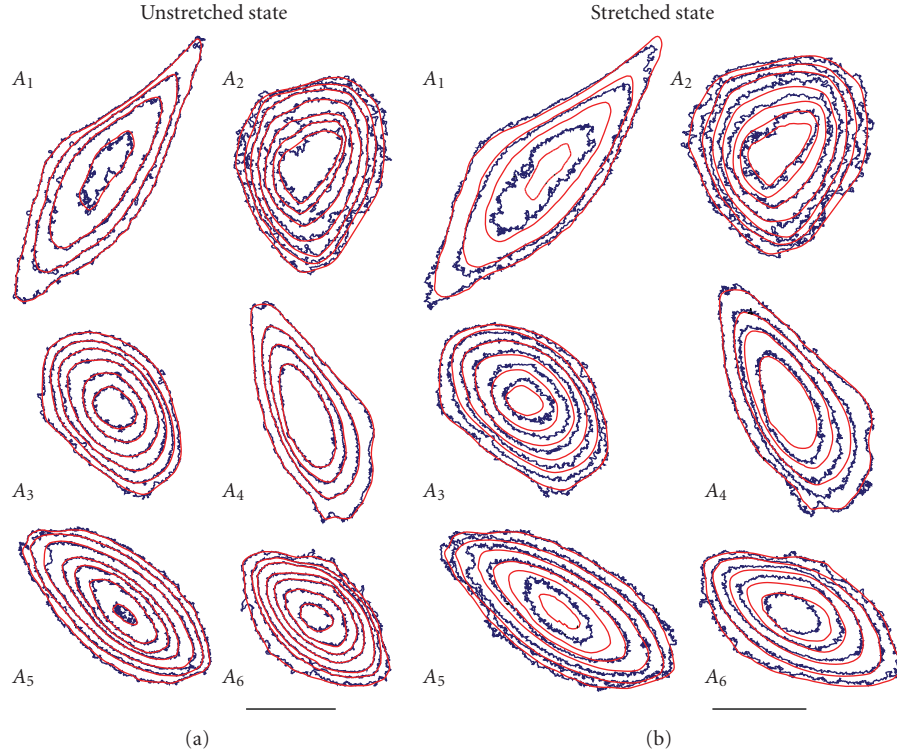


FIGURE 6: Comparisons of (a) contours measured in the unstretched state (blue lines) and those smoothed to make the 3D geometric models (red lines), and (b) contours measured in the stretched state (blue lines) and those predicted by the finite element analysis (red lines). The height interval between adjacent outlines is  $1 \mu\text{m}$ . Bar:  $20 \mu\text{m}$ .

TABLE 4: Distance error for the outline of each cell in the stretched state between the CLSM measurement and the results of the finite element analysis ( $n = 6$ ). At each height level for cells in the finite element analysis, the 2D mean displacement was calculated excluding the displacement component in the height direction.

Region	Average (SD) ( $\mu\text{m}$ )	Average (SD) with respect to mean displacement (%)
Top	1.28 (0.78)	278 (100)
Middle (upper half)	0.86 (0.43)	128 (65)
Middle (lower half)	0.55 (0.19)	48 (24)
Bottom	0.41 (0.12)	24 (7)

elasticity, which was (a)  $C = 850 \text{ Pa}$  and (b)  $C = 129 \text{ Pa}$ . In Figure 7(a), the deformed model  $B_7$  had two peak-displacement regions in the free-surface regions due to the stiff nucleus. In Figure 7(b), the deformed model  $B_8$  had almost horizontal isodisplacement lines, showing near uniform deformation at each height level. Figure 7(c) compares the displacement in the stretching direction in the major cross-section between models  $B_7$  (top panel) and  $B_8$  (bottom panel). The stiff nucleus restricted the deformations of itself and the cytoplasm in its vicinity, decreasing the height reduction of the cellular top and the nuclear elongation in the stretching direction when the substrate was stretched.

The sensitivity of the deformation of the cellular free surface to the elasticity of the cytoplasm and nucleus was evaluated. The difference between the 2D displacement of nodes

(height  $\geq 0$  in the unloaded state) on the cellular free surface in models  $B_1$  and  $B_2$  was  $0.069 \pm 0.077 \mu\text{m}$  or  $5.6 \pm 6.2\%$  (mean  $\pm$  SD) compared to the mean 2D displacement of these nodes. Among models  $B_1, \dots, B_8$ , the maximum difference was  $0.090 \pm 0.098 \mu\text{m}$  or  $7.2 \pm 7.9\%$  ( $B_1$  versus  $B_3, B_5$ , or  $B_8$ ; models  $B_3, B_5$ , and  $B_8$  had identical displacements). These errors were smaller than the spatial resolution of the images.

The sensitivity of the deformation of the cellular free surface to the magnitude of substrate stretching was also evaluated using model  $A_1$ . The difference between the substrate stretching and the mean 2D displacement of the nodes on the cellular free surface (height  $> 0$  in the unloaded state) was  $0.49 \pm 0.31 \mu\text{m}$  and  $33 \pm 21\%$  (mean  $\pm$  SD) between  $\varepsilon_x = 0.151$  and  $0.101$  with a constant  $\varepsilon_y = -0.031$ , and  $0.3 \pm 0.15 \mu\text{m}$  and  $15 \pm 10\%$  between  $\varepsilon_y = -0.031$  and  $0$  with a constant  $\varepsilon_x = 0.151$ .

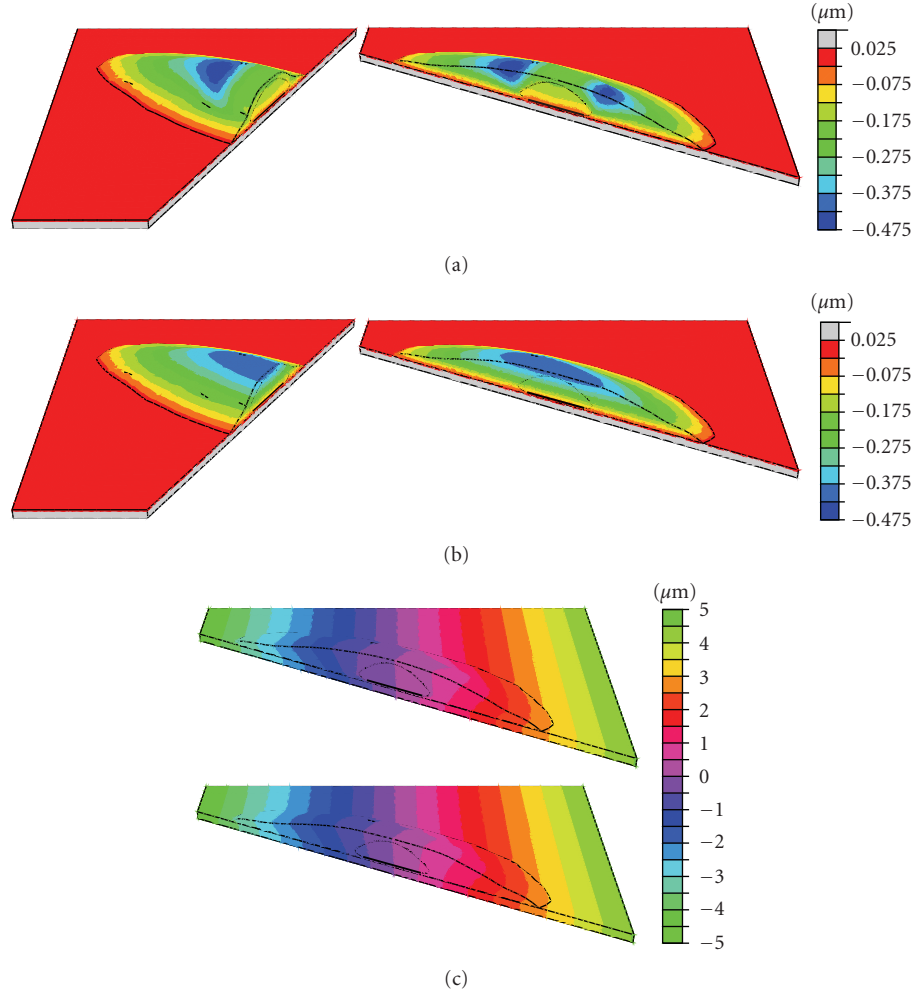


FIGURE 7: Comparisons of (a) the displacement in the height direction along the major and minor cross-sections for model  $B_7$  and (b) model  $B_8$ ; (c, top panel) displacement in the stretching direction along the major cross-section for model  $B_7$  and (c, bottom panel) model  $B_8$  under 15.1% stretching of the substrate associated with 3.0% transverse compression. In the figure, the substrate is stretched symmetrically in the right and left directions.

#### 4. Discussion

Published studies on the deformation of an entire cell typically analyzed cellular deformation independent of height position [2–6]. In confocal sectioning of chondrocytes, the outlines were compared between the uncompressed and compressed states only in the central plane of each cell [7]. Furthermore, in image-based 3D modeling of cells [8, 10, 16], the geometric change of an entire cell with the application of force or displacement that was seen in a numerical analysis was not compared with experimental results. By contrast, we obtained a contour map of cells in the unstretched and stretched states, enabling an analysis of the height-dependent deformation. Then, we compared the outline of cells on the substrate surface between the unstretched and stretched states, considering the deformation of the substrate. We also made finite element models and compared the theoretically predicted profiles with experimentally obtained outlines of cells at different heights.

These techniques will lead to more accurate understanding of the three-dimensional deformation of cells subjected to various forces and displacements.

Experimental and theoretical analyses of cellular deformation indicate that a hyperelastic material model is a practical approximation for describing the deformation of a cell after quasistatic stretching after completion of the stress relaxation. A finite element model by Yamada et al. [17] consisting of a neo-Hookean plasma membrane and incompressible cytoplasm caused slight buckling of the cellular free surface under uniaxial stretching of the substrate. Solid constituents in the cytoplasm must be requisite to support the flexible plasma membrane. Our model expressed the cytoplasm as a neo-Hookean material, which is more appropriate for describing the cell deformation.

To determine the morphometry of each cell, we dyed the cytoplasm with calcein-AM and determined a threshold value to obtain the cell boundary. Peeters et al. [18] showed a continuous change in the fluorescence intensity at the

boundary of a fluorescent bead. Thus, it is necessary to determine a threshold value for the cell boundary. We confirmed that well-determined thresholds in images before and after stretching indicate the same boundary. Although a threshold might define a larger or smaller region than the actual cell boundary, the cell body defined using the threshold is made of the same material.

There are fluorescent dyes that label the plasma membrane to identify a cell border. To the best of our knowledge, however, these have not been used for the purpose of extracting the 3D border from adherent cells. Such dyes might not be suitable for staining the fine details of all parts of the plasma membrane of adherent cells, both at the free surface and the cell bottom.

According to Table 4, our cell body model could be used to provide a practical reproduction of the cellular deformation, with possible small errors in the boundary for the lower half of the cell but significant errors for the upper half. This might have been due to a lack of volume with sufficient fluorescence intensity in the top region of a cell. By comparing the right image in Figure 3(b) and the contour labeled "55" in Figure 4(a), it is evident that lamellipodia and filopodia were not included in the 3D geometrical model. The volume of these podia was too small for the fluorescence intensity to be detected above the threshold.

A  $20 \times 20$ -pixel region in the cell bottom image was theoretically deformed to a  $23 \times 19.4$ -pixel region by the substrate deformation. Between these pixel regions, 70 pixels sharing 18% of the region were not identical. We ignored the error resulting from this difference because the  $20 \times 20$ -pixel region at the central portion of the cell bottom had a small fluorescence intensity gradient (see Figure 4). A complicated procedure would be required to determine the fluorescence fading rate between the unstretched and stretched states.

The basic models in the present study (models  $A_1, \dots, A_6$ ) assumed a homogeneous material due to the lack of data on microscopic or regional material properties. A cell consists of various organelles, such as the nucleus and cytoskeleton. Of these organelles, the nucleus has the greatest effect on the cell deformation. The displacement of the free surface differed by  $<0.1 \mu\text{m}$  or 7% of the mean displacement of nodes from that of the nucleus-free model under substrate stretching. This difference is at most one-fifth of the error in the lower region of cells in the experiment (see Table 4).

In reality, an endothelial cell consists of viscoelastic material [19], and its mechanical properties change when it remodels [20]. No well-defined 3D viscoelastic material model has yet been established, and the remodeling process has not been incorporated into a constitutive or structural model, which remains as a future problem.

In the present study, we only applied displacement boundary conditions and assumed a simple nucleus geometry, referring to the finite element model in Caille et al. [1]. Force boundary conditions, such as cell poking, should be considered to validate the material properties in the finite element model. The geometry and location of the nucleus are also important factors to describe the mechanical states of intracellular components. Modeling of cells on the basis of

double- or multistaining image data for the cytoplasm and nucleus, and considering stress fibers and focal adhesions, remain as areas of future study.

Prestress in the cytoskeletal network has been incorporated in the tensegrity model, which is a representative unit of the cytoplasm [16, 21]. So far, our finite element models represent homogenized behavior in the cytoplasm. Reproducing the microscopic stress distribution in cytoskeletal components is an area of future study that will also incorporate pretension in actin filaments.

## 5. Conclusion

This is the first study to measure and validate the 3D geometrical change of adherent cells when the substrate is stretched. The advantages of the 3D measurement and numerical deformation analysis are that they provide detailed data on the cellular deformation according to the height position, reflecting the cellular shape. We also analyzed the sensitivity of the elasticity of intracellular components on the cellular deformation. The present study provides a basis of adequate finite element modeling of cells under stretching of the vascular wall or substrate to investigate effects caused by the mechanical environment. Future studies should measure and model the cellular structure precisely and also reproduce the mechanical fields to correlate with intracellular responses such as stress fiber formation.

## Acknowledgment

This study was partially supported by a Grant-in-Aid for Scientific Research on Priority Areas (no. 15086213) from the Ministry of Education, Culture, Sports, Science, and Technology of Japan.

## References

- [1] N. Caille, O. Thoumine, Y. Tardy, and J.-J. Meister, "Contribution of the nucleus to the mechanical properties of endothelial cells," *Journal of Biomechanics*, vol. 35, no. 2, pp. 177–187, 2002.
- [2] K. A. Barbee, E. J. Macarak, and L. E. Thibault, "Strain measurements in cultured vascular smooth muscle cells subjected to mechanical deformation," *Annals of Biomedical Engineering*, vol. 22, no. 1, pp. 14–22, 1994.
- [3] N. Caille, Y. Tardy, and J.-J. Meister, "Assessment of strain field in endothelial cells subjected to uniaxial deformation of their substrate," *Annals of Biomedical Engineering*, vol. 26, no. 3, pp. 409–416, 1998.
- [4] S. I. Simon and G. W. Schmid-Schönbein, "Cytoplasmic strains and strain rates in motile polymorphonuclear leukocytes," *Biophysical Journal*, vol. 58, no. 2, pp. 319–332, 1990.
- [5] C. L. Gilchrist, S. W. Witvoet-Braam, F. Guilak, and L. A. Setton, "Measurement of intracellular strain on deformable substrates with texture correlation," *Journal of Biomechanics*, vol. 40, no. 4, pp. 786–794, 2007.
- [6] M. E. Wall, P. S. Weinhold, T. Siu, T. D. Brown, and A. J. Banes, "Comparison of cellular strain with applied substrate strain in vitro," *Journal of Biomechanics*, vol. 40, no. 1, pp. 173–181, 2007.

- [7] D. A. Lee, M. M. Knight, J. F. Bolton, B. D. Idowu, M. V. Kayser, and D. L. Bader, "Chondrocyte deformation within compressed agarose constructs at the cellular and sub-cellular levels," *Journal of Biomechanics*, vol. 33, no. 1, pp. 81–95, 2000.
- [8] T. Ohashi, H. Sugawara, T. Matsumoto, and M. Sato, "Surface topography measurement and intracellular stress analysis of cultured endothelial cells exposed to fluid shear stress," *JSME International Journal, Series C*, vol. 43, no. 4, pp. 780–786, 2000.
- [9] G. T. Charras and M. A. Horton, "Determination of cellular strains by combined atomic force microscopy and finite element modeling," *Biophysical Journal*, vol. 83, no. 2, pp. 858–879, 2002.
- [10] M. C. Ferko, A. Bhatnagar, M. B. Garcia, and P. J. Butler, "Finite-element analysis of a multicomponent model of sheared and focally adhered endothelial cells," *Annals of Biomedical Engineering*, vol. 35, pp. 208–223, 2007.
- [11] H. Yamada, D. Morita, J. Matsumura, T. Takemasa, and T. Yamaguchi, "Numerical simulation of stress fiber orientation in cultured endothelial cells under biaxial cyclic deformation using the strain limit hypothesis," *JSME International Journal, Series C*, vol. 45, no. 4, pp. 880–888, 2002.
- [12] H. Yamada and J. Matsumura, "Finite element analysis of the mechanical behavior of a vascular endothelial cell in culture under substrate stretch," *Transactions of JSME, Series A*, vol. 70, no. 5, pp. 710–716, 2004 (Japanese).
- [13] R. P. Jean, C. S. Chen, and A. A. Spector, "Finite-element analysis of the adhesion-cytoskeleton-nucleus mechanotransduction pathway during endothelial cell rounding: axisymmetric model," *Journal of Biomechanical Engineering*, vol. 127, no. 4, pp. 594–600, 2005.
- [14] P. Tracqui and J. Ohayon, "Transmission of mechanical stresses within the cytoskeleton of adherent cells: a theoretical analysis based on a multi-component cell model," *Acta Biotheoretica*, vol. 52, no. 4, pp. 323–341, 2004.
- [15] H. Yamada and H. Ando, "Orientation of apical and basal actin stress fibers in isolated and subconfluent endothelial cells as an early response to cyclic stretching," *Molecular and Cellular Biomechanics*, vol. 4, no. 1, pp. 1–12, 2007.
- [16] D. Stamenovic, "Effects of cytoskeletal prestress on cell rheological behavior," *Acta Biomaterialia*, vol. 1, no. 3, pp. 255–262, 2005.
- [17] H. Yamada, H. Ishiguro, and M. Tamagawa, "Mechanical behavior and structural changes of cells subjected to mechanical stimuli: deformation, freezing, and shock waves," in *Biomechanics at Micro- and Nanoscale Levels*, H. Wada, Ed., vol. 1, pp. 154–164, World Scientific, Singapore, 2005.
- [18] E. A. G. Peeters, C. V. C. Bouten, C. W. J. Oomens, D. L. Bader, L. H. E. H. Snoeckx, and F. P. T. Baaijens, "Anisotropic, three-dimensional deformation of single attached cells under compression," *Annals of Biomedical Engineering*, vol. 32, no. 10, pp. 1443–1452, 2004.
- [19] M. Sato, N. Ohshima, and R. M. Nerem, "Viscoelastic properties of cultured porcine aortic endothelial cells exposed to shear stress," *Journal of Biomechanics*, vol. 29, no. 4, pp. 461–467, 1996.
- [20] R. M. Nerem and D. Seliktar, "Vascular tissue engineering," *Annual Review of Biomedical Engineering*, vol. 3, pp. 225–243, 2001.
- [21] D. E. Ingber, "Tensegrity 1. Cell structure and hierarchical systems biology," *Journal of Cell Science*, vol. 116, pp. 1157–1173, 2003.

## Research Article

# Computer Aided Modeling of Human Mastoid Cavity Biomechanics Using Finite Element Analysis

**Chia-Fone Lee,<sup>1,2,3</sup> Peir-Rong Chen,<sup>2,3</sup> Wen-Jeng Lee,<sup>4</sup> Yuan-Fang Chou,<sup>5</sup> Jyh-Horng Chen,<sup>1,6</sup> and Tien-Chen Liu<sup>7</sup>**

<sup>1</sup> Institute of Biomedical Engineering, National Taiwan University, 790 Taipei, Taiwan

<sup>2</sup> Department of Otolaryngology, Buddhist Tzu Chi General Hospital, 790 Hualien, Taiwan

<sup>3</sup> Department of Medicine, Tzu Chi University, 790 Hualien, Taiwan

<sup>4</sup> Department of Medical Imaging, National Taiwan University Hospital, 100 Taipei, Taiwan

<sup>5</sup> Institute of Mechanical Engineering, College of Mechanical Engineering, National Taiwan University, 106 Taipei, Taiwan

<sup>6</sup> Institute of Electrical Engineering, College of Electrical Engineering and Computer Science, National Taiwan University, 106 Taipei, Taiwan

<sup>7</sup> Department of Otolaryngology, National Taiwan University Hospital, 100 Taipei, Taiwan

Correspondence should be addressed to Tien-Chen Liu, liuent@ntu.edu.tw

Received 27 April 2009; Accepted 16 June 2009

Academic Editor: João Manuel R. S. Tavares

Copyright © 2010 Chia-Fone Lee et al. This is an open access article distributed under the Creative Commons Attribution License, which permits unrestricted use, distribution, and reproduction in any medium, provided the original work is properly cited.

The aim of the present study was to analyze the human mastoid cavity on sound transmission using finite element method. Pressure distributions in the external ear canal and middle ear cavity at different frequencies were demonstrated. Our results showed that, first, blocking the aditus improves middle ear sound transmission in the 1500- to 2500-Hz range and decreases displacement in frequencies below 1000 Hz when compared with the normal ear. Second, at frequencies lower than 1000 Hz, the acoustic pressures were almost uniformly distributed in the external ear canal and middle ear cavity. At high frequencies, higher than 1000 Hz, the pressure distribution varied along the external ear canal and middle ear cavity. Third, opening the aditus, the pressures difference in dB between the middle ear cavity and external ear canal were larger than those of the closed mastoid cavity in low frequency (<1000 Hz). Finally, there was no significant difference in the acoustic pressure between the oval window and round window is noted and increased by 5 dB by blocking the aditus. These results suggest that our complete FE model including the mastoid cavity is potentially useful and can provide more information in the study of middle ear biomechanics.

## 1. Introduction

The human middle ear, including the tympanic membrane (TM) and the three auditory ossicles (malleus, incus, and stapes), is the mechanical system for sound transmission from the outer to the inner ear. A number of parameters such as the shape and stiffness of the TM, shape and volume of the external ear canal, and volume and pressure of the middle ear cavity directly affect acoustic-mechanical transmission through the middle ear. Changes in these parameters are often related to pathophysiologic conditions of the ear. The function of human hearing was investigated through the use of models. Among these models, the following models

for the middle ear represent the state of the art in the area. In general, there are two groups of models. The first group consists of electroacoustic circuit models based on the close link between acoustics and electrical engineering [1–8]. The second group is composed of structural mechanical models, mainly finite element (FE) models of the tympanic membrane and ossicles in humans [9–19] and in animals [20–22].

FE analysis is a computer simulation technique used in engineering and biomechanical analysis. The first FE model of the cat ear drum was reported by Funnell and Laszlo [20]. Since then, FE modeling of middle ear biomechanics has become a rapidly growing area of research. The advent

of high-resolution computed tomography (HRCT) made it possible to perform virtual instead of physical sectioning, and computer assistance facilitated the construction of reliable three-dimensional (3D) mathematical anatomic models. Using the combined technologies of FE analysis and 3D reconstruction of the middle ear from HRCT, we developed an FE model of the human middle ear with TM, ossicular bone, middle ear ligament, and middle ear boundaries [23]. This model was validated by comparing data from it to published experimental measurements, and it was tested in several otologic applications [24, 25].

To date, the FE model represents the precise geometric configurations of the ossicles, TM, and ligaments/muscles and has the capability for analysis of transmission of sound through the middle ear. The FE model should, however, also include the external ear canal, middle ear cavity, and cochlea to simulate the complete acoustic-mechanical transmission in the ear. Gan et al. [26] created a two-chamber FE model (ear canal and middle ear cavity) to further simulate middle ear mechanics. They reconstructed the 3D model from a set of histological images. But the mastoid cavity was not included in their FE model, possibly due to the limited size of the histologic images. Therefore, the effects of the mastoid cavity on the sound transmission were unclear. In this paper, we report a three-chamber (ear canal, middle ear, and mastoid cavity) FE model of the right ear, incorporating middle ear ossicles, external ear canal, middle ear cavity, and mastoid cavity. The geometry and surface generation were created from HRCT images obtained in a 47-year-old man. The model was then validated by comparing the results with published experimental measurements. Acoustic-structural coupled analysis was performed to determine the function of external ear canal, middle ear cavity, and mastoid cavity for acoustic-mechanical transmission through the human middle ear.

## 2. Materials and Methods

**2.1. High-Resolution Computed Tomography of Temporal Bone.** In this study, HRCT scanning was performed in a 47-year-old man with normal hearing and no previous otologic disorders. Otoscopic evaluation and pure tone audiometry were performed before HRCT examination. Temporal bone images obtained from the right ear were used for evaluation and reconstruction. The parameters of HRCT were described in our previous reports [23]. After capturing the images, the landmarks of the temporal bone were identified by an otolaryngologist and a radiologist (Figure 1(a)). All images were then transferred to an Amira visualization system for 3D reconstruction. Characteristic dimensions of the middle ear components were measured from the geometric model and compared with the published anatomic data and the data from our previous middle ear model [23].

**2.2. A 3D FE Model of the Middle Ear.** To prepare for FE analysis of the middle ear, the 3D model was translated into Patran (MSC Software, Perth, Australia) and ANSYS (ANSYS, Canonsburg, PA, USA): two commercially available

FE modeling packages. On the basis of the model, FE meshes of the ear were created using Patran. To facilitate the acoustic-structural coupled analysis, the mesh of the FE model was slightly modified in this study. The TM was meshed using 3 layers with a total of 4293 eight-node hexahedral solid elements instead of the shell element, because the coupled analysis requires the TM to be a 3D solid structure. Using one layer of shell element with acoustic-structure interfaces on both sides does not work because each node in the shell element would have the same pressure on each side of the shell. Finally, the vibration amplitudes in a mathematical model would be more precise and reasonable than one layer. Accordingly, the tympanic annulus was meshed using 3 layers with a total of 408 eight-node hexahedral solid elements instead of shell elements. Other meshes of the FE model remained the same in our previous middle ear model [23]. The ossicles, ligaments, and tendons are considered to be isotropic materials, whereas the TM is considered to be orthotropic material. The mechanical properties of the TM, ossicles, and joints in the model (Table 1) were adopted based on the results reported by Gan et al. [26]. The structural boundaries of the middle ear include the tympanic annulus, middle ear suspensory ligament, stapedial annular ligament, and cochlear fluid. Poisson's ratio was assumed to be 0.3 for all materials of the middle ear system. The element-damping matrix for the solid elements was expressed by

$$[C] = \alpha[M] + \beta[K], \quad (1)$$

where  $[M]$  and  $[K]$  were element mass and stiffness matrices of the solid and shell elements, respectively, and  $\alpha$  and  $\beta$  were the damping parameters. The action of the cochlear fluid on the stapes footplate was modeled as a set of 49 spring-dashpot elements distributed on the footplate as our previous work [23]. The detailed modeling for the boundary conditions is shown in Table 2 [26]. Figure 1(b) shows the FE model of the human right ear including the external ear canal, ossicles with attached ligaments/muscles, and tympanic cavity. Figure 1(c) shows the extended middle ear FE model to the aditus, mastoid antrum, and mastoid cavity. Figure 1(d) shows the tympanic cavity connects to the mastoid cavity through the aditus. The tympanic cavity and mastoid cavity were displayed transparently.

The air in the external ear canal, tympanic cavity, and mastoid cavity, which enclosed the air volume  $1442 \text{ mm}^3$ ,  $693 \text{ mm}^3$ , and  $6438 \text{ mm}^3$ , respectively, was meshed with acoustic elements. The external ear canal was expressed as a bent tube with rigid walls based on the dimensions obtained through HRCT scanning. The length of canal from the umbo to the entry section along the canal axis was about  $3.04 \text{ cm}$  and close to result of Egolf et al. [27]. The canal length superiorly was  $2.86 \text{ cm}$  and the length inferiorly was  $3.21 \text{ cm}$ . The cross-sectional area varied from  $65.45 \text{ mm}^2$  (near the TM) to  $96.19 \text{ mm}^2$  at the canal entrance. The published anatomical data for the external air volume would be ranged from  $830$  to  $1972 \text{ mm}^3$  [28]. A large difference in volume of the middle ear cavity

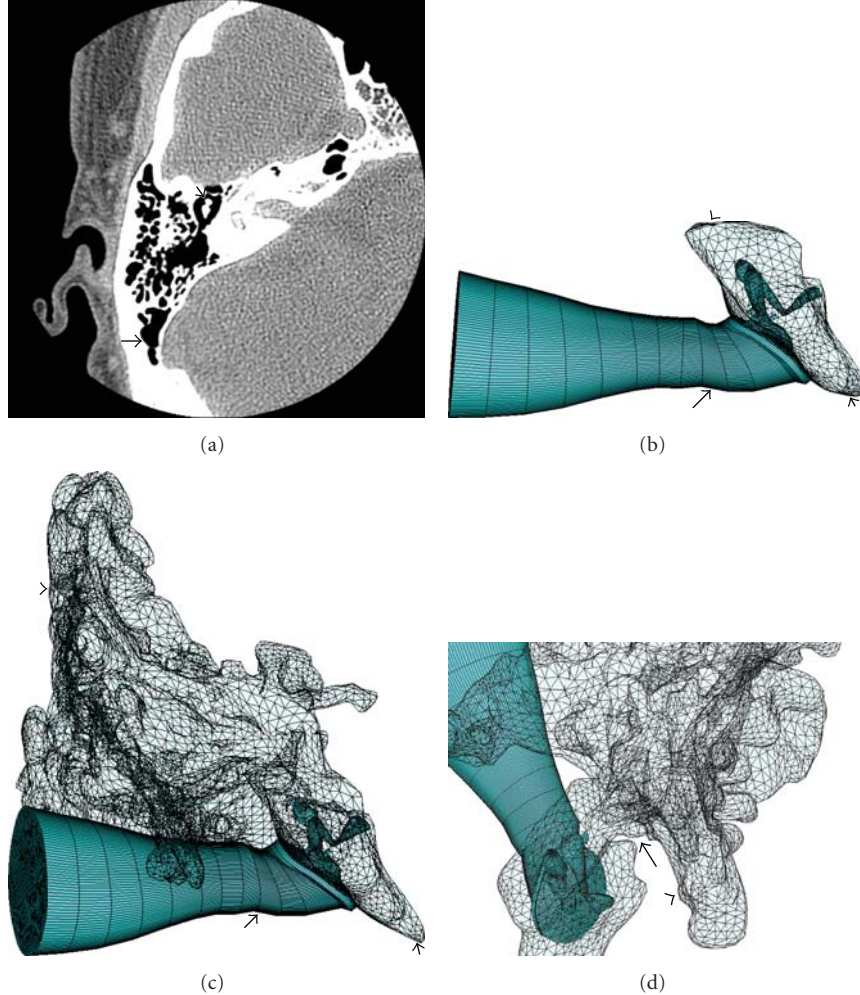


FIGURE 1: (a) Axial HRCT image of a normal right temporal bone, including ossicles (small arrow) and mastoid cavity (large arrow). (b) Finite element model of human right ear including tympanic membrane, ossicles (malleus, incus, and stapes), suspensory ligament/muscles, tympanic annulus, Eustachian tube (small arrow), external ear canal (large arrow) and tympanic cavity (arrow head) in anterior view. The tympanic cavity was expressed in transparency. (c) Finite element model of human right ear including tympanic membrane, ossicles (malleus, incus, and stapes), suspensory ligament/muscles, tympanic annulus, external ear canal (large arrow), Eustachian tube (small arrow), tympanic cavity, and mastoid cavity (arrow head) in anterior view. The middle ear cavity was expressed in transparency. (d) Finite element model of human right ear demonstrated the tympanic cavity was connected to the mastoid cavity (arrow head) through the aditus (arrow).

exists between individual subjects; this volume varies from 2000 to 22000 mm<sup>3</sup> [29]. The volume of tympanic cavity, however, is within the range of approximately 500–1000 mm<sup>3</sup> [30]. The volume of middle ear cavity is also within the range.

**2.3. FE Analysis.** The acoustic analysis in ANSYS (ANSYS Inc., Canonsburg, PA) programs only involves modeling the fluid medium and the surrounding structure [31]. A coupled acoustic analysis takes the fluid-structure interaction into account. The acoustic pressure in the fluid medium is determined by the wave equation. The interaction of the fluid and the structure at a mesh interface caused the acoustic pressure to exert a force applied to the structure and the structure motion produces an effective fluid load.

The governing finite element matrix equations produce the following:

$$\begin{bmatrix} M_s & 0 \\ \rho_0 R^T & M_f \end{bmatrix} \begin{bmatrix} \ddot{u} \\ \ddot{p} \end{bmatrix} + \begin{bmatrix} K_s & -R \\ 0 & K_f \end{bmatrix} \begin{bmatrix} u \\ p \end{bmatrix} = \begin{bmatrix} F_s \\ F_f \end{bmatrix}; \quad (2)$$

$p$  and  $u$  are the fluid pressure and the structure displacement, respectively.  $M_s$  is the structure mass matrix.  $K_s$  is the structure stiffness matrix. Correspondingly,  $M_f$  is the fluid mass matrix,  $\rho_0$  is the fluid density and  $K_f$  is the fluid stiffness matrix.  $F_f$  is the applied fluid pressure vector at the interface obtained by integrating the pressure over the area of the surface.  $R$  is a coupling matrix that represents the effective surface area associated with each node on the fluid-structure interface (FSI). Both the structural and acoustic load quantities that are produced at the acoustic-structure

TABLE 1: Mechanical properties used for the middle ear finite element model.

Structure	Data for the finite element model
<i>Eardrum</i>	
Density	$1.2 \text{ g/cm}^3$
Young's modulus (pars flaccida) (pars tensa)	$1.0 \times 10^7 \text{ N/m}^2$ $2.0 \times 10^7 \text{ N/m}^2$ (longitudinal direction) $3.5 \times 10^7 \text{ N/m}^2$ (radial direction)
Thickness	0.1 mm
<i>Malleus</i>	
Density	
Head	$2.55 \times 10^3 \text{ Kg/m}^3$
Neck	$4.53 \times 10^3 \text{ Kg/m}^3$
Handle	$3.70 \times 10^3 \text{ Kg/m}^3$
Young's modulus	$1.41 \times 10^{10} \text{ Kg/m}^2$
<i>Incus</i>	
Density	
Body	$2.36 \times 10^3 \text{ Kg/m}^3$
Short process	$2.26 \times 10^3 \text{ Kg/m}^3$
Long process	$5.08 \times 10^3 \text{ Kg/m}^3$
Young's modulus	$1.41 \times 10^{10} \text{ N/m}^2$
<i>Stapes</i>	
Density	$2.20 \times 10^3 \text{ Kg/m}^3$
Young's modulus	$1.41 \times 10^{10} \text{ N/m}^2$

TABLE 2: Structure boundary conditions used for the middle ear finite element model.

Middle ear components	Young's modulus or spring constant	Damping
Superior mallear ligament	$4.9 \times 10^6 \text{ N/m}^2$	$\alpha = 0 \text{ s}^{-1}$ $\beta = 0.0001 \text{ s}$
Lateral mallear ligament	$6.7 \times 10^6 \text{ N/m}^2$	
Posterior incudal ligament	$6.5 \times 10^6 \text{ N/m}^2$	
Anterior mallear ligament	$2.1 \times 10^7 \text{ N/m}^2$	
Posterior stapedial muscle	$5.2 \times 10^7 \text{ N/m}^2$	
Tensor tympani muscle	$7.0 \times 10^7 \text{ N/m}^2$	
Cochlear fluid	60 N/m	$0.06 \text{ N s/m}$
Stapedial annular ligament	9 N/m	0 N s/m

interface are functions of unknown nodal degree of freedom. Equation (2) implies that nodes on a fluid-structure interface have both displacement and pressure degree of freedom. The coupling matrix  $R$  also takes into account the direction of the normal vector defined for each pair of coincident acoustic and structural element faces that comprise the interface surface. The ear consists of solid structure and acoustic media that belong to different engineering disciplines and result in different boundary conditions. The air in the external ear canal and inside the middle ear cavity was modeled as acoustic elements and governed by an acoustic wave equation under the assumptions that the fluid is compressible and inviscid with uniform mean density and pressure:

$$\frac{1}{C^2} \frac{\partial^2 p}{\partial t^2} = \nabla^2 p, \quad (3)$$

where  $p$  is acoustic pressure,  $c$  is the speed of sound, and  $c = \sqrt{k/\rho_0}$  is the fluid medium,  $\rho_0$  the mean fluid density,  $k$  the bulk modulus of fluid, and  $t$  is the time. The speed of sound and density of the air were assumed as 343 m/s and 1.2 kg/m<sup>3</sup>, respectively. The acoustic absorption coefficient of FSI ( $\mu$ ) is defined as the fraction of absorbed acoustic energy to total incident energy [32, 33]. The absorption coefficient values are: 0.007 (TM), 0.02 (canal wall), 0.04 (cavity wall), 0.04 (ossicles), and 0.02 (ligament/muscles), respectively, [26].

**2.4. Validation of the FE Model.** The FE model was first tested and validated by comparing the responses of the middle ear system to harmonic pressure on the lateral surface of the TM between the FE analysis and published experimental measurements. Applied 120 dB SPL (20 Pa) to the canal was the same as McElveen's experiments, the harmonic

analysis was conducted on the model over a frequency range of 200–8000 by using ANSYS. McElveen et al. [34] conducted a total 6 temporal bone experiments to study the effect of mastoid cavity modification on middle ear sound transmission. Measurements of umbo displacement were made at 200 Hz intervals from 500 to 7000 Hz at the TM. After the initial baseline umbo displacement measurements, the aditus and antrum were blocked with a saline-filled balloon (Fogarty catheter) inserted through a hole in the tegmen made prior to taking the measurements and closed with clay. The balloon was inflated, the hole on the tegmen was closed with clay and the measurement was repeated. Peak-to peak umbo displacement, aditus open versus closed in McElveen's human temporal bone 3 was used for model validation.

### 3. Results

The umbo and predicted stapes footplate displacements while the aditus was open or blocked were converted to the frequency response curve of peak-to-peak displacement. Figure 2(a) contains both simulated umbo displacement and McElveen's data [34]. The predicted stapes footplate displacements are shown in Figure 2(b). Blocking the aditus decreases displacement in the low frequencies below 1000 Hz. Displacement in the mid-frequencies, 1500 and 2500 Hz, was increased by aditus blockage. The FE result showed a peak increase of vibration amplitude at an approximate frequency of 4000 Hz, with the amplitude response pattern similar to the experimental results and smoother than the experimental results. The effects of aditus blockage are small in this model. The effects might come from different volume sizes of mastoid cavity.

Figure 3(a) shows the FE model-predicted frequency response curves of relative acoustic pressure at several different locations in the canal and middle ear cavity (open the aditus) when a harmonic sound pressure of 120 dB SPL was applied at the canal entrance with the ear canal open. The position of measuring pressures in mastoid cavity is located in the central part and about 3.8 cm from the oval window, 4.2 cm from the round window and 3.1 cm from the incudostapedial joint. Likewise, Figure 3(b) demonstrates the FE model-predicted frequency response curves of relative acoustic pressure at several different locations in the canal and closed mastoid (blocking the aditus) cavity when a harmonic sound pressure of 120 dB SPL was applied at the canal entrance with the ear canal open. The FE result shows an 18-dB SPL increase of sound pressure around a frequency of 4000 Hz with a pressure response pattern similar to the experimental results. The small-dotted line in the figure is the experimental curve obtained by Shaw [35]. When the aditus was blocked (Figure 3(b)), the FE results showed that the pressure responses at four locations in the cavity were almost the same at frequencies below 4000 Hz. At frequencies higher than 4000 Hz, the difference of magnitude was within 5 dB. With open aditus (Figure 3(a)), the FE results showed that the pressure responses at five locations in the cavity were almost identical at frequencies below 700 Hz. At frequencies

higher than 700 Hz, the pressure difference in dB at the mastoid cavity was smaller than at the tympanic cavity. With open aditus, the pressure difference in dB differences between the canal entrance and middle ear cavity were larger than those of the closed cavity in low frequency (<1000 Hz). The FE acoustic pressure distributions in the ear canal and middle ear cavity were obtained at frequencies of 1000 and 8000 Hz, respectively, when a sound pressure of 120 dB SPL was delivered at the canal entrance (Figure 4). These results showed that acoustic pressure distributions in external ear canal and middle ear cavity were functions of frequency. At frequencies lower than 1000 Hz, the acoustic pressures were almost uniformly distributed in the external ear canal. At frequencies higher than 1000 Hz, the pressure distribution varied along the external ear canal and middle ear cavity. To demonstrate the pressure distribution in the middle ear cavity, we hid the external ear canal from the FE model and rescaled the magnitude bar (Figure 5). Likewise, the pressure distribution varied along the middle ear cavity.

### 4. Discussion

This model is the first one characterized by accurate structural dimensional and geometric shapes of middle ear structures, external ear canal, and mastoid cavity in the human. To confirm the validity of this model, the vibration amplitude of the umbo obtained with this model was compared with that derived from experimental measurement data. The predicted vibration amplitude of stapes was also shown. It was difficult to measure stapes vibration amplitude without opening the middle ear cavity. If a complete FE model of the middle ear were constructed, spatial variations in displacement on the TM, three ossicular vibrations, and spatial pressure distributions in the middle ear cavity and external ear canal could clarified without direct measurement, which are difficult to perform. It appeared that the results from the temporal bone experiments and the FE-predicted results match, namely that blocking the aditus improves middle ear sound transmission in the 1500 to 2500 Hz range and decreases displacement in the low frequencies below 1000 Hz when compared with the normal ear. Blocking the aditus eliminates the compliance of the mastoid cavity thus stiffening the TM and decreasing low frequency transmission, while opening the aditus increases middle ear cavity compliance, decrease TM stiffness and improves the low-frequency response. It has been reported that the effect of the mastoid cavity on the vibration of the TM is remarkable at low frequency and that it behaves like a spring [17, 30, 36]. The mastoid cavity would enhance sound transmission at low frequency (<1000 Hz) because the spring constant of the air in the mastoid cavity is inversely proportional to its volume. In McElveen's experimental results [34], blocking the aditus decreased transmission in two bones and increased transmission in one bone. The effects were small between results. Because of the small numbers of bone studies and the individual variations between bones, any conclusion about the clinical significance of the temporal bone results might be cautiously. The real

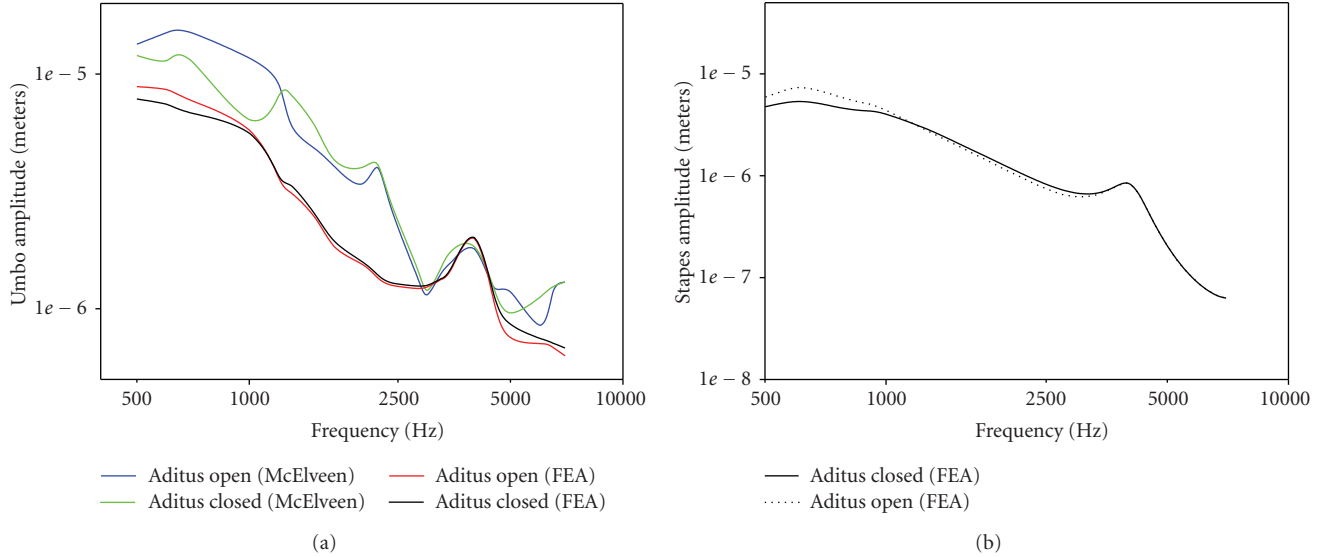


FIGURE 2: (a) Amplitude of umbo displacement versus frequency of the acoustic stimuli at 120 dB SPL (aditus open versus aditus closed) in the ear canal. The finite element model predicted umbo displacements were close to McElveen's experimental results. (b) Amplitude of predicted stapes footplate displacement versus frequency of the acoustic stimuli at 120 dB SPL (aditus open versus aditus closed).

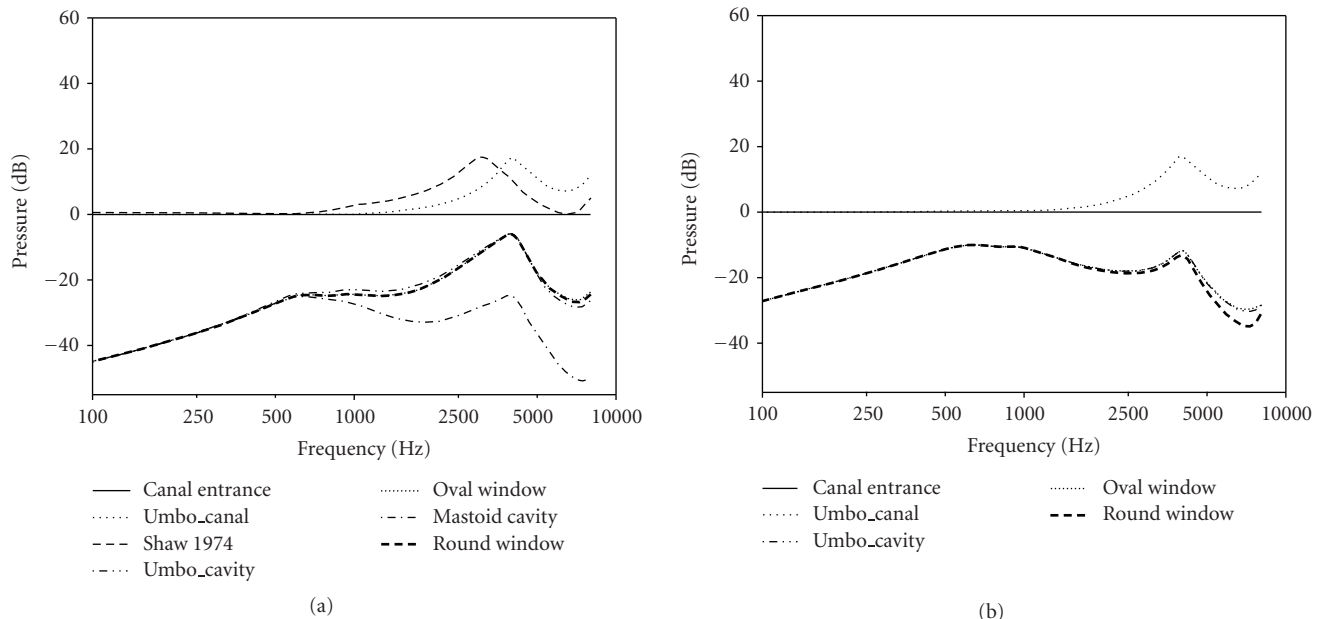


FIGURE 3: (a) FE frequency response curves of harmonic sound pressure at five locations inside middle ear cavity in the canal when aditus open. The 120 dB SPL was input at the canal entrance. The pressure magnitude was relative to the canal entrance. (b) FE frequency response curves of harmonic sound pressure at four locations inside middle ear cavity in the canal when aditus closed. The 120 dB SPL was input at the canal entrance. The pressure magnitude was relative to the canal entrance.

results could be affected by confounding variables including middle ear injury, stiffness of TM, and the mobility status of the ossicular chains. Therefore, more large numbers of temporal bone studies should be needed. Some small peaks in umbo displacement were noted in McElveen's results. According to umbo and stapes displacement measurements in temporal bones and living humans, in some 30% of ears, the tympanic membrane (TM) does not produce a smooth

frequency response over the important hearing frequencies [37]. Goode [38] reported that measurements of umbo displacement for a constant sound pressure level (SPL) at the TM in 22 frequencies between 200 and 6000 Hz showed peaks and valleys of more than 10 dB. This is possibly the result of previous injuries, both major and minor, to the TM, and perhaps to the ossicles [38]. Our FE model curve is lower than the experimental curve; however, the trend was similar

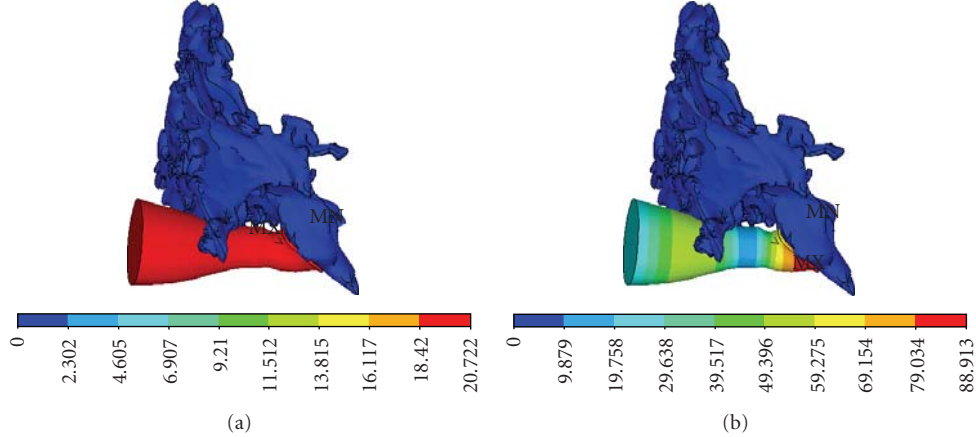


FIGURE 4: (a) Acoustic pressure distribution in the external ear canal and middle ear cavity predicted by the FE model at frequency of 1000 Hz. The sound pressure applied at the canal entrance was 120 dB SPL (20 Pa). The color bands represent different pressure levels relative to the canal entrance pressure. (b) Acoustic pressure distribution in the external ear canal and middle ear cavity predicted by the FE model at frequency of 8000 Hz. The sound pressure applied at the canal entrance was 120 dB SPL (20 Pa). The color bands represent different pressure levels relative to the canal entrance pressure.

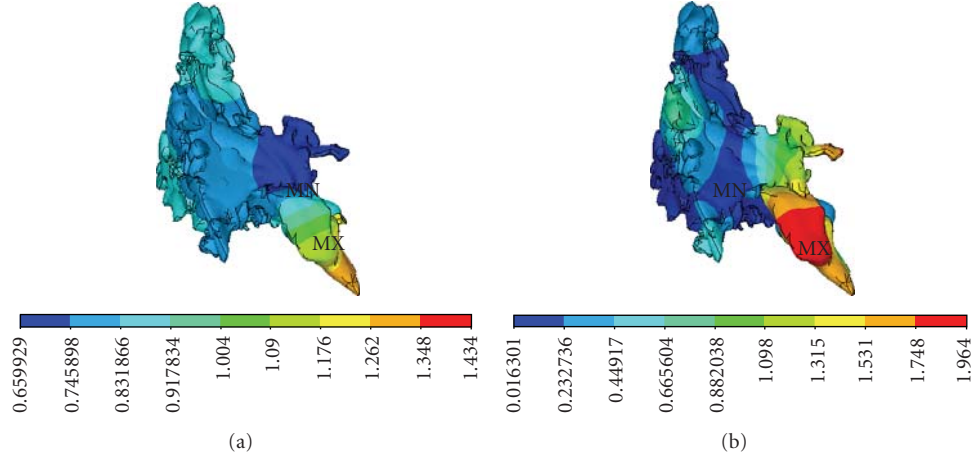


FIGURE 5: (a) Acoustic pressure distribution in middle ear cavity predicted by the FE model at frequency of 1000 Hz. The sound pressure applied at the canal entrance was 120 dB SPL (20 Pa). The color bands represent different pressure levels relative to the canal entrance pressure. The external ear canal was hidden. (b) Acoustic pressure distribution in middle ear cavity predicted by the FE model at frequency of 8000 Hz. The sound pressure applied at the canal entrance was 120 dB SPL (20 Pa). The color bands represent different pressure levels relative to the canal entrance pressure. The external ear canal was hidden.

to the experimental curve. The difference between the FE model and the experimental data may also result from the variations of individual temporal bone.

The acoustic pressure distributions in the external ear canal and middle ear cavity are spatially visualized and quantified by our FE model. Our result is the complete FE model, including the external ear canal, TM, ossicles, ligaments/muscles, tympanic cavity, and mastoid cavity. The results demonstrated that acoustic pressure distributions in ear canal and middle ear cavity are functions of frequency and different pressure measurement locations (Figure 3). The difference of acoustic pressure between the ear canal and middle ear cavity was caused by high acoustic impedance of the TM that was induced by attached middle ear and

inner ear structure. In the FE coupled analysis, the mastoid cavity effect was taken into the consideration for acoustic impedance. The air vibration in the middle ear cavity was lower than the air vibration in the canal. At low frequencies ( $f < 1000$  Hz), the acoustic pressure was uniformly distributed in the ear canal (Figure 4(a)). At high frequencies ( $f > 1000$  Hz), the pressure distribution varied along the canal (Figure 4(b)). The results reflect superposition of the incident and reflected sound wave from the TM and canal wall in the canal. The sound pressure difference in dB in the middle ear cavity is expected to vary with the air volume of the cavity (Figure 5). The acoustic pressure in the closed mastoid cavity is 10–25 dB lower than that of the canal entrance over the frequency range of 100–8000 Hz.

With open aditus, the acoustic pressure in the middle ear cavity is 10–45 dB lower than that of the canal entrance over the frequency range of 100–8000 Hz. This big drop of acoustic pressure in the cavity is caused by the high acoustic impedance of the TM induced by the attached middle ear and inner ear structure.

There was no significant difference of the acoustic pressure measured at different locations in the middle ear cavity at low frequency. As frequency increases, the pressure difference in dB between the oval window and round window is noted and increased by less than 5 dB. These results demonstrate that window pressure difference of the acoustic pathway for sound transmission to the inner ear is insignificant. The same conclusion is also obtained from experimental measurements on the temporal bone by Voss et al. [30], Peake et al. [4], and FE results by Gan et al. [26].

In conclusion, we created an FE model that not only includes the external ear canal and tympanic cavity but also the mastoid cavity, which can help us to understand the mastoid cavity effect on sound transmission. Tympanomastoid surgery modifies the middle ear cavity in various ways. These modifications might have important effects on sound transmission of the middle ear [34]. The acoustic effects of cavity modification by different types of tympanoplasty and mastoidectomy are difficult to determine clinically because TM and ossicular reconstruction are often undertaken as well. These results suggest that the FE model is potentially useful in the study of middle ear biomechanics and in the design and testing of the implantable middle ear hearing devices [39]. It would be possible to predict how middle ear function is affected by various kinds of middle ear pathologies and to understand how individual differences in middle ear structures affect that function prior to surgery. The model could be further improved in several aspects as finding more accurate boundary conditions and adding the structure of cochlea and the cochlear fluid into the model [40]. The overall thickness of TM (0.1 mm) was adopted in our model. Fay et al. [19] incorporates the measurement of the geometry of the ear canal, the 3D asymmetrical geometry of the eardrum and the details of the eardrum fiber structure. To develop a more comprehensive 3D FE model of human ear for multi-field FE analysis using detail TM structures and coupling the current FE model is our next goals. In addition, ligaments/tendons have a clear different behavior in tension and compression, in fact, stiffness in tension is much higher than in compression. The ligaments/tendons in the middle ear were traction free and essentially one-direction member. The behavior was dominant in axial direction. Therefore, if we chose the proper values, the hypothesis of isotropic behavior can be appropriated. A variety of mechanical tests have been reported to measure properties of soft tissue, such as uniaxial tensile, strip biaxial tension, and shear tests. In addition to experimental measurement, numerous material models have been developed to simulate the behavior of tissue in analytical ways [41]. Weiss et al. [42] used a hyperelastic material model with an exponential strain energy function to fit experimental curves of human medial collateral ligament through FEA. There are several nonlinear hyperelastic material models

available for analyzing mechanical properties of biological soft tissue, such as the Ogden, Mooney-Rivlin and Yeoh models. In the future, these methods can be used to improve our FE model of human ear. The further study will focus on how the alteration in structure, pathology, collagen fiber layer in tympanic membrane and different air volume sizes of mastoid cavity would affect the acoustic-mechanical transmission through the ear canal and middle ear to the inner ear.

## Acknowledgments

This work was supported by a grant from the National Taiwan University Hospital to T.C.L. (Grant no. NTUH 96A01) and a grant from the Buddhist Tzu Chi General Hospital to C.F.L. (Grant no. TCRD 9703, 9704, 9801, and 9802).

## References

- [1] Y. Onchi, "Mechanism of middle ear," *Journal of the Acoustical Society of America*, vol. 33, p. 794, 1961.
- [2] J. Zwislocki, "Analysis of middle ear function. I. Input impedance," *Journal of the Acoustical Society of America*, vol. 34, pp. 1514–1523, 1962.
- [3] C. A. Shera and G. Zweig, "Phenomenological characterization of eardrum transduction," *Journal of the Acoustical Society of America*, vol. 90, no. 1, pp. 253–262, 1991.
- [4] W. T. Peake, J. J. Rosowski, and T. J. Lynch III, "Middle-ear transmission: acoustic versus ossicular coupling in cat and human," *Hearing Research*, vol. 57, no. 2, pp. 245–268, 1992.
- [5] R. L. Goode, M. Killion, K. Nakamura, and S. Nishihara, "New knowledge about the function of the human middle ear: development of an improved analog model," *American Journal of Otology*, vol. 15, no. 2, pp. 145–154, 1994.
- [6] J. J. Rosowski and S. N. Merchant, "Mechanical and acoustic analysis of middle ear reconstruction," *American Journal of Otology*, vol. 16, no. 4, pp. 486–497, 1995.
- [7] H. Hudde and C. Weistenhöfer, "A three-dimensional circuit model of the middle ear," *Acustica*, vol. 83, no. 3, pp. 535–549, 1997.
- [8] S. Puria and J. B. Allen, "Measurements and model of the cat middle ear: evidence of tympanic membrane acoustic delay," *Journal of the Acoustical Society of America*, vol. 104, no. 6, pp. 3463–3481, 1998.
- [9] K. R. Williams and T. H. J. Lesser, "A finite element analysis of the natural frequencies of vibration of the human tympanic membrane I," *British Journal of Audiology*, vol. 24, no. 5, pp. 319–327, 1990.
- [10] H. Wada, T. Metoki, and T. Kobayashi, "Analysis of dynamic behavior of human middle ear using a finite-element method," *Journal of the Acoustical Society of America*, vol. 92, no. 6, pp. 3157–3168, 1992.
- [11] A. Eiber and A. Kauf, "Berechnete Verschiebung der Mittelohrknochen unter statischer Belastung," *HNO*, vol. 42, no. 12, pp. 754–759, 1994.
- [12] K. R. Williams, A. W. Blayney, and H.J. Rice, "Middle ear mechanics as examined by the finite element method," in *Middle Ear Mechanics in Research and Otosurgery: Proceedings of the International Workshop on Middle Ear Mechanics*, K. B. Hüttnerbrink, Ed., pp. 40–47, 1997.
- [13] H.-J. Beer, M. Bornitz, H.-J. Hardtke, et al., "Modelling of components of the human middle ear and simulation of their

- dynamic behaviour," *Audiology and Neuro-Otology*, vol. 4, no. 3-4, pp. 156–162, 1999.
- [14] M. Bornitz, T. Zahnert, H.-J. Hardtke, and K.-B. Hüttenbrink, "Identification of parameters for the middle ear model," *Audiology and Neuro-Otology*, vol. 4, no. 3-4, pp. 163–169, 1999.
- [15] P. J. Prendergast, P. Ferris, H. J. Rice, and A. W. Blayney, "Vibro-acoustic modelling of the outer and middle ear using the finite-element method," *Audiology and Neuro-Otology*, vol. 4, no. 3-4, pp. 185–191, 1999.
- [16] P. Ferris and P. J. Prendergast, "Middle-ear dynamics before and after ossicular replacement," *Journal of Biomechanics*, vol. 33, no. 5, pp. 581–590, 2000.
- [17] T. Koike, H. Wada, and T. Kobayashi, "Modeling of the human middle ear using the finite-element method," *Journal of the Acoustical Society of America*, vol. 111, no. 3, pp. 1306–1317, 2002.
- [18] R. Z. Gan, B. Feng, and Q. Sun, "Three-dimensional finite element modeling of human ear for sound transmission," *Annals of Biomedical Engineering*, vol. 32, no. 6, pp. 847–859, 2004.
- [19] J. Fay, S. Puria, W. F. Decraemer, and C. Steele, "Three approaches for estimating the elastic modulus of the tympanic membrane," *Journal of Biomechanics*, vol. 38, no. 9, pp. 1807–1815, 2005.
- [20] W. R. J. Funnell and C. Laszlo, "Modeling of the cat eardrum as a thin shell using the finite-element method," *Journal of the Acoustical Society of America*, vol. 63, no. 5, pp. 1461–1467, 1978.
- [21] W. R. Funnell, W. F. Decraemer, and S. M. Khanna, "On the damped frequency response of a finite-element model of the cat eardrum," *Journal of the Acoustical Society of America*, vol. 81, no. 6, pp. 1851–1859, 1987.
- [22] H. M. Ladak and W. R. J. Funnell, "Finite-element modeling of the normal and surgically repaired cat middle ear," *Journal of the Acoustical Society of America*, vol. 100, no. 2, pp. 933–944, 1996.
- [23] C.-F. Lee, P.-R. Chen, W.-J. Lee, J.-H. Chen, and T.-C. Liu, "Three-dimensional reconstruction and modeling of middle ear biomechanics by high-resolution computed tomography and finite element analysis," *Laryngoscope*, vol. 116, no. 5, pp. 711–716, 2006.
- [24] C.-F. Lee, L.-P. Hsu, P.-R. Chen, Y.-F. Chou, J.-H. Chen, and T.-C. Liu, "Biomechanical modeling and design optimization of cartilage myringoplasty using finite element analysis," *Audiology and Neurotology*, vol. 11, no. 6, pp. 380–388, 2006.
- [25] C.-F. Lee, J.-H. Chen, Y.-F. Chou, L.-P. Hsu, P.-R. Chen, and T.-C. Liu, "Optimal graft thickness for different sizes of tympanic membrane perforation in cartilage myringoplasty: a finite element analysis," *Laryngoscope*, vol. 117, no. 4, pp. 725–730, 2007.
- [26] R. Z. Gan, Q. Sun, B. Feng, and M. W. Wood, "Acoustic-structural coupled finite element analysis for sound transmission in human ear-pressure distributions," *Medical Engineering and Physics*, vol. 28, no. 5, pp. 395–404, 2006.
- [27] D. P. Egolf, D. K. Nelson, H. C. Howell III, and V. D. Larson, "Quantifying ear-canal geometry with multiple computer-assisted tomographic scans," *Journal of the Acoustical Society of America*, vol. 93, no. 5, pp. 2809–2819, 1993.
- [28] J. A. Donaldson and J. M. Miller, "Anatomy of the ear," in *Otolaryngology: Basic Sciences and Related Disciplines*, vol. 1, pp. 75–110, Saunders, Philadelphia, Pa, USA, 1973.
- [29] O. I. Molvær, F. M. Vallersnes, and M. Kringlebotn, "The size of the middle ear and the mastoid air cell. System measured by an acoustic method," *Acta Oto-Laryngologica*, vol. 85, no. 1-2, pp. 24–32, 1978.
- [30] S. E. Voss, J. J. Rosowski, S. N. Merchant, and W. T. Peake, "Acoustic responses of the human middle ear," *Hearing Research*, vol. 150, no. 1-2, pp. 43–69, 2000.
- [31] H. Debruyne and O. Lesaint, "About the significance of PD measurements in liquids," *IEEE Transactions on Dielectrics and Electrical Insulation*, vol. 10, no. 3, pp. 385–392, 2003.
- [32] A. D. Pierce, *Acoustic-An Introduction to Its Physical Principles and Applications*, McGraw-Hill, New York, NY, USA, 1981.
- [33] L. E. Kinsler, A. R. Frey, A. B. Coppens, and J. V. Sanders, *Fundamentals of Acoustics*, John Wiley & Sons, New York, NY, USA, 4th edition, 2002.
- [34] J. T. McElveen, C. Miller, R. L. Goode, and S. A. Falk, "Effect of mastoid cavity modification on middle ear sound transmission," *Annals of Otology, Rhinology and Laryngology*, vol. 91, no. 5, pp. 526–532, 1982.
- [35] E. N. G. Shaw, "The external ear," in *Handbook of Sensory Physiology*, W. D. Keidel and W. D. Nef, Eds., vol. 1, Springer, Berlin, Germany, 1974.
- [36] I. Kirikae, *The Structure and Function of Middle Ear*, Tokyo University Press, Tokyo, Japan, 1960.
- [37] R. L. Goode, K. Nakamura, and K. Gyo, "Comments on: acoustic transfer characteristics in human middle ears studied by a SQUID magnetometer method," *Journal of the Acoustical Society of America*, vol. 82, pp. 1646–1654, 1987.
- [38] R. L. Goode, "Current status and future of implantable electromagnetic hearing aids," *Otolaryngologic Clinics of North America*, vol. 28, no. 1, pp. 141–146, 1995.
- [39] C.-F. Lee, J.-H. Chen, Y.-F. Chou, and T.-C. Liu, "The optimal magnetic force for a novel actuator coupled to the tympanic membrane: a finite element analysis," *Biomedical Engineering*, vol. 19, no. 3, pp. 171–177, 2007.
- [40] R. Z. Gan, B. P. Reeves, and X. Wang, "Modeling of sound transmission from ear canal to cochlea," *Annals of Biomedical Engineering*, vol. 35, no. 12, pp. 2180–2195, 2007.
- [41] T. Cheng and R. Z. Gan, "Experimental measurement and modeling analysis on mechanical properties of tensor tympani tendon," *Medical Engineering and Physics*, vol. 30, no. 3, pp. 358–366, 2008.
- [42] J. A. Weiss, J. C. Gardiner, and C. Bonifasi-Lista, "Ligament material behavior is nonlinear, viscoelastic and rate-independent under shear loading," *Journal of Biomechanics*, vol. 35, no. 7, pp. 943–950, 2002.

## Research Article

# Recovery of Myocardial Kinematic Function without the Time History of External Loads

Heye Zhang, Bo Li, Alistair A. Young, and Peter J. Hunter

Bioengineering Institute, University of Auckland, Auckland 1142, New Zealand

Correspondence should be addressed to Heye Zhang, [heye.zhang@auckland.ac.nz](mailto:heye.zhang@auckland.ac.nz)

Received 30 April 2009; Accepted 24 June 2009

Academic Editor: João Manuel R. S. Tavares

Copyright © 2010 Heye Zhang et al. This is an open access article distributed under the Creative Commons Attribution License, which permits unrestricted use, distribution, and reproduction in any medium, provided the original work is properly cited.

A time-domain filtering algorithm is proposed to recover myocardial kinematic function using output-only measurements without the time history of external loads. The main contribution of this work is that the overall effect of all the external loads on the myocardium is treated as a random variable disturbed by the Gaussian white noise because the external loads of the myocardium are usually unknown in practical exercises. The kernel of our proposed algorithm is an iterative, multiframe, and sequential filtering procedure consisting of a Kalman filter and a least-squares filter. In our proposed implementation, the initial guess of myocardial kinematic function and residual innovation of all the state variables are first computed using a Kalman filter via state space equations only driven by the Gaussian white noise, and then the residual innovation is fed into a least-squares filter to estimate the total external loads of the myocardium. In the end, the initial guess of myocardial kinematic function is corrected using external loads provided by the least-squares filter. After the introduction of the whole structure of our algorithm, we demonstrate the ability of the framework on synthetic data and MR image sequences.

## 1. Introduction

Ischemic heart disease (IHD), or myocardial ischaemia, is a heart disease characterized by restricted blood supply to a certain area of muscle wall of the heart (myocardium), usually due to the blockage or shrinkage of the coronary artery. The restricted blood supply in the particular area of the myocardium can cause dysfunction or even permanent damage (infarction) if left untreated. In daily clinical practice, because of recent technological advances in cardiac imaging modalities, particularly magnetic resonance imaging (MRI), multislice computed tomography (CT), and echocardiography, assessment of the regional kinematic function of the myocardium has been largely applied to estimate the location of infarction and evaluate the seriousness of infarction by clinical specialists. In the medical image community, the idea to indicate IHD or infarction accurately via quantification of myocardial kinematic function has stimulated a huge number of computing algorithms to overcome practical difficulties, for example, relatively sparse spatial resolution and low temporal sampling rate of current imaging modalities. Most early works utilize pixel intensities

to evaluate myocardial kinematic function using one or even more imaging modalities [1–3], but the performance of these approaches varies largely because of the quality of the image. Recently, more and more feature points, such as tagging lines [4–6] or boundaries [7, 8], have been introduced as extra constraints to enhance the performance of intensity-based approaches, however, these intensity-based approaches still suffer from noise in the image data. The recovery of a dense motion field and deformation parameters for the entire myocardium from a sparse set of image-derived displacements/velocities seems an ill-posed problem which needs more physically meaningful constraints to obtain a unique solution in some optimal sense.

Therefore, a large number of strategies have been developed over the past two decades to introduce a variety of physically meaningful constraints into myocardial motion analysis, including notable examples of mathematically motivated regularization [9], deformable superquadrics [10], spatiotemporal B-Spline [11], Fisher estimator with smoothness and incompressibility assumptions [12], as well as finite-element method- (FEM-) based modal analysis [13–15]. From the introduction of biomechanical model-based

constraint [16–18] into the medical image community, the biomechanical model has attracted great attention because of its physiologically meaningful representation of myocardial dynamics. Contrary to previous frame-to-frame strategies with biomechanical model-based constraint, multiframe analysis strategies are gradually accepted since the periodic nature of myocardial dynamics is widely recognized. A number of image analysis works are motivated to adopt different biomechanical models from system point of view [19, 20]. In [21], the authors adopt system control theory [22] into medical image analysis by establishing a biomechanical model-based state-space framework for the multiframe estimation of the periodic myocardial motion: “the physical constraints take the role of the spatial regulator of the myocardial behavior and spatial filter/interpolator of the data measurements, while techniques from statistical filtering theory impose spatiotemporal constraints to facilitate the incorporation of multiframe information to generate optimal estimates of the myocardial kinematics in 2D.” The authors of [21] also apply a similar state-space filtering structure to estimate parameters of biomechanical models and myocardial motion simultaneously in [23, 24], but the filtering techniques in [23, 24] are realized by the extended Kalman filter and  $H_\infty$  filter, respectively. However, the computation of the Kalman filter has prohibited its popularity in 3D motion analysis. Thus, a reduced-rank Kalman filter was proposed to reduce the computation and estimate 3D myocardial kinematic function using a small number of principal modal components in [25]. In spite of the potential advantage of computational speed in [25], the effect of infarction might not be reflected by a small number of principal modal components because the influence of infarction to the whole myocardium could be localized and small. In the most recent works feedback, control techniques are also applied to estimate cardiac motion with a collocate state estimator [26] and parameters of biomechanical model using an extended Kalman filter [27] or  $H_\infty$  filter [28] separately. Despite sharing the same origin from the control theory, techniques in [26–28] still belong to the class of “deterministic models” as defined in [29], which are different from “stochastic models” in [21, 24]. However, the importance of external loads to the biomechanical model has not been addressed in multiframe medical image analysis in spite of a simple fact that the loading condition of each patient is not the same. Though different biomechanical constraints, from isotropic material to anisotropic material or from small deformation to large deformation, have been applied to myocardial motion analysis, most of works assume external loads of the biomechanical model as implicitly available forces from the image-derived boundary [18, 23, 24] or from a priori knowledge [26–28, 30]. In [31], external loads are obtained by a weighting between boundary-derived force from images and the electrical force from simulation. All these deterministic treatments of external loads are not patient-specific and a minor error in external loads might alert the dynamics of the same biomechanical model largely, which would damage the positive effect of model constraint eventually. In [32], a frame-to-frame statistical EM algorithm is applied to estimate the active forces, strains, and stresses

together despite the fact that the active forces are time-varying after the displacements of the myocardium are reconstructed by using the MRI-SPAMM tagging technique and a deformable model from images.

Inspired by the work [33] of input estimation in the inverse heating problem without the time history of external input, we proposed a biomechanical constrained sequential filtering framework which performs multiframe estimation of the nonrigid myocardial kinematic function and external loads of system simultaneously from medical image sequence. Our work is also developed from earlier works like the state-space-based motion recovery algorithms with the external loads constructed from boundaries [21, 24] and model-based filtering framework with external loads simulated from an electromechanical coupling model [30]. Contrary to previous approaches using deterministic approximation of external loads, our proposed framework treats external loads as a stochastic input after the biomechanical model is converted into a stochastic state-space representation, which is more rational because of largely unknown knowledge of external loads of each patient’s heart. Since the external loads in our approach are treated as a stochastic variable, we start to call external loads as input forces from here, which is a proper description in the stochastic control theory [22]. Therefore, the main difference of our work to previous multiframe estimation efforts is that rather than making ad hoc mathematical assumptions on the behavior of input forces, we allow uncertainties inside input forces because of unobservable loading condition of the heart, which is a better description of clinical situation from the stochastic control theory point of view. To achieve optimal estimation, we cyclically feed the updated estimation of input forces and imaging-derived data into the filtering framework until reaching largely data-driven convergence: a Kalman filter is first used to generate the residual innovation sequences without input forces, followed by a recursive least-square filter which is derived to use the sequences of residual innovation to compute values of input forces to the myocardium. Finally, myocardial kinematic function can be recovered by using the estimated input forces.

The outline of the paper is as follows. Section 2 describes the underlying myocardial dynamics, that is, the state-space representation of biomechanical model. The combination of the Kalman filter and the recursive least-square filter to recover input forces and correct the estimation of myocardial kinematic function is introduced in Section 3. We finally evaluate our algorithm in Section 4 and present the corresponding discussion and conclusion in Section 5.

## 2. Representation of Myocardial Dynamics

As a rule of thumb, the heart is a complex mechanical system in terms of large deformation and complicated material properties [34]. Many sophisticated models have been built over tremendous experiments to reproduce the behavior of the heart [34]. However, the complexities of these models limit their performance in understanding patient’s data because of high computational requirements. Furthermore,

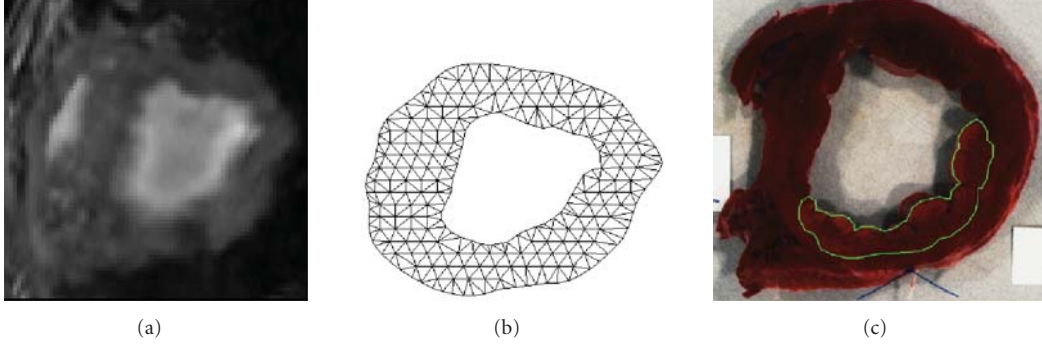


FIGURE 1: (a) Mid-ventricle MRI slice of a canine heart, (b) FEM representation of left ventricle constructed from MRI slice, and (c) TTC stained postmortem myocardium with the infarcted tissue highlighted.

some errors of initialization can be accumulated and amplified through the model dynamics because of the deterministic nature of these models. The purpose of this paper is to build a stochastic representation of myocardial dynamics, which relaxes the requirement of complexity and accuracy of the model by introducing uncertainties into the biomechanical model. In the following subsections, a deterministic finite-element representation of the myocardium using the law of linear elasticity is built, and then this representation plus its relation of measurement will be converted into stochastic state space equations. The reason to choose linear elasticity in this work is to construct a rationally realistic and computationally feasible analysis framework using imaging data and other available measurements, the structure, dynamics, and material of the myocardium. In the stochastic representation, the model errors, which could be caused by an imperfect model, insufficient discretization, or incorrect initialization, and measurement errors are properly addressed as noise terms in each state space equation. It is noted that other computational cardiac mechanics of materials also can be adopted into this stochastic framework.

**2.1. Law of Linear Elasticity.** In the current 2D implementation, we adopt an isotropic linear elastic material property, where the stress and strain relationship obeys Hooke's law [35], to approximate myocardial dynamics:

$$\sigma = S\varepsilon, \quad (1)$$

where  $\sigma$  is the stress tensor and  $\varepsilon$  is the strain tensor.

In the law of mechanical deformation, the infinitesimal strain tensor or Cauchy's strain tensor will be used to describe the deformation of an object with elastic material properties [35]. The infinitesimal strain tensor is calculated by

$$\varepsilon = \begin{bmatrix} \frac{\partial u_x}{\partial x} \\ \frac{\partial u_y}{\partial y} \\ \frac{\partial u_x}{\partial y} + \frac{\partial u_y}{\partial x} \end{bmatrix}, \quad (2)$$

where  $u_x$  is the displacement along  $x$  axis and  $u_y$  is the displacement along  $y$  axis in location  $(x, y)$ . In our 2D implementation, the plane strain condition is assumed. So the material constitutive matrix  $S$  is

$$S = \frac{E}{(1+\nu)(1-2\nu)} \begin{bmatrix} 1-\nu & \nu & 0 \\ \nu & 1-\nu & 0 \\ 0 & 0 & \frac{1-2\nu}{2} \end{bmatrix}, \quad (3)$$

where  $E$  is Young's modulus and  $\nu$  is Poisson's ratio [35]. In previous work [36], the values of these two myocardial material variables are specified as  $E = 75$  kpa and  $\nu = 0.47$ . In the following subsection, the finite-element representation, numerical discretization of the myocardium will be built using the material constitutive law established in the following subsection.

**2.2. Finite-Element Mesh of Myocardium.** The finite-element method has been a standard numerical method in solving partial differential equations. In this implementation, a triangular mesh is generated to represent a 2D myocardial slice, which is segmented in the MR images by a spatial-temporal active region model strategy [37]. The displacements of all the vertices in the mesh are calculated by an automatic nonrigid registration algorithm [38]. The finite-element mesh over one image plane and corresponding MR image are illustrated by Figure 1. Over the constraint of linear isotropic linear elasticity and the linear triangular finite-element mesh, the nodal displacement-based governing dynamic equation of each element is established under the principle of minimum potential energy. These equations finally can be assembled together in matrix form as [35]

$$M\ddot{U}(t) + C\dot{U}(t) + KU(t) = R(t), \quad (4)$$

where  $M$ ,  $C$ , and  $K$  are the mass, damping, and stiffness matrices, respectively,  $R$  is the load vector, and  $U$  is the displacement vector. Also  $M$  is a known function of material density and is assumed temporally constant for incompressible material,  $K$  is a function of material constitutive law, and is related to Young's modulus and Poisson's ratio which are again assumed constant. Finally,  $C$  is frequency dependent,

and we assume Rayleigh damping  $C = \alpha M + \beta K$  with small constant  $\alpha$  and  $\beta$  for the low damping myocardial tissue [35].

We need to point out that the input forces  $R$ , which are driven by electrical excitations and blood pressure, of the cardiac system are highly complicated. In clinical practice, observations of intraventricular blood pressures are too sparse and noisy. In spite of many efforts which are aimed to recover intracardiac electrical excitations from body surface potentials [39], the coupling of electrical excitations and active forces remain unknown in clinical practice because of difficulties. So it is a good strategy to assume the whole input forces to the cardiac system are a Gaussian random variable, which represents the unobservable nature. The uncertainties of input forces could be removed or reduced if new observations of input forces can be reliably collected in clinical practice in the future. In the ideal case, where the input forces are fully known, the least-square filter will vanish, and the Kalman filter will be able to recover the motion from images directly.

**2.3. Continuous State-Space Equations.** In order to apply our simultaneous estimation strategy as the structure in [33], the dynamic equation (4) needs to be transformed into a continuous stochastic state equation first. Let the state vector be  $x(t) = [U(t), \dot{U}(t)]^T$  and we can have

$$\dot{x}(t) = A_c x(t) + B_c W(t) + n(t), \quad (5)$$

where  $n(t)$  is the process noise which is an additive, zero-mean, white noise ( $E[n(t)] = 0$ ;  $E[n(t)n(s)'] = Q_n(t)\delta_{ts}$ , where  $Q_n$  is the process noise covariance). The input forces  $W(t)$ , the system matrices  $A_c$  and  $B_c$  are

$$\begin{aligned} W(t) &= [R(t)], \\ A_c &= \begin{bmatrix} 0 & I \\ -M^{-1}K & -M^{-1}C \end{bmatrix}, \\ B_c &= \begin{bmatrix} 0 \\ -M^{-1} \end{bmatrix}, \end{aligned} \quad (6)$$

the matrices  $B_c$  and  $W$  are not the same as the works in [21, 24] because we modify them for the estimation of input forces.

An associated measurement equation, which describes the observations provided by the images or imaging-derived data  $y(t)$  can be expressed in the form:

$$y(t) = Hx(t) + e(t), \quad (7)$$

where  $e(t)$  is the measurement noise which is additive, zero mean, and white ( $E[e(t)] = 0$ ;  $E[e(t)e(s)'] = R_e(t)\delta_{ts}$ , where  $R_e$  is the measurement noise covariance), independent of  $n(t)$ . Also,  $H$  is the measurement matrix which should be specified by the relation between state vector  $x(t)$  and measurement vector  $y(t)$ .

The process noise in (5) and the measurement noise in (7) are crucial in our stochastic approach. For example, linear elasticity is used in this work to approximate the dynamics

of the myocardium. However, it is not the most realistic material model for myocardial dynamics. The distance between linear elasticity and real myocardial dynamics will contribute to the process noise in (5), as uncertainties in model. Other errors, such as discretization and initialization, also can be treated as uncertainties in computational model, that is, the process noise in (5). How to obtain the proper process noise is still a great challenge and active topic in many state-space approaches [40]. So is the measurement noise. The process noise and the measurement noise are adjusted manually in this work because the aim of this work is to establish a proper stochastic framework to address the issue of input forces. However, it is worthy to explore the properties and effects of the process noise and the measurement noise of this framework in future work.

**2.4. Discrete State-Space Equations.** The MR images are usually collected distinctly over the whole cardiac cycle, so (7) should be discretized according to corresponding imaging instants. However, (5) also needs to be discretized so that it can be run in a computer. It should be noted that the continuous-discrete Kalman filter has been proposed to recover continuous myocardial kinematic function in [41]. However, the state equation is still discretized in a very small time step to approximate the effect of continuous dynamics in [41]. We discretize (5) and (7) over the imaging sampling interval  $T$ . Since the imaging sampling interval  $T$  is always a known constant, we can replace  $kT$  with  $k$  in

$$\begin{aligned} x(k+1) &= Ax(k) + BW(k) + n(k), \\ y(k) &= Hx(k) + e(k), \end{aligned} \quad (8)$$

$$A = e^{A_c T}, \quad B = A_c^{-1} (e^{A_c T} - I) B_c, \quad (9)$$

$A$  and  $B$  can be computed using Pade approximation [42]. The mathematical derivation of discrete state-space equations from continuous state-space equations is provided in [21]. Here if there are  $N$  sample nodes to represent the myocardium,  $A$  is a  $4N \times 4N$  matrix,  $B$  is a  $4N \times 2N$  matrix,  $x$  is a  $4N \times 1$  vector and  $W$  is a  $2N \times 1$  vector.

**2.5. Discrete State-Space Equations with Noisy Input Forces.** In order to model the input forces as a random variable, typically seen in estimation and tracking literature [33, 43], Equation (8) are transformed into stochastic equations with noisy input forces:

$$x(k+1) = Ax(k) + B[W(k) + n(k)], \quad (10)$$

$$y(k) = Hx(k) + e(k), \quad (11)$$

where  $n(k)$  and  $e(k)$  are the additive, zero-mean, white noises, but independent from each other. As can be seen in (10), the uncertainties in input forces  $W(k)$  are modeled by putting  $n(k)$  and  $W(k)$  together. So the input forces are disturbed by the noise  $n(k)$ , which represents the unobservable nature of the input force. Though the dynamic of state  $x$  is driven by the unobservable input forces now, we will provide an additional least-square filter to estimate the input forces and correct the estimation of state  $x$ .

### 3. Simultaneous Estimation of Myocardial Motion and Input Forces

To handle unknown input forces in (10), we propose a framework of simultaneous estimation of myocardial kinematic function and input forces, which consists of two parts: a Kalman filter and a recursive least-square filter. Let  $x^-$ ,  $\hat{x}(k)$ , and  $\bar{x}(k)$  denote the prediction of the true state  $x(k)$  without the input forces  $W(k)$ , the estimation of the true state  $x(k)$  without the input forces  $W(k)$ , and the estimation of the true state  $x(k)$  with the input forces  $W(k)$ , respectively. Then our proposed framework can be summarized below:

(1) Prediction without input forces:

$$\begin{aligned} x^-(k) &= A\bar{x}(k-1), \\ P^-(k) &= A\bar{P}(k-1)A^T + BQ_nB^T. \end{aligned} \quad (12)$$

(2) Update with measurements:

$$\begin{aligned} S(k) &= HP^-(k)H^T + R_e, \\ G(k) &= P^-(k)H^TS^{-1}(k), \\ \bar{P}(k) &= [1 - G(k)H]P^-(k), \\ \bar{z}(k) &= Y(k) - HX^-(k), \\ \bar{x}(k) &= x^-(k) + G(k)\bar{z}(k), \end{aligned} \quad (13)$$

where the covariance of residual innovation sequence  $\bar{z}(k)$  is  $S(k)$ .

(3) Estimation of input forces:

$$\begin{aligned} \Phi_S(k) &= H[AM_S(k-1) + I]B, \\ \Sigma &= \Phi_S(k)\gamma^{-1}P_b(k-1)\Phi_S^T(k) + S(k), \\ K_b(k) &= \gamma^{-1}P_b(k-1)\Phi_S^T(k)\Sigma^{-1}, \\ P_b(k) &= [I - K_b\Phi_S(k)]\gamma^{-1}P_b(k-1), \\ W(k) &= W(k-1) + K_b(k)[\bar{Z}(k) - \Phi_S(k)W(k-1)]. \end{aligned} \quad (14)$$

(4) Correction with input forces:

$$\begin{aligned} M_s(k) &= [I - G(k)H][AM_S(k-1) + I], \\ \hat{x}(k) &= \bar{x}(k) + M_s(k)BW(k). \end{aligned} \quad (15)$$

The detailed derivation of steps (3) and (4) can be found in the appendix of [33]. However  $\bar{P}(k)$  is the error covariance matrix of the Kalman filter without information of input forces,  $S(k)$  is the residual innovation covariance,  $G(k)$  is the Kalman gain,  $\Phi_S(k)$  and  $M_s(k)$  are the sensitivity matrices,  $\bar{z}(k)$  is the residual innovation,  $P_b(k)$  is the error covariance of the estimated input vector  $W(k)$ , and  $K_b(k)$  is the correction gain for the updating  $W(k)$ . Also,  $\Phi_S(k)$ ,  $M_s(k)$ ,  $K_b(k)$ , and  $P_b(k)$  are a  $4N \times 2N$  matrix, a  $4N \times 4N$  matrix, a  $4N \times 4N$  matrix, a  $2N \times 4N$  matrix, and a  $2N \times 2N$  matrix, respectively, if there are  $N$  nodes in the triangular mesh of the myocardium. When  $\gamma = 1$ , we will get the

usual sequential least-square estimator, which is only suitable for a constant input force system. In the system with time-varying input forces, however, we like to prevent  $K_b(k)$  from reducing to zero. This is accomplished by introducing the factor  $\gamma$ . By setting  $0 < \gamma < 1$ ,  $K_b(k)$  is effectively prevented from shrinking to zero. Hence, the corresponding least-square filter can preserve its updating ability continuously. However, the inherent data truncation effect brought by  $\gamma$  causes variance increases in  $W(k)$  in the estimation problem resulting from noise. Thus, it is necessary to compromise between fast adaptive capability and the loss of estimate accuracy.

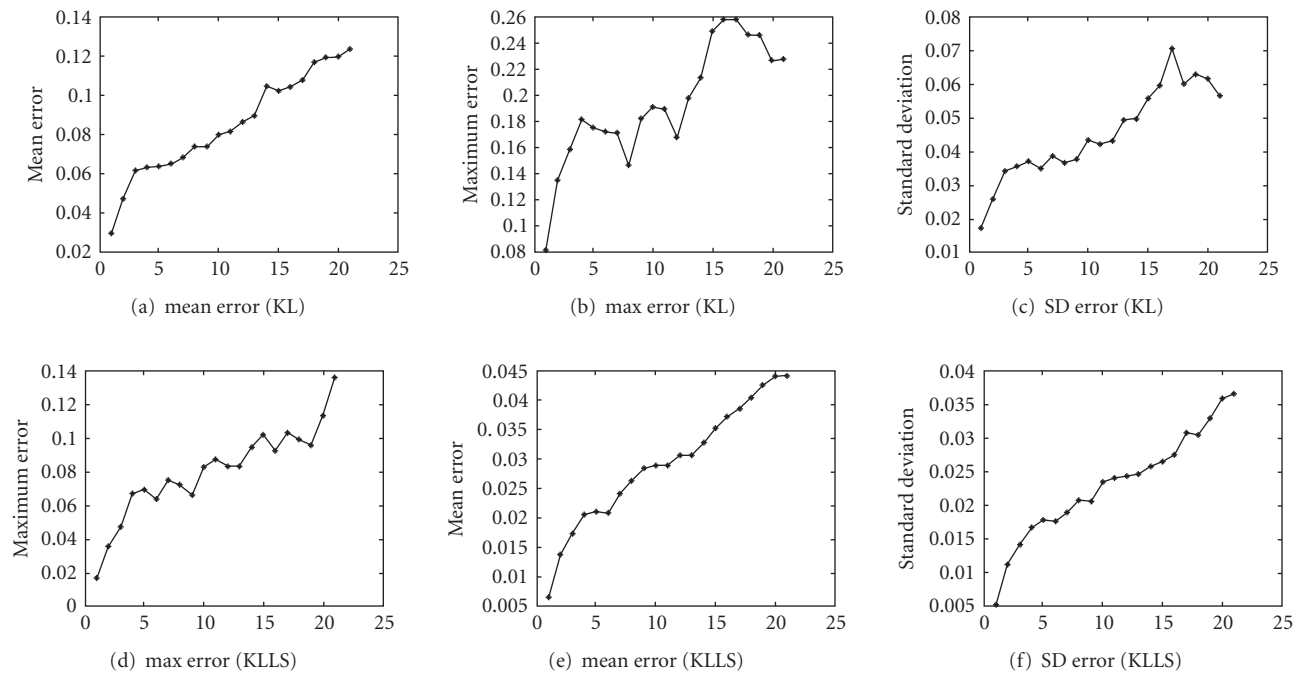
Here, the Kalman filter is used to generate  $G(k)$ ,  $S(k)$ , and  $\bar{z}(k)$ , based on the state transition matrix  $A$ , input matrix  $B$ , and process and measurement noise covariance matrices  $Q_n$  and  $R_e$ . The least-square filter is derived to compute the onset time histories of the unknown input forces by utilizing the Kalman gain, residual innovation covariance  $S(k)$ , and residual innovation  $\bar{z}(k)$ . In addition, our framework is initialized by setting  $\bar{x}(-1) = 0$ ,  $W(-1) = 0$ , and  $M_S(-1) = 0$ . Since  $\bar{P}(-1) = p \times I_{4N \times 4N}$  and  $P_b(-1) = p_b \times I_{4N \times 4N}$  are normally assumed, where  $I$  is the identity matrix,  $p$  and  $p_b$  are the constant scalar, we initialize  $p$  and  $p_b$  as large numbers, such as  $10^6$  and  $10^2$ , respectively. This has the effect of treating the errors in the initial estimation of the input forces as large. However, after a few time steps, the estimation results should converge to their actual values rapidly if the state-space equations can capture the system dynamics quickly. This also shows that the present technique is not sensitive to the errors in the initial estimation. Though  $Q_n$  and  $R_e$  should be determined according to the noise level in the input forces and measurements, it is adjusted manually in this work according to empirical experiences.

## 4. Experiments

**4.1. Synthetic Data.** Our filtering strategy is first validated in synthetic data of a 2D object undergoing body forces only in the vertical direction ( $y$ -axis) with the bottom being fixed. The magnitude of body forces in each triangular element is decided by the area of that element by setting the density of body forces to 1 Newton. Material properties and other parameters are taken as Young's modulus  $E = 75$  kpa, Poisson's ratio  $\nu = 0.4$ , damping coefficients  $\alpha = 0.01$  and  $\beta = 0.1$ . The simulation is generated by a general purpose finite-element software, Abaqus. However 21 sampling frames of the motion are acquired, with displacements and velocities in all nodes, as the ground truth. Then Gaussian noises (20 dB) are added in all nodes to generate noisy measurements. A single Kalman filter (KL) and our framework of the Kalman filter and the least-square filter (KLLS) are implemented for the estimation of kinematic function. In KL implementation, the nodal displacements with noise in the top of the synthetic object are used to construct input forces through the penalty method, which is the same as the work in [21]. The setting of process noise  $Q_n$  and measurement noise  $R_e$  is the same in KL and KLLS in order to maintain a fair comparison, where  $Q_n = 10^{-5}$  and  $R_e = 10^{-8}$ . In KLLS,  $\gamma$  is set to 0.82. The displacement magnitude and strain maps of the ground truth

TABLE 1: Differences between the ground truth and the KL/KLLS estimated nodal positions.

Method	Frame number	Maximum error	Mean error	Standard deviation
KL	number 4	0.181	0.063	0.036
	number 8	0.146	0.074	0.037
	number 12	0.168	0.086	0.043
	number 16	0.258	0.104	0.060
	number 20	0.227	0.120	0.062
KLLS	number 4	0.067	0.021	0.017
	number 8	0.072	0.026	0.021
	number 12	0.083	0.013	0.024
	number 16	0.093	0.031	0.028
	number 20	0.114	0.044	0.036

FIGURE 2: (a) Mean, (b) max, and (c) standard deviation errors of the Kalman filter; (d) mean, (e) max, and (f) standard deviation errors of the Kalman filter and the least-square filter; all the  $x$  axis in the figures are the numbering of frame.

and the estimated results for quantitative assessments and comparisons of two filtering strategies are shown in Figure 3. Overall point-by-point positional errors are measured by their mean and standard deviation. The mean is calculated by

$$\text{Mean} = \frac{1}{N} \sum_i^N |\text{Est}_i - \text{Tru}_i| \quad i = 1, \dots, N, \quad (16)$$

where  $N$  is the number of nodes, Est is the estimated nodal value and Tru is the true nodal value. The standard deviation is calculated by

$$\text{SD} = \sqrt{\frac{1}{N} \sum_i^N (\text{Est}_i - \text{Mean})^2} \quad i = 1, \dots, N, \quad (17)$$

where  $N$  is the number of nodes and SD is the standard deviation. The growth of errors in KL and KLLS are illustrated in Figure 2, which shows errors of KLLS has stable behavior in comparison with KL. From Table 1, we also can see the quantitative measures of accumulated errors: such as in frame #20, the maximum, mean and standard deviation of errors of KLLS are 0.114, 0.044, and 0.036; the maximum, mean and standard deviation of errors of KL are 0.227, 0.120, and 0.062. The comparison between the estimated forces and ground truth are also shown in Table 2. Overall, our framework shows superior performance over the same measurements with the same noise level because of simultaneous estimation of kinematic function and input forces, but a single Kalman filter with boundary forces fails here because of wrong input forces dominated by noisy displacements in boundary.

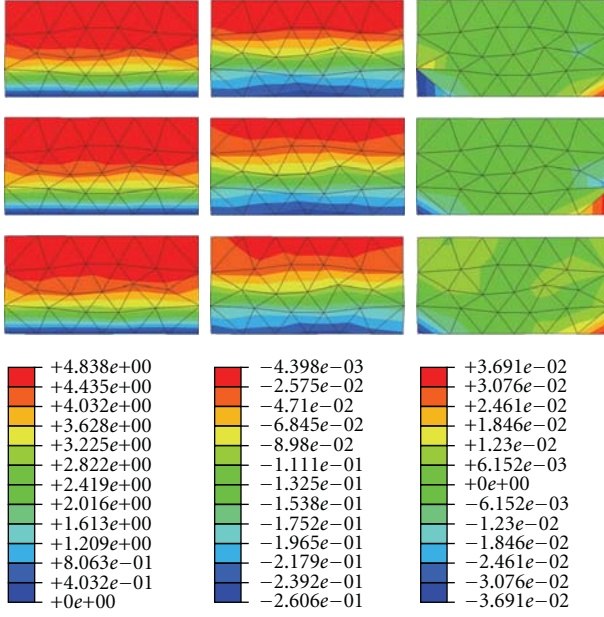


FIGURE 3: From first row to fourth row: ground truth, estimation results of our framework, estimation results of a single Kalman filter and color scale mapping. From first column to third column: magnitude maps of displacement, strain maps in  $y$ -axis and strain maps in  $xy$ -axis.

TABLE 2: Comparison of the magnitude to total nodal forces between ground truth and estimation (KLLS).

Frame number	Ground truth	Estimated result
number 4	3.82e + 003	3.24e + 003
number 8	3.81e + 003	3.22e + 003
number 12	3.78e + 003	2.99e + 003
number 16	3.73e + 003	2.99e + 003
number 20	3.70e + 003	2.89e + 003

**4.2. Canine Image Data.** The MR image data and representation of left ventricle (LV) are displayed in Figure 1. Myocardial displacements and velocities can be extracted using our previous multiframe algorithm [24] or other algorithms [19, 38, 44]. The infarcted tissue is highlighted in the triphenyl tetrazolium chloride (TTC) stained after mortem myocardium (Figure 1), which provides the clinical gold standard for the assessment of the image analysis results. The parameters of material properties of the myocardium are initialized as Young's modulus is set to 75 kpa, Poisson's ratio is set to 0.47, damping coefficients  $\alpha = 0.01$  and  $\beta = 0.1$ . The parameters of KLLS are initialized as the process noise  $Q_n$  is set to  $10^{-4}$ , measurement noise is set to  $10^{-10}$  and  $\gamma$  is set to 0.53. The estimated radial, circumferential, and RC shear strain maps are shown in Figure 4. The infarct tissue can be identified in the strain maps, and the most obvious difference is observed in the RC shear strain map, where the lower-right quarter of the myocardium has much larger strain than other normal tissues. These patterns are in

good agreement with the highlighted TTC-stained tissue in Figure 1, demonstrating the clinical relevance of our strategy.

## 5. Conclusion

In this paper, we have presented a biomechanically constrained filtering framework for the multiframe estimation of the nonrigid cardiac kinematics from medical image sequence. In spite of linear elasticity used to approximate myocardial system dynamics, our framework could allow convenient incorporation of other material constraints. The input estimation filtering formulation facilitates the considerations of input data uncertainty, and the Kalman filtering principles are adopted to achieve optimal estimation of the myocardial kinematics over corrected input forces. Quantitative validation has been conducted using synthetic data with known ground truth, and physiological experiment results are acquired from MR image sequences, as validated by post-mortem tissue staining.

The conventional Kalman filtering strategy consists of two steps: prediction and correction. The successful place of the conventional Kalman filtering strategy is computing the estimated state variables between predictions and measurements in minimum mean square sense. However, the predictions generated by the model could be faulty if the input term of the model is wrongly added, and then the error of estimations could be dominated by the imperfect predictions. In the case of myocardial dynamics, it will demand arduous work, including tremendous experiments, to determine patient's loading condition, which is not feasible in daily clinical practice. So it is reasonable to treat the loading, that is, input forces, of the heart as stochastic sources. In our particular application, it can be easily seen that the response of the cardiac system will vary largely with different loading conditions from (4). The forces constructed from boundaries or image features are obviously different from the real situation in the myocardium and a minor error from these image-derived forces could be amplified by (4) easily. Since the patient-specific observations of input forces in the cardiac system are still unavailable, it is meaningful to handle the uncertainties in input forces and measurements simultaneously, which can increase the accuracies of estimated state variables if estimated input forces are closed to ground truth.

Though this approach is inspired by [33] from the heating problem, it is closely related with previous state space approaches [21, 30, 41]. Works like [21, 30, 41] could be considered as one special situation of our approach where least-square filter vanishes if the external loading can be specified deterministically. The demanding computation also prohibits the performance of our filtering strategy in 3D because of burdensome computation of the Kalman filter and extra calculation of the least-square filter. Since the computation of the conventional 3D Kalman filter could be properly reduced by applying model reduction [25] or reduced rank filter [45], it will be worthy to apply similar techniques in our work. Further, the material properties of the biomechanical models may be estimated along with the motion properties through the augmentation of the state

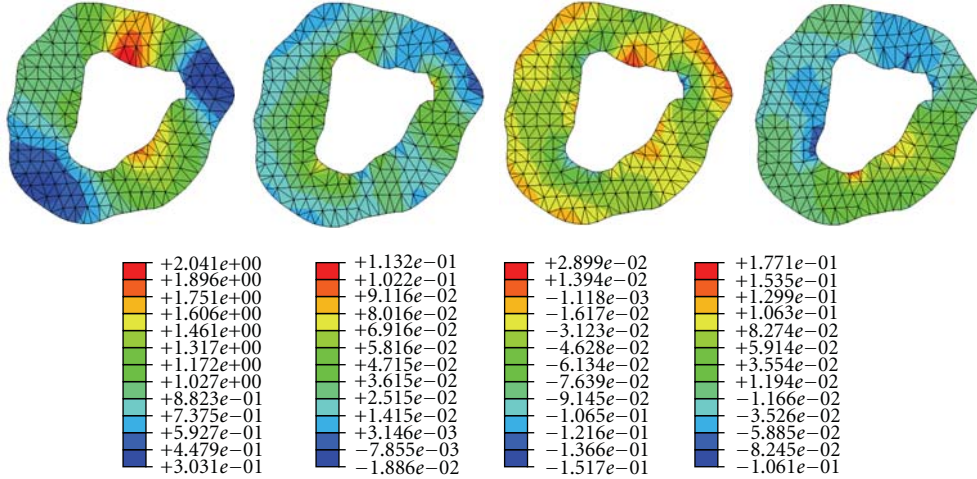


FIGURE 4: From left to right: estimated displacement magnitude, radial, circumferential, and RC shear strain maps for frame #9 (with respect to frame number 1).

vector by the material parameters and the construction of the nonlinear augmented state-space representation [24].

## Acknowledgments

This work is supported by The Wellcome Trust Fund. The authors would like to extend their gratitude to Dr. Albert Sinusas of Yale University for the canine experiment and imaging data. The valuable comments and suggestions from the anonymous reviewers are also greatly appreciated.

## References

- [1] S. C. Amartu and H. J. Vesselle, "A new approach to study cardiac motion: the optical flow of cine MR images," *Magnetic Resonance in Medicine*, vol. 29, no. 1, pp. 59–67, 1993.
- [2] M. J. Ledesma-Carbayo, J. Kybic, M. Desco, et al., "Spatiotemporal nonrigid registration for ultrasound cardiac motion estimation," *IEEE Transactions on Medical Imaging*, vol. 24, no. 9, pp. 1113–1126, 2005.
- [3] S. Song and R. Leahy, "Computation of 3D velocity fields from 3D cine CT images," *IEEE Transactions on Medical Imaging*, vol. 10, no. 3, pp. 295–306, 1991.
- [4] A. A. Amini, Y. Chen, M. Elayyadi, and P. Radeva, "Tag surface reconstruction and tracking of myocardial beads from SPAMM-MRI with parametric b-spline surfaces," *IEEE Transactions on Medical Imaging*, vol. 20, no. 2, pp. 94–103, 2001.
- [5] T. S. Denney, "Estimation and detection of myocardial tags in MR image without user-defined myocardial contours," *IEEE Transactions on Medical Imaging*, vol. 18, no. 4, pp. 330–344, 1999.
- [6] M. A. Guttman, J. L. Prince, and E. R. McVeigh, "Tag and contour detection in tagged MR images of the left ventricle," *IEEE Transactions on Medical Imaging*, vol. 13, no. 1, pp. 74–88, 1994.
- [7] A. A. Amini and J. S. Duncan, "Bending and stretching models for LV wall motion analysis from curves and surfaces," *Image and Vision Computing*, vol. 10, no. 6, pp. 418–430, 1992.
- [8] P. C. Shi, A. J. Sinusas, R. T. Constable, E. Ritman, and J. S. Duncan, "Point-tracked quantitative analysis of left ventricular surface motion from 3-D image sequences," *IEEE Transactions on Medical Imaging*, vol. 19, no. 1, pp. 36–50, 2000.
- [9] J. C. McEachen II and J. S. Duncan, "Shape-based tracking of left ventricular wall motion," *IEEE Transactions on Medical Imaging*, vol. 16, no. 3, pp. 270–283, 1997.
- [10] N. J. Pelc, M. Drangova, L. R. Pelc, et al., "Tracking of cyclical motion using phase contrast cine MRI velocity data," *Journal of Magnetic Resonance Imaging*, vol. 5, pp. 339–345, 1995.
- [11] J. Huang, D. Abendschein, V. G. Davila-Roman, and A. A. Amini, "Spatio-temporal tracking of myocardial deformations with a 4-D B-spline model from tagged MRI," *IEEE Transactions on Medical Imaging*, vol. 18, no. 10, pp. 957–972, 1999.
- [12] T. S. Denney and J. L. Prince, "Reconstruction of 3D left ventricular motion from planar tagged cardiac MR images: an estimation theoretic approach," *IEEE Transactions on Medical Imaging*, vol. 14, no. 4, pp. 625–635, 1995.
- [13] S. Benayoun and N. Ayache, "Dense non-rigid motion estimation in sequences of medical images using differential constraints," *International Journal of Computer Vision*, vol. 26, no. 1, pp. 25–40, 1998.
- [14] A. P. Pentland and B. Horowitz, "Recovery of nonrigid motion and structure," *IEEE Transactions on Pattern Analysis and Machine Intelligence*, vol. 13, no. 7, pp. 730–742, 1991.
- [15] S. Sclaroff and A. P. Pentland, "Modal matching for correspondence and recognition," *IEEE Transactions on Pattern Analysis and Machine Intelligence*, vol. 17, no. 6, pp. 545–561, 1995.
- [16] R. T. Constable, P. C. Shi, A. Sinusas, and J. Duncan, "Volumetric deformation analysis using mechanicsbased data fusion: applications in cardiac motion recovery," *International Journal of Computer Vision*, vol. 35, no. 1, pp. 87–107, 1999.
- [17] D. P. Dione, R. T. Constable, X. Papademetris, A. J. Sinusas, and J. S. Duncan, "Estimation of 3D left ventricular deformation from echocardiography," *Medical Image Analysis*, vol. 5, pp. 17–28, 2001.
- [18] D. P. Dione, R. T. Constable, X. Papademetris, A. J. Sinusas, and J. S. Duncan, "Estimation of 3D left ventricular deformation from medical images using biomechanical models," *IEEE*

- Transactions on Medical Imaging*, vol. 21, no. 7, pp. 786–799, 2002.
- [19] J. S. Duncan and N. Ayache, “Medical image analysis: progress over two decades and the challenges ahead,” *IEEE Transactions on Pattern Analysis and Machine Intelligence*, vol. 22, no. 1, pp. 85–106, 2000.
  - [20] A. F. Frangi, W. J. Niessen, and M. A. Viergever, “Three-dimensional modeling for functional analysis of cardiac images,” *IEEE Transactions on Medical Imaging*, vol. 20, no. 1, pp. 2–25, 2001.
  - [21] H. F. Liu and P. C. Shi, “State-space analysis of cardiac motion with biomechanical constraints,” *IEEE Transactions on Image Processing*, vol. 16, no. 4, pp. 901–917, 2007.
  - [22] Y. Bar-Shalom, X. Li, and T. Kirubarajan, *Estimation with Applications to Tracking and Navigation*, John Wiley & Sons, New York, NY, USA, 2000.
  - [23] H. F. Liu and P. C. Shi, “Cardiac motion and elasticity characterization with iterative sequential hinfinity criteria,” in *Medical Image Computing and Computer Assisted Intervention*, pp. 34–42, 2004.
  - [24] P. C. Shi and H. F. Liu, “Stochastic finite element framework for simultaneous estimation of cardiac kinematic functions and material parameters,” *Medical Image Analysis*, vol. 7, no. 4, pp. 445–464, 2003.
  - [25] K. C. L. Wong, L. Wang, H. Zhang, H. F. Liu, and P. C. Shi, “Computational complexity reduction for volumetric cardiac deformation recovery,” *Journal of Signal Processing Systems*, vol. 55, no. 1–3, pp. 281–296, 2009.
  - [26] P. Moireau, D. Chapelle, and P. Le Tallec, “Filtering for distributed mechanical systems using position measurements: perspectives in medical imaging,” *Inverse Problems*, vol. 25, no. 3, Article ID 035010, 25 pages, 2009.
  - [27] P. Moireau, D. Chapelle, and P. Le Tallec, “Joint state and parameter estimation for distributed mechanical systems,” *Computer Methods in Applied Mechanics and Engineering*, vol. 197, no. 6–8, pp. 659–677, 2008.
  - [28] D. Chapelle and P. Moireau, “Robus filter for joint state-parameters estimation in distributed mechanical system,” *Discrete and Continous Dynamical Systems*, vol. 23, no. 1–2, pp. 65–84, 2009.
  - [29] L. Ljung, “Asymptotic behavior of the extended kalman filter as a parameter estimator for linear systems,” *Computer Methods in Applied Mechanics and Engineering*, vol. 24, no. 1, pp. 36–50, 1979.
  - [30] C. L. Wong, H. Y. Zhang, and P. C. Shi, “Physiome model based state-space framework for cardiac kinematics recovery,” in *Medical Image Computing and Computer Assisted Intervention*, pp. 720–727, 2006.
  - [31] M. Sermesant, H. Delingette, and N. Ayache, “An electromechanical model of the heart for image analysis and simulation,” *IEEE Transactions on Medical Imaging*, vol. 25, no. 5, pp. 612–625, 2006.
  - [32] Z. H. Hu, D. Metaxas, and L. Axel, “In-vivo strain and stress estimation of the left ventricle from MRI images,” in *Medical Image Computing and Computer Assisted Intervention*, pp. 706–713, 2002.
  - [33] P. C. Tuan, C. C. Ji, L. W. Fong, and W. T. Huang, “An input estimation approach to on-line two-dimensional inverse heat conduction problems,” *Numerical Heat Transfer, Part B*, vol. 29, no. 3, pp. 345–363, 1996.
  - [34] L. Glass, P. Hunter, and A. McCulloch, *Theory of Heart: Biomechanics, Biophysics, and Nonlinear Dynamics of Cardiac Function*, Springer, New York, NY, USA, 1991.
  - [35] K. J. Bathe, *Finite Element Procedures*, Prentice-Hall, Englewood Cliffs, NJ, USA, 1996.
  - [36] H. Yamada, *Strength of Biological Material*, Williams and Wilkins, Baltimore, Md, USA, 1970.
  - [37] L. N. Wong, H. F. Liu, A. J. Sinusas, and P. C. Shi, “Simultaneous recovery of left ventricular shape and motion using meshfree particle framework,” in *Proceedings of IEEE International Symposium on Biomedical Imaging: From Nano to Macro*, pp. 1263–1266, 2004.
  - [38] B. Li, A. A. Young, and B. R. Cowan, “Validation of GPU accelerated non-rigid registration for the evaluation of cardiac function,” in *Medical Image Computing and Computer Assisted Intervention*, pp. 880–887, 2008.
  - [39] L. W. Wang, H. Y. Zhang, K. C. L. Wong, H. F. Liu, and P. C. Shi, “Noninvasive imaging of 3D cardiac electrophysiology,” in *Proceedings of IEEE International Symposium on Biomedical Imaging: From Nano to Macro*, pp. 632–635, 2006.
  - [40] P. F. J. Lermusiaux, “Adaptive modeling, adaptive data assimilation and adaptive sampling,” *Physica D*, vol. 230, no. 1–2, pp. 172–196, 2007.
  - [41] C. L. Wong, H. Y. Zhang, and P. C. Shi, “Cardiac motion recovery: continuous dynamics, discrete measurements, and optimal estimation,” in *Medical Image Computing and Computer Assisted Intervention*, pp. 744–751, 2006.
  - [42] G. H. Golub and C. F. Van Loan, *Matrix Computation*, Johns Hopkins University Press, Baltimore, Md, USA, 1983.
  - [43] T. Glad and L. Ljung, *Control Theory*, Taylor & Francis, London, UK, 2000.
  - [44] E. Haber, D. N. Metaxas, and L. Axel, “Motion analysis of the right ventricle from MRI images,” in *Medical Image Computing and Computer Assisted Intervention*, pp. 177–188, 1998.
  - [45] D. T. Pham, J. Verron, and M. C. Roubaud, “Singular evolutive extended kalman filter with eof initialization for data assimilation in oceanography,” *Journal of Marine Systems*, vol. 16, no. 3–4, pp. 323–340, 1998.

## Research Article

# In Vivo Measurement of Glenohumeral Joint Contact Patterns

**Michael J. Bey, Stephanie K. Kline, Roger Zael, Patricia A. Kolowich, and Terrence R. Lock**

*Department of Orthopaedic Surgery, Bone and Joint Center, Henry Ford Hospital, 2799 W. Grand Blvd., E&R 2015, Detroit, MI 48202, USA*

Correspondence should be addressed to Michael J. Bey, bey@bjc.hfh.edu

Received 15 April 2009; Accepted 27 June 2009

Academic Editor: João Manuel R. S. Tavares

Copyright © 2010 Michael J. Bey et al. This is an open access article distributed under the Creative Commons Attribution License, which permits unrestricted use, distribution, and reproduction in any medium, provided the original work is properly cited.

The objectives of this study were to describe a technique for measuring in-vivo glenohumeral joint contact patterns during dynamic activities and to demonstrate application of this technique. The experimental technique calculated joint contact patterns by combining CT-based 3D bone models with joint motion data that were accurately measured from biplane x-ray images. Joint contact patterns were calculated for the repaired and contralateral shoulders of 20 patients who had undergone rotator cuff repair. Significant differences in joint contact patterns were detected due to abduction angle and shoulder condition (i.e., repaired versus contralateral). Abduction angle had a significant effect on the superior/inferior contact center position, with the average joint contact center of the repaired shoulder 12.1% higher on the glenoid than the contralateral shoulder. This technique provides clinically relevant information by calculating in-vivo joint contact patterns during dynamic conditions and overcomes many limitations associated with conventional techniques for quantifying joint mechanics.

## 1. Introduction

The treatment of many pathologic shoulder conditions (e.g., rotator cuff tears, glenohumeral joint instability) relies implicitly on the belief that restoring normal glenohumeral joint mechanics is necessary to obtain a satisfactory clinical result. However, the measurement of glenohumeral joint mechanics—in particular, the patterns of contact between the humerus, and glenoid—has been a challenging task, especially under in vivo conditions. Previous research has measured glenohumeral joint mechanics under in-vitro conditions with cadaveric specimens (e.g., [1–3]), and under in vivo conditions with standard clinical imaging techniques such as magnetic resonance imaging (MRI) [4–8], fluoroscopy [9–12], and computed tomography (CT) [13]. However, there are limitations associated with these conventional measuring techniques. Specifically, cadaveric studies cannot accurately simulate in vivo conditions because muscle forces and joint forces are unknown. MRI and CT are largely restricted to acquiring images under static conditions and conventional fluoroscopy is not designed to accurately measure motion in three dimensions. Thus, these conventional measurement techniques were not designed to assess three-dimensional, in vivo glenohumeral joint contact patterns during dynamic activities. Therefore, the objectives

of this study are to (1) describe a technique for measuring in vivo glenohumeral joint contact patterns during dynamic activities, and (2) demonstrate application of this technique by characterizing differences between shoulders in patients who had undergone rotator cuff repair.

## 2. Methods

**2.1. Subjects.** Following institutional review board approval and informed consent, 20 subjects (13 males, 7 females; age:  $65.1 \pm 10.4$ ) enrolled in the study. Each subject had arthroscopic surgical repair of an isolated supraspinatus tendon tear approximately 4 months prior to participating in the study. All tears were directly repaired to bone using a double row technique [14] and an anterior acromioplasty was also performed. Each patient's shoulder was placed in a sling postoperatively. Active motion exercises were initiated at six weeks postsurgery, and progressive resistance training was initiated at 10–12 weeks postsurgery. The contralateral shoulder of each subject was asymptomatic, with no history of shoulder injury or surgery.

**2.2. Testing Setup.** Subjects were positioned with their shoulder centered within a biplane X-ray system [15]. The system consists of two 100 kW pulsed X-ray generators (EMD

Technologies CPX 3100CV, Quebec, Canada) and two 30 cm image intensifiers (Shimadzu AI5765HVP, Kyoto, Japan), optically coupled to synchronized high-speed video cameras (Phantom IV, Vision Research, Wayne, NJ, USA), configured in a custom gantry to enable a variety of motion studies. Subjects wore a lead-lined thyroid shield and protective vest during testing to minimize X-ray exposure.

**2.3. Testing Procedures.** Glenohumeral joint motion was assessed by tracking the 3D position of the humerus and scapula from images acquired from the biplane X-ray system. Images were acquired at 60 Hz with the X-ray generators in pulsed mode while subjects performed coronal-plane abduction. Subjects began this motion with their arm in a fully adducted neutral-rotation position, resting comfortably at their side. The ending position for this task was approximately 120° of humerothoracic motion, that is, the angle formed between the humerus and the torso. Subjects performed this motion while holding a 3-pound hand weight, or a weight less than this that was consistent with the patient's stage of rehabilitation. Subjects were instructed to perform this motion at a frequency of 0.25 Hz, so that one complete motion cycle took four seconds. The rate of shoulder motion was controlled using a metronome. Subjects performed three trials with a minimum of three minutes between trials to minimize fatigue. In addition, biplane X-ray images were acquired for a single static trial at the starting position. This static trial served as a reference position to which all glenohumeral joint motion data were compared. Both the repaired and contralateral shoulders were tested and the testing order was randomized.

Following testing, bilateral CT scans of the entire humerus and scapula were acquired (GE Medical Systems, LightSpeed16, Piscataway, NJ, USA). The scans were performed in axial mode with a slice thickness of 1.25 mm and an in-plane resolution of approximately 0.5 mm per pixel. The humerus and scapula were isolated from other bones and soft tissue using a semiautomatic segmentation technique (Mimics 10.1, Materialise, Leuven, Belgium). The CT volume was then interpolated using a feature-based interpolation technique and scaled to have cubic voxels with dimensions similar to the 2D pixel size in the biplane X-ray images.

**2.4. Measuring Glenohumeral Joint Motion.** The 3D position and orientation of the humerus and scapula were tracked from the biplane X-ray images using a 3D model-based tracking technique [16]. This technique uses a six degree-of-freedom optimization algorithm to find the best match between the biplane X-ray images and a pair of digitally reconstructed radiographs (DRRs) generated via ray-traced projection through the CT-based bone model. By optimizing the correlation between the two DRRs and the actual 2D biplane X-ray image pairs, the *in vivo* position and orientation of a given bone can be estimated. This model-based tracking technique has been shown to have an accuracy of better than  $\pm 0.4$  mm and  $\pm 0.5^\circ$  for measuring *in vivo* shoulder motion during dynamic activities [16].

Transformations between each bone's 3D position and anatomical axes were determined from the CT-based bone

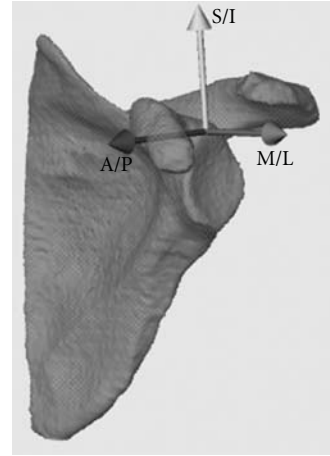


FIGURE 1: The contact center location was expressed relative to a subject-specific scapula coordinate system. The axes of the scapula coordinate system are aligned in the anterior/posterior (X axis), superior/inferior (Y axis), and medial/lateral (Z axis) directions.

models using custom software (based on Open Inventor 5.0, Mercury Computer Systems, Chelmsford, Mass, USA) that was developed to locate specific anatomical landmarks and construct standardized anatomical coordinate systems (Figure 1) [17]. To minimize side-to-side variability in kinematic measures due solely to anatomical axis locations, the same anatomical landmark locations identified on the humerus and scapula of the repaired shoulder were used for the contralateral shoulder. This was accomplished by mirror-imaging the contralateral shoulder CT-based bone models, manually coregistering these bone models with the repaired shoulder's CT-based bone models, and then transferring the anatomical landmark locations to the contralateral shoulder's CT-based bone models. Rotations of the humerus relative to the glenoid were calculated using a standard Euler angle sequence in which the first rotation defined the plane of elevation, the second rotation described the amount of elevation, and the third rotation represented the amount of internal/external rotation [18].

**2.5. Measuring Glenohumeral Joint Contact Patterns.** Glenohumeral joint contact patterns were determined by combining the joint motion measured from the biplane X-ray images with the subject-specific CT bone models. Briefly, the CT-based bone models were first converted into 3D surface models constructed of contiguous triangular tiles. A typical humerus or scapula model contained approximately 70 000 triangles of  $0.5 \text{ mm}^2$  each. To avoid unnecessary calculation, two specific regions of interest were identified: the humeral head and the glenoid. After co-registering the surface models with the kinematic data, the custom software calculated the 3D distance from every surface-triangle centroid on the humeral head to every surface-triangle centroid on the glenoid (Figure 2(a)). The contact center location was then determined by calculating the centroid of the closest  $200 \text{ mm}^2$  region of contact between the humerus and glenoid (Figure 2(b)). The 3D coordinates of this contact center

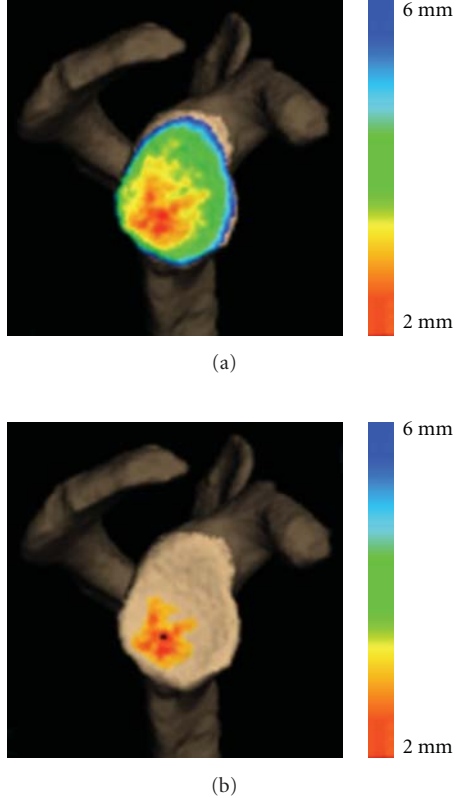


FIGURE 2: (a) Colormap of the minimum distance between the glenoid and humerus for a single frame of data. (b) The contact center location (indicated by the black dot) was calculated as the centroid of the closest  $200 \text{ mm}^2$  region between the humerus and glenoid.

location were then expressed relative to the scapula-based coordinate system, with the medial/lateral coordinate always located on the glenoid surface. This process was repeated for all frames of every trial. These calculations resulted in a 3D contact path, that is, a time-series of glenohumeral joint contact data at each point in time.

Due to differences in glenoid size between subjects, these glenohumeral joint contact data were normalized relative to the size of each subject's glenoid. Specifically, we first used custom software developed in our laboratory to manually measure the glenoid's maximum superior/inferior (S/I) and maximum anterior/posterior (A/P) dimensions from the CT-based bone models. For each subject, the 3D joint contact center coordinates were then normalized by (1) dividing the A/P contact center location by the maximum A/P glenoid dimension, and (2) dividing the S/I contact center location by the maximum S/I glenoid dimension. Thus, the data were expressed as a percentage of the maximum glenoid dimensions in both the A/P and S/I directions. These normalized contact center position data were then averaged across subjects in  $5^\circ$  increments from  $10^\circ$  to  $70^\circ$  of glenohumeral abduction.

**2.6. Outcome Measures.** To quantify differences in joint contact patterns between the repaired and contralateral shoulders, we calculated five outcome measures from the

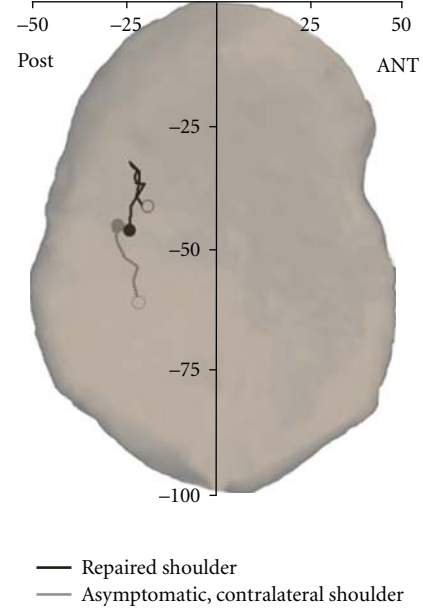


FIGURE 3: Average path of the glenohumeral joint contact center (superimposed on a typical glenoid) during coronal-plane abduction. For each path, the open circle ( $\circ$ ) indicates the starting position and the closed circle ( $\bullet$ ) indicates the ending position. ANT: anterior, POST: posterior.

normalized 3D contact center data. These outcome measures, averaged across all trials, included A/P contact center position, S/I contact center position, A/P contact position range, S/I contact position range, and contact path length.

**2.7. Statistical Analysis.** We used a two-way repeated measures ANOVA to assess the effects of glenohumeral joint abduction angle (from  $10^\circ$  to  $70^\circ$  in  $10^\circ$  increments) and shoulder condition (repaired versus contralateral) on the normalized A/P and S/I contact center position. The effect of shoulder condition (repaired versus contralateral) on average A/P contact center position, average S/I contact center position, A/P contact position range, S/I contact position range, and contact path length was assessed with a paired *t*-test. Significance was set at  $P < .05$ .

### 3. Results

The experimental technique presented here was sufficiently sensitive to detect differences in joint contact patterns as a function of both abduction angle and shoulder condition (i.e., repaired versus contralateral). The joint contact center position moved predominantly in the S/I direction and relatively little in the A/P direction during shoulder abduction in both the repaired and contralateral shoulders (Figure 3), with abduction angle having a significant effect on S/I contact center position ( $P = .004$ ) but not A/P contact center position ( $P = .675$ ). Interestingly, the path of the joint contact center changed direction during abduction in the repaired shoulders. Specifically, the joint contact center location moved superiorly on the glenoid

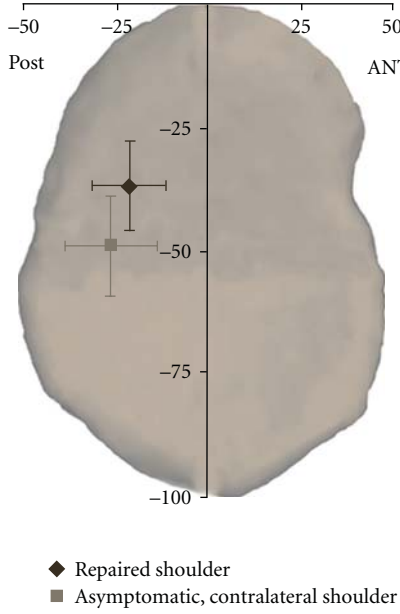


FIGURE 4: Average contact center position from  $10^\circ$  to  $70^\circ$  of coronal-plane abduction. Significant differences in both the average S/I ( $P = .01$ ) and A/P ( $P = .04$ ) contact center position were detected between the repaired and contralateral shoulders. ANT: anterior; POST: posterior.

from  $10^\circ$  to  $40^\circ$  of glenohumeral abduction, but then moved inferiorly on the glenoid from  $40^\circ$  to  $70^\circ$  of abduction (Figure 3). Consequently, the distance between the joint contact center locations associated with the repaired shoulders' starting position ( $10^\circ$  of glenohumeral abduction) and ending position ( $70^\circ$  of glenohumeral abduction) was only 1.5 mm. In contrast, the distance between the joint contact center locations at the starting and ending positions in the contralateral shoulders was 5.4 mm as the joint contact center path did not change direction during abduction.

Shoulder condition (i.e., repaired versus contralateral) had a significant effect on both the S/I ( $P < .001$ ) and A/P ( $P = .029$ ) contact center position. Specifically, the repaired shoulders' average joint contact center was  $12.1\% \pm 6.4\%$  higher on the glenoid ( $P = .01$ ) and  $3.7\% \pm 2.5\%$  more anterior on the glenoid ( $P = .04$ ) than the contralateral shoulders' average joint contact center (Figure 4). However, the study did not detect statistically significant differences between the repaired and contralateral shoulders in terms of A/P contact center range ( $P = .18$ , Figure 5), S/I contact center range ( $P = .10$ , Figure 5), or contact path length ( $P = .89$ , Figure 5).

#### 4. Discussion

This study describes a technique for measuring *in vivo* glenohumeral joint contact patterns during dynamic activities, and demonstrates application of this technique by characterizing differences between repaired and contralateral shoulders of patients who have undergone rotator cuff repair. The experimental method described here offers advantages

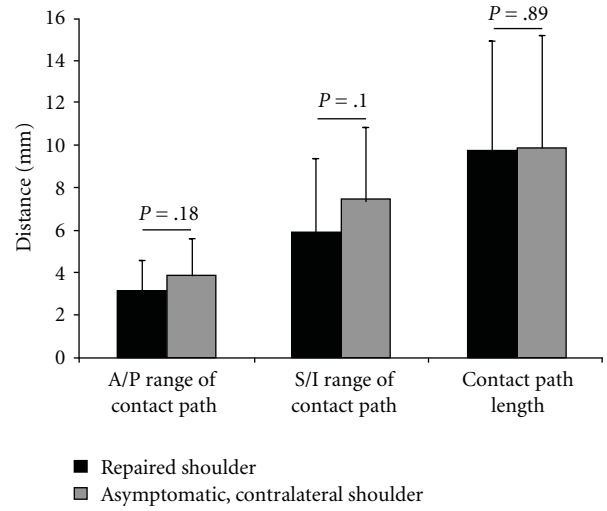


FIGURE 5: No statistically significant differences were detected between the repaired and contralateral shoulders in terms of A/P contact center position range ( $P = .18$ ), S/I contact center position range ( $P = .10$ ), or contact path length ( $P = .89$ ).

over conventional techniques for describing glenohumeral joint motion. Specifically, glenohumeral joint contact patterns provide a measure of joint function that may not be adequately captured when reporting only conventional measures of humeral rotation and translation. This is important, since many pathologic conditions of the shoulder (e.g., rotator cuff tear, glenohumeral joint instability) are believed to alter the glenohumeral joint articular mechanics, and procedures for treating these common conditions rely implicitly on the belief that restoring normal glenohumeral joint mechanics is necessary to obtain a satisfactory outcome. The approach described here of quantifying joint contact patterns has also been used by other investigators as a means of detecting functional differences associated with a specific clinical condition (e.g., distal radius malunion [19, 20]) that can not be detected using conventional kinematic parameters. Thus, joint contact patterns are perhaps not only a more sensitive measurement than conventional kinematics for detecting subtle differences in joint function but may also provide a more clinically relevant indication of the extent to which a conservative or surgical procedure has adequately restored normal joint function.

Glenohumeral joint contact patterns have been quantified in a number of cadaveric studies. For example, the effects of shoulder position on glenohumeral joint contact patterns have been studied in cadaver specimens using stereophotogrammetry [21–23]. Soslofsky et al. indicated that the glenoid contact location was primarily in the anterior half of the glenoid with the shoulder adducted, but moved posteriorly with increasing abduction [23]. In contrast, the current study demonstrated that the contact center was always located on the posterior half of the glenoid (in both the repaired and contralateral shoulders), and that there was little change in the A/P contact center location with increasing abduction. Furthermore, while the current

study demonstrated significant changes in the S/I contact center location with increasing abduction (Figure 3), the study by Soslowsky et al. reported no clear shift in the S/I direction in glenoid contact patterns with abduction. One plausible explanation that may help to reconcile these differences is that these previous cadaveric studies simulated scapular-plane abduction whereas the subjects in the current study elevated their shoulders in the coronal plane. Cadaveric studies have also investigated the effects of shoulder position, joint contact forces, muscles forces, and various simulated clinical conditions on joint contact area and joint contact pressures by inserting thin pressure-sensitive films or similar devices (e.g., Fuji film or Tekscan sensors) between the humerus and glenoid [1–3, 24, 25]. Although these types of cadaveric experiments have provided the bulk of existing knowledge about glenohumeral joint mechanics, cadaveric studies are not capable of accurately reproducing the complex muscle forces, joint forces, or joint motions that occur *in vivo*. Furthermore, given that rotator cuff disease typically develops slowly over many years, the inability to study biological response or disease progression is another significant limitation of cadaver studies.

One limitation of this technique for measuring joint contact patterns is that it neglects cartilage, since cartilage is difficult to image with both CT and conventional radiography. DeFrate and colleagues have suggested that neglecting cartilage could potentially lead to erroneous measures of joint contact in the knee due to variations in cartilage thickness across the femur and tibia [26]. Previous research has demonstrated that cartilage thickness varies with position on the glenoid and humeral head too, but that cartilage thickness has an inverse relationship between these articulating surfaces [27–30]. In particular, it has been shown that cartilage thickness for the humeral head is highest in the center and lowest at the periphery. In contrast, cartilage thickness on the glenoid is lowest in the center of the glenoid and higher at the periphery. The significance of this inverse relationship is that based on the data by Soslowsky and colleagues [27], the range of total cartilage thickness (i.e., the sum of glenoid cartilage thickness and humeral head cartilage thickness) over the regions of contact on the glenoid and humeral head during coronal-plane abduction varies by only 0.4 mm. Since the range of total cartilage thickness is equal to the uncertainty associated with the model-based tracking technique ( $\pm 0.4$  mm [16]), the current approach is not sufficiently accurate to detect changes in joint contact associated with subtle variations in total cartilage thickness. Thus, there is currently no advantage to including cartilage information in our subject-specific bone models. However, we anticipate additional technical enhancements will improve the accuracy of our model-based tracking technique, and therefore future efforts will focus on developing and validating (under conditions that provide a realistic simulation of *in vivo* testing conditions) a technique that includes cartilage in the estimation of joint contact patterns.

In summary, we have developed a technique for characterizing *in vivo* glenohumeral joint contact patterns during dynamic activities. This approach overcomes limitations

associated with cadaveric experiments and static imaging techniques. Future research efforts will use this experimental approach to objectively assess the glenohumeral joint contact patterns in asymptomatic normal individuals and those with pathologic conditions affecting the shoulder.

## Acknowledgments

This project was supported by grant number AR051912 from NIH/NIAMS.

## References

- [1] J. Yu, M. H. McGarry, Y.-S. Lee, L. V. Duong, and T. Q. Lee, “Biomechanical effects of supraspinatus repair on the glenohumeral joint,” *Journal of Shoulder and Elbow Surgery*, vol. 14, no. 1, supplement 1, pp. S65–S71, 2005.
- [2] R. Gupta and T. Q. Lee, “Positional-dependent changes in glenohumeral joint contact pressure and force: possible biomechanical etiology of posterior glenoid wear,” *Journal of Shoulder and Elbow Surgery*, vol. 14, no. 1, supplement 1, pp. S105–S110, 2005.
- [3] P. E. Greis, M. G. Scuderi, A. Mohr, K. N. Bachus, and R. T. Burks, “Glenohumeral articular contact areas and pressures following labral and osseous injury to the anteroinferior quadrant of the glenoid,” *Journal of Shoulder and Elbow Surgery*, vol. 11, no. 5, pp. 442–451, 2002.
- [4] H. Graichen, S. Hinterwimmer, R. von Eisenhart-Rothe, T. Vogl, K.-H. Englmeier, and F. Eckstein, “Effect of abducting and adducting muscle activity on glenohumeral translation, scapular kinematics and subacromial space width *in vivo*,” *Journal of Biomechanics*, vol. 38, no. 4, pp. 755–760, 2005.
- [5] S. Hinterwimmer, R. von Eisenhart-Rothe, M. Siebert, et al., “Influence of adducting and abducting muscle forces on the subacromial space width,” *Medicine and Science in Sports and Exercise*, vol. 35, no. 12, pp. 2055–2059, 2003.
- [6] G. P. Pappas, S. S. Blemker, C. F. Beaulieu, T. R. McAdams, S. T. Whalen, and G. E. Gold, “*In vivo* anatomy of the Neer and Hawkins sign positions for shoulder impingement,” *Journal of Shoulder and Elbow Surgery*, vol. 15, no. 1, pp. 40–49, 2006.
- [7] C. M. L. Werner, D. Weishaupt, S. Blumenthal, A. Curt, P. Favre, and C. Gerber, “Effect of experimental suprascapular nerve block on active glenohumeral translation *in vivo*,” *Journal of Orthopaedic Research*, vol. 24, no. 3, pp. 491–500, 2006.
- [8] H. Graichen, T. Stammberger, H. Bonel, E. Karl-Hans, M. Reiser, and F. Eckstein, “Glenohumeral translation during active and passive elevation of the shoulder—a 3D open-MRI study,” *Journal of Biomechanics*, vol. 33, no. 5, pp. 609–613, 2000.
- [9] M. Mahfouz, G. Nicholson, R. Komistek, D. Hovis, and M. Kubo, “*In vivo* determination of the dynamics of normal, rotator cuff-deficient, total, and reverse replacement shoulders,” *Journal of Bone and Joint Surgery A*, vol. 87, supplement 2, pp. 107–113, 2005.
- [10] C. W. A. Pfirrmann, M. Huser, G. Szekely, J. Hodler, and C. Gerber, “Evaluation of complex joint motion with computer-based analysis of fluoroscopic sequences,” *Investigative Radiology*, vol. 37, no. 2, pp. 73–76, 2002.
- [11] I. S. Talkhani and C. P. Kelly, “Movement analysis of asymptomatic normal shoulders: a preliminary study,” *Journal of Shoulder and Elbow Surgery*, vol. 10, no. 6, pp. 580–584, 2001.

- [12] D. G. Mandalidis, B. S. Mc Glone, R. F. Quigley, D. McInerney, and M. O'Brien, "Digital fluoroscopic assessment of the scapulohumeral rhythm," *Surgical and Radiologic Anatomy*, vol. 21, no. 4, pp. 241–246, 1999.
- [13] J.-P. Baeyens, P. Van Roy, A. De Schepper, G. Declercq, and J.-P. Clarijs, "Glenohumeral joint kinematics related to minor anterior instability of the shoulder at the end of the late preparatory phase of throwing," *Clinical Biomechanics*, vol. 16, no. 9, pp. 752–757, 2001.
- [14] I. K. Y. Lo and S. S. Burkhardt, "Double-row arthroscopic rotator cuff repair: re-establishing the footprint of the rotator cuff," *Arthroscopy*, vol. 19, no. 9, pp. 1035–1042, 2003.
- [15] S. Tashman and W. Anderst, "In-vivo measurement of dynamic joint motion using high speed biplane radiography and CT: application to canine ACL deficiency," *Journal of Biomechanical Engineering*, vol. 125, no. 2, pp. 238–245, 2003.
- [16] M. J. Bey, R. Zauel, S. K. Brock, and S. Tashman, "Validation of a new model-based tracking technique for measuring three-dimensional, in vivo glenohumeral joint kinematics," *Journal of Biomechanical Engineering*, vol. 128, no. 4, pp. 604–609, 2006.
- [17] G. Wu, F. C. T. van der Helm, H. E. J. Veeger, et al., "ISB recommendation on definitions of joint coordinate systems of various joints for the reporting of human joint motion—part II: shoulder, elbow, wrist and hand," *Journal of Biomechanics*, vol. 38, no. 5, pp. 981–992, 2005.
- [18] A. R. Karduna, P. W. McClure, L. A. Michener, and B. Sennett, "Dynamic measurements of three-dimensional scapular kinematics: a validation study," *Journal of Biomechanical Engineering*, vol. 123, no. 2, pp. 184–190, 2001.
- [19] J. J. Crisco, D. C. Moore, G. E. Marai, et al., "Effects of distal radius malunion on distal radioulnar joint mechanics—an in vivo study," *Journal of Orthopaedic Research*, vol. 25, no. 4, pp. 547–555, 2007.
- [20] G. E. Marai, D. H. Laidlaw, C. Demirralp, S. Andrews, C. M. Grimm, and J. J. Crisco, "Estimating joint contact areas and ligament lengths from bone kinematics and surfaces," *IEEE Transactions on Biomedical Engineering*, vol. 51, no. 5, pp. 790–799, 2004.
- [21] G. A. Ateshian, S. D. Kwak, L. J. Soslowsky, and V. C. Mow, "A stereophotogrammetric method for determining in situ contact areas in diarthrodial joints, and a comparison with other methods," *Journal of Biomechanics*, vol. 27, no. 1, pp. 111–124, 1994.
- [22] R. Kelkar, V. M. Wang, E. L. Flatow, et al., "Glenohumeral mechanics: a study of articular geometry, contact, and kinematics," *Journal of Shoulder and Elbow Surgery*, vol. 10, no. 1, pp. 73–84, 2001.
- [23] L. J. Soslowsky, E. L. Flatow, L. U. Bigliani, R. J. Pawluk, G. A. Ateshian, and V. C. Mow, "Quantitation of in situ contact areas at the glenohumeral joint: a biomechanical study," *Journal of Orthopaedic Research*, vol. 10, no. 4, pp. 524–534, 1992.
- [24] J. J. P. Warner, M. K. Bowen, X.-H. Deng, J. A. Hannafin, S. P. Arnoczyk, and R. F. Warren, "Articular contact patterns of the normal glenohumeral joint," *Journal of Shoulder and Elbow Surgery*, vol. 7, no. 4, pp. 381–388, 1998.
- [25] R. A. Creighton, B. J. Cole, G. P. Nicholson, A. A. Romeo, and E. P. Lorenz, "Effect of lateral meniscus allograft on shoulder articular contact areas and pressures," *Journal of Shoulder and Elbow Surgery*, vol. 16, no. 3, pp. 367–372, 2007.
- [26] L. E. DeFrate, H. Sun, T. J. Gill, H. E. Rubash, and G. Li, "In vivo tibiofemoral contact analysis using 3D MRI-based knee models," *Journal of Biomechanics*, vol. 37, no. 10, pp. 1499–1504, 2004.
- [27] L. J. Soslowsky, E. L. Flatow, L. U. Bigliani, and V. C. Mow, "Articular geometry of the glenohumeral joint," *Clinical Orthopaedics and Related Research*, no. 285, pp. 181–190, 1992.
- [28] J. Hodler, R. A. Loredo, C. Longo, D. Trudell, J. S. Yu, and D. Resnick, "Assessment of articular cartilage thickness of the humeral head: MR-anatomic correlation in cadavers," *American Journal of Roentgenology*, vol. 165, no. 3, pp. 615–620, 1995.
- [29] H. Graichen, J. Jakob, R. von Eisenhart-Rothe, K.-H. Englmeier, M. Reiser, and F. Eckstein, "Validation of cartilage volume and thickness measurements in the human shoulder with quantitative magnetic resonance imaging," *Osteoarthritis and Cartilage*, vol. 11, no. 7, pp. 475–482, 2003.
- [30] L. Yeh, S. Kwak, Y.-S. Kim, et al., "Evaluation of articular cartilage thickness of the humeral head and the glenoid fossa by MR arthrography: anatomic correlation in cadavers," *Skeletal Radiology*, vol. 27, no. 9, pp. 500–504, 1998.

## Research Article

# Adding Image Constraints to Inverse Kinematics for Human Motion Capture

**Antoni Jaume-i-Capó, Javier Varona, Manuel González-Hidalgo, and Francisco J. Perales**

Departament de Ciències Matemàtiques i Informàtica, Universitat de les Illes Balears, Ed. A. Turmeda,  
Ctra de Valldemossa Km 7.5, 07122 Palma, Spain

Correspondence should be addressed to Antoni Jaume-i-Capó, antoni.jaume@uib.es

Received 15 May 2009; Accepted 8 July 2009

Academic Editor: João Manuel R. S. Tavares

Copyright © 2010 Antoni Jaume-i-Capó et al. This is an open access article distributed under the Creative Commons Attribution License, which permits unrestricted use, distribution, and reproduction in any medium, provided the original work is properly cited.

In order to study human motion in biomechanical applications, a critical component is to accurately obtain the 3D joint positions of the user's body. Computer vision and inverse kinematics are used to achieve this objective without markers or special devices attached to the body. The problem of these systems is that the inverse kinematics is "blinded" with respect to the projection of body segments into the images used by the computer vision algorithms. In this paper, we present how to add image constraints to inverse kinematics in order to estimate human motion. Specifically, we explain how to define a criterion to use images in order to guide the posture reconstruction of the articulated chain. Tests with synthetic images show how the scheme performs well in an ideal situation. In order to test its potential in real situations, more experiments with task specific image sequences are also presented. By means of a quantitative study of different sequences, the results obtained show how this approach improves the performance of inverse kinematics in this application.

## 1. Introduction

In biomechanical applications that aim to study human motion, a critical component is to accurately obtain the 3D joints' positions of the user's body. Usually, the most common methods to obtain the joints' positions require a laboratory environment and the attachment of markers to the body. Modern biomechanical and clinical applications require the accurate capture of normal and pathological human movement without the artifacts associated with standard marker-based motion capture techniques such as soft tissue artifacts and the risk of artificial stimulus of taped on or strapped on markers [1]. Emerging techniques and research in computer vision are leading to the rapid development of the markerless approach to motion capture [2].

In computer vision, algorithms are designed to allow the system to analyze one or multiple image streams in order to recover human motion. However, the images are 2D and the human body representation is in 3D. This fact leads to the presence of ambiguities; there are a number of

possible 3D configurations of the human body that could explain a single image. In addition, these images can be noisy or incomplete (some joints or limbs are not visible). Therefore, we can only estimate the users posture. Inverse kinematics approaches can solve the body posture from their 3D position if we can clearly locate visible body parts such as face and hands. For example, in the work of Zou et al. [3], the angles of joints are estimated by inverse kinematics based on human skeleton constraints, and the coordinates of pixels in the body segments in the scene are determined by forward kinematics. Finally the human motion pose can be reconstructed by histogram matching. Their main drawback is that the algorithm does not handle human motion in the direction perpendicular to the image plane displacement. In the case of multiple cameras, ambiguities appear to be less significant. For example, by using two cameras to recover the user's posture in order to recognize the user's gestures for Human-Computer Interaction applications [4]. This work is also based on computer vision and inverse kinematics in order to recover human body posture.

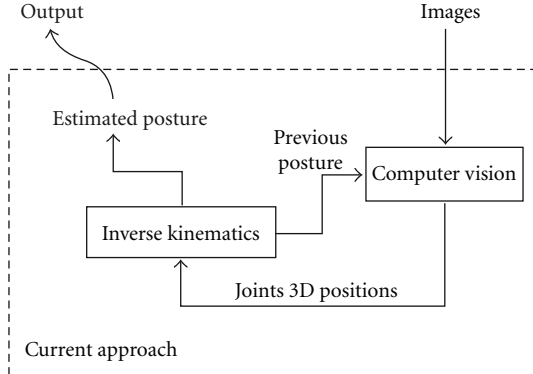


FIGURE 1: Current approach to combine computer vision and inverse kinematics.

However, previous works based on the combination of computer vision and inverse kinematics tend to simplify the approach by combining the results of both techniques that are applied by separate. As it is shown in Figure 1, current approaches are based on the detection of certain joints into the images by using Computer Vision algorithms and, therefore, estimate a plausible body posture by using Inverse Kinematics algorithms. In this way, the Inverse Kinematics algorithms are “blinded” with respect to the projection of body segments into the images. They only use biomechanical constraints to estimate the best position of the non-detected joints in the images.

In this paper we present a new approach where the objective is to include the image information directly onto the inverse kinematics scheme, see Figure 2. The idea is to use image constraints to solve the redundancy of kinematics solvers. In addition, we also explain that it is possible to use a preprocessed image, in other words, the computer vision algorithms could process the input images in order to make the problem more tractable or to enhance a desired image feature for specific applications. Finally, this scheme of posture reconstruction can be used with one or more views, that is, it can work using only one view but the results improve if more views of the performer are applied.

In order to show the viability of this scheme of 3D human posture recognition, different experiments have been conducted. First, using synthetic images in order to show how the scheme works in an ideal situation. This simple case shows how theoretically the scheme performs correctly. Next, in order to test its potential in real situations, experiments with real sequences are also presented. In these experiments an annotated sequence and a known database of human motions that contains motion capture data are used to make a quantitative study of different sequences in order to evaluate the performance of the presented approach.

This paper is organized as follows. In next section, current inverse kinematics approach is reviewed in order to introduce in Section 3 the image constraints. Section 4

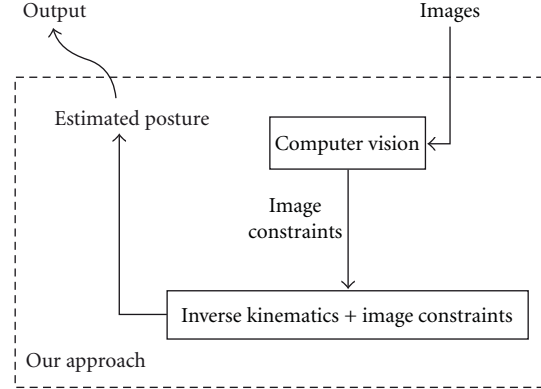


FIGURE 2: Our approach: Adding image constraints to inverse kinematics.

analyzes the obtained results in order to demonstrate the viability of this approach. Finally, conclusions are presented in the last section.

## 2. Inverse Kinematics

In order to capture human motion, the human body is usually modeled as an articulated chain, which consists of a set of rigid objects, called links, joined together by joints. To control the movement of an articulated chain it is common to use inverse kinematics (IK). IK is exploited to reconstruct an anatomically correct posture of the user (i.e., its joint state) considering the 3D locations of selected end-effectors which are used to constrain the posture.

For the moment, let us consider only a single frame of motion. Write the vector of joint angles as  $\theta = \{\theta_1, \dots, \theta_n\}$ . Assume that we would like to meet a set of constraints on joints positions as  $\mathbf{x} = \{x_1, \dots, x_m\}$  as functions of the joints degrees of freedom  $\theta$ . The problem of inverse kinematics is to obtain a  $\theta$  such that  $\mathbf{x} = \mathbf{g}(\theta)$ . Closed forms solutions are available for at least some parameters, when the limbs of the articulated chain are considered independently [5]. More often, one must see this as a numerical root finding problem based on the linearization of the set of constraints on joint positions,  $\mathbf{g}$ , considering small displacements about the current configuration,  $\theta$ ,

$$\Delta \mathbf{x} = \mathbf{J} \Delta \theta, \quad (1)$$

where  $\mathbf{J}$  is the  $m \times n$  Jacobian matrix

$$\mathbf{J} = \left( \frac{\partial g_i}{\partial \theta_j} \right), \quad i = 1, \dots, m; j = 1, \dots, n. \quad (2)$$

The resulting Jacobian matrix  $\mathbf{J}$  is inverted to map the desired constraint variation  $\Delta \mathbf{x}$  to a corresponding posture variation  $\Delta \theta$ . Using the pseudoinverse, noted by  $\mathbf{J}^+$ , the norm of the solution mapped by  $\mathbf{J}^+$  is minimal, that is, it is the

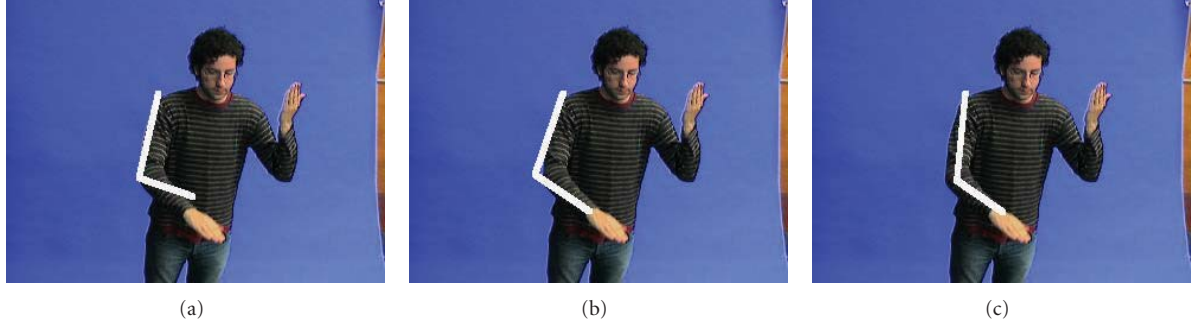


FIGURE 3: (a) Initial configuration of the articulated chain, (b) IK estimation, (c) result by adding the image constraint.

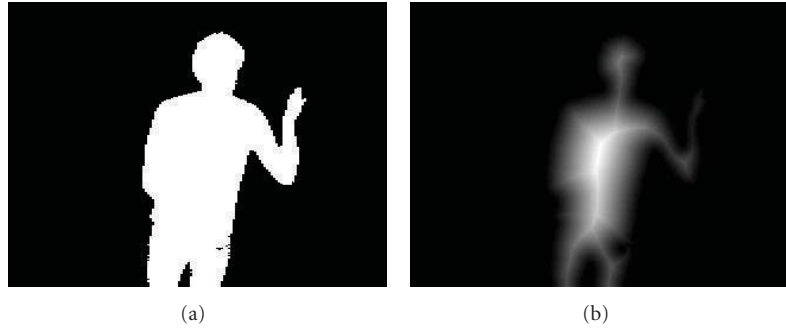


FIGURE 4: Image supports: (a) silhouette; (b) euclidean distance transform.

smallest posture variation realizing the desired constraint variation:

$$\Delta\boldsymbol{\theta} = \mathbf{J}^+ \Delta\mathbf{x}. \quad (3)$$

Since  $\text{rank}(\mathbf{J}) = m < n$ , there is an infinite number of solutions. For the positioning and animation of articulated figures in computer graphics, the weighting strategy [6] is frequently employed. In the field of robotics however, the strategy is to solve this inverse kinematics redundancy adding a secondary term (usually defined as secondary task) to (3) in order to minimize a criterion  $h(\boldsymbol{\theta})$ . In this formulation, redundancy solution is accomplished by moving the joints such that the end-effectors are moved in the desired way and the criterion  $h$  is always kept at a minimum. This was first exploited by Liégeois [7] who added a secondary task by projecting the negative gradient of  $h(\boldsymbol{\theta})$  into the null space of  $\mathbf{J}$ , see (4),

$$\Delta\boldsymbol{\theta} = \mathbf{J}^+ \Delta\mathbf{x} - \alpha(\mathbf{I}_n - \mathbf{J}^+ \mathbf{J}) \nabla h(\boldsymbol{\theta}), \quad (4)$$

where  $\mathbf{I}_n$  is the  $n \times n$  identity matrix, and  $\alpha$  is a positive gain factor which is configuration dependent. Definition of the secondary task by means of the criterion  $\nabla h(\boldsymbol{\theta})$  depends on the application. In following section, a criterion based on images will be defined in order to capture human motion.

### 3. The Image-Based constraint

As explained in previous section, it is possible to constrain the solutions of inverse kinematics by adding a scalar

criterion  $h(\boldsymbol{\theta})$ . Next, we explain how to define this criterion by using the images in order to guide the posture reconstruction of the articulated chain for human motion capture applications.

The definition of the image-based constraint is inspired in the works of Visual Servo Control [8]. Specifically, Marchand and Courty define different secondary tasks for controlling a camera in virtual environments [9]. For motion capture purposes, it should be taken into account that the human structure is highly redundant and, therefore, a large solution space exists. A solution is to generalize (4) to include more tasks by using the priority strategy [10]. In this case, the solution guarantees that a task associated with a high priority will be achieved as much as possible, while a low-priority constraint will be optimized only on the reduced solution space that does not disturb all higher priority tasks. However, for the sake of clarity, we only consider two tasks. It is straightforward to extend to more tasks when the image constraint has low priority. In addition, it is possible to use the Extended Jacobian method [11] in order to give a high priority to the image constraint.

For motion capture applications, we define  $h(\boldsymbol{\theta})$  in order to maximize the overlap between the projection of the articulated chain into the images and the human body. Consider the case of the Figure 3(a), where is shown the initial configuration of the articulated chain and the objective is to estimate the elbow's position with the 3D position of the hand as end-effector. By applying IK we obtain the result of Figure 3(b), where the elbow's estimation

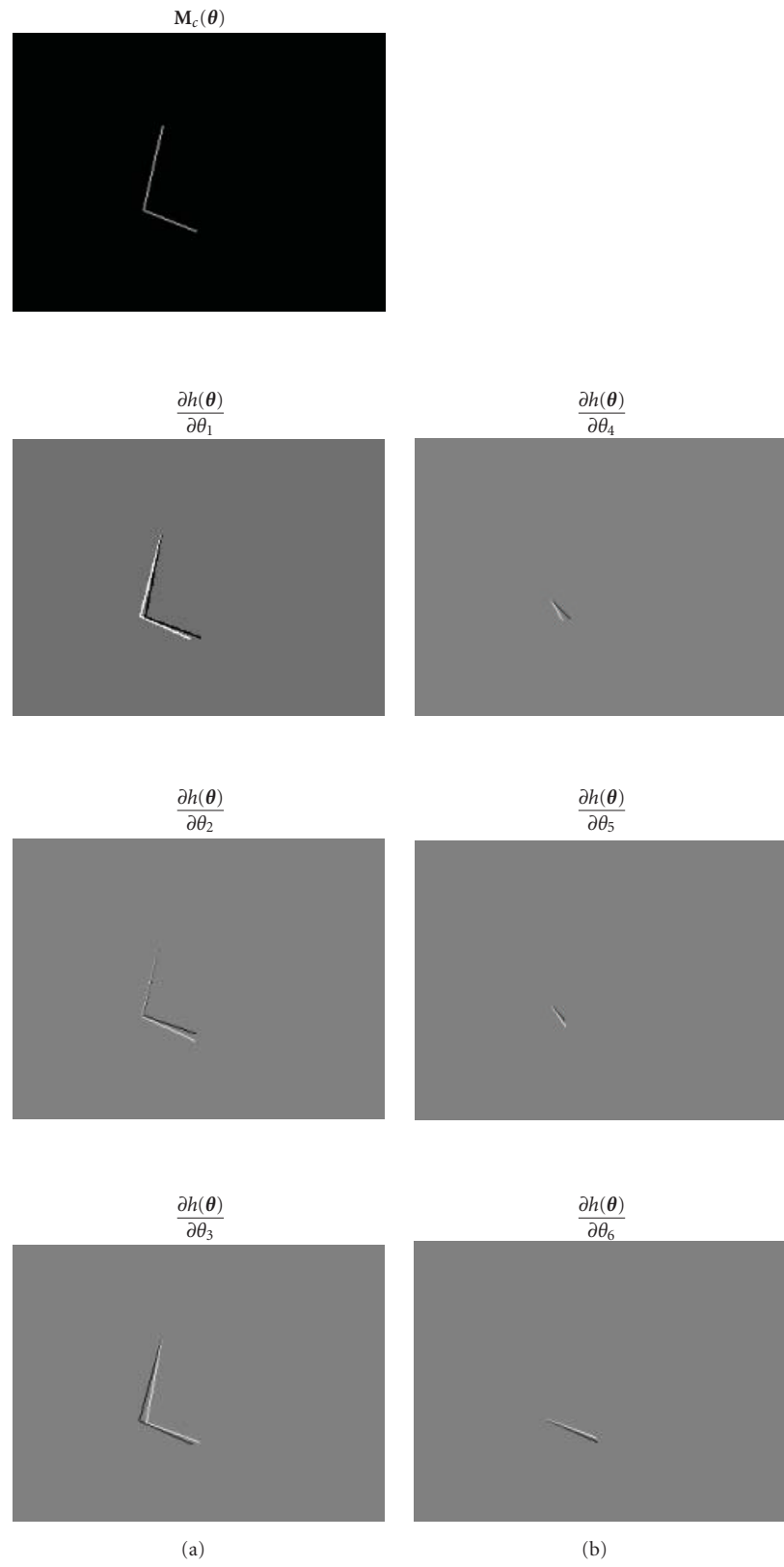


FIGURE 5: The  $M_c(\boldsymbol{\theta})$  function and its partial derivatives for the case of Figure 3.

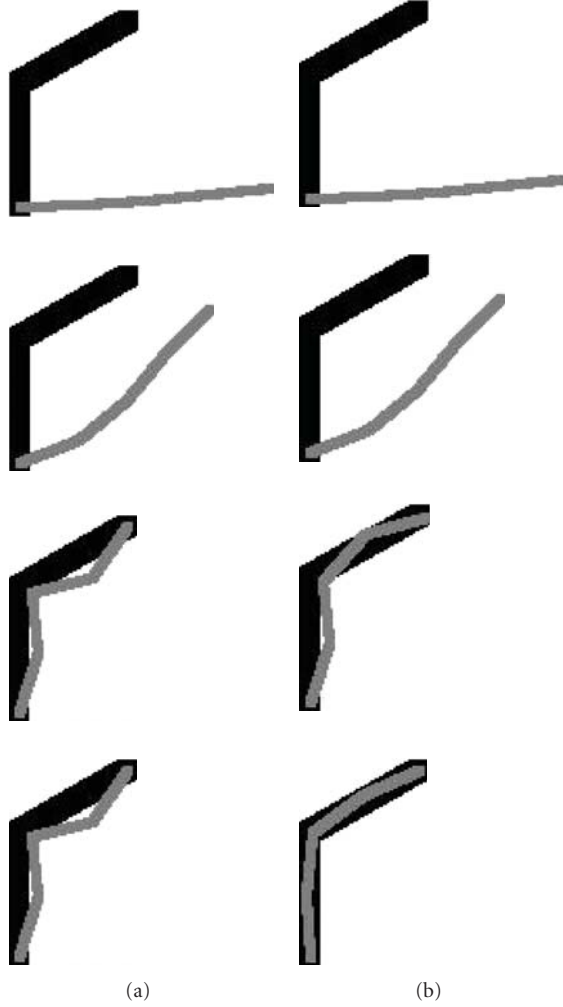


FIGURE 6: Experiment 1. From the initial configuration of the articulated chain (gray), both approaches try to reach the objective configuration (black). Left column, sequence applying inverse kinematics without image constraint. Right column, sequence applying inverse kinematics with image constraint.

lies outside of the body due its “blind” nature by using only the desired position of the end-effector. In order to solve this problem, we propose a criterion that tries to guide the articulated chain to the body projection into the image, Figure 3(c). Formally, let us to define  $h(\theta)$  as follows

$$h(\theta) = \frac{1}{n} \sum_c \sum_x \sum_y (\mathbf{I}_c(x, y) \cdot \mathbf{M}_c(x, y, \theta)), \quad (5)$$

where  $\mathbf{I}_c(x, y)$  represents the intensity of the 2D point  $(x, y)$  of the image  $c$  ( $c \geq 1$ ), which corresponds to a different view of the user, and  $n$  is the number of points  $(x, y)$  that belong to the desired image support  $\mathbf{I}_c$ . Applying a background subtraction algorithm [12], it is possible to directly use the silhouette as the image support,  $\mathbf{I}$ , of the articulated chain, see Figure 4(a). However, in order to get

a smooth surface we apply the euclidean distance transform [13] to the silhouette image, see Figure 4(b). Both operations are fast and do not introduce a significative delay in the algorithm.

In order to complete the definition of (5), let us to define the function  $\mathbf{M}_c(\theta)$ , which is the projection of the articulated chain into the image  $c$ . If  $\mathbf{X} = (X, Y, Z)$  are the coordinates of the  $i$ th joint in the 3D-space, and assuming knowing the calibration data in order to project the 3D coordinates into the 2D images, we define  $\mathbf{p}_{c,i} = (x, y)$  such as the 2D image coordinates of the projected  $i$ th joint into the image  $c$ . Assuming that the joints are ordered in a consecutive way, the  $\mathbf{M}_c(\theta)$  function is defined as follows:

$$\mathbf{M}_c(x, y, \theta) = \begin{cases} 1, & \text{if } (x, y) \in \overline{\mathbf{p}_{c,i}\mathbf{p}_{c,i+1}} \text{ for some } i \text{ joint,} \\ 0, & \text{otherwise,} \end{cases} \quad (6)$$

where  $\overline{\mathbf{p}_{c,i}\mathbf{p}_{c,i+1}}$  is the segment between the 3D joints’ projection into the image. Figure 5 shows the  $\mathbf{M}_c(\theta)$  function for the example of Figure 4 and its partial derivatives. Concluding, the image constraint is then given by the gradient of the criterion  $h(\theta)$  of (7)

$$\nabla h(\theta) = \left( \frac{\partial h(\theta)}{\partial \theta_j} \right), \quad j = 1, \dots, n, \quad (7)$$

where the partial derivative of the joint  $j$  is defined in (8)

$$\frac{\partial h(\theta)}{\partial \theta_j} = \frac{1}{n} \sum_c \sum_x \sum_y \left( \mathbf{I}_c(x, y) \cdot \frac{\partial \mathbf{M}_c(x, y, \theta)}{\partial \theta_j} \right). \quad (8)$$

## 4. Performance Evaluation

The proposed approach is evaluated using three different tests. The first test uses a virtual environment to show how the presented approach runs well in an ideal situation. The second test applies the proposed approach on a sequence of user’s motions to show how the presented approach performs well using real images. Finally, the third test compares the evaluation of the inverse kinematics approach, with and without image constraints, by using HumanEva dataset [14]. This dataset comprises four subjects performing six different types of actions recorded in seven calibrated video sequences from different viewpoints. Additionally, the video sequences are synchronized with their corresponding motion captured 3D pose parameters.

In addition, the complete algorithm (with and without image constraint) has been implemented in Visual C++ using the OpenCV libraries [15] and it has been tested in a realtime interaction context on an Intel Core2 QUAD Q6600 under Windows Vista. First, without the image constraint, we have obtained a performance of 21 frames per second

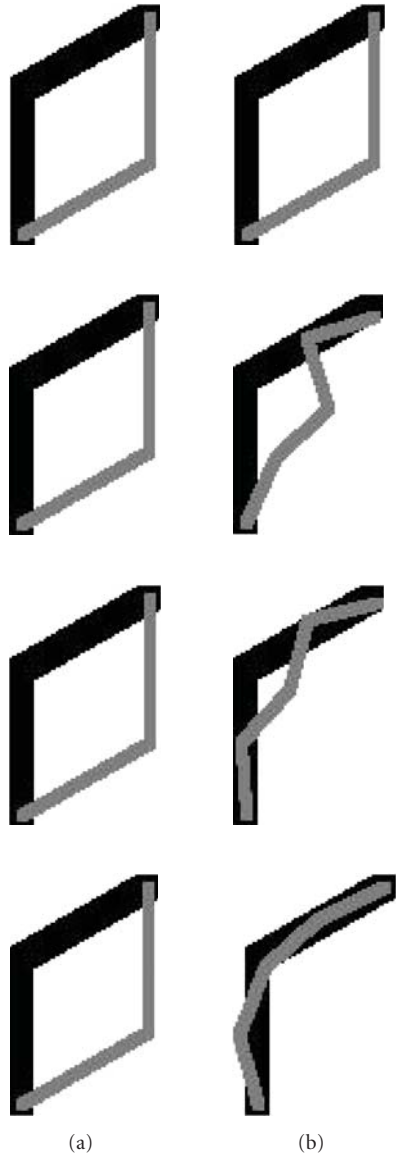


FIGURE 7: Experiment 2. Initial (gray) and objective (black) configuration with the same end effector position. Left column, sequence applying inverse kinematics without image constraint. Right column, sequence applying inverse kinematics with image constraint.

(with 15 steps of convergence). Second, with the image constraint, we have obtained a performance of 19 frames per second (with 15 steps of convergence). Therefore, its use in human-computer interaction applications is also possible. For other uses in non real-time applications the accuracy could be improved adding more steps of convergence.

**4.1. Virtual Environment.** First, we test the system in a virtual environment to show how the presented approach works in an ideal situation. We define an articulated chain in 2D space, composed by 4 segments, with a total of

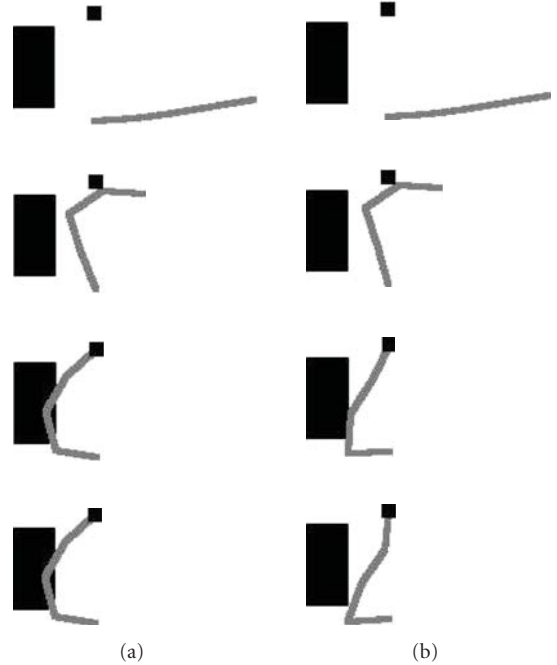


FIGURE 8: Experiment 3. From initial configuration of the chain (gray) the experiment try to avoid an object (black). Left column, sequence applying inverse kinematics without image constraint. Right column, sequence applying inverse kinematics with image constraint.

4 rotational joints of 1 DOF each one (i.e., a rotational joint for each segment). To test the system, we generate an initial configuration and an objective configuration of the articulated chain. Next, we apply the inverse kinematics approach, from initial configuration with and without image constraint, to estimate the objective configuration of the articulated chain.

In the first experiment, displayed in Figure 6, we generate an initial configuration and an objective configuration of the articulated chain, we apply the inverse kinematics approach, with and without image constraint. Without the image constraint, when the articulated chain reaches the end-effector the estimation of the objective configurations stops. On the other hand, by using image constraint it continues to try inserting the articulated chain inside the projection of the objective configuration, even if the articulated chain reaches the end-effector. In Figure 7 we display a second experiment where we generate an initial configuration and an objective configuration of the articulated chain, with the same end-effector. We apply the inverse kinematics approach, from the initial configuration, with and without image constraint. The results show that the inverse kinematics without the image constraint estimation does not change the initial configuration because the end-effector is reached. On the other hand, the inverse kinematics with image constraint enforces the chain to reach the image projection of the objective configuration. Figure 8 shows the last experiment in virtual environment, where the articulated chain tries to avoid an object

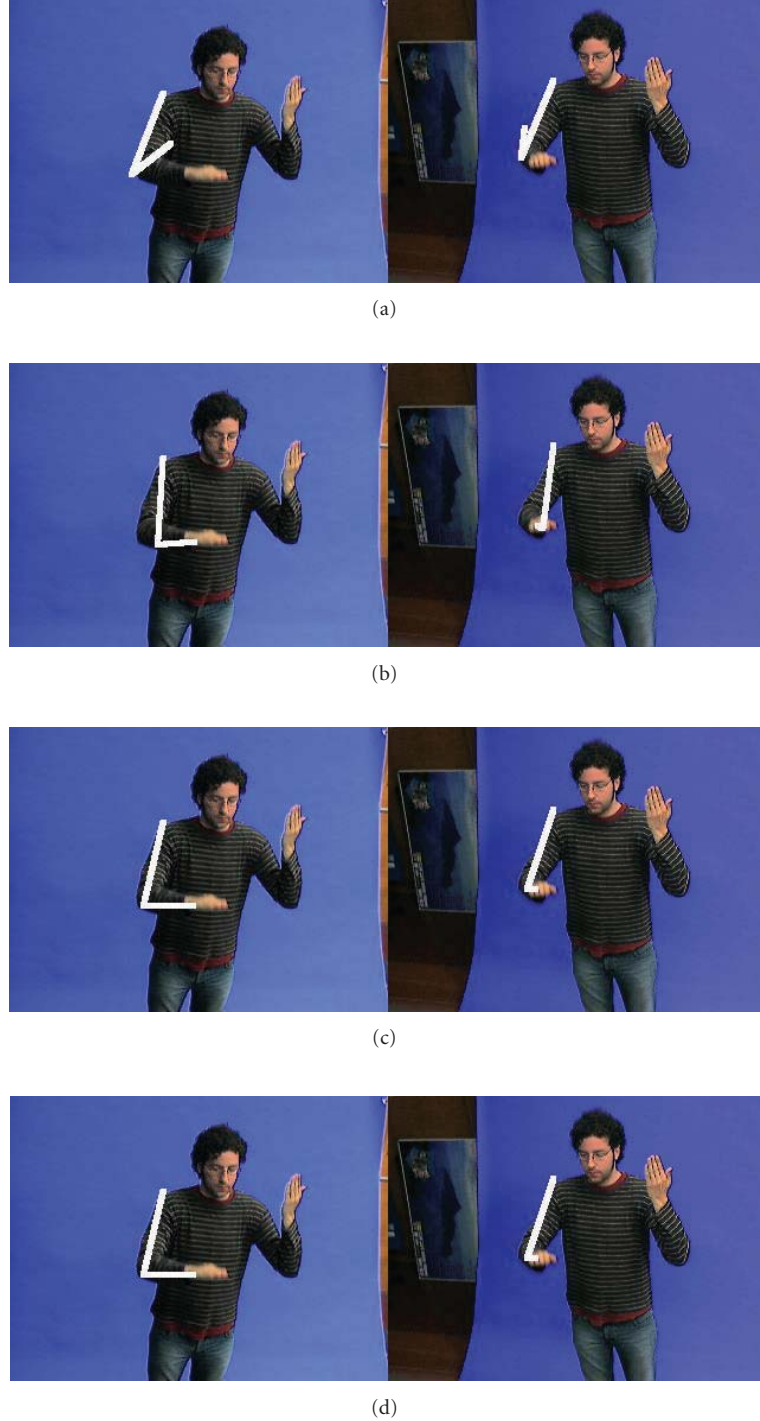


FIGURE 9: Working with real images. (a) Initial configuration of the articulated chain. (b) Arm estimation applying inverse kinematics approach. (c) And (d) arm estimation applying inverse kinematics with image constraints using one and two views respectively.

projected in an image. We define the initial configuration of the articulated chain, the objective end-effector, and a squared object. In this case, we use the image constraint to avoid the object. The experiments show that adding the image constraint outperforms inverse kinematics, in order to achieve the desired articulated chain configuration.

**4.2. Using Real Images.** In this test we apply the inverse kinematics with image constraint approach on a real stereoscopic sequence of human motions. Besides, the 3D joints' positions of the sequence are manually annotated for a quantitative comparison. The sequence has 450 frames corresponding to 15 seconds in real-time. The main objective of this test is to show that the proposed approach performs well with real

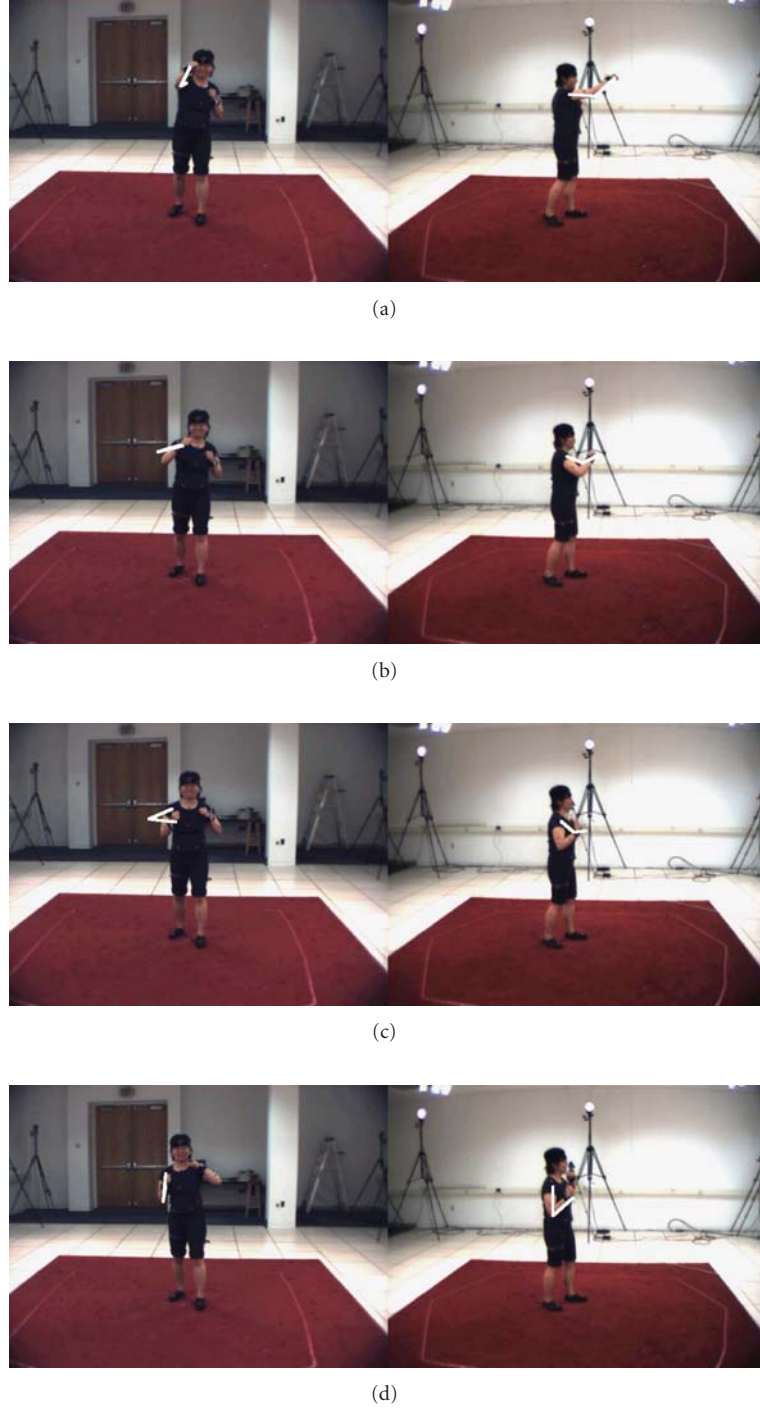


FIGURE 10: HumanEva *box* sequence for the subject 1, using Inverse kinematics.

images. In addition, this experiment shows that using this approach it is possible to solve the problem using only one image.

In Figure 9 is shown a frame of the stereoscopic sequence while applying the inverse kinematics approach with and without image constraint. We define an articulated chain in 3D space, with 2 rotational joints of 3 DOF each one. In the case of using image constraint, we apply

the approach firstly by using the left camera ( $c = 1$ ) and then, by using both cameras ( $c = 2$ ). The results show that when the inverse kinematics approach loses the elbow position, the inverse kinematics image constraint approach estimates the position of the elbow inside the silhouette. Using this stereoscopic sequence, there are not any significant differences between using one or both cameras.

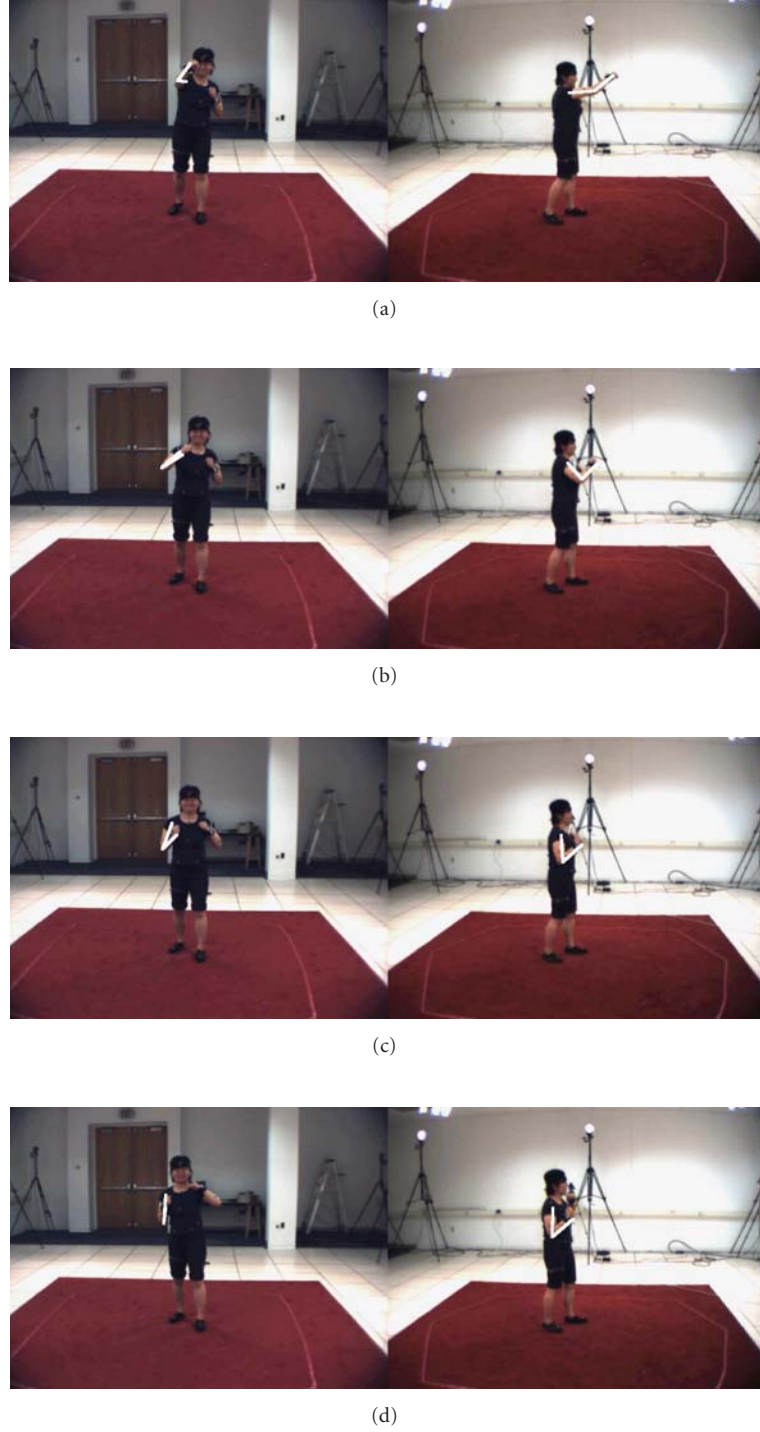


FIGURE 11: HumanEva box sequence for the subject 1, applying Inverse kinematics using image-based constraints.

In order to perform a quantitative evaluation the mean squared error is used. Formally, the error between an estimated 3D joint  $X^e$  and the truly performed one  $X^{GT}$  from ground truth data is computed as

$$D(\mathbf{X}^e, \mathbf{X}^{GT}) = \frac{1}{i} \sum \|\mathbf{X}^e - \mathbf{X}^{GT}\| \quad (9)$$

where  $i$  is the number of frames. Specifically, we compare the manually annotated elbows positions and the estimated elbows positions using the inverse kinematics with image constraints in the case of one view and in the case of two views. In addition, we also can compare with the results of the priority inverse kinematics (PIK) approach [16] because the same test sequence is used to evaluate its performance.

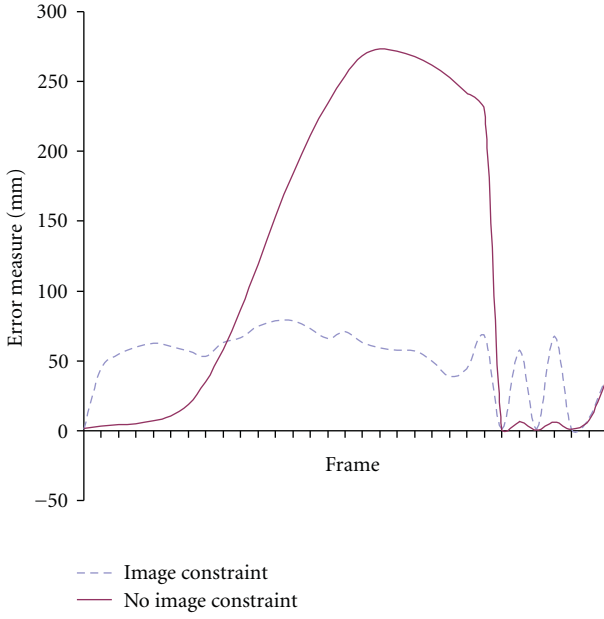


FIGURE 12: Elbow's estimation error by frame of the *box* sequence.

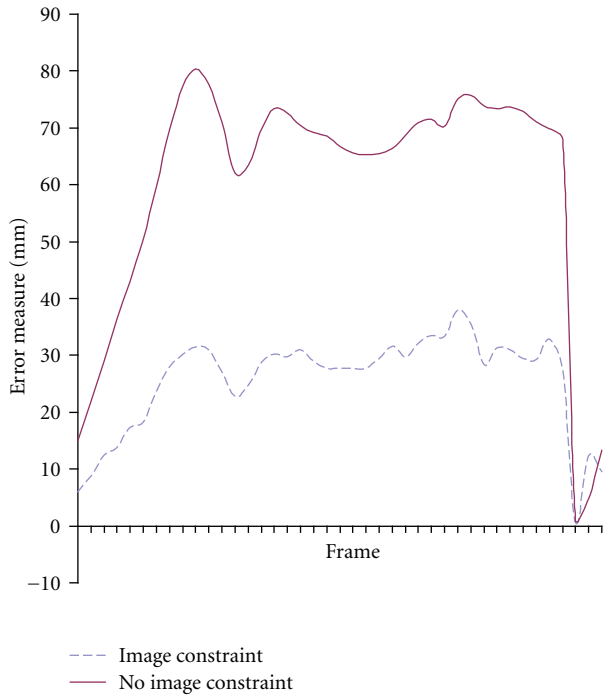


FIGURE 13: Knee's estimation error by frame of the *box* sequence.

Table 1 summarizes the results that shows how the inverse kinematics with image constraints has less error. It can also be observed how using the second view does not significantly improve the results.

TABLE 1: Comparison by using the manually annotated sequence.

	PIK (mm)	IBIK-1 view (mm)	IBIK-2 views (mm)
Left elbow	46.54	20.05	19.81
Right elbow	42.40	19.86	19.07

TABLE 2: Overall error of the estimation of the 3D positions of the internal joints for the two sequences (the elbow in the case of the arm and the knee in the case of the leg) for the two sequences.

	IK (mm)	IBIK (mm)
Box sequence	47.72	21.39
Walking sequence	40.69	16.35

**4.3. HumanEva Test.** This test evaluates our system using two views of two sequences of real motions, *walking* and *box*, of the subject 1 of HumanEva dataset. These sequences have a total of 3050 frames per view. Due to the fact that this database also contains the 3D positions of the joints by using markers, the objective of these experiments is to make a quantitative evaluation of our approach. We define an articulated chain in 3D space, with 2 rotational joints of 3 DOF each one, in order to estimate the configurations of the arm (for the *box* sequence) and the leg (for the *walking* sequence).

By using the mean square distance of (9), Table 2 shows the obtained results applying inverse kinematics with and without the image-based constraints.

Visual results for the *box* sequence are shown in Figures 10 and 11, where it is possible to see how the inverse kinematics approach loses the elbow position, and how, by adding the image-based constraints, the elbow's estimation lies inside the silhouette. This fact can also be observed in the graphic of Figure 12 where the elbow's estimation error by frame of the two approaches is displayed.

Figures 13, 14 and 15 show the results of the *walking* sequence, where a similar performance than previous sequence can also be observed. In this case, by adding the image-based constraint the recovered motion of the leg is more natural, avoiding the artifacts caused by the inverse kinematics approach in the knee's estimation.

## 5. Conclusion

The invasiveness of the sensor system, the high dimension of the posture space, and the modeling approximations in the mechanical model of the human body are sources of errors that accumulate and result in an approximate posture that could not be sufficient in biomechanical applications that study human motion precisely. Specifically, applications based on computer vision and inverse kinematics approaches presents the problem that no information was available to locate the internal joints and this forced the IK approach to make a somewhat arbitrary decision about what was the optimal angle for these joints.

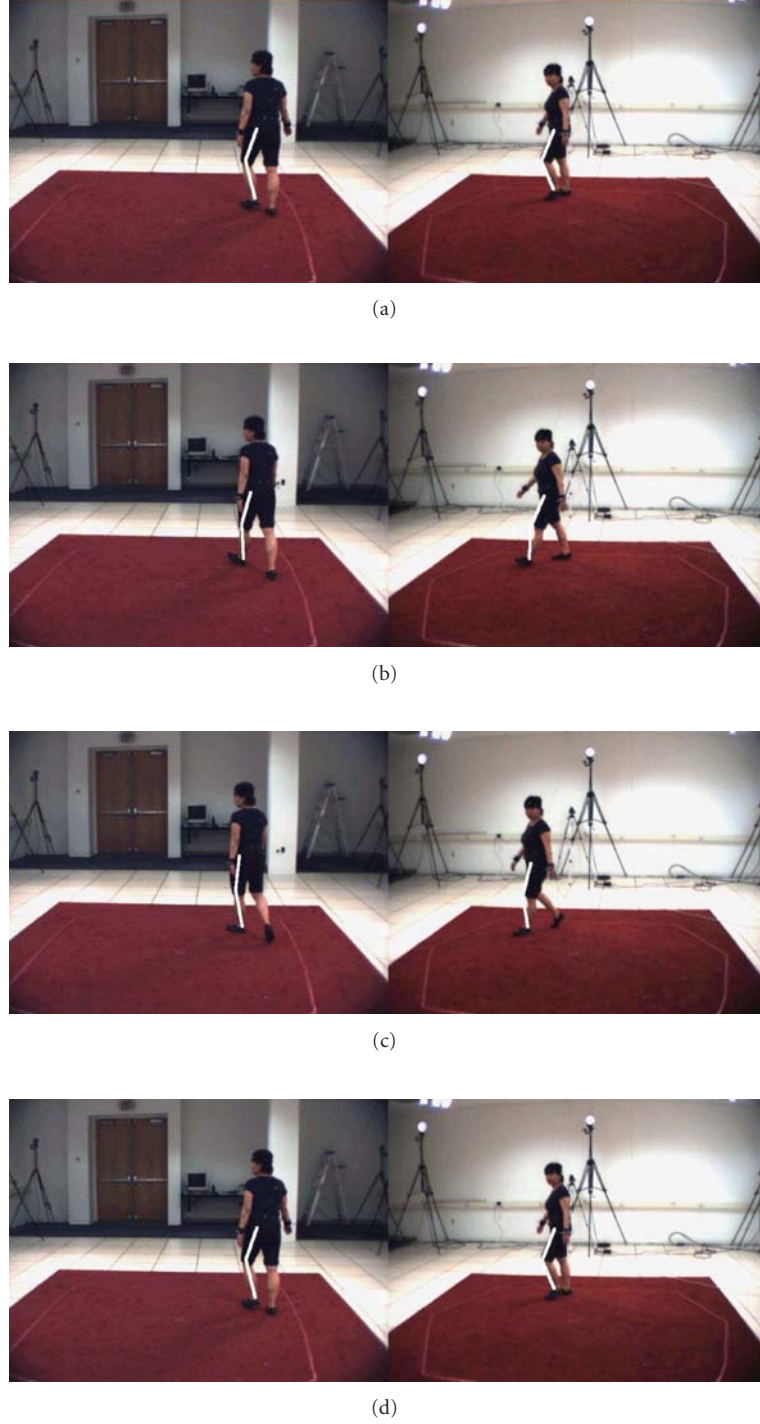


FIGURE 14: HumanEva *walking* sequence for the subject 1, applying Inverse kinematics estimation.

In this paper, we present how to add image constraints to the inverse kinematics formulation in order to solve this problem. We have proposed a criterion that tries to guide the articulated chain to the body projection into the image. In this way, impossible chain configurations are avoided. Experiments using synthetic images show how this approximation performs correctly and, how to solve difficult situations that occur when there are motions that do not

imply to the end-effectors. Besides, we have evaluated our approach using real images, including sequences of a known human motion database in order to compute quantitative results. The computed error, about 2 centimeters, can be considered as sufficiently small to permit its use in motion capture applications. Moreover, adding the image constraint implies that the solution of the kinematic chain is more independent on initial configuration.

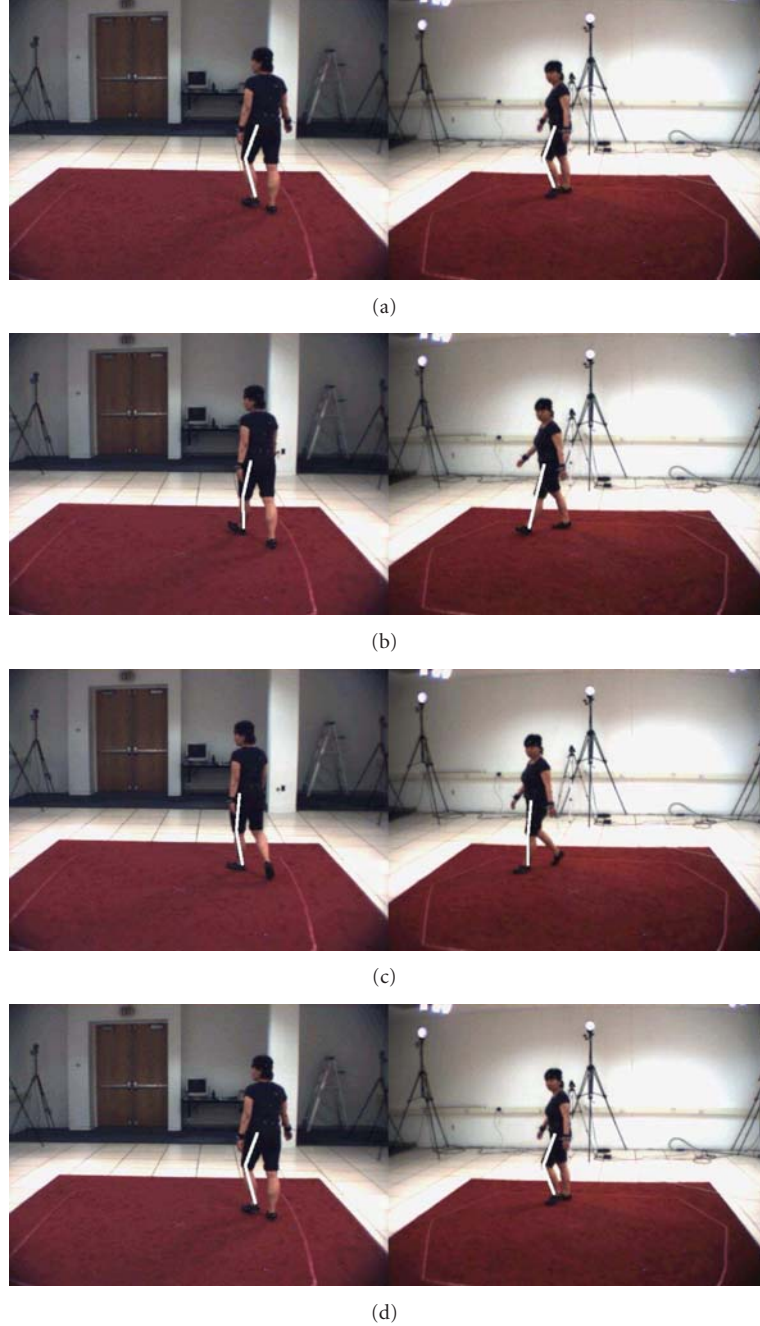


FIGURE 15: HumanEva *walking* sequence for the subject 1, applying Inverse kinematics using image-based constraints.

As future work, we plan to generalize this approach to include more tasks by using the priority strategy. In this way, it would be possible to use more complex models of the human body in to order to achieve better estimations.

## Acknowledgment

This work has been supported by the Spanish MEC under projects TIN2007-67993 and TIN2007-67896. Dr. J. Varona also acknowledge the support of a Ramon y Cajal (cofunded by the European Social Fund) Postdoctoral fellowship from the Spanish MEC.

## References

- [1] L. Mündermann, S. Corazza, and T. P. Andriacchi, "The evolution of methods for the capture of human movement leading to markerless motion capture for biomechanical applications," *Journal of NeuroEngineering and Rehabilitation*, vol. 3, article 6, 2006.
- [2] T. B. Moeslund, A. Hilton, and V. Krüger, "A survey of advances in vision-based human motion capture and analysis," *Computer Vision and Image Understanding*, vol. 104, no. 2-3, pp. 90–126, 2006.
- [3] B. Zou, S. Chen, C. Shi, and U. M. Providence, "Automatic reconstruction of 3D human motion pose from uncalibrated

- monocular video sequences based on markerless human motion tracking,” *Pattern Recognition*, vol. 42, no. 7, pp. 1559–1571, 2009.
- [4] J. Varona, A. Jaume-i-Capó, J. Gonzàlez, and F. J. Perales, “Toward natural interaction through visual recognition of body gestures in real-time,” *Interacting with Computers*, vol. 21, no. 1-2, pp. 3–10, 2009.
  - [5] D. Tolani, A. Goswami, and N. I. Badler, “Real-time inverse kinematics techniques for anthropomorphic limbs,” *Graphical Models*, vol. 62, no. 5, pp. 353–388, 2000.
  - [6] J. Zhao and N. I. Badler, “Inverse kinematics positioning using nonlinear programming for highly articulated figures,” *ACM Transactions on Graphics*, vol. 13, no. 4, pp. 313–336, 1994.
  - [7] A. Liégeois, “Automatic supervisory control of the configuration and behavior of multibody mechanisms,” *IEEE Transactions on Systems, Man and Cybernetics*, vol. 7, no. 12, pp. 868–871, 1977.
  - [8] F. Chaumette and S. Hutchinson, “Visual servo control. II. Advanced approaches [Tutorial],” *IEEE Robotics and Automation Magazine*, vol. 14, no. 1, pp. 109–118, 2007.
  - [9] E. Marchand and N. Courty, “Controlling a camera in a virtual environment,” *Visual Computer*, vol. 18, no. 1, pp. 1–19, 2002.
  - [10] P. Baerlocher and R. Boulic, “An inverse kinematics architecture enforcing an arbitrary number of strict priority levels,” *Visual Computer*, vol. 20, no. 6, pp. 402–417, 2004.
  - [11] C. A. Klein, C. Chu-Jenq, and S. Ahmed, “A new formulation of the extended Jacobian method and its use in mapping algorithmic singularities for kinematically redundant manipulators,” *IEEE Transactions on Robotics and Automation*, vol. 11, no. 1, pp. 50–55, 1995.
  - [12] T. Horprasert, D. Harwood, and L. S. Davis, “A statistical approach for real-time robust background subtraction and shadow detection,” in *Proceedings of the 7th IEEE International Conference on Computer Vision, Frame Rate Workshop (ICCV '99)*, pp. 1–19, Kerkyra, Greece, September 1999.
  - [13] D. G. Bailey, “An efficient euclidean distance transform,” in *Proceedings of the 10th International Workshop Combinatorial Image Analysis (IWCIA '04)*, pp. 394–408, Auckland, New Zealand, December 2004.
  - [14] L. Sigal and M. J. Black, “HumanEva: synchronized video and motion capture dataset for evaluation of articulated human motion,” Tech. Rep. CS-06-08, Brown University, Providence, RI, USA, 2006.
  - [15] G. R. Bradski and V. Pisarevsky, “Intel’s computer vision library: applications in calibration, stereo, segmentation, tracking, gesture, face and object recognition,” in *Proceedings of the IEEE Computer Society Conference on Computer Vision and Pattern Recognition (CVPR '00)*, vol. 2, pp. 796–797, Hilton Head Island, SC, USA, 2000.
  - [16] R. Boulic, J. Varona, L. Unzueta, M. Peinado, A. Suescun, and F. Perales, “Evaluation of on-line analytic and numeric inverse kinematics approaches driven by partial vision input,” *Virtual Reality*, vol. 10, no. 1, pp. 48–61, 2006.

## Research Article

# Segmentation, Reconstruction, and Analysis of Blood Thrombus Formation in 3D 2-Photon Microscopy Images

Jian Mu,<sup>1</sup> Xiaomin Liu,<sup>1</sup> Małgorzata M. Kamocka,<sup>2</sup> Zhiliang Xu,<sup>3</sup> Mark S. Alber,<sup>3</sup> Elliot D. Rosen,<sup>2</sup> and Danny Z. Chen<sup>1</sup>

<sup>1</sup>Department of Computer Science and Engineering, University of Notre Dame, Notre Dame, IN 46556, USA

<sup>2</sup>Department of Medical and Molecular Genetics, Indiana University School of Medicine, Indianapolis, IN 46202, USA

<sup>3</sup>Department of Mathematics, University of Notre Dame, Notre Dame, IN 46556, USA

Correspondence should be addressed to Jian Mu, jmu@nd.edu

Received 1 May 2009; Accepted 10 July 2009

Academic Editor: João Manuel R. S. Tavares

Copyright © 2010 Jian Mu et al. This is an open access article distributed under the Creative Commons Attribution License, which permits unrestricted use, distribution, and reproduction in any medium, provided the original work is properly cited.

We study the problem of segmenting, reconstructing, and analyzing the structure growth of thrombi (clots) in blood vessels *in vivo* based on 2-photon microscopic image data. First, we develop an algorithm for segmenting clots in 3D microscopic images based on density-based clustering and methods for dealing with imaging artifacts. Next, we apply the union-of-balls (or alpha-shape) algorithm to reconstruct the boundary of clots in 3D. Finally, we perform experimental studies and analysis on the reconstructed clots and obtain quantitative data of thrombus growth and structures. We conduct experiments on laser-induced injuries in vessels of two types of mice (the wild type and the type with low levels of coagulation factor VII) and analyze and compare the developing clot structures based on their reconstructed clots from image data. The results we obtain are of biomedical significance. Our quantitative analysis of the clot composition leads to better understanding of the thrombus development, and is valuable to the modeling and verification of computational simulation of thrombogenesis.

## 1. Introduction

Upon vascular injury, to prevent blood loss following a break in the blood vessel, components in the blood and vessel wall interact rapidly to form a thrombus (clot) to limit hemorrhage. Qualitative and, more importantly, quantitative analysis of the structures of developing thrombi formed *in vivo* is of significant biomedical importance. Such analysis can help identifying the factors altering thrombus growth and the structures affecting thrombus instability. A better understanding of the thrombus structures and properties is also valuable for the development of therapeutics for treating bleeding disorders.

Recent development of multiphoton intravital microscopy makes it possible to collect high-resolution, multi-channel images of developing thrombi. Thus, there is a need for computer-based methods for automatically analyzing 3D microscopic images of thrombi (i.e., stacks of 2D image slices of thrombus cross-sections). Such algorithms must be efficient, accurate, and robust, and be able to handle large

quantities of high-resolution 3D image data for quantitative analysis. In our multidisciplinary research, such algorithms can help us advance thrombus studies by providing a vital connection between the biological experimental models and the multiscale computational models of thrombogenesis (e.g., [1, 2]).

Segmentation and reconstruction on 3D microscopic images is an important yet challenging problem in biomedical imaging, and many approaches have been proposed for different imaging settings (e.g., [3, 4]). Thresholding algorithms extract a sought image object from the background based on a threshold value. There are different methods for determining the threshold value. Typical thresholding methods can be classified into three categories: (1) Histogram shape-based thresholding methods, (2) entropy based thresholding methods, and (3) spatial thresholding methods.

Histogram shape-based thresholding methods are based on the shape property of the histograms. A commonly used thresholding algorithm in this category is due to Otsu [5]

and aims to minimize the in-class variance and maximize the between-class variance. It assumes that the image to be thresholded contains two classes of pixels/voxels (e.g., the object and background), and computes the optimum threshold separating these two classes so that their combined spread (intraclass variance) is minimized. This is also equivalent to maximizing the inter-class variance. Sezan [6] performed the peak analysis by convolving the histogram function with a smoothing and differencing kernel and proposed the so-called peak-and-valley thresholding. Entropy-based thresholding algorithms exploit the entropy of the distribution of the gray levels. Johannsen and Bille [7] and Pal et al. [8] studied the Shannon entropy-based thresholding. Kapur et al. [9] strived to maximize the background and foreground entropies. Spatial thresholding methods utilize not only the gray value distribution but also the dependency of pixels in a neighborhood. Kirby and Rosenfeld [10] considered the local average gray levels for thresholding. Chanda and Majumder [11] used co-occurrence probabilities as indicators of the spatial dependency.

Unlike direct thresholding, density-based clustering methods (e.g., [12, 13]) group input points together based on not only the intensity of each point, but also the point density in its neighborhood. Thus, this approach can ignore isolated points while gathering points that are densely close to each other. It has been applied to several biomedical image segmentation problems [14–16]. Chan et al. [16] gave an automated density-based algorithm for segmenting gene expression in fluorescent confocal images, and reported that density-based segmentation outperforms direct thresholding on noisy images. However, in our setting, we noticed that applying only density-based clustering does not handle properly signal intensity fluctuation from 2D image slice to slice (the signals tend to become weaker as the slices are further away from the vessel wall). Hence, to deal with both the signal fluctuation and scattering isolated points in our problem, we develop an algorithm that combines Otsu's method [5] and density-based clustering [12, 13] to segment thrombi.

Our problem also presents other difficulties, such as fuzzy boundaries, photobleaching [17], and other imaging artifacts, which all add to the complexity of the problem. Such artifacts include movement of the vascular bed (e.g., due to animal breathing), the presence of fat and blood (caused by bleeding during tissue preparation for observation) around or on top of the vessel, and so forth. To overcome these difficulties, we first determine automatically the threshold for each type of channel values of voxels in every 2D image slice and classify the voxels using slice-specific threshold values. Then, clusters of clot voxels are obtained in 3D images using density-based clustering. Since clots contain nearby blood cells as part of their components, we also allow each cluster to include neighboring voxels for blood cells.

The main goal of our research is to establish a computer-aided platform for segmenting, reconstructing, and analyzing the development of thrombus structures in microscopic images (rather than, e.g., presenting a new image segmentation algorithm, although this paper does give a segmentation algorithm). Based on our image thrombus

segmentation/reconstruction strategies, we are able to set up an effective platform for studying clot structures. This platform enables us to identify sequences of 3D clot structures (from series of 3D images) as they grow in time, and perform quantitative analysis of clots and their dynamic shape changes. The analysis allows us to examine experimental results of actual thrombus development on laser-induced injuries in vessels of two types of mice (the wild type and the type with low levels of coagulation factor VII) captured *in vivo* by microscopic images, and compare such results quantitatively with the thrombus development predictions from a multiscale computational model [1, 2]. Thus, our platform can help refine and validate simulation results generated by the computational model, providing a valuable tool for furthering our understanding of thrombus development.

The rest of this paper is organized as follows. Section 2 presents our clot segmentation algorithm. Section 3 discusses our clot surface reconstruction strategies. Section 4 shows the experimental results. Section 5 provides quantitative analysis of various clot structures and properties. Section 6 summarizes our work and gives some concluding statements.

## 2. Clot Segmentation

A clot consists of several key components: Fibrin, platelets, as well as surrounding blood cells (leukocytes and red blood cells). Our microscopic images capture fluorescent signals of labeled thrombus components, with the following labeling scheme: *blue* is for plasma (dextran), *green* for fibrinogen/fibrin, *red* for platelets, and *black* for everything else (i.e., excluding the above three fluorescently tagged components), as shown in Figure 1. Therefore, our task is to identify and analyze the structures (or shapes) formed by red voxels and green voxels plus the surrounding voxels of “black” cells in 3D microscopic images.

As we observed from the image data, fibrin, platelets (or the red and green voxels), and surrounding black cells cluster together to form clots. However, other fibrin and platelet fluorophores also scatter around in the 3D images (since these clot components are supplied continuously by the blood flow along the vessel). That is, the scattering fluorophores may represent true data points. Thus, in this setting, while we see clusters of red and green points in the thrombi (plus surrounding black cells), the 3D space is also scattered with many other red and green points that are not part of any clot. Thus, our problem is to first identify the clusters (or galaxies) of discrete red/green points or voxels plus surrounding black voxels while at the same time ignore the “isolated” red/green points (or isolated stars), and then from the resulting clusters, reconstruct the (continuous) surfaces and volumes of the clots.

The input to our clot segmentation algorithm is a vertical sequence of 2D image slices (i.e., the slices are “parallel” to the vessel wall), called a *Z-stack*. Our algorithm consists of the following main steps: Section 2.1 threshold determination; Section 2.2 voxel classification; Section 2.3 density-based clustering; Section 2.4 black voxel inclusion.

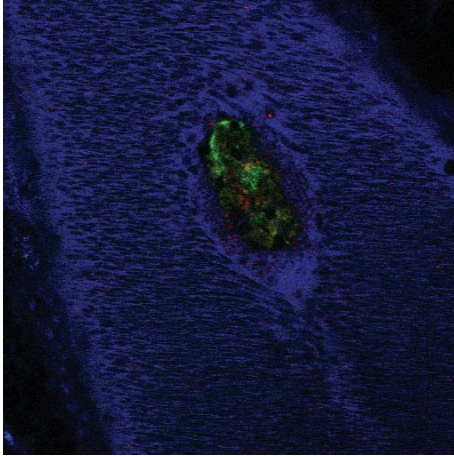


FIGURE 1: A sample input image slice (viewed better in color).

**2.1. Threshold Determination.** In our image setting, the voxel intensities often fluctuate throughout the slice sequence of a Z-stack, probably due to the setup and chosen parameters of the imaging facility for particular experiments. That is, the intensities of voxels can vary up and down (even substantially) from slice to slice, and from Z-stack to Z-stack. Actually, the information for each voxel consists of three values (called *channels*), representing the levels of red, green, and blue (each in the range of 0 to 255) of the voxel. Thus, we need to determine a specific threshold value for each channel of every individual slice for an input Z-stack (the threshold values of the three channels for different slices may be different).

Based on the outcomes of our preliminary experiments, we chose to apply Otsu's method [5] to compute the threshold values channel by channel and slice by slice. Assuming that the image to be thresholded contains two classes of pixels/voxels (e.g., object and background), Otsu's method computes the optimum threshold separating these two classes so that their combined spread (intraclass variance) is minimized. Although this method is efficient and works well for images with bimodal histograms, still it may not yield accurate segmentation results in our situation. Due to the scattering of many isolated red/green points, simple thresholding methods do not seem to be sufficient for identifying thrombi in our 2-photon microscopic images. We need to combine the thresholding method with the density-based clustering approach, as to be discussed in detail below.

**2.2. Voxel Classification.** In our image setting, since the information of any voxel consists of three channel values, representing its levels of red, green, and blue (each from 0 to 255), we need to classify each voxel as red, green, blue, or black (corresponding to the clot components of platelets, fibrin, plasma, and blood cells, respectively). Since the fluorescent signals in different channels of a voxel may not be independent of each other, there are many possible different combinations of channel values for a voxel. Thus,

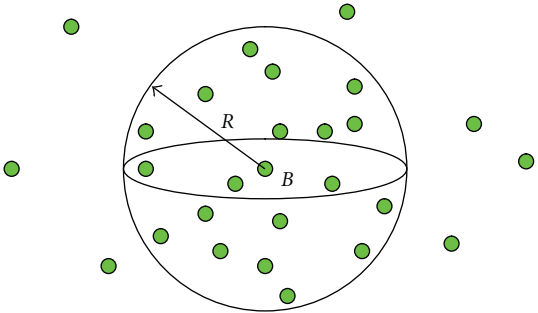


FIGURE 2: Illustrating the density-based clustering idea.

we need a method for voxel classification, based on the channel values of the voxels. Our classification method for each voxel  $v$  of every slice is as follows: Find the maximum value among the three channels of  $v$  (say, this value is red); if this red value is above the threshold of that slice for red, then  $v$  is classified as red; otherwise,  $v$  is black.

**2.3. Density-Based Clustering.** We apply Chen et al.'s density-based clustering (DBC) algorithm [12] to compute clusters of red/green voxels as well as ignoring isolated red/green voxels. Figure 2 illustrates the key concept of the DBC algorithm. The idea of density-based clustering is that, for two given parameters  $R$  (for the *neighborhood*) and  $D$  (for the *density*), if the 3D ball  $B$  of radius  $R$  centered at any red or green point contains at least (a mix of)  $D$  red/green points, then all the red/green points in the ball  $B$  are part of a cluster; further, if two clusters share any common red/green points, then they are merged into the same cluster.

As mentioned above, in the original images, there are many isolated red/green voxels (most of which are inactivated platelets and fibrin in the blood flow). Further, some platelets and fibrin may form relatively small or sparse clusters that are disconnected from the target clot and therefore should be ignored. One might consider applying filtering techniques (e.g., the median filter [18]) to remove such isolated data points and small clusters, since filtering techniques are often effective for removing noise in images. However, most filters have the undesired side-effects of changing the intensity values of certain voxels, blurring the boundary between different objects, or creating additional false positive points in the images. In our clot study, because we need to analyze the clot components quantitatively (both in the volume and on the surface), we prefer to keep the original voxel intensity values unchanged for the output precision of our quantitative analysis. The DBC approach can solve this kind of clustering problem without making any change to the image data. By using suitably chosen parameter values of the neighborhood  $R$  and density  $D$ , it allows us to identify large dense clusters (clots) and discard regions of low density (i.e., the background and isolated or small groups of inactivated platelet and fibrin voxels).

One important issue to the DBC approach is to choose appropriate values for the neighborhood parameter  $R$  and

density parameter  $D$ . A heuristic algorithm for determining the parameter values of  $R$  and  $D$  was given in [19]. This general heuristic method, however, may not always produce effective parameter values for all different applications and situations. Expert input and decisions are often needed in determining the actual parameter values of  $R$  and  $D$  in specific applications, such as our particular case.

Based on our experiments and evaluations, we choose the ball radius  $R = 5$  and the density value  $D = 80$ . The reason for using a “high” density value,  $D = 80$ , is as follows. After a cluster is produced by the DBC approach (in this step), we need to “expand” it (in the next step) by including the surrounding black voxels (to capture the nearby blood cells). The cluster expansion should not take blue voxels, but it should include nearby red/green voxels as well. Thus, this expansion process actually includes all surrounding non-blue voxels. With a relatively high density value, we preserve a dense cluster structure (although some “sparse” red/green voxels around the current cluster boundary may be excluded in the DBC process). This loss of information is compensated by allowing the clot to capture the nearby red/green/black voxels in the cluster expansion process.

The value of the ball radius  $R$  is determined as follows. For a given density parameter  $D = 80$ , if we set  $R = 5$ , then the threshold value for the density is about 15% (which means that at least 15% of the voxels inside the ball must belong to the point set of interest). The experimental results produced using these two parameters match well with the experts’ manually segmented results. If we set the  $R$  value to (say) 4, then accordingly the threshold is raised to about 30%. But, our experimental results show that this fails to capture some of the nearby voxels which the biologists think should be included as part of the clot. Of course, we could use larger values for  $R$  and  $D$ ; however, experimental results indicate that this does not make too much difference in the final results (i.e., the output clots). Yet, the larger values for  $R$  and  $D$  require considerably more computation. Therefore, the two parameter values we chose to use,  $D = 80$  and  $R = 5$ , are suitable for our purpose. In different imaging settings, the users may estimate the percentage of the undesired points (the undesired points may be noise, or as in our application, scattered points of interest) and come up with other appropriate parameter values.

**2.4. Black Voxel Inclusion.** In the previous steps, we only look for voxel clusters of platelets and fibrin. Actually, there are also some blood cells which appear as black voxels surrounding the clot structure. These blood cells are also part of the clot and should be taken into account. The goal of this step is to include these nearby black voxels into the clot and compensate the loss of red/green voxels around the cluster boundary due to the DBC clustering. For every cluster voxel, we examine its neighboring voxels and decide whether these voxels should be added to the clot. Such a voxel  $v$  is added to the clot if and only if  $v$  is not yet part of the clot and is non-blue. Here we use the 6-connected neighborhood (in 3D) for clot expansion. The expansion process continues iteratively until all surrounding non-blue voxels are taken by the clot.

### 3. Clot Surface Reconstruction

Each cluster produced by the above segmentation algorithm is merely a collection (or “cloud”) of discrete points (or voxels) in 3D. To obtain the clot formed by a point cloud, we need to “impose” some continuous “shape” to the voxel cluster in order to achieve structures such as the surface and volume of the clot. To construct the boundary of the clot, we first use the 3D morphological dilation method [20] to define a ball around each voxel of the cluster, resulting in the union of a cluster of balls in 3D. In this way, we connect or attach nearby discrete voxels into a continuous boundary of the clot. We then use the marching cube algorithm [21] to transform the dilated clot volume into meshed surfaces.

An alternative method is to apply the alpha shape algorithm [22] that selects a subset of the input points to define the “shape” boundary of an input point cloud based on a parameter  $\alpha$ . With different  $\alpha$  values, one can attain different levels of details of the clot surface. The  $\alpha$ -shape of the point cloud degenerates to the input point set as the value of  $\alpha$  approaches to 0, and it becomes the convex hull of the input point set as  $\alpha$  approaches to  $+\infty$ . This feature of the alpha shape algorithm may serve as a good tool for further analysis of the clot shapes, as the users can control the level of details on the clot surface based on their needs.

## 4. Experimental Results

In our experiments, we use a Zeiss LSM-510 Meta confocal/multiphoton microscopy system equipped with a tunable Titanium-Sapphire laser at the Indiana Center for Biological Microscopy. Direct laser-induced injuries are made in the mesentery veins of mice that either are normal (the wild type) or have different levels of coagulation factor VII (we use FVII to denote coagulation factor VII).

Our algorithms are performed on 17 wild-type injuries and 15 low FVII injuries. For each injury, we produce a sequence of 3D images (Z-stacks), every forty seconds per 3D image, for a total of 15 Z-stacks. Typically, each Z-stack consists of about 80 2D slices; each slice is of a size of  $512 \times 512$  voxels.

In the experiments, the development of thrombi is monitored by intravital multiphoton microscopy in a single optical plane. In addition to the confocal video microscopy in one plane, we can also generate a vertical stack of 2-photon images that can be compiled to form a 3D reconstruction of thrombi. This allows us to obtain a vertical stack of plane images (a Z-stack), or a series of Z-stacks (a 4D image with time as the 4th dimension). A key feature of this model that distinguishes it from other experimental models of intravital fluorescence video microscopy is that we record in 2-photon confocal mode.

**4.1. Evaluation.** We ran our algorithms on all the Z-stacks (about 480 of them) to reconstruct clots. Figure 3(b) shows an example of our 3D clot reconstruction.

To evaluate the effectiveness of our algorithms, a biologist manually identified clots from Z-stacks, assisted by the commercially available software Metamorph. Although

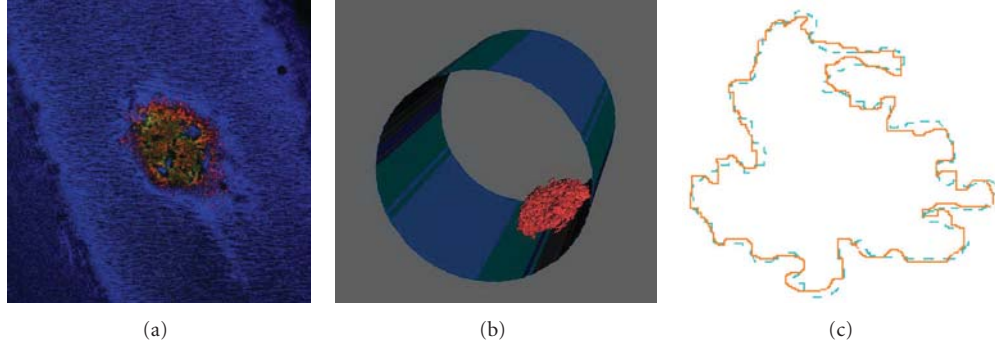


FIGURE 3: (a) One slice of an input Z-stack, (b) a reconstructed 3D clot attached to the vessel wall, (c) a 2D example of comparison and evaluation: expert-produced result (solid curve) and output by our algorithms (dashed curve).

Metamorph is a powerful tool for image acquisition, process, and analysis, manually generating segmentation results with it is still a very tedious and time-consuming process since it takes lots of human efforts to estimate parameter values. The biologist manually set the threshold for each voxel channel based on experience and segmented the thrombi on some 2D slices using Metamorph. As an example, a manually segmented result and the output of our algorithms on the same image data are compared in Figure 3(c). One can see that these two results match very well with each other. A quantitative comparison of the example shapes in Figure 3(c) is as follows. The area inside the solid curve: 16779; the area inside the dashed curve: 16957; the area of their intersection: 15505; the symmetric difference error: 2726.

**4.2. Implementation and Execution Time.** We implemented our image segmentation algorithm on a computer with a 1.73 GHz Pentium Dual-Core CPU and 2 GB memory. The reconstruction algorithm was implemented on a computer with a 2.5 GHz Intel Quad-Core CPU and 4 GB memory. The typical execution time is the following. That for a Z-stack of 80 slices, each slice of size  $512 \times 512$ , the segmentation and reconstruction run in well under one minute (about 15 seconds for segmentation and about 30 seconds for reconstruction).

## 5. Analysis Results

To determine the composition and volumes of the clots, we compute the number of voxels in each clot component. Table 1 compares the volume sizes of the clot components in two Z-stacks, one for a typical wild-type injury and the other for a typical FVII deficient type injury (here,  $(+, +, -)$ , e.g., means the red channel value and green channel value of a voxel are both above their corresponding thresholds, and the blue channel value is below its threshold).

Figure 4 shows some profile curves of the distributions of the clot components along the distance from the vessel wall.

Figure 5 gives a comparison between the thrombi in injuries of the wild-type and low FVII mice, which illustrates how thrombi develop over time and the effects of FVII.

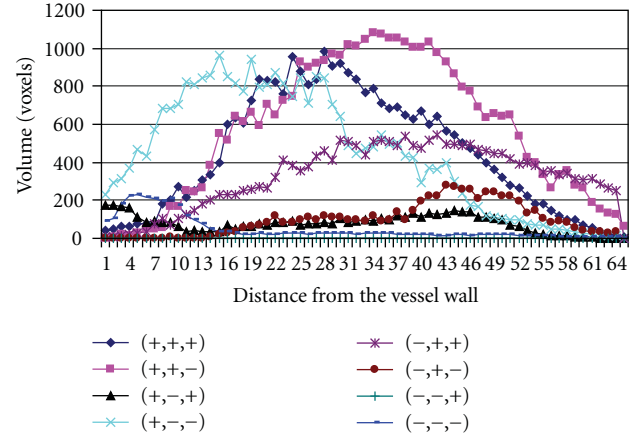


FIGURE 4: The profile curves of the distributions of the clot components.

Here, laser-induced injuries were made in mesentery venules (100 micron diameter). The results show that for a typical clot of the wild type, its volume increases rapidly at the earlier time points and then shrinks significantly soon after its peak; after a few minutes, the size of the clot becomes relatively stable and does not change much. In contrast, while platelets initially accumulate at the injury sites of low FVII mice, the clot structures are unstable and embolize from the vessel wall. Smaller thrombi do begin to form at later times as some fibrin starts to accumulate in the thrombi. The instability of the developing thrombi in the absence of FVIIa-mediated fibrin generation can be seen from Figure 5. The wild-type and low FVII thrombi also incorporate an increasing number of blood cells (such as leukocytes and/or erythrocytes).

Our analysis results show that, for a common wild-type injury, the size of the clot usually peaks in one or two minutes after the injury is made, and stabilizes about two minutes after the peak. However, for low FVII injuries, the size of the clot is not stable, with some significant ups and downs in the size. We also observe more blood cells covering the developing thrombi at later time points. Further, as time goes, we see an increasing number of

TABLE 1: (A) is for a wild-type injury and (B) is for an FVII deficient type injury. The thrombi were at 1 minute after the injury.

(R,G,B)	Vol. (A)	% (A)	Vol. (B)	% (B)
(+, +, +)	36843	14.1695	783	6.4244
(+, +, -)	114525	44.0452	1084	8.894
(+, -, +)	22596	8.6902	2853	23.4083
(+, -, -)	78190	30.0711	6875	56.4079
(-, +, +)	493	0.1896	8	0.0656
(-, +, -)	3014	1.1592	185	1.5179
(-, -, +)	0	0	0	0
(-, -, -)	4356	1.6753	400	3.2819

TABLE 2: Porosity of a wild-type clot at different time points: T1 (40 seconds after injury), T2 (80 seconds), and T6 (4 minutes).

Sample no.	T1	Porosity (%)	T2	Porosity (%)	T6	Porosity (%)
1	59325	20.90	63333	15.56	69012	7.98
2	57746	23.00	63794	14.94	69581	7.23
3	58120	22.51	64041	14.61	68837	8.22
4	58901	21.47	64183	14.42	68540	8.61
5	58311	22.25	64370	14.17	69904	6.79
6	58019	22.64	64494	14.01	69331	7.56
7	57908	22.79	64450	14.07	68799	8.27
8	57899	22.80	64323	14.24	68736	8.35
9	58062	22.58	64139	14.48	69012	7.98
10	57803	22.93	63916	14.78	69538	7.28

fibrin/fibrinogen on the clot surface. That is, at the beginning stage, there is a burst of platelets on the surface; however, the number of fibrin/fibrinogen gradually increases and becomes dominant. This is consistent with our hypothesis that the fibril network on the clot surface is an important factor which regulates thrombus growth and affects thrombus stability. Figure 6 to some extent justifies our hypothesis. It shows the composition of different components on the surfaces of the clots; the curves indicate that, for wild-type clots, the number of fibrin/fibrinogen gradually increases over time. However, low FVII clots do not show this trend. Here we use only two typical clots to illustrate our analysis. Other wild-type/low FVII clots show a similar fashion of growth.

Figure 7 shows how the shape of a wild-type clot changes in time (the clot structures are at 1, 1.5, and 4 minutes after a laser-induced injury was made on the vessel wall). We can clearly see in the figure that at later time points, fibrin/fibrinogen cells (green voxels in the figure) become dominant on the clot surface.

Other than the size and shape of a clot, another important factor that may be related to the blood flow is the permeability of the clot. A clot can be viewed as a porous medium, and its permeability is measured by its porosity. The porosity of a clot is represented by a percentage which indicates the proportion of the void (i.e., nonclot) space in a rectangular cuboid region which is entirely contained in the volume of the clot. This percentage represents the ratio of

the total volume of the void space over the total volume of the region of interest (the region normally includes both clot and void voxels). To ensure the robustness of the percentage value of porosity, after we select the initial position of the “box” (i.e., cuboid region), we gradually move the box around to check how consistent this ratio value is in nearby locations. (In this experiment, we moved the box along certain directions and used a step length of 2; for each box size, we produced 10 sample values.) During the process of moving the box, we maintain the same box size and make sure that the entire box is always inside the clot volume. Table 2 shows some experimental data. Here we use a box size of  $30 \times 50 \times 50$ . We counted the number of clot voxels inside the box and calculated the porosity (we only calculated the porosity of the wild-type clots, which grow in a more regular fashion).

From Table 2, one can see that at the earlier time points, a clot is more permeable than it is at the later time points. As time goes, the clot tends to become more and more compact. This is due largely to the fact that cells on and near the clot surface (most of these cells are platelets at earlier time points) are less adhesive to each other than cells in the inside and are easily flushed away by the blood flow. For further analysis, two of the coauthors of this paper, Drs. Alber and Xu, are leading a research effort aiming to construct a multiscale simulation model for predicting how clots grow under different flow conditions and different factors which may regulate the clot growth [2].

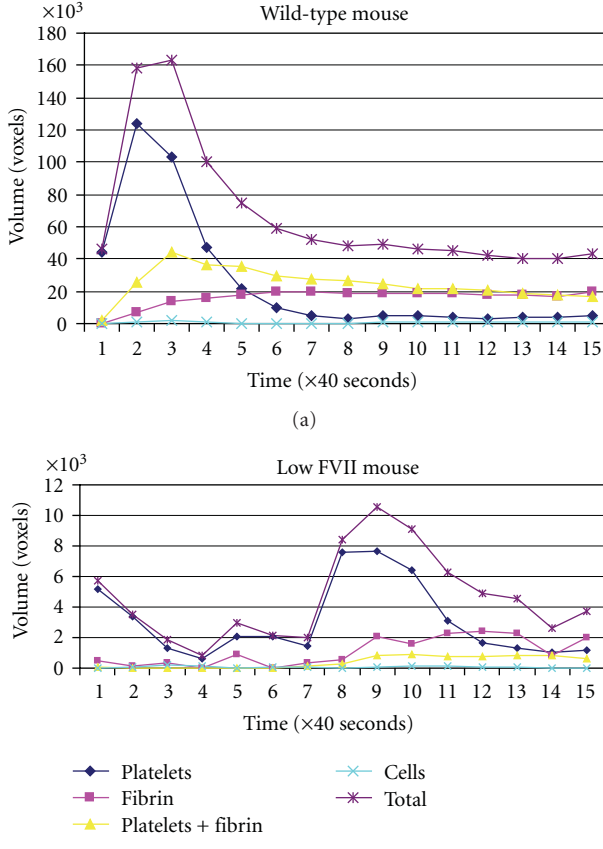


FIGURE 5: The effects of FVII on the structures of venous thrombi.

## 6. Conclusions

We presented a new approach for segmentation, reconstruction, and analysis of 3D thrombi in 2-photon microscopic images. Our method and platform have been applied to study the structural differences between thrombi formed in wild-type and low FVII mice. Thrombi in low FVII mice are smaller, have a lower fibrin content, and are less stable than those in wild-type mice.

Our platform for reconstruction and analysis of 3D thrombi from 2-photon microscopic images will be a valuable tool, allowing one to process a large amount of images in a relatively short time. The high-resolution quantitative structural analysis using our algorithms provides new metrics that are likely to be critical to characterizing and understanding biomedically relevant features of thrombi. For instance, the reconstructed structures of the developing thrombi (Figure 7) show the shapes of heterogeneous subdomains of the clot enriched with different thrombus components. Since these subdomains have different mechano-elastic properties, the interfaces between such subdomains are potential sites responsible for structural instability.

With the ability to provide a quantitative description of the thrombus structures, it will be possible to com-

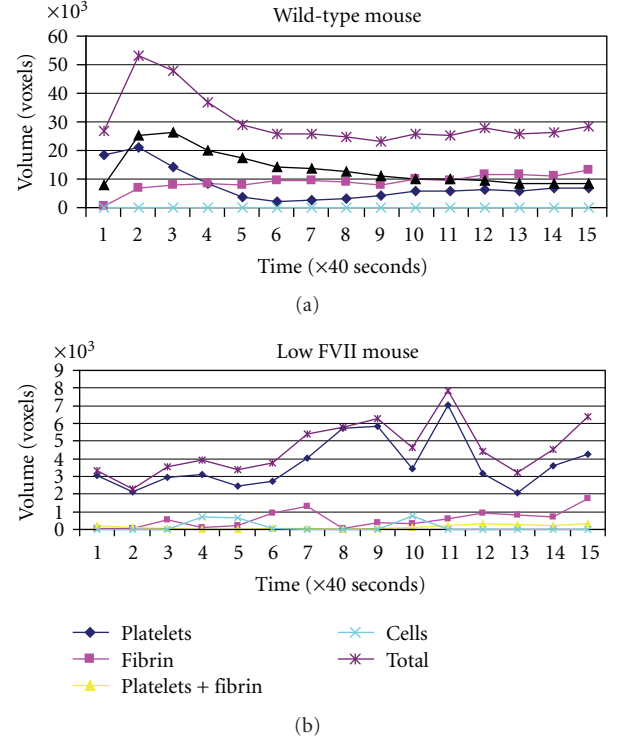


FIGURE 6: The composition of different components on the clot surface.

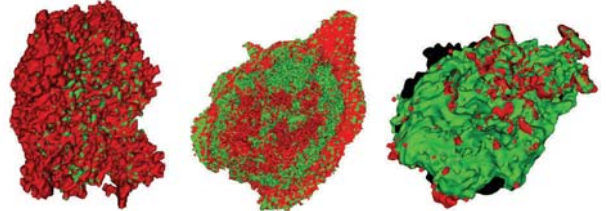


FIGURE 7: A reconstructed 3D clot as it changes in time (red for platelets, green for fibrinogen/fibrin, and black for other blood cells).

pare biological experimental thrombi monitored by multiphoton microscopy for their development *in vivo* with the predictions of a multiscale computational model of thrombogenesis [1, 2]. Such quantitative comparisons are essential to the refinement and validation of the simulation model. Currently, we have the individual modules and procedures of the programs working, and the effectiveness of our approaches has been shown by our experiments, as discussed in Sections 4 and 5. However, the software system as a whole is still under development (it is not yet ready and available as a software tool to the research community at this time, while we are working towards this goal). Nevertheless, we anticipate that the integration of the experimental and computational approaches for thrombogenesis made possible by our image processing strategies will provide an effective tool for analyzing and understanding the biomedically important yet complex processes of thrombus development.

## Acknowledgments

The authors would like to thank Amy Zollman for technical assistance and Professor Kenneth W. Dunn and Professor Sherry G. Clendenon for assistance with multiphoton microscopy. This research was supported in part by NSF Grants CCF-0515203, CCF-0916606, and DMS-0800612, NIH Grants R01-EB004640 and HL073750-01A1, and the INGEN Initiative to Indiana University School of Medicine. The work of X. Liu was supported in part by a graduate fellowship from the Center for Applied Mathematics, University of Notre Dame.

## References

- [1] Z. Xu, N. Chen, M. M. Kamocka, E. D. Rosen, and M. Alber, "A multiscale model of thrombus development," *Journal of the Royal Society Interface*, vol. 5, no. 24, pp. 705–722, 2008.
- [2] Z. Xu, N. Chen, S. C. Shadden, et al., "Study of blood flow impact on growth of thrombi using a multiscale model," *Soft Matter*, vol. 5, no. 4, pp. 769–779, 2009.
- [3] X. Yang, H. Beyenal, G. Harkin, and Z. Lewandowski, "Quantifying biofilm structure using image analysis," *Journal of Microbiological Methods*, vol. 39, no. 2, pp. 109–119, 1999.
- [4] T. Zhu, H. C. Zhao, J. Wu, and M. F. Hoylaerts, "Three-dimensional reconstruction of thrombus formation during photochemically induced arterial and venous thrombosis," *Annals of Biomedical Engineering*, vol. 31, no. 5, pp. 515–525, 2003.
- [5] N. Otsu, "A threshold selection method from gray-level histograms," *IEEE Transactions on Systems, Man, and Cybernetics*, vol. 9, no. 1, pp. 62–66, 1979.
- [6] M. I. Sezan, "A peak detection algorithm and its application to histogram-based image data reduction," *Graphical Models and Image Processing*, vol. 29, pp. 47–59, 1985.
- [7] G. Johannsen and J. Bille, "A threshold selection method using information measures," in *Proceedings of the 6th International Conference of Pattern Recognition (ICPR '82)*, pp. 140–143, Munich, Germany, 1982.
- [8] S. K. Pal, R. A. King, and A. A. Hashim, "Automatic grey level thresholding through index of fuzziness and entropy," *Pattern Recognition Letters*, vol. 1, no. 3, pp. 141–146, 1983.
- [9] J. N. Kapur, P. K. Sahoo, and A. K. C. Wong, "A new method for gray-level picture thresholding using the entropy of the histogram," *Computer Vision, Graphics, & Image Processing*, vol. 29, no. 3, pp. 273–285, 1985.
- [10] R. L. Kirby and A. Rosenfeld, "A note on the use of (gray level, local average gray level) space as an aid in threshold selection," *IEEE Transactions on Systems, Man and Cybernetics*, vol. 9, no. 12, pp. 860–864, 1979.
- [11] B. Chanda and D. D. Majumder, "A note on the use of the graylevel co-occurrence matrix in threshold selection," *Signal Processing*, vol. 15, no. 2, pp. 149–167, 1988.
- [12] D. Z. Chen, M. Smid, and B. Xu, "Geometric algorithms for density-based data clustering," *International Journal of Computational Geometry and Applications*, vol. 15, no. 3, pp. 239–260, 2005.
- [13] M. Ester, H.-P. Kriegel, J. Sander, and X. Xu, "A density-based algorithm for discovering clusters in large spatial databases with noise," in *Proceedings of 2nd International Conference on Knowledge Discovery and Data Mining (KDD '96)*, pp. 226–231, Portland, Ore, USA, 1996.
- [14] M. E. Celebi, Y. A. Aslandogan, and P. R. Bergstresser, "Mining biomedical images with density-based clustering," in *Proceedings of International Conference on Information Technology: Coding and Computing (ITCC '05)*, vol. 1, pp. 163–168, Las Vegas, Nev, USA, April 2005.
- [15] Y. Song, C. Xie, Y. Zhu, C. Li, and J. Chen, "Function based medical image clustering analysis and research," *Advances in Computer, Information, and Systems Sciences, and Engineering*, pp. 149–155, 2006.
- [16] P.-K. Chan, S.-H. Cheng, and T.-C. Poon, "Automated segmentation in confocal images using a density clustering method," *Journal of Electronic Imaging*, vol. 16, no. 4, Article ID 043003, 9 pages, 2007.
- [17] B. Herman, M. J. Parry-Hill, I. D. Johnson, and M. W. Davidson, "Introduction to optical microscopy," 2003, <http://micro.magnet.fsu.edu/primer/java/fluorescence/photobleaching/index.html>.
- [18] B. Weiss, "Fast median and bilateral filtering," *ACM Transactions on Graphics*, vol. 25, no. 3, pp. 519–526, 2006.
- [19] M. Ester, H.-P. Kriegel, J. Sander, and X. Xu, "A density-based algorithm for discovering clusters in large spatial databases with noise," in *Proceedings of the 2nd International Conference on Knowledge Discovery and Data Mining (KDD '96)*, pp. 226–231, Portland, Ore, USA, 1996.
- [20] E. R. Dougherty, *An Introduction to Morphological Image Processing*, SPIE Optical Engineering Press, Center for Imaging Science Rochester Institute of Technology, Bellingham, Wash, USA, 1992.
- [21] W. E. Lorensen and H. E. Cline, "Marching cubes: a high resolution 3D surface construction algorithm," *Computer Graphics*, vol. 21, no. 4, pp. 163–169, 1987.
- [22] H. Edelsbrunner and E. P. Mücke, "Three-dimensional alpha shapes," *ACM Transactions on Graphics*, vol. 13, no. 1, pp. 43–72, 1994.

## Research Article

# Evaluation of a Validation Method for MR Imaging-Based Motion Tracking Using Image Simulation

**Kevin M. Moerman,<sup>1</sup> Christian M. Kerskens,<sup>2</sup> Caitríona Lally,<sup>3</sup> Vittoria Flamini,<sup>3</sup> and Ciaran K. Simms<sup>1</sup>**

<sup>1</sup> Trinity Centre for Bioengineering, School of Engineering, Parsons Building, Trinity College, Dublin 2, Ireland

<sup>2</sup> Trinity College Institute of Neuroscience, Trinity College Dublin, Dublin, Ireland

<sup>3</sup> Mechanical and Manufacturing Engineering, Dublin City University, Dublin, Ireland

Correspondence should be addressed to Kevin M. Moerman, moermank@tcd.ie

Received 1 May 2009; Accepted 20 July 2009

Academic Editor: João Manuel R. S. Tavares

Copyright © 2010 Kevin M. Moerman et al. This is an open access article distributed under the Creative Commons Attribution License, which permits unrestricted use, distribution, and reproduction in any medium, provided the original work is properly cited.

Magnetic Resonance (MR) imaging-based motion and deformation tracking techniques combined with finite element (FE) analysis are a powerful method for soft tissue constitutive model parameter identification. However, deriving deformation data from MR images is complex and generally requires validation. In this paper a validation method is presented based on a silicone gel phantom containing contrasting spherical markers. Tracking of these markers provides a direct measure of deformation. Validation of in vivo medical imaging techniques is often challenging due to the lack of appropriate reference data and the validation method may lack an appropriate reference. This paper evaluates a validation method using simulated MR image data. This provided an appropriate reference and allowed different error sources to be studied independently and allowed evaluation of the method for various signal-to-noise ratios (SNRs). The geometric bias error was between  $0\text{--}5.560 \times 10^{-3}$  voxels while the noisy magnitude MR image simulations demonstrated errors under 0.1161 voxels (SNR: 5–35).

## 1. Introduction

The body responds to mechanical loading on several timescales (e.g., [1, 2]), but in vivo measurement of critical parameters such as muscle load, joint reaction force, and tissue stress/strain is usually not possible [3, 4]. In contrast, suitably validated computational models can predict all of these parameters, and they are therefore a powerful tool for understanding the musculoskeletal system [4, 5] and are in use in diverse applications from impact biomechanics [6, 7] to rehabilitation engineering [8, 9], surgical simulation [10, 11], and soft tissue drug transport [12].

Skeletal muscle tissue in compression is nonlinear elastic, anisotropic, and viscoelastic, and a constitutive model with very good predictive capabilities for in vitro porcine muscle has been proposed [13, 14]. However, validating this model for living human tissue presents significant difficulties. Some authors have used indentation tests on skeletal muscle [15, 16], but the tissue was then assumed to be isotropic and

linear in elastic and viscoelastic properties. In contrast, noninvasive imaging methods that allow detailed measurement of human soft tissue motion and deformation (due to known loading conditions) combined with inverse finite element (FE) analysis allow for the evaluation of more complex constitutive models.

The work presented here is part of a study aiming to use indentation tests on the human arm, tagged Magnetic Resonance (MR) imaging and inverse FE analysis to determine the mechanical properties of passive living human skeletal muscle tissue using the constitutive model described in [13, 14].

Recently the potential of using surface deformation measurements from 3D digital image correlation to assess mechanical states throughout the bulk of a tissue has been shown [17]. However MR imaging combined with deformation tracking techniques can provide 3D deformation data throughout the tissue volume and is ideal for the evaluation of constitutive models such as [13, 14]. MR imaging has

been used to study skin [18], heart [19], and recently also rat skeletal muscle [20] (though a simplified Neo-Hookean model was applied).

The techniques for tracking tissue deformation from (e.g., tagged) MR imaging are complex and require validation using an independent measure of deformation. Since physically implanting markers is not feasible and anatomic landmarks are either absent or difficult to track, alternative methods have been employed. Young et al. [21] recorded angular displacement of a silicone gel phantom using tagged MR images and evaluated the results using FE modelling and 2D surface deformation derived from optical tracking of lines painted on the phantom surface. Similarly, Moore et al. [22] used optical tracking of surface lines on a silicone rubber phantom to validate MR-based deformation measures. However simple tensile stretch was applied and only a 2D measure of surface deformation was used. There were also temporal synchronisation issues between the optical and MR image data. In both of the optical validations studies above the error related to the optical tracking method was not quantified. Other authors have used implantable markers. For instance Yeon et al. [23] used implanted crystals and sonomicrometric measurements for validation of tagged MR imaging of the canine heart. However the locations of the crystals were verified manually by mapping with respect to surface cardiac landmarks in the excised heart and matching problems between MR and sonomicrometric measurements occurred. Neu et al. [24, 25] evaluated a tagged MR imaging-based deformation tracking technique for cartilage using spherical marker tracking in a silicone soft tissue phantom. However the marker centres were determined by manually fitting a circle to each marker in two orthogonal directions and imaging was performed on excised tissue samples at high resolution (over 32 voxels across marker diameter) using a nonclinical 7.05T scanner.

This paper shows that validation of *in vivo* medical imaging techniques and image processing algorithms is challenging partially due to the lack of appropriate reference data. Although experimental validation methods using soft tissue MR imaging phantoms can be developed, the data derived from these often suffers uncertainties similar to those present in the target soft tissue. Therefore the validation method itself often lacks an appropriate reference. In this paper a novel technique for the validation of a 3D MR imaging-based motion and deformation tracking technique, applicable to 3D deformation, is presented. The validation method, based on marker tracking, was evaluated (and validated) using simulated magnitude MR image data because this allows full control and knowledge of marker locations and thus provides the final real “gold standard.” It addition this allows for the independent analysis of geometric bias and of method performance across a wide range of realistic noise conditions.

## 2. Methods

**2.1. The Tissue Phantom.** The proposed validation configuration is an MR compatible indentor used to apply deformation to a phantom and provides an independent

measure of deformation allowing validation of MR imaging-based motion and deformation tracking. A silicone gel soft tissue phantom was developed to represent deformation modes expected in the human upper arm due to external compression (see Figure 1), as such the phantom resembles a cylindrical soft tissue region containing a stiff bonelike core. The gel (SYLGARD 527 A&B Dow Corning, MI, USA) has similar MR [26] and mechanical [17] properties to human soft tissue and has been used in numerous MR imaging-based studies on soft tissue biomechanics [21, 24, 27–34]. Embedded in the gel are contrasting spherical polyoxymethylene balls of  $3 \pm 0.05$  mm diameter (The Precision Plastic Ball Co Ltd, Addingham, UK). The lack of signal in the markers in comparison to the high gel signal allows tracking.

**2.2. MR Imaging.** The type of image data used in the current study is T2 magnitude MR images. Deformation can be measured using marker tracking methods applied to full volume scans taken at each deformation step. A full volume scan was performed on the tissue phantom using a 3T scanner (Philips Achieva 3T, Best, The Netherlands). Cubic 0.5 mm voxels were used and the data was stored using the Digital Imaging and Communication in Medicine (DICOM) format. Figures 1(a) and 1(b) show an example of an MR image and tagged MR image of a region of the phantom. The voxel intensities of the images are 9 bit unsigned integers with values ranging from 0 to 511. The data was imported into Matlab 7.4 R2007a (The Mathworks Inc., USA) for image processing. The image data was normalised producing an average gel intensity of 0.39, while the marker intensity was zero.

**2.3. Marker Tracking Method.** To track the movement of markers from the 3D MR data an image processing algorithm was developed in Matlab (The Mathworks Inc., USA). The centre point of each marker at each time step can be found using 3 main steps: (1) *masking*, (2) *adjacency grouping*, and (3) *centre point calculation*.

**(1) Masking.** Masking was performed to identify the central voxels for each marker. To reduce computational time the mask was only applied to voxels that qualify (based on intensity threshold) as potentially belonging to a marker. In addition a sparse cross-shaped mask was designed (Figure 2(a)) with just 12 voxels (significantly less than nonsparse cubic or spherical masks which would be around 729 and 250 voxels, resp.). When the mask operates on a voxel  $v$  with image coordinates  $(i, j, k)$ , the image coordinates of the 12 (surrounding) mask voxels  $(i_m, j_m, k_m)$  can be defined as

$$\begin{pmatrix} i_m \\ j_m \\ k_m \end{pmatrix} = \begin{pmatrix} i + (1, -1, 0, 0, 0, 0, 4, -4, 0, 0, 0, 0) \\ j + (0, 0, 1, -1, 0, 0, 0, 0, 4, -4, 0, 0) \\ k + (0, 0, 0, 0, 1, -1, 0, 0, 0, 0, 4, -4) \end{pmatrix}. \quad (1)$$

Image processing masks are generally used as a spatial filter; however in this case the mask was used as a logic operator to find voxels matching the following criterion. A voxel  $v$  at

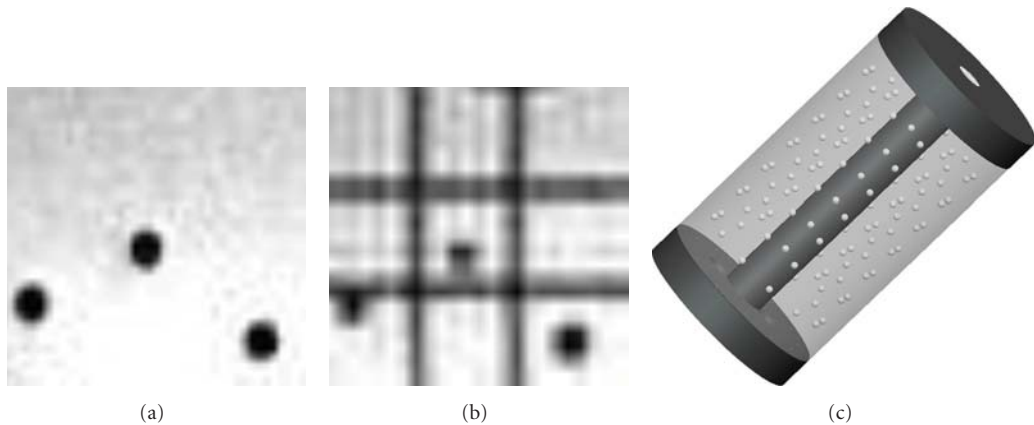


FIGURE 1: (a) An MR image of a gel region with markers, (b) a tagged MR image region, and (c) the silicone gel soft tissue phantom containing the spherical markers (white balls).

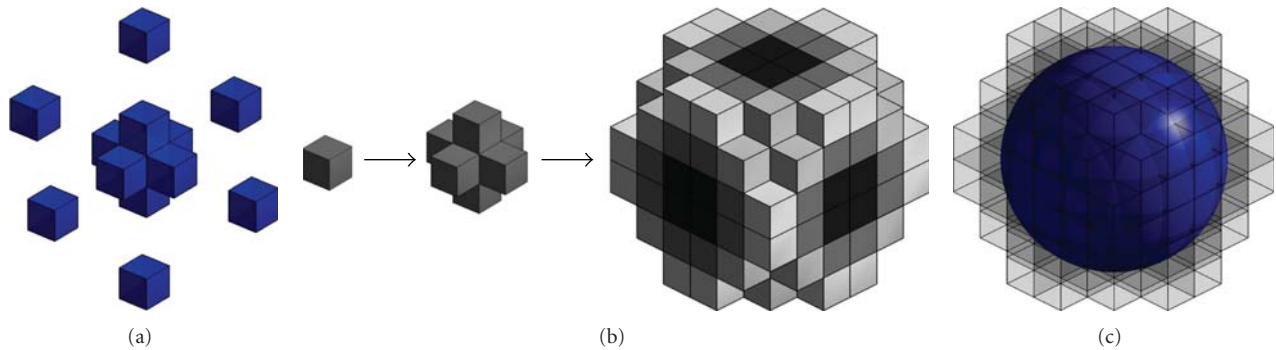


FIGURE 2: (a) The cross-shaped mask, (b) the adjacency-based grouping process, (c) a 3 mm diameter sphere placed at the calculated marker centre.

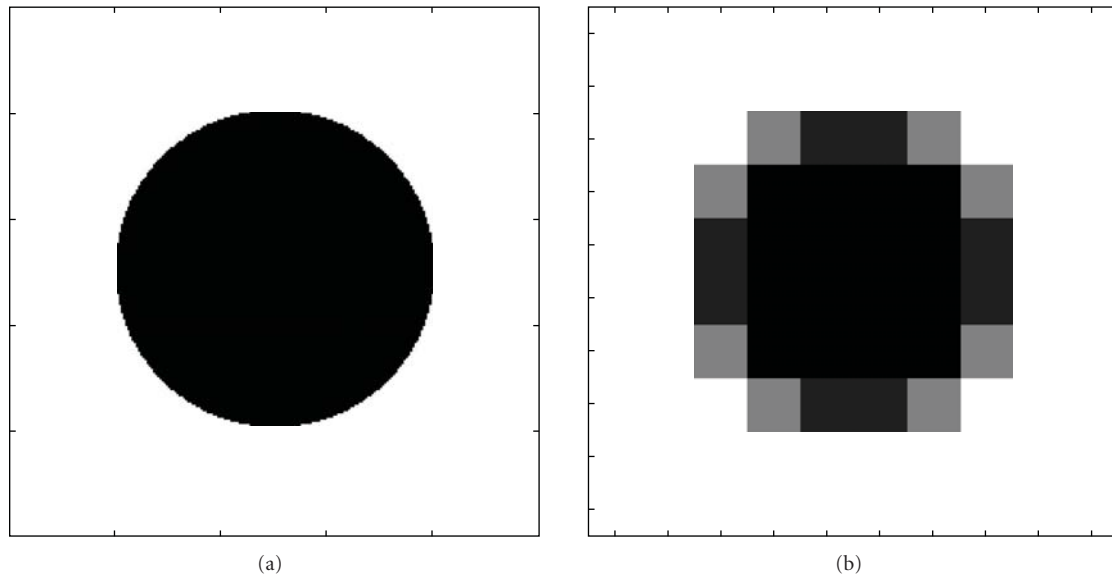


FIGURE 3: (a) A high resolution (uniform 0.02 mm voxels) binary mid-slice image of marker, (b) corresponding mid-slice at the MR acquisition resolution (uniform 0.5 mm voxels).

location  $(i, j, k)$  is classified as a central marker voxel when all the central cross-mask voxels (see cross-shape in Figure 2(a)) have intensities smaller than the intensity threshold  $T$  and all of the outer voxels (see outer voxels in Figure 2(a)) have intensities higher than or equal to the intensity threshold  $T$ . In other words the following pseudoequation needs to be true:

$$\begin{pmatrix} i_m(1 : 6) \\ j_m(1 : 6) \\ k_m(1 : 6) \end{pmatrix} < T \wedge \begin{pmatrix} i_m(7 : 12) \\ j_m(7 : 12) \\ k_m(7 : 12) \end{pmatrix} \geq T. \quad (2)$$

Here all of the first six mask voxels (indicated with  $1 : 6$ ), of the mask coordinate collection  $(i_m, j_m, k_m)$ , represent the central cross-elements and the last six (indicated with  $7 : 12$ ) represent the outer elements (see Figure 2(a)). Depending on the marker appearance in the image (see next section) up to 8 central marker voxels match this criterion and were found per marker.

(2) *Adjacency Grouping.* Calculating the marker centre point using only the central marker voxels identified using masking does not provide an accurate centre point determination (accurate to within a voxel at best) and is sensitive to marker appearance. The more voxels that are included (e.g., all) the better. To find and group voxels deemed to belong to the same marker a grouping algorithm was used. The central marker voxels found using masking were used as starting points to group objects using adjacency analysis. The adjacency grouping is a stepwise process. Adjacency coordinate groups (ACGs) are created for all the voxels found using masking. The process starts with one of the voxels found using masking  $v'$  and is assigned to be part of marker group  $M$ . The ACG for this voxel  $v'$  with coordinates  $(i', j', k')$  is defined as

$$\begin{pmatrix} i_f \\ j_f \\ k_f \end{pmatrix} = \begin{pmatrix} i' + (1, -1, 0, 0, 0, 0) \\ j' + (0, 0, 1, -1, 0, 0) \\ k' + (0, 0, 0, 0, 1, -1) \end{pmatrix}. \quad (3)$$

The ACG contains all the directly adjacent voxels of the voxel  $v'$  (its direct upper, lower, front, back, left, and right neighbours). Any voxel  $v$  with coordinates  $(i, j, k)$  is added to the marker group  $M$  when its intensity is lower than  $T$  and its coordinates are found within one of the ACGs of the marker  $M$ . When a voxel is added to the marker group  $M$  its ACG is added to the set of ACGs belonging to  $M$  and this process is repeated. Voxels are added to a marker group until the group is no longer growing.

Figure 2(b) shows how, starting with one central voxel, the surrounding low intensity voxels within the coordinate group  $(i_f, j_f, k_f)$  are added and when this is repeated all voxels representing the marker are grouped. After grouping, the dimensions and number of voxels of the object were compared to what is expected for normal markers (e.g., a diameter of under 6 voxels and consisting of under 250 voxels) to filter out possible objects other than markers.

(3) *Centre Point Calculation.* The centre point for each marker group was determined using weighted averaging. The centre coordinates  $(I_M, J_M, K_M)$  of a marker  $M$  composed of  $N$  voxels is defined as

$$(I_M \quad J_M \quad K_M) = \left( \frac{\sum_{a=1}^N w_a i_a}{\sum_{a=1}^N w_a} \quad \frac{\sum_{a=1}^N w_a j_a}{\sum_{a=1}^N w_a} \quad \frac{\sum_{a=1}^N w_a k_a}{\sum_{a=1}^N w_a} \right). \quad (4)$$

Here average  $i$ ,  $j$ , and  $k$  represent the coordinates of each of the voxels in the marker group. Since those voxels with intensities close to zero are more likely to belong to a marker than voxels with intensities close to the gel intensity, the weight  $w_a$  for a voxel with intensity  $z_a$  was defined as:

$$w_a = \left( 1 - \frac{z_a}{T} \right), \quad \text{with } w_a = 0 \text{ if } z_a > T. \quad (5)$$

Here  $T$  represents a threshold which for a noiseless image could be set equal to the gel intensity (the weight  $w_a$  then represents the volume fraction of marker material present in the voxel). The condition is added that when  $z_a$  is larger than  $T$  the weight  $w_a = 0$ .

**2.4. Evaluation of Marker Tracking Method Using Simulated Magnitude MR Image Data.** The marker tracking method was evaluated using simulated magnitude MR image data because this allows full control and knowledge of marker locations and thus provides the final real “gold standard.” The simulated data also allow one to isolate and study errors from different sources. The marker tracking method was evaluated using algorithms developed in Matlab (The Mathworks Inc., USA) and involves the following steps: (1) *simulation of a noiseless image and analysis of geometric bias*, and (2) *simulation of noisy magnitude MR data and analysis of the noise effects*. The final noisy image data allows one to evaluate the performance of the method under varying noise conditions while the noiseless image allows for evaluation of the geometric bias implicit in the method.

(1) *Simulation of a Noiseless Image and Analysis of Geometric Bias.* Since the marker image intensity values are zero, image data were simulated by multiplying an image representing gel volume fractions by the average normalised gel intensity. A 3D image space can be defined containing only markers and gel and can be expressed as a continuous binary function  $f(x, y, z)$ , where  $f = 0$  for all marker coordinates and  $f = 1$  for all gel coordinates. When this function is represented across voxels intermediate intensities arise as averaging occurs at each voxel where intensity is equivalent to the gel volume fraction within the voxel. The continuous binary function can however be approximated by a high-resolution binary image. Simulation of a volume fraction image at the desired (lower) resolution (cubic 0.5 mm voxels) then involves simple averaging of the high-resolution representation. High-resolution binary images were created at 25 times the acquisition resolution. A 2D mid-slice of a high-resolution (cubic 0.02 mm voxels) binary image is shown in Figure 3(a). At this resolution the marker sphere is represented by over 1.7 million voxels and the volume is represented with less than 0.07% error. Figure 3(b) shows

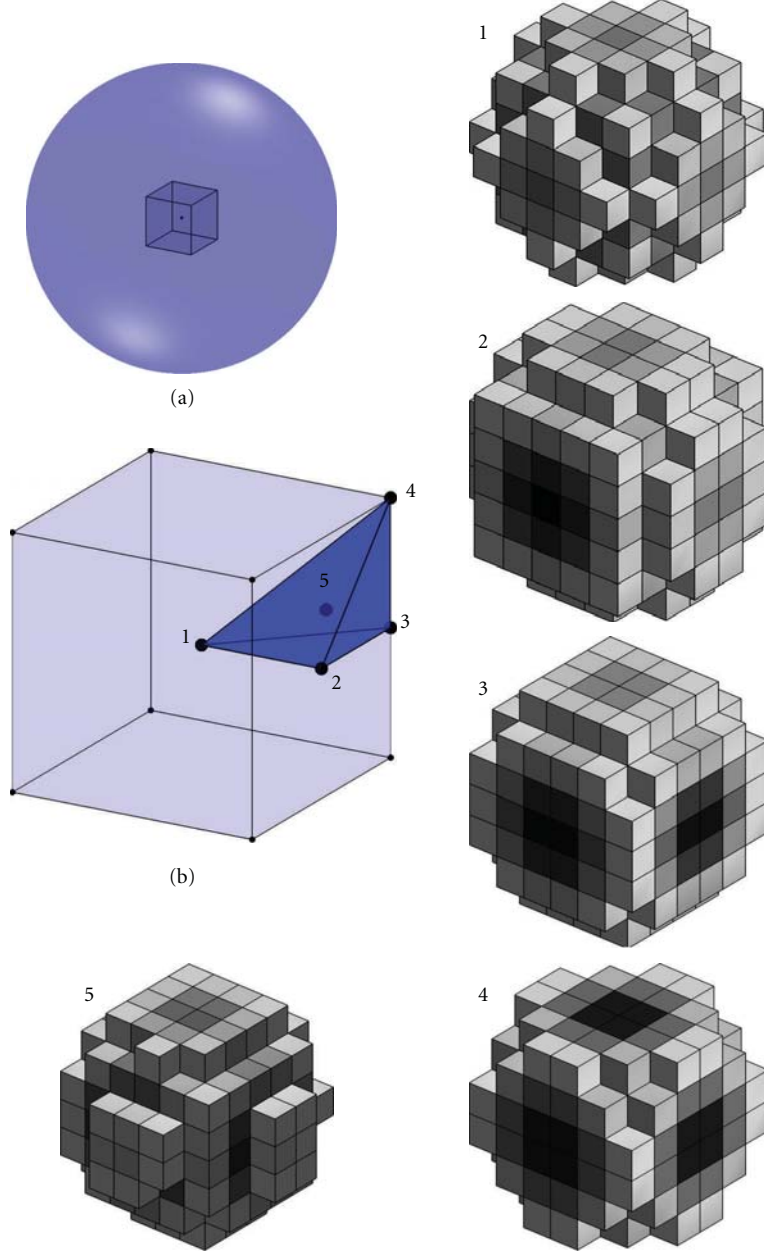


FIGURE 4: (a) A marker sphere showing OCV. (b) An OCV showing the tetrahedron in which the appearance of markers varies uniquely. The most symmetric appearances are 1 mid voxel, 2 mid face, 3 mid edge, and 4 voxel corner. Appearance 5 is in the middle of the tetrahedron and shows the resulting asymmetric appearance.

the corresponding volume fraction image at the averaged acquisition resolution (cubic 0.5 mm voxels). By multiplying the obtained volume fraction image with the appropriate gel intensity (average normalised intensity 0.39) a noiseless simulated image is obtained.

The appearance in Figure 3(b) is symmetric because the marker centre point coincides with a voxel corner. However the appearance of objects in images varies depending on their location due to averaging across the discrete elements, in this case voxels, which leads to a geometric bias affecting the marker tracking method. Figure 4(a) shows a marker

sphere and the voxel in which its centre point is found. This voxel is named the Object Central Voxel (OCV) (see also Figure 4(b)). When a marker centre point coincides with the centre of its OCV appearance 1 is obtained. Similarly 2 up to 4 demonstrate the appearance of a marker when its centre coincides with the middle of a voxel face, the middle of a voxel edge and a voxel corner, respectively. Obviously when a marker is moved exactly one voxel in a certain orthogonal direction its appearance has not changed but simply shifted. In fact each of these appearances is either symmetric or equivalent to several other appearances

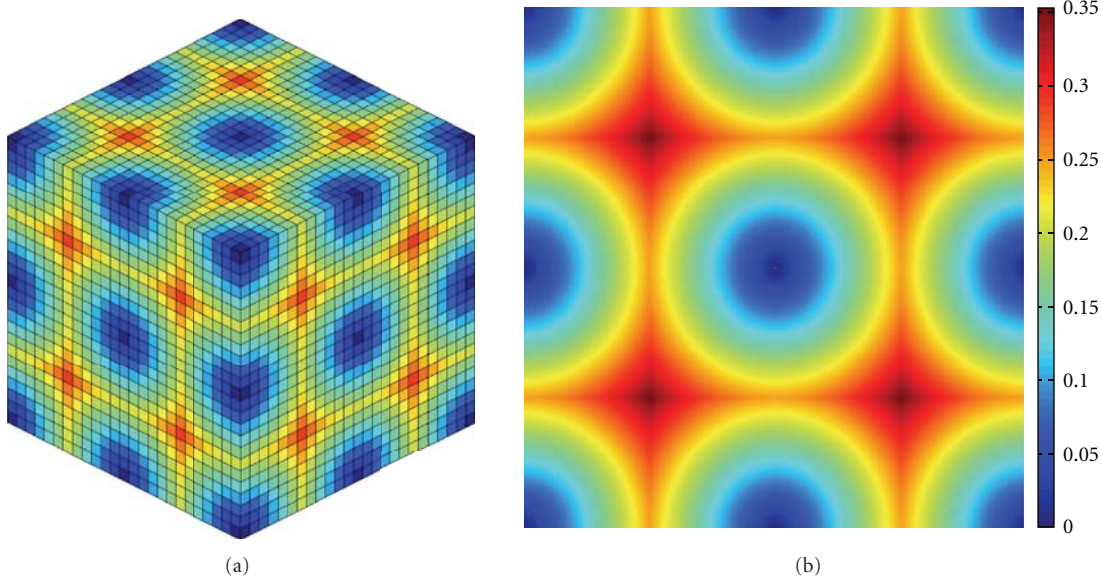


FIGURE 5: (a) A 3D plot representing the full OCV showing the expected type of geometric bias pattern, and (b) a 2D equivalent.

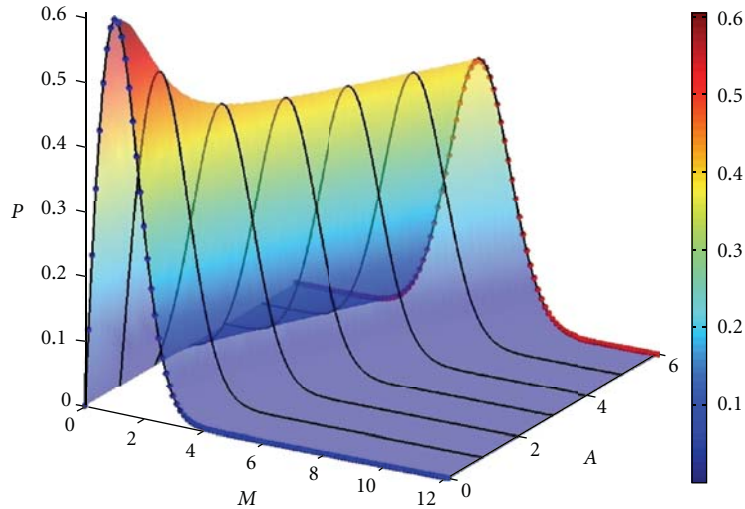


FIGURE 6: The Rician PDF at various  $A/\sigma_g$  ratios (0–6). When  $A/\sigma_g = 0$  the Rician PDF reduces to the Rayleigh distribution (blue dots) however as  $A/\sigma_g$  increases to over  $A/\sigma > 2$  the Rician PDF behaves approximately Gaussian (red dots at  $A/\sigma = 6$ ).

obtainable through varying location within the OCV (e.g., each voxel corner produces the same appearance while mid-edge appearances can be obtained through rotation and mirroring). Thus when the spherical markers (or any other symmetric shape) are averaged across a cubic voxel matrix the appearance varies uniquely within the blue tetrahedron shown in Figure 4(b). All other appearances can be obtained by rotation and mirroring of the appearances in this tetrahedron. Appearances 1–4 are the most symmetric appearances obtainable. Other appearances however can be asymmetric such as case 5 which is obtained when the marker centre coincides with the centre of the tetrahedron. Since the centre point calculation in the marker tracking method is based on an average of marker voxel coordinates, it is

sensitive to symmetry of the marker appearance and as such the error is also related to asymmetry.

It was hypothesised that since OCV points 1–4 in Figure 4 produce symmetric appearances the error here is low and that locations furthest away from these symmetries produce the worst error. If this hypothesis is true the error would follow a pattern similar to that shown in Figure 5 (a distance plot from the grid defined by the corner, mid-edge, and middle points) and assuming that each point has the same symmetry “weight,” the worst error should occur in the middle of the longest edge of the tetrahedron.

The geometric bias was investigated by simulating markers with their centre points coinciding with various locations within an OCV in the absence of noise. Due to the symmetry

in the appearances as discussed above, simulations were performed in 1 octant of the OCV only using a grid of points. For visualisation purposes the results were then mirrored to obtain bias measures across the full OCV (similar to Figure 5(a)) producing a  $19 \times 19 \times 19$  grid. A finer grid was then applied around the maximum bias to closely approximate the location of the real maximum bias. This process was repeated until the found maximum no longer varied significantly.

**(2) Simulation of Noisy Magnitude MR Data and Analysis of the Noise Effects.** Noise is present in all real MR images, and the performance of the marker tracking method needs to be evaluated in the presence of appropriate noise in the simulated image. During MR imaging, signal is acquired in the frequency domain using receiver coils. To move to the image domain the signal can be sampled at discrete locations and reconstructed using inverse Fourier Transforms. For each reconstructed image voxel in Cartesian space the signal can be expressed as a real signal  $A$  (represents the noiseless simulated image) plus a real noise component  $n_R$  and an imaginary noise component  $n_I$  [35]

$$s = s_R + s_I = A + n_R + i n_I, \quad \text{with } i = \sqrt{-1}. \quad (6)$$

These independent noise components are identically distributed (with zero mean) and their Probability Density Function (PDF) is Gaussian [35–37]. The magnitude  $m$  of a signal can be calculated using

$$m = \sqrt{(A + n_R)^2 + n_I^2}. \quad (7)$$

The image intensities in magnitude MR images in the presence of noise follow a Rician distribution [35–38] with a PDF [39, 40] given by

$$P_m(m | A, \sigma_g) = \frac{m}{\sigma_g^2} \exp\left(-\frac{(A^2 + m^2)}{2\sigma_g^2}\right) I_0\left(\frac{Am}{\sigma_g^2}\right) H(m), \quad (8)$$

where  $\sigma_g$  represents the standard deviation of the Gaussian noise,  $H$  represents the Heaviside step function (ensuring  $P_m = 0$  for  $m = 0$ ), and  $I_0$  is the 0 order modified Bessel function of the first kind. Figure 6 shows a surface plot of the Rician PDF for various  $A/\sigma_g$  (or SNR) ratios (Figure 6 was created using  $\sigma_g = 1$ , the SNR is therefore  $A/\sigma_g = A$ ). When the noise dominates and  $A/\sigma_g$  approaches zero the Rician PDF reduces to the Rayleigh PDF [35, 36] (see blue dots in Figure 6). However, when the signal dominates ( $A/\sigma_g > 2$  [36]) the Rician distribution behaves approximately Gaussian (red dots in Figure 6 are for a Gaussian PDF at  $A/\sigma_g = 6$ ) [35, 36]. With the knowledge that when  $A = 0$  the Rician PDF reduces to the Rayleigh PDF,  $\sigma_g$

can be estimated by analysis of background noise using [38]

$$\hat{\sigma}_g = \sqrt{\frac{1}{2N} \sum_{i=1}^N m_i^2}. \quad (9)$$

Using this equation, and analysis of the background of a normalised T2 MR image of the silicone gel phantom,  $\sigma_g$  was estimated to be 0.02. Based on the average normalised gel intensity of 0.39 this corresponds to an SNR of 19.5. However, to evaluate the performance of the marker tracking method in the presence of noise, images were simulated at the worst location found by the geometric bias at a SNR of 5 up to 35. Simulations were performed 10 000 times to obtain an estimate of the error distribution at the various SNR levels.

### 3. Results

The results are presented in two steps: (1) *evaluation of the geometric bias in the marker tracking method, and* (2) *evaluation of the performance on the marker tracking method in the presence of noise.*

**(1) Evaluation of the Geometric Bias in the Marker Tracking Method.** Figure 7(a) shows the geometric bias error in the absence of noise in an Object Central Voxel (OCV). The colour in each element is the error (in units of voxels) of the marker tracking method for each point on the 3D grid. Figure 7(b) shows 2D image slices through Figure 7(a) showing the best (1, 2) and worst locations (3). Analysis demonstrated that overall the geometric bias of the marker tracking method ranges from 0 to a maximum of  $5.560 \times 10^{-3}$  (with a mean of  $3.149 \times 10^{-3}$  and a standard deviation of  $7.771 \times 10^{-4}$  voxels. The error is 0 for the symmetric cases (1–4 in Figure 4) while the maximum error occurs in locations where a marker centre point coincides with 1/1.368th or 1/4.329th of a voxel; see, for example, white points in Figure 7(b) (e.g., at  $[i, j, k] = [0.731, 0.731, 0.731]$ ).

**(2) Evaluation of the Performance on the Marker Tracking Method in the Presence of Noise.** The performance of the marker tracking method for the noisy magnitude MR image simulations obtained from the 10 000 simulations at each SNR of 5 up to 35 is presented next. As the SNR increases from 5 to 35 the maximum, mean and minimum voxel errors vary according to Figure 8(a). The standard deviation is plotted in Figure 8(b). Although for  $T = 0.26$  the maximum stays below 0.1127 in all cases, the method performs better when  $T$  is chosen depending on SNR. To illustrate this Figure 9 shows results for the SNR range 15–35 using  $T = 0.32$ . Using a higher  $T$  means that the marker groups are composed of more voxels and thus a more accurate centre point can be calculated. The maximum voxel error for  $T = 0.26$  at an SNR = 19.5 (estimated SNR level) is  $4.254 \times 10^{-2}$  voxels; however using a  $T = 0.32$  in this case results in a more threefold increase of the accuracy as the maximum error is reduced to  $1.1611 \times 10^{-2}$  voxels. The optimum  $T$  value for a certain SNR can be determined using MR data simulations.

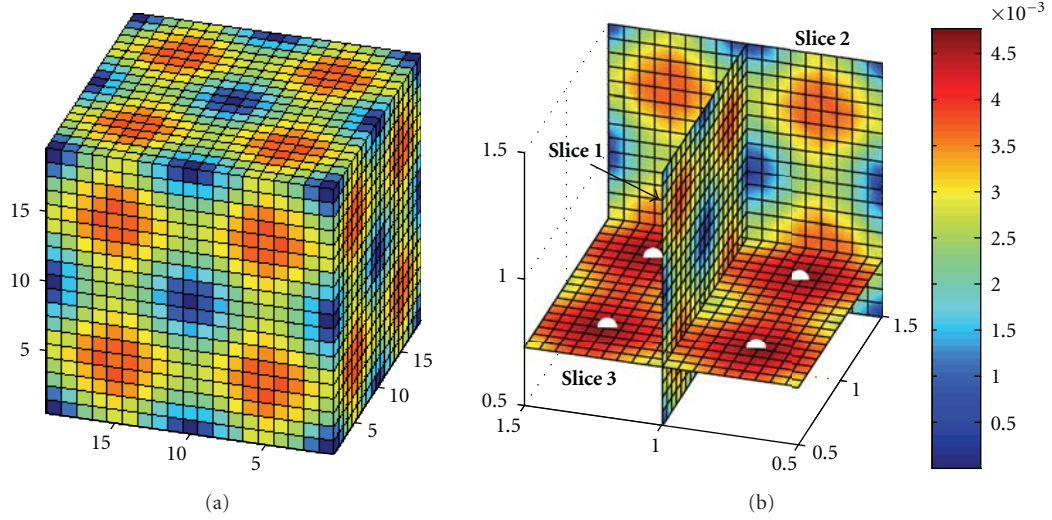


FIGURE 7: (a) The OCV showing the error of the marker tracking method, each grid locations tested. (b) Three 2D image slices through the OCV for the best (Slice 1 and 2) and worst locations (Slice 3).

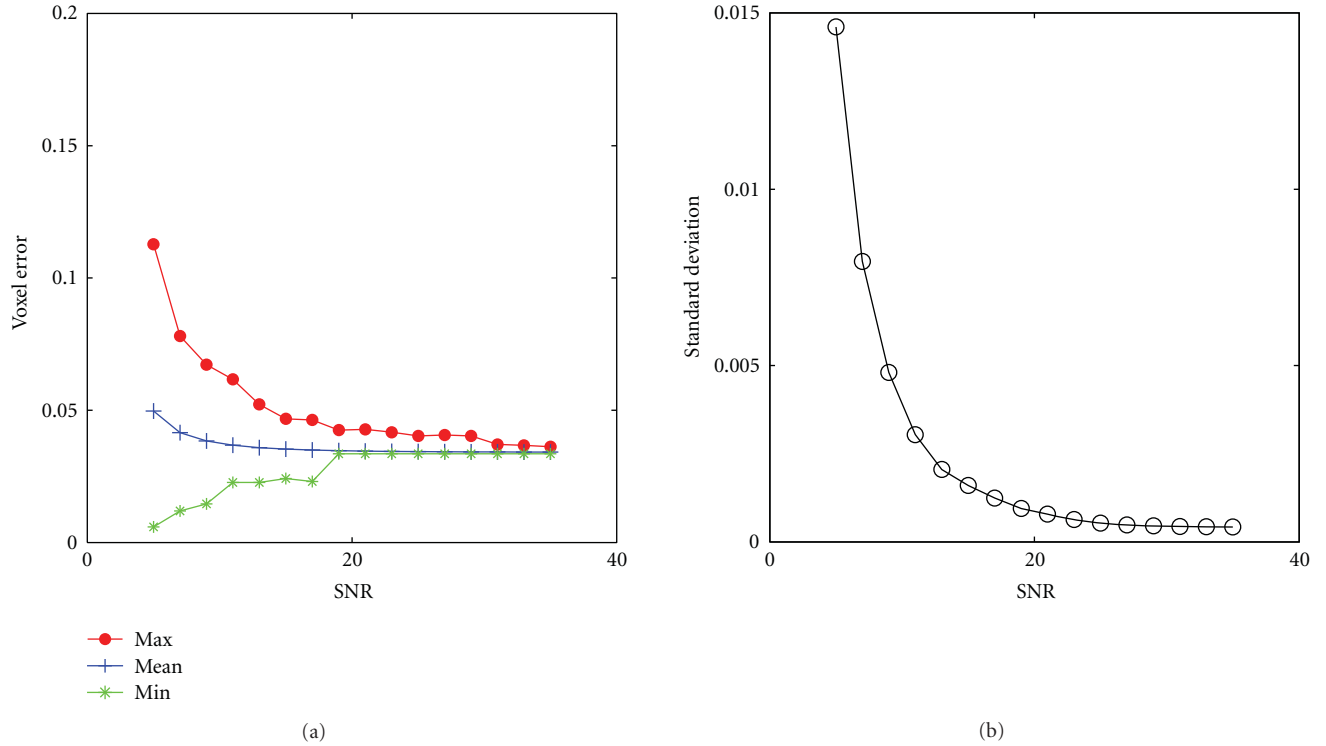


FIGURE 8: Results for SNR 5 up to 35 using  $T = 0.26$ . (a) The maximum (red dotted line), the mean (blue crossed line), and the minimum voxel error plotted against SNR, and (b) the standard deviation plotted against SNR.

Using simulations the error can be minimised for a given SNR by adjusting the  $T$  value.

#### 4. Discussion

Several MR imaging-based motion tracking algorithms have been proposed in the literature, for example, tagged MR

imaging [41] and phase contrast MR imaging [42], but these all rely upon validation of the algorithms proposed. A review of the literature showed that the validation methods used for existing techniques are frequently incomplete, and this paper presents a novel validation method for MR imaging based on motion tracking using a marker tracking algorithm which itself is validated against simulated MR image data. Simulated data was generated for the noise-free case as well

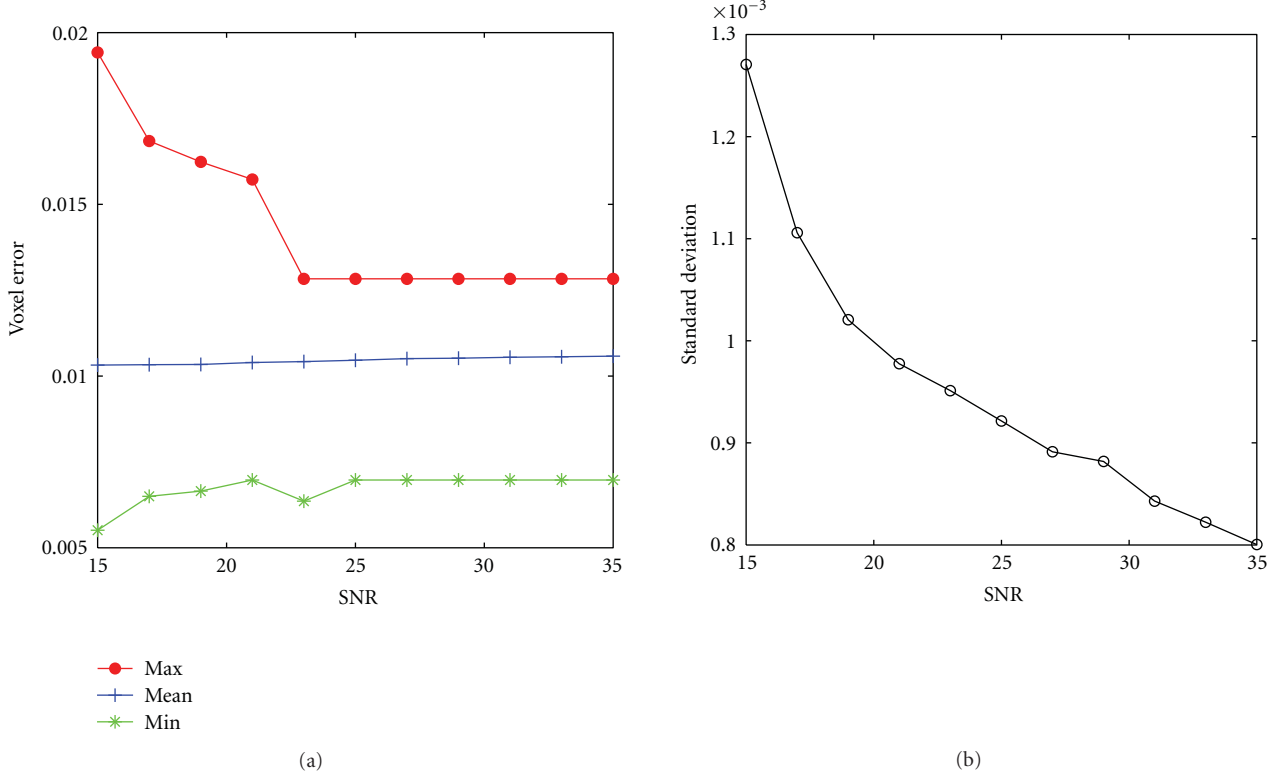


FIGURE 9: Results for SNR 15 up to 35 using  $T = 0.32$ . (a) The maximum (red dotted line), the mean (blue crossed line), and the minimum voxel error plotted against SNR, and (b) the standard deviation plotted against SNR.

as for a variety of different Rician distributed noise levels. The noise-free image data allowed analysis of the error related to the geometric bias independently from other error sources.

Therefore the method proved to be robust with geometric bias errors of between  $0\text{--}5.560 \times 10^{-3}$  voxels and errors due to noise remaining below 0.1127 voxels for all cases simulated with signal-to-noise ratios from 5 to 35. These results were achieved for a global threshold value  $T = 0.26$ . However altering the threshold value based on the SNR may result in a significant increase in accuracy. The optimum  $T$  value for a certain SNR can be determined using MR data simulations. Using simulations the error can be minimised for a given SNR by adjusting the  $T$  value.

The method proposed in this paper has two main advantages. The first is that the data used for validation is simulated and therefore can be chosen to have desired levels of noise. This permitted evaluation of the marker tracking method for different levels of noise which has not been done previously. Secondly, since this validation method is based on MR imaging, the marker tracking experiment and the MR imaging-based motion and deformation tracking can all be performed at the same time within the MR scanner.

Although this method has been developed for application to tagged MR imaging on the upper arm, the methods presented here are not limited to this application and can be applied to validate other types of MR imaging-based motion and deformation tracking techniques. Furthermore, these methods are independent of the chosen phantom shape.

## 5. Conclusion

A novel marker tracking method has been presented and validated using simulated MR image data. The marker tracking method is robust and the maximum geometric bias was  $5.560 \times 10^{-3}$  voxels while the error due to noise remains below 0.1127 voxels for Rician noise distributions with signal-to-noise ratios from 5 up to 35. This appears to be the only marker tracking algorithm suitable for the validation of MR-based motion and deformation tracking of soft tissue which has been validated against a “gold standard.”

## Acknowledgment

This work was funded by a Research Frontiers Grant (06/RF/ENMO76) awarded by Science Foundation Ireland.

## References

- [1] H. Lissner, M. Lebow, and F. Evans, “Experimental studies on the relation between acceleration and intracranial pressure changes in man,” *Surgery Gynecology & Obstetrics*, vol. 111, pp. 329–338, 1960.
- [2] L. M. McNamara and P. J. Prendergast, “Bone remodelling algorithms incorporating both strain and microdamage stimuli,” *Journal of Biomechanics*, vol. 40, no. 6, pp. 1381–1391, 2007.
- [3] J. Davis, K. R. Kaufman, and R. L. Lieber, “Correlation between active and passive isometric force and intramuscular

- pressure in the isolated rabbit tibialis anterior muscle," *Journal of Biomechanics*, vol. 36, no. 4, pp. 505–512, 2003.
- [4] A. Erdemir, S. McLean, W. Herzog, and A. J. van den Bogert, "Model-based estimation of muscle forces exerted during movements," *Clinical Biomechanics*, vol. 22, no. 2, pp. 131–154, 2007.
  - [5] D. Marjoux, D. Baumgartner, C. Deck, and R. Willinger, "Head injury prediction capability of the HIC, HIP, SIMon and ULP criteria," *Accident Analysis & Prevention*, vol. 40, no. 3, pp. 1135–1148, 2008.
  - [6] H. Muggenthaler, K. von Merten, S. Peldschus, et al., "Experimental tests for the validation of active numerical human models," *Forensic Science International*, vol. 177, no. 2-3, pp. 184–191, 2008.
  - [7] P. C. Ivancic, S. Ito, and M. M. Panjabi, "Dynamic sagittal flexibility coefficients of the human cervical spine," *Accident Analysis & Prevention*, vol. 39, no. 4, pp. 688–695, 2007.
  - [8] E. Linder-Ganz, N. Shabshin, Y. Itzchak, and A. Gefen, "Assessment of mechanical conditions in sub-dermal tissues during sitting: a combined experimental-MRI and finite element approach," *Journal of Biomechanics*, vol. 40, no. 7, pp. 1443–1454, 2007.
  - [9] E. Linder-Ganz, N. Shabshin, Y. Itzchak, Z. Yizhar, I. Siev-Ner, and A. Gefen, "Strains and stresses in sub-dermal tissues of the buttocks are greater in paraplegics than in healthy during sitting," *Journal of Biomechanics*, vol. 41, no. 3, pp. 567–580, 2008.
  - [10] Y.-J. Lim and S. De, "Real time simulation of nonlinear tissue response in virtual surgery using the point collocation-based method of finite spheres," *Computer Methods in Applied Mechanics and Engineering*, vol. 196, no. 31-32, pp. 3011–3024, 2007.
  - [11] M. A. Audette, V. Hayward, O. Astley, M. Doyon, G. A. McCallister, and K. Chinzei, "A PC-based system architecture for real-time finite element-based tool-specific surgical simulation," in *Proceedings of the 18th International Congress and Exhibition on Computer Assisted Radiology and Surgery (CARS '04)*, vol. 1268 of *International Congress Series*, pp. 378–383, June 2004.
  - [12] P. I. Wu and E. R. Edelman, "Structural biomechanics modulate intramuscular distribution of locally delivered drugs," *Journal of Biomechanics*, vol. 41, no. 13, pp. 2884–2891, 2008.
  - [13] M. Van Loocke, C. G. Lyons, and C. K. Simms, "A validated model of passive muscle in compression," *Journal of Biomechanics*, vol. 39, no. 16, pp. 2999–3009, 2006.
  - [14] M. Van Loocke, C. G. Lyons, and C. K. Simms, "Viscoelastic properties of passive skeletal muscle in compression: stress-relaxation behaviour and constitutive modelling," *Journal of Biomechanics*, vol. 41, no. 7, pp. 1555–1566, 2008.
  - [15] A. Gefen, N. Gefen, E. Linder-Ganz, and S. S. Margulies, "In vivo muscle stiffening under bone compression promotes deep pressure sores," *Journal of Biomechanical Engineering*, vol. 127, no. 3, pp. 512–524, 2005.
  - [16] A. Palevski, I. Glaich, S. Portnoy, E. Linder-Ganz, and A. Gefen, "Stress relaxation of porcine gluteus muscle subjected to sudden transverse deformation as related to pressure sore modeling," *Journal of Biomechanical Engineering*, vol. 128, no. 5, pp. 782–787, 2006.
  - [17] K. M. Moerman, C. A. Holt, S. L. Evans, and C. K. Simms, "Digital image correlation and finite element modelling as a method to determine mechanical properties of human soft tissue in vivo," *Journal of Biomechanics*, vol. 42, no. 8, pp. 1150–1153, 2009.
  - [18] M. Tada, N. Nagai, H. Yoshida, and T. Maeno, "Iterative FE analysis for non-invaseice material modeling of a fingertip with layered structure," in *Proceedings of the Eurohaptics*, Paris, France, 2006.
  - [19] J. C. Walker, M. B. Ratcliffe, P. Zhang, et al., "Magnetic resonance imaging-based finite element stress analysis after linear repair of left ventricular aneurysm," *Journal of Thoracic and Cardiovascular Surgery*, vol. 135, no. 5, pp. 1094–1102, 2008.
  - [20] K. K. Ceelen, A. Stekelenburg, J. L. J. Mulders, et al., "Validation of a numerical model of skeletal muscle compression with MR tagging: a contribution to pressure ulcer research," *Journal of Biomechanical Engineering*, vol. 130, no. 6, Article ID 061015, 8 pages, 2008.
  - [21] A. A. Young, L. Axel, L. Dougherty, D. K. Bogen, and C. S. Parenteau, "Validation of tagging with MR imaging to estimate material deformation," *Radiology*, vol. 188, no. 1, pp. 101–108, 1993.
  - [22] C. C. Moore, S. B. Reeder, and E. R. McVeigh, "Tagged MR imaging in a deforming phantom: photographic validation," *Radiology*, vol. 190, no. 3, pp. 765–769, 1994.
  - [23] S. B. Yeon, N. Reichek, B. A. Tallant, et al., "Validation of in vivo myocardial strain measurement by magnetic resonance tagging with sonomicrometry," *Journal of the American College of Cardiology*, vol. 38, no. 2, pp. 555–561, 2001.
  - [24] C. P. Neu, M. L. Hull, and J. H. Walton, "Error optimization of a three-dimensional magnetic resonance imaging tagging-based cartilage deformation technique," *Magnetic Resonance in Medicine*, vol. 54, no. 5, pp. 1290–1294, 2005.
  - [25] C. P. Neu, M. L. Hull, J. H. Walton, and M. H. Buonocore, "Toward an MRI-based method to determine three-dimensional deformations in articular cartilage," in *Proceedings of the Summer Bioengineering Conference*, Key Biscayne, Fla, USA, 2003.
  - [26] D. C. Goldstein, H. L. Kundel, M. E. Daube-Witherspoon, L. E. Thibault, and E. J. Goldstein, "A silicone gel phantom suitable for multimodality imaging," *Investigative Radiology*, vol. 22, no. 2, pp. 153–157, 1987.
  - [27] K. F. Augenstein, B. R. Cowan, I. J. LeGrice, P. M. F. Nielsen, and A. A. Young, "Method and apparatus for soft tissue material parameter estimation using tissue tagged magnetic resonance imaging," *Journal of Biomechanical Engineering*, vol. 127, no. 1, pp. 148–157, 2005.
  - [28] T. S. Denney Jr., J. L. Prince, M. J. Lopez, and E. R. McVeigh, "Optimal tag pattern validation using magnetic resonance imaging," in *Proceedings of the IEEE International Conference on Image Processing (ICIP '94)*, Austin, Tex, USA, 1994.
  - [29] A. S. Fahmy, A. Krieger, and N. F. Osman, "An integrated system for real-time detection of stiff masses with a single compression," *IEEE Transactions on Biomedical Engineering*, vol. 53, no. 7, pp. 1286–1293, 2006.
  - [30] D. L. Kraitchman, A. A. Young, C.-N. Chang, and L. Axel, "Semi-automatic tracking of myocardial motion in MR tagged images," *IEEE Transactions on Medical Imaging*, vol. 14, no. 3, pp. 422–433, 1995.
  - [31] N. F. Osman, "Detecting stiff masses using strain-encoded (SENC) imaging," *Magnetic Resonance in Medicine*, vol. 49, no. 3, pp. 605–608, 2003.
  - [32] S. Sampath, V. Parthasarathy, and J. L. Prince, "A phantom validation of the FastHARP pulse sequence," in *Proceedings of the IEEE International Symposium on Biomedical Imaging*, 2002.

- [33] B. T. Wyman, *Mechanical Evaluation of the Paced Heart Using Tagged Magnetic Resonance Imaging*, The Department of Biomedical Engineering, The Johns Hopkins University, Baltimore, Md, USA, 1999.
- [34] A. A. Young, D. L. Kraitchman, L. Dougherty, and L. Axel, “Tracking and finite element analysis of stripe deformation in magnetic resonance tagging,” *IEEE Transactions on Medical Imaging*, vol. 14, no. 3, pp. 413–421, 1995.
- [35] R. M. Henkelman, “Measurement of signal intensities in the presence of noise in MR images,” *Medical Physics*, vol. 12, no. 2, pp. 232–233, 1985.
- [36] H. Gudbjartsson and S. Patz, “The Rician distribution of noisy MRI data,” *Magnetic Resonance in Medicine*, vol. 34, no. 6, pp. 910–914, 1995.
- [37] A. Cárdenas-Blanco, C. Tejos, P. Irarrazaval, and I. Cameron, “Noise in magnitude magnetic resonance images,” *Concepts in Magnetic Resonance A*, vol. 32, no. 6, pp. 409–416, 2008.
- [38] S. Aja-Fernandez, C. Alberola-Lopez, and C.-F. Westin, “Noise and signal estimation in magnitude MRI and Rician distributed images: a LMMSE approach,” *IEEE Transactions on Image Processing*, vol. 17, no. 8, pp. 1383–1398, 2008.
- [39] S. O. Rice, “Mathematical analysis of random noise,” *Bell Systems Technical Journal*, vol. 23, pp. 282–332, 1944.
- [40] S. O. Rice, “Mathematical analysis of random noise,” *Bell Systems Technical Journal*, vol. 24, pp. 46–156, 1945.
- [41] L. Axel, A. Montillo, and D. Kim, “Tagged magnetic resonance imaging of the heart: a survey,” *Medical Image Analysis*, vol. 9, no. 4, pp. 376–393, 2005.
- [42] P. D. Gatehouse, J. Keegan, L. A. Crowe, et al., “Applications of phase-contrast flow and velocity imaging in cardiovascular MRI,” *European Radiology*, vol. 15, no. 10, pp. 2172–2184, 2005.

## Research Article

# Optical Flow Active Contours with Primitive Shape Priors for Echocardiography

Ali K. Hamou and Mahmoud R. El-Sakka

Department of Computer Science, University of Western ON, London, Ontario, Canada N6A 5B7

Correspondence should be addressed to Mahmoud R. El-Sakka, elsakka@csd.uwo.ca

Received 2 May 2009; Revised 28 July 2009; Accepted 5 August 2009

Academic Editor: João Manuel R. S. Tavares

Copyright © 2010 A. K. Hamou and M. R. El-Sakka. This is an open access article distributed under the Creative Commons Attribution License, which permits unrestricted use, distribution, and reproduction in any medium, provided the original work is properly cited.

Accurate delineation of object borders is highly desirable in echocardiography, especially at the left ventricle. Among other model-based techniques, active contours (or snakes) provide a unique and powerful approach to image analysis. In this work, we propose the use of a new external energy for a *gradient vector flow* (GVF) snake, being the optical flow of a moving sequence (modeling the mechanical movement of the heart). This external energy can provide additional information to the active contour model garnering adequate results for moving sequences. An automatic iterative primitive shape prior was also applied in order to further improve the results of a GVF snake, when dealing with especially noisy echocardiographic images. Results were compared with expert-defined segmentations yielding acceptable sensitivity, precision rate and overlap ratio performance.

## 1. Introduction

The assessment of cardiac function has been a major area of interest in the medical field. Normal heart function consists of pumping chambers (known as ventricles) which regulate the systemic and pulmonary circulation systems by delivering blood to the proper areas. Detection of nonnormal heart function in the *left ventricle* (LV), for instance, can cause systolic dysfunction, being the reduction in the ability to contract, or diastolic dysfunction, being the inability to fill efficiently. Along with mechanical functions, various heart structures may also fail causing cardiomyopathies, endangering the life of the host individual. Fortunately, many myopathies are treatable (with medication, implanted pacemakers, defibrillators, or ventricular assist devices) given early detection. Echocardiography, imaging the heart using ultrasound waves, facilitates the ability to do so.

The advent of real time ultrasonography provides the ability to image an entire LV and surrounding anatomy within one cardiac cycle (approximately one second). However, depending on the patient's "photogenicity" (impacting factors include and surrounding fatty tissues, calcifications, gender), these images are most likely marred by speckle artifacts. Many computer vision techniques attempt to

reduce such speckle noise by means of filtering [1] or incorporating the speckle effect directly into their algorithms [2]. Boundary detection techniques are employed in order to segment the wanted regions for analyses on the heart structures, such as endocardial borders [3], stress and strain of the septum wall [4], and wall motility [5] to name a few.

Various computer vision techniques have been introduced to accomplish boundary detection. Kass et al. [6] first proposed the original active contour model (commonly known as a snake or a deformable model). In their formulation, image segmentation was posed as an energy minimization problem.

Active contours treat the surface of an object as an elastic sheet that stretches and deforms when external and internal forces are applied to it. These models are physically-based, since their behavior is designed to mimic the physical laws that govern real-world objects [7]. Since this approach relied on variational calculus to find a solution, time complexity was one of the main drawbacks of this original model. Amini et al. [8] proposed an algorithm for using dynamic programming, in order to incorporate soft and hard constraints into the formulation, improving time complexity and results. Further improvements to time complexity were proposed by Williams et al. [9], by using a greedy algorithm while

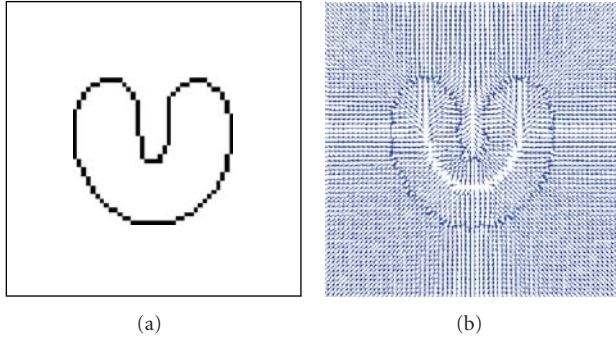


FIGURE 1: Example of gradient vector forces. (a) Standard U-Image. (b) Gradient Vector Flow of U-Image.

incorporating a simple curvature approximation. Issues with large capture ranges and concavities are solved by other advances, which include inflation forces [10], probabilistic models [11], oriented particles [12], and gradient vector flows [13]. For the purposes of this study, focus will be placed on those advances best suited for echocardiographic images.

Since the LV represents one of the most important heart functions, many semiautomatic techniques attempt to segment this region from surrounding tissues [3, 14, 15]. Yet, no universally accepted standard exists for segmenting echocardiographic images.

Papademetris et al. [15] took advantage of a b-splines parameterized deformable model for segmenting cardiac regions. The external energy consisted of the standard intensity term and a *markov random field* (MRF) texture-based term. The MRF is based on a combination of gradient, regional, and curvature data computed from the original image. Initial contours are manually placed for each 2D plane and are passed to a shape tracking algorithm. Displacements are probabilistically computed using a confidence measurement for the entire set. Final displacements are fed into an anisotropic linear elastic model which is computed vis-à-vis a Bayesian estimation framework. The manual placement of the contours makes this technique quite labour intensive.

Felix-Gonzalez and Valedes-Cristerna [14] proposed a segmentation technique for echocardiographic images using an *active surface model* (ASM). The ASM is made up of cubic splines and is based on a gradient descent procedure. When using gradient descent, the empirical setting of parameters is required based on the quality and types of images used. This makes this proposed technique extremely sensitive to its input. Furthermore, Felix-Gonzalez et al.'s work was only tested on two limited datasets.

Leung et al. [16] proposed the use of an *active appearance model* (AAM) and intensity, based registration for segmenting multiple 2D image slices. An AAM uses all the information in an image region covered by the target object, rather than just that near modeled edges. An AAM involves the principal component analysis of the various shapes and textures from several manually segmented 2D slices for training. The AAM makes use of the training set to converge the initial set mesh to the best textures on the image. However, this trained set required several manual

segmentations of the 2D image slices to tune it to the medium being used.

The *gradient vector flow* (GVF) [13] snake was introduced as a modification to the original snake model in order to overcome the capture range and curve concavity issues. However using the GVF snake on echocardiograms directly will not provide an adequate solution due to the complication of speckle noise and the existence of valves within the heart cavity, inhibiting a proper segmentation.

Zhou et al. [17] proposed the segmentation of MRI cardiac sequences using a generalized *fuzzy gradient vector flow* (FGVF) map along with a relative optical flow field. Optical flow measurements are computed on the cardiac sequence being considered, and a *maximum a posteriori probability* (MAP) was used as a window for the movement of the curve. The use of optical flow with GVF provides promising results; however this technique is used exclusively on clear MRI data, and hence the presence of speckle noise on echocardiographic images would require modifications of this technique. Both GVF and optical flow measurements will be used in the proposed technique.

In this paper, we propose to utilize optical flow measurements as an external energy of a GVF snake. We will show that there is ample information in the movement of tissues within the heart cavity that will provide the necessary knowledge to segment out the region of interest. We will further improve the results by providing means of incorporating an iterative prior knowledge process into the proposed solution which takes into account the primitive shape of an object during the active contour evolution cycle. The rest of the paper is organized as follows. Section 2 will outline each module of the proposed model. Section 3 will explain the experimental setup and results, and Section 4 will contain concluding comments.

## 2. Description of Model

**2.1. Parametric Active Contour Review.** A snake is an energy minimization problem. Its energy is represented by two forces (internal energy,  $E_{in}$ , and external energy,  $E_{ex}$ ) which work against each other. The total energy should converge to a local minimum—in the perfect case—at the desired boundary. The snake is defined as  $v(s) = [x(s), y(s)]^T$ , where  $s$  belongs to the interval  $[0, 1]$ . Hence, the total energy to be minimized,  $E_{AC}$ , to give the best fit between a snake and a desired object shape is

$$E_{AC} = \int_0^1 E_{in}(v(s)) + E_{ex}(v(s)) ds. \quad (1)$$

The internal energy decreases as the curve becomes smooth (by incorporating both elasticity and stiffness), whereas the external energy decreases as approaching the features of interest, such as image structures or edges.

The internal energy of the active contour formulation is further defined as

$$E_{in}(v(s)) = \alpha(s) \left| \frac{dv(s)}{ds} \right|^2 + \beta(s) \left| \frac{d^2v(s)}{ds^2} \right|^2, \quad (2)$$

where  $\alpha(s)$  and  $\beta(s)$  are weighting factors of elasticity and stiffness terms, respectively. The first-order term makes the snake's surface act like a membrane. The weight  $\alpha(s)$  controls the tension along the spine (stretching a balloon or elastic band). The second-order term makes the snake act like a thin plate. The weight  $\beta(s)$  controls the rigidity of the spine (bending a thin plate or wire).

A typical external energy formulation to identify edges for a given image,  $I(x, y)$ , is

$$E_{\text{ex}}(x, y) = -|\nabla I(x, y)|^2, \quad (3)$$

where  $\nabla$  denotes the gradient operator. In the case of a noisier image the edges are further smoothed:

$$E_{\text{ex}}(x, y) = -|\nabla(G_\sigma(x, y) * I(x, y))|^2 \quad (4)$$

where  $G_\sigma(x, y)$  is a two-dimensional Gaussian function with standard deviation  $\sigma$ , and  $*$  denotes a convolution operator. Since the contour may get trapped by the noisy areas of the image,  $\sigma$  must be large enough to compensate for the image noise that would interfere with the active contour's capture range. The standard snake algorithm also suffers from poor capture range because initialization and the inability to capture concavities. These problems are largely solved by the advent of the GVF snake [13].

The concavity problem exists due to the gradient vectors in an image generally have large magnitude only in the immediate vicinity of the boundary and are nearly zero at points away from the boundary. As such the capture range of the snake will be quite small. In order to resolve this, the gradient map is extended to points away from boundaries using a computational diffusion process. The GVF field is used as an external energy in the active contour and is characterized by the vector field  $z(x, y) = [u(x, y), v(x, y)]^T$  that minimizes the energy functional [13]:

$$E_{\text{GVF}} = \iint \mu(|\nabla u|^2 + |\nabla v|^2) + |\nabla f|^2 |z - \nabla f|^2 dx dy, \quad (5)$$

where  $f$  is an edge map derived from the image,  $\mu$  is the degree of smoothness of the field,  $u$  and  $v$  characterize the direction and strength of the field. Hence, when  $|\nabla f|$  is small, the energy will be dominated by the partial derivatives, yielding a slow field. Alternatively, when  $|\nabla f|$  is large, the latter term dominates and the function is minimized by setting  $z = \nabla f$ .

The external energy for the proposed scheme will be generated using a *virtual electric field* (VEF) [18] of  $f$  over the traditional GVF technique. Traditional GVF field generation is performed by optimizing the cost function represented in (5), which is quite a time consuming process. The VEF is defined by considering each edge pixel as a point charge within an electric field. This can be accomplished by convolving the edge map with the following two masks:

$$\begin{aligned} g_x(x, y) &= \frac{-c \cdot x}{(x^2 + y^2)^{3/2}}, \\ g_y(x, y) &= \frac{-c \cdot y}{(x^2 + y^2)^{3/2}}, \end{aligned} \quad (6)$$

where  $c = (4\pi\epsilon)^{-1}$  and  $\epsilon$  is sufficiently small constant. The resulting field yields a vector flow identical to a GVF field, given the masks are large enough. A smaller mask size would ignore outlying edges that would have little impact on the interested features since their range is quite far. However, since echoardiographic images contain many features throughout the image, quantizing any part of the edgemap is not an option. According to Park and Chung [18], an area of radius 32 around the feature should provide adequate flow vectors to accurately recreate a GVF field, without suffering from the high computational cost associated with vector flow generation. Figure 1 illustrates gradient vector forces, where Figure 1(b) shows an example of a vector flow field on the standard U-Image, shown in Figure 1(a), using  $65 \times 65$  masks generated from (6), which is identical to the original GVF field.

**2.2. Optical Flow Review.** Optical flow approximates the apparent motion of an object over a series of images (or time). The relationship between the optical flow in the image plane and the velocities of objects in the three-dimensional world is not necessarily obvious [19]. For the sake of convenience, most optical flow techniques consider a particularly simple world where the apparent velocity of brightness patterns can be directly identified with the movement of surfaces in the scene. This implies that objects maintaining structure but changing intensity would break this assumption.

Consider an image intensity  $I(x, y, t)$  at time  $t$ . Time, in this instance, implies the next frame in an image cine. Assuming that at a small distance away and some time later the given intensity is

$$\begin{aligned} I(x + \Delta x, y + \Delta y, t + \Delta t) &= I(x, y, t) + \frac{\partial I}{\partial x} \Delta x + \frac{\partial I}{\partial y} \Delta y + \frac{\partial I}{\partial t} \Delta t \\ &\quad + \text{higher order terms}. \end{aligned} \quad (7)$$

Given that the object started at position  $(x, y)$  at time  $t$ , and that it moved by a small distance of  $(\Delta x, \Delta y)$  over a period of time  $\Delta t$ , the following assumption can be made:

$$I(x + \Delta x, y + \Delta y, t + \Delta t) = I(x, y, t). \quad (8)$$

The assumption in (8) would only be true if the intensity of our object is the same at time  $t$  and  $t + \Delta t$ . Furthermore, if our  $\Delta x$ ,  $\Delta y$ , and  $\Delta t$  are very small, our higher-order terms would vanish, that is,

$$\frac{\partial I}{\partial x} \Delta x + \frac{\partial I}{\partial y} \Delta y + \frac{\partial I}{\partial t} \Delta t = 0. \quad (9)$$

Dividing (9) by  $\Delta t$  will yield

$$-\frac{\partial I}{\partial t} = \frac{\partial I}{\partial x} \frac{\Delta x}{\Delta t} + \frac{\partial I}{\partial y} \frac{\Delta y}{\Delta t}, \quad (10)$$

$$-I_t = \frac{\partial I}{\partial x} u + \frac{\partial I}{\partial y} v, \quad \text{where } u = \frac{\Delta x}{\Delta t}, \quad v = \frac{\Delta y}{\Delta t}. \quad (11)$$

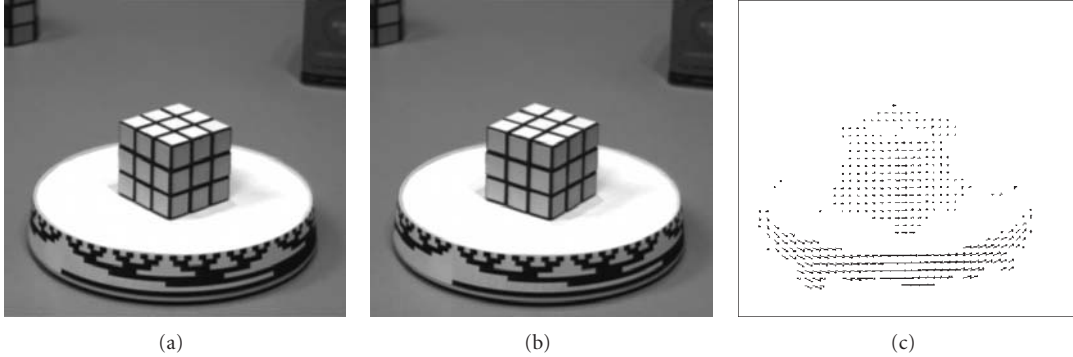


FIGURE 2: Example of an optical flow field on a Rubik's cube rotated image. (a) Cube at time  $t$ . (b) Cube at time  $t + \Delta t$ . (c) Optical flow of image (a) to (b) using Lucas-Kanade method (Originally published in Russell and Norving [22]).

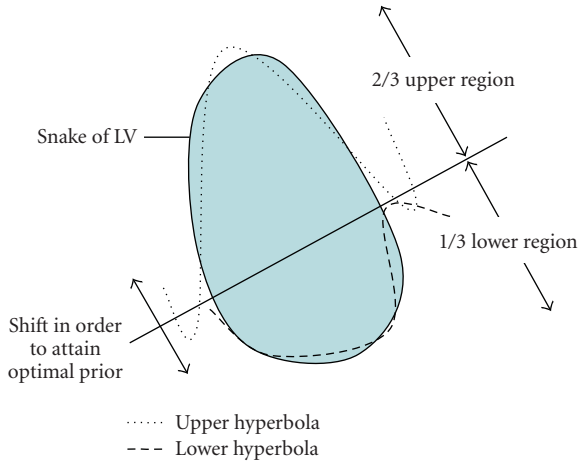


FIGURE 3: Generation of primitive priors on the active contour.

Equation (11) is known as the optical flow constraint equation, where  $I_t$ , at a particular pixel location  $(x, y)$ , is how fast its intensity at this location is changing with respect to time:  $u$  and  $v$  are the spatial rates of change for any given pixel (i.e., how fast an intensity is moving across an image). However, effectively estimating the component of the flow (along with intensity values) cannot directly be solved in this form since it will yield one equation per pixel for every two unknowns,  $u$  and  $v$ . In order to do so, additional constraints must be applied to this equation.

Lucas and Kanade [20] and Horn and Schunck [21] introduced two common methods for solving this problem using partial derivatives. The former assumes that the flow field is locally smooth (for a given static window size) and then solves (11) by means of a least squares approximation technique. The latter uses a global regularization parameter which assumes that images consist of objects undergoing rigid motion, resulting in a smooth optical flow over a relatively large area. Figure 2 depicts a visual representation of the optical flow of a simple Rubik's cube. Notice that the grayscale image has few shadows, helping to maintain consistency in the luminance of each pixel, hence yielding accurate results.

When dealing with noisy echocardiograms, a global regularization parameter will deal with the speckle better than the static window. This is due to the speckle noise remaining relatively static, lacking fluidity, throughout an image. Hence, the speckle will be “filtered”, since the optical flow calculations will fail to realize it within the frames.

Optical flow magnitudes will be combined with the image's edge maps (Section 2.4) in order to generate the external energy in (1) of the GVF snake. This would help to reduce artifacts due to static speckle noise, while also providing more information for the contour points to track (i.e., the tissue mass movement).

**2.3. Primitive Shape Prior Knowledge.** Since we are dealing with structures that have known shapes and sizes, and many real world models have been already measured, prior knowledge information can be directly used to increase the performance of a segmentation algorithm. Priors based on shape statistical models require modifications to the standard active contour model. An iterative solution can be incorporated directly into any optimization model by using the proposed framework which we first outlined in Hamou et al. [23].

Since it is desirable to incorporate shape priors without directly involving the user for training, automatic shape detection takes place on the set of discrete snake points  $v(s)$ . This is achieved by first generating the least squares fit polynomial(s) of the current  $v(s)$  points. For our left ventricle application, snake points are divided into an upper region and a lower region, which will be approximated by two separate third-order hyperbolas. These hyperbolas will better suit the shape of the left ventricle during both systole and diastole, though any shape prior can be represented by means of simple primitives. Least squares fitting technique is utilized to estimate the two hyperbolas coefficients. The axis separating the two regions is computed by taking the two-thirds upper and one-third lower bounds on all snake points. This separator can be tuned by shifting it upwards or downwards (either manually by the user or automatically by the system) in order to minimize the distance between the fitted hyperbolas and snake points. Priors are then generated by joining the fitted primitives to form one solid shape.

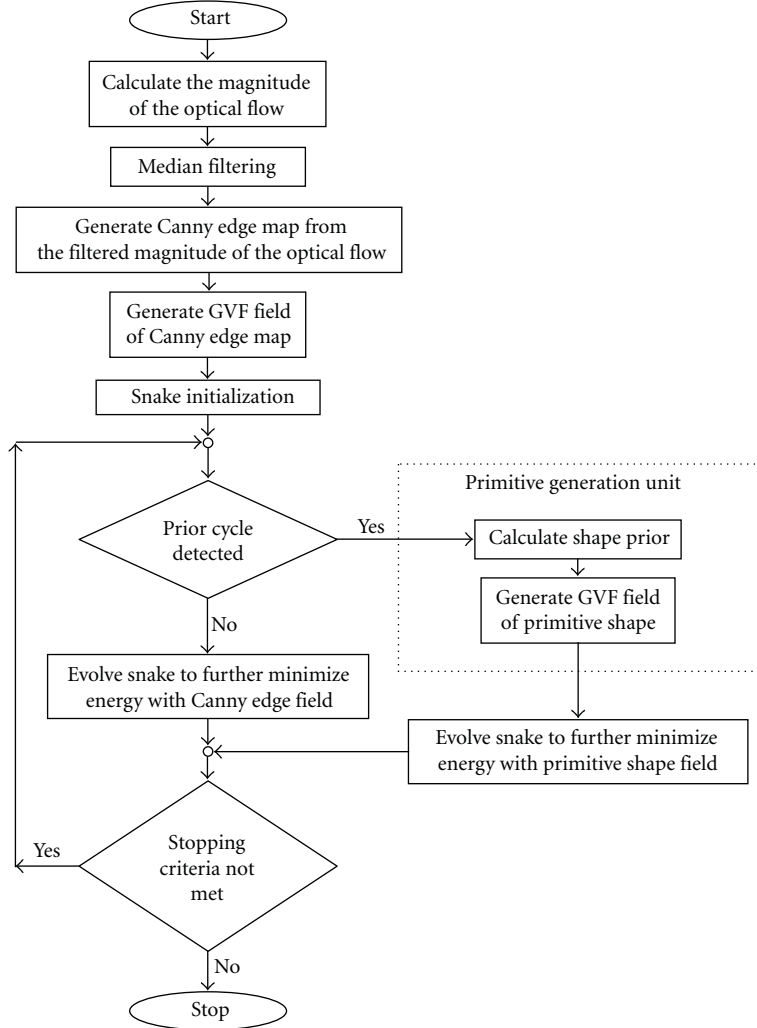


FIGURE 4: Top-level flow chart of the algorithm.

Primitives are bounded by the furthest easterly and westerly points by the snake points, in order to prevent the possibility of a nonconnecting shape.

Once the priors have been generated, its GVF field is computed. This new field will replace the existing external energy of the GVF snake for this specific snake iteration. Figure 3 portrays the process of generating a primitive prior for the left ventricle of the 4-chamber view image, where two intersecting hyperbolas are used (default shape for our left ventricle application).

The fitting of a primitive shape (or a series of primitives as needed for the left ventricle) to the snake points,  $v(s)$ , will help compensate for the noise that inhibits the snake from migrating past a certain point. It will also help retract the snake towards the primitive prior when an occluded border exists, common in many echocardiographic images. The user can control the number of cycles between any two consecutive prior calculation cycles (prior step parameter). This allows for the increase or decrease in the inherent effect of the prior knowledge to the snake's convergence cycle.

This primitive prior module is useful in the medical arena where the specialist or clinician has a clear understanding of the underlying structure being detected, such as a liver, an artery, or a heart. They can choose their desired primitive shape (or series of shapes) before curve evolution takes place.

**2.4. Complete System.** Figure 4 illustrates a top-level block diagram of the proposed system. It starts with the calculation of the optical flow magnitude on the image cines (*as explained in Section 2.2*). The estimated optical flow is preprocessed by median filtering. A Canny edge map of the filtered optical flow magnitude was generated and added to the original image edge map following normalization. The Canny detector was applied due to its use of nonmaximum suppression that further aids in the filtering of speckle noise. This result is used to generate the GVF for the snake's external energy. GVF snake evolution (*as explained in Section 2.1*) iterates to further minimize the energy function until a prior cycle condition is satisfied (*as explained in Section 2.3*), at which the prior cycle is initiated. At the prior cycle, a GVF is

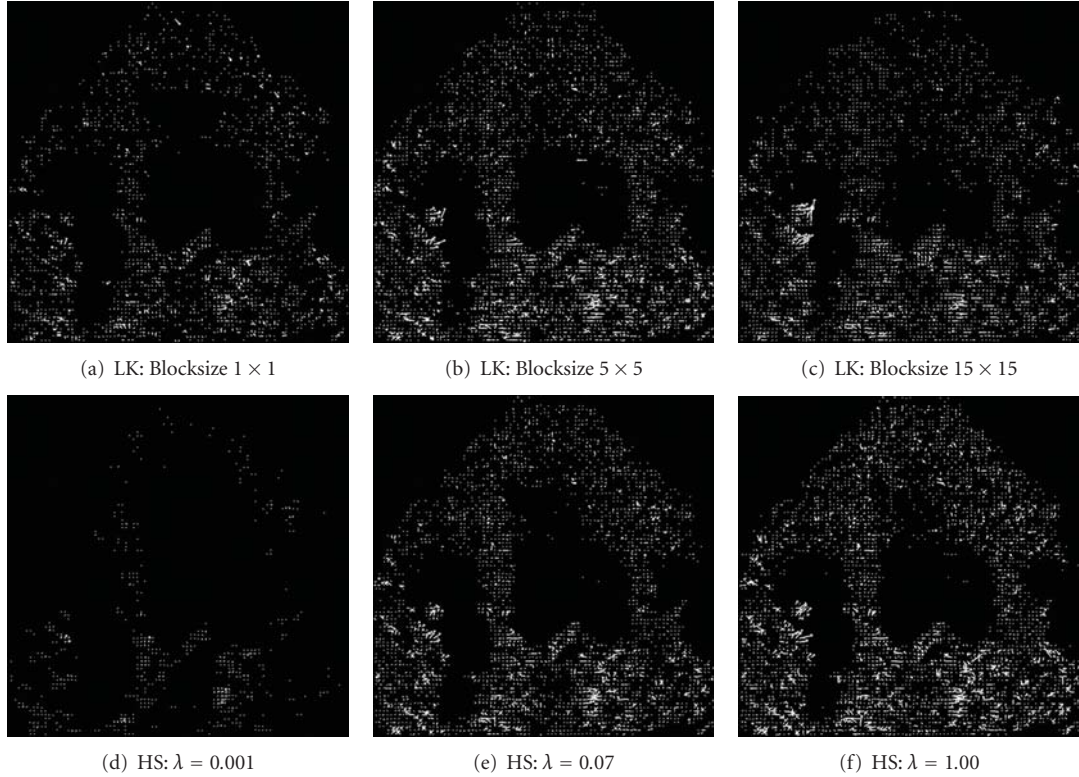


FIGURE 5: Optical flow fields on the left ventricle using Lucas-Kanade and Horn-Schunck methods.

generated from the prior and a single optimization iteration of the snake is executed before returning to the non-prior original snake iteration. This process is repeated until the snake is optimized and equilibrium is achieved.

### 3. Experimental Results

For this study, a series of B-mode echocardiogram cross sectional videos of the heart have been used to investigate the proposed snake algorithm. These videos were acquired using an SONOS 5500 by Philips Medical System. The transducer frequency was set at 2.5 MHz in order to insure adequate penetration of tissue, while maintaining good image quality. Longitudinal views of the heart, which nicely visualize the left ventricle, were acquired. The generated videos were treated as series of individual images in sequence.

For optical flow calculations, both Horn-Schunck and Lucas-Kanade were able to represent the motion of the heart, though Lucas-Kanade showed a greater number of scatter errors due to its local estimation of regions. As shown in Figure 5(a), at lower local window sizes, the low-level structure information was not represented. In Figure 5(b), where the window size is  $5 \times 5$ , noise starts to cloud the left ventricle structure, and in Figure 5(c), where the window size is  $15 \times 15$ , all information is lost by the noise. The high amount of speckle inherent to US images made it difficult to cope. The Horn-Schunck technique, with a global regularization parameter  $\lambda$  between 0.05 and 0.09, was able to compensate for the general speckle throughout the

US images while maintaining structural endocardial lining. Empirically, we found that smoothing greater than this, as exhibited in Figure 5(d), where  $\lambda = 0.001$ , would start to erode structural feature borders. Smoothing less than this, as exhibited in Figure 5(f), where  $\lambda = 1.00$ , would result in scatter and false flow measurements due to the noise. For this application, a regularization parameter of 0.07 was selected.

The mask size for generating the GVF field was set to 65 by 65 in order to calculate the point charges and is then normalized for active contour use. For left ventricle segmentation, the initial contour was set to be a small oval (of radius greater than 30 pixels along its minor axis and 60 pixels along its major), which was placed by the user within the left ventricle of the heart on the first image cine. Following image in the sequence would grab the previous segmented left ventricle contour and use it as its initial contour. Hence each dataset (or set of image sequences) was only initialized once.

Snake parameters  $\alpha$  and  $\beta$  were set to 4.0 and 0, respectively.  $\beta$  was set to 0 due to the influence of the prior knowledge component which offsets the curvature, whereas  $\alpha$  was set to 4.0 in order to make sure that the external and internal energies were neatly balanced. The prior step parameter was set to 5. By decreasing the value of this step parameter, greater shape regularity would occur, but it would take much longer for the snake to reach equilibrium. Empirically, we found that a prior step parameter of 5 was balanced enough to maintain the shape regularity of the snake, without greatly affecting the time complexity.

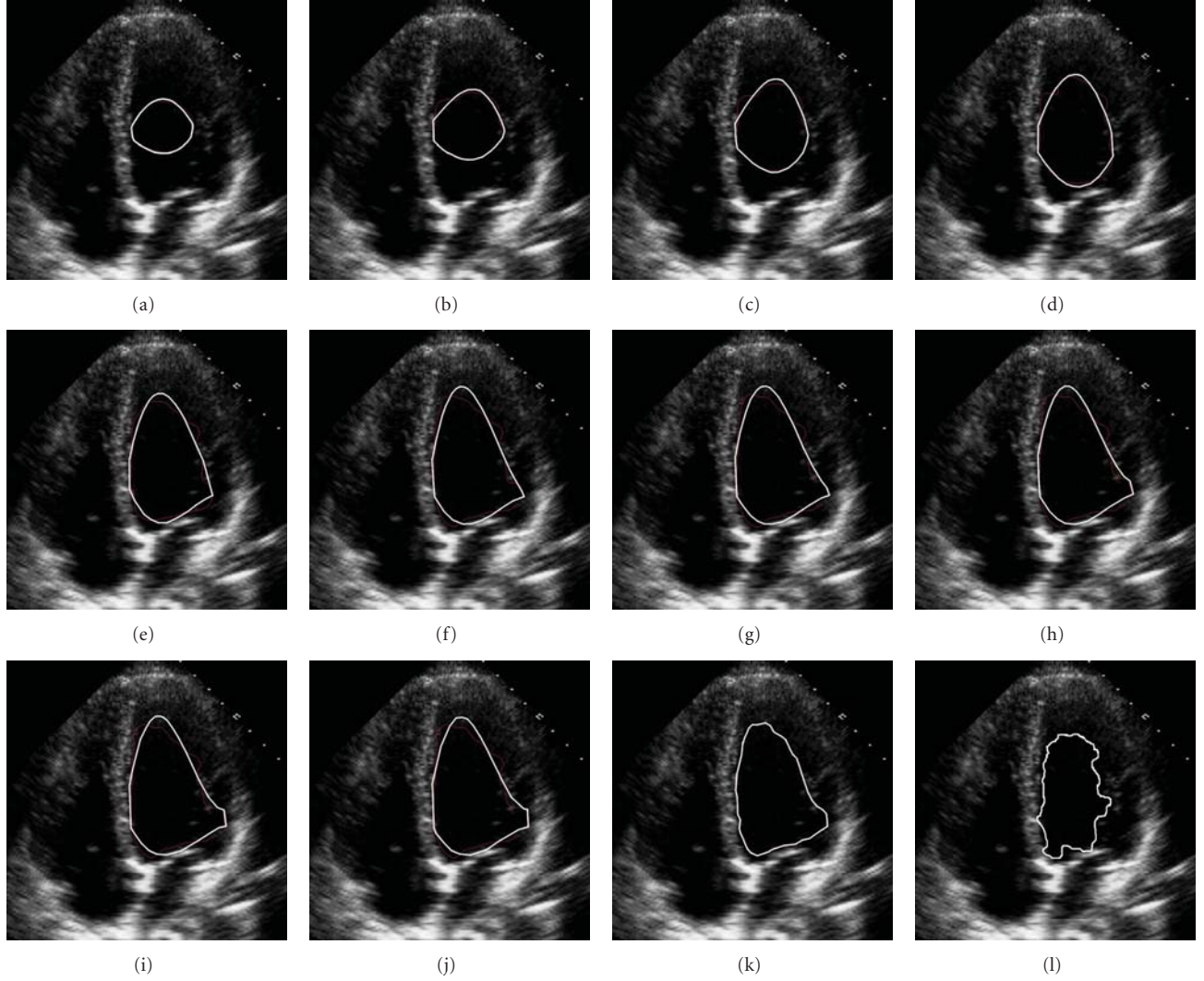


FIGURE 6: Example of a left ventricle segmentation using the proposed scheme. (a)-(j) Prior formulation steps, where the prior step parameter is set at every five iterations of energy optimization process. (k) and (l) represent the final segmentation of the left ventricle with and without utilizing shape priors, respectively.

During our experimentations, we assumed that equilibrium is achieved when there is less than 10% movement of contour points throughout the snake between two consecutive snake evolutions.

Since the proposed model is iterative, other adjustments can be made during the prior knowledge phase, such as increasing internal energy weights dependent on the distance of fitted priors to snake curve and other various optimizations without upsetting the actual active contour model, though none were done for the purposes of this experiment.

Figure 6 shows an example of a left ventricle segmentation using the proposed scheme. Figures 6(a)-6(j) illustrate the outcome of the proposed active contour iterations, where the prior step parameter is set to five iterations (in order to demonstrate the contour progression over the cycle). Figure 6(k) represents the final contour when utilizing the shape priors and the optical flow as an external energy.

Figure 6(l) shows the final contour when utilizing the optical flow as an external energy exclusively without shape priors. Examination reveals that the shape priors helped to maintain shape regularity and properly delineate the left ventricular endocardial lining, despite being disrupted by the speckle noise, artifacts, and valves movements.

Experiments were run on eight complete cardiac cycles from different patients. The performance of the proposed system was measured by comparing 130 indexed segmented image cines from the eight cardiac cycles to the manually delineated segmentations by an expert radiologist, representing the gold standard used.

Since the images at hand were mainly small segmented foregrounds (left ventricular surface area) against vast backgrounds, the system performance would best be measured by means of its *sensitivity*, *precision rate*, and *overlap ratio*. Let us consider the following metrics: a *true positive* pixel is a pixel that is considered part of the left ventricle by both of the

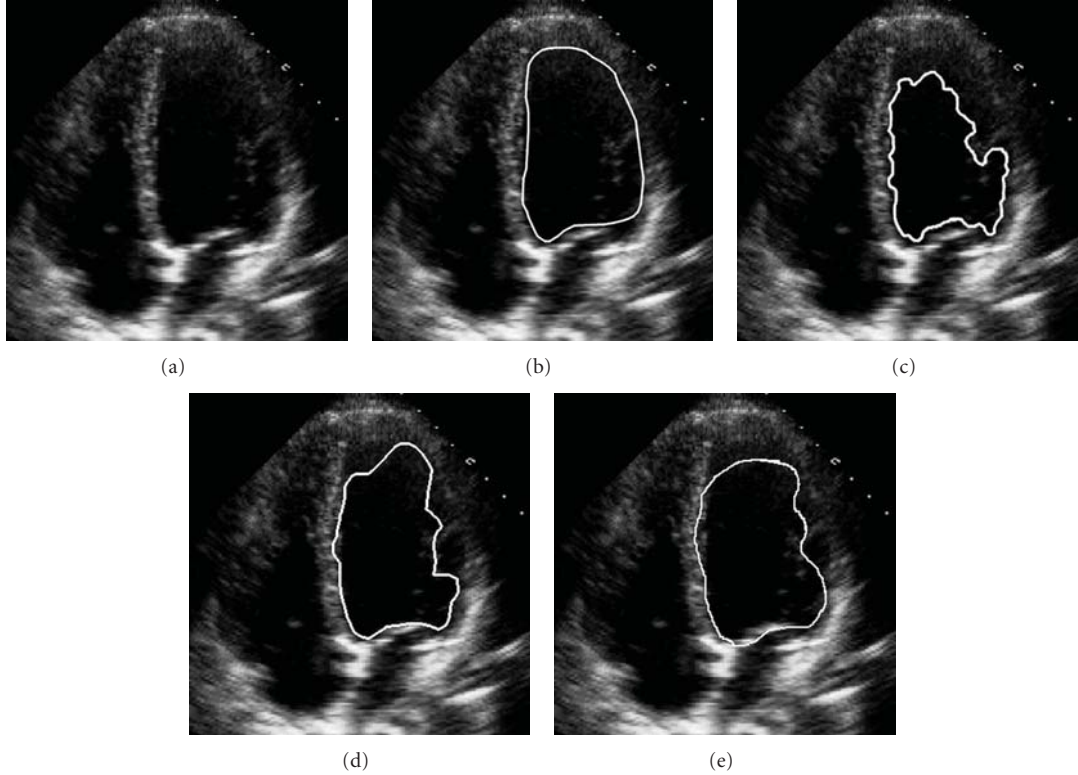


FIGURE 7: Example of segmenting a heart left ventricle. (a) Original left ventricle ultrasound image, (b) expert manual segmentation, (c) segmentation using standard GVF, (d) segmentation using GVF-optical flow without priors, and (e) segmentation using the proposed GVF-optical flow with priors.

proposed method and the gold standard. A *false positive* pixel is a pixel that is considered part of the left ventricle by the proposed method but it is not considered as such on the gold standard. A *false negative* pixel is a pixel that is not considered as part of the left ventricle by the proposed method; yet it is considered to be part of the ventricle according to the gold standard. The *sensitivity* is the percentage of the number of true positive pixels divided by the sum of the number of true positive pixels, and false negative pixels. In other words, it classifies how well a binary classification test correctly identifies a condition. *Precision rate* is the percentage of the number of true positive pixels divided by the sum of the number of true positive pixels and false positive pixels. In other words, it classifies how accurate the results of the test when the results are positive. *Overlap ratio* is the percentage of the number of true positive pixels divided by the sum of the number of true positive pixels, false positive pixels and false negative pixels.

The sensitivity, precision rate, and overlap ratio of the proposed system on the 130 segmented cines can be seen in Table 1. This was generated by combining the total metric aggregates across all 130 cines, and calculating the sensitivity, precision rate and overlap ratio measures. In comparison, the standard GVF snake's on the same dataset yields an adequate sensitivity this is due to over-segmentation by the GVF method, since the speckle tends to complicate image features. When optical flow is added to the GVF model some

of the inherent noise is filtered out (due to the static nature of the speckle); hence the segmentation results are improved. By using primitive priors to help the snake's regularity, results are further improved (as revealed in Table 1).

Figure 7 illustrates the segmentation of a heart left ventricle using various segmentation schemes. Figure 7(a) shows the original left ventricle of the heart ultrasound image, whereas Figure 7(b) shows an expert manual segmentation of the image shown in Figure 7(a). Figure 7(c) depicts the final contour using the original GVF snake model (yielding a sensitivity, precision rate and overlap ratio of 71.9%, 96.3% and 70.0%, resp.). Figure 7(d) shows the results of using optical flow GVF without priors (yielding 80.7%, 93.9%, and 76.7%). Figure 7(e) shows the final contour using our optical flow GVF snake with primitive priors (yielding a sensitivity, precision rate, and overlap ratio of 85.2%, 91.9%, and 79.2%, resp.). Examination of the figure reveals that the shape priors improve regularity by allowing the snake to overcome noise artifacts. This allows for proper delineation of the left ventricular endocardial lining. The standard GVF's precision rate is slightly higher in this example, since the GVF contour results in a severely under segmented region, hence having very few false positives. In our scheme, the motion information (optical flow) is used as structural information in the external energy of the snake. This motion information ignores much of the speckle, due to its static nature, preventing feature under segmentation.

TABLE 1: Sensitivity, precision rate, and overlap ratio of the proposed segmentation system.

	Sensitivity	Precision rate	Overlap ratio
Standard GVF snake	90.4%	70.2%	65.3%
GVF snake with optical flow only	92.8%	76.5%	72.2%
GVF snake with optical flow and priors	93.7%	80.9%	76.7%

## 4. Concluding Remarks

In this paper, we have shown that optical flow can be utilized as an external energy within the GVF active contour framework. We have demonstrated that an active contour method is able to make use of the knowledge derived from the apparent motion of tissue via optical flow measurements. This strengthens the principle that tissue movement should be considered within segmentation techniques, where the data facilitates it.

Furthermore, results were improved by using primitive shapes, which helped overcome the inherent difficulties in segmenting echocardiographic images, by maintaining shape regularity. The proposed prior technique does not require training samples that are expert delineated; rather they are built from the current active contour control points. Furthermore, different primitive priors can be used depending on the feature of interest to be segmented. Such segmentations would improve the calculation of various clinical measures by reducing the inconsistencies and variability between clinicians while simultaneously reducing the time for clinician interaction.

## Acknowledgment

This research is partially funded by the Natural Sciences and Engineering Research Council of Canada (NSERC). This support is greatly appreciated.

## References

- [1] B. Mazumdar, A. Mediratta, J. Bhattacharyya, and S. Banerjee, "A real time speckle noise cleaning filter for ultrasound images," in *Proceedings of the IEEE Symposium on Computer-Based Medical Systems (CBMS '06)*, pp. 341–346, 2006.
- [2] C. Tauber, H. Batatia, and A. Ayache, "Robust B-spline snakes for ultrasound image segmentation," *Journal of Signal Processing Systems*, vol. 54, no. 1–3, pp. 159–169, 2009.
- [3] M. Choy and J. Jin, "Morphological image analysis of left-ventricular endocardial borders in 2D echocardiograms," in *Medical Imaging 1996: Image Processing*, vol. 2710 of *Proceedings of SPIE*, pp. 852–863, Newport Beach, Calif, USA, February 1996.
- [4] J. Montagnat and H. Delingette, "Space and time shape constrained deformable surfaces for 4D medical image segmentation," in *Proceedings of the Medical Image Computing and Computer-Assisted Intervention (MICCAI '00)*, Lecture Notes in Computer Science, pp. 196–205, 2000.
- [5] A. Amini, P. Radeva, M. Elayyadi, and D. Li, "Measurement of 3D motion of myocardial material points from explicit B-surface reconstruction of tagged MRI data," in *Proceedings of the International Conference on Medical Image Computing and Computer Assisted Intervention*, vol. 1496 of *Lecture Notes in Computer Science*, pp. 110–118, 1998.
- [6] M. Kass, A. Witkin, and D. Terzopoulos, "Snakes: active contour models," *International Journal of Computer Vision*, vol. 1, no. 4, pp. 321–331, 1988.
- [7] L. Cohen, "On active contour models and balloons," *Computer Vision, Graphics, and Image Processing: Image Understanding*, vol. 53, no. 2, pp. 211–218, 1991.
- [8] A. Amini, T. Weymouth, and R. Jain, "Using dynamic programming for solving variational problems in vision," *IEEE Transactions on Pattern Analysis and Machine Intelligence*, vol. 12, no. 9, pp. 855–867, 1990.
- [9] D. J. Williams and M. Shah, "A fast algorithm for active contours and curvature estimation," *Computer Vision Graphics and Image Processing: Image Understanding*, vol. 55, no. 1, pp. 14–26, 1992.
- [10] L. Cohen and I. Cohen, "Finite-element methods for active contour models and balloons for 2-D and 3-D images," *IEEE Transactions on Pattern Analysis and Machine Intelligence*, vol. 15, no. 11, pp. 1131–1147, 1993.
- [11] H. Mallouche, J. de Guise, and Y. Goussard, "Probabilistic model of multiple dynamic curve matching for a semitransparent scene," in *Vision Geometry IV*, vol. 2573 of *Proceedings of SPIE*, pp. 148–157, San Diego, Calif, USA, July 1995.
- [12] R. Szeliski and D. Tonnesen, "Surface modeling with oriented particle systems," *Computer Graphics*, vol. 26, no. 2, pp. 185–194, 1992.
- [13] C. Xu and J. Prince, "Snakes, shapes, and gradient vector flow," *IEEE Transactions on Image Processing*, vol. 7, no. 3, pp. 359–369, 1998.
- [14] N. Felix-Gonzalez and R. Valdes-Cristerna, "3D echocardiographic segmentation using the mean-shift algorithm and an active surface model," in *Medical Imaging 2006: Image Processing*, vol. 6144 of *Proceedings of SPIE*, pp. 147–151, San Diego, Calif, USA, February 2006.
- [15] X. Papademetris, A. Sinusas, D. Dione, and J. Duncan, "3D cardiac deformation from ultrasound images," in *Proceedings of the International Conference on Medical Image Computing and Computer-Assisted Intervention (MICCAI '00)*, vol. 1679 of *Lecture Notes in Computer Science*, pp. 420–429, 1999.
- [16] K. Leung, M. van Stralen, G. van Burken, et al., "Sparse appearance model based registration of 3D ultrasound images," in *Medical Imaging and Augmented Reality*, vol. 4091 of *Lecture Notes in Computer Science*, pp. 236–243, 2006.
- [17] S. Zhou, B. Liang, and W. Chen, "A new method for robust contour tracking in cardiac image sequences," in *Proceedings of the 2nd IEEE International Symposium on Biomedical Imaging: Macro to Nano*, vol. 1, pp. 181–184, 2004.
- [18] H. Park and M. Chung, "A new external force for active contour model: virtual electric field," in *Proceedings of the International Conference on Visualization, Imaging and Image Processing (VIIP '02)*, pp. 103–106, 2002.
- [19] J. Barron, D. Fleet, and S. Beauchemin, "Performance of optical flow techniques," *International Journal of Computer Vision*, vol. 12, no. 1, pp. 43–77, 1994.
- [20] B. Lucas and T. Kanade, "An iterative image registration technique with an application to stereo vision," in *Proceedings of Imaging Understanding Workshop*, pp. 121–130, 1981.
- [21] B. Horn and B. Schunck, "Determining optical flow," *Artificial Intelligence Journal*, pp. 185–203, 1981.

- [22] S. Russell and P. Norvig, *AI, A Modern Approach*, Prentice Hall, Englewood Cliffs, NJ, USA, 1995.
- [23] A. K. Hamou, S. Osman, and M. R. El-Sakka, “Carotid ultrasound segmentation using DP active contours,” in *Proceedings of the International Conference on Image Analysis and Recognition (ICIAR '07)*, vol. 4633 of *Lecture Notes in Computer Science*, pp. 961–971, 2007.

## Research Article

# A New Method to Calibrate Attachment Angles of Data Loggers in Swimming Sharks

**Shizuka Kawatsu,<sup>1</sup> Katsufumi Sato,<sup>2</sup> Yuuki Watanabe,<sup>3</sup> Susumu Hyodo,<sup>1</sup> Jason P. Breves,<sup>4</sup> Bradley K. Fox,<sup>4</sup> E. Gordon Grau,<sup>4</sup> and Nobuyuki Miyazaki<sup>1</sup>**

<sup>1</sup> Ocean Research Institute, The University of Tokyo, 1-15-1 Minamidai, Nakano, Tokyo 164-0014, Japan

<sup>2</sup> International Coastal Research Center, Ocean Research Institute, The University of Tokyo, 2-106-1 Akahama, Otsuchi, Iwate 028-1102, Japan

<sup>3</sup> National Institute of Polar Research, 10-3 Midorimachi, Tachikawa, Tokyo 190-8518, Japan

<sup>4</sup> Hawaii Institute of Marine Biology, University of Hawaii, Kaneohe, HI 96744, USA

Correspondence should be addressed to Shizuka Kawatsu, kawatusame@ori.u-tokyo.ac.jp

Received 2 May 2009; Accepted 7 August 2009

Academic Editor: João Manuel R. S. Tavares

Copyright © 2010 Shizuka Kawatsu et al. This is an open access article distributed under the Creative Commons Attribution License, which permits unrestricted use, distribution, and reproduction in any medium, provided the original work is properly cited.

Recently, animal-borne accelerometers have been used to record the pitch angle of aquatic animals during swimming. When evaluating pitch angle, it is necessary to consider a discrepancy between the angle of an accelerometer and the long axis of an animal. In this study, we attached accelerometers to 17 free-ranging scalloped hammerhead shark (*Sphyrna lewini*) pups from Kaneohe Bay, Hawaii. Although there are methods to calibrate attachment angles of accelerometers, we confirmed that previous methods were not applicable for hammerhead pups. According to raw data, some sharks ascended with a negative angle, which differs from tank observations of captive sharks. In turn, we developed a new method to account for this discrepancy in swimming sharks by estimating the attachment angle from the relationship between vertical speed (m/s) and pitch angle obtained by each accelerometer. The new method can be utilized for field observation of a wide range of species.

## 1. Introduction

An accurate determination of pitch angle is critical to gain detailed information about the diving and foraging strategies of aquatic animals. For example, air-breathing aquatic animals that forage underwater control pitch angle and allocate their submerged time. In African penguins, steeper ascent angles presumably occur when they have depleted their oxygen stores and must return to the surface more quickly to breathe [1]. In macaroni penguins, pitch angle is significantly correlated with time spent at the bottom-phase of the dive [2]. A steep pitch angle during ascent indicates that they encountered a prey patch and a shallow pitch angle contributes to movement into a more profitable area in the following dive, due to increasing the horizontal distance [2]. While in fish, Nakaya [3] said that scalloped hammerhead sharks (*Sphyrna lewini*) have great maneuverability due to a movable large plate on head. Based

on the observation of swimming behavior, it is apparent that sharks make a sharp dorsal turn at the bottom, consume food items, and swim away along the bottom [3]. In this sequence, pitch angle is an important indicator of a feeding event.

Recent advances in the development of animal-borne accelerometers (data loggers) make it possible for researchers to monitor pitch angle of aquatic animals *in situ* by attaching an acceleration sensor (accelerometer) along the longitudinal axis of the body. When a data logger is positioned exactly parallel to the longitudinal axis of an animal, the calculated angle of the data logger is the same as the pitch angle of the animal. Nonetheless, it is impossible to align the logger exactly parallel to the longitudinal axis of an animal in field studies. A few methods have been previously described to account for the discrepancy between the pitch angle of data loggers and the longitudinal axis in field studies. In one instance, Watanuki et al. [4] designated the attachment angle to the lower back of seabirds as 0° when they were

at the water surface, a time in which they were essentially horizontal before release. This methodology is well suited for birds that can be maintained in a horizontal position at the water surface. However, for animals that have a flexible body, it is difficult to keep them positioned horizontally for an extended period of time. In addition, this methodology cannot be applied for obligate swimming fish because of fatal risk for lack of adequate gill ventilation. Another approach to account for the discrepancy between the pitch angle of data loggers and the longitudinal axis was reported by Sato et al. [5] in Weddell seal. In this study, the attachment angle was calculated by using the data logger along with the speed sensor. Sato et al. [5] used the data logger (UWE1000-PD2GT; 22 mm diameter, 124 mm length; 80 g in air; Little Leonardo Co., Tokyo, Japan) which contains a propeller and reported that the attachment angle for a specific dive of Weddell seal could be determined using equations including the number of propeller rotations, surging acceleration ( $m/s^2$ ), the acceleration of gravity ( $9.8 m/s^2$ ), and body angle (degrees). This methodology can only be applied for large animals due to the relatively large size of data loggers that have a propeller. Furthermore, this method is only applicable for diving animals that must come to the surface to breathe. Lastly, in a third study, the attachment angle in flatfish was assigned as  $0^\circ$  when they lay on the substrate as reported by Kawabe et al. [6]. This method is only applicable for benthic animals that remain on the bottom. There are currently no reported methods to apply for continuous swimming fish.

The previously described methods are specific for particular species and we therefore anticipated that they might not be suitable for use in hammerhead sharks. Scalloped hammerhead shark pups have flexible bodies and are obligatory swimmers [7]. In addition, their small body size allows only for use of the smallest logger available for field studies that can only record depth, temperature and 2-axes accelerations, but not speed. In this study, we attached data loggers to 17 free-ranging pups with the objective to establish a new method for calibrating the attachment angle of loggers in free-ranging sharks.

## 2. Materials and Methods

**2.1. Field Work.** Our field studies occurred in Kaneohe Bay, Hawaii ( $21.26^\circ N$ ,  $157.47^\circ W$ ) in August and October, 2007, and July/August, 2008. Kaneohe Bay is a nursery ground for the scalloped hammerhead shark (*Sphyrna lewini*) during summer months in which pups spend most of their time near the bottom [8]. In this study, juvenile scalloped hammerhead sharks were collected using hand lines with baited hooks. Upon capture, sharks were immediately transferred to the Hawaii Institute of Marine Biology, University of Hawaii, and placed in 3 m diameter tanks with flow-through seawater for 2–3 days. Sharks were fed squid twice a day and usually resumed feeding within 24 hours of capture. Release of the sharks into the field with data loggers did not occur until they resumed feeding in captivity for at least 48 hours. At this time, both total length (TL) and body mass (BM) were measured. For some sharks, BM was estimated from the

relationship ( $R^2 = 0.45$ ) between TL and BM of 20 pups from a previous experiment. Prior to release, a data logger was attached immediately anterior to the first dorsal fin using a plastic cable connected to a time-scheduled release system [9]. This cable ran through the soft plastic netting (3 cm  $\times$  5 cm) attached to the shark with dissolvable suture (Matsuda Medical Kogyo Co., Tokyo, Japan). Techniques used to attach the data loggers were done within a jet of seawater and designed to minimize stress. The time required to attach the data loggers was less than 5 minutes per individual and we let sharks respire forcibly along the way. After which time sharks were immediately released in the bay. All animal experiments were conducted according to the Guideline for Care and Use of Animals approved by the committees of University of Tokyo and University of Hawaii.

**2.2. Data Recovery.** An automatic time-scheduled release system that allows for loggers to be located and retrieved using VHF radio signals was used because the recapture of instrumented pups in Kaneohe Bay is not possible. The data loggers were attached to a float of copolymer foam (Nichiyu Giken Kogyo Co., Saitama, Japan), in the top of which a VHF radio transmitter with a 45 cm semirigid wire antenna (Advanced Telemetry Systems Inc., Isanti, MN, USA) was embedded. A plastic cable connected to a time-scheduled release mechanism (Little Leonardo Co.) bound the tag to the plastic netting which was attached to the pups. Tag retrieval followed the method reported in Baikal seals [10]. Devices were attached to 17 pups in total, of which we successfully retrieved 16 loggers. Of the 16 loggers, one data logger was released from a pup after 6 hours, 7 were released after 24 hours, 7 were released after 48 hours, and one was released after 72 hours.

**2.3. Instruments.** Acceleration data loggers (M190L-D2GT; Little Leonardo Co., Tokyo, Japan) were used to examine swimming behavior of pups. Each logger was 15 mm in diameter, 53 mm in length, had a mass of 18 g and recorded depth (1 Hz), 2-axes accelerations (for detecting caudal fin movement and pitch, 32 Hz for eight individuals and 16 Hz for eight individuals), and temperature (1 Hz). The total weight of the instruments deployed on pups, including devices for data recovery (such as float and VHF transmitter), was 50 g with a slight positive buoyancy in seawater. The measuring range for acceleration along two axes was  $\pm 29.4 m/s^2$ . Values recorded by the accelerometers were converted into acceleration ( $m/s^2$ ) with linear regression equations. To obtain the calibration equations, relative values recorded by each logger at  $90^\circ$  and  $-90^\circ$  from the horizontal level were regressed against the corresponding acceleration ( $9.8 m/s^2$  and  $-9.8 m/s^2$ , resp.).

**2.4. Data Analysis.** Two of the sixteen retrieved data loggers were not included in our analyses due to incomplete data records. Loggers were positioned so as to detect longitudinal (surging) and lateral (swaying) accelerations. Loggers attached on the animals measured both dynamic acceleration (such as tail beating activities) and static acceleration (such

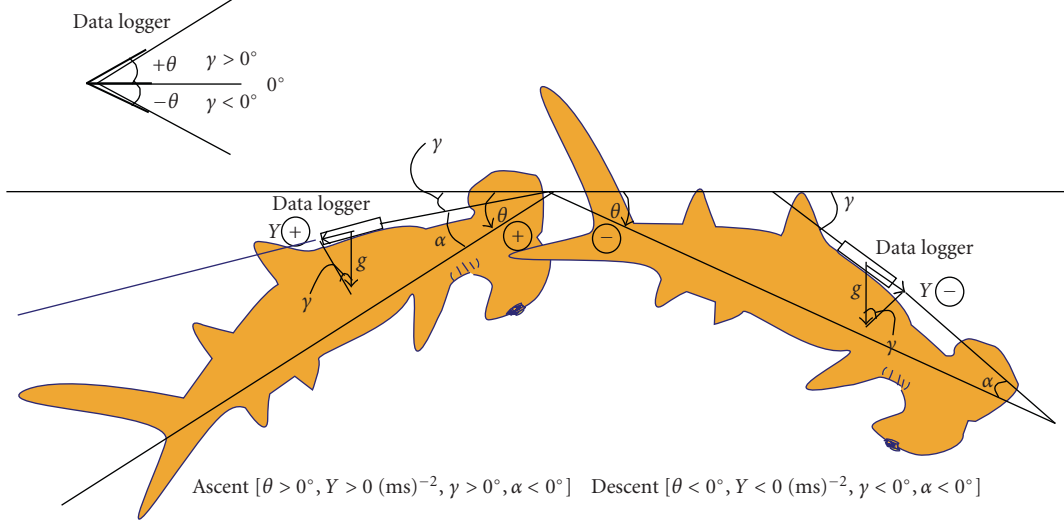


FIGURE 1: Attachment of a data-logger to the dorsal side of a hammerhead shark. Diagram shows the direction of surging acceleration  $Y$ , recorded by a D2GT logger placed on a shark, and gravity  $g$  ( $= 9.8 \text{ ms}^{-2}$ ), angle of surge axis of the logger to horizon ( $\gamma$ ), that of longitudinal axis to horizon ( $\theta$ ) defined as pitch angle (negative as the shark descends), and logger attachment angle ( $\alpha$ ).

as gravity). The acceleration sensor along the longitudinal body axis can measure acceleration in response to changes in the movements of animals such as stroking and change in pitch angle. High-frequency fluctuations in the surging acceleration records are believed to be caused by caudal fin movements. When the animal is still or moving at a constant speed, the gravity vector will change in response to pitch angle. Together, low-frequency fluctuations in the acceleration along the longitudinal axis (surging acceleration) are used to calculate the pitch angle [5, 11].

To remove the high-frequency component of acceleration caused by the tail beating, we extracted the low-frequency signals on surging accelerations of sharks with a filter in the IGOR Pro software (Wave Metrics Inc., USA; see also [5, 11]). Then, the low-frequency component of longitudinal acceleration ( $Y$ ) was converted to angle of the data-logger relative to the horizon ( $\gamma$  ranging from  $-90^\circ$  to  $90^\circ$ ) as follows:

$$\gamma = \alpha \sin\left(\frac{Y}{9.8}\right). \quad (1)$$

Following Sato et al. [5], the body angle of pups against the water surface ( $\theta$ , Figure 1) can be expressed by

$$\theta = \gamma - \alpha, \quad (2)$$

where  $\gamma$  is the angle of surge axis of the logger to horizon (degrees), and  $\alpha$  is the attachment angle of the logger against the longitudinal axis (degrees).  $\theta$  and  $\gamma$  while pups were descending (the data logger was tilting in a clockwise direction) were regarded as negative, and when ascending (the data logger was tilting in a counterclockwise direction),  $\theta$  and  $\gamma$  were regarded as positive.

At first, we estimated an attachment angle ( $\alpha_1$ ) using a previously reported method [4]. We corrected the values of body angle recorded in a holding tank horizontally for 10–20 seconds to  $0^\circ$ . We held a pup for 10–20 seconds with its

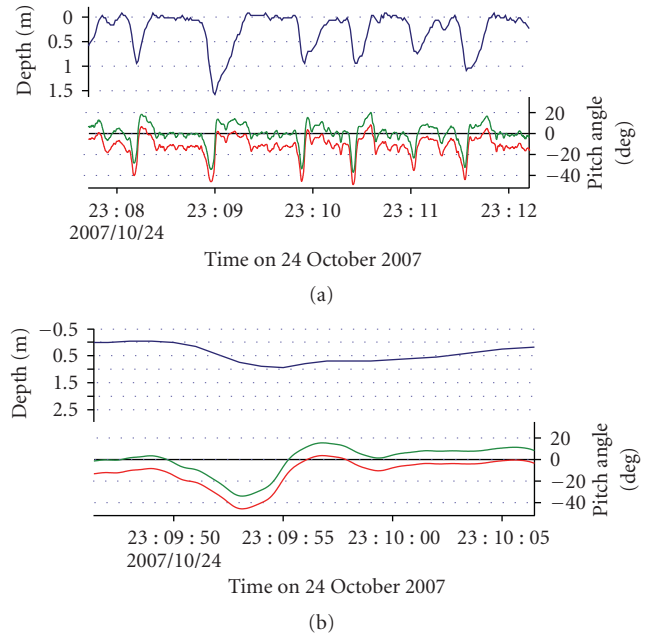


FIGURE 2: (a) An example of swimming depth (blue line) adjusted pitch angle by new method (green line) and by previous method (red line) of an individual pup (HI0703). (b) Enlarged part of Figure 2 shows that the adjusted pitch angle (green line) changed from a negative to positive value at the moment of ascent.

body level to the water surface and recorded the time. We assumed the pitch angle during previous recording periods to be flat ( $0^\circ$ ). Then, we subtracted the recorded angle during previous periods from each individual's pitch angle data over the period of logger deployment. Next, we obtained another attachment angle ( $\alpha_2$ ) using a new method that estimated the attachment angle from the relationship between vertical

TABLE 1: Morphological information and attachment angles of loggers derived from a previous method ( $\alpha_1$ ) and that following adjustment by a new method ( $\alpha_2$ ) for each shark.

Shark ID	Sex	Total length (cm)	Body mass (g)	$\alpha_1$ (degrees)	$\alpha_2$ (degrees)	Correlation coefficient	Data length (h)*
HI0702	F	54.5	727	-19.6	-43.6	-0.72	6
HI0703	M	58	870	-12.5	-24.3	-0.88	24
HI0704	F	54	935	-2.2	-20.5	-0.71	48
HI0705	F	56	760	-18.0	-36.4	-0.79	48
HI0706	M	55	750	-13.3	-25.3	-0.57	28
HI0707	F	56	780	-12.0	-23.9	-0.77	24
HI0709	M	54	745	-6.9	-19.9	-0.56	20
HI0801	F	54	575	-31.2	-31.9	-0.78	2
HI0802	F	54	575	-19.3	-22.7	-0.83	2
HI0803	—	58	717	-23.1	-40.1	-0.72	19
HI0804	—	58	717	-24.9	-44.1	-0.74	24
HI0805	—	57	681	-26.1	-55.2	-0.60	17
HI0807	M	54	575	-15.8	-40.4	-0.72	17
HI0808	F	57	681	-21.7	-17.3	-0.71	44

\*Data length (h) is not necessarily consistent with total recorded hours.

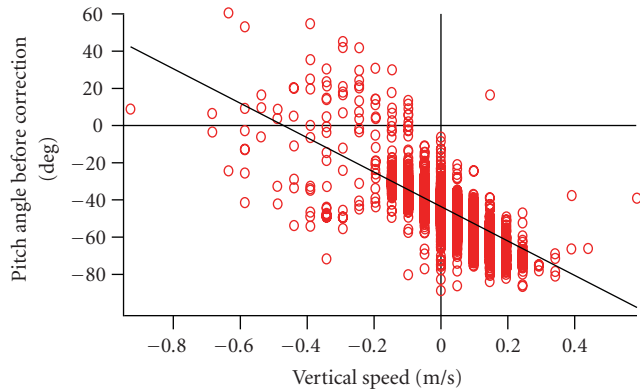


FIGURE 3: Example of the relationship between raw pitch angle ( $\gamma$ ) and vertical speed from an individual pup (HI0702). A negative vertical speed indicates ascent and a positive value indicates descent.

speed (m/s) and body angle. We compared raw pitch angle ( $\gamma$ ) with vertical speed per second to find a linear regression from each pup. There are indications that negatively buoyant fishes, such as sharks and sturgeon, may assume a positive pitch tilt during steady horizontal swimming as a behavioral mechanism to increase the total body area generating lift [12, 13]. Nonetheless, it can be assumed that the body axis of an animal is parallel to the direction of movement when the animal swims at a constant speed. With this assumption, we expected a descending pup to have a negative pitch angle while the pitch angle of an ascending pup would be positive. If a pup swims horizontally, the instantaneous pitch angle would be zero. When we analyzed the relationships between raw pitch angle and vertical speed per second, we found a linear regression from each pup. This regression line should pass through the origin coordinate if the logger angle is parallel to the longitudinal axis of the body. We considered the intercept of the regression line to be the attachment angle ( $\alpha_2$  degrees).

To confirm the utility of this new method, we observed instrumented banded dogfish (*Triakis scyllium*) in an experimental tank using a video camera. We attached a data logger (UWE190PD2GT: 22 mm diameter, 124 mm length; 80 g in air; Little Leonardo Co., Tokyo, Japan) using the same method as used for hammerhead pups. After the experiment, we compared the adjusted angle calculated from our new method with the adjusted angle obtained from video observations.

### 3. Results

As expected, we could not use previously reported methods to adjust pitch angle. Thus, we needed to develop a new method to calculate the attachment angle for hammerhead pups. A modulation of the pitch angle of a swimming shark is expected to correspond to fluctuations in the vertical speed rate (depth changes per second). The depth parameter therefore has the potential to provide information for the correction of pitch angle.

The first method reported by Watanuki et al. [4] provided us an estimated attachment angle ( $\alpha_1$ ) from 16 pups that varied between  $-40.9^\circ$  and  $-2.2^\circ$  (Table 1). When we applied this attachment angle to each pup, some individuals showed a negative angle when they ascended (Figure 2, red line). All the scatter plots made from the pitch angle before adjustment and the vertical speed provided a linear regression. A regression line was produced for each pup (Figure 3) with correlation coefficient (absolute value) higher than 0.56 (Table 1). The intercept of the regression line (adjustment angle  $\alpha_2$ ) varied from  $-55.2^\circ$  to  $-17.3^\circ$  (Table 1).  $\alpha_1$  and  $\alpha_2$  were regarded as negative when the data logger was tilting in a clockwise direction and positive when the data logger was tilting in a counterclockwise direction. As a result, all the data loggers attached to pups showed negative attachment angles.



FIGURE 4: An attachment angle of the data logger on the banded dogfish was  $14^\circ$  from visual analysis and  $13.7^\circ$  from the regression line method.

The attachment angles obtained from our new method differed from values obtained from the first method (Table 1). For example, an attachment angle of one individual (HI0702) from the first method was  $-19.6^\circ$  while the new method yielded an angle of  $-43.6^\circ$ . Both corrected pitch angles using the above values are indicated in Figure 2. The corrected pitch angle using the new methodology showed that the diving profile became negative during descent and positive during ascent (Figure 2(b)). Even considering the pitch tilt previously cited [12, 13], a negative pitch angle during ascent does not correctly represent the pitch angle of a pup. We concluded that the new methodology corresponds well with the diving profile. In banded dogfish held in an aquarium, the adjustment angle from the regression line method was  $13.7^\circ$ , while the observed tilt angle of the data logger was  $14^\circ$  when analyzed from video observations (Figure 4).

## 4. Discussion

The new regression line method we report has three advantages over previously described methods. First, the new method provides more accurate information about the correction angle since the corrected pitch angle using the new methodology corresponds well with the diving profile. It is difficult to fix sharks on their flat pitch angle because their bodies are flexible and a seemingly flat angle out of water is not necessarily the same as the rigid flat angle. Indeed, banded dogfish orient their heads slightly upward when resting at the bottom of an aquarium when compared with when they are held out of water. Second, the new method is considerably less invasive than the method that requires holding sharks level at the water surface. Our new method accounts for the fact that hammerhead shark pups are obligate swimmers that can only respire while swimming [7]. Third, it is possible to adjust the pitch angle without speed data. Sato et al. [5] developed another adjustment technique for a logger that contained a propeller so as to record speed in addition to depth, 2-axes accelerations, and temperature in the data logger we used. With this technique,

the animal does not need to be fixed flat, but it cannot be applied to smaller animals such as hammerhead shark pups, because a data logger including a speed sensor is too large and would likely impact behavior.

In conclusion, we developed a new method of analysis that enabled us to correct the pitch angle of hammerhead sharks equipped with a small accelerometer. For fish that display changes in pitch angle when making movements up and down in the water column, this new method to correct pitch angle in juvenile sharks can be applied for the acquisition of information in a wider range of species.

## Acknowledgments

The authors would like to thank the following people for their cooperation: Dr. Darren T. Lerner, Dr. Nicholas M. Whitney, and Dr. Tetsuya Hirano, University of Hawaii, Yoko Yamaguchi, Shin Takaki, and Souichirou Takabe, ORI for their assistance with the fieldwork, and Sho Tanaka, Fumitaka Noguchi, and Genjiro Nishi, Tokai University, for their assistance of aquarium investigations. This study was supported by the Sasakawa Scientific Research Grant from The Japan Science Society to S. K., the Pauley Foundation Summer Program 2008 at Hawaii Institute of Marine Biology to E. G. G., Japan-USA Research Cooperative Program from the Japan Society for the Promotion of Science to S. H., Grant in Aid from JSPS (19255001) to K. S., and program “Bio-Logging Science of the University of Tokyo (UTBLS)” led by N. M.

## References

- [1] R. P. Wilson and M.-P. Wilson, “The foraging behaviour of the African penguin *Spheniscus demersus*,” in *The Penguins: Ecology and Management*, pp. 244–265, Surrey Beatty and Sons, Sidney, Australia, 1995.
- [2] K. Sato, J.-B. Charrassin, C.-A. Bost, and Y. Naito, “Why do macaroni penguins choose shallow body angles that result in longer descent and ascent durations?” *Journal of Experimental Biology*, vol. 207, no. 23, pp. 4057–4065, 2004.
- [3] K. Nakaya, “Hydrodynamic function of the head in the hammerhead sharks (Elasmobranchii: Sphyrnidae),” *Copeia*, pp. 330–336, 1995.
- [4] Y. Watanuki, Y. Niizuma, G. W. Gabrielsen, K. Sato, and Y. Naito, “Stroke and glide of wing-propelled divers: deep diving seabirds adjust surge frequency to buoyancy change with depth,” *Proceedings of the Royal Society B*, vol. 270, no. 1514, pp. 483–488, 2003.
- [5] K. Sato, Y. Mitani, M. F. Cameron, D. B. Siniff, and Y. Naito, “Factors affecting stroking patterns and body angle in diving Weddell seals under natural conditions,” *Journal of Experimental Biology*, vol. 206, no. 9, pp. 1461–1470, 2003.
- [6] R. Kawabe, Y. Naito, K. Sato, K. Miyashita, and N. Yamashita, “Direct measurement of the swimming speed, tailbeat, and body angle of Japanese flounder (*Paralichthys olivaceus*),” *ICES Journal of Marine Science*, vol. 61, no. 7, pp. 1080–1087, 2004.
- [7] C. G. Lowe, “Kinematics and critical swimming speed of juvenile scalloped hammerhead sharks,” *Journal of Experimental Biology*, vol. 199, no. 12, pp. 2605–2610, 1996.

- [8] K. N. Holland, B. M. Wetherbee, J. D. Peterson, and C. G. Lowe, "Movements and distribution of hammerhead shark pups on their natal grounds," *Copeia*, pp. 495–502, 1993.
- [9] Y. Watanabe, E. A. Baranov, K. Sato, Y. Naito, and N. Miyazaki, "Foraging tactics of Baikal seals differ between day and night," *Marine Ecology Progress Series*, vol. 279, pp. 283–289, 2004.
- [10] Y. Watanabe, E. A. Baranov, K. Sato, Y. Naito, and N. Miyazaki, "Body density affects stroke patterns in Baikal seals," *Journal of Experimental Biology*, vol. 209, no. 17, pp. 3269–3280, 2006.
- [11] H. Tanaka, Y. Takagi, and Y. Naito, "Swimming speeds and buoyancy compensation of migrating adult chum salmon *Oncorhynchus keta* revealed by speed/depth/acceleration data logger," *Journal of Experimental Biology*, vol. 204, no. 22, pp. 3895–3904, 2001.
- [12] P. He and C. S. Wardle, "Tilting behavior of the Atlantic mackerel, *Scomber scombrus*, at low swimming speeds," *Journal of Fish Biology*, vol. 29, pp. 223–232, 1986.
- [13] C. D. Wilga and G. V. Lauder, "Functional morphology of the pectoral fins in bamboo sharks, *Chiloscyllium plagiosum*: benthic vs. pelagic station-holding," *Journal of Morphology*, vol. 249, no. 3, pp. 195–209, 2001.

## Research Article

# Analysis and Modelling of Muscles Motion during Whole Body Vibration

M. Cesarelli,<sup>1</sup> A. Fratini,<sup>1</sup> P. Bifulco,<sup>1</sup> A. La Gatta,<sup>2</sup> M. Romano,<sup>1</sup> and G. Pasquariello<sup>1</sup>

<sup>1</sup>Department of Biomedical Electronic and Telecommunication Engineering, University of Naples “Federico II”, 80125 Naples, Italy

<sup>2</sup>Math4Tech Centre, University of Ferrara, Ferrara, 44100 Ferrara, Italy

Correspondence should be addressed to M. Cesarelli, cesarell@unina.it

Received 1 May 2009; Accepted 3 August 2009

Academic Editor: João Manuel R. S. Tavares

Copyright © 2010 M. Cesarelli et al. This is an open access article distributed under the Creative Commons Attribution License, which permits unrestricted use, distribution, and reproduction in any medium, provided the original work is properly cited.

The aim of the study is to characterize the local muscles motion in individuals undergoing whole body mechanical stimulation. In this study we aim also to evaluate how subject positioning modifies vibration damping, altering local mechanical stimulus. Vibrations were delivered to subjects by the use of a vibrating platform, while stimulation frequency was increased linearly from 15 to 60 Hz. Two different subject postures were here analysed. Platform and muscles motion were monitored using tiny MEMS accelerometers; a contra lateral analysis was also presented. Muscle motion analysis revealed typical displacement trajectories: motion components were found not to be purely sinusoidal neither in phase to each other. Results also revealed a mechanical resonant-like behaviour at some muscles, similar to a second-order system response. Resonance frequencies and damping factors depended on subject and his positioning. Proper mechanical stimulation can maximize muscle spindle solicitation, which may produce a more effective muscle activation.

## 1. Introduction

Vibratory stimulations transferred to the whole body, that is, whole body vibrations (WBVs) treatments, have recently aroused a great deal of interest. WBVs are widely studied in the fields of exercise physiology, sport, and rehabilitation medicine [1–4]. Many studies have indeed accounted for their impact on metabolic and hormonal activity, neuromuscular response, and postural control [5–21].

WBV training aims to mechanically activate muscles by eliciting reflex neuromuscular activity. In such treatments, vibrations are generally delivered to the body as a whole by the use of vibrating plates, while muscular activity estimation is assessed analysing the simultaneous electromyography (EMG) activity, in particular the EMGs root mean square (RMS) values.

These vibrating devices produce vertical sinusoidal oscillations (or alternating rotation) of a platform across a frequency range from 10 to 80 Hz and peak-to-peak displacements from 1 to 10 mm [3, 22].

Mostly, individuals undergoing WBV treatments are requested to hold a specific position onto the plate. Vibratory

stimulation, impressed by the platform, transfers to the muscles through the body.

When vibration loads are applied, mechanical and metabolic responses arise from the neuromuscular system [2, 7, 9, 17]; muscles increase their activity to dampen the soft tissue oscillations that occur in response to vibrations. Specific WBV frequencies also seem to produce a higher EMGs RMS values than others [2].

Although EMG analysis is a common practice in estimating muscle response to vibratory stimulations, EMG is difficult to measure because vibrations induced in the tissues causes movement artifacts, which interfere with measurement of muscle activity [23, 24].

However, as reported in a previous study, there is a significant correlation between muscle motion and EMG activity [25]. Most of vibration-induced neuromuscular response occurs at the resonant frequencies of the tissues, concurring with the highest levels of muscle activity [23, 26–28].

Local mechanical stimulus characterization (i.e., muscle motion analysis) could be meaningful in discovering proper muscle stimulation and may contribute to suggest appropriate and effective WBV exercise protocols.

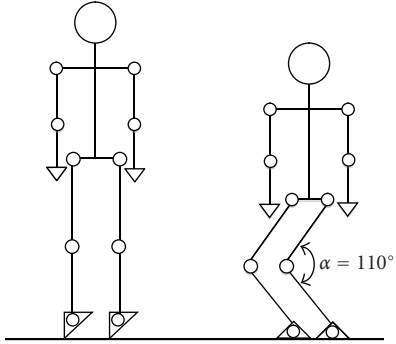


FIGURE 1: Body postures selected for the study.

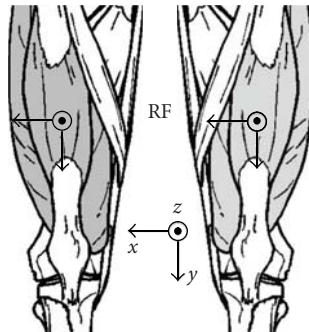


FIGURE 2: Example of accelerometer arrangement on muscles for both of the lower limbs. The picture shows the position and orientation of the accelerometer on RF muscles.

WBV effects depend on intensity, direction and frequency of vibratory stimulation; however, subject training posture should be considered as one of the most important factors involved.

This study concentrates on the characterization and modelling of the muscle motion in individuals exposed to whole body mechanical stimulation while holding different postures on platform. In our study we aim also to evaluate how subject positioning on the platform modifies vibration dumping through the body and in turn, the local vibratory stimulus. However, only two postures were analysed: hack squat position and upright position with heel raised.

Patients were impressed by a linear vibratory stimulation sweep in a frequency range from 15 to 60 Hz, while motions of the Rectus Femoris (RF), Biceps Femoris (BF)- (long head) and Gastrocnemius Lateralis (GL) were analyzed; a contralateral analysis between both of the lower limbs was also presented.

Muscle motion analysis showed typical 3D trajectories. Muscle displacement was found of different amount on each relative axis; motion components were also found not to be purely sinusoidal neither in phase to each other.

Results revealed a mechanical resonant-like behaviour at some muscles, very similar to a second-order system in the frequency range explored. A simple data fitting was then performed and it confirmed a high correlation ( $R^2_1$ ) between model and experimental data.

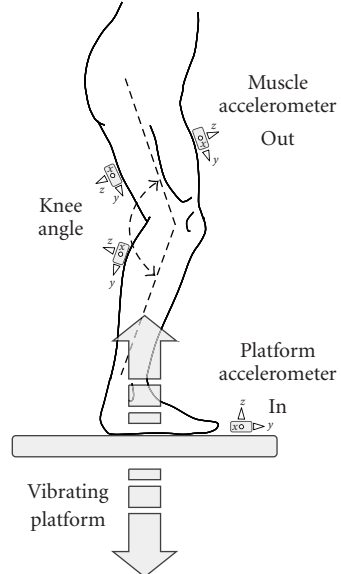


FIGURE 3: Scheme of measurement setup.

Contralateral analysis showed that the mechanical behaviour of muscles (both dominant and non dominant leg) was similar. Two limbs muscles motion resulted to be synchronous and symmetric with respect to the sagittal-plane.

## 2. Methods

**2.1. Subjects, Device, and Vibratory Stimulus.** Twenty healthy males (age  $22.6 \pm 2.2$  years, height  $176.7 \pm 8.4$  cm, weight  $74.0 \pm 10.1$  kg—athletically untrained), not affected by any known neurological or musculoskeletal disorder, were voluntarily involved in the study and gave their informed, written consent to participate. Vibrations were impressed by using a vibrating platform (TSEM S.p.A., Padova-Italy). Platform displacement was exclusively vertical, sinusoidal with an intensity (peak-to-peak displacement) set to 1.2 mm. The plate frequency was controlled from a function generator (Krohn-Hite 5300A) to obtain a linear vibratory stimulation sweep in a frequency range from 15 to 60 Hz. Frequency sweep time interval was set to 26 seconds, corresponding to an increase rate of about 1.7 Hz per second. All the subjects were familiarized with the device and proper positioning before recording; during the test subjects were requested to hold two positions (see Figure 1) without the use of any constraint:

- (i) P1: hack squat position: in the hack squat posture, subjects bent their legs at the knees with an angle of  $110^\circ$  between the lower legs and the upper legs;
- (ii) P2: upright on feet toes: in upright posture, subjects stand on their feet toes with heel raised.

These postures were selected as they are two of the manufacturers suggested positions for WBV training; they also reduce transmission of vibrations to patient's trunk and head [29].

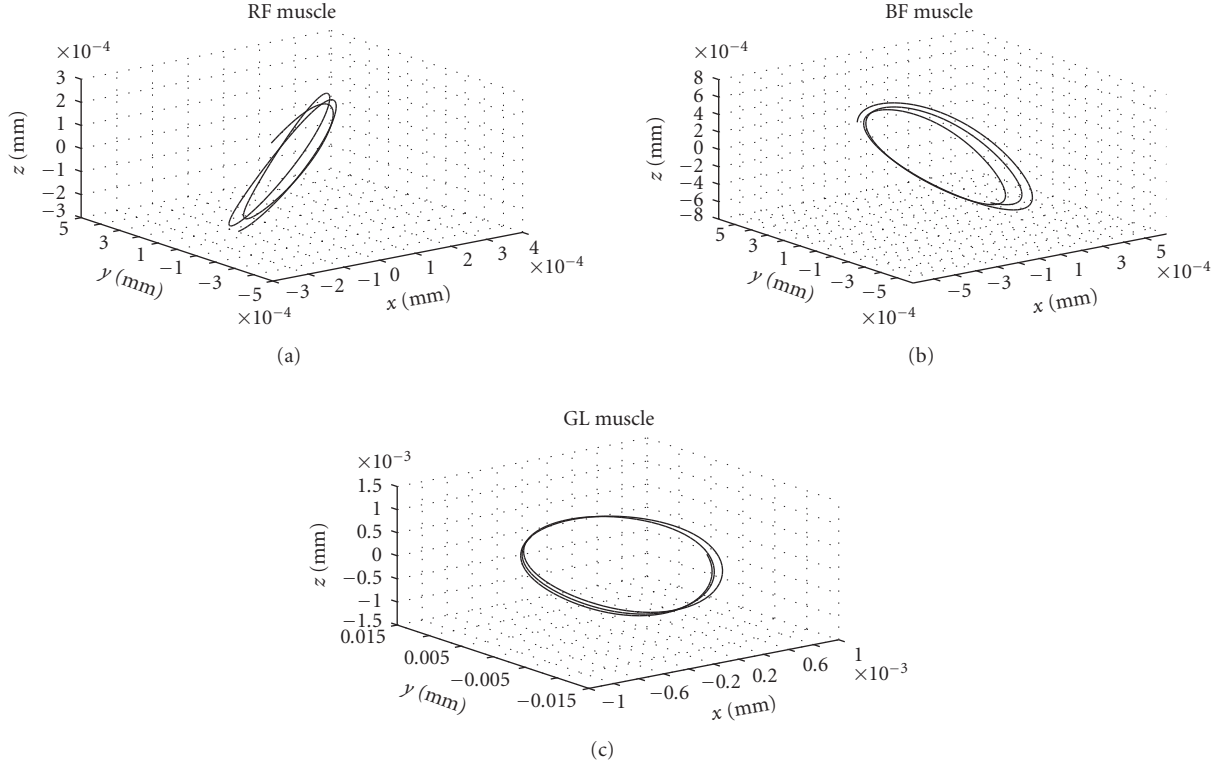


FIGURE 4: An example of three dimensional displacement of RF, BF and GL muscle belly under vibratory stimulation. The subject was holding the hack squat position while the frequency of the vibratory stimulus was around to 24 Hz. The figure depicts few cycles. The reference position for each muscle was placed at the accelerometer axis' origin.

Tiny and lightweight (less than 10 g) three-axial MEMS accelerometers (Freescale Semiconductors) were used to measure accelerations onto patient's skin and on the vibrating platform (the sensors were set to measure acceleration within a  $\pm 10$  g range).

The accelerometers were placed at 50% on the line from the anterior spina iliaca superior to the superior part of the patella for RF muscle, at 50% on the line between the ischial tuberosity and the lateral epicondyle of the tibia for BF muscle, at 1/3 of the line between the head of the fibula and the heel for GL muscle and at the centre of the vibration plate to monitor mechanical vibration (Figure 3). MEMS accelerometers were stuck onto muscles belly with medical adhesive tape (3 M). For each postural position, signals from the muscle bellies (both dominant and nondominant leg) were collected contemporaneously (Figure 2).

A PC multi-channel 16-bit data acquisition card (NI-DAQCard 6251) was used to acquire acceleration signals. All signals were sampled at 2048 Hz.

As mentioned, each of the acquisition (one for each posture), spaced with 60 seconds rest intervals, had a duration of 26 seconds; during this time interval the stimulation frequency, imposed by vibrating plate, raises linearly from 15 to 60 Hz.

**2.2. Accelerometer Data Processing.** Accelerations signals provided information related to muscle belly oscillation; they were preprocessed in order to exclude influence of

gravity and slow accommodation movements on motion information. Since gravity and subject's accommodation movements contributions are typically confined from 0 to 5 Hz [30], recordings have been high-pass filtered using a zero-phase 5th-order Butterworth with a cut off frequency of 10 Hz.

Muscle and platform displacements were estimated integrating twice the acceleration data after high-pass filtering on each axis. The resultant vectors were then estimated and analysed.

**2.3. Frequency Response of the Biomechanical System.** The frequency response of the biomechanical system was obtained processing the resultant displacement signals. The actual displacement of the vibrating plate (which was substantially constant in amplitude) was considered as the input signal, while the muscle displacement as system output.

Instantaneous frequency was computed for each vibration cycle by estimating two subsequent zero-crossings (with a positive slope) of the signal. Input displacement amplitude, output displacement amplitude and input/output phase difference were estimated for each cycle; gains were obtained by the input/output amplitude ratio. System gain and phase were then plotted against frequency (experimental system response).

**2.4. System Identification and Data Fitting.** A simple data fitting was performed supposing the system as a pure

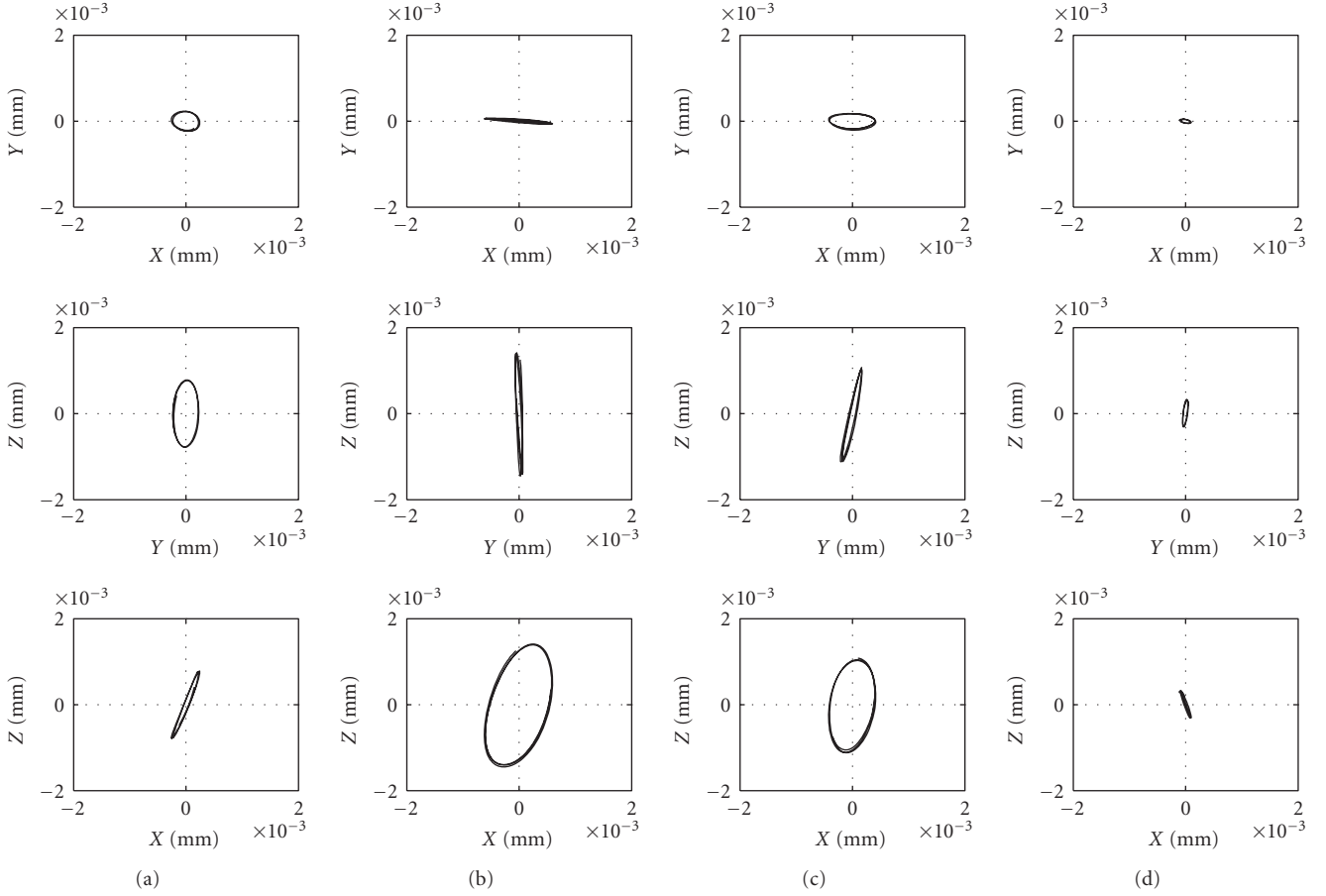


FIGURE 5: An example of the RF muscle belly trajectories over the  $(x, y)$ ,  $(y, z)$  and  $(x, z)$  planes, at different stimulation frequencies ((a) = 16 Hz, (b) = 25 Hz, (c) = 40 Hz, (d) = 50 Hz). The figure corresponds to P1 subject positioning.

second-order given by the following equation:

$$G(s) = K_{dc} \frac{1}{(s/\omega_n)^2 + 2\xi(s/\omega_n) + 1}, \quad (1)$$

where  $K_{dc}$  is the DC gain,  $\omega_n$  is the natural frequency, and  $\xi$  is the dumping ratio.

Model parameters ( $\omega_n$  and  $\xi$ ) were estimated by utilizing the values of the dominant peak (amplitude and frequency) of the experimental frequency response;  $K_{dc}$  coefficient was estimated minimizing the root mean squared error (RMSE) between model and experimental data.

**2.5. Contralateral Analysis.** A contralateral analysis on both of the lower limbs was also conducted by comparing the following:

- (i) muscle motion of dominant and nondominant leg,
- (ii) the estimated resonance frequencies.

In particular we evaluate the symmetry of muscle motion and the similarity of frequency response between lower limbs. For each posture and for all of the muscles analyzed we computed the correlation coefficient ( $R_s^2$ ) between the estimated frequency responses (amplitude) of the two limbs muscles.

### 3. Results

Muscle motion analysis showed peculiar three-dimensional trajectories. Muscle displacement components resulted different on each relative axis; they were also found not to be purely sinusoidal neither in phase to each other. In Figure 4 are shown typical 3D estimated muscle trajectory over time (few vibration cycles are represented).

Figures 5, 6 and 7 show some more details about the motion of the three analysed muscles over the frequency range explored. The image shows the projections of the trajectory over the three planes:  $X/Y$ ,  $Y/Z$  and  $X/Z$ , at different stimulation frequencies;

In general, acceleration components registered on muscle belly were not in phase one to another. They were also different in amplitude and showed a dissimilar behaviour with the frequency. In general the recorded accelerations confirmed a frequency-dependent increase.

From Figure 5 it is easy to identify a different mechanical response for each axis and, in turn for each plane. Displacements on  $x$ -,  $y$ - and  $z$ -axis resulted not always in phase, neither pure sinusoids (the figures were not exact ellipses).

From figures it is also noticeable that in position P1, RF and BF muscles movements were more pronounced on

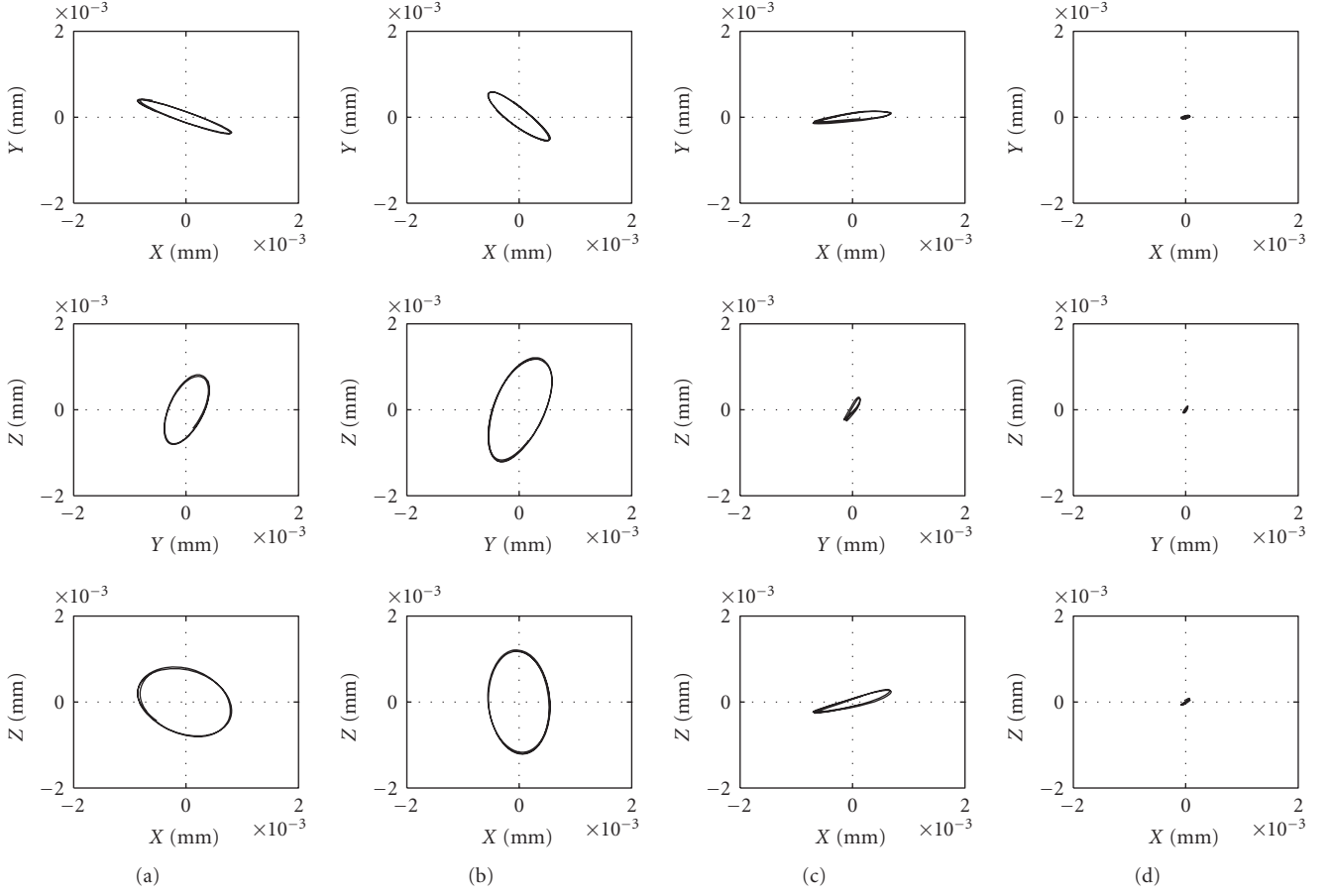


FIGURE 6: An example of the BF muscle belly trajectories over the  $(x, y)$ ,  $(y, z)$  and  $(x, z)$  planes, at different stimulation frequencies ((a) = 16 Hz, (b) = 25 Hz, (c) = 40 Hz, (d) = 50 Hz). The figure corresponds to P1 subject positioning.

$z$ -axis; the same result was found in all the subjects (see Figures 5 and 6).

In Figure 7 it is shown that in position P1 for GL muscle movements seemed to be more pronounced on  $y$  axis.

It is worth mentioning that resonant frequency and dumping factor were subject dependant.

In P1 position RF and BF resultant displacement showed a resonance-like profile over frequency; this was not evident for GL. In P2 position only the GL muscle showed a resonant-like profile while RF and BF displacements resulted highly dumped (mean normalized displacement  $\leq 0.4$  (mm)/(mm)). RF, BF and GL resonance frequencies and dumping factors depended on subject.

In Figure 9 is presented an example of the mechanical behaviour of the three examined muscles, over the frequency range of interest, for one subject and with respect to each posture.

For each posture described, the mechanical response of muscles showing a resonant-like profile was very similar to that of second-order system (Figure 10), as confirmed by the correlation coefficient  $R_1^2$  (Table 1).

In general, the contralateral analysis showed that the mechanical behaviour of muscles was similar.

In P1, mean difference between dominant and non dominant limb resonance frequencies ( $\Delta Fr$ ) was equal to  $0.26 (\pm 1.85)$  Hz for RF and  $0.39 (\pm 2.79)$  Hz for BF (Table 2). In P2,  $\Delta Fr$  for GL was equal to  $0.03 \pm 3.23$  Hz.  $R_2^2$  coefficient resulted very high, suggesting a similar motion of contralateral muscles (Table 2).

With respect to position P1, contralateral analysis revealed that motion of both RF muscles (dominant and non dominant leg) was synchronous and symmetric in the sagittal-plane: both RF muscles phase responses were almost identical along  $z$ - and  $y$ -axes (synchronicity), while they showed a difference of  $\pi$  rad along  $x$ -axis (symmetry with respect to sagittal plane). The same behaviour was found for both of BF muscles.

#### 4. Discussions

Interaction of human body with applied vertical whole body vibrations strongly depends on subject's characteristics: anatomy, positioning, muscle stiffness and other individual tissue mechanical properties; some authors also consider the possibility that vibratory stimulation impairs the "muscular memory" process responsible for predictive force [30].

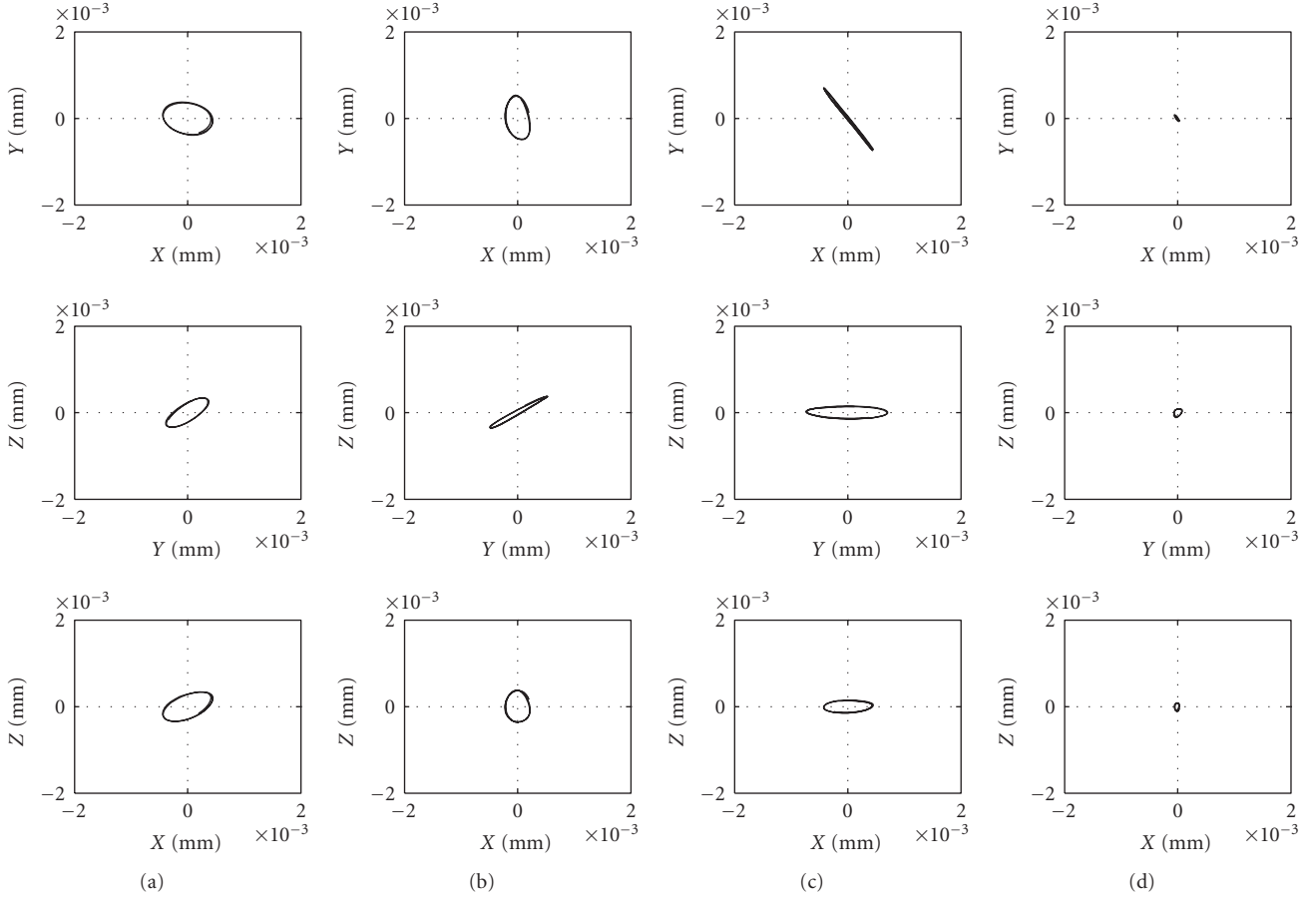


FIGURE 7: An example of the GL muscle belly trajectories over the  $(x, y)$ ,  $(y, z)$  and  $(x, z)$  planes, at different stimulation frequencies ((a) = 16 Hz, (b) = 25 Hz, (c) = 40 Hz, (d) = 50 Hz). The figure corresponds to P2 subject positioning.

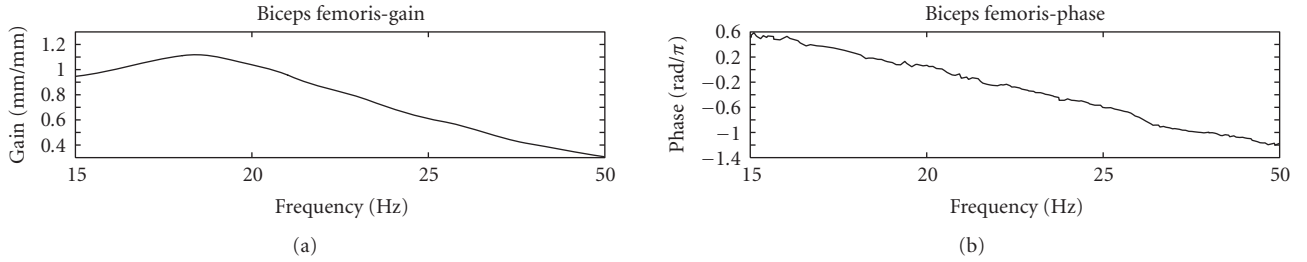


FIGURE 8: An example of BF frequency response—(a) amplitude and (b) phase—over frequency with respect to position P1.

Variations of the mentioned parameters modifies the kinematic chain, through which mechanical vibration propagates into the body, altering muscle local mechanical oscillations.

The effects of WBV on muscle motion (i.e., muscle stimulation) depend on intensity, direction and frequency of vibratory stimulation; however, subject training posture, as highlighted by our results, should be considered as one of the most important factors involved.

This study aimed to characterize different lower limb muscle motion in individuals exposed to vertical whole body mechanical stimulation. In our study we analysed how subject positioning on the platform modifies vibration

dumping and alters the local vibratory oscillation. Two postures were analysed: hack squat position and upright position with heel raised. Muscle motion was successfully measured using tiny and lightweight MEMS accelerometers.

RF, BF and GL muscles motion was here considered: such kinematics can be expressed as a summation of different terms: muscle mean position (depending exclusively on posture), its vibratory displacements and subjects small accommodation movements.

Those three kinematic components can be easily separated in the frequency domain: the stationary position and the slow, small postural adjustments are confined to the very

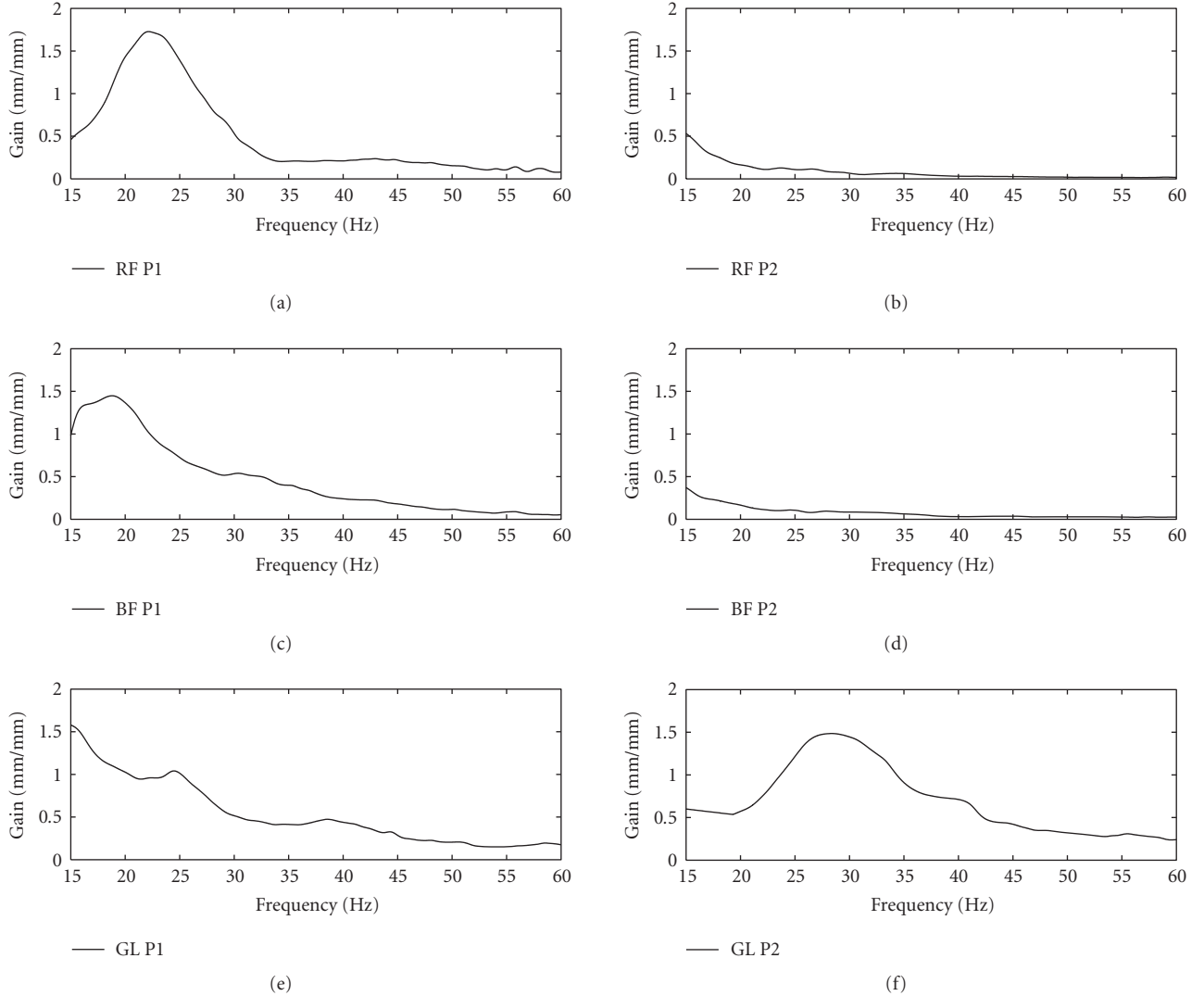


FIGURE 9: An example of estimated normalised resultant muscle displacements over frequency with respect to position P1 ((a) for Rectus Femoris, (c) for Biceps Femoris, (e) for Gastrocnemius Lateralis) and P2 ((b) for Rectus Femoris, (d) for Biceps Femoris, (f) for Gastrocnemius Lateralis).

TABLE 1: Frequency response parameters: mean  $\pm$  SD.

	Fr (Hz)	Mr (mm/mm)	Q	$R^2_1$
RF P1	$20.50 \pm 1.84$	$1.42 \pm 0.37$	$3.49 \pm 1.24$	$0.95 \pm 0.05$
BF P1	$19.90 \pm 2.44$	$1.12 \pm 0.18$	$2.56 \pm 1.06$	$0.95 \pm 0.06$
GL P2	$30.30 \pm 8.27$	$1.04 \pm 0.36$	$2.49 \pm 1.02$	$0.89 \pm 0.11$

low frequencies (0 to 5 Hz) [31], while frequency content of a muscle motion induced by vibration basically consists of the fundamental vibration frequency (i.e., from 15–60 Hz in these trials) and its superior harmonics.

Therefore, in order to consider only vibration related muscle oscillations, standard high pass filtering was combined with double integration providing reliable estimation of the actual muscle displacements.

Three-dimensional muscle motion resulted relatively complex: each of the motion component (along the relative

$x$ -,  $y$ -,  $z$ -axes) resulted not always purely sinusoidal neither in phase to each other.

RF and BF resonance were observed below 25 Hz while individuals maintain position P1; similarly a GL resonant response was found above 30 Hz in position P2.

The analysis of the resultant estimated displacements confirmed that BF and RF muscles achieved the maximum oscillation (i.e., receive the maximal vibration stimulation) in position P1 while GL maximal oscillation was achieved in position P2.

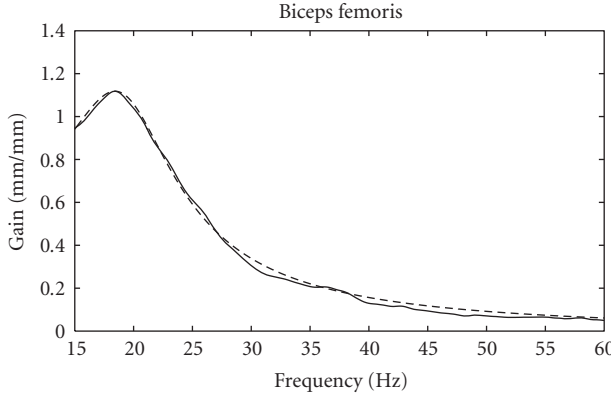


FIGURE 10: An example of second-order system data fitting: continuous line represent the estimated muscle transfer function while the dotted line shows the second-order approximation.

TABLE 2: Contra-lateral analysis: mean  $\pm$  SD.

	$\Delta F_r$ (Hz)	$R^2$
RF P1	$0.26 \pm 1.85$	$0.95 \pm 0.04$
BF P1	$0.39 \pm 2.79$	$0.95 \pm 0.03$
GL P1	X	$0.94 \pm 0.04$
RF P2	X	$0.88 \pm 0.09$
BF P2	X	$0.94 \pm 0.06$

It is worth mentioning that only for this posture/muscle combinations a resonant-like behaviour was clearly visible; however further investigations will be considered to assess the variability of muscle response after multiple vibratory stimulations and different rest periods.

Since experimental data resembled a second-order system like response (suggesting a kinematic equivalent behaviour of a wobbling damped oscillating mass) a simple data fitting was performed. The high correlation coefficient ( $R^2$ , see Table 1) between the empirical frequency response and analytical second-order transfer function then confirmed the validity of the assumption.

Contra-lateral analysis showed nonsignificant differences between dominant and nondominant lower limb; both lower limbs muscles motion resulted to be synchronous and symmetric with respect to the sagittal-plane.

However muscles mechanical resonance characteristics (frequency and dumping factor) depended on subject.

In conclusion, as highlighted in this study, vibratory induced muscle oscillations strongly depend on subject's posture; as suggested, our results confirmed the meaning of a proper positioning in vibratory stimulus transmission.

Since WBV training is included in many fitness and rehabilitation centres exercise programmes, improvements in current knowledge would be helpful in discovering effective exercise protocols.

Assuming the hypothesis of correlation between muscle motion and EMG activity [25], WBV muscle stimulation programmes have to take into account the posture hold by subject on platform, and in turn, the local muscle mechanical

oscillation (i.e., local muscle stimulation). In particular our results suggested that BF and RF muscles may receive the maximal stimulus in position P1 while the for GL muscle stimulation may be preferable position P2.

However, maximizing muscles motion could act in producing more muscle lengthening, and in turn higher muscle activation. In addition, since this study involved untrained male subjects, studies with female subjects should be performed to compare with the results obtained for male subjects.

## Acknowledgment

The authors are grateful to TSEM S.p.A. for providing vibrating platform device.

## References

- [1] J. R. Burke, M. C. Schutten, D. M. Koceja, and G. Kamen, "Age-dependent effects of muscle vibration and the Jendrassik maneuver on the patellar tendon reflex response," *Archives of Physical Medicine and Rehabilitation*, vol. 77, no. 6, pp. 600–604, 1996.
- [2] M. Cardinale and J. Lim, "Electromyography activity of vastus lateralis muscle during whole-body vibrations of different frequencies," *Journal of Strength and Conditioning Research*, vol. 17, no. 3, pp. 621–624, 2003.
- [3] M. Cardinale and J. Wakeling, "Whole body vibration exercise: are vibrations good for you?" *British Journal of Sports Medicine*, vol. 39, no. 9, pp. 585–589, 2005.
- [4] C. Delecluse, M. Roelants, and S. Verschueren, "Strength increase after whole-body vibration compared with resistance training," *Medicine and Science in Sports and Exercise*, vol. 35, no. 6, pp. 1033–1041, 2003.
- [5] J. E. Desmedt and E. Godaux, "Vibration-induced discharge patterns of single motor units in the masseter muscle in man," *Journal of Physiology*, vol. 253, no. 2, pp. 429–442, 1975.
- [6] C. Bosco, R. Colli, E. Introini, et al., "Adaptive responses of human skeletal muscle to vibration exposure," *Clinical Physiology*, vol. 19, no. 2, pp. 183–187, 1999.
- [7] C. Bosco, M. Cardinale, and O. Tsarpela, "Influence of vibration on mechanical power and electromyogram activity in human arm flexor muscles," *European Journal of Applied Physiology and Occupational Physiology*, vol. 79, no. 4, pp. 306–311, 1999.
- [8] I. Bautmans, E. Van Hees, J.-C. Lemper, and T. Mets, "The feasibility of whole body vibration in institutionalised elderly persons and its influence on muscle performance, balance and mobility: a randomised controlled trial," *BMC Geriatrics*, vol. 5, article 17, p. 8, 2005.
- [9] C. Bosco, M. Iacovelli, O. Tsarpela, et al., "Hormonal responses to whole-body vibration in men," *European Journal of Applied Physiology*, vol. 81, no. 6, pp. 449–454, 2000.
- [10] C. Bosco, M. Cardinale, O. Tsarpela, et al., "The influence of whole body vibration on jumping performance," *Biology of Sport*, vol. 15, no. 3, pp. 157–164, 1998.
- [11] J. A. Eisman, "Good, good, good... good vibrations: the best option for better bones?" *The Lancet*, vol. 358, no. 9297, pp. 1924–1925, 2001.
- [12] I. Homma, T. Nagai, T. Sakai, M. Ohashi, M. Beppu, and K. Yonemoto, "Effect of chest wall vibration on ventilation in patients with spinal cord lesion," *Journal of Applied Physiology*, vol. 50, no. 1, pp. 107–111, 1981.

- [13] V. B. Issurin, D. G. Liebermann, and G. Tenenbaum, "Effect of vibratory stimulation training on maximal force and flexibility," *Journal of Sports Sciences*, vol. 12, no. 6, pp. 561–566, 1994.
- [14] K. Kerschan-Schindl, S. Grampp, C. Henk, et al., "Whole-body vibration exercise leads to alterations in muscle blood volume," *Clinical Physiology*, vol. 21, no. 3, pp. 377–382, 2001.
- [15] S. Verschueren, M. Roelants, C. Delecluse, S. Swinnen, D. Vanderschueren, and S. Boonen, "Effect of 6-month whole body vibration training on hip density, muscle strength, and postural control in postmenopausal women: a randomized controlled pilot study," *Journal of Bone and Mineral Research*, vol. 19, no. 3, pp. 352–359, 2004.
- [16] C. D. Marsden, J. C. Meadows, and H. J. Hodgson, "Observations on the reflex response to muscle vibration in man and its voluntary control," *Brain*, vol. 92, no. 4, pp. 829–846, 1969.
- [17] J. Mester, P. Spitznfeil, J. Schwarzer, and F. Seifriz, "Biological reaction to vibration-Implications for sport," *Journal of Science and Medicine in Sport*, vol. 2, no. 3, pp. 211–226, 1999.
- [18] J. Mester, H. Kleinoder, and Z. Yue, "Vibration training: benefits and risks," *Journal of Biomechanics*, vol. 39, no. 6, pp. 1056–1065, 2006.
- [19] J. Rittweger, H. Schiessl, and D. Felsenberg, "Oxygen uptake during whole-body vibration exercise: comparison with squatting as a slow voluntary movement," *European Journal of Applied Physiology*, vol. 86, no. 2, pp. 169–173, 2001.
- [20] C. T. Rubin, R. Recker, D. Cullen, J. Ryaby, J. McCabe, and K. McLeod, "Prevention of postmenopausal bone loss by a low-magnitude, high-frequency mechanical stimuli: a clinical trial assessing compliance, efficacy, and safety," *Journal of Bone and Mineral Research*, vol. 19, no. 3, pp. 343–351, 2004.
- [21] S. Torvinen, P. Kannus, H. Sievänen, et al., "Effect of a vibration exposure on muscular performance and body balance. Randomized cross-over study," *Clinical Physiology and Functional Imaging*, vol. 22, no. 2, pp. 145–152, 2002.
- [22] C. Bosco, "Automatic device for optimized muscular stimulation," US patent no. WO01/56650, January 2001.
- [23] A. Fratini, M. Cesarelli, P. Bifulco, and M. Romano, "Relevance of motion artifact in electromyography recordings during vibration treatment," *Journal of Electromyography and Kinesiology*, vol. 19, no. 4, pp. 710–718, 2009.
- [24] H. De Talhouet and J. G. Webster, "The origin of skin-stretch-caused motion artifacts under electrodes," *Physiological Measurement*, vol. 17, no. 2, pp. 81–93, 1996.
- [25] A. Fratini, P. Bifulco, M. Cesarelli, G. Pasquariello, M. Romano, and A. La Gatta, "Correspondence between muscle motion and EMG activity during whole body vibration," in *Proceedings of the 4th European Conference of the International Federation for Medical and Biological Engineering (IFMBE '08)*, vol. 22, pp. 2069–2072, Antwerp, Belgium, 2008.
- [26] J. M. Wakeling and A.-M. Liphardt, "Task-specific recruitment of motor units for vibration damping," *Journal of Biomechanics*, vol. 39, no. 7, pp. 1342–1346, 2006.
- [27] J. M. Wakeling, B. M. Nigg, and A. I. Rozitis, "Muscle activity damps the soft tissue resonance that occurs in response to pulsed and continuous vibrations," *Journal of Applied Physiology*, vol. 93, no. 3, pp. 1093–1103, 2002.
- [28] J. E. Desmedt and E. Godaux, "Mechanism of the vibration paradox: excitatory and inhibitory effects of tendon vibration on single soleus muscle motor units in man," *Journal of Physiology*, vol. 285, pp. 197–207, 1978.
- [29] B. Harazin and J. Grzesik, "The transmission of vertical whole-body vibration to the body segments of standing subjects," *Journal of Sound and Vibration*, vol. 215, no. 4, pp. 775–787, 1998.
- [30] D. A. Nowak, K. Rosenkranz, J. Hermsdörfer, and J. Rothwell, "Memory for fingertip forces: passive hand muscle vibration interferes with predictive grip force scaling," *Experimental Brain Research*, vol. 156, no. 4, pp. 444–450, 2004.
- [31] T. E. Prieto, J. B. Myklebust, R. G. Hoffmann, E. G. Lovett, and B. M. Myklebust, "Measures of postural steadiness: differences between healthy young and elderly adults," *IEEE Transactions on Biomedical Engineering*, vol. 43, no. 9, pp. 956–966, 1996.

## Research Article

# Nonlinear Synchronization for Automatic Learning of 3D Pose Variability in Human Motion Sequences

M. Mozerov, I. Rius, X. Roca, and J. González

Computer Vision Center and Departament d'Informàtica, Universitat Autònoma de Barcelona,  
Campus UAB, Edifici O, 08193 Cerdanyola, Spain

Correspondence should be addressed to M. Mozerov, mozerov@cvc.uab.es

Received 1 May 2009; Revised 31 July 2009; Accepted 2 September 2009

Academic Editor: João Manuel R. S. Tavares

Copyright © 2010 M. Mozerov et al. This is an open access article distributed under the Creative Commons Attribution License, which permits unrestricted use, distribution, and reproduction in any medium, provided the original work is properly cited.

A dense matching algorithm that solves the problem of synchronizing prerecorded human motion sequences, which show different speeds and accelerations, is proposed. The approach is based on minimization of MRF energy and solves the problem by using Dynamic Programming. Additionally, an optimal sequence is automatically selected from the input dataset to be a time-scale pattern for all other sequences. The paper utilizes an action specific model which automatically learns the variability of 3D human postures observed in a set of training sequences. The model is trained using the public CMU motion capture dataset for the walking action, and a mean walking performance is automatically learnt. Additionally, statistics about the observed variability of the postures and motion direction are also computed at each time step. The synchronized motion sequences are used to learn a model of human motion for action recognition and full-body tracking purposes.

## 1. Introduction

Analysis of human motion in activities remains one of the most challenging open problems in computer vision [1–3].

The nature of the open problems and techniques used in human motion analysis approaches strongly depends on the goal of the final application. Hence, most approaches oriented to surveillance demand performing activity recognition tasks in real-time dealing with illumination changes and low-resolution images. Thus, they require robust techniques with a low computational cost, and mostly, they tend to use simple models and fast algorithms to achieve effective segmentation and recognition tasks in real-time.

In contrast, approaches focused on 3D tracking and reconstruction require to deal with a more detailed representation about the current posture that the human body exhibits [4–6]. The aim of full body tracking is to recover the body motion parameters from image sequences dealing with 2D projection ambiguities, occlusion of body parts, and loose fitting clothes among others.

Many action recognition and 3D body tracking works rely on proper models of human motion, which constrain the search space using a training dataset of prerecorded motions

[7–10]. Consequently, it is highly desirable to extract useful information from the training set of motion. Traditional treatment suffers from problems inadequate modeling of nonlinear dynamics: training sequences may be acquired under very different conditions, showing different durations, velocities, and accelerations during the performance of an action. As a result, it is difficult to collect useful statistics from the raw training data, and a method for synchronizing the whole training set is required. Similarly to our work, in [11] a variation of DP is used to match motion sequences acquired from a motion capture system. However, the overall approach is aimed to the optimization of a posterior key-frame search algorithm. Then, the output from this process is used for synthesizing realistic human motion by blending the training set.

The DP approach has been widely used in literature for stereo matching and image processing applications [12–14]. Such applications often demand fast calculations in real-time, robustness against image discontinuities, and unambiguous matching.

The DP technique is a core of the dynamic time warping (DTW) method. Dynamic time warping is often used in speech recognition to determine if two waveforms

represent the same spoken phrase [15]. In addition to speech recognition, dynamic time warping has also been found useful in many other disciplines, including data mining, gesture recognition, robotics, manufacturing, and medicine [16].

Initially DTW method was developed for the one-dimensional signal processing (in speech recognition, e.g.). So, for this kind of the signal the Euclidean distance minimization with a weak constraint (the derivative of the synchronization path is constrained) works very well. In our case the dimensionality of the signal is up to 37D and weak constraint does not yield satisfactory robustness due to the noise and the signal complexity. We propose to minimize a composite distance that consists of two terms: a distance itself and a smoothness term. Such kind of a distance has the same meaning of the energy in MRF optimization techniques.

The MRF energy minimization approach shows the perfect performance in stereo matching and segmentation. Likewise, we present a dense matching algorithm based on DP, which is used to synchronize human motion sequences of the same action class in the presence of different speeds and accelerations. The algorithm finds an optimal solution in real-time.

We introduce a median sequences or the best pattern for time synchronization, which is another contribution of this work. The median sequence is automatically selected from the training data following a minimum global distance criterion among other candidates of the same class.

We present an action-specific model of human motion suitable for many applications, that has been successfully used for full body tracking [4, 5, 17]. In this paper, we explore and extend its capabilities for gait analysis and recognition tasks. Our action-specific model is trained with 3D motion capture data for the walking action from the CMU Graphics Lab Motion capture database. In our work, human postures are represented by means of a full body 3D model composed of 12 limbs. Limbs' orientations are represented within the kinematic tree using their direction cosines [18]. As a result, we avoid singularities and abrupt changes due to the representation. Moreover, near configurations of the body limbs account for near positions in our representation at the expense of extra parameters to be included in the model. Then, PCA is applied to the training data to perform dimensionality reduction over the highly correlated input data. As a result, we obtain a lower-dimensional representation of human postures which is more suitable to describe human motion, since we found that each dimension on the PCA space describes a natural mode of variation of human motion. Additionally, the main modes of variation of human gait are naturally represented by means of the principal components found. This leads to a coarse-to-fine representation of human motion which relates the precision of the model with its complexity in a natural way and makes it suitable for different kinds of applications which demand more or less complexity in the model.

The synchronized version of the training set is utilized to learn an action-specific model of human motion. The observed variances from the synchronized postures of the training set are computed to determine which human

postures can be feasible during the performance of a particular action. This knowledge is subsequently used in a particle filter tracking framework to prune those predictions which are not likely to be found in that action.

This paper is organized as follows. Section 2 explains the principles of human action modeling. In Section 3 we introduce a new dense matching algorithm for human motion sequences synchronization. Section 4 shows some examples of data base syncronisation. Section 5 describes the action specific model and explains the procedure for learning its parameters from the synchronized training set. Section 6 summarizes our conclusions.

## 2. Human Action Model

The body model employed in our work is composed of twelve rigid body parts (hip, torso, shoulder, neck, two thighs, two legs, two arms, and two forearms) and fifteen joints; see Figure 1(a). These joints are structured in a hierarchical manner, constituting a kinematic tree, where the root is located at the hip. However, postures in the CMU database are represented using the XYZ position of each marker that was placed to the subject in an absolute world coordinates system. Therefore, we must select some principal markers in order to make the input motion capture data usable according to our human body representation. Figure 1(b) relates the absolute position of each joint from our human body model with the markers' used in the CMU database. For instance, in order to compute the position of joint 5 (head) in our representation, we should compute the mean position between the RFHD and LFHD markers from the CMU database, which correspond to the markers placed on each side of the head. Notice that our model considers the left and the right parts of the hip and the torso as a unique limb, and therefore we require a unique segment per each. Hence, we compute the position of joints 1 and 4 (hip and neck joints) as the mean between the previously computed joints 2 and 3, and 6 and 9, respectively.

We use directional cosines to represent relative orientations of the limbs within the kinematic tree [18]. As a result, we represent a human body posture  $\Psi$  using 37 parameters, that is,

$$\Psi = \{u, \theta_1^x, \theta_1^y, \theta_1^z, \dots, \theta_{12}^x, \theta_{12}^y, \theta_{12}^z\}, \quad (1)$$

where  $u$  is the normalized height of the pelvis, and  $\theta_l^x, \theta_l^y, \theta_l^z$  are the relative directional cosines for limb  $l$ , that is, the cosine of the angle between a limb  $l$  and each axis  $x$ ,  $y$ , and  $z$ , respectively. Directional cosines constitute a good representation method for body modeling, since it does not lead to discontinuities, in contrast to other methods such as Euler angles or spherical coordinates. Additionally, unlike quaternion, they have a direct geometric interpretation. However, given that we are using 3 parameters to determine only 2 DOFs for each limb, such representation generates a considerable redundancy of the vector space components. Therefore, we aim to find a more compact representation of the original data to avoid redundancy.

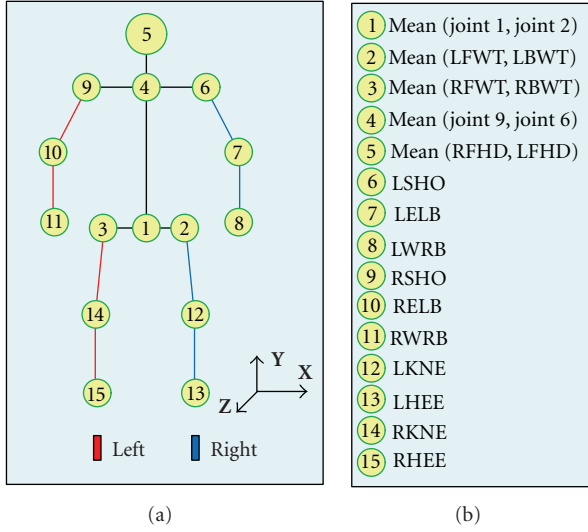


FIGURE 1: (a) Details of the human body model used; (b) the relationship to the marker set employed in the CMU database.

Let us introduce a particular performance of an action. A performance  $\Psi_i$  consists of a time-ordered sequence of postures

$$\Psi_i = \{\psi_i^1, \dots, \psi_i^{F_i}\}, \quad (2)$$

where  $i$  is an index indicating the number of performance, and  $F_i$  is the total number of postures that constitute the performance  $\Psi_i$ . We assume that each two consecutive postures are separated by a time interval  $\delta f$ , which depends on the frame rate of the prerecorded input sequences; thus the duration of a particular performance is  $T_i = \delta f F_i$ . Finally, an action  $A_k$  is defined by all the  $I_k$  performances that belong to that action  $A_k = \{\Psi_1, \dots, \Psi_{I_k}\}$ .

As we mentioned above, the original vector space is redundant. Additionally, the human body motion is intrinsically constrained, and these natural constraints lead to highly correlated data in the original space. Therefore, we aim to find a more compact representation of the original data to avoid redundancy. To do this, we consider a set of performances corresponding to a particular action  $A_k$  and perform the Principal Component Analysis (PCA) to all the postures that belong to that action. Eventually, the following eigenvector decomposition equation has to be solved:

$$\lambda_j \mathbf{e}_j = \Sigma_k \mathbf{e}_j, \quad (3)$$

where  $\Sigma_k$  stands for the  $37 \times 37$  covariance matrix calculated with all the postures of action  $A_k$ . As a result, each eigenvector  $\mathbf{e}_j$  corresponds to a mode of variation of human motion, and its corresponding eigenvalue  $\lambda_j$  is related to the variance specified by the eigenvector. In our case, each eigenvector reflects a natural mode of variation of human gait. To perform dimensionality reduction over the original data, we consider only the first  $b$  eigenvectors that span the new representation space for this action, hereafter *aSpace* [16]. We assume that the overall variance of a new

space approximately equals to the overall variance of the unreduced space:

$$\lambda_S = \sum_{j=1}^b \lambda_j \approx \sum_{j=1}^b \lambda_j + \varepsilon_b = \sum_{j=1}^{37} \lambda_j, \quad (4)$$

where  $\varepsilon_b$  is the *aSpace* approximation error.

Consequently, we use (4) to find the smallest number  $b$  of eigenvalues, which provide an appropriate approximation of the original data, and human postures are projected into the *aSpace* by

$$\tilde{\Psi} = [\mathbf{e}_1, \dots, \mathbf{e}_b]^T (\Psi - \bar{\Psi}), \quad (5)$$

where  $\Psi$  refers to the original posture,  $\tilde{\Psi}$  denotes the lower-dimensional version of the posture represented using the *aSpace*,  $[\mathbf{e}_1, \dots, \mathbf{e}_b]$  is the *aSpace* transformation matrix that correspond to the first  $b$  selected eigenvectors, and  $\bar{\Psi}$  is the posture mean value that is formed by averaging all postures, which are assumed to be transformed into the *aSpace*. As a result, we obtain a lower-dimensional representation of human postures which is more suitable to describe human motion, since we found that each dimension on the PCA space describes a natural mode of variation of human motion [16]. Choosing different values for  $b$  lead to models of more or less complexity in terms of their dimensionality. Hence, while the *gross-motion* (mainly, the motion of the torso, legs, and arms in low resolution) is explained by the very first eigenvectors, subtle motions in the PCA space representation require more eigenvectors to be considered. In other words, the initial 37-dimensional parametric space becomes the restricted  $b$ -dimensional parametric space.

The projection of the training sequences into the *aSpace* constitutes the input for our sequence synchronization algorithm. Hereafter, we consider a multidimensional signal  $\mathbf{x}_i(t)$  as an interpolated expansion of each training sequence  $\tilde{\Psi}_i = \{\tilde{\Psi}_i^1, \dots, \tilde{\Psi}_i^{F_i}\}$  such as

$$\tilde{\Psi}_i^f = \mathbf{x}_i(t) \quad \text{if } t = (f-1)\delta f; f = 1, \dots, F_i, \quad (6)$$

where the time domain of each action performance  $\mathbf{x}_i(t)$  is  $[0, T_i]$ .

### 3. Synchronization Algorithm

As stated before, the training sequences are acquired under very different conditions, showing different durations, velocities, and accelerations during the performance of a particular action. As a result, it is difficult to perform useful statistical analysis to the raw training set, since we cannot put in correspondence postures from different cycles of the same action. Therefore, a method for synchronizing the whole training set is required so that we can establish a mapping between postures from different cycles.

Let us assume that any two considered signals correspond to the identical action, but one runs faster than another (e.g., Figure 2(a)). Under the assumption that the rates ratio of

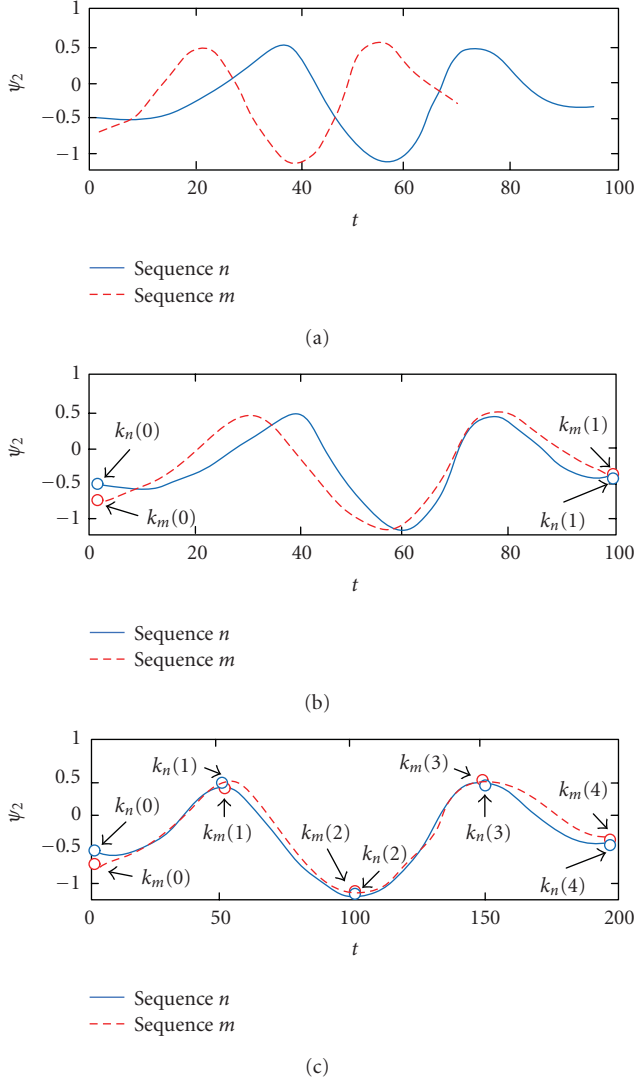


FIGURE 2: (a) Non synchronized one-dimensional sequences. (b) Linearly synchronized sequences. (c) Synchronized sequences using a set of key-frames.

the compared actions is a constant, the two signals might be easily linearly synchronized in the following way:

$$\mathbf{x}_n(t) \approx \mathbf{x}_{n,m}(t) = \mathbf{x}_m(\alpha t); \quad \alpha = \frac{T_m}{T_n}, \quad (7)$$

where  $\mathbf{x}_n$  and  $\mathbf{x}_m$  are the two compared multidimensional signals,  $T_n$  and  $T_m$  are the periods of the action performances  $n$  and  $m$ , and  $\tilde{\mathbf{x}}_{m,n}$  is linearly normalized version of  $\mathbf{x}_m$ ; hence  $T_n = T_{m,n}$ .

Unfortunately, in our research we rarely, if ever, have a constant rate ratio  $\alpha$ . An example, which is illustrated in Figure 2(b), shows that a simple normalization using (7) does not give us the needed signal fitting, and a nonlinear data synchronization method is needed. Further in the text we will assume that the linear synchronization is done and all the periods  $T_n$  possess the same value  $T$ .

The nonlinear data synchronization should be done by

$$\mathbf{x}_n(t) \approx \mathbf{x}_{n,m}(t) = \mathbf{x}_m(\tau); \quad \tau(t) = \int_0^t \alpha(t) dt, \quad (8)$$

where  $\mathbf{x}_{n,m}(t)$  is the best synchronized version of the action  $\mathbf{x}_m(t)$  to the action  $\mathbf{x}_n(t)$ . In literature the function  $\tau(t)$  is usually referred to as the distance-time function. It is not an apt turn of phrase indeed, and we suggest naming it as the rate-to-rate synchronization function instead.

The rate-to-rate synchronization function  $\tau(t)$  satisfies several useful constraints, that are

$$\tau(0) = 0; \quad \tau(T) = T; \quad \tau(t_k) \geq \tau(t_l) \quad \text{if } t_k > t_l. \quad (9)$$

One common approach for building the function  $\tau(t)$  is based on a key-frame model. This model assumes that the compared signals  $\mathbf{x}_n$  and  $\mathbf{x}_m$  have similar sets of singular points, that are  $\{t_n(0), \dots, t_n(p), \dots, t_n(P-1)\}$  and  $\{t_m(0), \dots, t_m(p), \dots, t_m(P-1)\}$  with the matching condition  $t_n(p) = t_m(p)$ . The aim is to detect and match these singular points; thus the signals  $\mathbf{x}_n$  and  $\mathbf{x}_m$  are synchronized. However, the singularity detection is an intricate problem itself, and to avoid the singularity detection stage we propose a dense matching. In this case a time interval  $t_n(p+1) - t_n(p)$  is constant, and in general  $t_n(p) \neq t_m(p)$ .

The function  $\tau(t)$  can be represented as  $\tau(t) = t(1 + \Delta_{n,m}(t))$ . In this case, the sought function  $\Delta_{n,m}(t)$  might synchronize two signals  $\mathbf{x}_n$  and  $\mathbf{x}_m$  by

$$\mathbf{x}_n(t) \approx \mathbf{x}_m(t + \Delta_{n,m}(t)t). \quad (10)$$

Let us introduce a formal measure of synchronization of two signals by

$$D_{n,m} = \int_0^T \|\mathbf{x}_n(t) - \mathbf{x}_m(t + \Delta_{n,m}(t)t)\| dt + \mu \int_0^T \left\| \frac{d\Delta_{n,m}(t)}{dt} \right\| dt, \quad (11)$$

where  $\|\bullet\|$  denotes one of possible vector distances, and  $D_{n,m}$  is referred to as the synchronization distance that consists of two parts, where the first integral represents the functional distance between the two signals, and the second integral is a regularization term, which expresses desirable smoothness constraints of the solution. The proposed distance function is simple and makes intuitive sense. It is natural to assume that the compared signals are synchronized better when the synchronization distance between them is minimal. Thus, the sought function  $\Delta_{n,m}(t)$  should minimize the synchronization distance between matched signals.

In the case of a discrete time representation, (11) can be rewritten as

$$D_{n,m} = \sum_{i=0}^{P-1} |\mathbf{x}_n(i\delta t) - \mathbf{x}_m((i + \Delta_{n,m}(i))\delta t)|^2 + \mu \sum_{i=0}^{P-1} |\Delta_{n,m}(i+1) - \Delta_{n,m}(i)|, \quad (12)$$

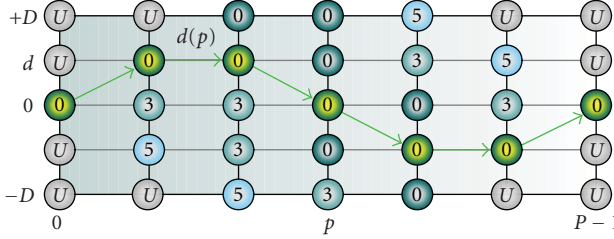


FIGURE 3: The optimal path through the DSI trellis.

where  $\delta t$  is a time sampling interval. Equation (9) implies

$$|\Delta_{n,m}(p+1) - \Delta_{n,m}(p)| \leq 1, \quad (13)$$

where index  $p = \{0, \dots, P-1\}$  satisfies  $\delta t P = T$ .

The synchronization problem is similar to the matching problem of two epipolar lines in a stereo image. In the case of the stereo image processing the parameter  $\Delta(t)$  is called disparity. For stereo matching a DSI representation is used. The DSI approach assumes that 2D DSI matrix has dimensions time  $0 \leq p < P$ , and disparity  $-D \leq d \leq D$ . Let  $E(d, p)$  denote the DSI cost value assigned to matrix element  $(d, p)$  and calculated by

$$E_{n,m}(p, d) = |\mathbf{x}_n(p\delta t) - \mathbf{x}_m(p\delta t + d\delta t)|^2. \quad (14)$$

Now we formulate an optimization problem as follows: find the time-disparity function  $\Delta_{n,m}(p)$ , which minimizes the synchronization distance between the compared signals  $\mathbf{x}_n$  and  $\mathbf{x}_m$ , that is,

$$\Delta_{n,m}(p) = \arg \min_d \sum_{i=0}^{<P} E_{n,m}(i, d(i)) + \mu \sum_{i=0}^{<P-1} |d(i+1) - d(i)|. \quad (15)$$

The discrete function  $\Delta(p)$  coincides with the optimal path through the DSI trellis as it is shown in Figure 3. Here term “optimal” means that the sum of the cost values along this path plus the weighted length of the path is minimal among all other possible paths.

The optimal path problem can be easily solved by using the method of dynamic programming. The method consists of step-by-step control and optimization that is given by a recurrence relation:

$$S(p, d) = E(p, d) + \min_{k \in 0, \pm 1} \{S(p-1, d+k) + \mu|d+k|\}, \\ S(0, d) = E(0, d), \quad (16)$$

where the scope of the minimization parameter  $k \in \{0, \pm 1\}$  is chosen in accordance with (13). By using the recurrence relation the minimal value of the objective function in (15) can be found at the last step of optimization. Next, the algorithm works in reverse order and recovers a sequence of optimal steps (using the lookup table  $K(p, d)$ ) of the stored

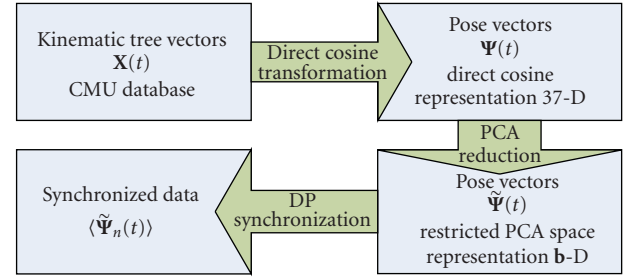


FIGURE 4: Flowchart of the synchronization method that is based on DP and PCA approaches.

values of the index  $k$  in the recurrence relation (16)) and eventually the optimal path by

$$\begin{aligned} d(p-1) &= d(p) + K(p, d(p)), \\ d(P-1) &= 0, \\ \Delta(p) &= d(p). \end{aligned} \quad (17)$$

Now the synchronized version of  $\mathbf{x}_m(t)$  might be easily calculated by

$$\mathbf{x}_{n,m}(p\delta t) = \mathbf{x}_m(p\delta t + \Delta_{n,m}(p)\delta t). \quad (18)$$

Here we assume that  $n$  is the number of the base rate sequences and  $m$  is the number of sequences to be synchronized.

The dense matching algorithm that synchronizes two arbitrary  $\mathbf{x}_n(t)$  and  $\mathbf{x}_m(t)$  prerecorded human motion sequences  $\mathbf{x}_n(t)$  and  $\mathbf{x}_m(t)$  is now summarized as follows.

- Prepare a 2D DSI matrix, and set initial cost values  $E_0$  using (14).
- Find the optimal path through the DSI using recurrence equations (16)-(17).
- Synchronize  $\mathbf{x}_m(t)$  to the rate of  $\mathbf{x}_n(t)$  using (18).

Our algorithm assumes that a particular sequence is chosen to be a time scale pattern for all other sequences. It is obvious that an arbitrary choice among the training set is not a reasonable solution, and now we aim to find a statistically proven rule that is able to make an optimal choice according to some appropriate criterion. Note that each synchronized pair of sequences  $(n, m)$  has its own synchronization distance calculated by (12). Then the full synchronization of all the sequences relative to the pattern sequences  $n$  has its own global distance:

$$C_n = \sum_{m \in A_k} C_{n,m}. \quad (19)$$

We propose to choose the synchronizing pattern sequence with minimal global distance. In statistical sense such signal can be considered as a median value over all the performances that belong to the set of  $A_k$  or can be referred to as “median” sequence.

The flowchart of the synchronization method that is based on DP and PCA approaches is illustrated in Figure 4.

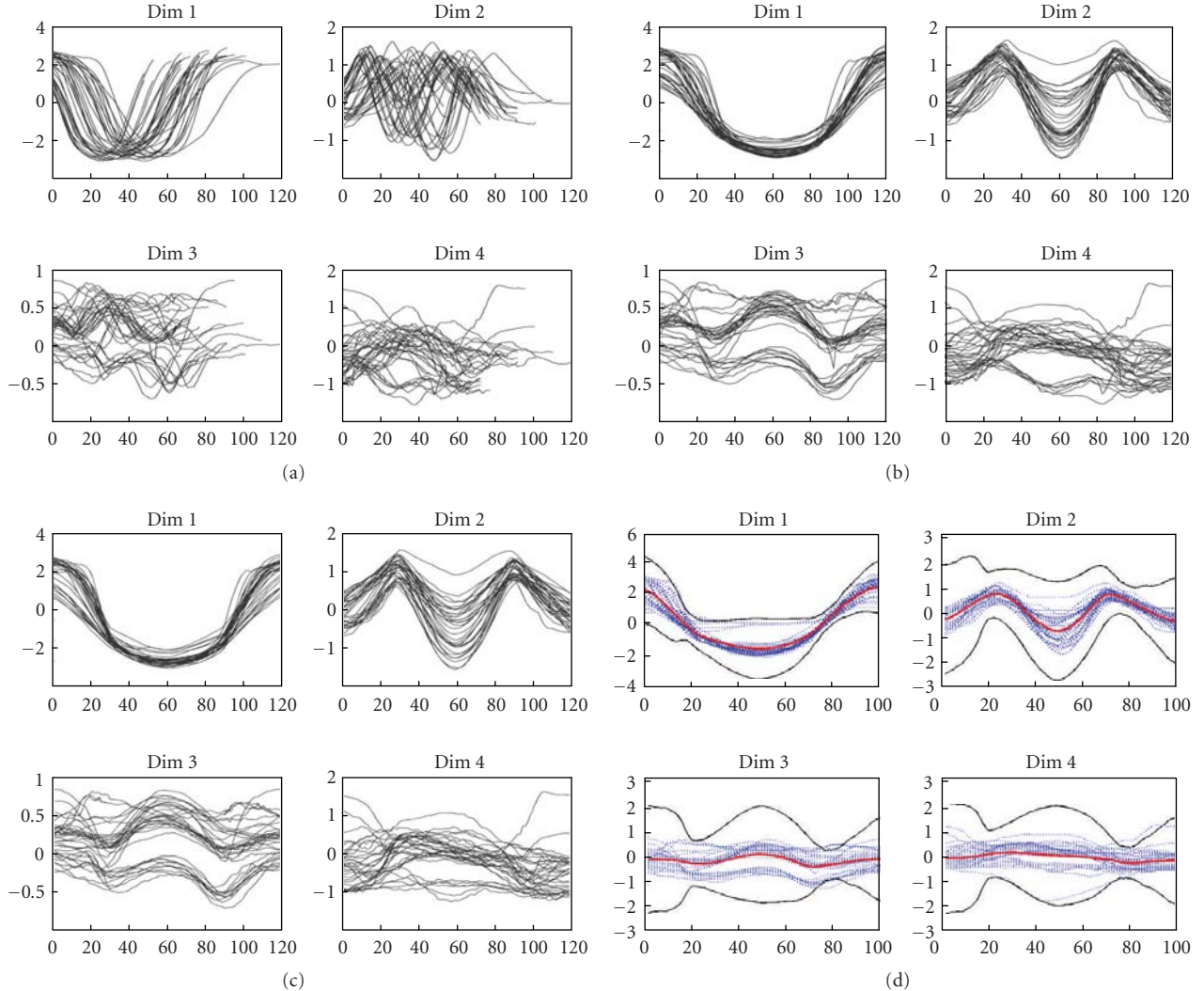


FIGURE 5: (a) Nonsynchronized training set. (b) Automatically synchronized training set with the proposed approach. (c) Manually synchronized training set with key-frames. (d) Learnt motion model for the bending action.

#### 4. Results of Synchronization

The synchronization method has been tested with many different training sets. In this section we demonstrate our result using 40 performances of a bending action. To build the *aSpace* representation, we choose the first 16 eigenvectors that captured 95% of the original data. The first 4 dimensions within the *aSpace* of the training sequences are illustrated in Figure 5(a). All the performances have different durations with 100 frames on average. The observed initial data shows different durations, speeds, and accelerations between the sequences. Such a mistiming makes very difficult to learn any common pattern from the data. The proposed synchronization algorithm was coded in C++ and run with a 3 GHz Pentium D processor. The time needed for synchronizing two arbitrary sequences taken from our database is  $1.5 \times 10^{-2}$  seconds and 0.6 seconds to synchronize the whole training set, which is illustrated in Figure 5(b).

To prove the correctness of our approach, we manually synchronized the same training set by selecting a set of 5 key-frames in each sequence by hand following a maximum curvature subjective criterion. Then, the training set was resampled; so each sequence had the same number of frames between each key-frame. In Figure 5(c), the first 4 dimensions within the *aSpace* of the resulting manually synchronized sequences are shown. We might observe that the results are very similar to the ones obtained with the proposed automatic synchronization method. The synchronized training set from Figure 5(b) has been used to learn an action-specific model of human motion for the bending action. The model learns a mean-performance for the synchronized training set and its observed variance at each posture. In Figure 5(d) the learnt action model for the bending action is plotted. The mean-performance corresponds to the solid red line while the black solid line depicts  $\pm 3$  times the learnt standard deviation at each

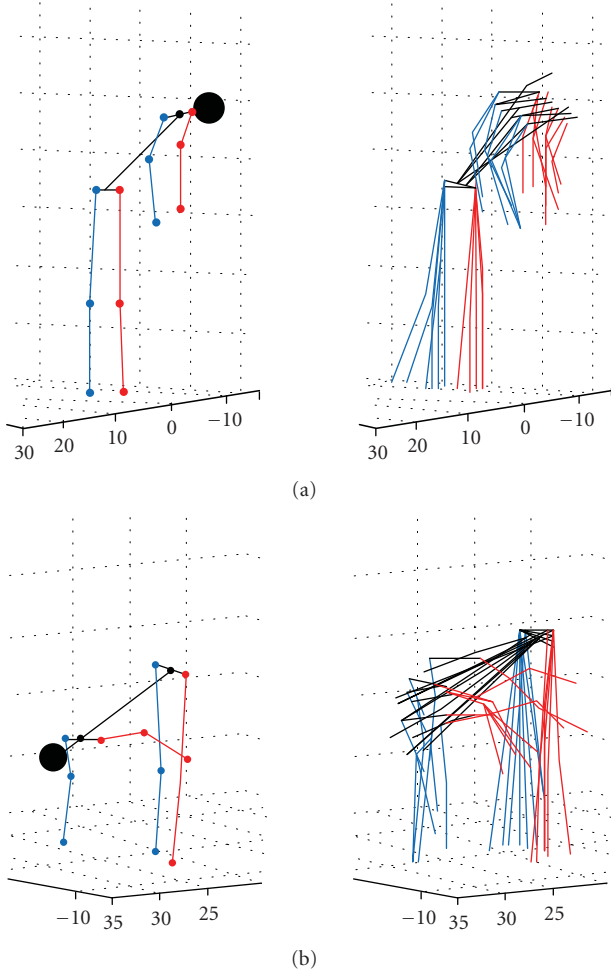


FIGURE 6: (a) and (b) Mean learnt postures from the action corresponding to frames 10 and 40 (left). Sampled postures using the learnt corresponding variances (right).

synchronized posture. The input training sequence set is depicted as dashed blue lines.

This motion model can be used in a particle filter framework as a priori knowledge on human motion. The learnt model would predict for the next time step only those postures which are feasible during the performance of a particular action. In other words, only those human postures which lie within the learnt variance boundaries from the mean performance are accepted by the motion model. In Figure 6 we show two postures corresponding to frames 10 and 40 from the learnt mean performance and a random set of accepted postures by the action model. We might observe that for each selected mean posture, only similar and meaningful postures are generated.

Additionally, to prove the advantage of our approach with respect to DTW we applied our algorithm with the cut objective function (without smoothness term), which is coincide with the DTW algorithm. In this case the synchronization process was not satisfactory: some selected mean postures were completely outliers or nonsimilar to any meaningful posture. It means that the smoothness factor  $\mu$

in (12) and (16) plays an important role. To find an optimal value of this parameter a visual criterion has been used (the manual synchronization that had been done before yields such a visual estimation technique). However, as a rule of thumb the parameter can be set equal to the mean value of the error term  $E(i,d)$ :

$$\mu = |\Lambda|^{-1} \sum_{i,d \in \Lambda} E(i,d), \quad (20)$$

where  $\Lambda$  is a domain of  $i$  and  $d$  indexes and  $|\Lambda|$  is the cardinality (or the number of elements) of the domain.

## 5. Learning the Motion Model

Once all the sequences share the same time pattern, we learn an action specific model which is accurate without loosing generality and suitable for many applications. In this section we consider the walking action and its model is useful for gait analysis, gait recognition, and tracking. Thus, we want to learn where the postures lie in the space used for representation, how they change over time as the action goes by, and what characteristics the different performances have in common which can be exploited for enabling the aforementioned tasks. In other words, we aim to characterize the shape of the synchronized version of the training set for the walking action in the PCA-like space. The process is as follows.

First, we extract from the training set  $\hat{A}_k = \{\hat{\psi}_1, \dots, \hat{\psi}_{I_k}\}$  a mean representation of the action by computing the mean performance  $\bar{\Psi}^{A_k} = \{\bar{\psi}^1, \dots, \bar{\psi}^F\}$  where each mean posture  $\bar{\psi}^t$  is defined as

$$\bar{\psi}^t = \sum_{i=1}^{I_k} \frac{\hat{\psi}_i^t}{I_k}, \quad t = 1, \dots, F. \quad (21)$$

$I_k$  is the number of training performances for the action  $\hat{A}_k$ ,  $\hat{\psi}_i^t$  corresponds to the  $t$ th posture from the  $i$ th training performance, and finally,  $F$  denotes the total number of postures of each synchronized performance.

Then, we want to quantify how much the training performances  $\hat{\psi}_i$  vary from the computed mean performance  $\bar{\Psi}^{A_k}$  of (21). Therefore, for each time step  $t$ , we compute the standard deviation  $\sigma^t$  of all the postures  $\bar{\psi}^t$  that share the same time stamp  $t$ , that is,

$$\sigma^t = \sqrt{\frac{1}{I_k} \sum_{i=1}^{I_k} (\hat{\psi}_i^t - \bar{\psi}^t)^2}. \quad (22)$$

Figure 7 shows the learned mean performance  $\bar{\Psi}^{A_k}$  (red solid line) and  $\pm 3$  times the computed standard deviation  $\sigma^t$  (dashed black line) for the walking action. We used  $b = 6$  dimensions for building the PCA space representation explaining the 93% of total variation of training data.

On the other hand, we are also interested in characterizing the temporal evolution of the action. Therefore, we compute the main direction of the motion  $\bar{v}_t$  for each

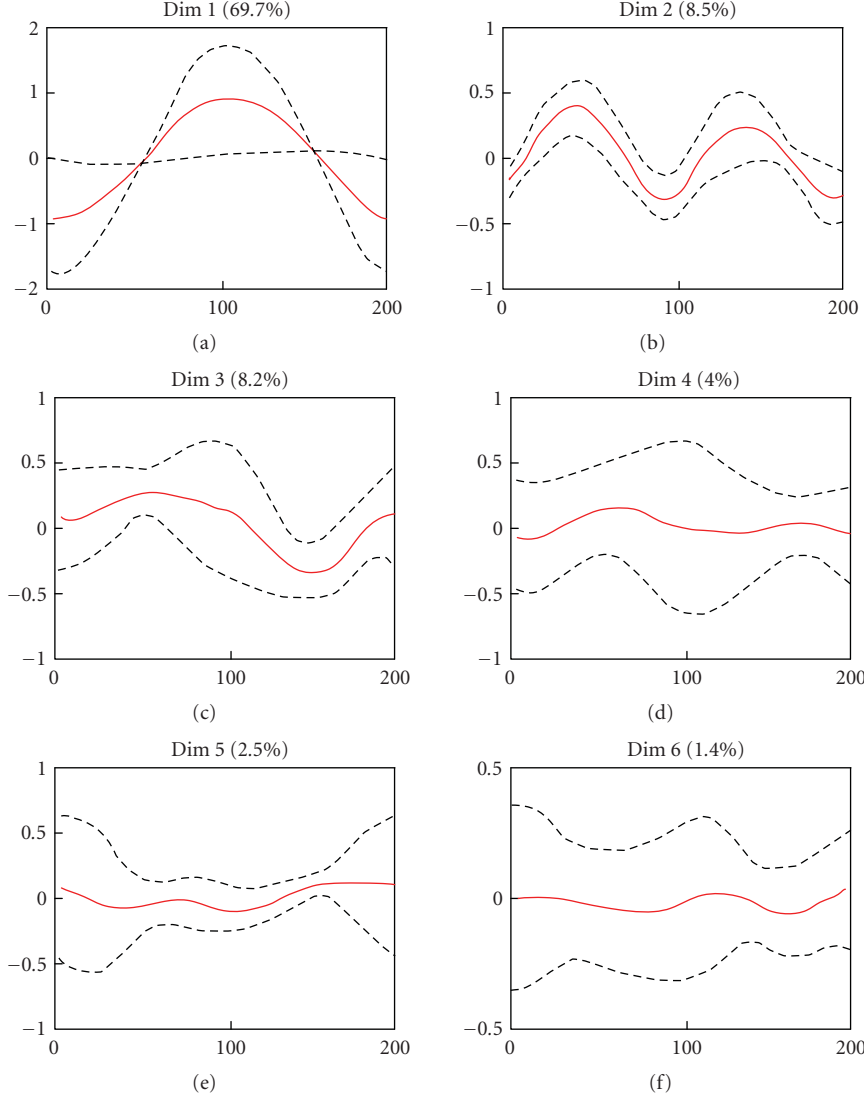


FIGURE 7: Learned mean performance  $\bar{\Psi}^{A_k}$  and standard deviation  $\sigma_t^t$  for the walking action.

subsequence of  $d$  postures from the mean performance  $\bar{\Psi}^{A_k}$ , that is,

$$\mathbf{v}_t = \frac{1}{d} \sum_{j=t}^{t-d+1} \frac{\bar{\Psi}^j - \bar{\Psi}^{j-1}}{\|\bar{\Psi}^j - \bar{\Psi}^{j-1}\|}; \quad \bar{\mathbf{v}}_t = \frac{\mathbf{v}_t}{\|\mathbf{v}_t\|}, \quad (23)$$

where  $\bar{\mathbf{v}}_t$  is a unitary vector representing the observed direction of motion averaged from the last  $d$  postures at a particular time step  $t$ . In Figure 8 the first 3 dimensions of the mean performance are plotted together with the direction vectors computed in (23).

Each black arrow corresponds to the unitary vector  $\bar{\mathbf{v}}_t$  computed at time  $t$ , scaled for visualization purposes. Hence, each vector encodes the mean observed motion's direction from time  $t - d$  to time  $t$ , where  $d$  stands for the length of the motion window considered. Additionally, selected postures from the mean performance have been sampled at times  $t = 1, 30, 55, 72, 100, 150$ , and  $168$  and overlaid in the graphic.

As a result, the action model  $\Gamma^{A_k}$  is defined by

$$\Gamma^{A_k} = \{\Omega^{A_k}, \bar{\Psi}^{A_k}, \sigma_t, \bar{\mathbf{v}}_t\}, \quad t = 1, \dots, F, \quad (24)$$

where  $\Omega^{A_k}$  is the PCA space definition for action  $A_k$ ,  $\bar{\Psi}^{A_k}$  is the mean performance, and  $\sigma_t$  and  $\bar{\mathbf{v}}_t$  correspond to the computed standard deviation and mean direction of motion at each time step  $t$ , respectively.

Finally, to handle the cyclic nature of the walking action, we concatenate the last postures in each cycle with the initial postures of the most close performance according to a Euclidean distance criterion within the PCA space. Additionally, the first and last  $d/2$  postures from the mean performance (where  $d$  is the length of the considered subsequences) are resampled using cubic spline interpolation in order to soft the transition between walking cycles. As a result, we are able to compute  $\sigma_t, \bar{\mathbf{v}}_t$  for the last postures of a full walking cycle.

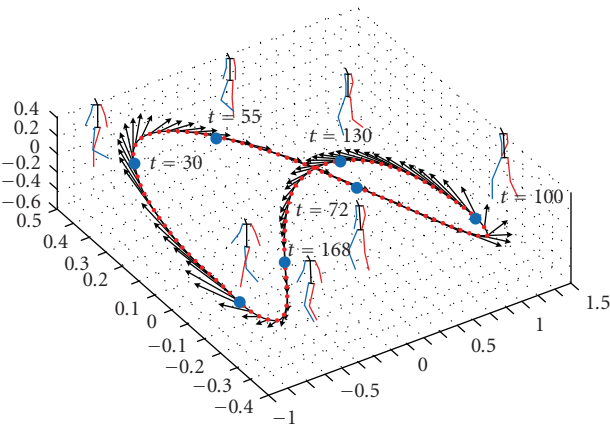


FIGURE 8: Sampled postures at different time steps, and learnt direction vectors  $\bar{v}_t$  from the mean performance for the walking action.

## 6. Conclusions and Future Work

In this paper, a novel dense matching algorithm for human motion sequences synchronization has been proposed. The technique utilizes dynamic programming and can be used in real-time applications. We also introduce the definition of the median sequence that is used to choose a time-scale pattern for all other sequences. The synchronized motion sequences are utilized to learn a model of human motion and to extract signal statistics. We have presented an action-specific model suitable for gait analysis, gait identification and tracking applications. The model is tested for the walking action and is automatically learnt from the public CMU motion capture database. As a result, we learnt the parameters of our action model which characterize the pose variability observed within a set of walking performances used for training.

The resulting action model consists of a representative manifold for the action, namely, the mean performance, the standard deviation from the mean performance. The action model can be used to classify which postures belong to the action or not. Moreover, the tradeoff between accuracy and generality of the model can be tuned using more or less dimensions for building the PCA space representation of human postures. Hence, using this coarse-to-fine representation, the main modes of variation correspond to meaningful natural motion modes. Thus, for example, we found that the main modes of variation for the walking action obtained from PCA explain the combined motion of both the legs and the arms, while in the bending action they mainly correspond to the motion of the torso.

Future research lines rely on obtaining the joint positions directly from image sequences. Previously, the action model has been successfully used in a probabilistic tracking framework for estimating the parameters of our 3D model from a sequence of 2D images. In [5] the action model improved the efficiency of the tracking algorithm by constraining the space of possible solutions only to the most feasible postures while performing a particular action, thus avoiding estimating

postures which are not likely to occur during an action. However, we need to develop robust image-based likelihood measures which evaluate the predictions from our action model according to the measurements obtained from images. Work based on extracting the image edges and the silhouette from the tracked subject is currently in progress. Hence, the pursued objective is to learn a piecewise linear model which evaluates the fitness of segmented edges and silhouettes to the 2D projection of the stick figure from our human body model. Methods for estimating the 6DOF of the human body within the scene, namely, 3D translation and orientation, also need to be improved.

## Acknowledgments

This work has been supported by EC Grant IST-027110 for the HERMES project and by the Spanish MEC under projects TIC2003-08865 and DPI-2004-5414. M. Mozerov acknowledges the support of the Ramon y Cajal research program, MEC, Spain.

## References

- [1] T. B. Moeslund and E. Granum, "A survey of computer vision-based human motion capture," *Computer Vision and Image Understanding*, vol. 81, no. 3, pp. 231–268, 2001.
- [2] T. B. Moeslund, A. Hilton, and V. Krüger, "A survey of advances in vision-based human motion capture and analysis," *Computer Vision and Image Understanding*, vol. 104, no. 2-3, pp. 90–126, 2006.
- [3] L. Wang, W. Hu, and T. Tan, "Recent developments in human motion analysis," *Pattern Recognition*, vol. 36, no. 3, pp. 585–601, 2003.
- [4] I. Rius, J. Varona, J. Gonzalez, and J. J. Villanueva, "Action spaces for efficient Bayesian tracking of human motion," in *Proceedings of the 18th International Conference on Pattern Recognition (ICPR '06)*, vol. 1, pp. 472–475, 2006.
- [5] I. Rius, J. Varona, X. Roca, and J. González, "Posture constraints for bayesian human motion tracking," in *Proceedings of the 4th International Conference on Articulated Motion and Deformable Objects (AMDO '06)*, vol. 4069, pp. 414–423, Port d'Andratx, Spain, July 2006.
- [6] L. Sigal and M. J. Black, "Measure locally, reason globally: occlusion-sensitive articulated pose estimation," in *Proceedings of the IEEE Computer Society Conference on Computer Vision and Pattern Recognition (CVPR '06)*, vol. 2, pp. 2041–2048, 2006.
- [7] J. González, J. Varona, X. Roca, and J. J. Villanueva, "Analysis of human walking based on *aSpaces*," in *Articulated Motion and Deformable Objects*, vol. 3179 of *Lecture Notes in Computer Science*, pp. 177–188, Springer, Berlin, Germany, 2004.
- [8] T. J. Roberts, S. J. McKenna, and I. W. Ricketts, "Adaptive learning of statistical appearance models for 3D human tracking," in *Proceedings of the British Machine Vision Conference (BMVC '02)*, pp. 121–165, Cardiff, UK, September 2002.
- [9] H. Sidenbladh, M. J. Black, and L. Sigal, "Implicit probabilistic models of human motion for synthesis and tracking," in *Proceedings of the 7th European Conference on Computer Vision Copenhagen (ECCV '02)*, vol. 2350 of *Lecture Notes in Computer Science*, pp. 784–800, Springer, Copenhagen, Denmark, May 2002.

- [10] R. Urtasun, D. J. Fleet, A. Hertzmann, and P. Fua, "Priors for people tracking from small training sets," in *Proceedings of the 10th IEEE International Conference on Computer Vision (ICCV '05)*, vol. 1, pp. 403–410, October 2005.
- [11] A. Nakazawa, S. Nakaoka, and K. Ikeuchi, "Matching and blending human motions using temporal scaleable dynamic programming," in *Proceedings of the IEEE/RSJ International Conference on Intelligent Robots and Systems (IROS '04)*, vol. 1, pp. 287–294, Sendai, Japan, September-October 2004.
- [12] Y. Bilu, P. K. Agarwal, and R. Kolodny, "Faster algorithms for optimal multiple sequence alignment based on pairwise comparisons," in *Proceedings of the IEEE/ACM Transactions on Computational Biology and Bioinformatics (TCBB '06)*, vol. 3, pp. 408–422, October-December 2006.
- [13] M. Gong and Y.-H. Yang, "Real-time stereo matching using orthogonal reliability-based dynamic programming," *IEEE Transactions on Image Processing*, vol. 16, no. 3, pp. 879–884, 2007.
- [14] J. L. Williams, J. W. Fisher III, and A. S. Willsky, "Approximate dynamic programming for communication-constrained sensor network management," *IEEE Transactions on Signal Processing*, vol. 55, no. 8, pp. 4300–4311, 2007.
- [15] J. Kruskall and M. Liberman, "The symmetric time warping problem: from continuous to discrete," in *Time Warps, String Edits, and Macromolecules: The Theory and Practice of Sequence Comparison*, pp. 125–161, Madison-Wesley, Reading, Mass, USA, 1983.
- [16] E. Keogh and M. Pazzani, "Derivative dynamic time warping," in *Proceedings of the 1st SIAM International Conference on Data Mining*, pp. 1–12, Chicago, Ill, USA, 2001.
- [17] I. Rius, D. Rowe, J. Gonzalez, and F. Xavier Roca, "3D action modeling and reconstruction for 2D human body tracking," in *Proceedings of the 3rd International Conference on Advances in Pattern Recognition (ICAPR '05)*, vol. 3687, pp. 146–154, Bath, UK, August 2005.
- [18] V. M. Zatsiorsky, *Kinematics of Human Motion*, chapter 1, Human Kinematics, 1998.

## Research Article

# Determination of Three-Dimensional Left Ventricle Motion to Analyze Ventricular Dyssynchrony in SPECT Images

**Marina de Sá Rebelo,<sup>1</sup> Ann Kirstine Hummelgaard Aarre,<sup>2</sup> Karen-Louise Clemmesen,<sup>2</sup> Simone Cristina Soares Brandão,<sup>1</sup> Maria Clementina Giorgi,<sup>1</sup> José Cláudio Meneghetti,<sup>1</sup> and Marco Antonio Gutierrez<sup>1</sup>**

<sup>1</sup>Heart Institute (InCor) do Hospital das Clínicas da Faculdade de Medicina da Universidade de São Paulo,  
Av. Dr. Enéas de Carvalho Aguiar, 44, CEP 05403000 São Paulo, Brazil

<sup>2</sup>Department of Health Science and Technology, Aalborg University, Fredrik Bajers Vej 7D2, DK-9220 Aalborg, Denmark

Correspondence should be addressed to Marina de Sá Rebelo, marina.rebelo@incor.usp.br

Received 29 April 2009; Revised 31 July 2009; Accepted 16 September 2009

Academic Editor: João Manuel R. S. Tavares

Copyright © 2010 Marina de Sá Rebelo et al. This is an open access article distributed under the Creative Commons Attribution License, which permits unrestricted use, distribution, and reproduction in any medium, provided the original work is properly cited.

A method to compute three-dimension (3D) left ventricle (LV) motion and its color coded visualization scheme for the qualitative analysis in SPECT images is proposed. It is used to investigate some aspects of Cardiac Resynchronization Therapy (CRT). The method was applied to 3D gated-SPECT images sets from normal subjects and patients with severe Idiopathic Heart Failure, before and after CRT. Color coded visualization maps representing the LV regional motion showed significant difference between patients and normal subjects. Moreover, they indicated a difference between the two groups. Numerical results of regional mean values representing the intensity and direction of movement in radial direction are presented. A difference of one order of magnitude in the intensity of the movement on patients in relation to the normal subjects was observed. Quantitative and qualitative parameters gave good indications of potential application of the technique to diagnosis and follow up of patients submitted to CRT.

## 1. Introduction

The automatic quantification of dynamic events, like the heart movement, is one of the most challenging applications in the field of medical image analysis. The normal Left Ventricle (LV) wall deformation occurring throughout the cardiac cycle may be affected by cardiac diseases. Thus, some pathological conditions could be identified by the change they produce in the expected normal movement [1].

Ventricular dyssynchrony is an example of a condition that modifies the normal behavior of the cardiac muscle [2]. Cardiac Resynchronization Therapy (CRT) is one of the procedures applied to patients with intraventricular dyssynchrony and aims to restore the normal contraction pattern by the stimulation of both right and left ventricles simultaneously [3]. Several studies have shown the effectiveness of CRT in patients with heart failure [4, 5]. However, among the patients submitted to CRT, 25–30% do not

respond to the treatment [6–9] (nonresponder). For this reason, when choosing CRT for a patient, several factors have to be considered. Besides being highly complex, it is an expensive therapy [10] and implantation of CRT device is not without risks to the patient [11]. The decision of recommending CRT to a patient is therefore a balance of these risks with its potential benefits.

At present, there is a lack of specific measures to characterize the degree of synchrony [12] as well as a factor, which prior to the application of the CRT, can discriminate patients who are going to respond to the therapy from those who are not. A number of researchers have been working to reach this goal in the last years [12–14]. Recently, several studies have used gated scintigraphic images to evaluate the ventricles synchrony by means of phase and amplitude images [10]. However, these two techniques involve a global analysis and may cause a loss of important information about the regional movement of the walls.

Electrocardiographic gating of Cardiac Single-Photon-Emission Computed Tomography (gated-SPECT) provides the clinician with a temporal set of 3D images that enables the visualization of the distribution of radioactive counts within the myocardium and surrounding structures throughout the cardiac cycle. It provides the ability to determine the severity of abnormalities in wall motion and wall thickening associated with myocardial dysfunction [15]. A number of techniques have been used in order to describe and quantify the nonrigid motion of the cardiac structures. Among these techniques, Optical Flow methods are used to accurately model nonrigid motion present during the cardiac cycle so that a one-to-one mapping is found between each voxel of two gated volumes [16, 17].

In previous works, we have described cardiac motion by means of the velocity flow field. The velocity estimation for each voxel in a volume was based on Optical Flow techniques [16]. In this technique, 3D LV motion is described by a series of 3D velocity vector fields computed automatically for each voxel on the sequence of cardiac volumes. The analysis and even the visualization of the velocity field in a cardiac volume are extremely difficult tasks, due to the high amount of information presented simultaneously. To make this bunch of information useful for diagnostic purposes, it is necessary to find compact and friendly representations for it.

In this work we propose a color coded visualization scheme for the qualitative analysis of the velocity components, with the definition of three movement directions. The coded velocity information obtained from Optical Flow in SPECT images is used to assess some aspects of CRT. In particular, we investigate the ability of velocity derived measurements to assess the effectiveness of CRT and velocity patterns that might be able to distinguish responder patients from the nonresponder, before the application of CRT. The assessment is performed on sets of images from thirty normal subjects and sixteen patients with idiopathic dilated cardiomyopathy.

## 2. Material and Methods

In this section the proposed methods to compute (Section 2.1) and analyze (Section 2.2) the left ventricle motion are described. In Section 2.3 the image acquisition protocol and data sets used for methods evaluation are presented, as well as the criteria used for classification of the patients as responders or nonresponders to the CRT.

### 2.1. Description of Heart Movement Through Velocity Fields

**2.1.1. Velocity Field Calculation.** The velocity fields are obtained by using an extension to 3D of the classical 2D Optical Flow [16, 17]. In this approach, two assumptions are imposed to the model. The first is a brightness constancy assumption and it assumes that the intensity of image elements is conserved between the image frames (called the OF constraint). The second assumption consists of a “smoothness” constraint and imposes that in a neighborhood the

voxels have similar velocities. The two assumptions are combined in a weighted function as follows:

$$\iiint \left[ (E_x u + E_y v + E_z w + E_t)^2 + \alpha^2 (u_x^2 + u_y^2 + u_z^2 + v_x^2 + v_y^2 + v_z^2 + w_x^2 + w_y^2 + w_z^2) \right] dx dy dz, \quad (1)$$

where the first term is the OF constraint, the second is a measure of the Optical Flow field smoothness, and  $\alpha$  is a weighting factor that controls the influence of the smoothness constraint.  $E_x$ ,  $E_y$ ,  $E_z$  and  $E_t$  are the image derivatives in the  $x$ ,  $y$ ,  $z$  and  $t$  directions;  $u$ ,  $v$  and  $w$  are the components of the local velocity vector  $\mathbf{v}$  along the  $x$ ,  $y$  and  $z$  directions, respectively.

The minimization of this function leads to a linear algebraic system, whose solution is the velocity component to each voxel and the coefficients are determined by the spatial and temporal derivatives of the images as follows:

$$\begin{aligned} u^{n+1} &= \bar{u}^n - \frac{E_x (E_x \bar{u}^n + E_y \bar{v}^n + E_z \bar{w}^n + E_t^n)}{\alpha^2 + E_x^2 + E_y^2 + E_z^2}, \\ v^{n+1} &= \bar{v}^n - \frac{E_y (E_x \bar{u}^n + E_y \bar{v}^n + E_z \bar{w}^n + E_t^n)}{\alpha^2 + E_x^2 + E_y^2 + E_z^2}, \\ w^{n+1} &= \bar{w}^n - \frac{E_z (E_x \bar{u}^n + E_y \bar{v}^n + E_z \bar{w}^n + E_t^n)}{\alpha^2 + E_x^2 + E_y^2 + E_z^2}, \end{aligned} \quad (2)$$

where  $\bar{u}$ ,  $\bar{v}$ , and  $\bar{w}$  are the mean velocities in each direction, for the voxels in a neighborhood of a given voxel, and  $n$  is the iteration index.

**2.1.2. Computational Description of the Left Ventricular Movement.** Generally speaking, the heart can be described as a nonrigid object that deforms throughout the cardiac cycle and has very complex mechanical properties [16]. To simplify the analysis of the left ventricular movement, it can be described in terms of contraction/expansion and torsion. In order to qualitatively evaluate the movement of the LV, three movement directions were defined, each with two possible orientations. These directions are depicted in Figure 1. Radial movement is described as a contraction towards the center of the LV during systole and as an expansion from the center during diastole. Horizontal rotation represents the clockwise and counterclockwise movement of the cardiac walls and the vertical rotation represents the movement towards the base (upwards) during systole and towards the apex during diastole. For the apex, only the radial component, which is the major component of its movement, is analyzed.

### 2.2. Qualitative Analysis of the Movement: Color Coding the Velocity Field in Spherical Coordinates

**2.2.1. Spherical Coordinate System.** The solution to the algebraic linear system presented in (1) gives the values of

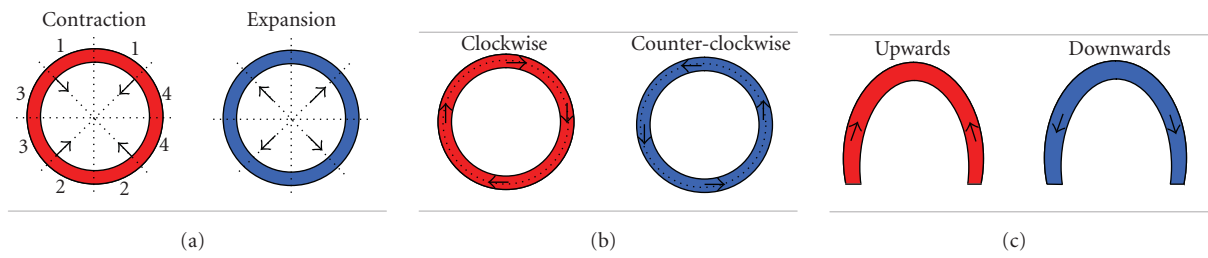


FIGURE 1: Motion directions defined in the cardiac cycle: (a) radial movement in terms of contraction and expansion; (b) horizontal rotation is either clockwise or counterclockwise; and (c) vertical rotation is upwards or downwards. The two orientations for each direction are colored by the defined coding scheme (see Section 2.1.1). Movements are depicted using the short axis view in (a) and (b) and the horizontal long axis view in (c). The LV walls are depicted in (a) left: region 1 is the anterior wall; region 2 is the inferior wall; region 3 is the septal wall; and region 4 is the lateral wall. (The nomenclatures of cardiac planes and wall segments used in this work follow the recommendations of the American Heart Association, as described in Cerqueira et al. [18].)

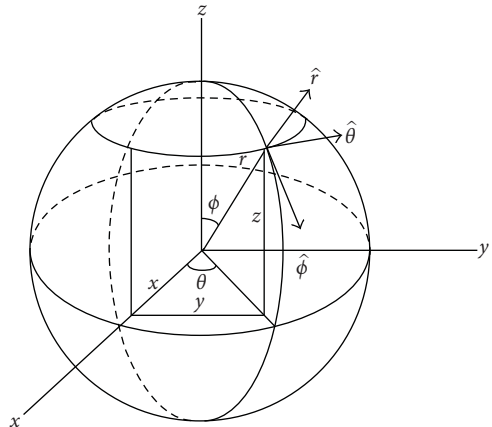


FIGURE 2: Unit vectors in spherical coordinates.

the velocity components for each voxel of the cardiac volume in Cartesian coordinates. However, the spherical coordinate system is a more suited system for the description of the movements presented in the former item. For this reason, the visualization module first performs a transformation of the velocities obtained in  $x$ ,  $y$ , and  $z$  directions to the unit vectors in the directions  $r$ ,  $\theta$ ,  $\phi$  in the spherical coordinate system (Figure 2).

The radial movement can be described by the unit vector for the  $r$  component, the horizontal rotation by the unit vector for the  $\theta$  component, and the vertical movement by the unit vector for the  $\phi$  component.

The center of the spherical coordinate system is essential when representing the left ventricular motion, as the origin is the reference point for the motion. The results for the velocity components are going to be highly dependent on the choice of this point. How to choose the center of the left ventricle is not a simple task. The anatomical center or the center of mass might be used as a central point, but this choice would fail to find the center in images from patients with myocardial infarction or any disease in which the counts are decreased at certain regions of the cardiac muscle. In this

work, the center is defined as the geometrical center of the LV and is selected manually by a trained physician.

**2.2.2. Color Scheme.** A desired feature of the visualization scheme is that all information concerning a movement direction be presented in a single image. Thus each image must present information about the orientation and the intensity of the velocity component. The color coding scheme is therefore defined as following: for each component, the color assigned to a voxel indicates the orientation of the movement, being either positive or negative, and the strength of the color indicates the intensity of the velocity vector in this direction.

Positive and negative orientations for each movement direction are defined as follows:

- (i) *Radial*: expansion is positive; contraction is negative,
- (ii) *Horizontal rotation*: clockwise rotation is negative, and counterclockwise rotation is positive;
- (iii) *Vertical rotation*: downwards motion is positive, and upwards rotation is negative.

In order to indicate velocity intensity, a discrete lookup table is used. In this table, the absence of motion is depicted as white, positive values are depicted as blue, and negative values are depicted as red. The positive and negative colors are divided into 128 steps by changing their saturation, such that strong movement is represented by a strong color, and a weaker movement has a lighter color. Figure 3 shows an example of a color scheme, in which the color variation follows a linear scale. Logarithm scales can be used for better visualization of weak movements.

**2.3. Acquisition and Processing of Patient Images.** The method was applied to 3D gated-SPECT ( $^{99}\text{mTc}$ -MIBI) images obtained from sixteen patients with idiopathic dilated cardiomyopathy, chronic heart failure in New York Heart Association functional class III or IV, LV Ejection Fraction  $<35\%$  and left bundle branch block (QRS  $\geq 120$  milliseconds), referred for implantation of a CRT device. The proposed protocol was approved by the Ethics Committee

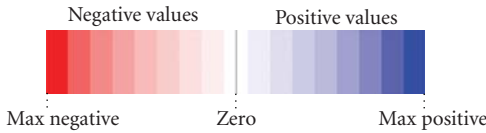


FIGURE 3: Color scheme for presenting information on both the intensity and orientation of the velocity: orientations with negative values are red, and orientations with positive values are blue. The faster a movement is, the stronger the color that represents it will be.

of the University of São Paulo Medical School and an informed consent was obtained from all study subjects and/or their families. The image acquisitions were performed at the Nuclear Medicine Department of the Heart Institute (InCor) HCFMUSP. All acquisitions were performed after the intravenous injection of 10 mCi of [technetium-99 m] sestamibi at rest in a dual-head rotating gamma camera (ADAC Cardio-MD with a LEAP Collimator). The acquisition process is synchronized with the electrocardiogram and the cardiac cycle was divided into 8 frames/cycle. A total of 64 projections were obtained over a semicircular 180-deg orbit. All projection images were stored using a  $64 \times 64$ , 16-bit matrix. The transverse tomograms were reconstructed with a thickness of 1 pixel/slice (6.47 mm). The volume of transverse tomograms was reoriented, and sets of slices perpendicular to the long axis (short axis view) and of slices parallel to the long axis (vertical long axis view and horizontal long axis view) were created. For each patient the images were acquired in two different conditions: at rest and after pharmacological induced stress.

From the group of sixteen patients, eight were responders to the CRT (Group1), and eight patients were nonresponders (Group2). For each patient, the rest and stress data sets were analyzed before to and after CRT, respectively. This gave a total of 64 gated-SPECT data sets included in this analysis. Before the implantation of the CRT device, the clinical condition of the patients was assessed and they were subsequently scanned with three different image modalities: gated-SPECT, echocardiography, and gated blood pool imaging. The aim was to gain an estimated left ventricular Ejection Fraction (EF) from each image modality, for later use as a quantitative measure of the response. After a three-month follow-up, the patients were submitted to the same procedures as prior to CRT. The majority of patients improve immediately their EF or functional class post-CRT implant. Estimates of the EF from each image modality were acquired a second time and compared with the estimated baseline EF. A positive response to CRT was defined as an increase of at least 5 percent points in one or more of the three modalities in addition to a positive clinical assessment. Patients who showed a positive response are named *responders*, and the ones who did not are named *nonresponders*.

The method was also applied to image sets of thirty normal subjects (The normal subjects whose images were used in this work were part of a Research protocol approved by the Ethics committee of the University of São Paulo Medical School.), whose acquisition protocol is the same as the one described for the patient images.

### 3. Results: Application of the Method to Investigate Some Aspects of CRT

**3.1. Results for Normal Subjects.** By analyzing normal left ventricles, the resulting visualization of the motion patterns can be compared with the motion expected from the heart physiology (seen in Figure 1).

As an example, Figure 4 shows the results obtained for one normal subject using the velocity color coding scheme. The Figure depicts the velocity images for the three movement directions in a slice from the midcavity portion at both diastole (line 1) and systole (line 2). Column (a) presents the images of the radial component, column (b) presents the images of the horizontal rotation component, and column (c) presents the images of the vertical component. The color table used in Figure 4 (as in the remaining figures of this text) is adjusted to the maximum value of each map.

**3.1.1. Radial Movement.** During systole, as the left ventricle ejects blood, the myocardium contracts starting at the apex and moving upwards to the base. Simultaneously, the septal and lateral walls move towards the center of the left ventricle. Therefore, the expected result in systole is the contraction which is presented in the Figure 4, line 2, column a. In this image, the contraction movement is represented by different tones of red, indicating the contraction with varying intensities. After ejection the heart enters the diastole, where the overall motion is opposite of the contraction. The expected colors are therefore also the opposite of the ones observed in systole. The results of a normal wall behavior can be observed in Figure 4, line 1, column a, where the expansion movement is depicted as different tones of blue.

**3.1.2. Horizontal Rotation.** The analysis of this movement is quite complicated. If one studies the anatomy and physiology of the subepicardial and subendocardial myofibres during both systole and diastole, it would be expected that images would show opposite rotations in the outer and inner sides of the myocardium. This could not be seen in any of the slices of any subjects. Instead, it seems like different rotary motions govern at different parts of the myocardium. The results in the midcavity slices form four corners, where opposing corners have movements with the same direction (see Figure 4, lines 1 and 2, column b). This pattern was similar in all normal left ventricles, hence it was assumed as the normal pattern in the horizontal motion. The results obtained show the expected opposite relationship between systole and diastole.

**3.1.3. Vertical Rotation.** In the ejection phase, the apex is pressed upwards during contraction to force the blood out through the aortic valve. The expected result of the vertical rotation in systole is therefore an upwards rotation, which is coded as red, this is also seen in Figure 4, line 2, column c. In diastole, the images show movement in the opposite direction.

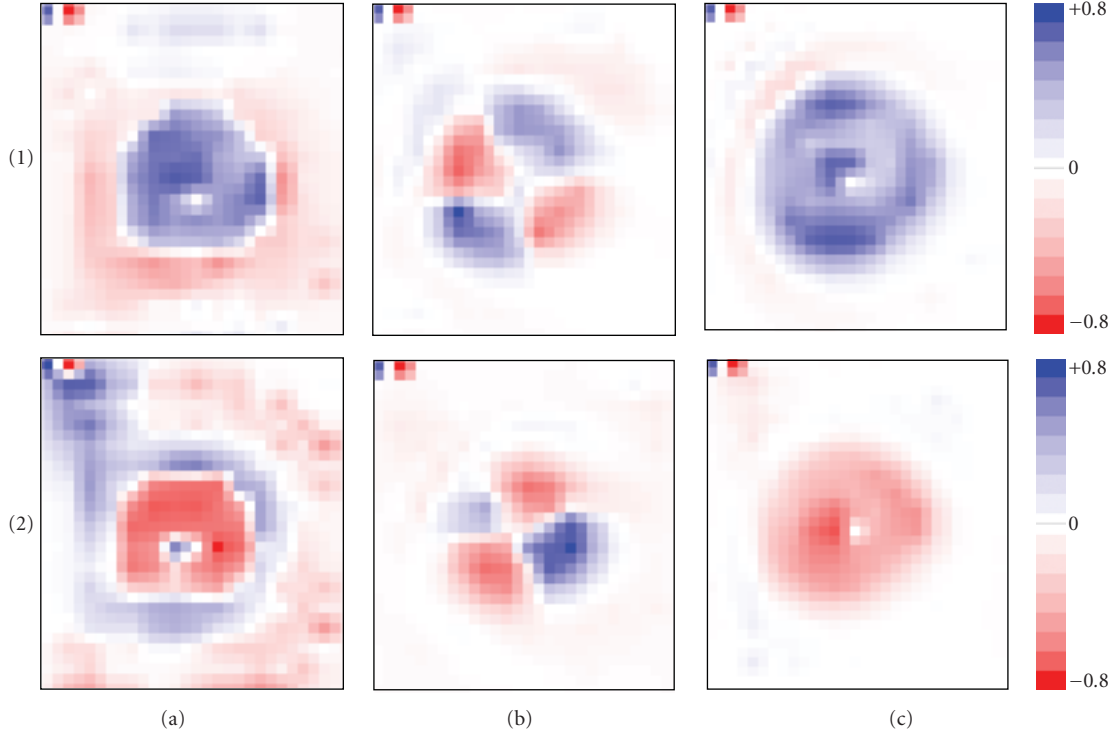


FIGURE 4: Velocity images of a normal subject in a slice from the midcavity portion of the LV. Line 1 presents diastolic images and line 2 presents systolic images. Column (a) depicts the images of the radial component. The several tones of blue in the myocardium in Line 1 represent the expansion while the tones of red in the same region in Line 2 represent the contraction. Column (b) presents the images of the horizontal rotation component. The tones of blue represent counterclockwise rotation while the tones of red represent clockwise rotation. Column (c) presents the images of the vertical component. The tones of blue represent downward motion while the tones of red represent upward motion. The color scale is shown at the top right of the figure.

### 3.2. Results for Patients

**3.2.1. Radial Movement.** In both groups of patients, the dyssynchrony of the movement can be observed in the radial movement. After CRT, Group1 should achieve an improved synchronization in the radial motion. This can be seen in most of the analyzed patients, where improvement in synchrony between septal and lateral wall is detected in both systole and diastole. Figure 5 shows an example of such a patient.

Prior to CRT a dyssynchrony is present in form of a blue (expanding) septal wall and a red (contracting) lateral wall. In the image after CRT, an improved synchrony is visible; here the blue color in the circle is replaced by a weak red color. During diastole in Figure 5, only the lateral wall is expanding before CRT, as the septal wall was expanding in systole. After CRT a more synchronous expansion is detected. It is seen that the overall intensity of the movement is weaker when compared to the normal subjects. The analysis of synchrony in the Group2 showed that there was no improvement in most of patients, as expected.

**3.2.2. Horizontal Rotation.** The images obtained before CRT present patterns quite different from the one assumed as the normal pattern. However, most of the results for Group1 after CRT are like the pattern found for the normal left

ventricles; an example is shown in Figure 6. The example in Figure 6 further shows that the desired opposite relationship between systole and diastole is present.

For Group2 no such pattern in the horizontal rotation was detected. One patient showed a pattern similar to a normal pattern in systole, but a worsening in diastole, while others showed the opposite or a mixture of rotations. None of the patients had a similar pattern of improvement or deterioration in synchrony. The intensity of motion was similar prior to and after CRT in all patients in systole, but in diastole half of the patients had a high intensity in horizontal rotation before CRT, which decreased after CRT. This behavior of noticeable decreased velocity intensity values was not detected in the Group1.

**3.2.3. Vertical Rotation.** A dyssynchrony in the vertical rotation is present in varying degrees in the results, which is expected for heart failure patients. Most of Group1 patients showed an improvement after CRT. For Group2, however, the normal pattern was hardly obtained even after CRT. In the case of horizontal rotation mentioned in the former section, some Group2 patients had a high intensity in diastole. The same patients had a high intensity in the vertical rotation in diastole. As it was seen in the horizontal rotation, the intensity of the vertical rotation also decreased after CRT. Figure 7 presents the results for a Group1 patient

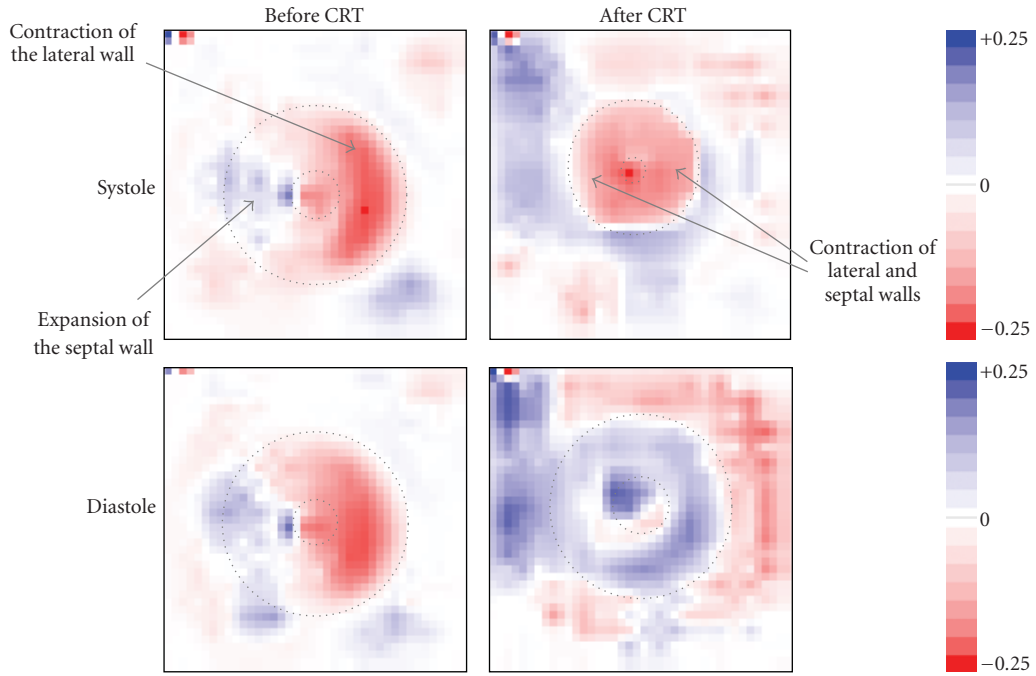


FIGURE 5: Radial motion of a Group1 patient. A slice from the midcavity is shown in systole and diastole, before and after CRT. In systole before CRT, the arrows indicate the septal and lateral walls. It can be noticed that in the septal wall, pixels present positive values—blue color—while in the lateral wall they present negative values—red color. The expected normal movement would be an overall contraction of the walls, represented by red color. Such movement can be seen in systole after CRT. The arrows in the figure indicate the global contraction movement depicted in tones of reds. The color scale is shown at the top right of the figure.

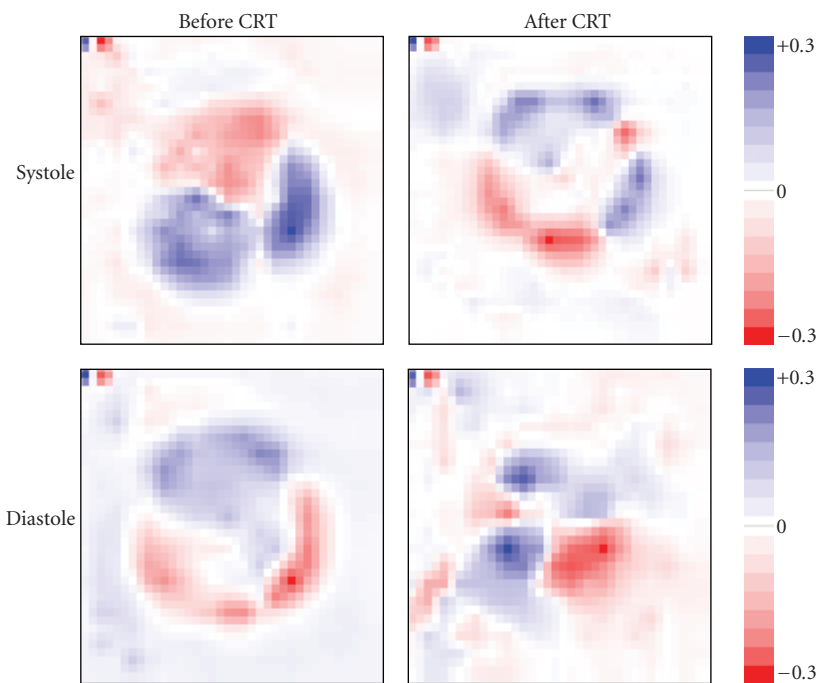


FIGURE 6: Horizontal motion of a Group1 patient. A slice from the midcavity is shown in systole and diastole, and before and after CRT. A movement pattern similar to the normal is seen after CRT in both systole and diastole. The color scale is shown at the top right of the figure.

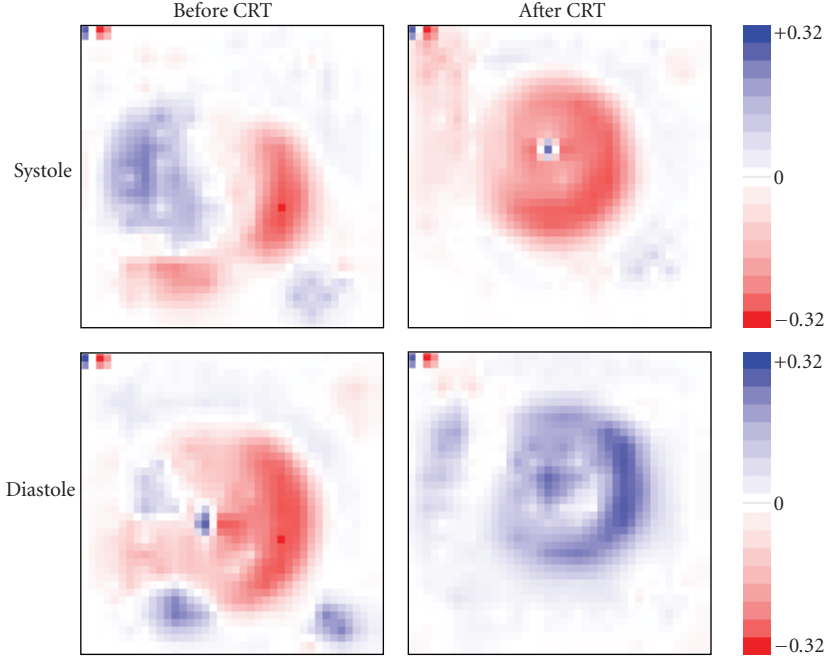


FIGURE 7: Vertical rotation in a Group1 patient. Middle slices shown during systole and diastole before and after CRT. The pattern is similar to the normal pattern before and after CRT as well as in systole and diastole. The color scale is shown at the top right of the figure.

**3.3. Analysis of Radial Movement—Normal and Patient.** Table 1 presents the normalized mean velocity values for the radial motion of the anterior, inferior, septal, and lateral walls (Figure 1(a)) for the LV midcavity portion. It presents the values found for one normal subject and one patient of each group (responder and nonresponder).

The comparison between patients (Group1 and Group2) and normal subjects shows that not only the synchrony of the movement is compromised, but the intensity is seriously decreased in this set of patients, which reflects the impaired heart function. The numerical values representing the quantity of movement of the normal subjects are ten times higher than the patients. Although this quantity does not change considerably before and after the CRT, the responder patient presents an overall increase in the clinical conditions due to the fact that the synchrony of the movement has been restored. This fact can be seen in Table 1 by the change in the expected sign for the measurement. Patients from the Group2 did not present this improvement in synchrony.

#### 4. Discussion and Conclusions

The analysis of the velocity field from cardiac volumes can give important clues about the dynamic events occurring during the cardiac cycle, which may help to understand how some treatments improve heart function. In this work, the results were presented in a slice of the short axis view and we proposed a scheme for displaying the wall movements which are displayed using a compressive color code that integrates orientation and intensity of the velocity vector at each voxel.

The most important feature of this method is its capability to evaluate LV motion in a more comprehensive way since it allows a regional analysis by assessing the movement in three predefined directions. Other techniques (like echocardiography and phase images derived from Fourier transform of radionuclide ventriculography or even gated single photon emission computed tomography) use previously defined points (or regions) and establish a comparison between them or evaluate indices that characterize global LV synchrony [2, 7, 10, 19].

In this study, the results from the normal subjects were used as the reference for normality in each of the directions. The representation of the velocity components in a color coded image has shown to be an efficient tool for regional inspection of the LV wall movement that could improve the optimal site of LV electrode implant. Actually, the method allows a local analysis, since the results are obtained for each voxel of the volume. This is an important advantage of this method when compared to other global techniques such as phase and amplitude.

Table 1 shows a quantitative comparison of one data set obtained in normal controls, and two patients, one who responded to CRT and one nonresponder. A difference of one order of magnitude in the intensity of the movement on patients in relation to the normal subjects was observed. The evaluation of radial motion before CRT in a nonresponder patient (group 2) showed a movement pattern different from normal in both phases of the cardiac cycle. The responder (group 1) showed motion in the opposite direction from normal controls only in inferior and septal walls. This fact could suggest that responders are different from nonresponders

TABLE 1: Mean intensity values for radial motion of one normal subject and two patients, one of Group1 and one of Group2, before and after CRT. Values presented for the walls depicted in Figure 1—anterior, inferior, septal, and lateral—for the LV midcavity portion. The computed intensity values are mapped to a scale that allows a maximum of +1 and a correspondent minimum of -1.

	Anterior wall		Inferior wall		Septal wall		Lateral wall	
	Diast	Syst	Diast	Syst	Diast	Syst	Diast	Syst
Expected orientation	+	-	+	-	+	-	+	-
Normal	+0.738	-0.344	+0.474	-0.278	+0.404	-0.144	+0.808	-0.600
Group1 before	+0.006	-0.056	-0.038	+0.016	-0.008	+0.056	+0.066	-0.062
	+0.026	-0.044	+0.020	+0.028	+0.028	-0.044	+0.100	-0.062
Group2 Before	0.000	+0.016	-0.026	+0.068	-0.030	+0.040	+0.046	+0.062
	-0.028	+0.068	+0.128	-0.004	-0.006	-0.004	+0.104	-0.002

Diast: values in diastole; Syst: values in systole; Expected orientation of the movement: + is expansion and - is contraction; Group1 before: responder patient before CRT; Group1 after: responder patient after CRT; Group2 before: patient nonresponder before CRT; Group2 after: patient nonresponder after CRT.

before therapy. After therapy, the direction of the motion of inferior and lateral walls of the nonresponder became similar to normal controls, but not the direction of anterior and septal walls. The group 1 patient showed a normal motion pattern except in inferior wall after therapy. The qualitative and quantitative parameters obtained with this method could add information to a better selection of patients who would respond to TRC and provide a measurable tool to the follow-up in this population.

*Limitations.* the spherical coordinate system was chosen for calculating the orientation and intensity of the left ventricular motion. A key issue to the proposed scheme is the center of the spherical coordinate system since it is the reference point for the motions and therefore essential in the visualization of the velocity components. A change in center will influence both the intensity and orientation of the left ventricular motion. Choosing the center is difficult as it should be the exact point or axis from which the motion starts and ends. In the present work, the center was determined manually by a trained observer as the geometrical center of the LV.

Another limitation is the poor resolution of SPECT images that sometimes makes it difficult to analyze the movements. It must be added, however, that the proposed method is not applicable to nuclear medicine imaging only and can be extended to other modalities.

*Future Perspectives and Conclusions.* the results are preliminary indications obtained via a qualitative assessment. Quantitative indexes can be created based on these images that would be able to quantitatively assess both the effectiveness and prediction of CRT response. These indexes could be based on the creation of normal distributions of the velocity field for each direction. An alternative and elegant approach for defining quantitative tools for the analysis of the movement patterns is the creation of a functional bull's eye [20–23]. Once the bull's eyes of the described movement patterns have been built, many studies can be performed for the assessment of the patient's condition. In order to find an index to predict response to CRT therapy, extensive clinical studies must be performed and involve the acquisition of

a statistically significant number of images from normal subjects and patients.

In this study, the left ventricular three-wall movements were studied using a compressive color code that characterizes the integration of orientation and intensity of the velocity vector at each voxel. This new technique of myocardial synchronization assessment might be able to distinguish responder patients from the nonresponders and improve the follow up of patients who underwent CRT.

## Acknowledgments

The authors would like to thank Dr. Ramon Moreno, Maurício Higa, and Carlos Santos for their valuable discussions at the elaboration of this work. This work was supported in part by the Foundation of Aid for Research of São Paulo State (FAPESP) Grant no. 2006/06612-4, the National Council for Scientific and Technological Development (CNPq) Grant no. 300499/2005-1, the National Institute of Science and Technology—Medicine Assisted by Scientific Computing INCT MACC, and the Zerbini Foundation.

## References

- [1] E. W. Remme, A. A. Young, K. F. Augenstein, B. Cowan, and P. J. Hunter, “Extraction and quantification of left ventricular deformation modes,” *IEEE Transactions on Biomedical Engineering*, vol. 51, no. 11, pp. 1923–1931, 2004.
- [2] J. Chen, E. V. Garcia, R. D. Folks, et al., “Onset of left ventricular mechanical contraction as determined by phase analysis of ECG-gated myocardial perfusion SPECT imaging: development of a diagnostic tool for assessment of cardiac mechanical dyssynchrony,” *Journal of Nuclear Cardiology*, vol. 12, no. 6, pp. 687–695, 2005.
- [3] K. Rioual, E. Unanua, S. Laguitton, et al., “MSCT labelling for pre-operative planning in cardiac resynchronization therapy,” *Computerized Medical Imaging and Graphics*, vol. 29, no. 6, pp. 431–439, 2005.
- [4] A. Auricchio and W. T. Abraham, “Cardiac resynchronization therapy: current state of the art: cost versus benefit,” *Circulation*, vol. 109, no. 3, pp. 300–307, 2004.
- [5] C. Linde, F. Braunschweig, F. Gadler, C. Bailleul, and J.-C. Daubert, “Long-term improvements in quality of life by

- biventricular pacing in patients with chronic heart failure: results from the MULTisite STimulation In Cardiomyopathy Study (MUSTIC)," *American Journal of Cardiology*, vol. 91, no. 9, pp. 1090–1095, 2003.
- [6] G. Lecoq, C. Leclercq, E. Leray, et al., "Clinical and electrocardiographic predictors of a positive response to cardiac resynchronization therapy in advanced heart failure," *European Heart Journal*, vol. 26, no. 11, pp. 1094–1100, 2005.
- [7] G. B. Bleeker, J. J. Bax, J. W.-H. Fung, et al., "Clinical versus echocardiographic parameters to assess response to cardiac resynchronization therapy," *American Journal of Cardiology*, vol. 97, no. 2, pp. 260–263, 2006.
- [8] C.-M. Yu, G. B. Bleeker, J. W.-H. Fung, et al., "Left ventricular reverse remodeling but not clinical improvement predicts long-term survival after cardiac resynchronization therapy," *Circulation*, vol. 112, no. 11, pp. 1580–1586, 2005.
- [9] S. Yeim, P. Bordachar, S. Reuter, et al., "Predictors of a positive response to biventricular pacing in patients with severe heart failure and ventricular conduction delay," *Pacing and Clinical Electrophysiology*, vol. 30, no. 8, pp. 970–975, 2007.
- [10] S. C. S. Brandão, M. C. P. Giorgi, R. T. de Miche, et al., "Ventricular synchrony in patients with dilated cardiomyopathy and normal individuals: assessment by radionuclide ventriculography," *Arquivos Brasileiros de Cardiologia*, vol. 88, no. 5, pp. 596–601, 2007.
- [11] S. A. Strickberger, J. Conti, E. G. Daoud, et al., "Patient selection for cardiac resynchronization therapy: from the Council on Clinical Cardiology Subcommittee on Electrocardiography and Arrhythmias and the Quality of Care and Outcomes Research Interdisciplinary Working Group, in collaboration with the Heart Rhythm Society," *Circulation*, vol. 111, no. 16, pp. 2146–2150, 2005.
- [12] J. W. O'Connell, C. Schreck, M. Moles, et al., "A unique method by which to quantitate synchrony with equilibrium radionuclide angiography," *Journal of Nuclear Cardiology*, vol. 12, no. 4, pp. 441–450, 2005.
- [13] J. Declerck, J. Feldmar, and N. Ayache, "Definition of a four-dimensional continuous planispheric transformation for the tracking and the analysis of left-ventricle motion," *Medical Image Analysis*, vol. 2, no. 2, pp. 197–213, 1998.
- [14] S. R. R. Tecelão, J. J. M. Zwanenburg, J. P. A. Kuijjer, et al., "Quantitative comparison of 2D and 3D circumferential strain using MRI tagging in normal and LBBB hearts," *Magnetic Resonance in Medicine*, vol. 57, no. 3, pp. 485–493, 2007.
- [15] G. J. Klein, B. W. Reutter, and R. H. Huesman, "Non-rigid summing of gated PET via optical flow," *IEEE Transactions on Nuclear Science*, vol. 44, no. 4, pp. 1509–1512, 1997.
- [16] M. A. Gutierrez, M. S. Rebelo, S. S. Furui, and J. C. Meneghetti, "Automatic quantification of three-dimensional kinetic energy in gated myocardial perfusion single-photon-emission computerized tomography improved by a multiresolution technique," *Journal of Electronic Imaging*, vol. 12, no. 1, pp. 118–124, 2003.
- [17] B. K. P. Horn and B. G. Schunck, "Determining optical flow," *Artificial Intelligence*, vol. 17, no. 1–3, pp. 185–203, 1981.
- [18] M. D. Cerqueira, N. J. Weissman, V. Dilsizian, et al., "Standardized myocardial segmentation and nomenclature for tomographic imaging of the heart: a statement for healthcare professionals from the Cardiac Imaging Committee of the Council on Clinical Cardiology of the American Heart Association," *Circulation*, vol. 105, no. 4, pp. 539–542, 2002.
- [19] S. C. S. Brandão, S. A. D. Nishioka, M. C. P. Giorgi, et al., "Cardiac resynchronization therapy evaluated by myocardial scintigraphy with  $^{99m}\text{TC}$ -MIBI: changes in left ventricular uptake, dyssynchrony, and function," *European Journal of Nuclear Medicine and Molecular Imaging*, vol. 36, no. 6, pp. 986–996, 2009.
- [20] R. J. Qureshi and S. A. Husain, "Design of an expert system for diagnosis of coronary artery disease using myocardial perfusion imaging," in *Proceedings of the National Conference on Emerging Technologies*, pp. 100–105, 2004.
- [21] N. Rougon, C. Petitjean, F. Prêteux, P. Cluzel, and P. Grenier, "A non-rigid registration approach for quantifying myocardial contraction in tagged MRI using generalized information measures," *Medical Image Analysis*, vol. 9, no. 4, pp. 353–375, 2005.
- [22] O. Gérard, A. C. Billon, J.-M. Rouet, M. Jacob, M. Fradkin, and C. Allouche, "Efficient model-based quantification of left ventricular function in 3-D echocardiography," *IEEE Transactions on Medical Imaging*, vol. 21, no. 9, pp. 1059–1068, 2002.
- [23] J.-W. Lin, A. F. Laine, and S. R. Bergmann, "Improving PET-based physiological quantification through methods of wavelet denoising," *IEEE Transactions on Biomedical Engineering*, vol. 48, no. 2, pp. 202–212, 2001.

## Research Article

# 3D Elbow Kinematics with Monoplanar Fluoroscopy: *In Silico* Evaluation

L. Tersi, S. Fantozzi, and R. Stagni

Department of Electronics, Computer Science and Systems (DEIS), University of Bologna, Via Venezia 52, I 47023 Cesena, Italy

Correspondence should be addressed to L. Tersi, luca.tersi@unibo.it

Received 1 May 2009; Revised 6 August 2009; Accepted 14 September 2009

Academic Editor: João Manuel R. S. Tavares

Copyright © 2010 L. Tersi et al. This is an open access article distributed under the Creative Commons Attribution License, which permits unrestricted use, distribution, and reproduction in any medium, provided the original work is properly cited.

An *in-silico* assessment of the performance of 3D video-fluoroscopy for the analysis of the kinematics of long bones is proposed. A reliable knowledge of *in-vivo* joints kinematics in physiological conditions is fundamental in the clinical field. 3D video-fluoroscopy theoretically permits a mm/deg level of accuracy in joint motion analysis, but the optimization algorithm for the pose estimation is highly dependent on the geometry of the bone segment analyzed. An automated technique based on distance maps and tangency condition was applied to the elbow bones. The convergence domain was explored to quantify and optimize measurement accuracy in terms of bias and precision. By conditioning the optimization algorithm using simple image features, the estimation error had small dispersion (interquartile range within 0.5 and 0.025 mm/deg for out-of-plane and in-plane pose parameters, resp.), but with occasional bias and outliers. 3D video-fluoroscopy produced promising results for the elbow joint, but further *in-vitro* validation studies should be carried out.

## 1. Introduction

3D video-fluoroscopy is a technique for the evaluation of joint kinematics based on the alignment of 3D models of bones or prostheses and series of 2D radiographic images representing the relevant monoplanar or biplanar projections [1]. The joint kinematics is reconstructed calculating, independently for each video-frame, the 6 degrees of freedom (DOF) absolute pose (3 translations and 3 rotations) of each body segment, and then calculating the 6 DOFs of their relative pose.

Reliable knowledge of *in-vivo* joint kinematics, in physiological conditions, is fundamental for various clinical applications: (i) the study of prosthesis design must aim at the replication of intact joint biomechanical function [2, 3]; (ii) the development of quantitative diagnostic tools can help the detection of pathological alterations in motion [4], and (iii) the outcomes of orthopaedic surgery must be quantified to find correlation with the recovery of physiological joint motor activities [5, 6]. Moreover, from a methodological point of view, accurate methods are necessary to validate and to evaluate errors associated with non-invasive techniques

for the quantification of motion (i.e., inertial sensors, stereophotogrammetry [7]). 3D video-fluoroscopy could provide this knowledge, because it theoretically permits to achieve a millimetre/degree accuracy level in joint motion analysis [8, 9], with relatively high dynamic performances (up to more than 50 fps with modern fluoroscopes), sufficient to analyze the motion during activities of daily living, and simple joint-specific tasks that can be performed inside the fluoroscopic volume (Figure 1).

*In-vivo* knee tasks, such as squat, stair climbing, chair raising and sitting or step up-down, were widely analysed with 3D video-fluoroscopy in replaced [10–13] and intact knee [14]. 3D video-fluoroscopy was also applied to quantify the *in-vivo* kinematics of ankle [15] and hip [16, 17] joints.

To estimate the 6 DOF of a bone segment in a frame acquired by video-fluoroscopy, a 3D model of the bone is virtually moved until it is best aligned to the relevant 2D image. This automatic procedure is typically carried out by means of an iterative optimization algorithms. Different metrics have been used to quantify a cost or a fitness function for the optimization such as: (i) the euclidean distance between the contour of the virtual projection of

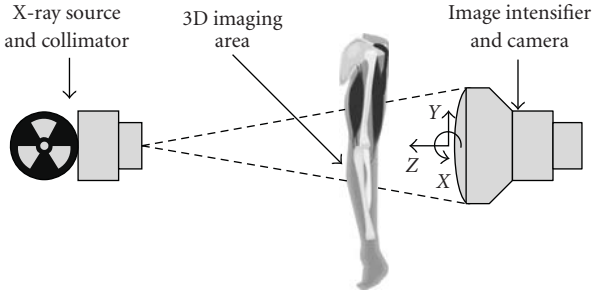


FIGURE 1: Configuration of a single-plane fluoroscopic acquisition system.

the model and the contour extracted from the fluoroscopic image [8, 18], (ii) the root mean square distance between the projection lines and the model surface [2], (iii) similarity measures between the fluoroscopic image and digitally reconstructed radiographies [19–23].

Promising accuracy levels have been reported for the intact knee joint: 0.23 mm for translation, 1.2 deg for rotation with biplanar fluoroscopy [22]; and 0.42 mm for in-plane and 5.6 mm for out-of-plane translations, 1.3 deg for rotation for monoplanar fluoroscopy [24]. However, these accuracies cannot a priori be considered valid for the other joints. Even if biplanar fluoroscopy is more robust, the present work focused on monoplanar fluoroscopy because it can investigate bigger volume with smaller X-ray dose for the patient.

The performance of 3D-fluoroscopy is affected by the geometry of the bone segments analysed, and its accuracy could vary considerably because local minima, caused by symmetries of the models surfaces, or by occlusions, could severely interfere with a correct estimation of the pose. Therefore, the technique is highly dependent on the initial guess of the pose for the optimization which is typically specified manually. However, the extent to which the intervention of the operator can affect the final reliability of the pose estimation has not been clarified yet. Therefore, 3D video-fluoroscopy might currently still be operator-dependent [18] and the application of 3D video-fluoroscopy is still too cumbersome to be suitable for routine clinical practice. The high potential of the method for routine clinical applications cannot be exploited without a concrete automation of the procedure, involving an automatic estimation of the initial guess of the pose. Therefore, the convergence domain of the optimization must be characterized in detail, exploring how different algorithms behave around reference poses.

Currently, no fluoroscopic methods have been applied to the *in-vivo* kinematics of the elbow joint. This joint has, however, been characterized *ex-vivo* [25], with Roentgen Stereophotogrammetric Analysis (RSA) [26, 27], and electromagnetic tracking systems [28], as well as *in-vivo* with non-invasive technique such as infrared stereo-photogrammetry [29], or nuclear magnetic resonance (MRI) [30]. Infrared stereo-photogrammetry, however, suffers accuracy limits due to soft tissue artifacts (20–48% of loss of rotational motion of the upper arm [31, 32]), while MRI fails to

detect the effect of the active contribution of muscles to the motion. Even though fluoroscopy has not yet been applied to the elbow, this joint is of particular interest for its validation because it is characterized by (i) a high degree of bone superimposition, (ii) being composed by thin long bones (in contrast with the typical morphology of knee prosthesis), and (iii) marked longitudinal cylindrical symmetries (especially for the radius). These aspects make the fluoroscopic analysis of the intact elbow considerably difficult, thus particularly suitable for a validation study.

To significantly improve the quality and the robustness of 3D video-fluoroscopy, it is necessary to understand the effect of the various sources of errors on the final accuracy. For this purpose, an analytic approach is necessary in order to find appropriate solutions to each single defect of the method.

In the present study, we analysed, by means of computer simulation, the convergence property of a modified version of the pose estimation algorithm proposed by Lavallée and Szelinsky [33] and based on adaptive distance maps (ADM), in order to better understand the influence of local minima and to optimize the pose estimation in terms of accuracy and precision. This algorithm was chosen because of its light computational weight and because it permits to achieve good accuracies even with incomplete contours [2], which can arise from occlusions or image blurring due to the bone motion.

In this evaluation study we considered (i) the geometric characteristic of the bone models, (ii) the resolution of the fluoroscopic projections, and (iii) the resolution of ADM as the only sources of errors. Confounding effects caused by the geometric distortions, by errors in the calibration of the fluoroscopic models, or by the incompleteness of the bone contours were disregarded in the present study.

The aim of the present study was to investigate the suitability of 3D video-fluoroscopy for the analysis of elbow bones kinematics, through a detailed exploration of the convergence domain of the minimization algorithm, in order to quantify and optimize measurement accuracy in terms of bias and precision.

## 2. Material and Methods

**2.1. Pose Estimation Algorithm.** An established technique was implemented to estimate the 3D pose of an object of known 3D geometry given its monoplanar fluoroscopic projection [2]. The algorithm was originally proposed by Lavallée and Szeliski [33] for biplanar projection, and is based on 3D adaptive distance maps. In brief, (i) the fluoroscope is virtually modelled with a perspective projection model; (ii) the 3D pose estimation is obtained with an iterative procedure that finds the best alignment between a bone surface model and its 2D fluoroscopic projection (typically a  $1024 \times 1024$  DICOM image). In the present study, the bone surface was modelled with triangles meshes, however different representation can be used (i.e., cloud of points, NURBS). The resolution of the meshes was not relevant, because the images for the alignment were generated *in-silico* projecting exactly the same models. There was, thus, a perfect correspondence between the 3D model and the projection

independently from the meshes properties. The quality of the alignment is represented by a cost function defined as:

$$\text{RMSD}(p) = \sqrt{\frac{1}{n} \sum_{i=1}^n [d(S_m(p), l_i)]^2}. \quad (1)$$

RMSD is the root mean square distance between the surface  $S_m(p)$  of the model  $m$  positioned in the pose  $p = (Tx\ T_y\ T_z, \Theta_x, \Theta_y, \Theta_z)$  and  $n$  projection lines  $l$ . The projection lines  $l$  represent the X-rays that generated the edge points of the bone segment projection extracted by a Canny edge detector [34] in the fluoroscopic image and is expressed in parametric form

$$l_i : C_i + \left( \frac{F - C_i}{L_i} \right) \lambda, \quad \lambda \in [0, L_i], \quad (2)$$

where  $F = (F_x, F_y, F_z)$  is a point representing the X-ray source position (*focus*),  $C_i = (C_{ix}, C_{iy}, C_{iz})$  is the  $i$ th of the  $n$  points of the contour, both expressed in the fluoroscopic system of reference, and  $L_i$  is their distance:

$$L_i = \|F - C_i\| \quad (3)$$

To quantify RMSD,  $l_i$  is sampled and, for each sampling point  $P_k^i = l_i(\lambda_k)$ , the distance from  $S_m(p)$  is computed. The distance of the projection line from the surface is then defined as the minimum distance among those of the line sampling points:

$$d(S_m(p), l_i) = \min_k (d(S_m(p), P_k^i)). \quad (4)$$

The best alignment condition is finally identified finding the values of the pose  $p$  that minimize the RMSD with the Levenberg–Marquardt (LM) method [35]:

$$\text{RMSD}_{\min} = \min_p (\text{RMSD}(p)). \quad (5)$$

The VXL [36] implementation of LM was used in the present work.

For a faster quantification of the distance  $d(S_m, l_i)$  between the line and the model surface, and to define the sampling step of  $l_i$ , adaptive distance maps (ADM) of the models surface were pre-computed and stored. Briefly, the ADM is an octree-based representation of an object [37]. In this representation, the volume outside and inside the surface of the object is non-uniformly discretized. The map assigns to each point of the discretization the corresponding signed distance from the surface of the model: positive if outside, negative if inside the object. The distance is computed as the minimum distance between the discretization point and the surface of model of the bone. The structure of the ADM is an octree which is built with an iterative procedure which subdivides a cube (also called octant) iteratively in other 8 half-side octants only if it contains at least one point of the mesh. The octree is then refined to avoid discontinuities between the levels of subdivision of two adjacent octants. The vertices of the octants are the volume discretization points. The distance of a generic point from the surface is then

computed with a tri-linear interpolation of the distances of the 8 vertices of the smallest octant containing the point. The octant side dimension gets smaller closer to the surface, thus the interpolation error becomes negligible. In the present work, the resolution of the octree (smallest octant side) will be referred as DMR (Distance Map Resolution). For a further improvement of the algorithm speed, also the sampling step of the projection lines is adaptive. The sampling step varies accordingly to the local resolution of the ADM and gets smaller closer to the surface. If  $s_k^i$  is the side of the smallest octant containing the sampled point  $P_k^i$  then the next point to evaluate the distance will be

$$\begin{aligned} P_{k+1}^i &= l_i(\lambda_{k+1}), \\ \lambda_{k+1} &= \lambda_k + \frac{s_k^i}{2}. \end{aligned} \quad (6)$$

Finally,  $l_i$  is resampled around the closest point to the surface with a uniform step length ten times smaller than DMR.

A global reference frame was defined with the  $x$  and  $y$  axis parallel and  $z$ -axis perpendicular to the image plane, with the origin in the centre of the image plane. The Euler  $zxy$  convention was used for rotations. The field of view was represented with a diameter of 400 mm. The X-ray source was virtually placed in  $F = (0, 0, 1000)$  mm, representing a typical distance of a standard fluoroscope, and pixel spacing was fixed at 0.34 mm. The effects on the final accuracy of the errors associated to the identification of the principal point ( $xy$ -coordinates of the X-ray source) and principal distance ( $z$ -coordinate of the X-ray source) were disregarded in the present study as already quantified elsewhere [38]. The X-rays were represented by a beam of straight lines and the effect of the geometrical image distortions, caused by the electronics of the image formation chain of real fluoroscopes [39], was not considered in the present study because, dealing with real images, the geometrical distortion can be efficiently corrected using a global spatial warping techniques [40, 41].

In the implementation of the LM minimization algorithm, 3 parameters must be specified: (i) the convergence tolerance on the RMSD ( $f_{tol}$ ), (ii) the convergence tolerance on the 6 DOF of the pose  $p$  ( $x_{tol}$ ), and (iii) the step length for forward (FD) Jacobian computation ( $\text{eps}$ ).

**2.2. Algorithm Convergence Properties.** High resolution models of humerus, ulna, and radius were downloaded from the official site of the European project VAKHUM (contract #IST-1999-10954 [42]) and used in the performed simulations. For each model two ADM were calculated and stored with DMR equal to 0.5 and 1 mm.

An anatomical reference frame was associated to each bone model according to the ISB recommendations [43]. Each model was then placed in a reference pose (parallel to  $xy$ -plane, lateral view, out of plane translation  $T_z = 200$  mm) simulating a typical fluoroscopic frame. Flat shaded projections were generated and the complete contour was extracted and then used for the alignment (Figure 2).

The sensitivity of the cost function to each DOF of  $p$  was analysed. The RMSD function was evaluated keeping 5 DOF constant and varying a single DOF at a time, with

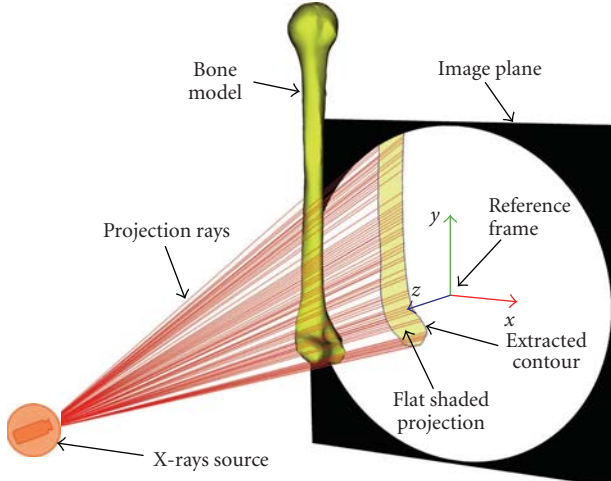


FIGURE 2: Perspective projection model. The bone model is placed in a reference position and a flat shaded projection is generated. The contour points are extracted and the projection lines are back projected towards the X-rays source.

a step of 0.1 mm/deg, around the reference pose, from  $-30$  to  $30$  mm/deg for translations and rotations, respectively. The analysis was repeated for humerus, ulna and radius. This permitted to evaluate how the shape and the symmetry of the different bone models influence the minimization. The RMSD with respect to each DOF analysed, can be represented as a cusp. The sensitivity ( $S$ ) of RMSD to the variation of the pose parameters, was defined as the average absolute slope between the left and the right tangents of the curve around its minimum (Figure 3):

$$S_p = \frac{1}{2} \left( \left| \frac{\text{RMSD}(p_m) - \text{RMSD}(p_m + \Delta p)}{\Delta p} \right| + \left| \frac{\text{RMSD}(p_m) - \text{RMSD}(p_m - \Delta p)}{\Delta p} \right| \right), \quad (7)$$

where  $p_m$  is the value of the generic pose parameter  $p$  correspondent to the minimum of RMSD.

A detailed convergence domain analysis was carried out for different sets of simulation parameters. The minimization was started from 1000 randomly-chosen initial-condition poses among 117649 permutations obtained varying the translations ( $\Delta T_x$ ,  $\Delta T_y$ ,  $\Delta T_z$ ) and rotations ( $\Delta \Theta_x$ ,  $\Delta \Theta_y$ ,  $\Delta \Theta_z$ ) between the values  $-10$ ,  $-7$ ,  $-3$ ,  $0$ ,  $3$ ,  $7$ ,  $10$  mm/deg, respectively, around the reference pose. The simulations parameters were initially varied using different values for DMR (0.5–1 mm), and eps ( $10^{-1}$ – $10^{-4}$  mm/deg) while  $x_{\text{tol}}$  and  $f_{\text{tol}}$  were both kept fixed at  $10^{-3}$  mm/deg.

**2.3. Algorithm Conditioning.** Different authors stressed that the minimization of RMSD is affected by local minima and by the large differences in the sensitivity to the various DOF [13, 24]. If the minimization starts from initial conditions inside a local minima basin, the pose estimation will be incorrect. Two different solutions were implemented and

compared in order to better deal with the problem of local minima.

The first, proposed by Fregly et al. [24], involved the sequential (*seq*) minimization of the DOF in order of sensitivity. For this purpose, three groups of DOF were formed: (i) in-plane pose parameters ( $T_x$ ,  $T_y$ ,  $\Theta_z$ ); (ii) out-of-plane rotations ( $\Theta_x$ ,  $\Theta_y$ ); (iii) out-of-plane translation ( $T_z$ ). After this three sequential minimization, the RMSD was finally further minimized with respect to the 6 DOF simultaneously.

The second solution (*feat*) involved the use of features extracted from the image to get closer to the real pose before starting the minimization. Two features were calculated on the bone-contour points: (i) the direction of maximum variance of the distribution, and (ii) the farthest point from the field of view border among the projections of the bone-contour point along the maximum variance axis. The first feature was used to evaluate a first guess for the bone model orientation around the projection axis ( $\Theta_z$ ), while the in-plane translation components ( $T_x$ ,  $T_y$ ) were estimated using the second feature. The three DOF were modified iteratively until convergence, and then the minimization was started as previously described.

The analysis was repeated for each bone model, using *seq*, *feat* and *seq-feat* together, with 2 values of eps ( $10^{-1}$ – $10^{-4}$  mm/deg) and DMR = 0.5 mm.

**2.4. Data Analysis.** For each set of parameters, the final deviations between estimated and reference poses, and the relevant residual RMSD were quantified. Bias and precision of the final estimates of the pose were quantified calculating for each DOF the median ( $m$ ) and the interquartile range (*iqr*). For bias results, a Student's *t*-test ( $P < .05$ ) was performed to determine if the values were statistically different from zero, indicating the presence of a systematic error. Moreover, to measure how outlier-prone the distributions were, the kurtosis ( $k$ ) was also calculated.

To investigate the effects of the different minimization parameters (DMR, eps, *seq*, *feat*, bone models and initial deviations) on the final estimates and RMSD, an n-way analysis of variance (ANOVA) was performed considering a significance level  $\alpha = 0.05$  (with Bonferroni adjustment for multiple comparisons).

### 3. Results

**3.1. Sensitivity Analysis.** The cusp shape of RMSD with respect to each DOF, except  $T_z$ , was verified, while with respect to  $T_z$ , RMSD showed a rounder trend. In particular the trend of the cost function for the humerus is shown in Figure 3. Similar trends were obtained also for the ulna and the radius models.

For all the bone models analysed, the sensitivity analysis highlighted the presence of an evident global minimum in correspondence of the reference pose ( $\Delta T_i = 0$  and  $\Delta \theta_i = 0$ ,  $i = x, y, z$ ). This was true for all the 6 DOF but with higher sensitivity for the in-plane DOF, see Table 1. In particular, the highest sensitivity was obtained

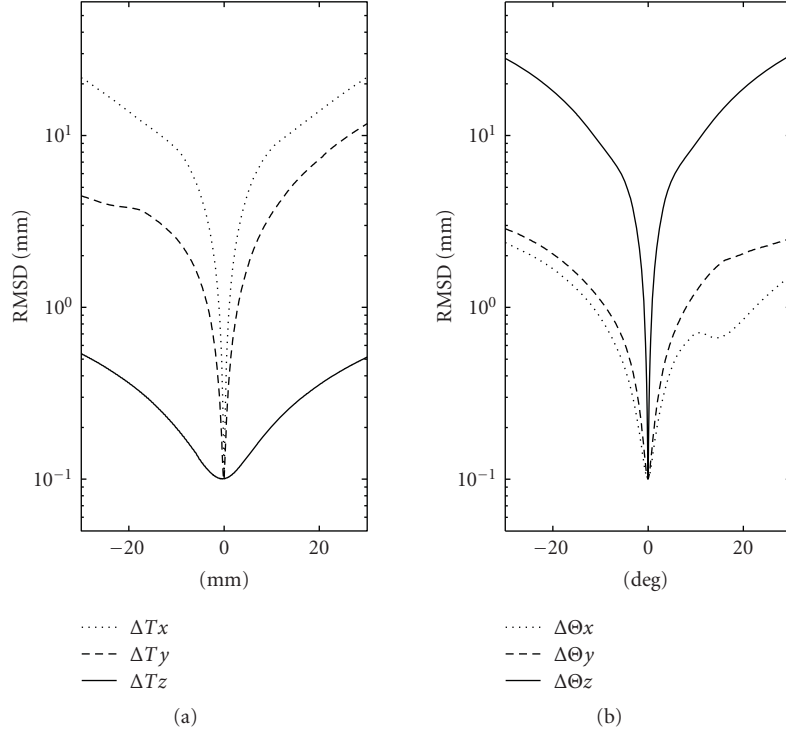


FIGURE 3: The root mean square distance RMSD plotted against the perturbation on the translations (a) and rotations (b) for the humerus bone. The RMSD forms a cusp around its minimum.

for  $\Theta z$  (mean value  $8.5e-1 \text{ mm} \cdot \text{deg}^{-1}$ ) while the smallest was obtained for  $T z$  (mean value  $1.2e-3 \text{ mm} \cdot \text{mm}^{-1}$ ). A clear local minimum, however, is shown for the humerus at approximately  $\Delta\theta x = 15 \text{ deg}$  (Figure 3), but was not found for the other bone models. All the sensitivity values of the radius, excepted  $S_{Tx}$  and  $S_{\theta z}$ , were approximately one order of magnitude smaller than those of ulna and humerus. The RMSD versus  $\Delta T y$  was asymmetric: since the analysed bone models were defined with the epicondyles in the middle of the imaging field, the RMSD grew faster when the model is moved further out of the imaging field ( $\Delta T y > 0 \text{ mm}$ ), slower in the opposite direction. The same behaviour was found also for ulna and radius, but, since the bone models were defined in the opposite part of the imaging field, the RMSD grew faster in the opposite direction, thus for  $\Delta T y < 0 \text{ mm}$ .

**3.2. Distance Map Resolution.** Results of the convergence domain analysis without conditioning (DMR = 1 mm and 0.5 mm;  $\text{eps} = 10^{-4} \text{ mm}/\text{deg}$ ) showed that a median error lower than 1 mm/deg was produced for each bone model and each DOF. The distributions, however, had large dispersions especially for  $T z$  and  $\Theta x$  ( $iqr > 5 \text{ mm}/\text{deg}$ ). Nevertheless, also for the other DOF we found numerous outliers:  $k$  ranged from a minimum of 8 ( $T y$  of the radius, DMR = 0.5 mm) to a maximum of 866 ( $\Theta z$  of the radius, DMR = 1 mm). For all three bone models, with  $\text{eps} = 10^{-1} \text{ mm}/\text{deg}$ , the  $iqr$  was larger than 1 mm/deg for in plane DOF and  $\Theta y$ , and larger than 10 mm/deg for  $\Theta x$  and  $T z$ . Generally, for all three

models and both values of  $\text{eps}$ , the interquartile ranges were always smaller when using a DMR = 0.5 mm rather than 1 mm ( $P < .05$ ). We report in Table 2 the results obtained for the radius, representing the most problematic case.

**3.3. Sequential Alignment.** The sequential alignment with DMR = 0.5 mm slightly decreased the number of local minima and outliers identified by the LM algorithm (Figure 4):  $k$  ranged from a minimum of 1.4 ( $T x$  of the ulna,  $\text{eps} = 10^{-4} \text{ mm}$ ) to a maximum of 265 ( $T z$  of the humerus,  $\text{eps} = 10^{-4} \text{ mm}$ ). The mean value of  $k$  between the models and the DOF was equal to 31 for  $\text{eps} = 10^{-4} \text{ mm}$ , and equal to 25 for  $\text{eps} = 10^{-1} \text{ mm}$ .

Using  $\text{eps} = 10^{-4} \text{ mm}/\text{deg}$ , the optimization of  $T x$ ,  $\Theta z$  and  $\Theta y$  resulted in median  $< 0.04 \text{ mm}/\text{deg}$ ,  $iqr < 0.10 \text{ mm}/\text{deg}$  even if  $\Theta y$  had a large number of outliers.  $T y$  had a median  $< 0.1 \text{ mm}/\text{deg}$ , with  $iqr < 0.50 \text{ mm}/\text{deg}$ : Figure 4 shows the outliers gathered together only for positive values of  $T y$ . Especially for the radius, the minimization process of  $\Theta x$  and  $T z$  tended to prematurely stop during its descent towards the global minimum, resulting in large dispersions (median  $< 0.05 \text{ mm}/\text{deg}$ ,  $iqr = 5.10 \text{ deg}$  and  $iqr = 4.10 \text{ mm}$ , respectively).

Increasing the step  $\text{eps}$  to  $10^{-1} \text{ mm}/\text{deg}$ , for all the three models, the median values for  $\Theta x$  and  $T z$  were smaller than  $0.08 \text{ mm}/\text{deg}$ , with a dispersion lower than  $0.45 \text{ mm}/\text{deg}$ .

**3.4. Features.** A further reduction of the number of outliers was introduced by the use of features to estimate an initial

TABLE 1: Sensitivity of the RMSD to the variation of the 6 DOF.

Model	$S_{Tx}$ [mm·mm $^{-1}$ ]	$S_{Ty}$ [mm·mm $^{-1}$ ]	$S_{Tz}$ [mm·mm $^{-1}$ ]	$S_{\Theta_x}$ [mm·deg $^{-1}$ ]	$S_{\Theta_y}$ [mm·deg $^{-1}$ ]	$S_{\Theta_z}$ [mm·deg $^{-1}$ ]
humerus	$5.5e-1$	$9.6e-2$	$1.5e-3$	$8.2e-3$	$1.6e-2$	$8.0e-1$
radius	$5.7e-1$	$7.6e-2$	$0.5e-3$	$1.0e-3$	$0.3e-2$	$9.2e-1$
ulna	$5.3e-1$	$1.6e-1$	$1.5e-3$	$5.0e-3$	$2.0e-2$	$8.4e-1$

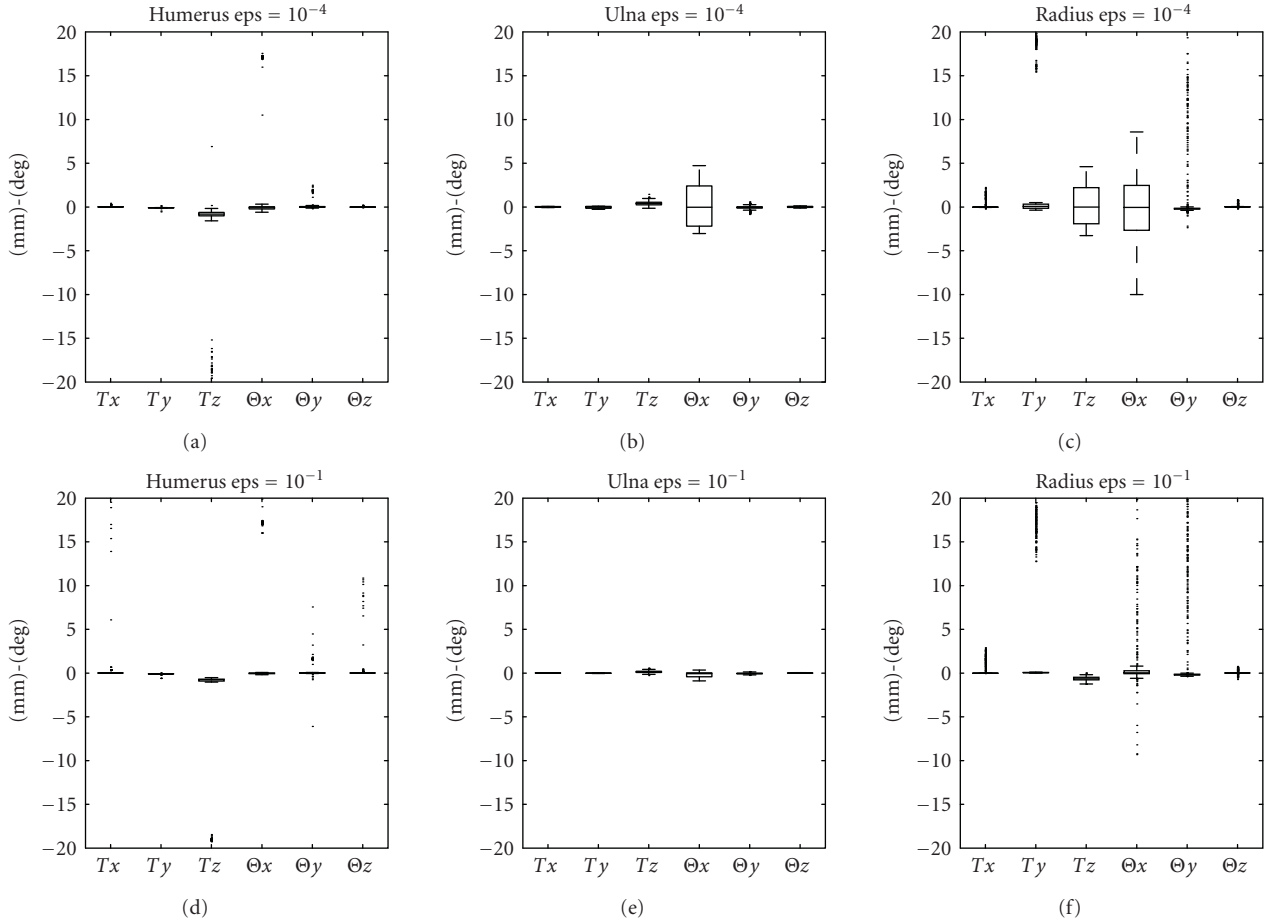
FIGURE 4: Box and whisker plots of the *seq* alignment with DMR = 0.5, (panels a, b, c)  $\epsilon = 10^{-4}$  mm/deg, or  $\epsilon = 10^{-1}$  mm/deg (panels d, e, f).

TABLE 2: Effects of the distance map resolution on the pose parameters estimates for the radius model.

DOF	DMR = 1 mm			DMR = 0.5 mm		
	$m$	$iqr$	$k$	$m$	$iqr$	$k$
$T_x$ [mm]	-0.03	0.01	20.2	-0.02	0.01	50.7
$T_y$ [mm]	0.26	0.75	8.4	0.21	0.48	9.7
$T_z$ [mm]	0.79	7.15	16.6	-0.2	4.41	47.3
$\Theta_x$ [deg]	-0.05	8.5	76.8	-0.11	5.5	74.1
$\Theta_y$ [deg]	-0.22	0.12	140.2	-0.19	0.1	293.7
$\Theta_z$ [deg]	0.02	0.02	307.8	0.01	0.02	866.2

guess for the in-plane DOF, (Figure 5). As for the sequential alignment, the use of a big step ( $\epsilon = 10^{-1}$ ) for the FD Jacobian computation, increased the precision of the

estimations of  $\Theta_x$  and  $T_z$  (for the radius  $iqr = 0.31$  deg and  $iqr = 0.24$  mm, resp.). The estimation of  $T_z$  was biased for the humerus and radius with medians approximately equal to -0.7 mm, as was  $\Theta_y$  of the radius (median equal to 0.2 deg), while for the other DOF and for the ulna the median values were always lower than 0.01 mm/deg. Considering the humerus and both the values of  $\epsilon$ , the LM algorithm sometimes converged to the local minimum shown in Figure 5 ( $T_z \approx -18$  mm,  $\Theta_x \approx +18$  mm), keeping the value of  $k$  high (medium values: 62 for the humerus, 2.8 for the ulna, 3.3 for the radius).

**3.5. Features and Sequential Alignment.** The simultaneous use of *feat* and *seq* had no significant effect on the final RMSD, nor on the errors of the single DOF estimates ( $P > .05$ ). The final results obtained for humerus, ulna and radius

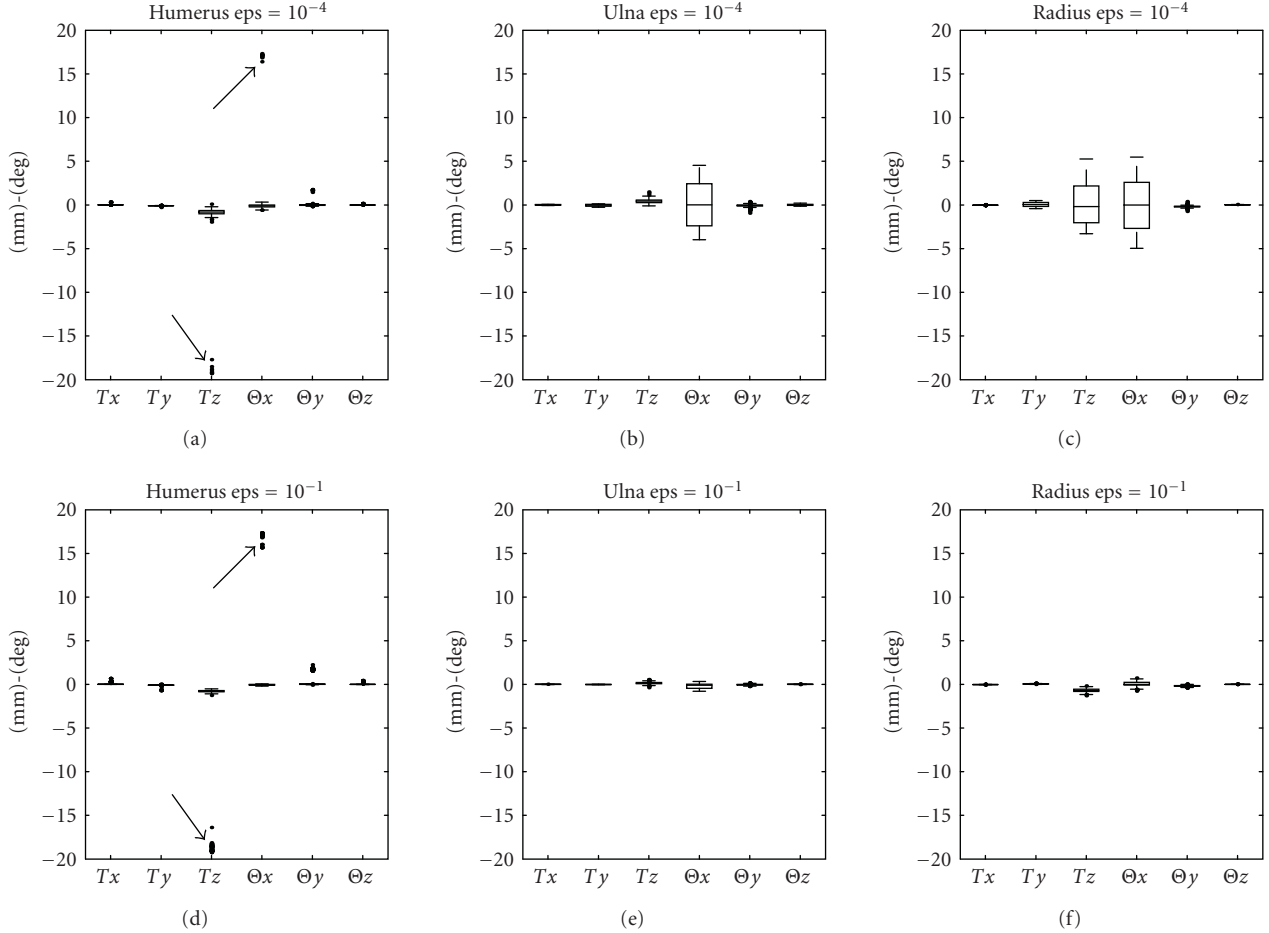


FIGURE 5: Box and whisker plots of the *feat* alignment with DMR = 0.5, (panels a, b, c)  $\text{eps} = 10^{-4}$  mm/deg, or  $\text{eps} = 10^{-1}$  mm/deg (panels d, e, f).

with  $\text{eps} = 10^{-1}$  mm/deg, and DMR = 0.5 mm are reported in Table 3. The *t*-test showed that the final estimates were always statistically different from 0, thus biased.

#### 4. Discussion

In this work, a sensitivity analysis and a convergence domain analysis of the minimization algorithm for the pose estimation in 3D video-fluoroscopy were addressed.

The sensitivity analysis showed that the cost function (RMSD) varies differently with each DOF: the in-plane pose parameters have a sensitivity at least one order of magnitude larger than the out-of-plane pose parameters. Moreover, the performed simulation showed that the cost function could have different behaviours depending on the analysed segment (Figure 3): considering  $\Theta x$ , we found a clear local minimum for the humerus but not for ulna and radius. For all three models, the RMSD with respect to  $Ty$  showed an asymmetric trend. That is due to the fact that only a partial part of the bone is included in the imaging field (Figure 2), thus, given the long diaphysis of the bone, two different scenarios occur while moving the model along the  $y$ -axis: if the models moves further into the imaging field,

the projection lines coming from the bone contour points intersect or pass near to the model surface, continuing to give only a little contribution to the increment of the cost function. On the other hand, if the model moves further out of the imaging field, there is no model surface for part of the projection lines to intersect with, increasing their contribution to the cost function. The findings about the RMSD explained the behaviour of the unconditioned LM algorithm, which was found to be noticeably sensitive to the local minima of the RMSD. Given the longitudinal cylindrical symmetry, the estimations of the pose of long bones were affected by large dispersions not only for  $Tz$ , as previously thoroughly reported for the knee prostheses, but also for  $\Theta x$  (see Table 2). Moreover, for the DOF with relative small *iqr* such as the in-plane pose parameters, the values of  $k$  were high ( $>8$ ), that is the distributions were affected by large number of outliers. The ANOVA confirmed the hypothesis that the higher is the resolution of the distance map (DMR) the more the accuracy and the precision of the technique increase ( $P < .05$ ). However, given the limits of the resolution of the fluoroscopic image and of the surface model mesh, a further increasing of DMR would be unnecessary. For the unconditioned minimization, varying the step for the

TABLE 3: Final accuracy in terms of median ( $m$ ), interquartile range ( $iqr$ ) and kurtosis ( $k$ ) of the pose estimations, for the three bone models with the *seq-feat* alignment.

DOF	Humerus			Ulna			Radius		
	$m$	$iqr$	$k$	$m$	$iqr$	$k$	$m$	$iqr$	$k$
$T_x$ [mm]	0.003	0.004	14.0	0.005	0.008	3.0	-0.021	0.006	4.8
$T_y$ [mm]	-0.087	0.005	73.7	-0.018	0.025	2.2	0.051	0.025	3.1
$T_z$ [mm]	-0.766	0.153	5.0	0.132	0.155	3.3	-0.692	0.260	3.1
$\Theta_x$ [deg]	-0.045	0.090	4.9	-0.071	0.474	2.0	0.017	0.317	3.1
$\Theta_y$ [deg]	0.011	0.032	5.6	-0.044	0.086	3.2	-0.195	0.073	4.2
$\Theta_z$ [deg]	0.001	0.011	26.8	0.007	0.019	2.9	0.007	0.003	4.9

FD Jacobian computation (eps) from  $10^{-4}$  to  $10^{-1}$  mm/deg induced a further instability.

To solve the convergence problems of the LM algorithm, the effect of the *seq* alignment on the minimization process was evaluated. When the initial conditions are too far from the reference pose, if not conditioned, the pure algorithm tries to explore the value of the cost function varying all the 6 DOF simultaneously, risking to move the less sensitive DOF away from the global solution. With the *seq* alignments, instead, the DOF with larger convergence domain are aligned in a first step, while the more critical (out-of-plane) DOF are minimized only when closed to the reference pose. Although this technique leads to an improvement of the precision of the estimate (Figure 4), the algorithm is still sensitive to local minima, or to local low-sensitivity areas of the cost function that can occur also for the in-plane pose parameters, such as for  $T_y$  (Figure 3). This could be the cause for the still high number of outliers (mean of  $k > 25$ ) obtained with the *seq* alignment. Varying eps from  $10^{-4}$  to  $10^{-1}$  mm/deg permitted to improve the performance of the optimization avoiding the early convergence for the less sensitive DOF ( $T_z$  and  $\Theta_x$ , Figure 4). However the problems of convergence are not completely solved, probably because two different DOF could have a correlated effect on the RMSD, thus, a sequential minimization could interfere with a proper descending to the global minimum.

The use of features completely avoided the problems of the *seq* alignment, because, differently from *seq*, the *feat* alignment is completely independent from the RMSD and, thus, from its local minima. For our simulations, we used two simple features: (i) the direction of maximum variance of the distribution of bone-contour points to extrapolate  $\Theta_z$ , and (ii) a characteristic point such as the farthest from the field of view border for  $T_x$ ,  $T_y$ . These features are particularly suitable for long bones, which cannot be completely included in the field of view; for short bones or prosthesis, however, the mean of the coordinates of the contour points can equally be used. These minimization settings, together with a FD Jacobian step  $\text{eps} = 10^{-1}$  (bigger enough to filter small noisy fluctuation of the RMSD), permitted to significantly reduce  $m$ ,  $iqr$ , and  $k$ .

Even if the combined effects of *feat* and *seq* did not introduce further improvements ( $P$ -value  $> .05$ ), with a fine tuning of the minimization parameters, a high level of precision can be achieved ( $iqr < 0.025$  mm/deg for

in-plane pose parameters,  $iqr < 0.5$  mm/deg for out-of-plane pose parameters) but with a high variability between the models (i.e., considering  $\Theta_x$ ,  $iqr$  equal to 0.09 deg for the humerus, and equal to 0.47 deg for the ulna), confirming the hypothesis that the performances of the method should be assessed for each bone model to be analysed. The results also showed that the final estimate is biased. This is due to the intrinsic limitations of the technique given by the resolution of the fluoroscopic projections and of the distance maps. Moreover, in spite of the fine tuning of the optimization parameters, the local minima showed in Figure 3 of the RMSD versus  $\Theta_x$  for the humerus, seldom caused the LM minimization algorithm to detect false poses. These false poses can generally be easily identified by an operator with a visual feedback of the alignment and, in such cases, the minimization can be repeated starting from a different initial condition.

The results of this study confirm that the accuracy and the precision that can be achieved, especially with the *feat* alignment, allow the technique to be suitable for the kinematic study of the elbow, but without excluding the complete independence by the operator.

## 5. Conclusions

In the present work, we proposed an analytical process to evaluate the performance of 3D video-fluoroscopy for its application to the analysis of kinematics of long bones, by means of *in-silico* simulations. The effects of the dominant sources of error such as bone symmetries, distance map resolution and image spacing, were investigated. Solutions were proposed to improve the accuracy and the precision of the method.

Given the high variability of the morphology of the bones or prostheses that could be analysed with 3D video-fluoroscopy, different performance assessment studies should be carried out before undertaking any new application of the technique, especially for clinical purpose. We focused on the elbow because it allowed to investigate different characteristics of 3D video-fluoroscopy applied to long bones. Compared to knee prosthesis, which have been deeply studied during the past years with 3D fluoroscopy [10–12], the marked cylindrical longitudinal symmetries of long bones constitute a dominant disturbing factor that could interfere with the final accuracy of the technique.



FIGURE 6: Real fluoroscopic image of the elbow: note the superimposition of bones and the low-contrast contours and the results of the Canny edge detection for the humerus.

The robustness of the alignment algorithm applied to the elbow joint was completely characterized. Even if the convergences to local minima was not completely avoided, with a proper conditioning and a fine tuning of the minimization algorithm parameters, excellent results can be achieved in term of low bias and high precision. Moreover, the methods and the findings addressed in this work focusing on monoplanar projections, can easily be extended also to biplanar 3D video-fluoroscopy.

In order to achieve a complete automation of the pose estimation algorithm, the problem of local minima should be completely solved. Robust optimization algorithms based on simulated annealing [13] or on Unscented Kalman Filtering [44] have been proposed. These techniques will be implemented and evaluated in future works in combination with the conditioning of minimization based on *feat* and *seq* which was proven to effectively improve the performance of LM. However, the bias errors committed will not be avoided with either of these robust techniques, because the errors are due to characteristics intrinsic to the monoplanar fluoroscopic analysis. Furthermore, when considering other sources of error typical of real fluoroscopic sessions such as the geometric distortions, surface model inaccuracies, errors in the calibration of the fluoroscopic models, and incompleteness of the bone contours, the accuracy would certainly worsen (Figure 6).

Again, all these considerations are to confirm that for application to the kinematics of any particular joint, a detailed validation study should be carried out, especially for clinical studies. The accuracy and the precision achieved with the *feat* alignment, allow the technique to be suitable for the kinematic study of the elbow, and most likely even of other long bones, however further *in-vitro* validation must be carried out.

## References

- [1] R. Stagni, S. Fantozzi, A. G. Cutti, and A. Cappello, "Kinematic analysistechniques and their application in biomechanics," in *Biomedical Systemtechnolog: Muscular Skeletal System*, C. Leondes, Ed., vol. 4, pp. 135–183, World Scientific, 2009.
- [2] S. Zuffi, A. Leardini, F. Catani, S. Fantozzi, and A. Cappello, "A model-based method for the reconstruction of total knee replacement kinematics," *IEEE Transactions on Medical Imaging*, vol. 18, no. 10, pp. 981–991, 1999.
- [3] S. Hirokawa, M. Abrar Hossain, Y. Kihara, and S. Ariyoshi, "A 3D kinematic estimation of knee prosthesis using X-ray projection images: clinical assessment of the improved algorithm for fluoroscopy images," *Medical and Biological Engineering and Computing*, vol. 46, no. 12, pp. 1253–1262, 2008.
- [4] P. M. Ludewig and J. F. Reynolds, "The association of scapular kinematics and glenohumeral joint pathologies," *Journal of Orthopaedic & Sports Physical Therapy*, vol. 39, no. 2, pp. 90–104, 2009.
- [5] S. Tashman, P. Kolowich, D. Collon, K. Anderson, and W. Anderst, "Dynamic function of the ACL-reconstructed knee during running," *Clinical Orthopaedics and Related Research*, vol. 454, pp. 66–73, 2007.
- [6] D. A. Dennis, M. R. Mahfouz, R. D. Komistek, and W. Hoff, "In vivo determination of normal and anterior cruciate ligament-deficient knee kinematics," *Journal of Biomechanics*, vol. 38, no. 2, pp. 241–253, 2005.
- [7] A. Cappello, R. Stagni, S. Fantozzi, and A. Leardini, "Soft tissue artifact compensation in knee kinematics by double anatomical landmark calibration: performance of a novel method during selected motor tasks," *IEEE Transactions on Biomedical Engineering*, vol. 52, no. 6, pp. 992–998, 2005.
- [8] S. A. Banks and W. A. Hodge, "Accurate measurement of three-dimensional knee replacement kinematics using single-plane fluoroscopy," *IEEE Transactions on Biomedical Engineering*, vol. 43, no. 6, pp. 638–649, 1996.
- [9] J. B. Stiehl, R. D. Komistek, D. A. Dennis, R. D. Paxson, and W. A. Hoff, "Fluoroscopic analysis of kinematics after posterior-cruciate-retaining knee arthroplasty," *The Journal of Bone and Joint Surgery. British*, vol. 77, no. 6, pp. 884–889, 1995.
- [10] S. Fantozzi, A. Leardini, S. A. Banks, M. Marcacci, S. Giannini, and F. Catani, "Dynamic in-vivo tibio-femoral and bearing motions in mobile bearing knee arthroplasty," *Knee Surgery, Sports Traumatology, Arthroscopy*, vol. 12, no. 2, pp. 144–151, 2004.
- [11] D. A. Dennis, R. D. Komistek, M. R. Mahfouz, B. D. Haas, and J. B. Stiehl, "Multicenter determination of in vivo kinematics after total knee arthroplasty," *Clinical Orthopaedics and Related Research*, no. 416, pp. 37–57, 2003.
- [12] S. A. Banks, G. D. Markovich, and W. A. Hodge, "In vivo kinematics of cruciate-retaining and -substituting knee arthroplasties," *The Journal of Arthroplasty*, vol. 12, no. 3, pp. 297–304, 1997.
- [13] M. R. Mahfouz, W. A. Hoff, R. D. Komistek, and D. A. Dennis, "A robust method for registration of three-dimensional knee implant models to two-dimensional fluoroscopy images," *IEEE Transactions on Medical Imaging*, vol. 22, no. 12, pp. 1561–1574, 2003.
- [14] R. D. Komistek, D. A. Dennis, and M. Mahfouz, "In vivo fluoroscopic analysis of the normal human knee," *Clinical Orthopaedics and Related Research*, no. 410, pp. 69–81, 2003.
- [15] R. D. Komistek, J. B. Stiehl, F. F. Buechel, E. J. Northcut, and M. E. Hajner, "A determination of ankle kinematics using

- fluoroscopy," *Foot and Ankle International*, vol. 21, no. 4, pp. 343–350, 2000.
- [16] D. A. Dennis, R. D. Komistek, E. J. Northcut, J. A. Ochoa, and A. Ritchie, "In vivo" determination of hip joint separation and the forces generated due to impact loading conditions," *Journal of Biomechanics*, vol. 34, no. 5, pp. 623–629, 2001.
  - [17] R. D. Komistek, D. A. Dennis, J. A. Ochoa, B. D. Haas, and C. Hammill, "In vivo comparison of hip separation after metal-on-metal or metal-on-polyethylene total hip arthroplasty," *The Journal of Bone and Joint Surgery. American*, vol. 84, no. 10, pp. 1836–1841, 2002.
  - [18] W. A. Hoff, R. D. Komistek, D. A. Dennis, S. M. Gabriel, and S. A. Walker, "Three-dimensional determination of femoral-tibial contact positions under in vivo conditions using fluoroscopy," *Clinical Biomechanics*, vol. 13, no. 7, pp. 455–472, 1998.
  - [19] D. Tomazevic, B. Likar, T. Slivnik, and F. Pernus, "3-D/2-D registration of CT and MR to X-ray images," *IEEE Transactions on Medical Imaging*, vol. 22, no. 11, pp. 1407–1416, 2003.
  - [20] D. B. Russakoff, T. Rohlfing, K. Mori, et al., "Fast generation of digitally reconstructed radiographs using attenuation fields with application to 2D-3D image registration," *IEEE Transactions on Medical Imaging*, vol. 24, no. 11, pp. 1441–1454, 2005.
  - [21] P. W. de Bruin, B. L. Kaptein, B. C. Stoel, J. H. C. Reiber, P. M. Rozing, and E. R. Valstar, "Image-based RSA: roentgen stereophotogrammetric analysis based on 2D-3D image registration," *Journal of Biomechanics*, vol. 41, no. 1, pp. 155–164, 2008.
  - [22] B.-M. You, P. Siy, W. Anderst, and S. Tashman, "In vivo measurement of 3-D skeletal kinematics from sequences of biplane radiographs: application to knee kinematics," *IEEE Transactions on Medical Imaging*, vol. 20, no. 6, pp. 514–525, 2001.
  - [23] W. Anderst, R. Zauel, J. Bishop, E. Demps, and S. Tashman, "Validation of three-dimensional model-based tibio-femoral tracking during running," *Medical Engineering & Physics*, vol. 31, no. 1, pp. 10–16, 2009.
  - [24] B. J. Fregly, H. A. Rahman, and S. A. Banks, "Theoretical accuracy of model-based shape matching for measuring natural knee kinematics with single-plane fluoroscopy," *Journal of Biomechanical Engineering*, vol. 127, no. 4, pp. 692–699, 2005.
  - [25] H. E. J. Veeger, B. Yu, K.-N. An, and R. H. Rozendal, "Parameters for modeling the upper extremity," *Journal of Biomechanics*, vol. 30, no. 6, pp. 647–652, 1997.
  - [26] A. Ericson, A. Arndt, A. Stark, P. Wretenberg, and A. Lundberg, "Variation in the position and orientation of the elbow flexion axis," *The Journal of Bone and Joint Surgery. British*, vol. 85, no. 4, pp. 538–544, 2003.
  - [27] D. Eygendaal, E. R. Valstar, J. O. Söjbjerg, and P. M. Rozing, "Biomechanical evaluation of the elbow using roentgen stereophotogrammetric analysis," *Clinical Orthopaedics and Related Research*, no. 396, pp. 100–105, 2002.
  - [28] F. Schuind, S. O'Driscoll, S. Korinek, K. N. An, and B. F. Morey, "Loose-hinge total elbow arthroplasty: an experimental study of the effects of implant alignment on three-dimensional elbow kinematics," *The Journal of Arthroplasty*, vol. 10, no. 5, pp. 670–678, 1995.
  - [29] R. Schmidt, C. Disselhorst-Klug, J. Silny, and G. Rau, "A marker-based measurement procedure for unconstrained wrist and elbow motions," *Journal of Biomechanics*, vol. 32, no. 6, pp. 615–621, 1999.
  - [30] A. Goto, H. Moritomo, T. Murase, et al., "In vivo elbow biomechanical analysis during flexion: three-dimensional motion analysis using magnetic resonance imaging," *Journal of Shoulder and Elbow Surgery*, vol. 13, no. 4, pp. 441–447, 2004.
  - [31] A. G. Cutti, G. Paolini, M. Troncoss, A. Cappello, and A. Davalli, "Soft tissue artefact assessment in humeral axial rotation," *Gait & Posture*, vol. 21, no. 3, pp. 341–349, 2005.
  - [32] R. Stagni, S. Fantozzi, A. Cappello, and A. Leardini, "Quantification of soft tissue artefact in motion analysis by combining 3D fluoroscopy and stereophotogrammetry: a study on two subjects," *Clinical Biomechanics*, vol. 20, no. 3, pp. 320–329, 2005.
  - [33] S. Lavallee and R. Szeliski, "Recovering the position and orientation of free-form objects from image contours using 3D distance maps," *IEEE Transactions on Pattern Analysis and Machine Intelligence*, vol. 17, no. 4, pp. 378–390, 1995.
  - [34] J. Canny, "A computational approach to edge detection," *IEEE Transactions on Pattern Analysis and Machine Intelligence*, vol. 8, no. 6, pp. 679–698, 1986.
  - [35] D. W. Marquardt, "An algorithm for least-squares estimation of nonlinear parameters," *SIAM Journal on Applied Mathematics*, vol. 11, no. 2, pp. 431–441, 1963.
  - [36] "VXL—C++ Libraries for Computer Vision," July 2009, <http://vxl.sourceforge.net>.
  - [37] M.-M. Yau and S. N. Srihari, "A hierarchical data structure for multidimensional digital images," *Communications of the ACM*, vol. 26, no. 7, pp. 504–515, 1983.
  - [38] J. Chouteau, J. L. Lerat, R. Testa, B. Moyen, and S. A. Banks, "Effects of radiograph projection parameter uncertainty on TKA kinematics from model-image registration," *Journal of Biomechanics*, vol. 40, no. 16, pp. 3744–3747, 2007.
  - [39] E. Gronenschild, "Correction for geometric image distortion in the x-ray imaging chain: local technique versus global technique," *Medical Physics*, vol. 26, no. 12, pp. 2602–2616, 1999.
  - [40] E. Gronenschild, "The accuracy and reproducibility of a global method to correct for geometric image distortion in the X-ray imaging chain," *Medical Physics*, vol. 24, no. 12, pp. 1875–1888, 1997.
  - [41] S. Fantozzi, A. Cappello, and A. Leardini, "A global method based on thin-plate splines for correction of geometric distortion: an application to fluoroscopic images," *Medical Physics*, vol. 30, no. 2, pp. 124–131, 2003.
  - [42] "Virtual animation of the kinematics of the human for industrial, educational and research purposes," August 2009, <http://www.ulb.ac.be/project/vakhum/public.dataset/public-data.htm>.
  - [43] G. Wu, F. C. T. van der Helm, H. E. J. (DirkJan) Veeger, et al., "ISB recommendation on definitions of joint coordinate systems of various joints for the reporting of human joint motion—part II: shoulder, elbow, wrist and hand," *Journal of Biomechanics*, vol. 38, no. 5, pp. 981–992, 2005.
  - [44] R. H. Gong, P. Abolmaesumi, and J. Stewart, "A robust technique for 2D-3D registration," in *Proceedings of the 28th Annual International Conference of the IEEE Engineering in Medicine and Biology*, pp. 1433–1436, New York, NY, USA, August-September 2006.

## Research Article

# Efficient and Low-Cost 3D Structured Light System Based on a Modified Number-Theoretic Approach

**Tomislav Pribanić,<sup>1</sup> Hrvoje Džapo,<sup>1</sup> and Joaquim Salvi<sup>2</sup>**

<sup>1</sup>Faculty of Electrical Engineering and Computing, University of Zagreb, Unska 3, 10000 Zagreb, Croatia

<sup>2</sup>Institute of Informatics and Applications, University of Girona, Avenue Lluís Santalo s/n, 17071 Girona, Spain

Correspondence should be addressed to Tomislav Pribanić, tomislav.pribanic@fer.hr

Received 8 May 2009; Revised 10 August 2009; Accepted 24 October 2009

Academic Editor: João Manuel R. S. Tavares

Copyright © 2010 Tomislav Pribanić et al. This is an open access article distributed under the Creative Commons Attribution License, which permits unrestricted use, distribution, and reproduction in any medium, provided the original work is properly cited.

3D scanning based on structured light (SL) has been proven to be a powerful tool to measure the three-dimensional shape of surfaces, especially in biomechanics. We define a set of conditions that an optimal SL strategy should fulfill in the case of static scenes and then we present an efficient solution based on improving the number-theoretic approach (NTA). The proposal is compared to the well-known Gray code (GC) plus phase shift (PS) technique and the original NTA, all satisfying the same set of conditions but obtaining significant improvements with our implementation. The technique is validated in biomechanical applications such as the scanning of a footprint left on a “foam box” typically made for that purpose, where one of the ultimate goals could be the production of a shoe insole.

## 1. Introduction

Structured light (SL) upgrades a passive stereo camera system and becomes a powerful tool to achieve dense 3D acquisition [1]. In the simplest case, one of the cameras is typically replaced by a pattern projector such as a digital light projector (DLP) or a liquid crystal display (LCD). The task of the projector is to project patterns (images) with a given texture so that pattern pixels are coded in a certain way. Consequently, on the object's surface the projector imposes a known code (texture) that is then acquired by a camera. The detection of correspondences between projected and imaged codes allows triangulation and hence the computation of the 3D position of those codes on the measuring surface [2].

Considering the typical restrictions of the large number of SL methods, we define a set of conditions (SoCs) that optimal SL patterns should comply with the following.

- (1) Every pixel of the projected pattern should contain the entire code and therefore potentially yield a corresponding 3D point. This will create the conditions for high-resolution 3D reconstruction.

- (2) There should be high distance between the code words of neighboring pixels. This will allow high sensitivity to spatial depth resolution.
- (3) There should be robustness to object color/albedo reflectance properties. Any particular color calibration adjustments or restrictions to the ambient light should be avoided. This will assure almost immediate system use and applicability to various types of object surfaces and ambient light scenarios.
- (4) There should be robustness to objects with sharp discontinuities and depth changes. This will guard against the problem of possible code perturbation and its misinterpretation during the decodification stage.
- (5) The patterns should assure full 3D reconstruction where all three spatial coordinates of the object shape are attainable. In other words, ultimately computing only the depth coordinate with respect to one reference plane will not be satisfactory.
- (6) Simple image processing of the acquired patterns, ideally the only image processing used, should consist

of addition, multiplication, comparison, and look-up table indexing. More complex image processing, such as finding edges, corners, detecting various shapes, centers of stripes, and color thresholding, should be avoided. Simple image processing will allow relatively easy implementation from a software point of view and fast processing, hopefully comparable with state-of-the-art commercial products.

- (7) Only off-the-shelf components should be used. No special devices such as special lights sources or colorimeters should be part of the system. This will allow easy and affordable implementation from a hardware point of view.

One of the most powerful SL methods is phase shifting (PS), classified into time multiplexing strategies [3]. PS projects a sequence of periodic intensity patterns, so that every subsequent pattern is offset by a fraction of its period with respect to the previous pattern, covering the entire period. As a result, the so-called relative phase map (also periodic) is obtained, in which values readily available from the relative phase map are said to be wrapped in the range modulo  $2\pi$ . Note that if there were not unwrapping problem, PS would perfectly fit SoC. A widely accepted solution to solve ambiguity of a single PS wrapped map is to combine it with Gray code (GC) [4]. The GC+PS technique is very effective and frequently regarded as the method of choice for the reconstruction of static objects [5]. In this case, the particular pattern period used to create the PS wrapped map is usually determined by the GC word length, since GC essentially codes the areas within every pattern period. However, there are research fields such as interferometry, where it is particularly convenient to work with patterns with variable periodicity. This type of research proposed a rather simple unwrapping solution called spatial unwrapping, which basically only works well on smooth surfaces since it assumes during the unwrapping procedure that the phase difference between neighboring pixels is less than  $\pi$ . An extension of this technique proposed an additional color-coded pattern, giving so a rough estimate to be used during the spatial unwrapping, at the expense that a colored pattern is basically restricted to color neutral objects [6]. Specially made hardware can be used to solve the problem of unwrapping [7]. Other proposed solutions concerned temporal phase unwrapping [8], which uses several wrapped PS maps and occasionally is referred to as multiple phase shifting (MPS). The simplest MPS unwrapping principle comes down to summing the wrapped phase differences between individual PS maps. Unfortunately, in order to achieve accurate 3D reconstruction, the amount of PS maps is typically fairly large in practice, for example, 20–30 maps as shown in [8]. Significant improvements appeared when the number of PS maps was reduced from  $N$  to  $\log_2 N$  [9], during which the periods of various PS maps follow a shorter exponential or other sequence [10, 11]. A very appealing approach was originally introduced by Gushov and Solodkin (referred to further as the G-S method) [12]. G-S is based on the number theoretic approach (NTA) where only two

patterns, with a larger number of periods, are considered, which is in theory sufficient to provide highly accurate 3D results (note that the number of periods has a direct effect on condition 2 in SoC). G-S is very fast since it comes down to the use of linear equations in which the inputs are simply the wrapped phases. Unfortunately, the straightforward implementation is very affected by unavoidable errors in wrapped phase computations. An interesting improvement is presented in [13] where the matrix of possible solutions is defined. Unfortunately, the computational time is related to the size of the search space, which dictates the probability that the right solution is contained within. Other usual improvements were offered in the form of more evolved 3D system design or the construction of look-up tables (LUTs), both of which might not be practical [14–16]. A typical problem with LUT is finite size, which limits the physical resolution. An alternative is to increase the size of LUT which leads to an increase in cost and computing time.

In this work we propose an MPS method based on significant improvements of a basic G-S. Our method checks and corrects, if necessary, the wrapped phase values obtained before the unwrapping computation is performed. In consequence, we do not need to use any LUT. We can readily use the wrapped values within the original G-S method to obtain a reliable unwrapped map. Consequently, our method is not influenced by wrapped phase computation inaccuracies as the original G-S method is and, besides, it is faster than common LUT-based (search) methods.

The remainder of this paper is structured as follows. In Section 2, we briefly explain the original G-S method and how it can be adapted to MPS pointing out the major problems. In Section 3, we present our proposal for overcoming such limitations and compare it to other SL techniques. Section 4 presents the setup of our system. Section 5 includes an experimental evaluation of our method compared to the original G-S and GC+PS. Finally, we conclude by recalling the major points of the presented work.

## 2. Application of the Number-Theoretic Approach in Multiphase Shifting

Two integer numbers  $\Phi_{ABS}$  and  $\varphi_R$  are in congruence if they give the same remainder when they are divided by a given number  $\lambda$ . Hence,  $\Phi_{ABS}$  and  $\varphi_R$  are said to be congruent modulo  $\lambda$ , as depicted in,

$$\Phi_{ABS} \equiv \varphi_R \pmod{\lambda}. \quad (1)$$

G-S takes advantage of a simultaneous solution to the following congruence equations:

$$\begin{aligned} \Phi_{ABS} &\equiv \varphi_{R1} \pmod{\lambda_1}, \\ \Phi_{ABS} &\equiv \varphi_{R2} \pmod{\lambda_2}, \\ &\vdots \\ \Phi_{ABS} &\equiv \varphi_{Rk} \pmod{\lambda_k}, \end{aligned} \quad (2)$$

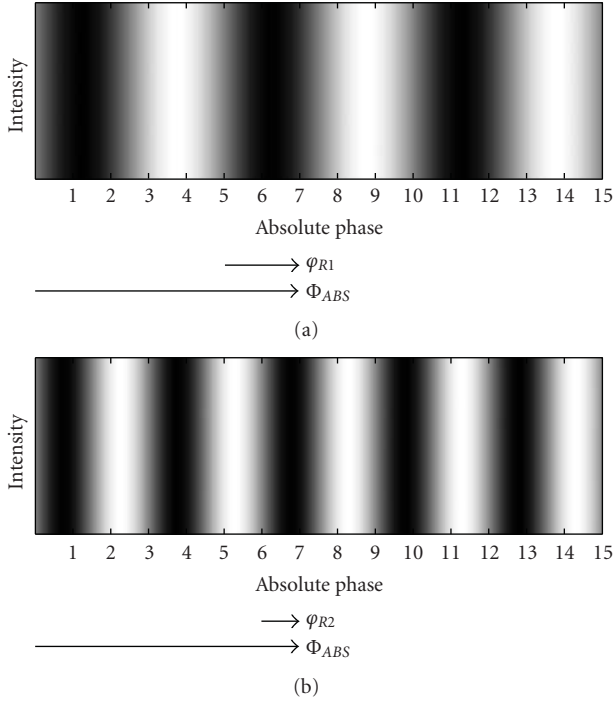


FIGURE 1: An example of two periodic intensity patterns and their relation to wrapped PS values.

where  $\Phi_{ABS}$  and  $\varphi_{R_i}$  are integers and  $\lambda_i$  are positive integers but also relative primes. A solution to (2) is provided by the famous Chinese remainder theorem [17] depicted in,

$$\Phi_{ABS} \equiv \sum_{i=1}^k \varphi_{R_i} \cdot e_i \pmod{\lambda_1 \cdot \lambda_2 \cdots \lambda_k}, \quad (3)$$

where the coefficients  $e_i$  can be computed as follows:

$$\begin{aligned} e_i &\equiv 1 \pmod{\lambda_i}, \\ e_i &\equiv 0 \pmod{\lambda_j}, \quad i \neq j. \end{aligned} \quad (4)$$

Next consider, as shown in Figure 1, an ideal appearance of two sinusoidal periodic patterns (corresponding to wavelengths  $\lambda_1 = 5$  and  $\lambda_2 = 3$ , resp.) which are meant to be projected and shifted. The abscissa axis corresponds to the unwrapped phase. Hence, every abscissa coordinate has a wrapped phase value, acquired throughout the pattern projection and shifting process, relative to the beginning of a period (e.g.,  $\varphi_{R1}=2$  or  $\varphi_{R2}=1$  as shown in Figure 1). Evidently, the following conditions hold:

$$\Phi_{ABS} = k_1 \cdot \lambda_1 + \varphi_{R1} = k_2 \cdot \lambda_2 + \varphi_{R2}, \quad (5)$$

where  $k_1$  and  $k_2$  are the number of periods typically unknown in practice, but necessary to reach some corresponding  $\Phi_{ABS}$  unwrapped value given some known  $\varphi_{R1}$  and  $\varphi_{R2}$ . Note that both  $\Phi_{ABS}$  and  $\varphi_{R1}$  divided by  $\lambda_1$  give the same remainder,  $\varphi_{R1}$ . Similarly  $\Phi_{ABS}$  and  $\varphi_{R2}$  divided by  $\lambda_2$  give the same remainder,  $\varphi_{R2}$ . Hence, we can set up a system of congruence equations (2) and find a solution for  $\Phi_{ABS}$  (3).

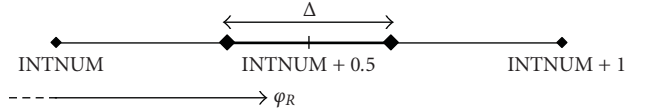


FIGURE 2: Segment on the unwrapped phase axis between two integer numbers [INTNUM, INTNUM+1].

Until now and for simplicity we have assumed integer values for the wrapped phases  $\varphi_{R1}$  and  $\varphi_{R2}$ . Of course, in practice,  $\varphi_{R1}$  and  $\varphi_{R2}$  are real numbers. Usually, the integer part is considered as an initial guess for computing  $\Phi_{ABS}$  in (3). Then, ideally, the fractional parts  $\varphi_{R1FRAC}$  and  $\varphi_{R2FRAC}$  of both wrapped phases should be equal. However, in order to minimize noise influence, in practice, the mean values of both fractional parts are added to the initially computed  $\Phi_{ABS}$  in order to find the ultimate solution for the unwrapped phase. The well-known problem in the original G-S method was that  $\varphi_{R1}$  and  $\varphi_{R2}$  were rounded and then used in (3). Consider that, due to noise, just one of the wrapped phases is slightly above an integer, when it should actually be just below that integer. Evidently, rounding (discarding a fractional part) gives a wrong input in (3), which is even magnified in the computation with the corresponding coefficient  $e_i$ . Consequently, the unwrapped phase  $\Phi_{ABS}$  will be quite apart from the correct one.

### 3. Proposition of a New Method

Our improvement is based on the fact that we actually have two major policies when computing an integer apart from the rational wrapped values: either rounding to the nearest integer or rounding to the nearest integer towards zero (alternatively infinity). In principle, all these types of rounding would work just fine. The only question is how to assure that all the wrapped phases are rounded towards the same corresponding value on the unwrapped phase axis and that, consequently, the rounding process provides the correct integer pair  $(\varphi_{R1}, \varphi_{R2})$  to be used in (3). This is essentially the key issue, which is neglected in the original G-S method.

Consider, as depicted in Figure 2, a segment extracted from the unwrapped phase axis in the interval between two integer values [INTNUM, INTNUM+1]. Additionally, there is an interval with width  $\Delta$  positioned exactly and symmetrically around the midpoint of [INTNUM, INTNUM+1]. Our proposed method checks whether either of the wrapped phases with their fractional parts are around the midpoint of the segment [INTNUM, INTNUM+1], enclosed with  $\Delta$ . If that is the case, we simply round towards zero to the nearest integer. On the contrary, we assume that the wrapped phases are close to the integer value on the unwrapped phase axis (i.e., close to INTNUM or INTNUM+1) and it is more accurate to round towards the nearest integer. Hence, the core of our method lies in choosing an optimal value for the interval  $\Delta$ . Recall that only in the ideal case  $\varphi_{RiFRAC}$  are equal. If  $\Delta$  is too small, the risk that none of the wrapped phases will fall within  $\Delta$  increases. So, in the case that one wrapped phase is above  $\text{INTNUM} + (0.5 + \Delta/2)$  while the other is below

$\text{INTNUM} + (0.5 - \Delta/2)$ , rounding to the nearest integer will cause an erroneous integer pair  $(\varphi_{R1}, \varphi_{R2})$ . Besides, if  $\Delta$  is too big, one of the wrapped phases might be within  $\Delta$ , but the other could even be outside the interval  $[\text{INTNUM}, \text{INTNUM}+1]$ . In this case, rounding to the smaller integer will yield an erroneous integer pair  $(\varphi_{R1}, \varphi_{R2})$ .

Besides making an informal and rather intuitive argument for the size of  $\Delta$ , one should note the following. The rigorous mathematical formulation for the size of  $\Delta$  effectively means a comprehensive analytical modeling of the noise sources, present during the computation of (un)wrapped phases. To name only a few factors, the noise sensitivity partly depends on the projector-camera physical setup and on the number of pattern periods, as explained in detail in [14]. Furthermore, the acquired image noise would have to be estimated, which depends on the quality of the camera and the projector, the lighting conditions and the object reflectance properties, among other aspects. On top of all that, the number of projected and shifted images also influences the computation of the wrapped phases. Evidently, the precise inclusion of all these factors in an a priori estimate of the size of delta is not an easy task and it is beyond the scope of this work. However, in practice, to acknowledge the influence of the above-mentioned factors we use a commercially available camera and projector, assuming it to be obvious that the results can only improve using better quality equipment. The chosen camera-projector physical setup is typical for a large number of 3D scanners. Next, we show a series of experiments with various commonly used pattern periods and in which we reach the point where the increase of pattern periods does not contribute to any gain in the reconstruction accuracy. We require no special ambient light conditions. In other words, we have extensively tested our chosen  $\Delta$  under “common and widely acceptable” conditions. More specifically, the size  $\Delta$  is determined for our setup partly intuitively and partly (confirmed) experimentally. We started computing the unwrapped phases with  $\Delta = 0.0$  (which is equivalent to an original G-S method), gradually increasing  $\Delta$  by adding 0.01. Then we realized that  $\Delta = 0.3$  assures an excellent result for the computation of the correct wrapped values, as shown in this work. We emphasize that for a given camera/projector setup and choice of pattern period, the computation of  $\Delta$  has to be done only once.

For completeness, we briefly recall that PS wrapped phase values  $\varphi_R$  for every pixel are computed solely from the image intensities  $I_i$  of the  $i$ th shifted and projected image, as shown in:

$$I_i = I_0 + A \cdot \sin(\varphi_R - \varphi_i), \quad (6)$$

where  $I_0$  is the intensity when no source of projection is present (ambient light),  $A$  reflects the amplitude of the projected (detected in image) sine signal, and  $\varphi_i$  are the equally distributed shifts to cover the entire period. Note that the value of  $A$  implicitly includes also the effect of the albedo/reflectance variation of a surface patch in the space which is projected into a particular pixel. Fortunately, an optimum result for the wrapped  $\varphi_R$  can be found through

a least square minimization of the difference between the left and the right sides of (6) [18]. Then for a number of images  $N \geq 3$  we obtain an expression for  $\varphi_R$  that ideally only depends on  $I_i$

$$\varphi_R = \text{atan} \left( - \sum_{i=0}^{N-1} I_i \cdot \cos(\varphi_i), \sum_{i=0}^{N-1} I_i \cdot \sin(\varphi_i) \right), \quad (7)$$

where  $\text{atan}$  is here the four quadrant inverse tangent function, yielding angle  $\varphi_R$  in the interval  $[-\pi, \pi]$ .

In the following paragraphs we summarize the key computational steps of our method.

*Step 1.* Given the periodic sine pattern, with the period length  $\lambda_1$ , compute the wrapped phase values  $\varphi_{R1}$  using the PS approach as explained through (6) and (7). Repeat this procedure for the other periodic sine pattern with the period length  $\lambda_2$  in order to find out another set of wrapped phase values  $\varphi_{R2}$ .

*Step 2.* Compute the coefficients  $e_i$  in the equation using, for instance, the extended Euclidean algorithm [19].

*Step 3.* For any camera pixel and its corresponding wrapped phases pair  $(\varphi_{R1}, \varphi_{R2})$ , set  $\Delta = 0.3$  and proceed as follows. Round the wrapped phase values to the closest *smaller* integer, if either of their fractional parts is within interval  $[0.5 - \Delta/2, 0.5 + \Delta/2]$ . Otherwise round it to the closest integer.

*Step 4.* Given the computed coefficients  $e_i$  and rounded wrapped values, compute the initial unwrapped value using (3). Refine this initial solution by adding the mean value of the wrapped phases’ fractional parts, which were previously discarded during the rounding process.

*Step 5.* Verify by visual inspection that the unwrapped phase map image is correct. This is relatively easy since an inappropriate value for  $\Delta$  will give distinctly wrong unwrapped phase values (not just slightly wrong ones invisible to a human eye), for example, Figure 4(a) versus 4(b). If necessary, repeat Step 3 and Step 4 using another value for  $\Delta$ . Recall that the determination of  $\Delta$  size is normally executed only once after the spatial arrangement of the camera/projector setup and patterns periods are defined.

Comparing the performance of our solution to other SL methods may not be straightforward. Nevertheless, in order to appreciate MPS methods and in particular the one we propose in this paper, we now briefly review the state-of-the-art in SL, pointing out that they violate at least one of the SoC (stated in the introduction of this paper) required for optimal SL patterns. According to one of the latest surveys, one group of SL strategies can be categorized as spatial neighborhood [3]. Spatial neighborhood concentrates, in the majority of cases, all the coding schemes in a unique pattern, which is evidently a clear advantage for the acquisition of moving scenes. As the name suggests, the codeword that labels a certain point of the pattern is obtained from a neighborhood of points around that point. Commonly used cues for (de)codification can be different single or

multiple shapes, for example, stripes or slits [20, 21], lines [22, 23], circles [24, 25], squares [26], which are either colored or have gray level intensities. The main problem here is a high sensitivity to colorful surfaces and/or code misinterpretation due to sharp changes in the object's depth (surface discontinuities). Up to a certain extent, both problems can be relaxed thanks to a color/reflectance calibration [27, 28] and dynamic programming [29, 30]. Another SL category is the so-called direct codification, where pattern points are encoded using a spectrum of gray level intensity [31] or colors [32], in which case the method is typically restricted for color neutral objects. Besides the problems of using color already mentioned, sometimes it is even necessary to use complicated hardware to project the color spectrum [33]. There have been some attempts to make improvements [34], but the biggest drawback in this category is the high sensitivity to noise, because the distance between adjacent codewords is nearly zero [35]. A somewhat special SL category is the Fourier transform profilometry (FTP), originally introduced in [36]. FTP is based ideally on imaging only a unique sinusoidal pattern while object depth is obtained from Fourier transformation computation, filtration in spatial frequency domain, and inverse Fourier transformation calculation [37]. Unfortunately, the computed 3D depth is commonly restricted and highly dependent on the system parameters, which can be improved through the projection of an extra  $\pi$ -phase shifted pattern [38]. However, an extra pattern makes the method inapplicable for moving scenes, unless a prior knowledge about the object speed is known [39]. There are attempts to perform a  $\pi$ -phase shifted FTP constructing a single composite pattern either with or without a color codification [40, 41]. Despite attempted improvements, the major drawback (motionless scenes) remains, as in any other (multi)frequency method: FTP faces the problem of blurred depth acquisition largely due to the nontrivial choice of the carrier frequencies related to the filtering step [42]. In conclusion, one of the very few known SL methods that do fulfill the SoC is the GC+PS approach which is extensively compared to our proposal. Other time-multiplexing methods aim to improve some shortcomings such as reducing the number of projection patterns at the expense of increasing the number of projected grey levels [43], or even trying to combine time-multiplexing with spatial neighborhood [44]. However, assuming that the number of patterns is not critical, all these methods are generally inferior to the classic GC+PS approach.

#### 4. System Setup Description

Our 3D structured light system is composed of a calibrated pair of Point Grey Research (PGR) Dragonfly 2 FireWire camera and an Acer X1260 DLP video projector, which are rigidly attached on a bar. Camera images have a resolution of  $1024 \times 768$  pixels. The distance of the camera and projector from the center of the calibration volume is about 900 mm and the baseline between the cameras and the projector is approximately 500 mm. The angle between the optical axes of the camera and the projector is of about  $30^\circ$ .

Although a camera wand calibration is generally regarded as the most user friendly calibration approach, it normally assumes the use of infrared camera system [45, 46]. Usually, a second best alternative is a plane calibration. Therefore, the camera was calibrated using a 2D calibration pattern with  $11 \times 8$  white circles on a black background. The diameter of the circles was 15 mm and they were 10 mm apart. The camera calibration algorithm used closely resembles the one explained in [47]. We have acquired 18 images of the 2D calibration plate taken from different orientations and locations throughout the calibration volume, which was of about 400 mm (width)  $\times$  450 mm (height)  $\times$  400 mm (depth). The centroids of the white calibration circles served not only to calibrate camera, but also to calibrate the projector. For every spatial position of the 2D calibration pattern (during camera calibration) we have projected the proposed pattern both in vertical and horizontal directions with respect to the projector image axis. We have searched for unique pattern codes (along both projector image axes) of centroids in the 2D pattern, and as we knew their 3D position (defined by the 2D calibration pattern), we were able to calibrate the projector using the same camera calibration algorithm [47]. For the camera the mean error and standard deviations between the detected calibration point's positions on the images and the positions provided by the calibration model using computed calibration parameters were 0.090 pixels and 0.066 pixels, respectively. Similarly for the projector, the mean error and standard deviations were 0.149 pixels and 0.114 pixels, respectively.

#### 5. Experimental Results

We have compared our proposed method to the original G-S and to GC+PS. In order to evaluate the accuracy, we have reconstructed a flat color neutral surface (plane). Ideally, all the acquired 3D points should lie on the plane, but in practice they do not. Hence, a common practice to evaluate accuracy in this case is to interpolate the plane from the entire set of 3D points and then to compute the distances (errors) of all these points to the interpolated plane. In Table 1 we provide the mean and standard deviations of such distances. We show representative results from one of the flat surface positions in the calibration volume, number of pattern periods, and GC word length. Moreover, on the very same flat surface we have also taped a color pattern composed of  $32 \times 24$  squares of various colors randomly generated as shown in Figure 3. For some other position within the calibration volume, we have conducted the same accuracy analysis as we did for the color neutral surface. The first thing to consider in Table 1 is the improvement in the obtained accuracy as long as we increase the number of periodic pattern periods and the length of the Gray codeword. This is in accordance with the theoretical expectations that increasing the code word distances between adjacent pixels should improve the depth computation accuracy. Given the other parameters of our 3D system (e.g., spatial sensor arrangement, camera and projector features, calibration), it seems that patterns of more than 20 periods do not

TABLE 1: Mean error and standard deviations of distances for total of  $N$  reconstructed points with respect to the fitted plane through those  $N$  points.  $p_1$  and  $p_2$  show the chosen number of periods for periodic patterns used to construct wrapped PS maps.  $m$  is the Gray code word length.

Proposed method							
$p_1$	$p_2$	$N$	Pale plane		$N$	Colorful plane	
			Mean (mm)	Std (mm)		Mean (mm)	Std (mm)
3	5		0.559	0.427		0.675	0.610
5	7		0.269	0.251		0.443	0.422
7	11	121491	0.241	0.183	108846	0.341	0.329
13	17		0.177	0.143		0.253	0.227
19	25		0.152	0.122		0.232	0.215
25	29		0.149	0.119		0.224	0.239
G-S method							
$p_1$	$p_2$	$N$	Pale plane		$N$	Colorful plane	
			Mean (mm)	Std (mm)		Mean (mm)	Std (mm)
3	5	112345	0.525	0.435	100567	0.667	0.593
5	7	93217	0.284	0.253	78456	0.468	0.489
7	11	67589	0.230	0.175	63976	0.337	0.318
13	17	63271	0.175	0.139	57349	0.244	0.220
19	25	54321	0.157	0.129	49345	0.228	0.217
25	29	52891	0.151	0.125	47975	0.209	0.226
GC+PS							
$m$	$p_1$	$N$	Pale plane		$N$	Colorful plane	
			Mean (mm)	Std (mm)		Mean (mm)	Std (mm)
2	4		0.934	1.061		1.287	1.398
3	8		0.284	0.281		0.456	0.432
4	16	121491	0.193	0.217	108846	0.231	0.219
5	32		0.158	0.127		0.240	0.231
6	64		0.153	0.131		0.232	0.212

contribute to an increase in accuracy. In addition, eventually the three methods provide about the same level of accuracy. However, the original G-S method suffers from a serious decrease in attainable resolution. Due to the discussed noise intrinsic in G-S, for a large number of pixels it is not possible to unwrap the phase correctly. As expected, the problem becomes more serious when the periods are increased since the number of potentially noisy pixels then increases considerably. To visualize the effect of such invalid pixels, Figure 4 shows an unwrapped phase map of a flat surface using both our method and the G-S method (pattern periods used in both cases were  $p_1 = 15$ ,  $p_2 = 19$ ). However, it is important to note that although the reduced resolution might be acceptable, it needs costly image processing to automatically detect those invalid pixels. For all practical purposes, if the number of invalid pixels becomes excessive, it is very hard to detect them all and at the same time avoid discarding correct pixels, which leads to an additional decrease of resolution. Besides, it is possible that some of the invalid pixels remain undetected. To detect them, we have simply used a  $3 \times 3$  pixel scanning mask, where we have computed for every pixel the abrupt changes of unwrapped values in a neighborhood of  $n$  pixels. Although it worked reasonably well, recall that according to our idea about

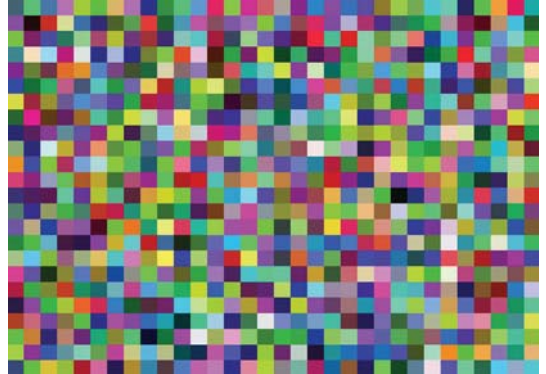


FIGURE 3: Evaluation method for colorful surfaces. The figure shows a randomly generated colorful pattern which is printed and stuck on the measuring surface.

an optimal SL strategy (see SoC), such additional image processing should certainly be avoided and full projector resolution should be used.

The comparison of our method to the powerful GC+PS does not appear to be significantly different (see Table 1).

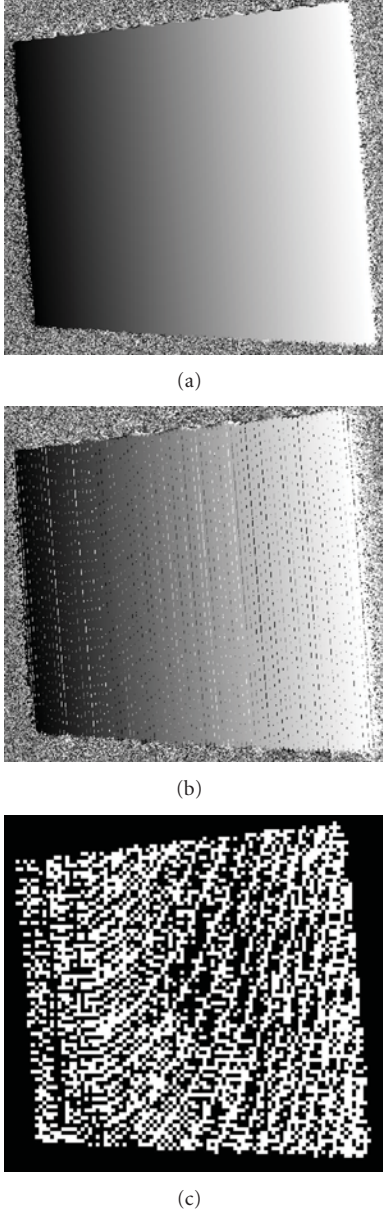


FIGURE 4: Appearance of the unwrapped phase map using the (a) proposed method and (b) the original G-S method; (c) shows (emphasized) in black all pixels with an incorrect unwrapped phase obtained by (b).

However, it is not straightforward to compare our method to GC+PS, since the patterns used are not exactly the same. The fact is that the length of the GC word of  $m$  bits typically determines the number of periods  $2^m$  to be used. The clear advantage of our method is when either GC images cannot be conveniently generated or some other arbitrary pattern periods are relatively easily available, such as in interferometry. In terms of color robustness we have appreciated a slight decrease in the accuracy for all the tested methods. That was surely expected to a certain extent, since the theoretical assumption of the full robustness to colorful surface is only a substantial idealization, which is particularly

hard to fulfill in the areas where abrupt changes of albedo take place.

As part of the qualitative evaluation of our method we have chosen to scan a foot impression from a “foam box” as shown in Figure 5 from three different viewing angles. We could acquire only the sole of the foot, without any lateral parts. In that case, a view similar to Figure 5(a) would be probably sufficient. Indeed that is how many commercial laser-based 3D systems dedicated particularly to the scanning of the foot (impressions) operate. However, in many applications (foot modeling), it may also be interesting to acquire parts of the lateral foot surface. Furthermore, to overcome the problem of occluded and/or shadow regions we have taken four scans. The problem of 3D surface registration from multiple views was solved using three white circular markers on our foam box [48]. In most cases our developed software automatically detects those markers on various images. If automatic detection fails, a user can manually add a rectangle around the white markers to roughly point out, for the underlying software, where the registration markers are.

Figure 6 shows a 3D reconstruction result acquired from the single view corresponding to Figure 5(a). In more detail, Figure 6(a) is a mesh visualized from the top and Figure 6(b) is the same color mesh shown from the bottom. It is customary to perform visualization with the help of colors where certain shades correspond to the depth of the impression in a foam box. Additionally, many professional software outputs 3D data in a variety of standard 3D file formats [49]. We have chosen to output our 3D scans in the STL format. Figure 7 shows the surface mesh visualization based on STL format of the registered model of the four scans. Very often the raw 3D data is smoothed prior to subsequent processing and modeling. The top row of Figure 7 shows the appearance of raw data, while the bottom row is a smoothed surface. The particular smoothing we have used is very basic: for every 3D raw data point we have defined a 1.5 mm cube in which that particular point was in the center. The new 3D position of a point was computed as the mean value of all its neighbors within a cube.

Although there are a number of systems available on the market to specifically scan the foot itself or impressions in a foam box [50–53], most of them are rather expensive and hardly applicable to a wide range of applications since they are aimed basically and exclusively at one particular application. In fact, many manufacturers offer different type of scanners for different applications [54–57]. Additionally, they are frequently made from a custom-designed (often patented as well) system of laser scanning heads and/or image sensors [58, 59]. However, our goal was to propose a widely applicable 3D structured light scanner that would also be cost effective, consisting of off-the-shelf components available to a large number of researchers.

Therefore, to visualize the performance of our technique reconstructing live subjects (only ideally perfectly static, but potentially moving surfaces), we have chosen as an example the reconstruction of a human face. Figure 8(a) is the camera image of the human face at a given instant of the projection; Figure 8(b) shows the dense 3D raw data obtained by our

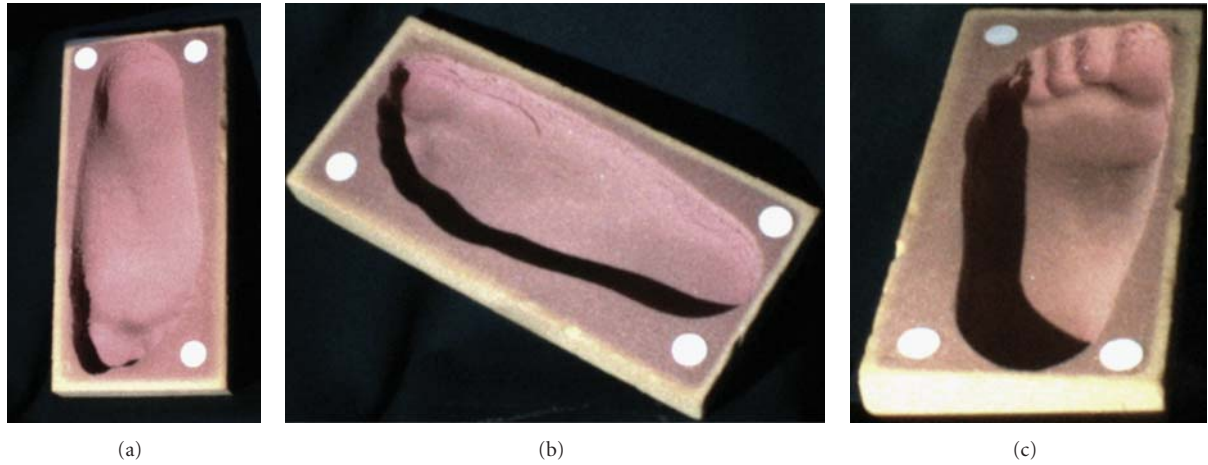


FIGURE 5: Images from three different views of the foot impression from our “foam box.”

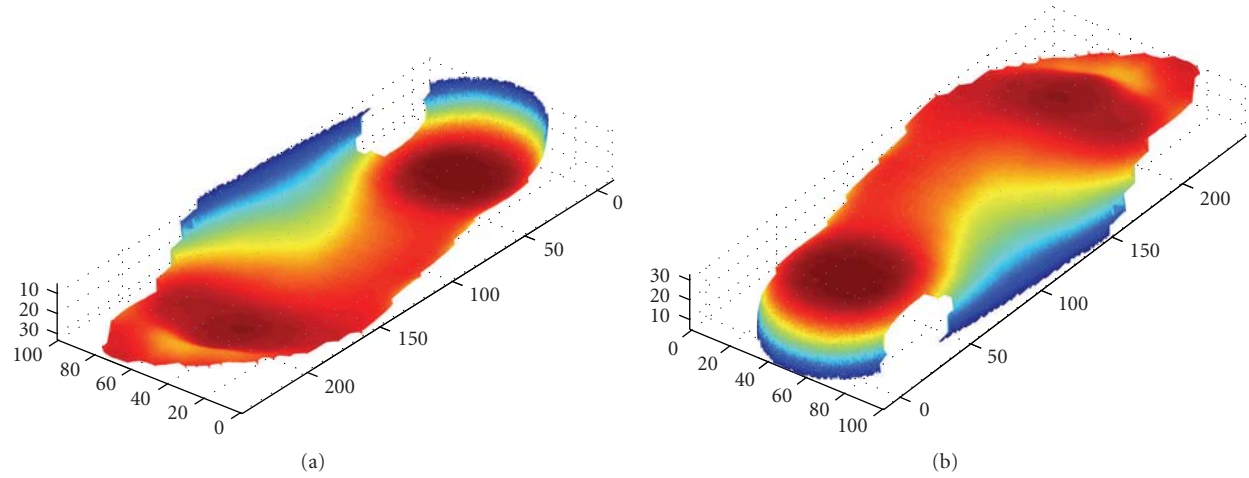


FIGURE 6: Impression from the foam box reconstructed from the single view: (a) the top perspective (b) the bottom perspective. Colors correspond to the different depth of the impression. The distribution of the colors is defined using jet color map in Matlab.

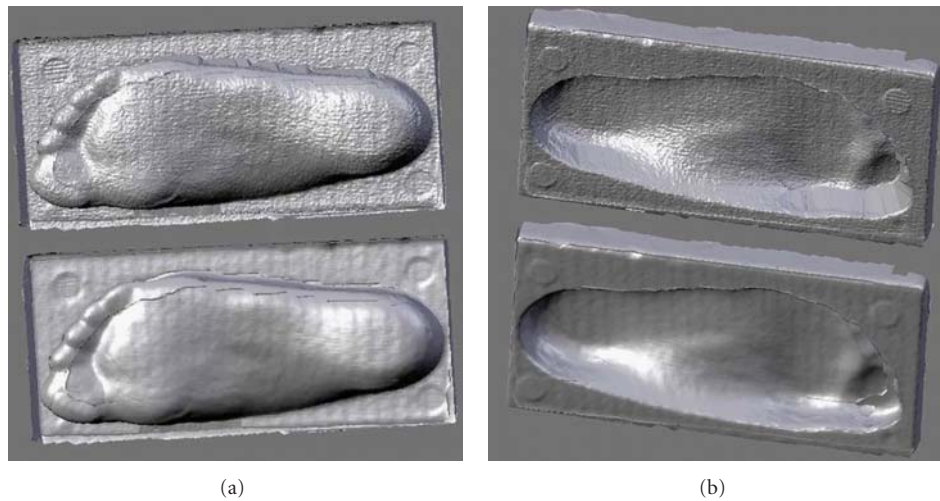


FIGURE 7: Reconstruction of a foam box from the multiple views. The results are shown from two perspectives ((a) and (b)). In addition, the top parts of the figure show the 3D raw data and the bottom parts represent the smoothed surface.

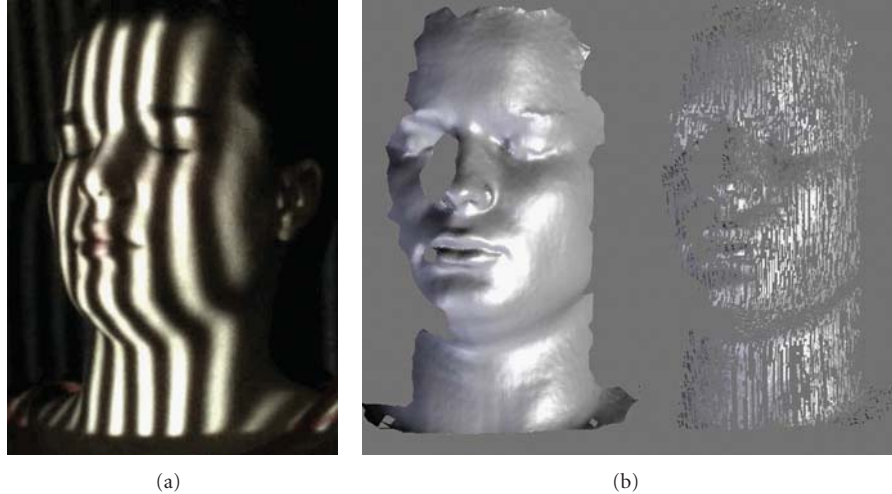


FIGURE 8: An example of 3D human face reconstruction. (a) Image during pattern projection. (b) Acquired mesh surface: left, dense reconstruction obtained by our method; right, sparse reconstruction obtained by the G-S method.

method compared to the sparse 3D raw data originally obtained by G-S. Note that due to camera occlusion, mainly the left part of the human face was measured. This is of course an inherent drawback of basically all the optical 3D scanners. Alternatively, one could add an additional camera or try to perform a multiview surface registration, as mentioned above.

## 6. Conclusion

Our proposed 3D structured light scanner is based on, one of the most powerful structured light projection strategies, multiphase shifting. MPS is a representative of the so-called time multiplexing strategy. Following a coarse-to-fine paradigm, it can achieve high measurement accuracy, a feature certainly desired in biomechanics. To solve the main problem related to MPS, phase unwrapping, we have proposed a relatively simple method which involves a modification of the common G-S method. Comparing results to the original G-S method clearly demonstrated the superiority in terms of better 3D resolution and easier and faster image processing of our approach. Comparing our method to the well-known GC+PS reveals the same achieved accuracy, with the advantage that our method is easily applicable to a larger variety of chosen pattern periods. Besides, our method clearly fulfills several highly appreciated conditions (SoC) stated in the introduction concerning optimal SL strategy, which are not very common in SL methods. The acquired reconstruction accuracy is in line with most of the scanners available on the market. In addition, we have demonstrated how our approach performs for a biomechanics application: the scanning of a footprint in a given foam box. At the same time we have discussed the potential wider use in other applications involving living (moving) subjects, such as the scanning of the human face. Note that our scanner consists of a common (cheap) projector and a well-known yet affordable

camera. That fact warrants its implementation by a large number of researchers.

## Acknowledgments

An important part of the shown work was steered through a visiting research enjoyed by the corresponding author at the Fraunhofer Institute for Computer Graphics Research (IGD) in Darmstadt, Germany. Special thanks go to Professor Dr.-Ing. Georgios Sakas and his Cognitive Computing & Medical Imaging Department for all the support provided at the time.

## References

- [1] J. F. Orr and J. C. Shelton, *Optical Measurement Methods in Biomechanics*, Chapman & Hall, Boca Raton, Fla, USA, 1997.
- [2] N. L. Chang, "Efficient dense correspondences using temporally encoded light patterns," in *Proceedings of the IEEE International Workshop on Projector-Camera Systems in Conjunction with International Conference on Computer Vision (ICCV '03)*, pp. 1–8, Nice, France, 2003.
- [3] J. Salvi, J. Pagés, and J. Batlle, "Pattern codification strategies in structured light systems," *Pattern Recognition*, vol. 37, no. 4, pp. 827–849, 2004.
- [4] G. Sansoni, A. Patrioli, and F. Docchio, "OPL-3D: a novel, portable optical digitizer for fast acquisition of free-form surfaces," *Review of Scientific Instruments*, vol. 74, no. 4, pp. 2593–2603, 2003.
- [5] G. Wiora, "High resolution measurement of phase-shift amplitude and numeric object phase calculation," in *Vision Geometry IX*, vol. 4117 of *Proceedings of SPIE*, pp. 289–299, San Diego, Calif, USA, 2000.
- [6] S. S. Gorthi and K. R. Lolla, "A new approach for simple and rapid shape measurement of objects with surface discontinuities," in *Optical Measurement Systems for Industrial Inspection IV*, vol. 5856 of *Proceedings of SPIE*, pp. 184–194, Bellingham, Wash, USA, 2005.

- [7] N. Ono, T. Shimizu, T. Kurihara, and S. Ando, "Real-time 3-D imager based on spatio-temporal phase unwrapping," in *Proceedings of the SICE Annual Conference*, pp. 2544–2547, Sapporo, Japan, August 2004.
- [8] H. O. Saldner and J. M. Huntley, "Temporal phase unwrapping: application to surface profiling of discontinuous objects," *Applied Optics*, vol. 36, no. 13, pp. 2770–2775, 1997.
- [9] J. M. Huntley and H. O. Saldner, "Shape measurement by temporal phase unwrapping: comparison of unwrapping algorithms," *Measurement Science and Technology*, vol. 8, no. 9, pp. 986–992, 1997.
- [10] W. Nadeborn, P. Andrä, and W. Osten, "A robust procedure for absolute phase measurement," *Optics and Lasers in Engineering*, vol. 24, no. 2-3, pp. 245–260, 1996.
- [11] J.-D. Tian, X. Peng, and X. Zhao, "A pitch-variation moiré fringes method of temporal phase unwrapping profilometry," *Optoelectronics Letters*, vol. 3, no. 3, pp. 215–218, 2007.
- [12] V. I. Gushov and Y. N. Solodkin, "Automatic processing of fringe patterns in integer interferometers," *Optics and Lasers in Engineering*, vol. 14, no. 4-5, pp. 311–324, 1991.
- [13] C. E. Towers, D. P. Towers, and J. D. C. Jones, "Time efficient Chinese remainder theorem algorithm for full-field fringe phase analysis in multi-wavelength interferometry," *Optics Express*, vol. 12, no. 6, pp. 1136–1143, 2004.
- [14] J. Burke, T. Bothe, W. Osten, and C. Hess, "Reverse engineering by fringe projection," in *Interferometry XI: Applications*, vol. 4778 of *Proceedings of SPIE*, pp. 312–324, Seattle, Wash, USA, July 2002.
- [15] M. Takeda, Q. Gu, M. Kinoshita, H. Takai, and Y. Takahashi, "Frequency-multiplex Fourier-transform profilometry: a single-shot three-dimensional shape measurement of objects with large height discontinuities and/or surface isolations," *Applied Optics*, vol. 36, no. 22, pp. 5347–5354, 1997.
- [16] J. Zhong and Y. Zhang, "Absolute phase-measurement technique based on number theory in multifrequency grating projection profilometry," *Applied Optics*, vol. 40, no. 4, pp. 492–500, 2001.
- [17] P. Ribenboim, *Algebraic Numbers*, John Wiley & Sons, New York, NY, USA, 1972.
- [18] C. J. Morgan, "Least-squares estimation in phase-measurement interferometry," *Optics Letters*, vol. 7, no. 8, pp. 368–370, 1982.
- [19] K. H. Rosen, *Elementary Number Theory and Its Applications*, Addison-Wesley, Reading, Mass, USA, 1988.
- [20] M. Tehrani, A. Saghaeian, and O. Mohajerani, "A new approach to 3D modeling using structured light pattern," in *Proceedings of the 3rd International Conference on Information and Communication Technologies (ICTTA '08)*, pp. 1–5, Damascus, Syria, 2008.
- [21] J. Pagés, J. Salvi, and J. Forest, "Optimised de Bruijn patterns for one-shot shape acquisition," *Image and Vision Computing*, vol. 23, no. 8, pp. 707–720, 2005.
- [22] H. Kawasaki, R. Furukawa, R. Sagawa, and Y. Yagi, "Dynamic scene shape reconstruction using a single structured light pattern," in *Proceedings of the 26th IEEE Conference on Computer Vision and Pattern Recognition (CVPR '08)*, pp. 1–8, Anchorage, Alaska, USA, June 2008.
- [23] T. P. Koninckx and L. Van Gool, "Real-time range acquisition by adaptive structured light," *IEEE Transactions on Pattern Analysis and Machine Intelligence*, vol. 28, no. 3, pp. 432–445, 2006.
- [24] P. M. Griffin, L. S. Narasimhan, and S. R. Yee, "Generation of uniquely encoded light patterns for range data acquisition," *Pattern Recognition*, vol. 25, no. 6, pp. 609–616, 1992.
- [25] C. Albitar, P. Graebing, and C. Doignon, "Design of a monochromatic pattern for a robust structured light coding," in *Proceedings of the IEEE International Conference on Image Processing (ICIP '07)*, pp. 529–532, San Antonio, Tex, USA, October 2007.
- [26] M. Ito and A. Ishii, "A three-level checkerboard pattern (TCP) projection method for curved surface measurement," *Pattern Recognition*, vol. 28, no. 1, pp. 27–40, 1995.
- [27] D. Caspi, N. Kiryati, and J. Shamir, "Range imaging with adaptive color structured light," *IEEE Transactions on Pattern Analysis and Machine Intelligence*, vol. 20, no. 5, pp. 470–480, 1998.
- [28] F. Forster, "A high-resolution and high accuracy real-time 3D sensor based on structured light," in *Proceedings of the 3rd International Symposium on 3D Data Processing, Visualization, and Transmission (3DPVT '06)*, pp. 208–215, Chapel Hill, NC, USA, 2006.
- [29] P. Fechteler and P. Eisert, "Adaptive colour classification for structured light systems," *IET Computer Vision*, vol. 3, no. 2, pp. 49–59, 2009.
- [30] L. Zhang, B. Curless, and S. Seitz, "Rapid shape acquisition using color structured light and multi-pass dynamic programming," in *Proceedings of the 1st International Symposium on 3D Data Processing, Visualization, and Transmission (3DPVT '02)*, pp. 24–36, Padova, Italy, June 2002.
- [31] B. Carrihill and R. Hummel, "Experiments with the intensity ratio depth sensor," *Computer Vision, Graphics, & Image Processing*, vol. 32, no. 3, pp. 337–358, 1985.
- [32] C. Wust and D. W. Capson, "Surface profile measurement using color fringe projection," *Machine Vision and Applications*, vol. 4, no. 3, pp. 193–203, 1991.
- [33] J. Tajima and M. Iwakawa, "3-D data acquisition by rainbow range finder," in *Proceedings of the 10th International Conference on Pattern Recognition (ICPR '90)*, vol. 1, pp. 309–313, Atlantic City, NJ, USA, June 1990.
- [34] T. Sato, "Multispectral pattern projection range finder," in *Three-Dimensional Image Capture and Applications II*, vol. 3640 of *Proceedings of SPIE*, pp. 28–37, San Jose, Calif, USA, 1999.
- [35] G. Chazan and N. Kiryati, "Pyramidal intensity-ratio depth sensor," Tech. Rep. 121, Department of Electrical Engineering, Center for Communication and Information Technologies, Technion, Haifa, Israel, 1995.
- [36] M. Takeda and K. Mutoh, "Fourier transform profilometry for the automatic measurement of 3-D object shapes," *Applied Optics*, vol. 22, no. 24, pp. 3977–3982, 1983.
- [37] X. Su and W. Chen, "Fourier transform profilometry: a review," *Optics and Lasers in Engineering*, vol. 35, no. 5, pp. 263–284, 2001.
- [38] J. Li, X. Su, and L. Gou, "An improved Fourier transform profilometry for automatic measurement of 3-D object shapes," *Optical Engineering*, vol. 29, no. 12, pp. 1439–1444, 1990.
- [39] E. Hu and Y. He, "Surface profile measurement of moving objects by using an improved  $\pi$  phase-shifting Fourier transform profilometry," *Optics and Lasers in Engineering*, vol. 47, no. 1, pp. 57–61, 2009.
- [40] W. Chen, P. Bu, S. Zheng, and X. Su, "Study on Fourier transforms profilometry based on bi-color projecting," *Optics and Laser Technology*, vol. 39, no. 4, pp. 821–827, 2007.
- [41] H.-M. Yue, X.-Y. Su, and Y.-Z. Liu, "Fourier transform profilometry based on composite structured light pattern," *Optics and Laser Technology*, vol. 39, no. 6, pp. 1170–1175, 2007.

- [42] C. Guan, L. G. Hassebrook, and D. L. Lau, "Composite structured light pattern for three-dimensional video," *Optics Express*, vol. 11, no. 5, pp. 406–417, 2003.
- [43] E. Horn and N. Kiryati, "Toward optimal structured light patterns," *Image and Vision Computing*, vol. 17, no. 2, pp. 87–97, 1999.
- [44] I. Ishii, K. Yamamoto, K. Doi, and T. Tsuji, "High-speed 3D image acquisition using coded structured light projection," in *Proceedings of the IEEE/RSJ International Conference on Intelligent Robots and Systems (IROS '07)*, pp. 925–930, San Diego, Calif, USA, October 2007.
- [45] T. Pribanić, P. Sturm, and M. Cifrek, "Calibration of 3D kinematic systems using orthogonality constraints," *Machine Vision and Applications*, vol. 18, no. 6, pp. 367–381, 2007.
- [46] T. Pribanić, P. Sturm, and S. Peharec, "Wand-based calibration of 3D kinematic system," *IET Computer Vision*, vol. 3, no. 3, pp. 124–129, 2009.
- [47] Z. Zhang, "A flexible new technique for camera calibration," *IEEE Transactions on Pattern Analysis and Machine Intelligence*, vol. 22, no. 11, pp. 1330–1334, 2000.
- [48] J. Salvi, C. Matabosch, D. Fofi, and J. Forest, "A review of recent range image registration methods with accuracy evaluation," *Image and Vision Computing*, vol. 25, no. 5, pp. 578–596, 2007.
- [49] Paracontour modelling software, September 2009, <http://www.londonorthotics.co.uk/loc-technology/foot-scanner.html>.
- [50] "FotoScan 3D," September 2009, <http://www.precision3d.co.uk>.
- [51] InFoot, September 2009, <http://www.iwl.jp/main/products.html>.
- [52] "EcoPlan," September 2009, [http://www.shoemaster.co.uk/products/eco\\_plan.html](http://www.shoemaster.co.uk/products/eco_plan.html).
- [53] "CanFit-Plus," September 2009, <http://www.vorum.com>.
- [54] Breuckman, September 2009, <http://www.creativecadcam.net/3d-white-light-scanner.html>.
- [55] Inspeck, September 2009, <http://www.inspeck.com>.
- [56] Cyberware, September 2009, <http://www.cyberware.com>.
- [57] "DigiScan dental scanner," September 2009, <http://www.rsi-gmbh.de/public/en/rsi/news.htm>.
- [58] Scanny3D, September 2009, <http://www.scanny3d.com>.
- [59] Steinbichler, September 2009, <http://www.central-scanning.co.uk>.

## Research Article

# Toward the Development of Virtual Surgical Tools to Aid Orthopaedic FE Analyses

Srinivas C. Tadepalli,<sup>1,2</sup> Kiran H. Shivanna,<sup>2</sup> Vincent A. Magnotta,<sup>2,3</sup>  
Nicole A. Kallemeyn,<sup>1,2</sup> and Nicole M. Grosland<sup>1,2,4</sup>

<sup>1</sup> Seamans Center for the Engineering Arts and Sciences, Department of Biomedical Engineering, The University of Iowa, Iowa City, IA 52242, USA

<sup>2</sup> Center for Computer Aided Design, The University of Iowa, 116 Engineering Research Facility, 330 S. Madison Street, Iowa City, IA 52242, USA

<sup>3</sup> Department of Radiology, University of Iowa Hospitals and Clinics, 200 Hawkins Drive, Iowa City, IA 52242, USA

<sup>4</sup> Department of Orthopaedics and Rehabilitation, University of Iowa Hospitals and Clinics, 200 Hawkins Drive, Iowa City, IA 52242, USA

Correspondence should be addressed to Nicole M. Grosland, nicole-grosland@uiowa.edu

Received 18 May 2009; Revised 8 October 2009; Accepted 28 October 2009

Academic Editor: João Manuel R. S. Tavares

Copyright © 2010 Srinivas C. Tadepalli et al. This is an open access article distributed under the Creative Commons Attribution License, which permits unrestricted use, distribution, and reproduction in any medium, provided the original work is properly cited.

Computational models of joint anatomy and function provide a means for biomechanists, physicians, and physical therapists to understand the effects of repetitive motion, acute injury, and degenerative diseases. Finite element models, for example, may be used to predict the outcome of a surgical intervention or to improve the design of prosthetic implants. Countless models have been developed over the years to address a myriad of orthopaedic procedures. Unfortunately, few studies have incorporated patient-specific models. Historically, baseline anatomic models have been used due to the demands associated with model development. Moreover, surgical simulations impose additional modeling challenges. Current meshing practices do not readily accommodate the inclusion of implants. Our goal is to develop a suite of tools (virtual instruments and guides) which enable surgical procedures to be readily simulated and to facilitate the development of all-hexahedral finite element mesh definitions.

## 1. Introduction

Orthopaedic surgeons use both surgical and nonsurgical techniques to treat musculoskeletal trauma, sports injuries, degenerative diseases, infections, tumors, and congenital conditions. Orthopaedic surgical operations are associated with the rearrangement of both hard and soft tissues, oftentimes leading to dramatic changes in structural geometry. The primary objective of a surgical correction is typically the maintenance or restoration of function. Due to the complexity of the anatomy under consideration and the biomechanical behavior of the tissues, the impact of a surgical procedure may not always be predicted on the basis of the surgeon's intuition and experience alone. Computational modeling using individual tomographic data can provide valuable information for surgeons during the planning stage. Specifically, the finite element method

provides a means to predict surgical outcome based on factors such as bony cuts (osteotomy), bone fragment/segment repositioning, the addition of instrumentation, and the host tissue response. Countless models have been developed over the years addressing procedures ranging from fusions to total joint replacements [1–14]. Unfortunately, few studies have incorporated patient-specific models. Historically, baseline anatomic models have been used due to the time devoted solely to model development. Moreover, surgical simulations impose an additional level of complexity and accompanying set of challenges. Current meshing practices do not readily accommodate the inclusion of implants. The challenges that accompany traditional modeling techniques are magnified when an implant is to be introduced in the model. Consequently, the time devoted to mesh development increases considerably, and hence such models may often prove impractical.

In pursuit of making patient-specific modeling a reality, we have made advancements in automating the patient-specific bony geometry definitions from CT and/or MR image datasets [15–17] and toward easing the development of corresponding patient-specific finite element (FE) mesh definitions via a custom-written software package, IA-FEMesh [18]. Our goal is to further advance these efforts by developing tools to simulate a variety of surgical procedures, thereby interactively incorporating implants into such models. One day, such models may aid the surgeon in preoperative planning or in the engineering of implant design, ultimately resulting in an improved clinical outcome. Toward that end, our goal is to develop a suite of tools which enable the user to readily simulate a surgical procedure and mesh the resulting structure with an all-hexahedral mesh. Historically, commercial preprocessors were developed for traditional engineering applications where the structures of interest can readily be broken down into geometric primitives, thus making hexahedral mesh development feasible. To capture the geometric complexity of anatomic structures often necessitates the use of a tetrahedral mesh. Hexahedral elements, however, are often preferred for their superior numerical performance as compared to tetrahedral elements [19, 20]. A mathematical argument in favor of the hexahedral element is that the volume defined by one element must be represented by at least five tetrahedral elements, which in turn yields a system matrix that is computationally more expensive. In contrast to the favorable numerical quality of hexahedral meshes, mesh generation is a difficult task.

Herein, we present a general framework for computer-assisted planning of orthopaedic interventions based on finite element modeling via the reconstruction of patient's anatomy from 3D image datasets. To date we have developed a prototype program and an easy to use workflow that interacts with IA-FEMesh, allowing the user to perform a series of surgical manipulations on a bony surface. This tool supports the same datatypes utilized by IA-FEMesh enabling the resulting surfaces to be imported into IA-FEMesh for mesh generation. Herein we demonstrate these surgical capabilities by simulating and meshing a cervical laminoplasty procedure.

## 2. Surgical Simulation Techniques

To enable the development of patient-/subject-specific models, the generation of an anatomic model begins with a collection of CT and MR images. CT images facilitate the delineation of the bony anatomy while also providing patient-specific material properties, while MR images allow soft tissues such as cartilage, ligaments and tendons, as well as muscles to be defined. The process of delineating the anatomic structures can be performed via a variety of techniques including manual, semiautomated, and fully automated techniques. The ability to define geometrically accurate representations of bony structures has previously been studied by DeVries et al. [21]. While defining the phalanx bones of the hand, good agreement was found between manual raters (Jaccard metric = 0.91) and physical laser

scans of the same specimens (surface distance = 0.20 mm). To facilitate the creation of the anatomic models both semi-automated techniques such as the expectation-maximization algorithms [16] as well as artificial neural networks (ANNs) [17] have been explored. In this paper, the BRAINS2 software was used to manually segment the regions of interest [22–25]. This software offers a variety of tools to facilitate the delineation of anatomical structures including thresholding, region growing, and clipping. These functions were used in conjunction with the manual editing tools to delineate the bones of the hand, wrist, and spine as shown in the following examples. For the models described in this paper, cadaveric specimens were imaged on a Siemens Sensation 64 slice computed tomography (CT) scanner [matrix = 512 × 512 pixels, field of view (FOV) = 172 mm, kilovolts peak (kVp) = 120, current = 94 mA, exposure = 105 mA]. The in-plane resolution for the hand and wrist was 0.34 mm with a slice thickness of 0.40 mm, while the spine was imaged with an in-plane resolution of 0.5 mm and 0.6 mm slice thickness. Once the regions of interest were manually delineated, a surface was generated from the binary segmentation, smoothed via Laplacian smoothing, and exported in STL format from BRAINS2.

The surgical simulation tools described here operate on the surface definitions of the anatomical structures. The surfaces generated in BRAINS2 are loaded into the surgical simulation software to initiate surgical planning. The user is provided several tools to manipulate the quality of the initial surface. For example, the ability to subdivide [26], decimate [27], and smooth the triangles of a given surface is afforded to the user. Figure 1 illustrates various triangulated surface definitions for a carpal bone of the wrist (i.e., capitate). Figures 1(a) and 1(b) illustrate the original triangulated mesh represented in shaded and wireframe form, respectively. Figure 1(c) shows the same surface having each triangle subdivided into 4 new triangles. Additionally, Figure 1(d) highlights the ability to decimate the surface, thereby decreasing the total number of triangles representing the surface. Care must be taken when decimating a surface so that the fidelity of the surface definition is not lost. In terms of smoothing, the user is able to use both Laplacian [28] and windowed sinc [29] smoothing functions. Future work will allow the user to visualize changes in the surface representation that result from these operations.

**2.1. Cutting a Bone via a Planar Cut.** An osteotomy, for example, is a surgical operation whereby a bone is cut to shorten, lengthen, or change its alignment. We have developed tools to cut a bone, thereby yielding two distinct bone segments. Moreover, tools have also been introduced to cut away the bony surface in preparation for implant insertion.

**2.1.1. Performing an Osteotomy.** To cut a bone, and retain the individual bony segments, a box widget has been introduced. The box may be interactively positioned (translated and rotated) with respect to the bone, the size of which is controlled via handles provided along each face normal of the box widget (Figure 2). Consequently, the user has the

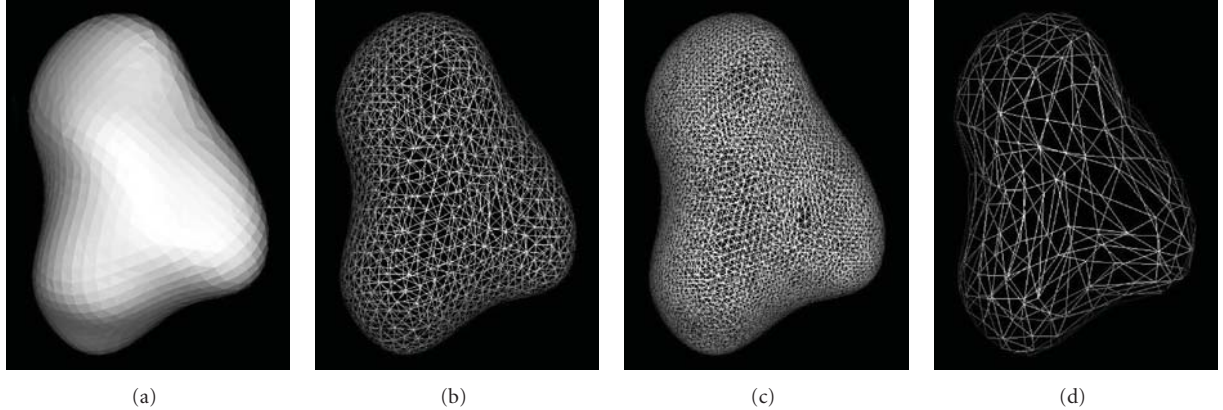


FIGURE 1: The capitate bone—the original triangulated surface represented as (a) a shaded and (b) wireframe surface. (c) Each triangle of the original mesh was subdivided 4 times and (d) the mesh was decimated to reduce the overall number of triangles.

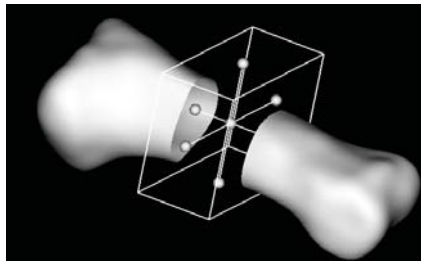


FIGURE 2: Box clip widget used to generate two bony segments.

ability to adjust the box by repositioning each face, thereby enabling a variety of cuts to be simulated. Once the box widget is of the desired length, width, and orientation, the segment of interest (i.e., inside/outside the box) is removed. The surface(s) that results from clipping the original closed surface with the box widget will no longer be closed; consequently, the resulting surfaces must be patched at the location of the simulated cut in order mesh the structure. This has been accomplished using Delaunay triangulation [28]. Rather than maintain a single surface definition, care was taken to assign separate surface definitions to the individual bony segments, thereby permitting the segments to be repositioned relative to one another.

**2.1.2. Removing Bone/Bony Surface.** To cut a bone in preparation for an implant, planar cuts are often made with the aid of a guide. Consequently, a 3D plane widget available in VTK has been used. The widget is represented by a plane with four corner vertices and a normal vector. Similar to the box widget, the plane can be moved interactively and positioned precisely with respect to the host bone. Thereafter, the desired bony surface is retained and the open face patched.

**2.2. Surface Boolean Operations.** Boolean operations (intersection, difference, or union) [30] provide the ideal tool for introducing an implant within a host bone (Figure 3). The software supports calculations for the intersection and union

of two surfaces, as well as the ability to subtract one surface from another. Boolean operations are often used to construct complex objects from simple geometric primitives. We have extended this to include complex anatomic surfaces and surfaces representing implants. The surgical simulation software allows the user to interactively create and size surfaces for simple geometric primitives including cylinders, rectangular blocks, and spheres. In addition, a surface representing a surgical tool and/or implant can be imported and interactively positioned relative to the bone. Once the two surfaces are in the proper position, Boolean operations can be used to manipulate the bony surface. For example, a Boolean operation between a cylindrical surface and the bony surface definition may be used to mimic a drill hole (Figure 4). Again, in order to mesh the structure, the resulting representation must be a closed surface. Consequently, the patching algorithm described previously was used to close the bony surface.

**2.3. Meshing the Resulting Surface Definition.** Once the surface has been cut/drilled (Figure 4) according to the desired surgical procedure, building blocks may be created and an all-hexahedral FE mesh generated using IA-FEMesh (Figure 5). The meshing algorithms currently available in IA-FEMesh dictate that the nodes be projected to the closest point on the surface. Consequently, the position of the building blocks controls the nodal placement. The resulting mesh quality can be evaluated/improved using the tools available in IA-FEMesh [18] prior to exporting the resulting mesh to an FE solver for analysis. Moreover, material properties (user defined and/or image-based) and boundary conditions can be assigned within IA-FEMesh. Although the current meshing practices are feasible as they stand, improvements can be made. For example, during mesh improvement (i.e., smoothing) there is a tendency for the nodes to pull away from the desired surface toward the newly introduced cut/hole (Figure 5). As a result, in the long term we propose to improve upon these meshing strategies by introducing feature edge detection, meshing, and smoothing techniques that preserve these features.

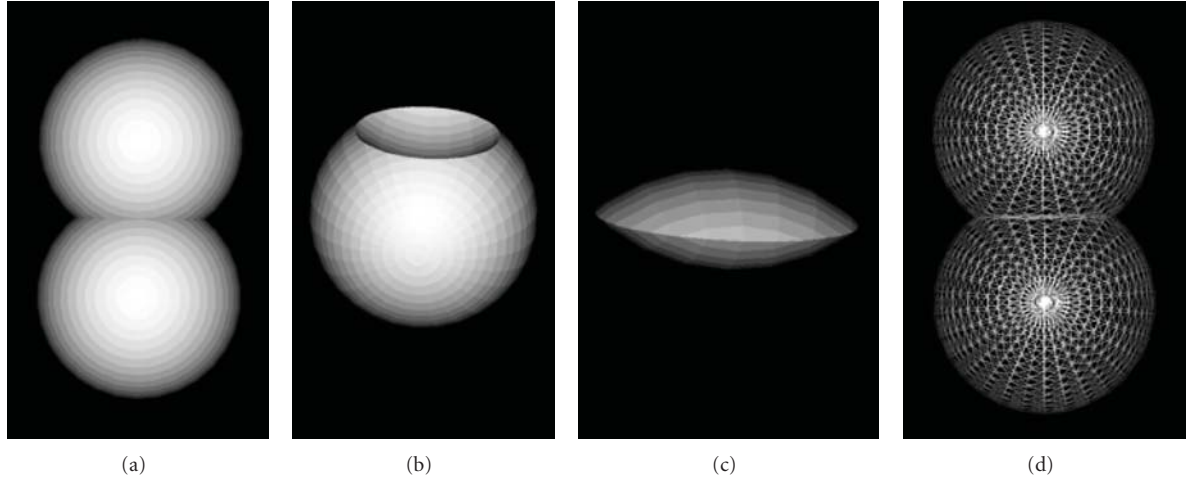


FIGURE 3: Boolean operations performed on (a) two spherical surfaces, (b) subtract, (c) intersection, and (d) union.

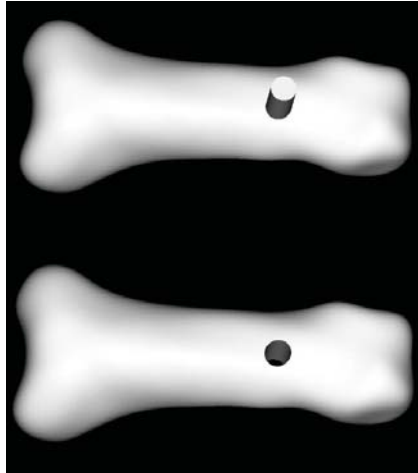


FIGURE 4: Introducing a cylindrical drill hole through the bone.

### 3. Results—A Clinically Relevant Application

While the description above outlines the features of the surgical simulation software, this section describes a clinical application used to test the feasibility of using these tools to evaluate patient-specific surgical procedures.

For example, the procedure of choice for decompression of the cervical spine depends on a variety of factors including the source and location of the compression, the number of vertebral segments involved, cervical alignment, and surgeon experience [31]. Consider, for example, cervical laminoplasty. Laminoplasty was originally developed in Japan [32] to avoid the delayed sequelae of laminectomy without fusion. This procedure initially gained popularity as a treatment for ossification of the posterior longitudinal ligament, but is increasingly being used to treat cases of cervical spondylotic myelopathy. Nevertheless, controversy persists as to whether or not cervical laminoplasty should become the treatment of choice for multilevel cervical stenosis with myelopathy.

Laminoplasty increases the effective diameter of the spinal canal by shifting the laminae dorsally with use of either a single door with a single lateral hinge, or a double door with lateral hinges on both sides. In contrast to laminectomy, laminoplasty retains a covering of the posterior laminar bone and ligamentum flavum over the spinal cord thereby minimizing instability, limits constriction of the dura from extradural scar formation [33, 34], and obviates the need for fusion. Early descriptions of laminoplasty kept the door open with use of suture or wire tethering the spinous process to the hinge side facet joint or capsular tissue [35]. More recent techniques include insertion of an autogenous spinous process graft, allograft bone, or synthetic spacers to keep the door open. Fixation with use of miniplates fixed to the lamina and lateral mass has been reported by multiple authors, without major complications [36–38].

Despite the success of cervical laminoplasty, questions still remain. To address such questions, we recently applied the surgical tools to simulate a cervical laminoplasty using a miniplate at C5 (Figure 6) [39–41]. For this study, a single cadaveric specimen was imaged as described previously. The C5 vertebral body was manually segmented from the CT dataset and the resulting surface loaded into the software to simulate the surgical procedure. The box widget was used to create a bicortical defect on one side, while a Boolean operation between the bony surface definition and a cylindrical surface was used to create a unicortical, or hinge, defect on the contralateral side. A cylindrical surface was also used to create drill holes on either side of the bicortical defect, while the planar widget was used to resect the spinous process. Thereafter, the resulting surface was meshed using a modified building block technique [42] (Figure 6(f)). The final mesh consisted of 29 254 elements. To our knowledge, this is the most refined all-hexahedral mesh of a vertebra reported in the literature. Moreover, the quality of the resulting mesh was as good, if not superior to those developed previously using commercial packages. The minimum, average, and maximum element volumes were 0.053, 0.419, 5.365, respectively, with a variance of 0.187. The

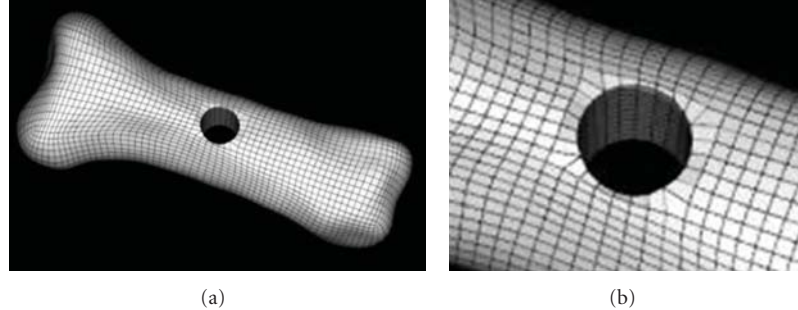


FIGURE 5: Multiblock mesh generated about a through hole. The magnified view of the hole illustrates a subtle loss of mesh fidelity due to smoothing immediately adjacent to the hole.

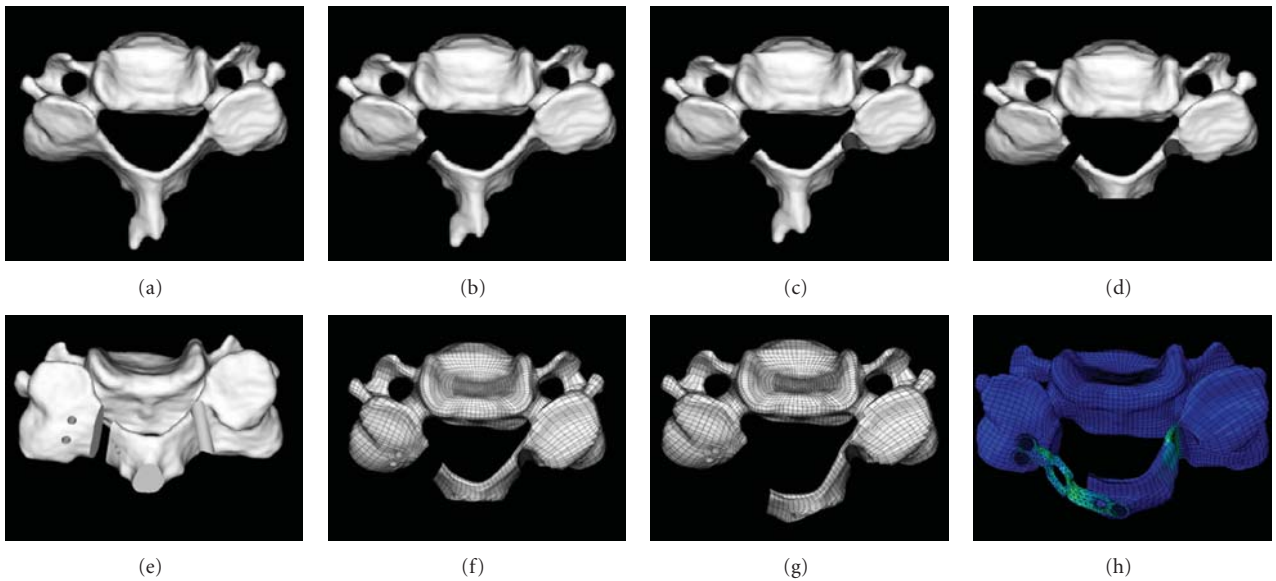


FIGURE 6: Laminoplasty procedure performed on vertebra C5. (a) Intact C5 surface, (b) bicortical defect, (c) contralateral hinge defect introduced, (d) spinous process resected, (e) drill holes introduced, (f) FE mesh, (g) hinge opened and the calculated stresses are input as initial conditions for the (h) plated model.

minimum, average, and maximum Jacobian quality metrics were 0.032, 0.339, 3.776, respectively, with a variance of 0.107. Moreover, FE meshes of the laminoplasty plate and accompanying screws were created. The model was used to predict the potential for fracture at the hinge while opening the posterior elements for plate insertion. Moreover, the stresses induced in the bone as the hinge was opened were incorporated in the plated model as initial conditions. This allowed us to examine the load transfer to the plate/screws as the hinge tried to close postoperatively, in the absence of external loading. The load to failure was predicted by the model under various loading conditions and compared to experimental studies under similar test conditions [39–41].

A substantial increase in the spinal canal area (38%) and diameter (29%) was predicted via the FE model, which compared favorably with the measurements obtained experimentally. It was evident from the finite element analysis and cadaveric testing that the introduction of the hinge reduced

the strength of the lamina by 5- to 9-fold depending on the direction of loading. The stresses in the region of the hinge exceeded the yield strength of the cortical bone indicative of failure, while the stresses in the laminoplasty constructs (i.e., miniplates) were below the yield strength of titanium. Using these meshing techniques, efforts are currently underway to simulate a multilevel laminoplasty in a C27 model and address the flexibility of the spine postoperatively.

#### 4. Discussion

The broad objective of our research plan is to augment IA-FEMesh with a suite of surgical tools, thereby enabling the software to be used to readily simulate/model a variety of surgical procedures. In pursuit of this objective we have developed an easy to use workflow for the manipulation of surfaces representing anatomical structures to simulate surgical procedures. While some of these features exist in other CAD/CAM software (e.g., SOLIDWORKS, VISI) as

well as finite element packages (e.g., ABAQUS CAE or ANSYS), implementing a surgical simulation tool within these packages requires a large learning curve, multiple pieces of software with different user interfaces, and significantly more time to generate the model as compared to the workflow presented here. The software presented here provides the same workflow and user interface as utilized in IA-FEMesh allowing users to perform the surgical simulations and generate the model in a matter of minutes.

In future work, we will merge the functionality described in this paper directly into the IA-FEMesh software, providing a complete surgical simulation workflow within a single software package. In addition, we are proposing to develop unique technologies to manipulate the anatomic surface definitions, enhance the multiblock meshing practices, and to improve the resulting mesh definitions. A promising means to improve the mesh definition of both anatomic structures and implants has proven to be feature recognition [43, 44]. This toolkit holds the potential to enable the user to readily simulate surgical interventions, introduce implants, and mesh the resulting models with all-hexahedral elements using multiblock meshing techniques. Our goal is to provide a meshing environment capable of meshing not only anatomic structures, but implants as well. Moreover, establishing the interactions between the two for analysis is imperative. Our long-term goal is to provide a user friendly meshing environment for researchers interested in FE analyses.

Ultimately, these tools and interactions could be coupled with three-dimensional visualization and haptic feedback that could not only serve as a simulation tool, but also a training tool for young physician scientists. This would allow new surgical procedures to be developed and evaluated in mathematical models before transitioning this work to animal models or clinical applications.

## Acknowledgments

The authors gratefully acknowledge the financial support provided in part by an award (R01EB005973) from the National Institute of Biomedical Imaging and Bioengineering, National Institutes of Health and The University of Iowa Presidential Graduate Fellowship.

## References

- [1] A. Gebert, J. Peters, N. E. Bishop, F. Westphal, and M. M. Morlock, "Influence of press-fit parameters on the primary stability of uncemented femoral resurfacing implants," *Medical Engineering and Physics*, vol. 31, no. 1, pp. 160–164, 2009.
- [2] Y. S. Lee, T. Q. Lee, and J. H. Keyak, "Effect of an UHMWPE patellar component on stress fields in the patella: a finite element analysis," *Knee Surgery, Sports Traumatology, Arthroscopy*, vol. 17, no. 1, pp. 71–82, 2009.
- [3] T. Zander, A. Rohlmann, and G. Bergmann, "Influence of different artificial disc kinematics on spine biomechanics," *Clinical Biomechanics*, vol. 24, no. 2, pp. 135–142, 2009.
- [4] J. Folgado, P. R. Fernandes, C. R. Jacobs, and V. D. Pellegrini, "Influence of femoral stem geometry, material and extent of porous coating on bone ingrowth and atrophy in cementless total hip arthroplasty: an iterative finite element model," *Computer Methods in Biomechanics and Biomedical Engineering*, vol. 12, no. 2, pp. 135–145, 2009.
- [5] A. Completo, J. A. Simões, and F. Fonseca, "Revision total knee arthroplasty: the influence of femoral stems in load sharing and stability," *Knee*, vol. 16, no. 4, pp. 275–279, 2009.
- [6] M. R. Abdul-Kadir, U. Hansen, R. Klabunde, D. Lucas, and A. Amis, "Finite element modelling of primary hip stem stability: the effect of interference fit," *Journal of Biomechanics*, vol. 41, no. 3, pp. 587–594, 2008.
- [7] Y. H. Kim, O. S. Kwon, and K. Kim, "Analysis of biomechanical effect of stem-end design in revision TKA using digital Korean model," *Clinical Biomechanics*, vol. 23, no. 7, pp. 853–858, 2008.
- [8] S. Checa, M. Taylor, and A. New, "Influence of an interpositional spacer on the behaviour of the tibiofemoral joint: a finite element study," *Clinical Biomechanics*, vol. 23, no. 8, pp. 1044–1052, 2008.
- [9] D. D. D'Lima, N. Steklov, B. J. Fregly, S. A. Banks, and C. W. Colwell Jr., "In vivo contact stresses during activities of daily living after knee arthroplasty," *Journal of Orthopaedic Research*, vol. 26, no. 12, pp. 1549–1555, 2008.
- [10] B. Zielinska and T. L. H. Donahue, "3D finite element model of meniscectomy: changes in joint contact behavior," *Journal of Biomechanical Engineering*, vol. 128, no. 1, pp. 115–123, 2006.
- [11] D. Janssen, J. Stolk, and N. Verdonschot, "Finite element analysis of the long-term fixation strength of cemented ceramic cups," *Proceedings of the Institution of Mechanical Engineers, Part H*, vol. 220, no. 4, pp. 533–539, 2006.
- [12] J. P. Halloran, A. J. Petrella, and P. J. Rullkoetter, "Explicit finite element modeling of total knee replacement mechanics," *Journal of Biomechanics*, vol. 38, no. 2, pp. 323–331, 2005.
- [13] E. Peña, B. Calvo, M. A. Martínez, D. Palanca, and M. Doblaré, "Finite element analysis of the effect of meniscal tears and meniscectomies on human knee biomechanics," *Clinical Biomechanics*, vol. 20, no. 5, pp. 498–507, 2005.
- [14] A. R. Hopkins, U. N. Hansen, and A. A. Amis, "Finite element models of total shoulder replacement: application of boundary conditions," *Computer Methods in Biomechanics and Biomedical Engineering*, vol. 8, no. 1, pp. 39–44, 2005.
- [15] E. Gassman, *The validation of an automated image segmentation technique for the development of anatomic finite element models*, M.S. thesis, Department of Biomedical Engineering, The University of Iowa, Iowa City, Iowa, USA, 2006.
- [16] A. J. Ramme, N. Devries, N. A. Kallemeyn, V. A. Magnotta, and N. M. Grosland, "Semi-automated phalanx bone segmentation using the expectation maximization algorithm," *Journal of Digital Imaging*, vol. 22, no. 5, pp. 483–491, 2009.
- [17] E. E. Gassman, S. M. Powell, N. A. Kallemeyn, et al., "Automated bony region identification using artificial neural networks: reliability and validation measurements," *Skeletal Radiology*, vol. 37, no. 4, pp. 313–319, 2008.
- [18] N. M. Grosland, K. H. Shivanna, V. A. Magnotta, et al., "IA-FEMesh: an open-source, interactive, multiblock approach to anatomic finite element model development," *Computer Methods and Programs in Biomedicine*, vol. 94, no. 1, pp. 96–107, 2009.
- [19] S. Benzley, E. Perry, K. Merkley, B. Clark, and G. Sjaardema, "A comparison of all-hexahedra and all-tetrahedra finite element meshes for elastic and elasto-plastic analysis," in *Proceedings 4th International Meshing Roundtable (IMR '95)*, pp. 179–191, 1995.

- [20] A. O. Cifuentes and A. Kalbag, "A performance study of tetrahedral and hexahedral elements in 3-D finite element structural analysis," *Finite Elements in Analysis and Design*, vol. 12, no. 3-4, pp. 313–318, 1992.
- [21] N. A. DeVries, E. E. Gassman, N. A. Kallmeyn, K. H. Shivanna, V. A. Magnotta, and N. M. Grosland, "Validation of phalanx bone three-dimensional surface segmentation from computed tomography images using laser scanning," *Skeletal Radiology*, vol. 37, no. 1, pp. 35–42, 2008.
- [22] V. A. Magnotta, G. Harris, N. C. Andreasen, D. S. O'Leary, W. T. C. Yuh, and D. Heckel, "Structural MR image processing using the BRAINS2 toolbox," *Computerized Medical Imaging and Graphics*, vol. 26, no. 4, pp. 251–264, 2002.
- [23] V. A. Magnotta, D. Heckel, N. C. Andreasen, et al., "Measurement of brain structures with artificial neural networks: two- and three-dimensional applications," *Radiology*, vol. 211, no. 3, pp. 781–790, 1999.
- [24] N. C. Andreasen, G. Cohen, G. Harris, et al., "Image processing for the study of brain structure and function: problems and programs," *Journal of Neuropsychiatry and Clinical Neurosciences*, vol. 4, no. 2, pp. 125–133, 1992.
- [25] N. C. Andreasen, T. Cizadlo, G. Harris, et al., "Voxel processing techniques for the antemortem study of neuroanatomy and neuropathology using magnetic resonance imaging," *Journal of Neuropsychiatry and Clinical Neurosciences*, vol. 5, no. 2, pp. 121–130, 1993.
- [26] T. Loop and H.-J. Priebe, "Recovery after anesthesia with remifentanil combined with propofol, desflurane, or sevoflurane for otorhinolaryngeal surgery," *Anesthesia and Analgesia*, vol. 91, no. 1, pp. 123–129, 2000.
- [27] M. Garland and P. S. Heckbert, "Surface simplification using quadric error metrics," in *Proceedings of the 24th Annual Conference on Computer Graphics (SIGGRAPH '97)*, pp. 209–216, 1997.
- [28] D. A. Field, "Laplacian smoothing and Delaunay triangulations," *Communications in Applied Numerical Methods*, vol. 4, no. 6, pp. 709–712, 1988.
- [29] G. Taubin, T. Zhang, and G. Golub, "Optimal surface smoothing as filter design," in *Proceedings of the 4th European Conference on Computer Vision (ECCV '96)*, pp. 283–292, 1996.
- [30] <http://staff.science.uva.nl/~dshamoni/myprojects/Boolean.html>.
- [31] J. J. Hale, K. I. Gruson, and J. M. Spivak, "Laminoplasty: a review of its role in compressive cervical myelopathy," *Spine Journal*, vol. 6, supplement 6, pp. S289–S298, 2006.
- [32] M. Oyama, S. Hattori, and N. Moriwaki, "A new method of cervical laminoplasty," *Central Japan Journal of Orthopaedic Surgery & Traumatology*, vol. 16, pp. 792–794, 1973.
- [33] Y. Mikawa, J. Shikata, and T. Yamamoto, "Spinal deformity and instability after multilevel cervical laminectomy," *Spine*, vol. 12, no. 1, pp. 6–11, 1987.
- [34] Y. Ishida, K. Suzuki, K. Ohmori, Y. Kikata, and Y. Hattori, "Critical analysis of extensive cervical laminectomy," *Neurosurgery*, vol. 24, no. 2, pp. 215–222, 1989.
- [35] K. Hirabayashi and K. Satomi, "Operative procedure and results of expansive open-door laminoplasty," *Spine*, vol. 13, no. 7, pp. 870–876, 1988.
- [36] H. Deutsch, P. V. Mummaneni, G. E. Rodts, and R. W. Haid, "Posterior cervical laminoplasty using a new plating system: technical note," *Journal of Spinal Disorders and Techniques*, vol. 17, no. 4, pp. 317–320, 2004.
- [37] M. F. O'Brien, D. Peterson, A. T. H. Casey, and H. A. Crockard, "A novel technique for laminoplasty augmentation of spinal canal area using titanium miniplate stabilization: a computerized morphometric analysis," *Spine*, vol. 21, no. 4, pp. 474–484, 1996.
- [38] T. Goto, K. Ohata, T. Takami, et al., "Hydroxyapatite laminar spacers and titanium miniplates in cervical laminoplasty," *Journal of Neurosurgery*, vol. 97, supplement 3, pp. 323–329, 2002.
- [39] S. Tadepalli, A. Gandhi, D. Fredericks, J. Smucker, and N. Grosland, "Cervical laminoplasty construct stability: experimental and finite element investigation," in *Proceedings of the Annual meeting for the American Society of Biomechanics*, State College, PA, USA, August 2009.
- [40] S. Tadepalli, N. Kallamayn, K. Shivanna, J. Smucker, D. Fredericks, and N. Grosland, "Cervical laminoplasty construct stability: a finite element study," in *Proceedings of the ASME Summer Bioengineering Conference*, June 2008.
- [41] S. Tadepalli, "Patient-specific hexahedral mesh generation for orthopaedic surgical planning of cervical laminoplasty," in *Biomedical Engineering*, The University of Iowa, Iowa City, Iowa, USA, 2009.
- [42] N. A. Kallmeyn, S. C. Tadepalli, K. H. Shivanna, and N. M. Grosland, "An interactive multiblock approach to meshing the spine," *Computer Methods and Programs in Biomedicine*, vol. 95, no. 3, pp. 227–235, 2009.
- [43] S. C. Tadepalli, K. H. Shivanna, V. A. Magnotta, and N. M. Grosland, "Patient-specific orthopaedic surgical planning: image datasets to FE models," in *Proceedings of the 31st Annual Meeting of the American Society of Biomechanics*, Palo Alto, CA, 2007.
- [44] K. Shivanna, S. Tadepalli, V. Magnotta, and N. Grosland, "Feature based all hexahedral mesh generation in orthopaedic biomechanics," in *Proceedings of the American Society of Biomechanics*, August 2009.

## Research Article

# Soft Tissue Structure Modelling for Use in Orthopaedic Applications and Musculoskeletal Biomechanics

E. A. Audenaert,<sup>1</sup> P. Mahieu,<sup>1</sup> T. van Hoof,<sup>2</sup> and C. Pattyn<sup>1</sup>

<sup>1</sup>Department of Orthopedic Surgery and Traumatology, Ghent University Hospital, De Pintelaan 185, 9000 Ghent, Belgium

<sup>2</sup>Department of Human Anatomy, Embryology, Histology and Medical Physics, University of Ghent, Ghent, Belgium

Correspondence should be addressed to E. A. Audenaert, emmanuel.audenaert@ugent.be

Received 6 May 2009; Revised 31 August 2009; Accepted 28 October 2009

Academic Editor: João Manuel R. S. Tavares

Copyright © 2010 E. A. Audenaert et al. This is an open access article distributed under the Creative Commons Attribution License, which permits unrestricted use, distribution, and reproduction in any medium, provided the original work is properly cited.

We present our methodology for the three-dimensional anatomical and geometrical description of soft tissues, relevant for orthopaedic surgical applications and musculoskeletal biomechanics. The technique involves the segmentation and geometrical description of muscles and neurovascular structures from high-resolution computer tomography scanning for the reconstruction of generic anatomical models. These models can be used for quantitative interpretation of anatomical and biomechanical aspects of different soft tissue structures. This approach should allow the use of these data in other application fields, such as musculoskeletal modelling, simulations for radiation therapy, and databases for use in minimally invasive, navigated and robotic surgery.

## 1. Introduction

In the last decade, technology revolutionized medical imaging, biomechanical modelling and surgical techniques in the field of orthopaedics. These advances have demonstrated the necessity and feasibility of supportive technologies in clinical practice, including image processing technologies, computer-assisted preoperative planning, image-guided and robotic assisted surgery.

Knowledge of the anatomical-geometrical manipulation of bone, muscles, and neighbouring nervous and vascular structures is essential for safe computed preoperative planning, during navigated and robotic-assisted surgical applications, and for the correct interpretation of post-operative outcomes. All this requires the development of anatomical models that provide digitized data that can be used for geometrical visualization, reconstruction and biomechanical analysis of both preoperative and postoperative anatomy, including the origin, insertion, location and lapses of the muscle fascicles and neurovascular structures surrounding the different joints, as well as detailed three-dimensional data of all osseous anatomical structures involved. The resulting data should obviously not only

be anatomically correct but also generalizing, simple in format and easy to communicate, handle and manipulate.

Currently, musculoskeletal imaging techniques such as magnetic resonance imaging (MRI) and conventional computer tomography (CT) can potentially provide a source for such complete anatomical models. Among the various imaging modalities for visualization of bony anatomy, CT is by far the ultimate medium, with the highest resolution. Soft tissue structures such as muscles, vascular tissues and nerves are significantly better visualized on MRI, and image-fusion techniques have been developed to combine the advantages in reconstruction of different imaging modalities into a single specimen [2, 3]. However, computational restraints and constraints of clinical reality, for example, time, cost, radiation exposure, and last but not least image distortion when large metallic implants are used, currently preclude the creation of full complex customized models of a region of interest. This gap can be bridged by creating idealized generic musculoskeletal models that can be scaled, morphed and fitted into a patient-specific model, using limited imaging and morphometric data of the patient and a database created from cadaver studies, where bone and functionally

relevant soft tissues such as muscles and neurovascular species are collected in detail [4–6]. To create generic models that include detailed bony as well as soft tissue anatomy, CT scanning of cadaver models was performed. Soft tissues were contrasted to allow semi-automated data retrieval in a format that would permit data processing for geometrical visualization in different applications and for biomechanical simulations or treatment planning. Nerve and vascular tissue were mathematically described as tubular structures. Muscle tissue was represented as single fibres, surfaces or solid volumes. This allows these data to be used for the construction of subject-specific data on generic anatomically based models. Alternatively, subject-specific anatomically based models can be constructed by customization/transformation of generic finite element geometric models [7, 8].

## 2. Preparation of the Anatomical Model

Muscle fascicle positions and orientations were predefined on a cadaver model by suturing 0.7-mm flexible copper wires to the muscles, from origin to insertion, following the fibre paths. The brachial plexus, as an example of anatomical complex neural tissue, was carefully dissected and injected with an iodine contrast mixture (Visipaque). A CT multislice scan (Siemens Somatom Volume Zoom) with a slice thickness of 1 mm was performed. The scan started above the occiput and continued down below the hip joint, resulting in about 750 slices. Each slice has  $512 \times 512$  pixels, and each pixel had a grey value in the Hounsfield scale of 4096 grey scale values, meaning that it is represented with a 12-bit value. Voxel size was  $0.88 \text{ mm}^3$ . A total data set from a single scan was therefore  $512 \times 512 \times 750 \times 12 = 2.36 \text{ GB}$  or about 300 MB. (Figure 1)

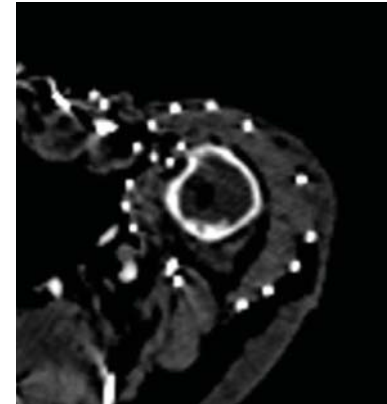
## 3. Segmentation and 3D Reconstruction of Muscle Fibre Paths and Surface Anatomy

The commercially available Mimics software package (Materialise NV, Heverlee, Belgium) was used for a density based segmentation and reconstruction of the different metallic markers and neurovascular structures. The software package was chosen because it allows for semi-automated segmentation using thresholding, dynamic region growing, multislice editing, Boolean operations and hole filling. Contrary the neurovascular structures, the segmentation could be performed more easily and fully automated due to the uniform and high density of the metallic markers.

Postprocessing of the segmented volumes was then performed for the mathematical definition of the orientation and position of the metallic markers used to define the muscle fibre paths. The algorithm to describe fibre positions for use in biomechanical simulations was based on the original description by Van der Helm et al. [20] A point cloud, generally consisting of more than 2000 points representing each marked muscle fibre, was sorted in  $x$ ,  $y$  or  $z$  according to the dominant anatomical direction of the fibre path.



(a)



(b)

FIGURE 1: (a) Metallic markers were attached to the outer surface of each muscle following the muscle fibre paths. (b) Axial CT image following model preparation.

A centreline defining the muscle fibre path was created based on a cluster method algorithm. The clustering algorithm was designed to provide a piecewise segmentation of the structure at interest from beginning to ending, orthogonal to its dominant anatomical direction. Subsequently, a variable  $t (0 \leq t \leq 1)$  was generated in such way that  $d(l)/d(t) \approx l$ , where  $l$  is the total length of the centreline polygon defining the muscle fibre path. This allows to define equidistant parts within the muscle fibre path, a feature that will be used later in the error estimation of the fitting procedure and further surface modelling of the muscle. Furthermore, the insertion ( $t = 1$ ) and origin ( $t = 0$ ) are easily deductible. Polynomials were fitted by a least-squares criterion using vectors  $t_x$ ,  $t_y$ ,  $t_z$ , which are polynomial functions of the variable  $t (0 \leq t \leq 1)$ , to represent all muscle fibre paths:

$$\begin{aligned} x &= a_0 + a_1 t + \dots + a_n t^n \\ y &= b_0 + b_1 t + \dots + b_n t^n \\ z &= c_0 + c_1 t + \dots + c_n t^n \end{aligned} \quad (1)$$

or

$$\begin{bmatrix} x_1 & y_1 & z_1 \\ x_2 & y_2 & z_2 \\ \vdots & \vdots & \vdots \\ x_N & y_N & z_N \end{bmatrix} = \begin{bmatrix} 1 & t_1 & t_1^2 & \dots & t_1^n \\ 1 & t_2 & t_2^2 & \dots & t_2^n \\ \vdots & \vdots & \vdots & \ddots & \vdots \\ 1 & t_N & t_N^2 & \dots & t_N^n \end{bmatrix} \begin{bmatrix} a_0 & b_0 & c_0 \\ a_1 & b_1 & c_1 \\ \vdots & \vdots & \vdots \\ a_n & b_n & c_n \end{bmatrix} \quad (2)$$

The mean resultant error in  $x_i$ ,  $y_i$  and  $z_i$  was expressed as

$$e = \frac{1}{N} \sum_{n=1}^N \text{norm} \begin{bmatrix} x_{i,m} - x_{c,m} \\ y_{i,m} - y_{c,m} \\ z_{i,m} - z_{c,m} \end{bmatrix}, \quad (3)$$

where  $N$  is the number of points defining the centreline,  $x_{i,m}$ ,  $y_{i,m}$  and  $z_{i,m}$  are the predicted points on the t-polynomial, and  $x_{c,m}$ ,  $y_{c,m}$ ,  $z_{c,m}$  the corresponding points on the centreline.

Finally to visualize the position and geometry of muscles, a surface patch was generated using the fitted t-polynomials representing the segmented muscle fibres and a cubic spline interpolation of  $n$  equidistant points on the t-polynomials. (Figure 2)

This method allows to represent each muscle as a limited number of fibres, described by a small  $n$  by 3 matrix, from which fibre origin, insertion, 3D positions and muscle surfaces can be easily obtained for use in scalable generic anatomical models. Figure 3 demonstrates the above as the pectoralis major muscle was represented both as a surface patch and a limited number of separated muscle fibres defining the muscles origin and insertional area.

#### 4. Parametric Reconstruction of Neurovascular Tissues

Numerous vessel extraction techniques and algorithms have been described in the literature. Some of those are applicable to tubular objects that show similar characteristics to vessels, in our case nervous tissue. An interesting overview and classification of most available methods was provided by Kirbas and Quek [9]. The choice of a specific algorithm mainly depends on the intended use of its output parameters. As we intend to generate orientation and general morphology, for use in generic models, we need an extraction technique that provides a simple description of curvature and vessel diameter. We therefore opted for a generalized cylinder model. The generalized cylinder is a volume created by cross-section swept along a path, the vessel centreline. The centreline is represented by a 3D cubic B-spline, in our case simplified by a polynomial approximation.

Similar to the muscle fibre paths, the Mimics software package (Materialise NV, Heverlee, Belgium) was used for initial segmentation of the neurovascular tissue. As the nervous tissue was injected with a contrasting mixture and vessels are air-filled structures in a cadaveric model, semi-automated segmentation of the tissues could be performed using thresholding, dynamic region growing, multislice editing, Boolean operations and hole filling.

Postprocessing of the segmented data of the different nervous and vascular structures was performed to define the orientation, morphology and position of these structures. A centreline of the different nervous and vascular components was generated as previously described for the muscle fibre paths. Nerves and vessels were approximated as tubular structures, of which the local radius was defined using the previously described clustering algorithm. Each cluster represented a piecewise elliptical section of the tube corresponding with the shape of the vessel or nerve. The norm of the projection orthogonal to the centreline of the vector defined by the maximum distance ( $r_{\max}$ ) between the centreline ( $v$ ) and the elliptical section, represented the approximated local radius of a cylinder sectioned by that specific cluster:

$$r = \|r_{\max}\| * \cos \left( \cos^{-1} \left( \frac{v \cdot r_{\max}}{\|v\| \|r_{\max}\|} \right) - \frac{\pi}{2} \right) \quad (4)$$

A variable  $t$  ( $0 \leq t \leq 1$ ) was generated in such way that  $d(l)/d(t) \approx l$ , where  $l$  is the total length of the centreline polygon defining the anatomical structure. A polynomial function of  $t$  ( $0 \leq t \leq 1$ ) was fitted to the centreline and its corresponding radii by a least-squares criterion. The output of the algorithm was a set of directed, 4-dimensional points indicating the  $(x, y, z)$  spatial position of each sequential vessel or nerve skeleton point with an associated radius at each point. The total generated equation consisted of  $x, y, z$  representing the centreline, and  $r$  representing the radius:

$$\begin{aligned} x &= a_0 + a_1 t + \dots + a_n t^n \\ y &= b_0 + b_1 t + \dots + b_n t^n \\ z &= c_0 + c_1 t + \dots + c_n t^n \\ r &= d_0 + d_1 t + \dots + d_n t^n \end{aligned} \quad (5)$$

or

$$\begin{bmatrix} x_1 & y_1 & z_1 & r_1 \\ x_2 & y_2 & z_2 & r_2 \\ \vdots & \vdots & \vdots & \vdots \\ x_N & y_N & z_N & r_N \end{bmatrix} = \begin{bmatrix} 1 & t_1 & t_1^2 & \dots & t_1^n \\ 1 & t_2 & t_2^2 & \dots & t_2^n \\ \vdots & \vdots & \vdots & \ddots & \vdots \\ 1 & t_N & t_N^2 & \dots & t_N^n \end{bmatrix} \begin{bmatrix} a_0 & b_0 & c_0 & d_0 \\ a_1 & b_1 & c_1 & d_1 \\ \vdots & \vdots & \vdots & \vdots \\ a_n & b_n & c_n & d_n \end{bmatrix} \quad (6)$$

The surface of the vessels and nerves were then modelled as curved tubes with variable radii in three dimensional space, based on estimating Frenet-Serret frames along the t-polynomial as originally described by Zerroug and Neftaia [10]. Although easy to implement, the Frenet-Serret formulation model and tube model are known to suffer from serious drawbacks of discontinuities and non-intuitive twisting behaviour at infliction points along the curve [9].

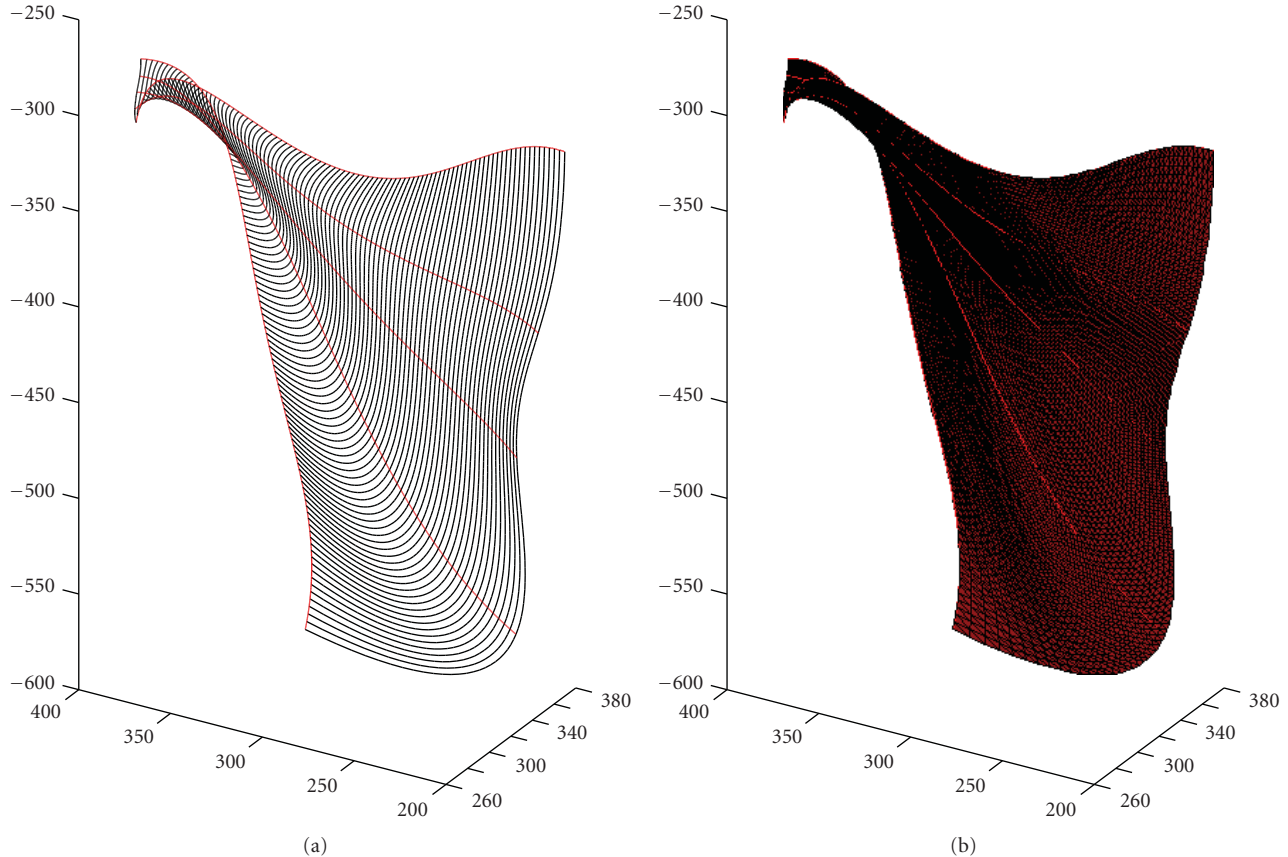


FIGURE 2: Muscle surfaces are reconstructed by cubic spline interpolation of  $n$  equidistant point on the fitted t-polynomials. The given example represents the latissimus dorsi muscle.

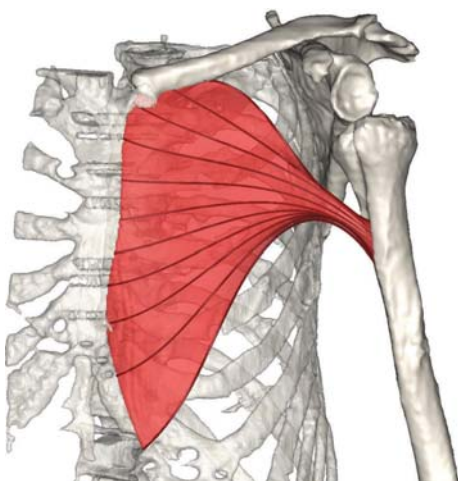


FIGURE 3: Illustration of the pectoralis major muscle including the muscle surface patch and a limited number of muscle fibres.

One way around this is to calculate the frame not using the second derivative of the curve (which becomes parallel to the tangent at these inflection points) but using an arbitrary vector that is never parallel to the tangent. (Figure 2)

We realize that the above description to obtain the vessel or nerve centreline and radius is approximative and by no means comparable to the advanced algorithms for vessel extraction used in today's automated radiological diagnostic systems. The method obviously is not intended for the diagnosis or description of local morphological abnormalities, but for the generation of generic anatomical models. The algorithm is easily reproducible and computationally fast. Moreover, it delivers anatomy as a generalized model in a format that is easy to communicate and manipulate. The entire subclavian artery for example is represented by a 4 by 4 matrix. Because of these features, our method fulfils the requirements of a generic model aimed at applications in orthopaedics and musculoskeletal biomechanics

## 5. Anatomical Model Reconstructions, Challenging Cases

To demonstrate the robustness of our method the following muscles were chosen for their complex anatomical structure: Latissimus dorsi, Trapezius and Deltoid muscle. In general 3rd or 4th-order t-polynomials were sufficient to approximate the different muscle fibre paths. Muscles of less complex morphology will probably be adequately represented by even lower degree functions. The use of t-polynomials

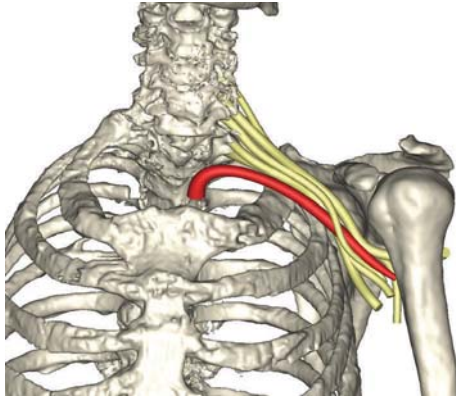
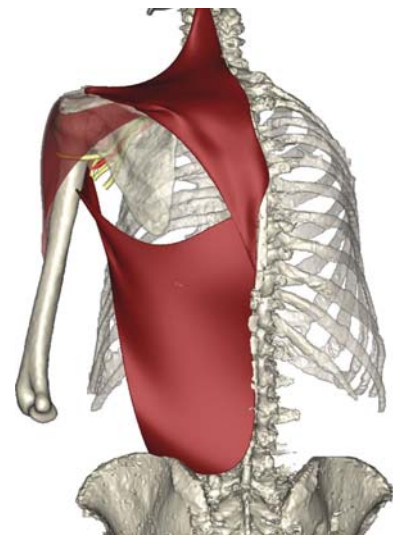


FIGURE 4: Surface reconstruction of the brachial plexus and intersecting subclavian artery.



(a)



(b)

FIGURE 5: Front (a) and back (b) view of a partially reconstructed soft tissue model including the deltoid, latissimus dorsi and trapezius muscle, the subclavian artery and brachial plexus.

## 6. Transition to Volumetric Muscle Models

Muscles are geometrically positioned between bone and other neighbouring muscles. Once the outer surfaces of all possible delimiting structures are derived, the remaining volume described by each muscle can therefore be predicted on a layer by layer basis. (Figure 6)

However, the transition to volumetric data requires though a muscle-specific approach. Muscles close to the bony skeleton such as the rotator cuff muscles, for example, the supraspinatus, infraspinatus and subscapularis muscle, fill discrete cavities onto the scapular body. The muscle's volume is therefore defined by the bony surface delimiting the muscle's inner surface, the scapular body, and the muscle's outer surface as previously obtained. To describe the path of muscle fibres on the inner surface of these muscles,

the problem can be approached as a minimizing geodesic path on the delimiting bony surfaces [1].

Superficial muscle layers on the other hand tend to cover the deeper layers as an elastic membrane. For these, the previously obtained outer surface can be defined as a conformation of this elastic membrane of high potential energy, which is then progressively released to a position of lesser potential energy without penetration of any delimiting structure, for example, bony surfaces or underlying muscles. This can be achieved by defining a finite number of spring elements connecting the surface nodes on the previously obtained muscle's outer surface.

This surface is composed of  $N$ -by- $N$  nodes, each describing  $(N - 1)$ -by- $(N - 1)$  tetragons. For each tetragon the respective centroid is defined. These are then used to define

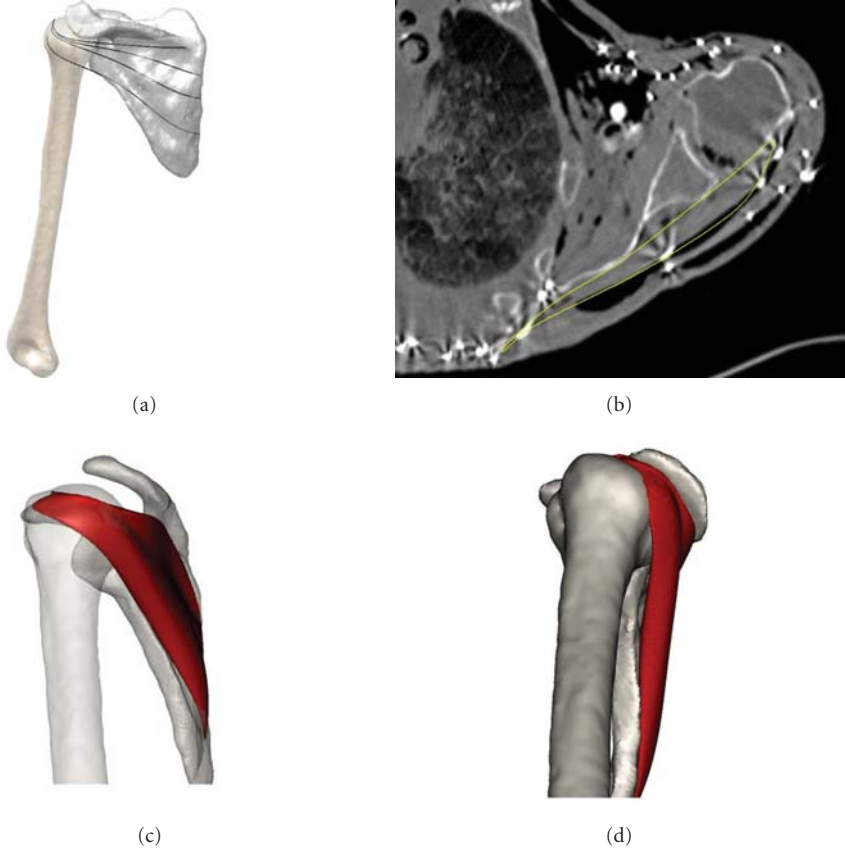


FIGURE 6: (a) Reconstruction of muscle fibre paths on the inner surface of the infraspinatus muscle. (b) Contour of the infraspinatus volume on the axial view. (c) & (d) Volumetric mesh of the infraspinatus muscle.

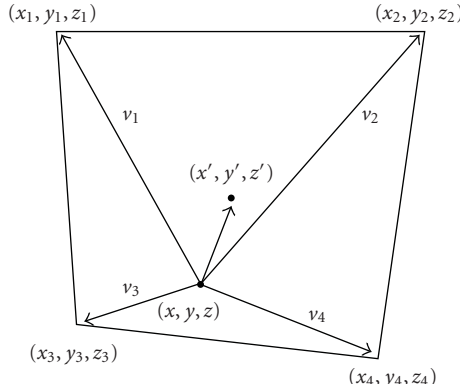


FIGURE 7: Each tetragon of the surface mesh is considered as a spring system. The central node is displaced to a new position by iteratively finding a new force-balancing state.

the basic element in the further optimization procedure. The movement of each original node is iteratively calculated by using the locations of its adjacent previously defined centroids only. Each edge connecting the central node with its neighbouring centroids can be seen as a linear spring with an initial length of zero.

Let  $v_i$  be the vector from the central node to the  $i$  the neighbouring centroid:

$$v_i = (x_i - x, y_i - y, z_i - z) \quad (7)$$

The sum of the spring forces acting on the central node is:

$$F = K \sum_{i=1}^k v_i, \quad (8)$$

where  $K$  is the spring constant, and  $k$  is the number of neighbouring centroids.

Considering that all the springs have initial lengths of zero, we can compute the potential energy of the system as:

$$E_p = \sum_{i=1}^4 \frac{1}{2} K \left( \|v_i\|_{L_2} \right)^2 \quad (9)$$

The cost function to be minimized is the sum of the squared lengths of the edges shared by the same centroid:

$$f(x, y, z) = \sum_{i=1}^4 \left( (x - x_i)^2 + (y - y_i)^2 + (z - z_i)^2 \right) \quad (10)$$

We can obtain position  $(x, y, z)$  that minimizes the cost function by simply finding the geometric centre of the neighbouring centroids:

$$\frac{\partial f}{\partial x} = \frac{\partial f}{\partial y} = \frac{\partial f}{\partial z} = 0$$

$$x = \frac{1}{4} \sum_{i=1}^4 x_i; \quad y = \frac{1}{4} \sum_{i=1}^4 y_i; \quad z = \frac{1}{4} \sum_{i=1}^4 z_i \quad (11)$$

In case the algorithm results in a node displacement that would cause penetration of any local obstacle, the surface point on the obstacle closest to the local minimum is withheld. The process is repeated until a steady state is obtained, defining the inner surface of muscle. Upon closure of both the inner and outer surfaces, the volume describing the muscle at interest remains. (Figure 7)

## 7. Application in Orthopaedic Simulations

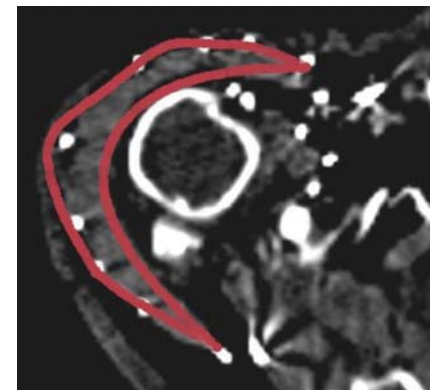
An implementation of the technique and its applications can be illustrated in reversed shoulder arthroplasty or nonanatomical shoulder replacement. Compared to normal shoulder anatomy, this prosthesis is a reverse ball-and-socket design, which results in important anatomical and biomechanical changes around the shoulder joint. Not only does the design produce significant changes in muscle moment arms, several anatomical structures are translated or stretched [11–13].

A cadaver model was prepared as outlined above for the description of normal anatomy. Next, a plastic model of a reversed shoulder prosthesis obtained by rapid prototyping was surgically implanted. The model was then scanned a second time in order to allow model reconstruction following nonanatomical shoulder replacement. (Figure 8)

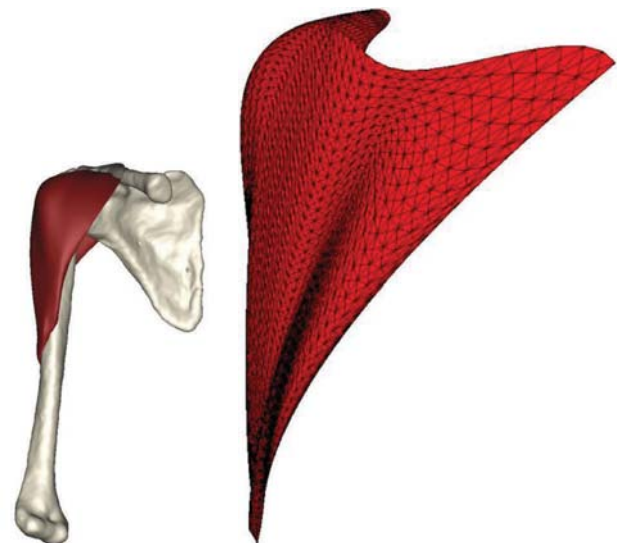
The preoperative and postoperative specimens were studied with use of a helical CT scan (Siemens/volume zoom). Scanning parameters were similar to those described earlier. The shoulder of the specimen was positioned in adduction-internal rotation and the elbow in approximately 90 degrees of flexion. The cervical spine was placed in a neutral position and both wrists were placed and strapped down on the lower abdomen. (Figure 9)

The CT images of the first and the second session were uploaded separately into the Mimics software package for further segmentation and 3D reconstruction (Materialise N.V., Heverlee, Belgium). Thresholding for bone, air, the iodine-contrasted tissues and the metallic markers was the first action performed to create a segmentation mask. Then, each region of interest was further selected.

Our method allows for a detailed analysis of changes in geometrical and biomechanical parameters, caused by the surgical procedure. For example measurement of excursion, elongation and displacement of the brachial plexus nerves after reversed prosthesis surgery of the shoulder joint following model preparation as outlined in the present paper has previously been described in detail [12].



(a)



(b)

(c)



(d)

FIGURE 8: (a) Contour of the deltoid volumetric mesh on an axial CT image. (b) The deltoid volume was created by fusion of the calculated inner and outer surfaces. (c) Separate visualization of the inner en outer surface mesh of the deltoid muscle.

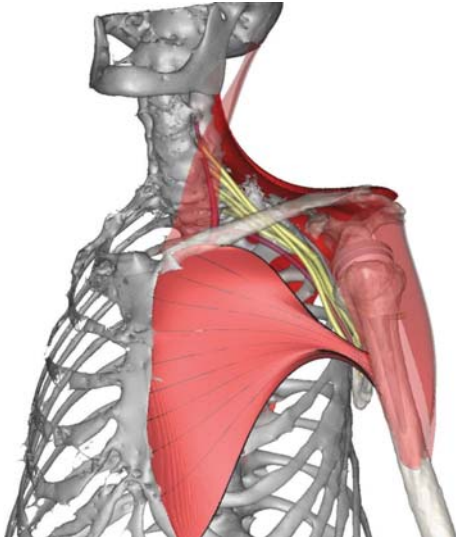


FIGURE 9: Postoperative reconstruction with a reversed shoulder prosthesis *in situ*. Reconstruction of the brachial plexus, brachial artery and surface reconstruction of the sternocleidomastoides, deltoid, pectoralis major (with fibre directions) and trapezius.

## 8. Conclusions

Technological assistance in orthopaedic surgery has progressed mainly from the combination of pre-and intraoperative imaging modalities on rigid osseous structures, sometimes combined with the use of tracking systems [14]. Few studies have focused on functional and surgically relevant deformable soft tissues other than skin and fat, such as muscle, vascular and nervous structures, and the postoperative outcome related to their surgical manipulation in orthopaedic applications [12]. Mainly due to the different nature of the treated pathologies, other surgical disciplines have evolved in a completely different, and compared to orthopaedics, mainly soft tissue focused direction, for example, augmented reality, soft tissue navigation and haptic technology applications in abdominal and pelvic surgery and soft tissue models for use in virtual reality training for minimally invasive and laparoscopic surgery [15, 16].

Parallel to the technological advances in computer and robotic aided orthopaedic surgery, musculoskeletal modelling has evolved greatly and appears to be close on the verge of integrating biomechanical simulations of soft tissue structures with intraoperative image guidance on bony anatomy [17–19]. Such near future improvements require general data that can bridge the gap between the two technological modalities and can be used for the development and validation of the fused endproduct.

Although a variety of anatomical data sets and reports on anthropometric scaling of bone and muscle attachment sites, usually within the context of biomechanical modelling, are available, few studies in the literature have focused on the digitization and parametric description of complete soft tissue anatomical models for direct application in modelling or computer-assisted surgical techniques in orthopaedics [5, 6, 12, 20–22].

Anatomical datasets for biomechanical analysis of an orthopaedic intervention usually describe the anatomy of a normal model, from which surgical manipulation of muscles and the corresponding biomechanical effect can be calculated [20, 23]. The classical example and gold standard for comparison remains the work published by Van der Helm et al. [20] who used a 3D-palpator and digitizer for the polynomial description of position and geometry of muscle and muscle attachment sites in the upper and lower limb. A variety of wrapping algorithms are then available for the full description of muscle fibre positions for biomechanical simulation of a specific surgical procedure [21, 24–26]. However, currently no data or method exists that can be used for the validation of such mathematically reconstructed anatomy, nor are there data on the choice and position of wrapping objects used to create the resulting simulation environment. Finally, functional and surgically relevant structures such as vessels and nerves have never been included in these simulations, although surgery affects their position and length and can compromise the postoperative outcome [12]. For nervous structures for example, it has been shown that a nerve strain of 5–10% already impairs axonal transport and nerve conduction [27].

The present method allows for such analysis. Following anatomical preparation, estimation of muscle and joint parameters necessary for biomechanical analysis and 3D imaging of the cadaver model, a specific surgical procedure can be performed and the resulting deflection and positions of relevant soft tissues can be visualized and geometrically analyzed. Wrapping objects for use in biomechanical simulations can be estimated and validated from both the reconstructed bony surfaces and the resulting deflections of the reconstructed muscle fascicles and surface models. In the field of navigated and computer-assisted surgery, the geometrical description of soft tissues is particularly useful to create a virtual environment that is reassuring and familiar to the operating surgeon, and to alert him that caution must be exerted during surgery in the proximity of fragile structures such as vessels and nerves.

The technique and its applications obviously have limitations. In the transition from generic to customized models, care should be taken in extrapolating the results; not because the validity of the model is being questioned, but because of the subject specificity, ethnic and racial variations, and the not uncommon occurrence of anatomical variants [6].

Despite this important limitation we believe that, for the current status of technology in imaging, surgical navigation and biomechanical analysis, the described technique offers a number of advantages that might aid in the further development of biomechanical models and computer-assisted surgical applications as well as for the closer integration of both.

## Acknowledgments

We are grateful to the Ghent University Department of Anatomy, Embryology, Histology and Medical Physics for providing the cadaver specimen used in this study. This

work was supported by the Institute for the Promotion of Innovation through Science and Technology in Flanders (I.W.T-Vlaanderen).

## References

- [1] E. W. Dijkstra, "A note on two problems in connexion with graphs," *Numerische Mathematik*, vol. 1, no. 1, pp. 269–271, 1959.
- [2] N. Archip, R. Rohling, V. Dessenne, P.-J. Erard, and L. P. Nolte, "Anatomical structure modeling from medical images," *Computer Methods and Programs in Biomedicine*, vol. 82, no. 3, pp. 203–215, 2006.
- [3] K. G. Baum, M. Helguera, and A. Krol, "Fusion viewer: a new tool for fusion and visualization of multimodal medical data sets," *Journal of Digital Imaging*, vol. 21, supplement 1, pp. S59–S68, 2008.
- [4] G. T. Gomes, E. A. Audenaert, L. De Wilde, and K. D'Herde, "Individualizing biomechanical shoulder models using scaling, morphing and fittings," in *Proceedings of the 1st ECCOMAS Thematic Conference on Computational Vision and Medical Image Processing (VIPIMAGE '07)*, pp. 319–322, Porto, Portugal, October 2008.
- [5] B. L. Kaptein and F. C. T. van der Helm, "Estimating muscle attachment contours by transforming geometrical bone models," *Journal of Biomechanics*, vol. 37, no. 3, pp. 263–273, 2004.
- [6] R. Matias, C. Andrade, and A. Veloso, "A transformation method to estimate muscle attachments based on three bony landmarks," *Journal of Biomechanics*, vol. 42, no. 3, pp. 331–335, 2009.
- [7] J. W. Fernandez, P. Mithraratne, S. F. Thrupp, M. H. Tawhai, and P. J. Hunter, "Anatomically based geometric modelling of the musculo-skeletal system and other organs," *Biomechanics and Modeling in Mechanobiology*, vol. 2, no. 3, pp. 139–155, 2004.
- [8] J. H. Challis, "A procedure for determining rigid body transformation parameters," *Journal of Biomechanics*, vol. 28, no. 6, pp. 733–737, 1995.
- [9] C. Kirbas and F. Quek, "A review of vessel extraction techniques and algorithms," *ACM Computing Surveys*, vol. 36, no. 2, pp. 81–121, 2004.
- [10] M. Zerroug and R. Nevatia, "Quasi-invariant properties and 3-D shape recovery of non-straight, non-constant generalized cylinders," in *Proceedings of the IEEE Conference on Computer Vision and Pattern Recognition*, pp. 96–103, New York, NY, USA, June 1993.
- [11] A. Terrier, A. Reist, F. Merlini, and A. Farron, "Simulated joint and muscle forces in reversed and anatomic shoulder prostheses," *Journal of Bone and Joint Surgery. British*, vol. 90, no. 6, pp. 751–756, 2008.
- [12] T. Van Hoof, G. T. Gomes, E. Audenaert, K. Verstraete, I. Kerckaert, and K. D'Herde, "3D computerized model for measuring strain and displacement of the brachial plexus following placement of reverse shoulder prosthesis," *Anatomical Record*, vol. 291, no. 9, pp. 1173–1185, 2008.
- [13] P. Boileau, D. J. Watkinson, A. M. Hatzidakis, and F. Balg, "Grammont reverse prosthesis: design, rationale, and biomechanics," *Journal of Shoulder and Elbow Surgery*, vol. 14, no. 1, supplement 1, pp. 147S–161S, 2005.
- [14] A. D. Pearle, D. Kendoff, and V. Musahl, "Perspectives on computer-assisted orthopaedic surgery: movement toward quantitative orthopaedic surgery," *Journal of Bone and Joint Surgery. American*, vol. 91, supplement 1, pp. 7–12, 2009.
- [15] N. Famaey and J. V. Sloten, "Soft tissue modelling for applications in virtual surgery and surgical robotics," *Computer Methods in Biomechanics and Biomedical Engineering*, vol. 11, no. 4, pp. 351–366, 2008.
- [16] D. Teber, M. Baumhauer, E. O. Guven, and J. Rassweiler, "Robotic and imaging in urological surgery," *Current Opinion in Urology*, vol. 19, no. 1, pp. 108–113, 2009.
- [17] O. de Leest, P. M. Rozing, L. A. Rozendaal, and F. C. T. van der Helm, "Influence of glenohumeral prosthesis geometry and placement on shoulder muscle forces," *Clinical Orthopaedics and Related Research*, no. 330, pp. 222–233, 1996.
- [18] S. L. Delp, J. P. Loan, M. G. Hoy, F. E. Zajac, E. L. Topp, and J. M. Rosen, "An interactive graphics-based model of the lower extremity to study orthopaedic surgical procedures," *IEEE Transactions on Biomedical Engineering*, vol. 37, no. 8, pp. 757–767, 1990.
- [19] D. J. Magermans, E. K. J. Chadwick, H. E. J. Veeger, F. C. T. van der Helm, and P. M. Rozing, "Biomechanical analysis of tendon transfers for massive rotator cuff tears," *Clinical Biomechanics*, vol. 19, no. 4, pp. 350–357, 2004.
- [20] F. C. T. van der Helm, H. E. J. Veeger, G. M. Pronk, L. H. V. Van der Woude, and R. H. Rozendal, "Geometry parameters for musculoskeletal modelling of the shoulder system," *Journal of Biomechanics*, vol. 25, no. 2, pp. 129–144, 1992.
- [21] I. W. Charlton and G. R. Johnson, "Application of spherical and cylindrical wrapping algorithms in a musculoskeletal model of the upper limb," *Journal of Biomechanics*, vol. 34, no. 9, pp. 1209–1216, 2001.
- [22] T. M. Kepple, A. S. Arnold, S. J. Stanhope, and K. L. Siegel, "Assessment of a method to estimate muscle attachments from surface landmarks: a 3D computer graphics approach," *Journal of Biomechanics*, vol. 27, no. 3, pp. 365–371, 1994.
- [23] M. D. Klein Horsman, H. F. J. M. Koopman, F. C. T. van der Helm, L. P. Prose, and H. E. J. Veeger, "Morphological muscle and joint parameters for musculoskeletal modelling of the lower extremity," *Clinical Biomechanics*, vol. 22, no. 2, pp. 239–247, 2007.
- [24] A. Audenaert and E. Audenaert, "Global optimization method for combined spherical-cylindrical wrapping in musculoskeletal upper limb modelling," *Computer Methods and Programs in Biomedicine*, vol. 92, no. 1, pp. 8–19, 2008.
- [25] F. Gao, M. Damsgaard, J. Rasmussen, and S. Christensen, "Computational method for muscle-path representation in musculoskeletal models," *Biological Cybernetics*, vol. 87, no. 3, pp. 199–210, 2002.
- [26] S. P. Marsden, D. C. Swailes, and G. R. Johnson, "Algorithms for exact multi-object muscle wrapping and application to the deltoid muscle wrapping around the humerus," *Proceedings of the Institution of Mechanical Engineers, Part H*, vol. 222, no. 7, pp. 1081–1095, 2008.
- [27] K. Ogata and M. Naito, "Blood flow of peripheral nerve effects of dissection stretching and compression," *Journal of Hand Surgery British*, vol. 11, no. 1, pp. 10–14, 1986.

## Research Article

# Imaging Arterial Fibres Using Diffusion Tensor Imaging—Feasibility Study and Preliminary Results

Vittoria Flamini,<sup>1</sup> Christian Kerskens,<sup>2</sup> Kevin M. Moerman,<sup>3</sup>  
Ciaran K. Simms,<sup>3</sup> and Caitríona Lally<sup>1,3</sup>

<sup>1</sup> School of Mechanical and Manufacturing Engineering, Dublin City University, Dublin 9, Ireland

<sup>2</sup> Trinity College Institute for Neuroscience, Trinity College Dublin, Dublin 2, Ireland

<sup>3</sup> Trinity Centre for Bioengineering, School of Engineering, Trinity College Dublin, Dublin 2, Ireland

Correspondence should be addressed to Caitríona Lally, triona.lally@dcu.ie

Received 1 May 2009; Revised 13 August 2009; Accepted 21 November 2009

Academic Editor: João Manuel R. S. Tavares

Copyright © 2010 Vittoria Flamini et al. This is an open access article distributed under the Creative Commons Attribution License, which permits unrestricted use, distribution, and reproduction in any medium, provided the original work is properly cited.

MR diffusion tensor imaging (DTI) was used to analyze the fibrous structure of aortic tissue. A fresh porcine aorta was imaged at 7T using a spin echo sequence with the following parameters: matrix  $128 \times 128$  pixel; slice thickness 0.5 mm; interslice spacing 0.1 mm; number of slices 16; echo time 20.3 s; field of view 28 mm  $\times$  28 mm. Eigenvectors from the diffusion tensor images were calculated for the central image slice and the averaged tensors and the eigenvector corresponding to the largest eigenvalue showed two distinct angles corresponding to near  $0^\circ$  and  $180^\circ$  to the transverse plane of the aorta. Fibre tractography within the aortic volume imaged confirmed that fibre angles were oriented helically with lead angles of  $15 \pm 2.5^\circ$  and  $175 \pm 2.5^\circ$ . The findings correspond to current histological and microscopy data on the fibrous structure of aortic tissue, and therefore the eigenvector maps and fibre tractography appear to reflect the alignment of the fibers in the aorta. In view of current efforts to develop noninvasive diagnostic tools for cardiovascular diseases, DTI may offer a technique to assess the structural properties of arterial tissue and hence any changes or degradation in arterial tissue.

## 1. Introduction

Cardiovascular diseases are the leading cause of death in the Western world, accounting for nearly half of all the deaths in Europe [1]. The most common arterial diseases are as a result of alterations in the structure of the arterial wall [2, 3]. Principally, these structural alterations are due to either degeneration of arterial tissue such as in the case of aneurysms [3], or the accumulation of lipids within an artery which can form plaques and stiffen the vessel, as in atherosclerosis [2]. Arterial diseases often progress without symptoms to a point where they sufficiently compromise the circulatory system and subsequently cause a sudden, often fatal event. In fact, aneurysms can dilate an arterial vessel to the point where the vessel tears as a result of the blood pressure, causing a massive haemorrhage [3]. Atherosclerotic plaques can grow within an arterial lumen obstructing blood flow and hence oxygen supply to an organ, causing ischemia

[2]. Ischemia can result in serious damage to vital organs and ultimately can result in myocardial infarction or stroke.

Since arterial diseases may develop in a symptomless way, the best way to diagnose and treat such diseases is by means of preventive medicine and screening [2, 4]. The optimal screening technique should be noninvasive and capable of detecting early signs of alterations in the arterial structure.

Many hemodynamic studies have investigated the onset of arterial disease in an attempt to provide early indicators of arterial disease that may be detected during diagnostic screening [4, 5]. They have shown that the arterial wall is an active structure which is subjected to loading and able to respond to environmental changes. In these studies attention has been focussed on alterations in the blood flow pattern in arteries which can create an imbalance in the complex relationship between the forces that regulate the remodelling of the arteries [4, 6–8]. In fact, an injury in the arterial wall or a change in the fluid shear force can trigger an abnormal

proliferation of the cells, thus causing atherosclerosis. These studies show that the arterial wall is capable of remodelling and it continuously adapts tending towards an optimal balance between stress and strain [4, 7]. In other words, it could be inferred that arterial diseases can be studied by means of solid mechanics and that a disease could be the result of a change in the vessel mechanical properties [9]. This approach could improve the understanding of atherosclerosis and could also be used in determining the aetiology of aneurysms, which, is as yet not completely understood [3].

In order to perform *in vivo* studies on the solid mechanics of arteries a noninvasive technique that would expose the patient to minimal harm must be used. Noninvasive techniques that are commonly used for the study of arterial diseases include Computed Tomography Angiography (CTA) [10], Magnetic Resonance Angiography (MRA) [11], X-Ray Angiography [12], and colour Doppler Ultrasound [13]. These imaging modalities are limited as they can only image the blood flow and cannot be used to study the mechanics of the arterial wall. They can therefore only provide information on the effect of arterial disease on blood flow and not the underlying cause. Conventional imaging techniques like Computed Tomography (CT) [14] and Magnetic Resonance Imaging (MRI) [15] can be used to image the arterial wall; however they can only provide an anatomical description of a vessel which is insufficient for full mechanical characterization.

In the 1990s, researchers developed an MRI application capable of analysing *in vivo* the axonal structure of the brain called Diffusion Tensor Imaging (DTI) [16]. DTI is capable of describing the degree of anisotropy of a tissue by analysing the diffusion of water molecules. This motion, which is normally random and hence the same in every direction, that is, isotropic, is altered and constrained in a biological tissue, that is, anisotropic, due to the composition of the underlying microstructure [17]. DTI consists of measuring the diffusion coefficients of water molecules in different directions for each pixel of the image and then creating a diffusion tensor for each pixel [18]. Furthermore, the direction of greatest diffusion, represented by the first eigenvector of the diffusion tensor, can be used to provide information on the fibrous architecture of the tissue, because water molecules will diffuse preferentially along fibres rather than across them [17]. The process of determining the fibre architecture from the diffusion tensor is called fibre tractography [19]. Since the development of DTI and fibre tractography [16, 19], these methods have been successfully applied to the brain [20], the heart [21, 22], skeletal muscle [23], cartilage [24, 25], and bone [26]. The combination of DTI and fibre tractography has enabled the architecture of the fibrous components of these tissues to be established *in vivo*.

Arterial tissue can be regarded as a fibre-reinforced material, because different kinds of fibres are present in the arterial wall. The arterial wall can be divided in three layers, each one with its own properties [7, 27]. The inner one is extremely thin and is called the intima. It is composed of endothelium and subendothelium and its role

consists of protecting the other layers from plasma lipids and lipoproteins. The middle layer is the media, where both elastic laminae and smooth muscle cells (SMCs) are present. In histological studies reported by Rhodin [27], the elastic laminae are described to be concentrically arranged, while SMCs are reportedly oriented diagonally at small angles, forming a spiral around the vessel. The outer layer is the adventitia, which is dense fibroelastic tissue without smooth muscle cells. Large elastic arteries, such as the aorta, contain high levels of elastin fibres in the media in order that they can withstand the pulsatile pressure waveform produced by the heart whilst more muscular arteries contain higher levels of smooth muscle cells and collagen and lower levels of elastin [7, 27]. The quantity and distribution of fibres within the arterial wall and their quality is therefore a direct measure of the mechanical strength and the health of arterial tissue [9].

In this study the aim was to assess the applicability of DTI for determining the fibre structure of arterial tissue. In particular, DTI was evaluated to establish if it could determine the helical and near circumferential arrangement of fibres within the aorta that has been extensively reported to be present within arterial tissue.

## 2. Materials and Methods

A porcine aorta was harvested from a six-month-old pig of Irish breed. The thoracic-abdominal section of the aorta was cut from the complete aorta. The vessel was 122 mm long and had a thickness of 2 mm in the proximal section and 1.5 mm in the distal one. The external connective tissue was removed from the aorta, and the vessel was placed in a custom designed cylindrical chamber filled with water. The chamber had dimensions of 32 mm diameter and 200 mm length. The chamber was designed to fit a circular polarised whole body Radio Frequency coil for a 7T Biospec (Bruker Biospin, Germany) Magnetic Resonance Imaging (MRI) scanner. The sample was scanned within 24 hours of slaughter according to the following Diffusion Tensor Imaging (DTI) acquisition protocol: spin echo sequence; matrix  $128 \times 128$  pixel; slice thickness 0.5 mm; interslice spacing 0.1 mm; number of slices 16; echo time 20.3 s; field of view 28 mm  $\times$  28 mm.

Diffusion Tensor Imaging is characterised by the application of a diffusion sensitivity gradient over at least six noncoplanar directions and by the application of a particular  $b$  value, where the  $b$  value is a measure of the sensitivity to diffusion, defined as follows:

$$\frac{S}{S_0} = \exp(-bD), \quad (1)$$

where  $S$  is the signal of the image analysed with an encoding gradient,  $S_0$  is the signal of a reference image (i.e., one taken with a null gradient), and  $D$  is the diffusion tensor [17]. The  $b$  value influences the signal-to-noise ratio and also describes the impact that the diffusion has on the image: when the  $b$  value increases, water molecular diffusion increases and therefore the signal of the image,  $S$ , diminishes along the direction of the gradient and the signal-to-noise

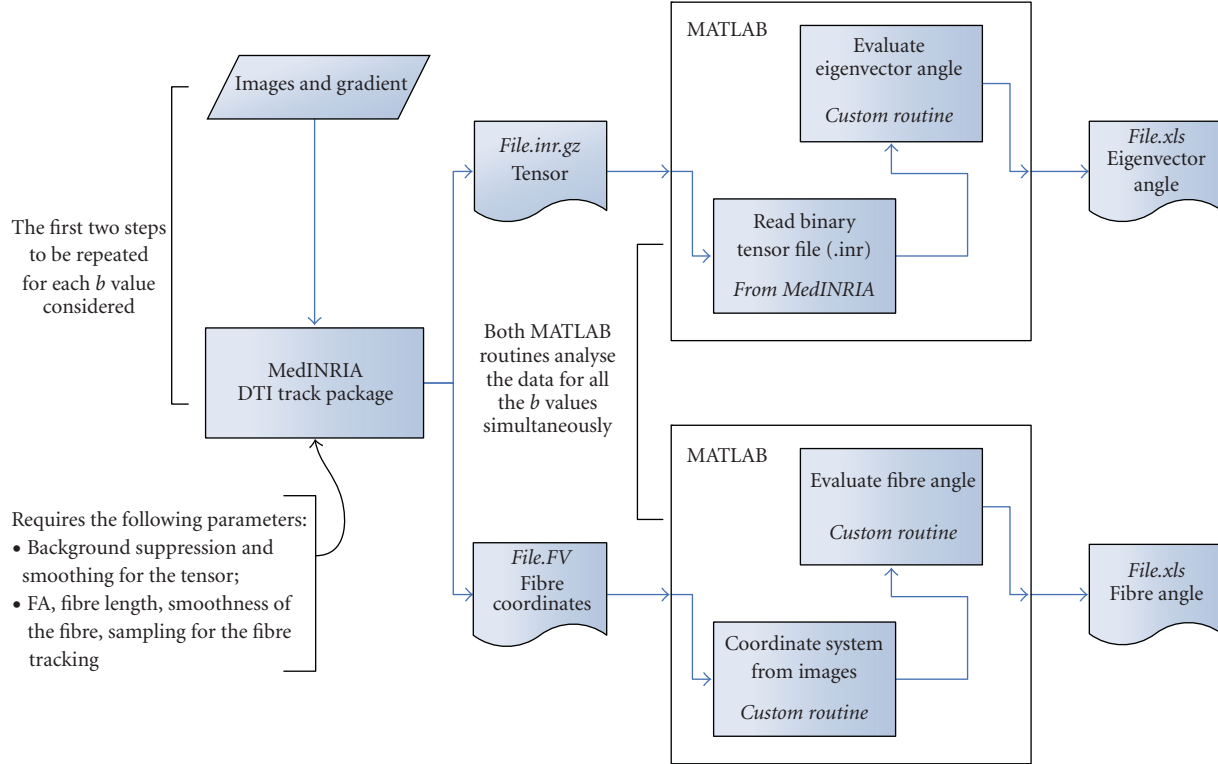


FIGURE 1: Flow chart indicating the various stages in the image postprocessing sequence.

ratio decreases [28, 29]. In contrast, for low  $b$  values the signal-to-noise ratio can be high but diffusion of water molecules along fibres is so low that fibre tracking may be impeded. The  $b$  value and the gradient are connected: the  $b$  value is proportional to gradient parameters such as amplitude, duration, and time spacing and the most suitable value depends on the tissue type being imaged [29, 30]. Therefore an optimal  $b$  value for arterial tissue had to be determined. In this study the gradient was applied over six diffusion directions and scans were repeated for six different  $b$  values; in particular the values analysed were: 200, 400, 600, 800, 1200, and 1600 s/mm<sup>2</sup>. Five repetitions of each measurement were taken and then averaged using a custom routine implemented in MATLAB. Averaging the measurements over five repetitions ensured that the results were more robust; however, measurements obtained from only one repetition where only the central slice of the image was considered and where all the slices were considered showed very little deviation from the averaged results of the five repetitions; see Tables 1 and 2, respectively.

By analysing the images taken for different diffusion directions for each pixel it is possible to derive a tensor that contains the information regarding the local diffusivity. Moreover, eigenvalues and eigenvectors can be extrapolated from each diffusion tensor [18]. Diffusion eigenvalues are important for the determination of a parameter called fractional anisotropy (FA) [30]. The FA is an index of the anisotropy of diffusion in the tissue and ranges between 0 and 1, with 0 being isotropy and 1 being complete

anisotropy. The fractional anisotropy is defined according to (2), where  $D$  is the diffusion tensor,  $\lambda_1$ ,  $\lambda_2$ ,  $\lambda_3$  are its eigenvalues, and  $\text{tr}(D)$  is the trace of  $D$  [30]:

$$\text{FA} = \sqrt{\frac{3}{2}} \sqrt{\frac{(\lambda_1 - \bar{D})^2 + (\lambda_2 - \bar{D})^2 + (\lambda_3 - \bar{D})^2}{\lambda_1^2 + \lambda_2^2 + \lambda_3^2}}, \quad (2)$$

$$\bar{D} = \frac{\text{tr}(D)}{3}.$$

In addition, diffusion eigenvectors are important for the determination of fibres patterns; the first eigenvector (i.e., the vector corresponding to the largest eigenvalue of the tensor) represents the direction of maximal diffusion and therefore it represents the predominant fibre direction [17, 19]. Fibre tractography can be defined as the pixelwise interpolation of the directions of the first eigenvector. Different interpolation algorithms are available, and in this study the algorithm implemented for the DTI fibre analysis was that available in the software MedINRIA (Sophia Antipolis, France). This software was chosen because it is optimised for DTI on clinical datasets. In fact, in order to reduce the noise which is common in these kinds of acquisitions, MedINRIA applies a maximum likelihood strategy. The estimation of the tensor, together with the use of Log-Euclidean metrics for tensor processing, improves the quality of the fibres reconstructed, which are tracked by using a streamline algorithm [31]. Using MedINRIA the diffusion tensor for each  $b$  value was evaluated and the fibre tractography was performed. In order

TABLE 1: Evaluation of the difference in the eigenvector angles between each repetition and the average over all the repetitions for the central slice of the image.

		Angles between 0°–90°		Angles between 90°–180°	
		Most prevalent angle range (°)	% of occurrence	Most prevalent angle range (°)	% of occurrence
Repetition n.1	b1	5 ± 2.5	7.29	175 ± 2.5	4.19
	b2	5 ± 2.5	9.12	175 ± 2.5	6.50
	b3	5 ± 2.5	12.35	175 ± 2.5	8.42
	b4	5 ± 2.5	13.49	175 ± 2.5	11.00
	b5	5 ± 2.5	15.76	175 ± 2.5	10.87
	b6	5 ± 2.5	17.50	175 ± 2.5	10.87
Repetition n.2	b1	5 ± 2.5	8.64	175 ± 2.5	5.94
	b2	5 ± 2.5	10.74	175 ± 2.5	8.77
	b3	5 ± 2.5	13.23	175 ± 2.5	12.31
	b4	5 ± 2.5	15.58	175 ± 2.5	12.13
	b5	5 ± 2.5	17.29	175 ± 2.5	13.66
	b6	5 ± 2.5	18.33	175 ± 2.5	15.28
Repetition n.3	b1	5 ± 2.5	9.04	175 ± 2.5	6.90
	b2	5 ± 2.5	14.14	175 ± 2.5	10.13
	b3	5 ± 2.5	13.71	175 ± 2.5	11.39
	b4	5 ± 2.5	17.63	175 ± 2.5	11.39
	b5	5 ± 2.5	19.21	175 ± 2.5	10.43
	b6	5 ± 2.5	19.07	175 ± 2.5	14.01
Repetition n.4	b1	5 ± 2.5	8.77	175 ± 2.5	5.46
	b2	5 ± 2.5	13.18	175 ± 2.5	8.90
	b3	5 ± 2.5	13.05	175 ± 2.5	10.91
	b4	5 ± 2.5	14.80	175 ± 2.5	11.65
	b5	5 ± 2.5	18.07	175 ± 2.5	12.75
	b6	5 ± 2.5	16.89	175 ± 2.5	11.48
Repetition n.5	b1	5 ± 2.5	8.47	175 ± 2.5	6.11
	b2	5 ± 2.5	10.30	175 ± 2.5	8.77
	b3	5 ± 2.5	14.80	175 ± 2.5	11.48
	b4	5 ± 2.5	16.06	175 ± 2.5	12.13
	b5	5 ± 2.5	19.82	175 ± 2.5	13.09
	b6	5 ± 2.5	19.82	175 ± 2.5	13.09
Averaged repetitions	b1	20 ± 2.5	9.15	160 ± 2.5	8.77
	b2	5 ± 2.5	11.41	175 ± 2.5	10.88
	b3	5 ± 2.5	15.28	175 ± 2.5	12.39
	b4	5 ± 2.5	17.92	175 ± 2.5	11.62
	b5	5 ± 2.5	19.01	175 ± 2.5	15.14
	b6	5 ± 2.5	18.56	175 ± 2.5	15.14

to proceed with the fibre tractography a region of interest (ROI) was manually defined that corresponded to the area between the external and internal boundary of the aorta, as delineated from the central image slice of the aorta. The software then tracked all the fibres passing through that ROI. The fibre tractography parameters were determined through previous DTI empirical measurements on aortic tissue and these parameters include the FA, the sampling pixel number, the minimum fibre length in mm and the smoothing interpolation of the fibres. These parameters were defined as follows: the FA was set to 0.2, the value for

which no fibres were tracked in the water; the sampling pixel number was set to 3, the number of pixels used to determine the initial fibre vector direction; the minimum fibre length was set to 10 mm; and the smoothing of the interpolated fibre was set to 20% [32]; see the appendix for more details on the process used to determine these parameters.

Subsequently, in MATLAB (Natick, MA, USA) two custom routines were implemented, one for the analysis of the tensor and one for the analysis of the orientation of fibres; see Figure 1. The tensor analysis consisted of the extrapolation of the first eigenvector from the tensor, and

TABLE 2: Evaluation of the difference in the eigenvector angles between each repetition and the average over all of the repetitions. In this case the measurement is averaged over all of the slices of the volume.

		Angles between 0°–90°		Angles between 90°–180°	
		Most prevalent angle range (°)	% of occurrence	Most prevalent angle range(°)	% of occurrence
Repetition n.1	b1	5 ± 2.5	7.09	175 ± 2.5	4.36
	b2	5 ± 2.5	9.76	175 ± 2.5	6.72
	b3	5 ± 2.5	11.33	175 ± 2.5	8.42
	b4	5 ± 2.5	12.55	175 ± 2.5	10.06
	b5	5 ± 2.5	15.08	175 ± 2.5	10.72
	b6	5 ± 2.5	14.99	175 ± 2.5	10.43
Repetition n.2	b1	5 ± 2.5	8.69	175 ± 2.5	5.50
	b2	5 ± 2.5	10.85	175 ± 2.5	8.34
	b3	5 ± 2.5	12.70	175 ± 2.5	10.13
	b4	5 ± 2.5	14.21	175 ± 2.5	11.15
	b5	5 ± 2.5	16.28	175 ± 2.5	11.37
	b6	5 ± 2.5	15.63	175 ± 2.5	12.48
Repetition n.3	b1	5 ± 2.5	8.18	175 ± 2.5	6.35
	b2	5 ± 2.5	11.59	175 ± 2.5	9.21
	b3	5 ± 2.5	12.96	175 ± 2.5	10.72
	b4	5 ± 2.5	15.93	175 ± 2.5	11.24
	b5	5 ± 2.5	16.19	175 ± 2.5	11.48
	b6	5 ± 2.5	17.59	175 ± 2.5	12.72
Repetition n.4	b1	5 ± 2.5	8.12	175 ± 2.5	5.52
	b2	5 ± 2.5	11.48	175 ± 2.5	9.54
	b3	5 ± 2.5	12.85	175 ± 2.5	10.32
	b4	5 ± 2.5	14.45	175 ± 2.5	11.04
	b5	5 ± 2.5	16.17	175 ± 2.5	11.11
	b6	5 ± 2.5	16.80	175 ± 2.5	11.26
Repetition n.5	b1	5 ± 2.5	7.42	175 ± 2.5	5.63
	b2	5 ± 2.5	11.46	175 ± 2.5	8.36
	b3	5 ± 2.5	12.44	175 ± 2.5	10.10
	b4	5 ± 2.5	13.29	175 ± 2.5	12.00
	b5	5 ± 2.5	16.24	175 ± 2.5	12.31
	b6	5 ± 2.5	16.24	175 ± 2.5	12.31
Averaged repetition	b1	20 ± 2.5	9.14	175 ± 2.5	7.45
	b2	5 ± 2.5	10.28	175 ± 2.5	9.35
	b3	5 ± 2.5	12.57	175 ± 2.5	10.14
	b4	5 ± 2.5	14.65	175 ± 2.5	10.48
	b5	5 ± 2.5	13.45	175 ± 2.5	13.20
	b6	5 ± 2.5	14.03	175 ± 2.5	13.31

the determination of the angle it formed with the  $x$ - $y$  plane, as illustrated in Figure 2(a). This was conducted on a single slice of the image (the central one). In order to study the consistency of the results over the length of the sample, the average of the tensor over all the slices was considered, and the angle of the eigenvector calculated. In both cases the study was focused on the ROI defined in MedINRIA.

The fibre distribution was analysed in another routine that assumed each fibre to be a portion of a helix. Consequently, the fibres could be represented by the following set of equations which are the general equations for a helix [33]:

$$\begin{aligned} x &= R \cos(t), \\ y &= R \sin(t), \\ z &= ct, \end{aligned} \quad (3)$$

where  $t$  is the angle with the  $x$  axis,  $R$  is the radius and  $c$  is the lead. From these equations the definition of the helix angle can be derived and used to define the lead fibre angle, that is, the angle shown in Figure 2(b), as follows:

$$\tan(\theta) = \frac{c}{R}. \quad (4)$$

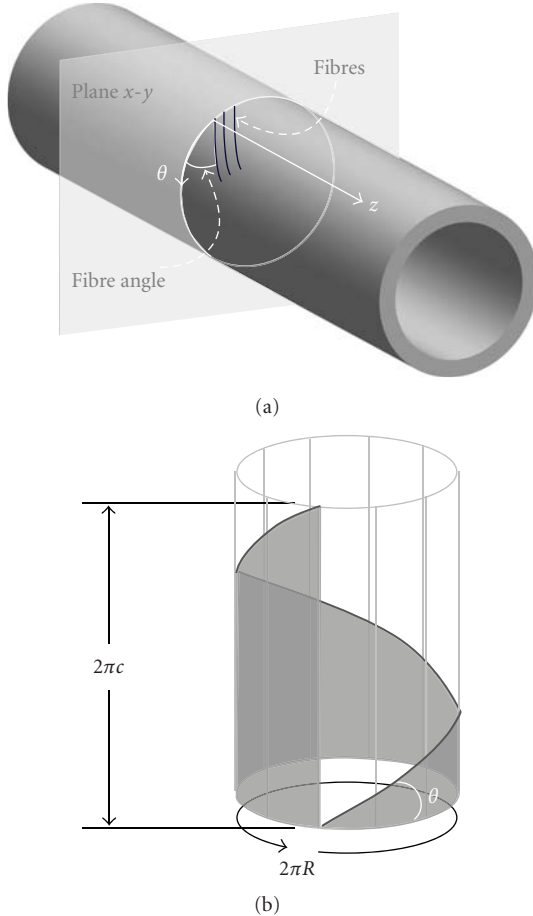


FIGURE 2: (a) Convention for the lead fibre angles calculated in this study; (b) definition of the fibre angle.

In order to apply these equations the fibres' coordinates, which were stored in an ASCII coded text file, needed to be converted from the image reference system to cylindrical coordinates, and therefore a centre had to be determined. Therefore, the ROI mask was used to determine the centre of mass of the aortic section and this was taken as the origin of the reference cylindrical coordinate system. Once the coordinates were converted, (4) was applied and the resultant fibre angle distribution was computed. For each fibre, the fibre angle was evaluated for each point of the fibre and then the median was taken. Test helices were created in MATLAB for the purpose of testing this routine. The helices had known angles ( $30^\circ$ ,  $45^\circ$ , and  $-30^\circ$ ), and the routine described above was successful in determining their lead angles.

### 3. Results

The process of determining the fibrous structure of the aortic tissue is illustrated in Figure 3, where all of the steps in the imaging and postprocessing procedure are shown. Firstly, the anatomical image resulting from the scan is used to determine the ROI; see Figures 3(a) and 3(b). Secondly, the diffusion tensor is analysed in MATLAB and the angle

between the first eigenvector and the  $x$ - $y$  plane determined and mapped onto the ROI; see Figures 3(c) and 3(d). From both of these images it can be seen that the region of the aorta in the image is still recognisable using the tensor map. Finally, the tensor is analysed using MedINRIA and the fibres tracked through the ROI of the aorta; see Figures 3(e) and 3(f). From these images it can be seen that the fibres plotted are distributed throughout the thickness of the aorta and that they are predominantly oriented circumferentially within the  $x$ - $y$  plane of the aorta.

The results for the tensor orientation were analysed for different  $b$  values to determine the influence of the  $b$  value on the tensor angles obtained. For the tensor representing the central slice and the averaged tensor, the angle between the first eigenvector and the  $x$ - $y$  plane had greater variability for small  $b$  values and became increasingly more consistent at higher  $b$  values; see Figures 4 and 5. Two dominant eigenvector angles, close to  $0^\circ$  and  $180^\circ$ , are evident for the analysis of the tensors of the central slice image for all  $b$  values (Figure 4), whilst three, close to  $0^\circ$ ,  $90^\circ$  and  $180^\circ$ , are present in the averaged images (Figure 5). However, by using the parameters defined above to carry out the fibre tractography such that the fibre angles were tracked, two dominant fibre angles were found between  $15^\circ \pm 2.5^\circ$  and  $175^\circ \pm 2.5^\circ$ , respectively (Figures 6 and 7). These angles were found to be independent of the  $b$  value applied during the imaging sequence. In the fibre tractography plots (Figures 6 and 7), the fibre angle distribution is evaluated over bands of  $5^\circ$ , and centred in the middle of each band.

### 4. Discussion and Conclusions

The arterial wall constitutes a highly organized tissue which must withstand a complex network of forces acting on it, as shown by Burton [6] and Peterson et al. [34]. The organisation of the tissue is therefore of utmost importance, as it has to offer distensibility and resistance [7]. The arterial tissue mechanical properties are derived from its microstructure which is constituted by collagen, elastin fibres, SMCs, and ground substances [27]. The fibrous components reinforce the structure and their distribution generally corresponds to the direction of maximum stress [6, 7]. The orientation of arterial fibrous components has been studied with many different techniques including histology [27], scanning electron microscopy (SEM) [35], confocal electron microscopy [36], and confocal laser scanning microscopy [37]. All of these techniques were consistent in finding that arterial tissue fibres are woven according to a helical pattern with a small pitch. In particular, in the study from O'Connell et al. [37], where the three-dimensional architecture of arterial fibres was reconstructed by means of microscopy, they demonstrated that all three fibrous constituents of the artery (i.e., collagen, elastin fibres, and SMCs) are aligned predominantly in the circumferential direction and in particular approximately  $\pm 10^\circ$  from the circumferential direction. The results presented in the current study are in accordance with this result. Firstly, by looking at Tables 1 and 2 it can be seen that in every repetition (as well as in the averaged

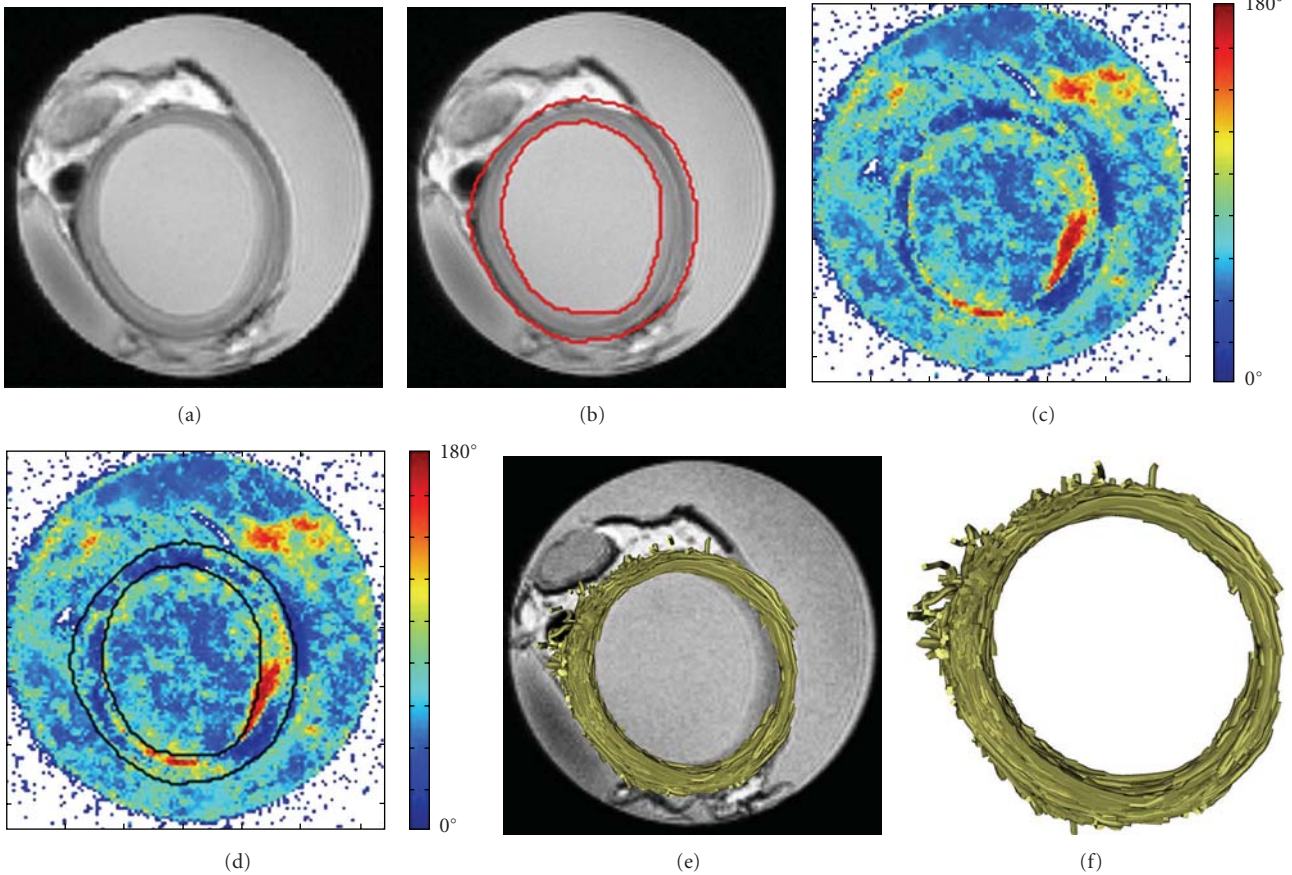


FIGURE 3: Steps in the DTI procedure and image postprocessing; (a) MRI anatomical scan, (b) the ROI of the aorta, (c) a map of the angle of the first eigenvector with the  $x$ - $y$  plane, (d) a map of the angle of the first eigenvector with the  $x$ - $y$  plane with the ROI clearly identified, (e) the results of the tractography process with the fibres superimposed on the reference image, and (f) the aortic fibres within the ROI alone.

repetitions) the eigenvector angle is predominantly oriented in the range of  $5 \pm 2.5^\circ$  and  $175 \pm 2.5^\circ$ . The tensor maps, where the angle of the first eigenvector with the  $x$ - $y$  plane is mapped, also show that the main diffusion direction has a small angle. In particular, by looking at the map for a single slice, it is clear to see that only the angular extremes,  $0^\circ$  and  $180^\circ$ , are evident on the contour map of the artery (Figure 4). This trend was seen in all individual slices where the eigenvector of the diffusion tensor was determined; however, when considering the overall sample, as in Figure 4, areas with eigenvectors at  $90^\circ$  to the  $x$ - $y$  plane are also present. By comparing the maps of the pixelwise eigenvectors for individual slices (central slices are shown in Figure 4) to that of the averaged tensor (Figure 5), it appears that some changes in the diffusion direction occur in parts of the vessel such that pixels with  $0^\circ$  and  $180^\circ$  eigenvector angles in different slices when averaged result in an angle of  $90^\circ$ . Therefore, analysis of the averaged tensor gives an indication of changes in the diffusion along the length of the vessel whilst individual slices give information on the local diffusion and may be indicators of fibre directions in specific regions of the vessel.

To establish fibre directions more conclusively, fibre tractography needs to be performed and the fibre tractography

on the diffusion tensors in the current study identified dominant fibre angles of  $15 \pm 2.5^\circ$  and  $175 \pm 2.5^\circ$ , as seen in Figures 6 and 7. This is consistent with the fibre direction reported in the literature for arterial tissue by O'Connell et al. [37]. This result is also in agreement with the eigenvector angles obtained directly from the diffusion tensor. Differences between the eigenvector angles and the fibre angles are to be expected due to the fact that these can be regarded as two different entities. In fact, even though the determination of the fibres is based on eigenvector angles, it is the three-dimensional eigenvector arrangement that dictates the fibre together with the constraints imposed by the tractography algorithm.

All of these results support the use of DTI as a means of obtaining a reliable description of the natural fibre orientation of arterial tissue in a noninvasive way; whereas techniques such as histology and microscopy need the tissue to be harvested and fixed. Harvesting the vessel, whilst clearly invasive, also has implications for the structural properties since that it removes any *in situ* longitudinal or circumferential prestretches. Moreover, with most of these techniques only small bi-dimensional portions of the arterial wall can be analysed, while with DTI it is possible to obtain the global, three-dimensional, fibre orientations.

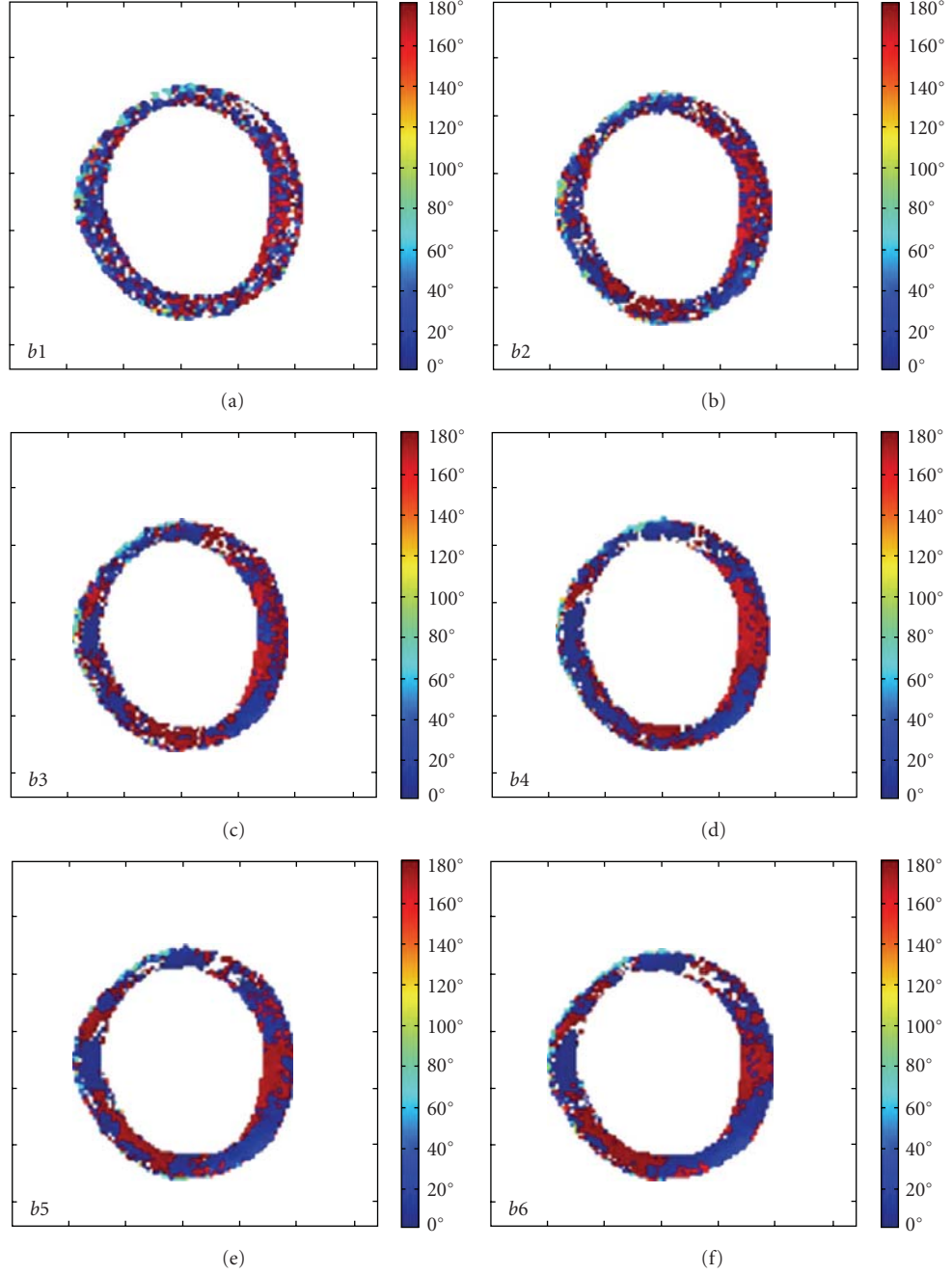


FIGURE 4: Contour maps of the angle between the first eigenvector and the  $x$ - $y$  plane for the central slices of the image data sets for the different  $b$  values.

Another interesting feature of this study is the determination of the most appropriate  $b$  value for the analysis of the fibrous orientation within the arterial wall. The optimal  $b$  value in DTI is dependant on the tissue being studied; for example, a value of  $1000 \text{ s/mm}^2$  has been reported for cartilage [24], whilst  $400 \text{ s/mm}^2$  has been used for the medial nerve in the human wrist [28, 38], and values between 500 and  $800 \text{ s/mm}^2$  for the myocardium [39, 40]. The  $b$  value appears to be connected with the composition of the tissue

studied and therefore can be used for the diagnosis of diseases that alter such composition [41, 42].

To the best of the authors' knowledge a suitable  $b$  value for DTI of arteries has not been reported to date and therefore a range of increasing  $b$  values were used in this feasibility study. To find the optimal  $b$  value the information in each image set for this range of  $b$  values had to be analysed, in particular the amount of significant data obtained in each image had to be quantified. For each  $b$  value the

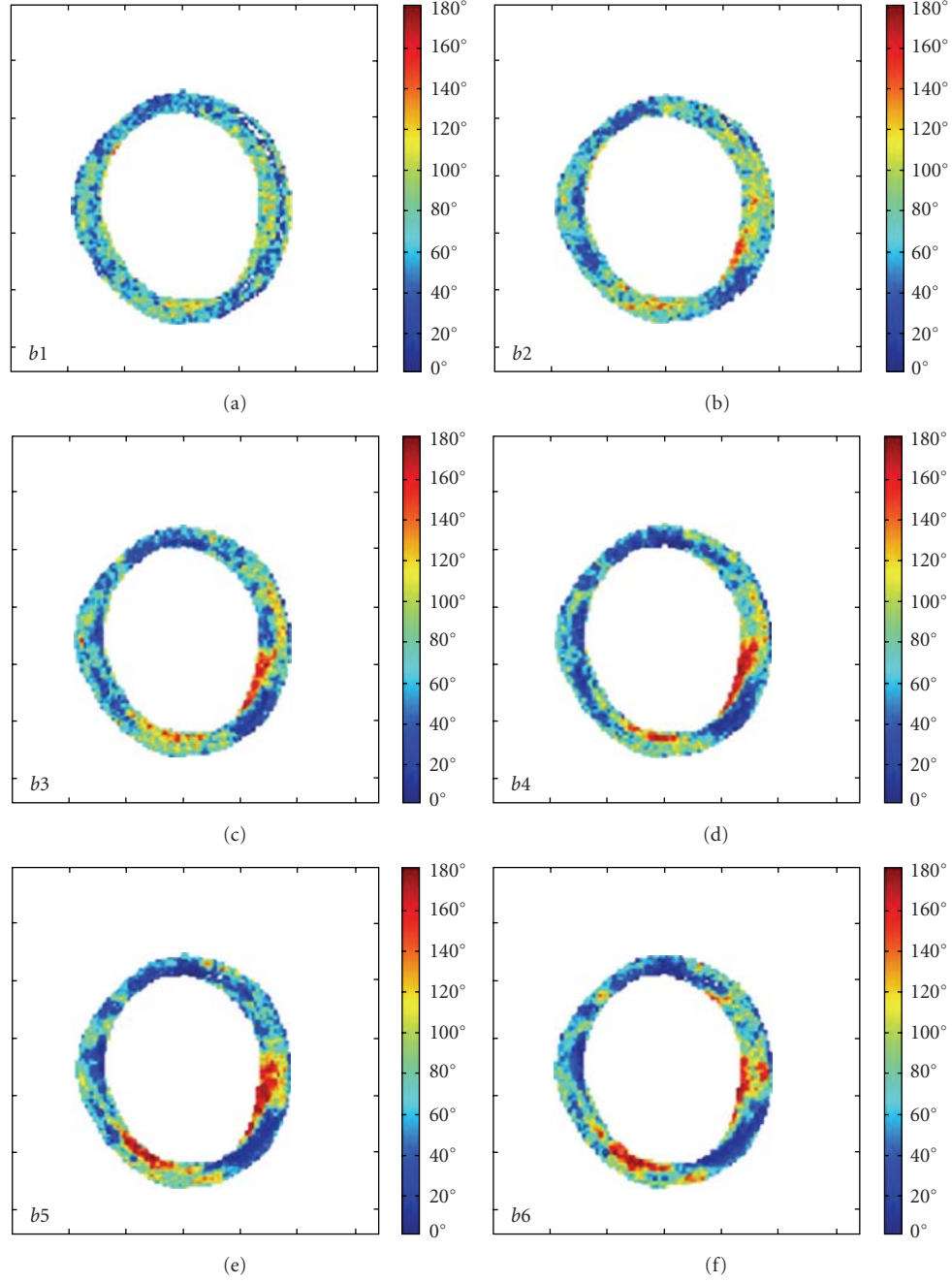
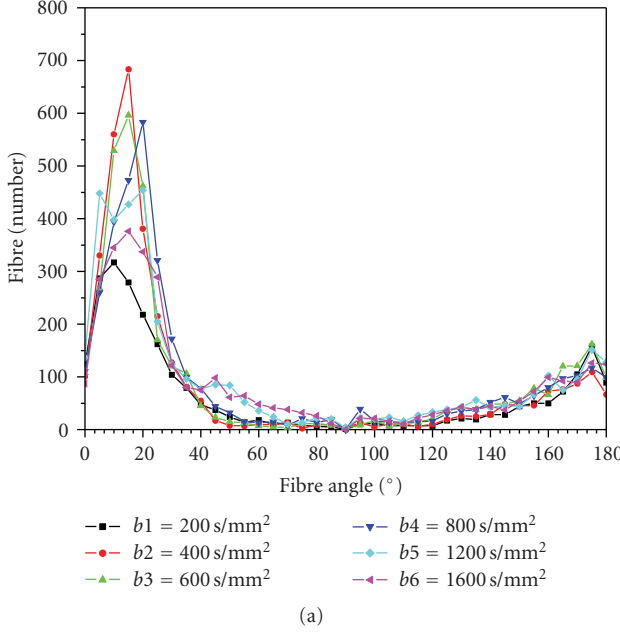


FIGURE 5: Contour maps of the angle between the first eigenvector and the  $x$ - $y$  plane for the averaged tensors of the image data sets for the different  $b$  values.

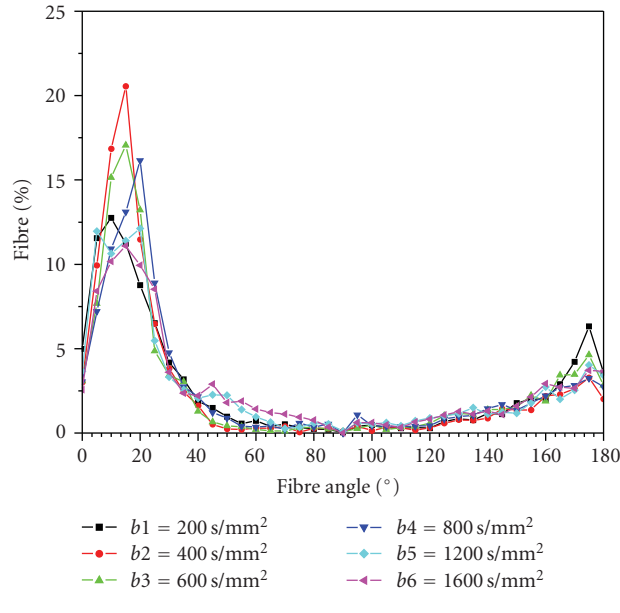
tensor maps and the fibre tracts were analysed and data such as the eigenvector angle and fibre angle distribution were extrapolated. Finally, these data were compared over the different  $b$  values in order to define the optimal one. It is possible to make this comparison by looking at the results shown in Figures 4–6.

For  $b$  values less than or equal to  $600 \text{ s/mm}^2$  it can be seen that while there is agreement with higher  $b$  values in terms of the fibre angles plotted (Figures 6 and 7), the corresponding tensor map is not coherent. It can be seen in

Figures 4 and 5 that for  $b1$  and  $b2$  a variety of angles are obtained; whereas for higher  $b$  values and in particular for  $b4$ , the angles determined converge on two dominant angles. This is supported also by an analysis of the eigenvector angle orientation for the different repetitions. Tables 1 and 2 show that for  $b1$  the orientation registered in the average of the repetitions is different from that obtained for each single repetition. This is due to the higher level of incoherence of pixel values at  $b1$  over the different repetitions.



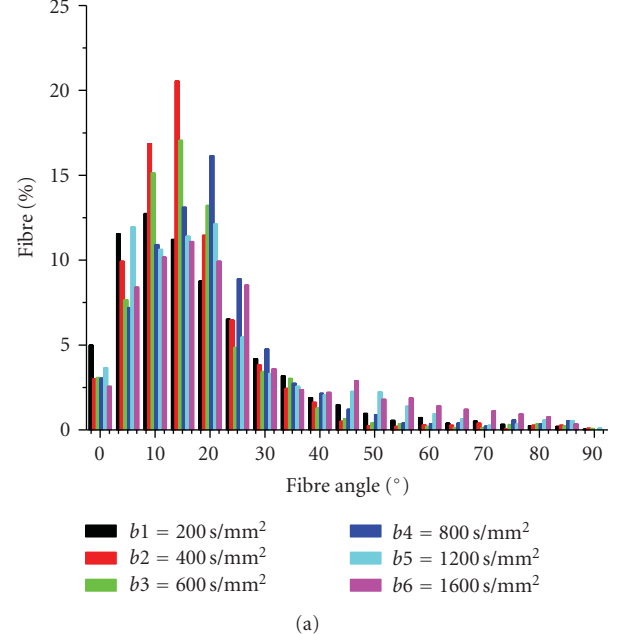
(a)



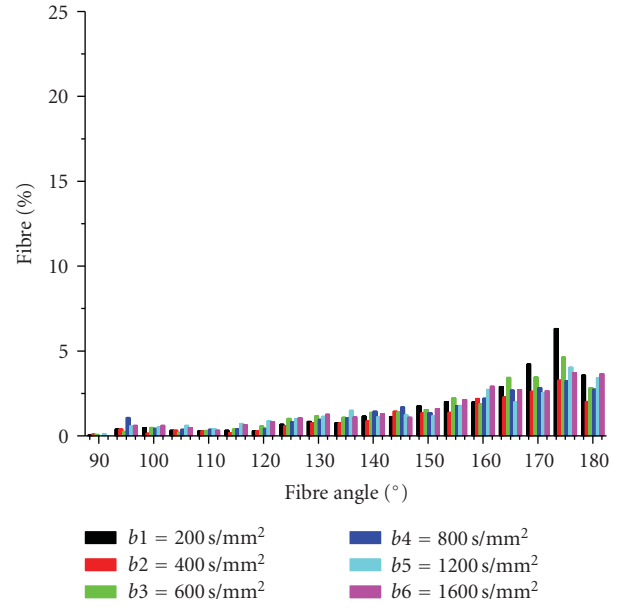
(b)

FIGURE 6: Distribution of the fibre angles over the analysed volume for different  $b$  values, (a) number of fibres; (b) percentages of fibres. The fibre angles are evaluated over bands of 5° and centered in the middle of each band.

At the same time, for  $b$  values higher than 800  $\text{s/mm}^2$ , the tensor maps show small changes, especially in Figure 5. This is confirmed in Figure 6 where the number of fibres with intermediate angles, especially in the range between 40°–90° obtained for  $b_5$  and  $b_6$  are higher than at  $b_4$ . In addition, the highest number of fibres is tracked for values in the range  $b_2$  to  $b_4$  whilst the number reduces from  $b_2$  to  $b_1$ , and  $b_4$  to  $b_6$ . These results suggest that the optimal  $b$  value for arteries may be around 800  $\text{s/mm}^2$  ( $b_4$ ), as this is the value



(a)



(b)

FIGURE 7: Histogram representing the fibre angle distribution for different  $b$  values. For ease of representation it has been split into two graphs: (a) 0° to 90°; (b) 90° to 180°. The angles are evaluated over bands of 5° and centered in the middle of each band.

for which there is a balance between the eigenvector angles in the tensor maps and the fibre data obtained by the fibre tracking procedure.

A limitation of this study is a lack of direct validation of these results through histology [27] or through other microscopic techniques [35–37]. The main objective of this study, however, was to use DTI for imaging the arterial structure and to compare the preliminary results obtained with the data available in the literature in order to show

the feasibility of this approach. Another limitation was the analysis of a vessel in the unloaded configuration, whereby the circumferential stretch was preserved, but the longitudinal stretch was lost. Taking these limitations into account it is still clear that DTI of arterial tissue is feasible and that it can be used to successfully image the fibrous structure of arterial tissue in a noninvasive way.

In the future, DTI of an arterial vessel in a longitudinally tethered state and loaded with a pulsatile lumen pressure will be carried out, and finally the technique will be translated to an *in vivo* setting. The result of this procedure will be a noninvasive imaging technique with the potential to study the fibrous architecture of arteries *in vivo* which can be used for early diagnosis of arterial diseases.

## Appendix

The appropriate tensor and tractography parameters were defined by means of a number of sensitivity tests. In order to obtain the most suitable value for each parameter, a range of values were applied and the differences observed between the results obtained considered, to establish the most suitable parameter for this particular application.

For the tensor parameters, the background suppression and the tensor smoothing had to be set. The background suppression consists in setting a threshold on the signal of the image under which no tensor will be estimated, based on the reference image  $S_0$ . This value was set to 1,000 (compared to a maximum signal of 32,766) in order not to interfere with the fibre tracking due to the fact that some areas of the arterial tissue were nearly as dark as the background. Regarding the tensor smoothing, a feature available in MedINRIA to reduce the noise of the tensor was set to "high," because by analysing the different FA maps, this was found to be the only value that would suppress the effect of the surrounding water.

For the fibre tractography, the optimal FA threshold, the minimum fibre length, the smoothness of the fibres, and the sampling parameters had to be established. The FA value was analysed first. Fractional anisotropy can be regarded as a tool to erase the noise and therefore the threshold value of FA influenced the amount of fibres tracked in the total image volume. The optimal FA should track fibres predominantly in the region of interest. For the aorta encased in fluid, extremely low FA threshold values ( $<0.15$ ) resulted in large amounts of fibres being tracked in the water volume, while high FA threshold values ( $>0.3$ ) resulted in very few fibres being tracked even in the aortic volume. Empirically we found that for an FA threshold value of 0.2 most of the fibres were tracked in the aortic volume and almost none in the water. Following the establishment of a suitable FA value, the effect of the minimum length of the fibre tracked was considered. Over two different sets of images, three different fibre lengths were considered; 5, 10, and 15 mm. For a setting of 5 mm many fragmented fibres were tracked while for 15 mm only a few fibres, albeit extremely long fibres, were tracked. By comparison to available histological data on aortic tissue, a minimum fibre length of 10 mm showed an optimal tradeoff between the number of fibres and their length for all the different  $b$

values and enabled a suitable sample from which average fibre directions could be ascertained. The value of 10 mm corresponds to one third of the planar resolution of the image. The influence of the smoothness parameter on the fibres tracked was also addressed. This parameter defines the smoothness of the curvature of the final fibre and ensures that large discontinuities in curvature from pixel to pixel of the image are identified such that they cannot be considered one fibre. For the chosen fibre length of 10 mm, variations in the smoothness value over a large range (20%–80%) showed that the fibre number tracked is relatively insensitive to this parameter and a value of 20% was applied to all subsequent images. Finally, the sampling parameter was investigated. The sampling parameter accounts for the number of pixels used for the determination of the fibre. A sampling parameter of one pixel, although extremely accurate, is computationally expensive. Empirically we found that a sampling parameter of three, where fibre tracking is only performed in one voxel out of each three, yields very good accuracy by comparison to a sampling of one pixel and reduces the computational time considerably [32].

## List of Symbols

- $S_0$ : Image with a null gradient (reference image)
- $S$ : Image corresponding to an encoding gradient
- $bi$ : Sensitivity to diffusion factor,  $i = [1\text{--}6]$
- $D$ : Diffusion tensor
- $\lambda_i$ : Eigenvalues,  $i = [1, 2, 3]$
- $t$ : Angle with the  $x$  axis
- $c$ : Helix lead constant
- $R$ : Helix radius
- $\theta$ : Fibre angle.

## Acknowledgment

This project is funded by a Research Frontiers Grant (06/RF/ENM076) awarded by Science Foundation Ireland.

## References

- [1] S. Petersen, V. Peto, M. Rayner, J. Leal, R. Luengo-Fernandez, and A. Gray, *European Cardiovascular Disease Statistics*, Department of Public Health, University of Oxford, Oxford, UK, 2005.
- [2] M. A. Crowther, "Pathogenesis of atherosclerosis," in *ASH Education Program Book*, pp. 436–441, American Society of Hematology, 2005.
- [3] N. Sakalihasan, R. Limet, and O. D. Defawe, "Abdominal aortic aneurysm," *The Lancet*, vol. 365, no. 9470, pp. 1577–1589, 2005.
- [4] G. Pasterkamp, D. P. V. de Kleijn, and C. Borst, "Arterial remodeling in atherosclerosis, restenosis and after alteration of blood flow: potential mechanisms and clinical implications," *Cardiovascular Research*, vol. 45, no. 4, pp. 843–852, 2000.
- [5] D. N. Ku, "Blood flow in arteries," *Annual Review of Fluid Mechanics*, vol. 29, pp. 399–434, 1997.
- [6] A. C. Burton, "Physical principles of circulatory phenomena: the physical equilibria of the heart and blood vessels,"

- in *Handbook of Physiology*, American Physiological Society, Bethesda, Md, USA, 1959.
- [7] G. S. Kassab, "Biomechanics of the cardiovascular system: the aorta as an illustratory example," *Journal of the Royal Society Interface*, vol. 3, no. 11, pp. 719–740, 2006.
  - [8] R. A. Peattie, T. J. Riehle, and E. I. Bluth, "Pulsatile flow in fusiform models of abdominal aortic aneurysms: flow fields, velocity patterns and flow-induced wall stresses," *Journal of Biomechanical Engineering*, vol. 126, no. 4, pp. 438–446, 2004.
  - [9] L. de Figueiredo Borges, R. G. Jaldin, R. R. Dias, N. A. G. Stolf, J.-B. Michel, and P. S. Gutierrez, "Collagen is reduced and disrupted in human aneurysms and dissections of ascending aorta," *Human Pathology*, vol. 39, no. 3, pp. 437–443, 2008.
  - [10] G. G. Hartnell, "Imaging of aortic aneurysms and dissection: CT and MRI," *Journal of Thoracic Imaging*, vol. 16, no. 1, pp. 35–46, 2001.
  - [11] S. G. Ruehm, M. Goyen, J. Barkhausen, et al., "Rapid magnetic resonance angiography for detection of atherosclerosis," *The Lancet*, vol. 357, no. 9262, pp. 1086–1091, 2001.
  - [12] C. Blondel, R. Vaillant, F. Devernay, G. Malandain, and N. Ayache, "Automatic binocular 3D reconstruction of coronary artery centerlines from rotational X-ray angiography," in *Proceedings of the Computer Assisted Radiology and Surgery*, pp. 1073–1078, 2002.
  - [13] J. Golzarian, S. Murgo, L. Dussaussois, et al., "Evaluation of abdominal aortic aneurysm after endoluminal treatment: comparison of color Doppler sonography with biphasic helical CT," *American Journal of Roentgenology*, vol. 178, no. 3, pp. 623–628, 2002.
  - [14] Z. A. Fayad, V. Fuster, K. Nikolaou, and C. Becker, "Computed tomography and magnetic resonance imaging for noninvasive coronary angiography and plaque imaging: current and potential future concepts," *Circulation*, vol. 106, no. 15, pp. 2026–2034, 2002.
  - [15] J.-F. Toussaint, G. M. LaMuraglia, J. F. Southern, V. Fuster, and H. L. Kantor, "Magnetic resonance images lipid, fibrous, calcified, hemorrhagic, and thrombotic components of human atherosclerosis in vivo," *Circulation*, vol. 94, no. 5, pp. 932–938, 1996.
  - [16] P. J. Basser and C. Pierpaoli, "Microstructural and physiological features of tissues elucidated by quantitative-diffusion-tensor MRI," *Journal of Magnetic Resonance, Series B*, vol. 111, no. 3, pp. 209–219, 1996.
  - [17] P. J. Basser and D. K. Jones, "Diffusion-tensor MRI: theory, experimental design and data analysis—a technical review," *NMR in Biomedicine*, vol. 15, no. 7–8, pp. 456–467, 2002.
  - [18] P. B. Kingsley, "Introduction to diffusion tensor imaging mathematics—part I: tensors, rotations, and eigenvectors," *Concepts in Magnetic Resonance Part A*, vol. 28, no. 2, pp. 101–122, 2006.
  - [19] S. Mori and P. C. M. Van Zijl, "Fiber tracking: principles and strategies—a technical review," *NMR in Biomedicine*, vol. 15, no. 7–8, pp. 468–480, 2002.
  - [20] S. Mori and J. Zhang, "Principles of diffusion tensor imaging and its applications to basic neuroscience research," *Neuron*, vol. 51, no. 5, pp. 527–539, 2006.
  - [21] T. G. Reese, R. M. Weisskoff, R. N. Smith, B. R. Rosen, R. E. Dinsmore, and V. J. Wedeen, "Imaging myocardial fiber architecture in vivo with magnetic resonance," *Magnetic Resonance in Medicine*, vol. 34, no. 6, pp. 786–791, 1995.
  - [22] G. D. Buckberg, A. Mahajan, B. Jung, M. Markl, J. Hennig, and M. Ballester-Rodes, "MRI myocardial motion and fiber tracking: a confirmation of knowledge from different imaging modalities," *European Journal of Cardio-Thoracic Surgery*, vol. 29, supplement 1, pp. S165–S177, 2006.
  - [23] D. A. Lansdown, Z. Ding, M. Waddington, J. L. Hornberger, and B. M. Damon, "Quantitative diffusion tensor MRI-based fiber tracking of human skeletal muscle," *Journal of Applied Physiology*, vol. 103, no. 2, pp. 673–681, 2007.
  - [24] L. Filidoro, O. Dietrich, J. Weber, et al., "High-resolution diffusion tensor imaging of human patellar cartilage: feasibility and preliminary findings," *Magnetic Resonance in Medicine*, vol. 53, no. 5, pp. 993–998, 2005.
  - [25] P. Julkunen, R. K. Korhonen, M. J. Nissi, and J. S. Jurvelin, "Mechanical characterization of articular cartilage by combining magnetic resonance imaging and finite-element analysis—a potential functional imaging technique," *Physics in Medicine and Biology*, vol. 53, no. 9, pp. 2425–2438, 2008.
  - [26] S. Capuani, C. Rossi, M. Alesiani, and B. Maraviglia, "Diffusion tensor imaging to study anisotropy in a particular porous system: the trabecular bone network," *Solid State Nuclear Magnetic Resonance*, vol. 28, no. 2–4, pp. 266–272, 2005.
  - [27] J. A. G. Rhodin, "Architecture of the vessel wall," in *Handbook of Physiology*, American Physiological Society, Bethesda, Md, USA, 1980.
  - [28] G. Andreisek, L. M. White, A. Kassner, G. Tomlinson, and M. S. Sussman, "Diffusion tensor imaging and fiber tractography of the median nerve at 1.5 T: optimization of *b* value," *Skeletal Radiology*, vol. 38, no. 1, pp. 51–59, 2009.
  - [29] P. Mukherjee, J. I. Berman, S. W. Chung, C. P. Hess, and R. G. Henry, "Diffusion tensor MR imaging and fiber tractography: theoretic underpinnings," *American Journal of Neuroradiology*, vol. 29, no. 4, pp. 632–641, 2008.
  - [30] P. B. Kingsley, "Introduction to diffusion tensor imaging mathematics—part II: anisotropy, diffusion-weighting factors, and gradient encoding schemes," *Concepts in Magnetic Resonance Part A*, vol. 28, no. 2, pp. 123–154, 2006.
  - [31] P. Fillard, X. Pennec, V. Arsigny, and N. Ayache, "Clinical DT-MRI estimation, smoothing, and fiber tracking with log-Euclidean metrics," *IEEE Transactions on Medical Imaging*, vol. 26, no. 11, pp. 1472–1482, 2007.
  - [32] P. Fillard, J. C. Souplet, and N. Toussaint, *Medical Image Navigation and Research Tool by INRIA (MedINRIA)*, INRIA Sophia Antipolis, Sophia Antipolis, France, 2007.
  - [33] E. Kreyszig, *Advanced Engineering Mathematics*, John Wiley & Sons, New York, NY, USA, 1999.
  - [34] L. H. Peterson, R. E. Jensen, and J. Parnell, "Mechanical properties of arteries in vivo," *Circulation Research*, vol. 8, no. 3, pp. 622–639, 1980.
  - [35] J. M. Clark and S. Glagov, "Transmural organization of the arterial media. The lamellar unit revisited," *Arteriosclerosis, Thrombosis, and Vascular Biology*, vol. 5, no. 1, pp. 19–34, 1985.
  - [36] P. Farand, A. Garon, and G. E. Plante, "Structure of large arteries: orientation of elastin in rabbit aortic internal elastic lamina and in the elastic lamellae of aortic media," *Microvascular Research*, vol. 73, no. 2, pp. 95–99, 2007.
  - [37] M. K. O'Connell, S. Murthy, S. Phan, et al., "The three-dimensional micro- and nanostructure of the aortic medial lamellar unit measured using 3D confocal and electron microscopy imaging," *Matrix Biology*, vol. 27, no. 3, pp. 171–181, 2008.
  - [38] C. Khalil, C. Hancart, V. Le Thuc, C. Chantelot, D. Chechin, and A. Cotten, "Diffusion tensor imaging and tractography of the median nerve in carpal tunnel syndrome: preliminary results," *European Radiology*, vol. 18, no. 10, pp. 2283–2291, 2008.

- [39] J. Chen, S.-K. Song, W. Liu, et al., "Remodeling of cardiac fiber structure after infarction in rats quantified with diffusion tensor MRI," *American Journal of Physiology*, vol. 285, no. 3, pp. H946–H954, 2003.
- [40] W.-Y. I. Tseng, V. J. Wedeen, T. G. Reese, R. N. Smith, and E. F. Halpern, "Diffusion tensor MRI of myocardial fibers and sheets: correspondence with visible cut-face texture," *Journal of Magnetic Resonance Imaging*, vol. 17, no. 1, pp. 31–42, 2003.
- [41] G. Tang, Y. Liu, W. Li, J. Yao, B. Li, and P. Li, "Optimization of b value in diffusion-weighted MRI for the differential diagnosis of benign and malignant vertebral fractures," *Skeletal Radiology*, vol. 36, no. 11, pp. 1035–1041, 2007.
- [42] H. S. Seo, K.-H. Chang, D. G. Na, B. J. Kwon, and D. H. Lee, "High b-value diffusion ( $b = 3000 \text{ s/mm}^2$ ) MR imaging in cerebral gliomas at 3T: visual and quantitative comparisons with  $b = 1000 \text{ s/mm}^2$ ," *American Journal of Neuroradiology*, vol. 29, no. 3, pp. 458–463, 2008.